FEUP Universidade do Porto
Faculdade de Engenharia

AN INTEGRAL PROBABILISTIC APPROACH FOR FATIGUE LIFETIME PREDICTION OF MECHANICAL AND STRUCTURAL COMPONENTS

José António Fonseca de Oliveira Correia
2014

Thesis presented to the Faculty of Engineering of the University of Porto
for the Doctor Degree in Civil Engineering

Supervisors
Rui Artur Bártolo Calçada *Full Professor*
Abílio Manuel Pinho de Jesus *Assistant Professor*
Alfonso Carlos Fernández-Canteli *Full Professor*

GOVERNO DE PORTUGAL
FCT Fundação para a Ciência e a Tecnologia
UNIÃO EUROPEIA Fundo Social Europeu
QREN QUADRO DE REFERÊNCIA ESTRATÉGICO NACIONAL PORTUGAL 2007.2013
POPH PROGRAMA OPERACIONAL POTENCIAL HUMANO

RESUMO

O objecto principal desta dissertação consiste no desenvolvimento de uma abordagem probabilística integrada para a previsão da vida à fadiga de componentes mecânicos ou estruturais sujeitos a campos de tensões/deformações não uniformes, tendo em consideração as fases de iniciação e de propagação de fendas fadiga. O modelo probabilístico desenvolvido por Castillo e Fernández-Canteli para descrição dos campos *p*-*S*-*N* e *p*-*ε*-*N*, foi usado como base nos desenvolvimentos originais propostos.

As falhas por fadiga são um dos motivos de preocupação para as pontes metálicas, devido à probabilidade de o aço deteriorar-se sob tensões variáveis. Esta tese apresenta uma caracterização do comportamento à fadiga de diferentes materiais representativos de um grupo de pontes metálicas rebitadas antigas Portuguesas, nomeadamente as pontes Eiffel, Luiz I, Fão, Pinhão e Trezói. A partir da análise dos resultados é claro que os materiais mais velhos são ferros pudelados, um precursor dos aços de construção modernos, sendo este último utilizado em pontes mais recentes como é o caso da ponte de Trezói. Os dados gerados e compilados da literatura são essenciais para as estimativas da vida residual, considerando ambas as fases de iniciação e de propagação de fendas, no âmbito de abordagens locais de fadiga e da Mecânica da Fractura, respectivamente.

As previsões de rotura, o projecto de engenharia e a análise de risco em fadiga não são possíveis sem o apoio de modelos de fadiga probabilísticos. Nesta dissertação propõe-se uma generalização do modelo probabilístico de base, proposto por Castillo e Fernández-Canteli para descrever os campos *S*-*N* e ε_a-*N*. Vários parâmetros usados na descrição do dano de fadiga, tendo em conta diversos aspectos do fenómeno de fadiga, são testados no contexto da generalização proposta. Em particular, é demonstrada a adequabilidade do modelo probabilístico para correlacionar parâmetros energéticos propostos quer para fadiga uniaxial quer para fadiga multiaxial.

Têm sido propostos na literatura modelos de propagação de fendas de fadiga baseados nas histórias de tensões/deformações elastoplásticas na extremidade da fenda recorrendo a relações deformação-vida, sendo o processo de propagação de fendas entendido como um processo de sucessivas reinicializações abrangendo elementos representativos do material. O modelo UniGrow encaixa-se nessa classe particular de modelos de propagação de fendas por fadiga, sendo um modelo baseado em tensões residuais. Nesta

investigação é proposta uma extensão do modelo UniGrow é proposto para a determinação de campos probabilísticos de propagação de fendas de fadiga, em particular os campos *p−da/dN−ΔK−R*. O aspecto chave na modelação proposta é a substituição do modelo de deformação-vida determinístico por um campo de deformação-vida probabilístico baseado na distribuição de Weibull. A utilização de um parâmetro de dano por fadiga sensível à tensão média permite a formulação de um modelo de propagação representando os efeitos da tensão média. O modelo de propagação de fendas por fadiga probabilístico resultante é demonstrado para dois materiais representativos de pontes metálicas rebitadas Portuguesas antigas (pontes Eiffel e Fão), e para aços correntes, nomeadamente o aço de construção S355 e o aço P355NL1, cobrindo distintas razões de tensões, *R*.

Propõe-se também uma abordagem local unificada para modelação quer da fase de iniciação quer da fase de propagação de fendas por fadiga. Neste trabalho, dois detalhes, um feito de aço P355NL1 e o outro feito de ferro pudelado da ponte Eiffel, são modelados de modo a gerar curvas *S-N* para diferentes razões de tensões, *R*. As previsões são comparadas com resultados experimentais disponíveis obtendo-se uma boa correlação.

Esta investigação finaliza com algumas interpretações probabilísticas do dano acumulado por fadiga sob carregamentos de amplitude variável, apoiado pelo campo probabilístico de Weibull e da sua variável normalizada *V*, sendo esta última adoptada como uma medida de dano. Em particular, é proposto um método para associar uma função de distribuição acumulada para o número de Miner clássico, sem a necessidade de se realizar programas experimentais de amplitude variável intensivos. Esta abordagem é discutida e aplicada a provetes lisos feitos de aço P355NL1 e a uma ligação rebitada construída em ferro pudelado original da ponte Fão.

ABSTRACT

This thesis aims at developing an integral probabilistic approach for fatigue lifetime prediction of mechanical or structural components with non-uniform stress/strain fields taking into account both the fatigue crack initiation and fatigue crack propagation phases. The base probabilistic model developed by Castillo and Fernández-Canteli for the *p-ε-N* and the *p-S-N* fields were explored to this end in several original contributions.

Fatigue failures are of concern for steel bridges due to the likelihood of the steel to deteriorate under variable stresses. Therefore, besides the modelling activities, this thesis presents the characterization of the fatigue behaviour of different materials from a representative group of Portuguese old metallic riveted bridges, namely the Eiffel, Luiz I, Fão, Pinhão and Trezói bridges. Some of these results are generated by the author, others are collected from literature. The older materials are puddle iron, precursor of the modern construction steels, the latter being used in the Trezói bridge. The generated data are essential for residual fatigue life estimations, considering both crack initiation and propagation phases, respectively, in the framework of Local Approaches to fatigue and Linear Elastic Fracture Mechanics.

Failure prediction, engineering design and risk analysis in fatigue are not possible without the support of probabilistic fatigue models. Therefore, a generalization of the basic probabilistic model proposed by Castillo and Fernández-Canteli to describe the *S-N* and ε_a-*N* fields is proposed in order to cover several fatigue damage parameters often associated in the literature to the fatigue phenomenon. Energetic parameters for uniaxial and multiaxial fatigue are satisfactory correlated with the base probabilistic model by Castillo and Fernández-Canteli.

A class of fatigue crack growth models based on elastoplastic stress–strain histories at the crack tip region and strain-life fatigue damage models have been proposed, the fatigue crack propagation being understood as a process of continuous crack initializations, over elementary material blocks, which may be governed by strain-life data of the plain (smooth) material. The UniGrow model fits this particular class of fatigue crack propagation models, being a residual stress based model. An extension of the UniGrow model is proposed to derive probabilistic fatigue crack propagation data, in particular the *p–da/dN–ΔK–R* fields. The key issue

in the proposed modelling is the replacement of the deterministic strain-life model by an existing probabilistic strain-life field based on Weibull distribution. The use of a fatigue damage parameter sensitive to mean stress allowed the formulation of the propagation model accounting for mean stress effects. The resulting probabilistic fatigue crack propagation model is demonstrated for two materials representative of old Portuguese metallic riveted bridges (Eiffel and Fão bridges), and for current steels, namely the S355 construction steel and the P355NL1 steel, covering distinct stress R−ratios.

It is also proposed a unified local approach in order to model both crack initiation and crack propagation. In this thesis, two notched details, one made of P355NL1 steel and another made of puddle iron from the Eiffel bridge, are modelled in order to generate S-N curves for distinct stress R-ratios. The predictions are compared with available experimental data. The probabilistic S-N field is proposed for the notched details and a good correlation of the available experimental data is observed.

This research finalizes with some probabilistic interpretations of fatigue damage accumulation under variable amplitude data, supported by the probabilistic Weibull field and its normalized variable V that is adopted as a damage measure. In particular, an approach is proposed to associate a cumulative distribution function to the classical Miner number without the need of performing extensive variable amplitude testing aiming. This approach is discussed and applied to smooth specimens made of P355NL1 steel and to a riveted joint made of a puddle iron original from the Fão bridge.

To woman of my life Maria João and to my family, as recognition of deep gratitude.

ACKNOWLEDGEMENTS

I would like to express my sincere gratitude to everyone who, by their support, encouragement, help or remarks have contributed to the fulfilment of this work.

Thanks to my supervisors, Prof. Rui Calçada, Prof. Abílio De Jesus and Prof. Alfonso Fernández-Canteli, by the helpful discussions and useful comments.

A special acknowledgement to Prof. Abílio de Jesus that gave me the opportunity of being the scientist I am today, looking forward to know many new issues.

I would like to thank the Portuguese Science Foundation (FCT) for the financial support through the doctoral grant SFRH/BD/66497/2009 and the project PTDC/EMEPME/78833/2006.

I sincerely want to thank the School of Sciences and Technology of the University of Trás-os-Montes e Alto Douro, the Faculty of Engineering of the University of Porto and Department of Construction and Manufacturing Engineering of the University of Oviedo, by the support and facilities that were made available to me.

Thanks to my friend, Xavier Cruz, and colleagues of the Projetos JAFOC, Lda. for the personal support. Most important, I would like to thank, *woman of my life Maria João* and my family, for all their love and support.

And I would like to thank to the rest of the people that supported me in one or another way.

José A.F.O. Correia

September 30, 2014

CONTENTS

LIST OF FIGURES

LIST OF TABLES

NOMENCLATURE

LATIN

a	crack length
a_i	Initial crack size
a_f	Critical crack size
Δa_i	Crack increment
A	parameter related to threshold lifetime in probabilistic fatigue model; elongation at fracture
b	Fatigue strength exponent
B	Linear regression parameter; parameter related to threshold lifetime in probabilistic fatigue model; thickness
c	Fatigue ductility exponent
C	Material constant; parameter related to endurance limit in probabilistic fatigue model
C_1, C_{el}, C_{pl}	Material constant
COV	Coefficient of variation
da/dN	Fatigue crack growth rate
$d\varepsilon/dt$	Average strain rate
E	Modulus of elasticity
E_{Tk}	slope of the k_{th} segment of the uniaxial cyclic stress-strain curve
f	Function of the stress intensity factor range; Frequency; yield function
f_y	Higher yield stress
f_u	Ultimate tensile strength
F_{max}	Maximum force
FP	Fatemi fatigue parameter
ΔF	Force range
$H(x)$	Heaviside function
K	Stress intensity factor; Applied stress intensity factor; Strain hardening coefficient; Material constant
K'	Cyclic strength coefficient
K_C , K_{IC}	Fracture toughness

K_f	Fatigue notch factor
K_i	Stress intensity factor at the elementary block i
K_I	Stress intensity factor in mode I
K_{max}	Maximum stress intensity factor
$K_{max,applied}$	Applied maximum stress intensity factor
$K_{max,tot}$	Total maximum stress intensity factor
K_{min}	Minimum stress intensity factor
K_{op}	Opening Stress intensity factor
K_r, $K_{residual}$	Residual stress concentration factor
K_t	Total tress concentration factor
ΔK	Stress intensity factor range
$\overline{\Delta K}$	Equivalent stress intensity range
$\Delta K_{applied}$	Applied stress intensity factor range
ΔK_{eff}	Effective stress intensity factor range
$\Delta K_{max,tot}$	Total maximum stress intensity factor range
ΔK_{th}	Threshold of stress intensity factor range
ΔK_{RMS}	Stress intensity factor range of the root mean square
ΔJ	Strain energy release density
L, L_1, L_2	Characteristic length
LM	Logarithmic Miner number
m, m_1, m_{el}, m_{pl}	Material constant
$m(x,a)$	Weight function
M	Miner number
n	Strain hardening exponent
n'	Cyclic strain-hardening exponent
n_{pi}	Number of cycles accumulated at stress σ_i
N	Number of cycles (fatigue life)
N^*	Normalized number of cycles
N_0	Reference number of cycles; Threshold value of lifetime
N_C	Number of cycles to the reference value of the fatigue strength
N_D	Number of cycles to the fatigue limit for constant amplitude stress ranges
N_f	Number of cycles to failure
N_i	Number of cycles in crack initiation; Number of cycles of the specimen i
N_L	Limiting Number of cycles
N_p	Number of cycles in crack propagation
N_{fpi}	Number of cycles to failure at stress σ_i
N_{sv}	Number of subvolumes

N_T	Total number of cycles
$2N_f$	Reversals to failure
$2N_t$	Transition Number of reversals
ΔN	Increment on cycles
p	Material constant; Probabilistic to failure
q	Material constant
r	Crack tip polar coordinate
R, R_σ	Stress ratio
R_ε	Strain ratio
R_p	Size of the reversed plastic zone
R_{RMS}	Stress ratio of the root mean square
R_y	Size of the monotonic plastic zone
R^2	Determination coefficient
S_{gross}	Gross cross-section
S_{ij}	deviatoric stress tensor
S_{net}	Net cross-section
T	Period
SWT	Smith, Watson and Topper fatigue damage parameter
u_y	Crack opening displacement
U	Effective stress intensity ratio
W	Characteristic length; Width
ΔW	Total strain energy range
ΔW^{E+}	Elastic strain energy range associated with the tensile stress
ΔW^{P}	Plastic strain energy density
ΔW^{P}_{0}	Plastic strain energy range at the fatigue limit
ΔW^{t}	Elastic tensile strain energy density
ΔW^{t}_{0}	Total strain energy range to limit fatigue
x	Distance from the crack tip
X	Independent variable defined as Log(Δσ)
X_{ij}	Back stress tensor
y	Distance in the *y* direction
Y	Dependent variable defined as Log(N_f)
w	Walker constant
w_i	Weights
w_k	Weighting factor for subvolume k
v, V	Normalizing variable in probabilistic fatigue model
Z	Reduction in cross-section at failure

GREEK

α, α_t, α_P, α_E	Material constant
β	Shape parameter of Weibull model
γ	Curve fitting parameter; Fatigue crack growth equation exponent
$\Delta\gamma$	Shear strain range
δ	Scale parameter of Weibull model; Elementary material blocks of length
δ^*	Elementary material blocks of length in the process zone
δ_{ij}	Kronecker delta
$\delta\sigma_0$	Increase of the proportional limit stress
ε	Strain
ε_a	Amplitude Strain; Principal in-plane strain (axial direction)
ε_{a0}	Strain range fatigue limit
ε'_f	Fatigue ductility coefficient
$\varepsilon^e{}_i$	Principal elastic strain
ε_k	Strain of the breakpoint in the uniaxial cyclic stress-strain curve
ε_{max}	Maximum strain
$\varepsilon^P{}_{ij}$	Plastic strain tensor
$\dot{\varepsilon}^P_{ij}$	Plastic strain increment
ε_r	Radial strain
$\tilde{\varepsilon}^{ep}_{x,i}$	Average elastoplastic strain along the x direction at the elementary block i
$\tilde{\varepsilon}^{ep}_{y,i}$	Average elastoplastic strain along the y direction at the elementary block i
ε_t	Principal in-plane strain (transversal direction)
ε_u	Walker strain
$\Delta\varepsilon$	Strain range
$\Delta\varepsilon^E$	Elastic strain range
$\Delta\varepsilon^P$	Plastic strain range
$\Delta\varepsilon^p_{ij}$	Plastic strain increment for the entire volume
$\Delta\varepsilon_t$	Transition total strain range
η	Material property
θ	Crack tip polar coordinate
κ, κ_t	Material constant
λ	Threshold parameter of Weibull model; Plastic multiplier
ν	Poisson ratio
$\bar{\nu}$	Effective Poisson ratio
ρ^*	Notch tip radius; Elementary material block size
ρ_c	Critical blunt tip radius

$\overline{\rho}$	Multiaxial constraint ratio
σ	Stress
σ_0	Cyclic yield stress; Stress fatigue limit
σ_a	Stress amplitude
σ_{ced}	Monotonic yield stress
$\tilde{\sigma}^{ep}_{eq,i}$	Average equivalent elastoplastic stress at the elementary material block i
σ'_f	Fatigue strength coefficient
σ_i	Principal stress
σ_{ij}	Stress tensor
σ_k	Material yield parameter; Stress of the breakpoint in the uniaxial cyclic stress-strain curve
σ_h	Hydrostatic stress
σ_M, σ_{max}	Maximum stress
σ_M*	Normalized maximum stress
σ_m, σ_{min}	Minimum stress
σ_m*	Normalized minimum stress
σ_{med}	Mean stress
$\sigma_{n,max}$	Maximum normal stress on the critical plane
σ_x	Elastic stress along the x direction
$\tilde{\sigma}^{ep}_{x,i}$	Average elastoplastic stress along the x direction at the elementary block i
$\tilde{\sigma}^{e}_{x,i}$	Average elastic stress along the x direction at the elementary block i
σ_y	Yield stress; Elastic stress along the y direction
$\tilde{\sigma}^{e}_{y,i}$	Average elastic stress along the y direction at the elementary block i
$\tilde{\sigma}^{ep}_{y,i}$	Average elastoplastic stress along the y direction at the elementary block i
$\sigma_{y,k}$	Yield stress for each subvolume
σ_r, $\sigma_{residual}$	Residual stress
σ_{st}	Ultimate strength
σ_u	Ultimate Strength
σ_∞	Stress fatigue limit
$\Delta\sigma$	Stress range
$\Delta\sigma$*	Normalized stress range
$\Delta\sigma_0$	Endurance fatigue limit
$\Delta\sigma_C$	Reference value of the fatigue strength at N_C = 2 million cycles
$\Delta\sigma_D$	Fatigue limit for constant amplitude stress ranges at the number of cycles N_D
$\Delta\sigma_f$	Stress range fatigue limit
$\Delta\sigma_{gross}$	Stress range computed on the gross cross-section
$\Delta\sigma_i$	Stress range of the specimen i
$\Delta\sigma_L$	Cut-off limit for stress ranges at the number of cycle N_L

$\Delta\sigma_{net}$	Stress range calculated in the net cross-section
$\Delta\sigma_{norm}$	Normalized stress range
τ_{xy}	Shear stress in the xy plane
ψ	Plastic function; fatigue damage parameter
ψ_0	Fatigue damage threshold
ψ^*	Normalized fatigue damage parameter

ACRONYMS

AASHTO	American Association of State Highway and Transportation Officials
ANSYS	Swanson Analysis Systems
ASTM	American society for testing and materials
APK	Association pour la Promotion de l'Enseignement de la Construction Acier
BS	British Standards Institution
CT	Compact tension
EC3	Eurocode 3
EIFS	Equivalent initial flaw size
EPS	Equivalent pre-crack size
FM	Fracture mechanics
FORM	First-order reliability method
IDMEC	Institute of Mechanical Engineering
LCF	Low cycle fatigue
HRR	Hutchinson-Rice-Rosengren
LEFM	Linear elastic fracture mechanics
MCS	Monte-Carlo simulation
MT	Middle tension
NDI	Nondestructive inspection
NP	Norma Portuguesa
RKE	Rice-Kujawski-Ellyin
RMS	Root mean square
SORM	Second-order reliability method
SWT	Smith, Watson and Topper

CHAPTER I

INTRODUCTION

1.1. MOTIVATION

Deterministic fatigue approaches have deserved a major attention of researchers despite the well-known probabilistic nature of fatigue damage. Probabilistic based approaches are mandatory alternatives since they account for scatter of fatigue results and allow us the establishment of safety margins in fatigue life predictions, constituting an important tool to assist design activities. Despite the relevance of the probabilistic approaches for fatigue, most important current design codes are still based on deterministic approaches [1].

The simplest way to account for scatter in fatigue is to characterize the variability of individual fatigue properties (e.g. fatigue limit), using probabilistic distributions. However, the formulation of probabilistic models is a more attractive idea. For example, it is preferable to have a general probabilistic model to describe the complete *S*-*N* field than dispose of a *S*-*N* field defined by the distribution of the fatigue limit plus a set of individual distributions for the fatigue lives under singly specific stress levels.

Probabilistic models are not dissociated from probabilistic distributions, the most common in fatigue being the LogNormal and the extreme distributions of Weibull and Gumbel. Recent contributions by Castillo and Fernández-Canteli [2] resulted in an innovative use of the referred extreme distributions for the description of the whole

probabilistic *S-N* and ε-*N* fields. With this approach, new possibilities for the derivation of probabilistic models emerge, taking into account this basic model. This thesis furnishes some contributions in this respect.

Probabilistic fatigue models have been essentially directed to *S-N* based fatigue approaches while strain based and Fracture Mechanics based fatigue approaches have deserved less attention with respect to their probabilistic modelling. Therefore, contributions in this domain are welcome. The *S-N* fatigue approach may be used to characterize the fatigue behaviour of plain material being also applied directly ~~on~~ to the design of mechanical/structural components. Many design codes follows this approach typically to correlate existing experimental data, the details being categorised by classes (e.g. EC3 [3] and AASTHO [4]). This type of approach requires intensive testing of a variety of details in order to account for the several sources of scatter in materials and geometric/mechanical characteristics. The idea of using basic S-N data from plain material to generate *S-N* curves for mechanical/structural components by resorting to a convenient model is very appellative for engineers since it allows testing times to be shorten with consequent costs reduction. Contributions on probabilistic fatigue modelling of mechanical/structural components are presented in this thesis.

Old metallic bridges are more prone to fatigue failures than modern metallic bridges since the former have suffered very long operational lives and are made of materials precursors of structural steels, characterized by higher heterogeneity of fatigue properties. Since this abundance of heterogeneities leads to increasing scatter of the fatigue properties the application of probabilistic approaches are even more justified for materials and structural components from this type of constructions. Reliability analysis of bridges is becoming a very common approach, in which the structural resistance, including fatigue, needs to be properly accounted for in a probabilistic form.

1.2. OBJECTIVES

The main objective of this study is the development of procedures for probabilistic modeling and assessment of mechanical or structural components, characterized by stress concentrations. The prediction of probabilistic *S*-*N* fields (*p*-*S*-*N* fields) is pursued, resorting to basic fatigue data of the materials, obtained from smooth specimens as reference information.

It is intended the proposition of new advances for the probabilistic models developed by Castillo and Fernández-Canteli [2] for the *p*-*ε*-*N* and the *p*-*S*-*N* fields. These models have successfully being applied to correlate stress-life and strain-life data of smooth specimens or components [5,6]. The objective in this case is to develop a set of procedures allowing an extension of these models to the structural or mechanical components to be achieved, which generally exhibit stress concentrations being responsible of non-uniform stress/strains distributions. Both crack initiation and crack propagation phases should be accounted for in the proposed models.

Besides the probabilistic models developments, the execution of experimental fatigue studies on materials from old ancient bridges is also envisaged. These test results will complement existing database of fatigue test results being developed at Institute of Mechanical Engineering (IDMEC). This experimental data, together with other literature data available for steels, will be used as the basis for models identification and validation in this document.

1.3. ORGANISATION OF THE THESIS

The thesis begins with an ***introduction*** (Chapter I), in which the motivation, objectives and structure of the thesis are presented.

The introduction is followed by a ***literature review on fatigue*** (Chapter II) that comprises the following topics: a historic perspective on fatigue, stages of fatigue damage, review of the main factors influencing fatigue damage, distinct approaches to fatigue modelling including global *S*-*N* approaches, local approaches and Fracture Mechanics based approaches. Also local approaches for fatigue crack propagation modelling are reviewed

since they will be the basis for further developments presented in this thesis. A global overview of probabilistic models for fatigue are presented with special emphasis given to the probabilistic models by Castillo and Fernández-Canteli [2].

In the Chapter III, entitled ***fatigue behaviour of materials and connections from ancient Portuguese riveted steel bridges***, fatigue data from materials of old riveted bridges will be presented. In particular strain-life, cyclic elastoplastic and fatigue crack propagation behaviours are characterized for several materials from ancient bridges. In addition to the material characterization, *S-N* fatigue data from riveted joints are also presented in this chapter. Both data, obtained from fatigue testing by the author and data disseminated in the literature, are gathered and compiled in this chapter to yield a reference compilation of fatigue data representative of Portuguese bridges.

Chapter IV proposes a generalization of the basic probabilistic model ($p–\varepsilon–N$ *or* $p–\sigma–N$) proposed by Castillo and Fernández-Canteli [2] for complex fatigue damage parameters. Several fatigue damage parameters covering many aspects of the fatigue phenomenon are proposed as reference parameters for the model and tested. Damage parameters able to reproduce mean stress effects, several alternatives of energetic parameters as well as multiaxial fatigue damage parameters are correlated using the probabilistic model.

In Chapter V, entitled ***procedure to derive probabilistic fatigue crack propagation fields***, *p-da/dN-ΔK-R* fields are aimed at. To this purpose, local approaches for fatigue crack modelling are used. Resorting to a probabilistic representation of the basic fatigue data (smooth specimen data) of the material, probabilistic fatigue crack growth fields are derived taking into account stress ratio effects. In this chapter, an assessment and extension of the model proposed by Noroozi *et al.* [7,8,9] is proposed to predict the fatigue crack propagation rates. This model is applied to derive probabilistic fatigue crack propagation fields for two materials, namely S355 construction steel, and P355NL1 pressure vessel steel, both representative from old Portuguese metallic riveted bridges (Eiffel and Fão bridges) covering distinct stress *R*-ratios.

The Chapter VI entitled ***procedure to derive probabilistic S-N fields for structural details*** present an extension of the model proposed by Noroozi et al. [7,8] in order to model fatigue crack propagation based on the local strain approach to fatigue. It aims at the determination of the fatigue crack propagation life for structural details taking into account both crack initiation and crack propagation phases. In this chapter, the local approaches to fatigue are also applied to two details to derive both probabilistic fatigue crack propagation fields (*p–S–N_p–R fields*) and fatigue crack initiation fields (*p–S–N_i–R fields*). The global prediction of the probabilistic *S–N_f* field is presented in a unified approach. Fatigue crack initiation is understood as the failure of the first elementary material block at notch root, and fatigue crack propagation is understood as the failure of successive elementary material blocks along the crack path.

Chapter VII is entitled ***a probabilistic interpretation of fatigue damage under variable amplitude loading***. In this chapter the probabilistic field of Castillo and Fernández-Canteli [2] is explored for situations of variable amplitude loading, where damage accumulation theories are required. Alternative damage measures, such as the classical Miner and logarithmic Miner, are used allowing a comparison between theoretical lifetime prediction and experimental results to be made using the normalized *V* variable of the probabilistic model. In this study, variable amplitude fatigue data available for the P355NL1 steel (smooth specimens) and for a riveted joint made of a puddle iron original from the Fão bridge are used.

The thesis finishes with Chapter VIII, where the main conclusions of the work performed and the proposals for further work are presented.

The Annex contains a relation of the scientific articles published by the author of the thesis during its preparation.

1.4. REFERENCES

[1] Schijve J. Statistical distribution functions and fatigue of structures. International Journal of Fatigue, 2005; 27, 1031–1039.

[2] Castillo E, Fernández-Canteli A. A Unified Statistical Methodology for Modeling Fatigue Damage. Springer, 2009.

[3] CEN-TC 250. EN 1993-1-9: Eurocode 3, Design of steel structures – Part 1-9: Fatigue. European Committee for Standardization, Brussels; 2003.

[4] AASHTO. AASHTO LRFD: bridge design specification; 1995.

[5] De Jesus AMP, Pinto H, Fernández-Canteli A, Castillo E, Correia JAFO. Fatigue assessment of a riveted shear splice based on a probabilistic model. International Journal of Fatigue 32 (2010), pp. 453–462.

[6] De Jesus AMP, Ripoll MLR, Fernández-Canteli A, Castillo E, Pereira HFSG. Probabilistic fatigue assessment of a notched detail taking into account mean stress effects. Journal of Pressure Vessel Technology, Transactions of the ASME 134 (2012), 2: 021203 - 9.

[7] Noroozi AH, Glinka G, Lambert S. A two parameter driving force for fatigue crack growth analysis. International Journal of Fatigue 2005; 27: 1277-1296.

[8] Noroozi AH, Glinka G, Lambert S. A study of the stress ratio effects on fatigue crack growth using the unified two-parameter fatigue crack growth driving force. International Journal of Fatigue 2007; 29:1616-1633.

[9] Noroozi AH, Glinka G, Lambert S. Prediction of fatigue crack growth under constant amplitude loading and a single overload based on elasto-plastic crack tip stresses and strains. Engineering Fracture Mechanics 2008; 75: 188-206.

CHAPTER II

A LITERATURE REVIEW ON FATIGUE

2.1. INTRODUCTION

Nowadays scientists, engineers and skilled technicians are fully aware of fatigue damage phenomenon. A proof of this collective consciousness is the definition of fatigue given in ASTM E1823 standard that defines fatigue as “The process of progressive localized permanent structural change occurring in a material subjected to conditions that produce fluctuating stresses and strains at some point or points and that may culminate in cracks or complete fracture after a sufficient number of fluctuations”. The inclusion of fatigue design procedures in design codes of current practice is also another significant indication of this collective awareness about the fatigue phenomenon and its consequences on safety of structures and mechanical components. Despite significant advance and maturity in fatigue phenomenon understanding, various specialized scientific journals focused on this topic reveal that fatigue phenomenon is not yet fully understood and progress for its better understanding is still possible.

This chapter presents an overview of the fatigue approaches being followed in the literature. Firstly, a brief overview of the fatigue history is introduced. Thereafter, a summary of the main fatigue approaches being currently followed in the literature is presented. Then the chapter focuses on probabilistic fatigue approaches available in the literature.

2.2. AN OVERVIEW OF FATIGUE HISTORY

The current state-of-the-art of fatigue is only possible due the uncountable contributions about along the last 177 years. It is impossible to refer to all these contributions in this document, but some of them deserve to be highlighted since they became milestones of the fatigue history.

Fatigue history alleged started with the pioneer works by the German Mines Engineer Albert who conducted the first fatigue experiments on conveyor chains and published the first known fatigue results, in 1837. In 1842 Rankine discussed the fatigue strength of railway axles. In 1853, Morin in his book on Strength of Materials presented a discussion about safe life design to be applied to axles of horse-drawn mail coaches. Maintenance plans were referred to including cracks reparation and sections transitions being identified as main location for those cracks. The term “fatigue” was first attributed to Braithwaite in 1854, who described in a paper fatigue failures in several machinery equipment. A discussion about allowable stresses for fatigue-loaded components was also presented. In the period of 1837-1958 many accidents due to fatigue failure of railway cars axles were reported, which resulted in numerous victims [1].

The period between 1858 and 1870 was definitively marked by the contributions of Wöhler who became a milestone in Fatigue. Wöhler conducted experiments on railway axles. He was responsible for the design and construction of the earliest testing machines. He was the first to note the role of the stress amplitude and mean stress on fatigue damage. He also performed important work on service loads measurement and design for finite life. It is interesting to note that his fatigue results were presented in a tabular form and only his successor, Spangenberg, introduced the graphical representation of the fatigue data in the form of curves, named as *S*-*N* curves, using linear abscissas and ordinates. Since 1936, these S-*N* curves started to be called Wöhler curves as a recognition to Wöhler’s contributions to fatigue. The representation of the *S*-*N* curves in the finite life region using bi-logarithmic axes was due to Basquin who first suggested the use of the power relation to correlate fatigue data [1].

Between 1870 and 1905, the contributions of Bauschinger were fundamental to

understand the cyclic plasticity of metals, which was the basis of the Low-Cycle-Fatigue, developed about 50 years later by Coffin and Manson. Kirsch, in 1898, was the first to calculate the stress concentration factor of 3.0 for a cylindrical hole in an infinite plate. Stress concentration factors have been revealed intrinsically linked to fatigue, due to local nature of the fatigue damage. Ewing and Humfrey, in 1903, observed slip bands on the surface of rotating-bending specimens, which consisted the first metallurgical description of the fatigue process [1].

In the 1905-1920 period the first full-scale fatigue test on large aircraft component was carried out. Fatigue tests on components were performed to improve its fatigue strength. The term notch effect appeared in the literature. The names of Smith, Haigh, Gough, Griffith, Inglis, Kommers, Moore, among others, appear in the literature [1].

In the period of 1920-1945, the main research lines on fatigue were established and/or developed, many of them are still currently being investigated. For example [1]:

- Investigations on variable amplitude loading. For this topic, contributions by Gassner were important. Also damage accumulation theories were developed, with emphasis on works by Palmgren (1937) and Miner (1945) who proposed the linear damage accumulation theory known as Miner rule [2].
- Foundations of Fracture Mechanics by Griffith (1920).
- First crack propagation tests, in 1936, by Forest.
- Statistical methods in strength of materials by Weibull (1939).
- Statistical evaluation of large number of fatigue experiments by Müller-Stock.
- Mechanical methods to improve fatigue strength by compressive residual stresses were developed.
- In this period books and conferences on fatigue started to appear.

In the period 1945-1960 the foundations of the Low-Cycle-Fatigue were established due to the contributions of Coffin and Manson (1955) [3,4]. Motivated by the aircraft industry, the “fail safe” and “safe life” design approaches were discussed. Miner’s rule was intensively investigated to verify its validity and alternative rules were proposed to overcome the limitations of the linear damage rule. Irwin in 1958, following the previous

works by Griffith, realized that the stress intensity factor was the leading parameter to control the static strength of cracked bodies. This contribution led to the Linear Elastic Fracture Mechanics [1].

After 1960 we assist to the development of the Fracture Mechanics and its application to fatigue. One inevitable contribution is the one proposed by Paris (1962) who first recognized the relation between fatigue and Fracture Mechanics [5]. The so-called Paris relation was a pioneer contribution in this field. After this relation, an uncountable number of crack propagation relations have been proposed to overcome known limitations of the Paris relation [6]. Elber (1963) gave also an important contribution for the understanding of fatigue crack growth under variable amplitude loading, introducing the "crack closure" concept [7,8]. With the development of fracture mechanics, "damage tolerance" design was adopted in some structures, particularly in Aeronautics.

The development of testing machines, namely single axis and multiaxial servohydraulic testing machines a promoted the development of fatigue studies in the field of variable amplitude loading and multiaxial fatigue. More recently, the development of resonance testing machines permitted studies in the very-high-cycle fatigue regime.

Despite the very significant advances in fatigue understanding and the current fatigue design practice for structures and mechanical components under dynamic loads, many topics require more research, such as [1]:

- Prediction of fatigue life under variable amplitude loading not fully solved, including fatigue crack propagation.
- The transferability to actual components of fatigue data obtained with specimens has not been sufficiently investigated.
- Corrosion fatigue is another complex and unsolved problem.
- The combination of high temperature and fatigue needs further investigation.
- Multiaxial fatigue, mainly for non-proportional loading and variable amplitude loading.

Real problems combine very often various sources of complications which makes them very challenging. This is the case of large structures like bridges, which are subjected to

multiaxial, variable amplitude loading, whereby the old ones, may also exhibit corrosion. Concerning the old materials from these bridges, they show unusual high scatter on its fatigue properties, which demands the use of probabilistic approaches.

2.3. GENERAL CONSIDERATIONS

2.3.1. Stages of fatigue damage

Microscopic investigations in the beginning of the 20th century have shown that fatigue crack nuclei start as invisible micro-cracks in slip bands. Later on, more microscopic information on the growth of small cracks became available. Indications pointed out that it may take place almost immediately if a cyclic stress above the fatigue limit is applied. The fatigue limit is the cyclic stress level below which a fatigue failure does not occur. In spite of early crack nucleation, micro-cracks remain invisible for a considerable part of the total fatigue life. Once cracks become visible, the remaining fatigue life of a laboratory specimen is usually a small percentage of the total life [9]. The latter percentage may be much larger for real structures such as ships, aircraft, bridges, etc.

After a micro-crack has nucleated, crack growth can still be a slow and erratic process, due to effects of the micro structure, e.g. grain boundaries. However, after some micro-crack growth has occurred away from the nucleation site, a more regular is observed. This is the beginning of the real crack growth period. Various steps in the fatigue life are indicated in Figure 2.1. The important point is that the fatigue life until failure consists of two periods: the crack initiation period and the crack growth period. Differentiating between the two periods is of great importance because several surface conditions do affect the initiation period, but have a negligible influence on the crack growth period. It should already be noted that fatigue prediction methods are different for the two periods [9]. The stress concentration factor, K_t, is the important parameter for predictions on crack initiation. The stress intensity factor, K, is used for predictions on crack growth.

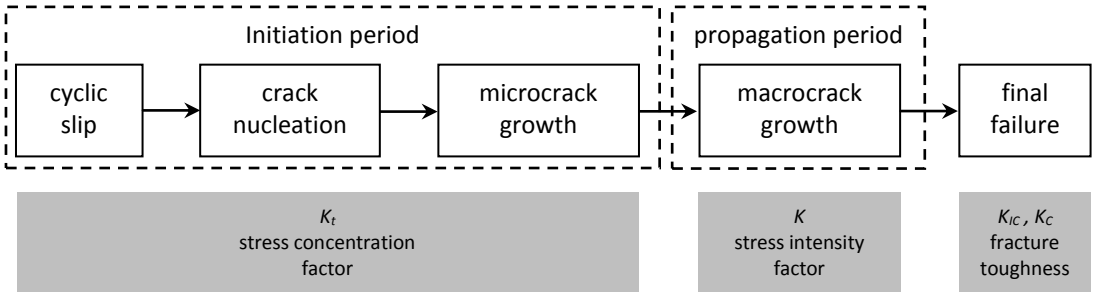

Figure 2.1 – Different phases of the fatigue life and relevant factors.

2.3.1.1. Fatigue Crack initiation

Fatigue crack initiation and crack growth are a consequence of cyclic slip bands. It implies cyclic plastic deformation as a result of moving dislocations. Fatigue occurs at stress amplitudes below the yield stress. At such a low stress level, plastic deformation is limited to a small number of grains of the material. This micro-plasticity can occur more easily in grains at the material surface because the surrounding material is present at one side only.

Cyclic slip requires a cyclic shear stress. On a micro scale the shear stress is not homogeneously distributed through the material. The shear stress on crystallographic slip planes differs from grain to grain, depending on the size and shape of the grains, crystallographic orientation of the grains, and elastic anisotropy of the material. In some grains at the material surface, these conditions are more favourable for cyclic slip than in other surface grains. Another significant aspect is that slip during the increase of the load also implies some strain hardening in the slip band. As a consequence, upon unloading a larger shear stress will be present on the same slip band, but now in the reversed direction. Reversed slip will thus preferably occur in the same slip band. As a consequence, reversed slip, although occurring in the same slip band, will occur on adjacent parallel slip planes.

The lower restraint on cyclic slip at the material surface has been mentioned as a favourable condition for crack initiation at the free surface. However, more arguments for crack initiation at the material surface are present. A very practical reason is the inhomogeneous stress distribution due to a notch effect of a hole or some other geometric discontinuity. Because of an inhomogeneous stress distribution, a peak stress

occurs at the surface (stress concentration). Furthermore, surface roughness also promotes crack initiation at the material surface. It is concluded that, the crack initiation period fatigue is a material surface phenomenon.

2.3.1.2. Fatigue crack growth

As long as the size of the micro-crack is still in the order of a single grain, the micro-crack is obviously present in an elastically anisotropic material with a crystalline structure and a number of different slip systems. The micro-crack contributes to an inhomogeneous stress distribution on a micro level, with a stress concentration at the tip of the micro-crack. As a result, more than one slip system may be activated. Moreover, if the crack is growing into the material in some adjacent grains, the constraint on slip displacements will increase due to the presence of the neighbouring grains. Similarly, it will become increasingly difficult to accommodate the slip displacements by a single slip system only, i.e. on parallel crystallographic planes. It should occur on slip planes in different directions. The micro-crack growth direction will then deviate from the initial slip band orientation. In general, there is a tendency to grow perpendicular to the loading direction (Figure 2.2) [9].

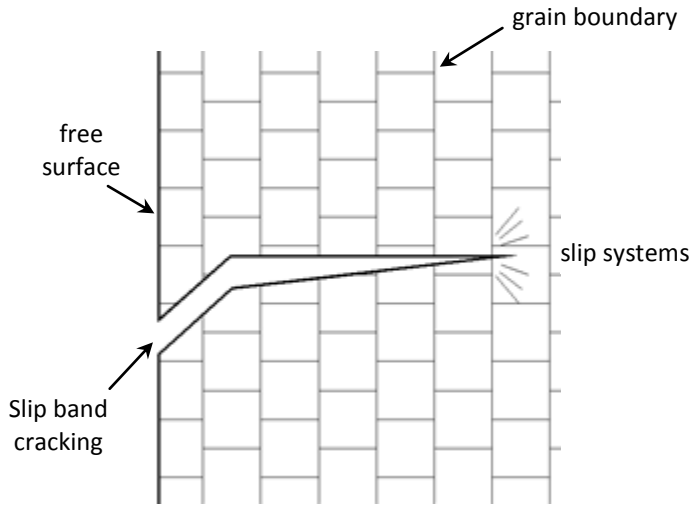

Figure 2.2 – Cross section of micro-crack.

The micro-crack growth is dependent on cyclic plasticity; barriers to slip can imply a threshold for crack growth. In the literature, several observations are reported on initially

inhomogeneous microcrack growth, which starts with a relatively high crack growth rate and then slows down or even stops due to material structural barriers. Two important surface aspects are no longer relevant. The lower restraint on cyclic slip at the surface is not applicable at the interior of the material, where inclusions or other kind of irregularities may act as trigger for crack initiation. Secondly, surface roughness and other surface conditions do not affect crack growth [9].

Crack growth resistance, when the crack penetrates into the material, depends on the material as a bulk property.

2.3.2. Review of main factors influencing fatigue damage

Since the pioneer research of Wöhler in metals, fatigue damage is unquestionably associated to stresses or strains varying in time. The increase in the amplitude of variation of the stresses/strains will result in accelerated fatigue damage. The typical way to express fatigue damage for materials, mechanical components or structural details is to use *S-N* curves, which are proposed based on constant amplitude (or range) loading. Figure 2.3 shows typical *S-N* curves for constant amplitude (or range) loading, which relates the stress amplitude (or range) with the number of cycles to failure. Some *S-N* curves may exhibit a clear horizontal plateau for high fatigue lives, representing a fatigue limit; however, some *S-N* curves may show a continuous reduction of fatigue strength for high fatigue lives, representing the case of a material/component not exhibiting a fatigue limit. The latter case corresponds to aluminium alloys and some high strength steels. For these materials, the fatigue limit is established as the stress range for a predefined high number of cycles.

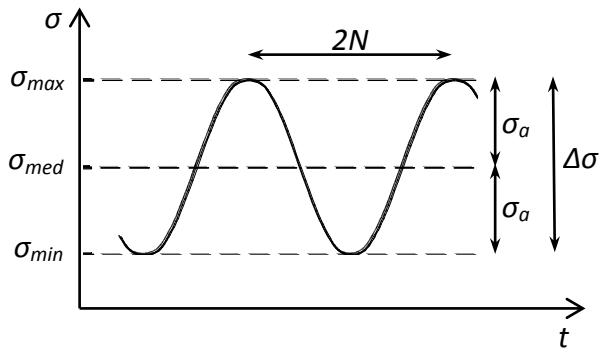

Maximum stress, σ_{max}

Minimum stress, σ_{min}

Stress range, $\Delta\sigma=\sigma_{max}-\sigma_{min}$

Stress amplitude, $\sigma_a=(\sigma_{max}-\sigma_{min})/2$

Mean stress, $\sigma_{med}=(\sigma_{max}+\sigma_{min})/2$

Stress ratio, $R=\sigma_{min}/\sigma_{max}$

a)

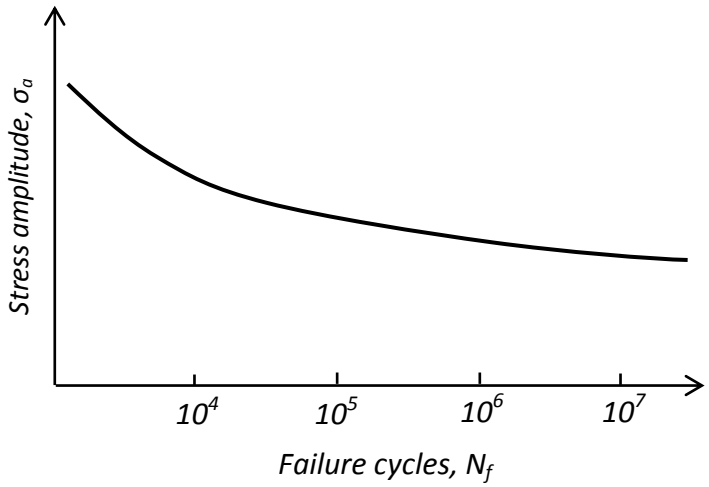

b)

Figure 2.3 – *S-N* representation: a) Constant amplitude loading definition; b) *S-N* diagram.

The *S-N* curves are typically established using the amplitude of stresses, the stress range or the maximum stress of the cycle as the leading damage parameter. Each *S-N* curve is generally derived for a fixed parameter related to the stress level of the cycle, such as the mean stress itself, the maximum or minimum stress or the stress ratio. In general, the fatigue strength decreases with increasing stress level. Figure 2.4a shows an example of a family of *S-N* curves, with the stress amplitude as a leading damage parameter. This figure illustrates the influence of the stress level on the *S-N* curves. It is clear that the fatigue limit depends on the applied stress level. The influence of the stress level on the fatigue strength, in particular of the mean stress, may be described using constant amplitude diagrams such as the ones proposed by Gerber, Soderberg and Goodman, illustrated in Figure 2.4b. These diagrams are used to express the influence of the mean stress on the fatigue limit, as well as the fatigue strength for a prescribed fatigue life. Besides these diagrams, stress level effects may be accounted in many other different ways, which are dependent on fatigue models being used [10].

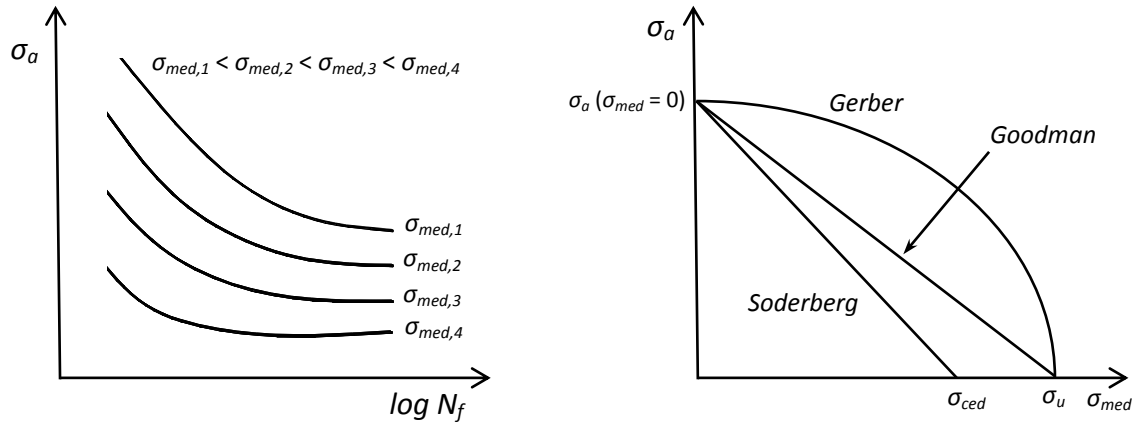

Figure 2.4 – Stress level effect on fatigue resistance:
a) influence of mean stress on S-N curves; b) constant life diagrams.

Besides the stress range or amplitude, as the main fatigue parameter, and mean stresses stress level, as the secondary fatigue parameter, which are two consensual factors influencing fatigue damage in any type of materials, other factors may influence fatigue damage, depending on the nature of material. Considering the case of the carbon and low-alloy steels, the following factors may have an impact on fatigue damage [11]: i) static strength level; ii) ductility; iii) cleanliness of the steel; iv) residual stresses; v) surface finish conditions; vi) aggressive environments.

Generally, mechanical components and structural details show stress concentrations due to surface discontinuities. This stress concentration is responsible for the fatigue strength reduction. However the fatigue strength reduction is not generally proportional to the stress concentration factor, K_t, associated to the geometric discontinuity. In general, a lower fatigue strength reduction is found, which is accounted by a fatigue notch factor, K_f. This fatigue notch factor corresponds to the ratio of the fatigue strength of a smooth specimen to the fatigue strength of a notched specimen, at the same number of cycles to failure. In general the fatigue notch factor depends on fatigue life and stress level. This factor decreases with increasing stress levels and decreasing fatigue lives, due to plastic deformation at notch root. The fatigue notch factor, K_f, tends to the stress concentration factor, K_t, fatigue notch sensitivity of the material increases.

Methodologies for the fatigue design of notched components under elastic dominant conditions (high-cycle fatigue), were introduced by Neuber [12,13] and Peterson [14].

More recently, the theory of critical distances bring new impulse to this topic [15,16].

2.4. FATIGUE LIFE PREDICTION METHODS

2.4.1. Global S-N approaches

Numerous studies have been conducted to understand the cyclic behaviour of steel bridge members and to formulate reliable fatigue-resistant design proposals. Fatigue problems are complex in nature and not easily understandable or feasible to be precisely modelled since a multitude of factors, which are not always independent, control the structural response to cyclic loading. Consequently, design and evaluation procedures are typically empirical in nature. Because no unified theory can reliably predict fatigue response, experimental testing is usually performed to describe the fatigue strength of structural members. Small-scale specimens, as well as full-scale specimens, have both been used to understand the fatigue behaviour of structural members [17].

Depending on the specific research program undertaken and the *S-N* field region covered by the experimentation, different intuitive models (parabolic, hyperbolic, linear, piecewise linear, etc.) have been proposed in the literature to fit experimental data [17,18,19]. Some of these models are shown in Table 2.1. However, unfortunately, not all are physically valid models.

Fatigue curves, plotted as straight lines when stress range, $\Delta\sigma$, and fatigue life, N_f, are expressed in logarithmic scale, as illustrated in Figure 2.5, are traditionally used to describe the cyclic response of a given structural detail.

Constant amplitude σ_a , or stress range $\Delta\sigma$, will result in a value of the cyclic life, *N*. A number of specimens must be tested to establish the representative *S-N* strength of a particular structural detail. Discrepancies between the predicted mean strength and the test results often occurs because so many factors influence the strength [17,19].

Table 2.1 – Models proposed in the literature for *S-N* curves [18].

Model	Function Form
Wöhler (1870)	$\log N = A - B \cdot \Delta\sigma;\ \ \Delta\sigma \geq \Delta\sigma_0$
Basquin (1910)	$\log N = A - B \cdot \log \Delta\sigma;\ \ \Delta\sigma \geq \Delta\sigma_0$
Strohmeyer (1914)	$\log N = A - B \cdot \log\left(\Delta\sigma - \Delta\sigma_0\right)$
Palmgren (1924)	$\log\left(N + D\right) = A - B \cdot \log\left(\Delta\sigma - \Delta\sigma_0\right)$
Palmgren (1924)	$\log N = A - B \cdot \log\left(\Delta\sigma - \Delta\sigma_0\right)$
Weibull (1949)	$\log\left(N + D\right) = A - B \cdot \log\left(\left(\Delta\sigma - \Delta\sigma_0\right)/\left(\Delta\sigma_{st} - \Delta\sigma_0\right)\right)$
Stüssi (1955)	$\log N = A - B \cdot \log\left(\left(\Delta\sigma - \Delta\sigma_0\right)/\left(\Delta\sigma_{st} - \Delta\sigma\right)\right)$
Bastenaire (1972)	$\left(\log N - B\right) \cdot \left(\Delta\sigma - \Delta\sigma_0\right) = A \cdot \exp\left[-C \cdot \left(\Delta\sigma - \Delta\sigma_0\right)\right]$
Spindel-Haibach (1981)	$\log\left(N/N_0\right) = \dfrac{\lambda + \delta \cdot \left(-\log\left(1-p\right)\right)^{1/\beta}}{\log\left(\Delta\sigma/\Delta\sigma_0\right)}$
Castillo et al. (1985)	$\log\left(N/N_0\right) = A \cdot \log\left(\Delta\sigma/\Delta\sigma_0\right) - B \cdot \log\left(\Delta\sigma/\Delta\sigma_0\right) + B \cdot \left\{\left(1/\alpha\right) \cdot \log\left[1 + \left(\Delta\sigma/\Delta\sigma_0\right)^{-2\alpha}\right]\right\}$
Kohout and Vechet (2001)	$\log\left(\Delta\sigma/\Delta\sigma_\infty\right) = \log\left(\dfrac{N + N_1}{N + N_2}\right)$
Pascual and Meeker (1999)	$\log N = A - B \cdot \log\left(\Delta\sigma - \Delta\sigma_0\right)$

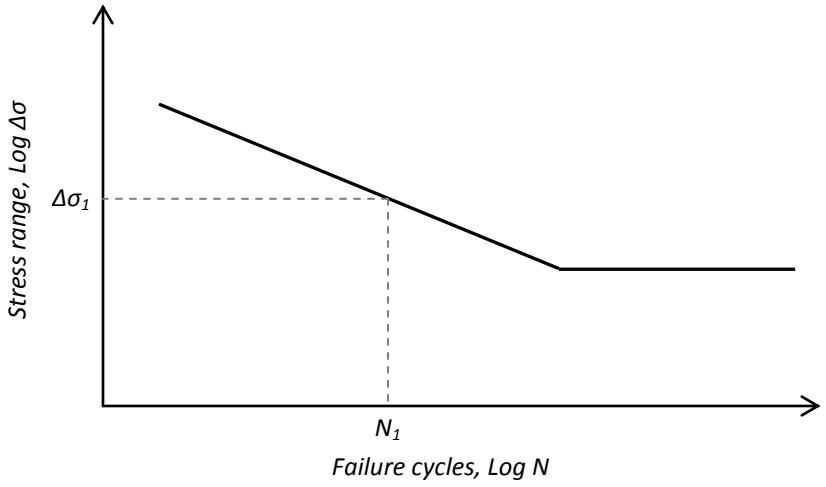

Figure 2.5 – Stress range versus number of cycles to failure.

Practice design codes [20] adopt the following form for the *S-N* curve, proposed by Basquin:

$$\Delta\sigma^m N_f = C \tag{2.1}$$

where *C* and *m* are material constants. Alternatively, the mean or median *S-N* curves may be represented using the following linear model [21,22], which is more suitable for parameters identification using linear regression analysis:

$$Y = A + B \cdot X \tag{2.2}$$

where *Y* is the dependent variable defined as $Log(N_f)$, *X* is the independent variable defined as $Log(\Delta\sigma)$, *A* and *B* are linear regression parameters. Consequently it is possible to rewrite the *S-N* curve in the following forms [21,22]:

$$\begin{cases} Log(N_f) = A + B \cdot Log(\Delta\sigma) \\ Log(\Delta\sigma) = -\dfrac{A}{B} + \dfrac{1}{B} \cdot Log(N_f) \end{cases} \tag{2.3}$$

where *A* and *B* are linear regression parameters which are related to the *C* and *m* constants:

$$\begin{cases} C = 10^A \\ m = -B \end{cases} \tag{2.4}$$

To carry out an assessment of the remaining fatigue life of old steel bridges and crane structures, critical structural details have to be identified and categorised. The treatment of fatigue life in structural details are described by design rules of several European and North American standards [19,23], such as, Eurocode 3 [24], BS 5400 [25] and AASHTO [26] standards.

The fatigue resistance of riveted shear splices of old metallic riveted bridges are not mentioned in Eurocode 3 [24,27]. A reasonable assumption is that a riveted shear splice is the same as a splice that uses non-preloaded high-strength bolts. In this case, Eurocode 3 prescribes the use of Detail Category 112 [19]. The Eurocode rule is plotted in Fig. 2.6. Both Åkesson & Edlund [19,28] and Helmerich et a [19,29] have suggested Eurocode Detail Category 71 for riveted shear splices. This is a better choice than Detail Category 112, though it is substantially conservative for stress ranges less than about 60 MPa. Taras and Greiner [30] have performed a statistical analysis of a significant amount of experimental fatigue data available in literature for riveted joints from old bridges. These authors suggest the categorization of the riveted joints into five categories, using a slope, *m*=5 for the design curve, instead of the *m*=3 given in the design codes for the joints,

EC3-1-9 [24]. Two of the categories are the single and double shear splices under tensile loading. For double shear riveted joints, Taras and Greiner [30] proposed a design *S-N* curve with a slope, *m*=5 and a fatigue strength of 90MPa at 2×10^6 cycles whereas for single shear riveted joints, a design *S-N* curve with a slope, *m*=5 and a fatigue strength of 71MPa at 2×10^6 cycles is suggested. In addition, they refer that mean stress effects must be accounted for riveted joints and suggested the use of a normalized stress range to allow comparison between experimental fatigue lifetimes to be made.

With the advent of the Eurocodes, development of national standards in Europe has ceased. However, riveted shear splices are specifically mentioned in BS 5400, so that they can be further handled in this frame. The riveted shear splice detail is described in BS 5400 as their Class D. This standard does distinguish between riveted shear splices and bolted shear splices, in contrast to Eurocode 3. However, the fatigue life rule provided by this standard for riveted shear splices is neither satisfactory [19].

The AASHTO standard also provides a fatigue life rule specifically for riveted shear splices (AASHTO Category D). This standard is widely used by railroads in North America. Among the standards reviewed, it is the one that most closely reflects the recent test data [19].

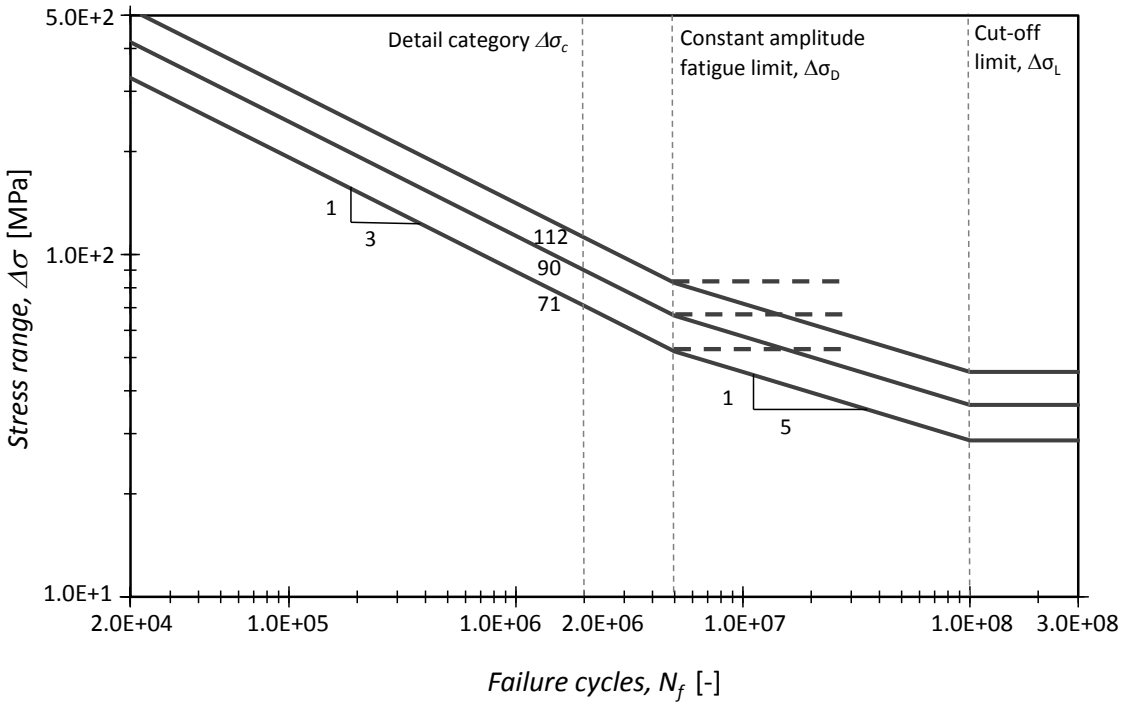

Figure 2.6 –Fatigue strength curve for nominal stress range EN 1993-1-9 [24].

2.4.2. Local approaches

Fatigue design philosophy has evolved from fatigue limit and infinite life criteria to approaches based on finite life behaviour [31,32]. The local approaches use fatigue damage parameters to correlate fatigue test results, especially for crack initiation life.

In order to predict the fatigue life under a specified condition, different fatigue damage parameters have been proposed to correlate fatigue life. The local approaches are generally divided into three categories, i.e., stress-based, strain-based and energy-based methods, when stress, strain or energy are respectively used as the fatigue damage parameter.

Models to account for the stress level effect referring to the stress-based, strain-based and energy-based methods have been proposed. These models are presented in the following.

2.4.2.1. Stress-based method

The stress-life method uses the alternating stress amplitude to predict the number of cycles to failure. This method is based on comparing the stress amplitude to a stress amplitude versus fatigue life curve (*S-N* diagram). The *S-N* curves are based on empirical formulas derived from experimental data. The stress-life method is generally only used for high cycle fatigue, because under low cycle fatigue the stress-strain relationship becomes nonlinear [31]. Similar to S-N curves, the relation between stress amplitude, $\Delta\sigma/2$, and the number of cycles to failure, N_f, can be approximated by a straight line when the stress amplitude and the fatigue life are both expressed on a logarithmic scale, thus resulting in:

$$\frac{\Delta\sigma}{2} = \sigma'_f \cdot (N_f)^b \tag{2.5}$$

where σ'_f is the fatigue strength coefficient, and *b* is the fatigue strength exponent.

For many loading cases, the mean stress is not zero. Although the stress level effect is often neglected in fatigue life calculations for welded details, the high residual stresses in such details tend to obliterate any possible effect of applied stress level. However, in non-

welded details, the effect of stress level must be accounted for in the fatigue life calculations.

Morrow [33,34] proposed a correction to account for the mean stress effect as follows:

$$\frac{\Delta\sigma}{2} = \left(\sigma'_f - \sigma_m\right)\cdot\left(N_f\right)^b \tag{2.6}$$

where σ_m is the mean stress and the other variables are the same as for Equation (2.5). The effect of the tensile mean stress is thus equivalent to a reduction of the fatigue strength coefficient. The model assumes that a given combination of stress amplitude, $\Delta\sigma/2$, and mean stress, σ_m, is expected to have the same fatigue life as a fully reversed stress amplitude of $(\Delta\sigma/2)_{-1}$, where:

$$\left(\frac{\Delta\sigma}{2}\right)_{-1} = \frac{\Delta\sigma/2}{1-\sigma_m/\sigma'_f} \tag{2.7}$$

The Morrow correction for stress-based method was found to work reasonably well for structural grades of steels [35].

2.4.2.2. Strain-based method

The strain-based method has found wide applications in fatigue analysis, especially for calculation of fatigue crack initiation. In contrast to the stress-based method, the strains-based method considers the plastic deformation that may occur in localized regions where fatigue cracks initiate. The strain-based method assumes the material in highly strained areas, such as at a notch root, behaves similarly to material in a smooth specimen under cyclic strain controlled loading with the same strain [34].

The strain-based method uses a strain versus life curve along with the cyclic stress versus strain curve of the material instead of the *S-N* curve used in the stress-based method. The coefficients and exponents that define these curves are treated as fatigue properties of the material. At the early developmental stages for the technique, there were insufficient fatigue data to quantify the fatigue properties of many engineering metals and various equations were proposed to correlate the fatigue properties to the tensile properties [34]. The generalized adoption of closed-loop mechanical testing systems and the

development of the strain-based method have largely eliminated the need for these empirical equations, and there is abundance of data defining the fatigue properties of numerous engineering metals [36].

For engineering materials at room temperature, cyclic hardening or softening usually takes place rapidly at first and then approaches to a stable condition. The stable cyclic stress versus strain curve is often defined using the Ramberg-Osgood equation [35-37]. The curve can be determined from several companion specimens cycled at various constant strain amplitudes or from a single specimen in conformity with the incremental step test method [34].

For Equation (2.8), the elastic component of the strain amplitude, $\Delta\varepsilon^E/2$, can be obtained as follows:

$$\Delta\varepsilon^E/2 = \frac{\sigma'_f}{E}\cdot\left(N_f\right)^b \tag{2.8}$$

where E is the modulus of elasticity. The plastic strain amplitude, $\Delta\varepsilon^P/2$, versus fatigue life can also be linearized on a logarithmic scale for low cycle fatigue. The relationship between the plastic strain amplitude and fatigue crack initiation life can be expressed in the following form:

$$\Delta\varepsilon^P/2 = \varepsilon'_f\cdot\left(N_f\right)^c \tag{2.9}$$

where ε'_f is the fatigue ductility coefficient, and c is the fatigue ductility exponent, both determined experimentally.

By adding the elastic and plastic components of strain amplitude, given respectively by Equations (2.8) and (2.9), the relationship between the total strain amplitude, $\Delta\varepsilon/2$, and fatigue life can be expressed as (see Figure 2.7):

$$\Delta\varepsilon/2 = \Delta\varepsilon^E/2 + \Delta\varepsilon^P/2 = \frac{\sigma'_f}{E}\cdot\left(N_f\right)^b + \varepsilon'_f\cdot\left(N_f\right)^c \tag{2.10}$$

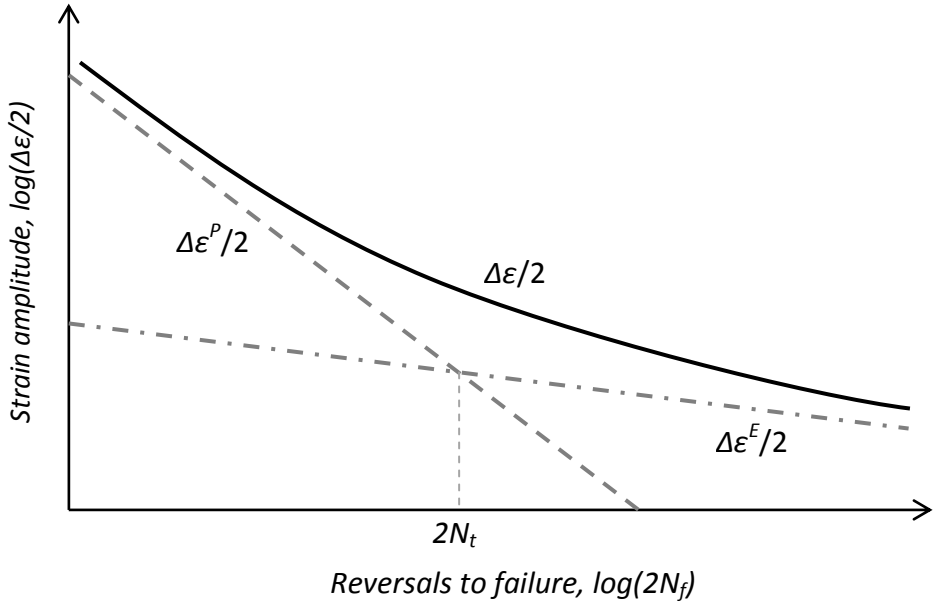

Figure 2.7 – Schematic plot of elastic, plastic and total strain amplitudes versus reversals to failure.

On its turn, the cyclic stress versus strain curve can be modelled by the Ramberg-Osgood equation as follows:

$$\Delta\varepsilon/2 = \frac{\Delta\sigma/2}{E} + \left(\frac{\Delta\sigma/2}{K'}\right)^{1/n'} \tag{2.11}$$

where *K'* is the cyclic strength coefficient and *n'* is the cyclic strain-hardening exponent. For the strain-based method, the mean stress effect can be corrected by the Smith, Watson and Topper (*SWT*) model [38]. The model appears to provide good results for a wide range of materials and is a good choice for general use [35]. The *SWT* model assumes that the fatigue life for any level of mean stress is a function of the product of the maximum stress and strain amplitude, $\sigma_{max}.\Delta\varepsilon/2$. The model can be expressed as:

$$\sigma_{\max} \cdot \Delta\varepsilon/2 = \frac{(\sigma'_f)^2}{E} \cdot (N_f)^{2b} + \sigma'_f \cdot \varepsilon'_f \cdot (N_f)^{b+c} \tag{2.12}$$

where the intervening parameters are defined as earlier.

2.4.2.3. Energy-based method

Experimental observations have confirmed the significant role that plastic deformation plays in the fatigue damage process. As cyclic plastic deformation is related to slip along crystallographic planes and dislocation movement, cyclic stress is related to the resistance

to such movement at the microscopic level and strain energy is dissipated during such irreversible deformations [31,32]. The energy-based method uses energy as a damage parameter to characterize fatigue, emphasizing the interrelation between stress, strain, and the fatigue damage process. It unifies high and low cycle fatigue, and has the potential to bridge fatigue data obtained in different laboratories using specimens of different geometry and size and tested under different controls [39,40]. As a relatively new method (mainly developed in the last two decades), it has not been widely used but the method seems promising.

Commonly, the total absorbed energy to the point of fatigue failure is assumed to depend on the total number of cycles sustained whereas the fatigue damage arising in each cycle is assumed to relate directly to the area under the hysteresis loops of the stress versus strain curve obtained during cyclic loading [31]. Various measures of energy have been proposed depending on the stress level, as for instance, the plastic strain energy density per cycle (ΔW^P). The ΔW^P criterion is more appropriate when the plastic strains are large, and while it is believed to be less suitable for small strain magnitude because during high cycle fatigue the plastic strain energy is very small and difficult to be measured accurately. The plastic plus elastic tensile strain energy density per cycle, ΔW^t, was proposed to predict the mean stress effect [41] and is believed to be more recommendable for deformation controlled situations.

Energy approaches are based on the assumption that fatigue damage is directly related to the area under the hysteresis loops resulting during cyclic loading the latter being related to the plastic deformation taking place during a load cycle, which on its turn relates to the fatigue damage sustained.

Ellyin and Kujawski [42] suggested the use of the total strain energy range per reversal, ΔW, can be written as:

$$\Delta W = \tfrac{1}{2}\Delta W^P + \tfrac{1}{2}\Delta\sigma\Delta\varepsilon \tag{2.13}$$

$$\Delta W^t = \Delta W^P + \frac{\sigma_{\max}^2}{2E} \tag{2.14}$$

where $\Delta\sigma$ is the stress range, $\Delta\varepsilon$ is the strain range and σ_{max} is the maximum stress.

The ΔW^t criterion is believed to be more appropriate to predict the mean stress effect, defined by the following expression:

$$\Delta W^t = \kappa_t \left(2N_f\right)^{\alpha_t} + \Delta W_0^t \tag{2.15}$$

where α_t<0 and κ_t>0 are constants, N_f is the number of cycles to failure and ΔW_0^t is the total strain energy range, ΔW^t, corresponding to fatigue limit. Ellyin [31] developed a more general expression that explicitly includes the mean stress in the formulation as follows:

$$D = \Delta W^P + f\left(\frac{\sigma_m}{\Delta\sigma/2}\right)\frac{\left(\Delta\sigma/2\right)^2}{2E} = \kappa_t \left(N_f\right)^{\alpha_t} + \Delta W_0^t \tag{2.16}$$

$$f\left(\frac{\sigma_m}{\Delta\sigma/2}\right) = 1 + \eta\left(\frac{\sigma_m}{\Delta\sigma/2}\right) \tag{2.17}$$

where the coefficient η is a material property, which varying from 0 to 1, characterizes the material sensitivity with respect to mean stress. It can be evaluated from a few fatigue tests conducted at different mean stress levels in the high cycle region.

2.4.3. Fracture Mechanics based approaches

2.4.3.1. An overview of fatigue crack propagation laws

With the development of the Fracture Mechanics, new opportunities for fatigue modelling emerged in the literature. The key contribution in this field is attributed to Paris and his co-authors [5] who first recognized the relation between the stress intensity factor at an existing crack tip and the crack advance under cyclic loading:

$$\frac{da}{dN} = f\left(\Delta K\right) \tag{2.18}$$

where da/dN is the fatigue crack growth rate; ΔK is the stress intensity factor range and f is a function of the stress intensity factor range to be defined. A simple power function was proposed by Paris, between the fatigue crack growth rate and the stress intensity factor range, at a given crack tip [5]:

$$\frac{da}{dN} = C\Delta K^m \tag{2.19}$$

where C and m are material constants. This crack propagation relation was verified to be

valid for a specific fatigue crack propagation regime, particularly in the fatigue crack propagation regime II, which lies in between the near threshold fatigue crack propagation regime (regime I) and the near unstable crack propagation regime (regime III), as illustrated in Figure 2.8.

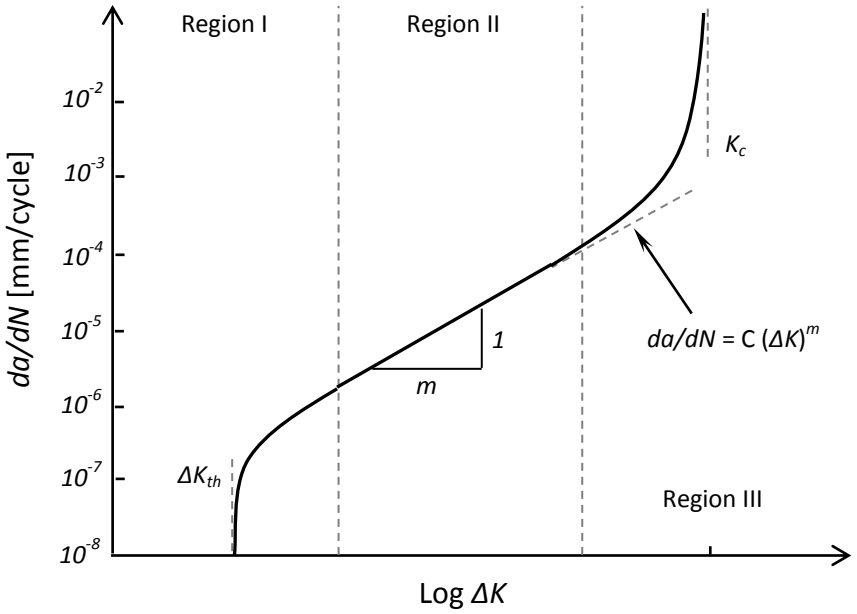

Figure 2.8 – Fatigue crack propagation regimes.

Despite its significant contribution, the Paris relation shows important limitations that were overcome by proposals of alternative and more complex fatigue crack propagation relations. An extensive review of numerous fatigue crack propagation relations was given by Beden *et al.* [6], either for constant and variable amplitude loading. The stress ratio effect is an important load parameter influencing the fatigue crack propagation rate, which is not accounted by the simple Paris model. Walker [43] proposed an alternative relation to overcome this limitation of the Paris model:

$$\frac{da}{dN} = C\left[\frac{\Delta K}{(1-R)^{1-\gamma}}\right]^m \tag{2.20}$$

This model introduces a third curve fitting parameter, γ, besides the *C* and *m* parameters already existing in the Paris model. For *R*=0, this relation coincides with the Paris relation. The γ parameter can be computed as the value that best consolidates the data along a single straight line on the log-log plot of *da/dN versus* $\overline{\Delta K}$, with $\overline{\Delta K}$ defined as:

$$\overline{\Delta K} = \frac{\Delta K}{(1-R)^{1-\gamma}} \tag{2.21}$$

With his proposal, Walker introduced the two-parameter approaches for fatigue crack propagation. The Walker fatigue crack propagation relation can be rewritten in the following form:

$$\frac{da}{dN} = C\left[\Delta K^{\gamma} \cdot K_{max}^{1-\gamma}\right]^m = C\left[\Delta K^{1-p} \cdot K_{max}^{p}\right]^m \tag{2.22}$$

Dinda and Kujawski [44] proposed a variation of the previous equation, excluding the compressive part of the stress intensity factor range:

$$\frac{da}{dN} = C\left[\left(\Delta K^{+}\right)^{1-p} \cdot K_{max}^{p}\right]^m \tag{2.23}$$

This type of fatigue crack propagation formulation, based on two-parameter crack driving force, was also followed by other authors. This is the case of the proposal by Donald and Paris [45] and Vasudevan *et al.* [46]. The latter authors considered that crack propagation may occur only if two thresholds are exceeded, namely, both ΔK and K_{max}.

Both Paris and Walker models are valid for the crack propagation in regime II whereas Forman proposed an extension of Walker model to the propagation regime III [47]:

$$\frac{da}{dN} = \frac{C\Delta K^m}{(1-R)(K_c - K_{max})} \tag{2.24}$$

Hartman and Schijve [48] extended Forman equation to cover the three crack propagation regimes:

$$\frac{da}{dN} = \frac{C\left(\Delta K - \Delta K_{th}\right)^m}{(1-R)K_c - \Delta K} \tag{2.25}$$

This relation results in a sigmoidal shaped curve with vertical asymptotes at $K_{max}=K_c$ and $\Delta K=\Delta K_{th}$. This relation suffers a limitation related to the stress ratio dependency of the ΔK_{th}, which is not directly contemplated in the relation. Many other fatigue crack propagation relations have been proposed in the literature, which are not accounted for in this review. Only some of the more relevant historical ones are being referred to. The

above relations make use of the ΔK parameter which is a Linear Elastic Fracture Mechanics parameter. Therefore, those relations are only applicable for cracks with limited plasticity ahead of the crack tip. For generalized elastoplastic conditions, some authors have proposed the use of Elastoplastic Fracture Mechanics parameters to correlate the fatigue crack growth, as is the case of the J-Integral, as proposed by Dowling and Begley [49]:

$$\frac{da}{dN} = C\Delta J^m \tag{2.26}$$

This equation is similar to the Paris relation (fits data in region II), but can be advantageously applied in situations of large scale yielding.

The previous referred relations have being suggested for constant amplitude loading conditions. For variable amplitude loading conditions they may be considered inappropriate due to load interactions that may significantly alter the growth behavior of a crack. For example, it is well know that an overload may induce retardation effects on crack propagation. Wheeler [50] proposed a model to simulate the retardation effects induced by single overloads, introducing a retardation parameter in the propagation law. The retardation parameter accounts for the interference between the crack tip plasticity zone induced by the overload and the steady state plasticity zone. This model does not account for underloads and interactions of multiple underloads and overloads. The Wheeler model was further advanced by Willenborg [51] to allow for underloads. One fatigue crack propagation model worldwide reputable is the NASGRO model, which is based on the Willenborg model. NASGRO model extends the Willenborg model in order to account for the reduction of retardation due to underloads.

Elber [7,8] furnished an important contribution in the fatigue crack growth study by introducing the crack closure concept to explain the crack growth under variable amplitude loading. Elber argued that a load cycle is only effective in driving the growth of a fatigue crack if the crack tip is fully open. He introduced the effective stress intensity ratio, *U*, defined as:

$$U = \frac{\Delta K_{eff}}{\Delta K} = \frac{K_{max} - K_{op}}{K_{max} - K_{min}} \tag{2.27}$$

where K_{max}, K_{min} and K_{op} are respectively the maximum, minimum and opening stress intensity factors. Any fatigue crack propagation relation above referred may be rewritten using the effective stress intensity factor range, ΔK_{eff}. For example, the Paris relation may be rewritten as:

$$\frac{da}{dN} = C\left(\Delta K_{eff}\right)^m = C\left(U\Delta K\right)^m \tag{2.28}$$

Crack closure is assumed in this approach to be responsible for the load interaction effects. The application of the crack closure model requires the accurate definition of the U and K_{op} parameters for specific materials, loading types and region on the fatigue rate curve. The crack closure approach is an alternative approach, competing with the residual stress approach induced by plasticity around the crack tip approach, the first becoming very popular.

For variable amplitude loading characterized by approximate random stress spectra, sequential effects are not relevant and for these conditions previously referred models that not account for load interaction effects are sufficient to make life predictions. Those models may be integrated cycle-by-cycle. Alternatively some authors [52] proposed the use of the Miner model to define an effective stress intensity factor according to the following relation:

$$\Delta K_{eff} = \left(\sum \frac{n_i \Delta K_i^m}{N_T} \right)^{1/m} \tag{2.29}$$

where ΔK_{eff} is the effective stress intensity factor; N_T is the total number of cycles; N_i is the number of cycles with a stress intensity factor range of ΔK_i and m is a constant.

Hudson [53] proposed the use of the root mean square (RMS) of the minimum and maximum stresses, which will be used to compute ΔK_{RMS} and R_{RMS} required for the fatigue crack propagation model, such as the Forman relation. This model will provide the average crack propagation for the analysed spectrum loading.

The models proposed by Castillo and Fernández-Canteli [54] represent a new solution for the fatigue crack propagation based on the assumption of the crack growth curve

becoming a cumulative distribution function. The inconvenience of dimensional parameters in existing crack propagation models is overcome in this new proposal by means of dimensional analysis, carried out on influent variables leading to adimensional normalized parameters. One additional alternative explored by authors is the Gumbel cumulative distribution function. The proposed model (see details at reference [54]) is defined by:

$$\frac{log\,\Delta K^{*} - log\,\Delta K^{*}_{th}}{log\,\Delta K^{*}_{up} - log\,\Delta K^{*}_{th}} = exp\left[-exp\left(\frac{\alpha - log\dfrac{da^{*}}{dN^{*}}}{\gamma} \right) \right] \tag{2.30}$$

This model depends on four parameters, α, γ, ΔK^{*}_{th} and ΔK^{*}_{up} which may be computed by least-square techniques [54]. The '*' in the variables of the model means normalized variables. For example, they can be normalized, as suggested by the authors, using the following relations:

$$a^{*} = \frac{a}{W}; N^{*} = \frac{N}{N_0}; \Delta K^{*} = \frac{K_{max} - K_{min}}{K_c}; \Delta K^{*}_{up} = \frac{\Delta K_{up}}{K_c}; \Delta K^{*}_{th} = \frac{\Delta K_{th}}{K_c} \tag{2.31}$$

with the intervening parameters defined as:

a= crack length;

W=characteristic length (e.g. specimen length)

N=Number of cycles;

N_0= reference number of cycles;

K_{max}, K_{min}=maximum and minimum stress intensity factors;

ΔK_{th}=threshold intensity factor range;

ΔK_{up}=limit stress intensity factor range;

K_c=material characteristic fracture toughness.

2.4.3.2. Fatigue modelling of structural details or mechanical components based on Fracture Mechanics

In the preceding section, a review of fatigue crack propagation laws was presented. The availability of accurate fatigue crack propagation laws is the key for reliable fatigue life

predictions of mechanical components or structural details. The most common use of the fracture mechanics based on fatigue crack propagation relations, consists in residual fatigue life assessment of mechanical components or structural details containing initial known defects acting like cracks. This can be accomplished integrating the crack propagation law, according to the following expression:

$$\frac{da}{dN} = f(\Delta K, R, ...) \Rightarrow N_f = \int_{a_i}^{a_f} \frac{da}{f(\Delta K, R, ...)} \tag{2.32}$$

where a_i is the initial crack size and a_f the critical crack size, which is defined by the unstable crack propagation, dictated by the material toughness, or plastic failure at the net section.

Besides residual fatigue life calculations, which is the basis of a damage tolerance analysis, the integration of fatigue crack growth relations can be used to compute the total fatigue life of components. In these cases, the crack initiation is disregarded and the fatigue life is understood as a process of fatigue crack propagation. The main difficulty implied in this approach is the determination of the initial crack size for the crack growth analysis. One practical solution in using an empirically assumed crack length, such as 0.25–1 mm for metals [55-57] whereby the assumption of such macro-crack could underestimate the fatigue life of the component. Some authors complement this approach with a local approach based on strain-life relations to compute the number of cycles to initiate such macro-crack [32,58]. This approach shows a drawback related to the definition of the precise size of the initial crack within the range above referred. In many cases, a calibration process is required.

An alternative way is to use an initial defect measured from nondestructive inspection [59]. However, this technique fails if the initial defect size is below the detection capability of the *NDI* technique. A conservative assumption corresponds to the consideration of an initial defect coinciding with the size of the *NDI* detection limit [60]. A common approach is to postulate an equivalent initial flaw size (*EIFS*) in an attempt to determine the initial crack size for fracture mechanics-based life prediction. The *EIFS* accounts for the initial quality, both from manufacturing and bulk material properties of structural details. The calculation of *EIFS* is usually performed using a trial and error back-

extrapolation (inverse) methodology. This procedure uses fatigue crack growth analysis with an assumed initial crack geometry and size to match the material failure data (stress-life) [61]. Yang and Manning [62] used this back-extrapolation technique to obtain the EIFS distribution of Al 2024-T351. White *et al.* [63] resort to a probabilistic fracture approach to derive the equivalent pre-crack size, which is also based on the back-extrapolation method. Molent *et al.* [64] used a back projection of the experimental crack growth curve to time zero to derive the *EPS* for Al 7050. The major problem using the back-extrapolation method is that the obtained *EIFS* seems to be dependent on the stress level [65]. It is desirable to view *EIFS* as a material property indicating the initial quality of the material and not connected to the applied stress level; this would make the *EIFS* applicable to a wide range of stress levels. However, it should be noted that *EIFS* is not a physical quantity. It is a quantity extrapolated from experimental data simply to facilitate life prediction by using only long crack growth analysis and avoiding the difficulties of short crack growth modeling. Widespread use of *EIFS* concept has not been realized due to the large amount of test data required to develop a reliable *EIFS* distribution [66].

When the uncertainties associated with *EIFS* need to be included, the problem becomes more involved. Due to the inherent variability of fatigue crack growth data, failure data, and also the modeling approximations in the fatigue crack growth analysis, the uncertainties of *EIFS* need to be carefully considered in a probabilistic life prediction. The back-extrapolation method makes the computation of probabilistic *EIFS* distribution very expensive, because Monte Carlo simulation is usually coupled with iterative fatigue crack growth analysis [67,68]. To overcome such inconveniences associated to the application of the *EIFS* concept above referred, reference [61] presents a new probabilistic *EIFS* calculation methodology based on the Kitagawa–Takahashi diagram. The *EIFS* is determined by matching the infinite life of a component with and without an assumed initial crack. The proposed methodology only uses the fatigue limit data and the fatigue crack threshold stress intensity factor. The statistics of *EIFS* are directly calculated without solving inverse fatigue crack growth analysis.

The Fracture Mechanics based fatigue approach has also been used to simulate technical crack initiation which, according Savaidis et al. [69], corresponds to a crack size of 1 mm.

These authors applied the Elastoplastic Fracture Mechanics (J-integral based crack growth law) to simulate the propagation of incipient postulated micro-cracks, which are obtained by back extrapolation. They applied the model to predict technical crack formation at notched details. Besides the Elastoplastic Fracture Mechanics framework, they considered crack closure effects.

2.4.4. Local approaches for fatigue crack propagation modelling

A link between the local approaches to fatigue, typically used to simulate fatigue crack initiation, and fatigue crack propagation has been demonstrated and explored by some authors [31,70-76]. These approaches recognize fatigue crack propagation as a process of continuous crack re-initializations. The local approaches to fatigue are applied to the plastic process zone ahead of the crack tip to simulate the fatigue crack growth. Basically, to predict fatigue crack growth, it is necessary to predict the stress/strain fields ahead of the crack tip and to apply a failure criterion to model the crack separation. An averaging process over a characteristic length is required due to the singularity introduced by the crack tip. The various approaches differ among each other in the way the geometry of the crack is defined, the expressions used to compute the local stresses and strains, the damage model and the characteristic length along which the damage model parameters are computed.

Glinka published a study in 1985, where a notch stress-strain analysis approach was applied to model fatigue crack growth. The crack was assumed to have a notch with a tip radius, ρ^* and the material ahead of the crack tip was assumed to be divided into elemental blocks of finite linear dimension, ρ^* (see Figure 2.9). The crack growth was assumed as the failure of successive elemental blocks, the fatigue crack growth rate being defined by the following relation:

$$\frac{da}{dN} = \frac{\rho^*}{N_f} \tag{2.33}$$

where N_f represents the number of cycles to fail the elemental block of dimension, ρ^*.

To simulate the elemental block failure, the Coffin-Manson relation, later modified by

Morrow, to account for mean stress effects, was applied using the elastoplastic stress/strains computed using the basis elastic solution for a blunt crack and the density energy criterion by the same author. The basis elastic solution was derived using the effective stress intensity range, which takes into account the crack closure effects. The author was able to correlate fatigue crack propagation data in the region I and II of fatigue crack propagation. This early work by Glinka was resumed twenty years later by Glinka and his collaborators, namely Noroozi, Lambert and Mikheevskiy [72-75]. The basic premises of the early work by Glinka were followed, but a more sophisticated procedure to compute the elastoplastic stress/strains at the representative material element was adopted. Instead of the crack closure correction, compressive residual stresses were computed due to the cyclic elastoplastic action. These compressive residual stresses are used to correct the stress intensity factor range leading to a net stress intensity range, which is used to correct the elastoplastic stress/strain field. This approach was demonstrated to work well for both constant and variable amplitude loading [72-75].

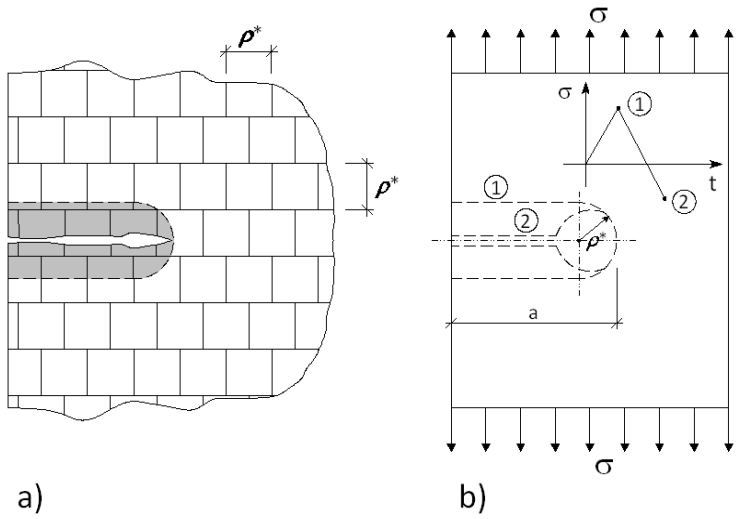

Figure 2.9 - The discrete material model and the crack tip geometry at the maximum and minimum load: (a) crack and the discrete elementary material blocks. (b) The crack model at the tensile maximum and compressive minimum loads used for the linear elastic stress analysis [72-74].

Ellyin and Kujawshi [31] proposed a low-cycle fatigue-based crack propagation model. This model is based on the assumption of three important plastic regions ahead of the crack tip for a propagating crack (see Figure 2.10). The region I is the process zone, denoted by δ^*. The behaviour of this process zone is modelled with an energetic damage parameter, $\Delta\sigma \cdot \Delta\varepsilon^p$, proposed by Ellyin. The damage parameter is evaluated using

analytical solutions for the plastic field ahead of a crack with a critical blunt tip radius ρ_c. Two analytical plastic fields were explored, namely the *HRR* (Hutchinson-Rice-Rosengren) and *RKE* (Rice-Kujawski-Ellyin) fields [31]. The crack tip blunting is responsible for finite damage parameters as the distance to the crack tip approaches to zero.

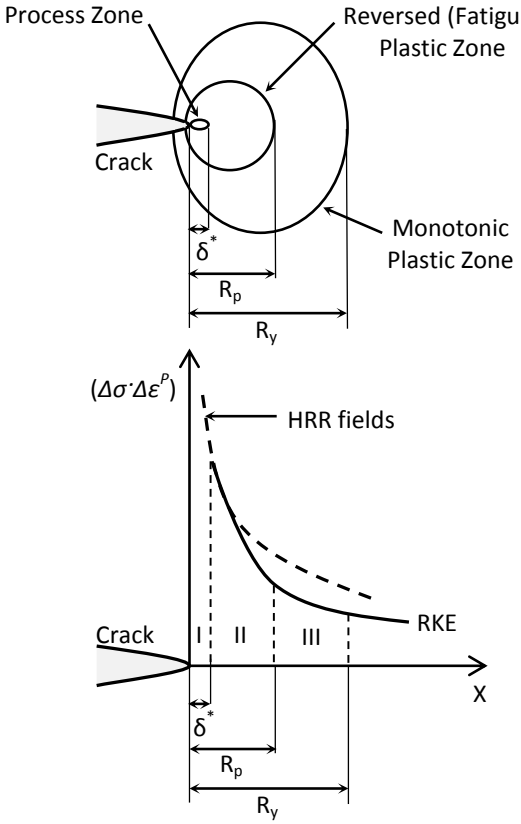

Figure 2.10 – Three regions in the front of the fatigue crack according to the Ellyin model [31].

The fatigue crack growth model uses the hysteretic energy in front of the crack as a criterion for the crack advance. This energy can be computed using the following relations:

$$\Delta W^P = \left(\frac{1-n'}{1+n'}\right)\Delta\sigma_{eq}\cdot\Delta\varepsilon_{eq}^p = \left(\frac{1-n'}{1+n'}\right)\frac{\Delta K^2}{Er\psi(n',\theta)} \tag{2.34}$$

where n' is the cyclic strain hardening exponent, E is the Young modulus, ΔK is the stress intensity factor range, r and θ are the polar coordinates associated to a crack tip origin and ψ is a plastic function which depends on the analytical method used to assess the plastic field ahead of the crack tip. Two possibilities were proposed by Ellyin, namely for *HRR* and *RKE* fields. Assuming that crack propagates along the plane y=0, what implies that θ=0 and r=x, the blunt crack tip will be attained in the computation of the damage

parameter, resulting:

$$\Delta W^P = \left(\frac{1-n'}{1+n'}\right)\frac{\Delta K^2}{E\psi(n',0)\left(\delta^* + \rho_c\right)} \tag{2.35}$$

The damage parameter will be related to the number of cycles to failure using both Basquin [77] and Coffin-Manson [3,4] relations:

$$\Delta W^P = 4\left(\frac{1-n'}{1+n'}\right)\varepsilon'_f\sigma'_f\left(2N_f\right)^{b+c} \tag{2.36}$$

From previous two equations, one may relate the crack advance distance δ^* with the increment on cycles, ΔN:

$$\frac{da}{dN} = \frac{\delta^*}{\Delta N} = \frac{\Delta K^2}{4E\varepsilon'_f\sigma'\psi(n')}\frac{\left(2\Delta N\right)^{-(b+c)}}{\Delta N} - \frac{\rho_c}{\Delta N} \tag{2.37}$$

The critical blunting radius, ρ_c may be computed for threshold fatigue crack propagation conditions, resulting the final expression for the fatigue crack growth rate as:

$$\frac{da}{dN} = 2\delta^*\left[\frac{\Delta K^2 - \Delta K_{th}^2}{4E\varepsilon'_f\sigma'_f\delta^*\psi(n')}\right]^{-\frac{1}{(b+c)}} \tag{2.38}$$

where ΔK_{th} is the threshold stress intensity factor range. The δ^* is assumed as a material constant to be identified by experimental data analysis. This parameter is assumed to be related to the microstructure and /or microfailure mechanisms. This parameter is in general higher than grain size. To account for the stress ratio effects on the crack propagation model, the authors introduced the mean stress influence on the model as well as an effective stress intensity range.

Peeker and Niemi [71] also proposed a model for fatigue crack propagation based on the local strain approach to fatigue. Besides the fatigue crack propagation modelling, their proposition also included the fatigue crack initiation modelling from notches (see a schematic representation in Figure 2.11). Therefore, an integrated approach was proposed by these authors, innovative with respect to the proposals by Ellyin and Glinka. These authors used the Morrow strain-life equation [33,34] with a mean stress correction to compute the damage of each element, with size δ, used to discretize the

crack path. Elastoplastic stress and strains are computed at each element using Ramberg-Osgood [37] relation together with the Glinka's equivalent strain energy density approach [78]. To apply the elastoplastic approach, the average elastic stresses at each element were computed from elastic solutions based on stress concentration factors (elements at crack initiators) and stress intensity factor/Fracture Mechanics solutions (elements at crack front). These authors also considered the possibility of simultaneous damaging of elements, using the linear summation damage rule. In order to unify the procedure for both crack initiation and crack propagation, the authors introduced the concept of a fictitious stress intensity factor range for notches in order to result the same stress field as resulting from the stress concentration factor. In order to extend the proposed methodology to variable amplitude loading, the authors adopted the crack closure concept to define effective stress intensity factor ranges that will be used to compute the elastic stress fields in the elements ahead of the crack tip.

The model proposed by Peeker and Niemi [71] allowed the description of the near threshold fatigue crack propagation data and the stable crack growth. For the near threshold fatigue crack propagation, the authors derived the following analytical relation:

$$\frac{da}{dN} = C_{el}\Delta K^{m_{el}}$$
$$C_{el} = 2\delta\left[\left(\sigma'_f - \sigma_m\right)\sqrt{2\pi\delta}\right]^{\frac{1}{b'}} \qquad (2.39)$$
$$m_{el} = -\frac{1}{b'}$$

For the stable crack growth, the authors derived the following relations:

$$\frac{da}{dN} = C_{pl}\Delta K^{m_{pl}}$$
$$C_{pl} = 2\delta\left[\varepsilon'\left(\frac{4\pi\delta K'E}{n'+1}\right)^{\frac{1}{n'+1}}\right]^{\frac{1}{c'}} \qquad (2.40)$$
$$m_{pl} = -\frac{2}{c'\left(n'+1\right)}$$

The superposition of the previous two relations led to the following analytical expression for the fatigue crack propagation law:

$$\frac{da}{dN} = \frac{1}{\frac{1}{C_{pl}\Delta K^{m_{pl}}} + \frac{1}{C_{el}\Delta K^{m_{el}}}} \tag{2.41}$$

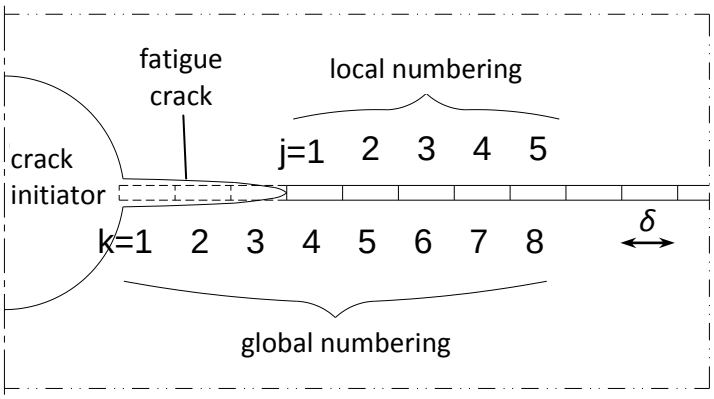

Figure 2.11 – Crack discretization with elements according to the model proposed by Peeker and Niemi [71].

The size of the elements used to discretize the crack path is determined taking into account two criteria: a) the size must be large enough to represent the local material properties by their mean value using continuous variables, and b) its size should be related to material micro-structural parameters, such as the material grain-size. For structural steels, the criteria result in an average element size of 0.1 mm=100μm [71].

Hurley and Evans [76] also proposed a local strain approach to the fatigue crack propagation modelling of a Ti 6246 alloy. These authors proposed the process damage zone being equal to the cyclic plastic zone ahead of the crack tip. The elastoplastic stress/strains at crack tip were computed by means of a non-linear finite element analysis and allowing the damage state of the cyclic plastic zone to be determined. The fatigue life of the process zone was computed using the Walker strain that was correlated directly with the fatigue life, from the experimental data using a power relation. This Walker strain is defined according to the following relation:

$$\varepsilon_W = \frac{\sigma_{max}}{E}\left(\frac{\Delta\varepsilon E}{\sigma_{max}}\right)^w \tag{2.42}$$

where σ_{max} is the maximum stress, E is the Young modulus, $\Delta\varepsilon$ is the strain range and w is a constant varying between 0 and 1. These authors applied the following definition of

the cyclic plastic zone, which is assumed to equal the process damage zone under plane strain conditions:

$$\Delta a_i = \frac{1}{3\pi}\left(\frac{\Delta K}{2\sigma_0}\right)^2 \tag{2.43}$$

where σ_0 is the cyclic yield stress and ΔK the stress intensity factor range computed from the numerical model. The approach proposed by these authors was much simpler than those proposed by the previous authors. It was supported by numerical models disregarding analytical aspects that allowed other authors to demonstrate the relation between these local approaches to fatigue crack modelling and the fracture mechanics approaches for fatigue crack propagation modelling.

2.5. PROBABILISTIC APPROACHES TO FATIGUE

Neglecting the probabilistic nature of the fatigue process by using a deterministic approach when lifetime predictions are intended contradicts the principles of structural integrity criteria and would have devastating consequences for the metallic bridges, aeronautic and machines industry, among others. Such limiting deterministic approaches can only be justified as long as the state of knowledge does not allow the development and proposition of more suitable probabilistic models for practical use.

Many sources of scatter may affect fatigue results (e.g. material variability, production variables). In order to allow the establishment of adequate safety levels on mechanical components/structural details, the several sources of scatter must be conveniently accounted for, the probabilistic approaches to fatigue appearing as an answer to this concern.

2.5.1 Global overview of probabilistic models for fatigue

One concern of the probabilistic approaches to fatigue is to account for the scatter in the *S-N* curves, and make possible the definition of appropriate reliability levels when they are applied in fatigue assessments. In reference [79], a discussion about the typical scatter in the *S-N* curve was presented. This scatter raises as the fatigue life increases and

stress amplitude decreases (see Figure 2.12).

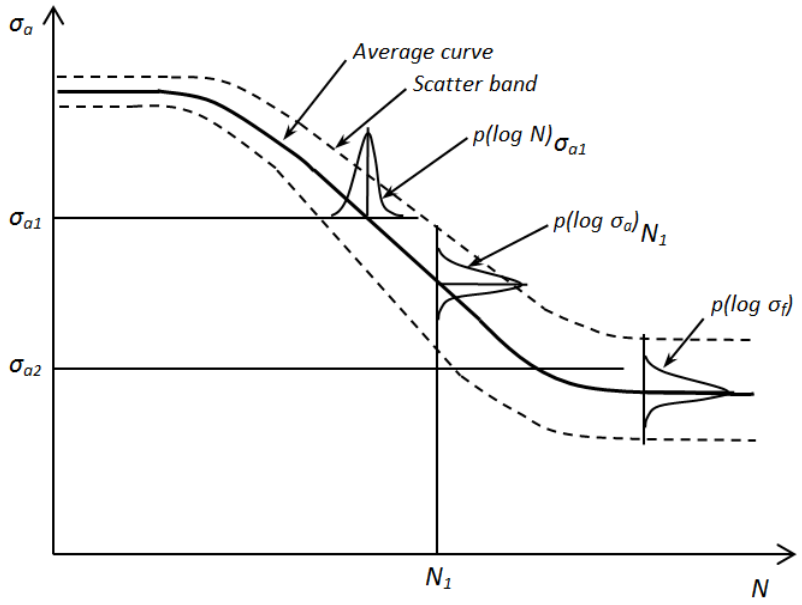

Figure 2.12 – Typical scatter band in a *S-N* curve [79].

In the engineering practice, the scatter of the *S-N* curves is accounted for by a very simple practical approach: performing a linear regression analysis on $log(N_f)$ vs. $Log\ (\sigma_a)$ data and determining a mean *S-N* curve with the respective standard deviation, assuming a LogNormal distribution for the number of cycles given the stress range. Afterwards, safety margins are established using the lower two-sigma or three-sigma design curve method. This means that the design curve can be derived by shifting the median strain–life curve in log coordinates to the left by two or three times the sample standard deviation. This is the case of the majority of existing design codes (e.g. EC3, BS5400, AASHTO). This fails to account for the statistical distribution of the results with respect to the sample size and the possible reliability/confidence levels required. Also it does not account for the variable scatter along the fatigue domain and may be not adequate for very high cycle fatigue lives. This process is already established in materials standards such as the ASTM E739 [80].

Zhao *et al.* [81] proposed a probabilistic fatigue *S–N* field including the super-long life regime for a railway axle steel. The curves and the fatigue limits, which are connected together in concurrent probability levels, are estimated by the test data in the mid-long life regime. The proposed field seek the improvement of existing code *S-N* curves which is commented by the authors to be very conservative for long-term fatigue lives. In this

study the LogNormal distribution was assumed for the fatigue lives given the stress amplitude.

Schijve [79] presented a discussion about statistical distribution functions that are popular on fatigue assessment of structures. According to this author, the statistical distributions for fatigue problems cannot be derived from a physical description of the fatigue phenomenon, in spite of the fact that the knowledge about fatigue damage of a material is fairly well developed in a qualitative way. As a consequence, a statistical distribution function must be assumed. In reference [79] an analysis of the *log(N)* normal, the 3-parameter Weibull and the 3-parameter $log(N-N_0)$ normal distributions were discussed using experimental fatigue data relative to series of similar fatigue tests (imposing stress ranges and measuring fatigue lives). A good fit of test results in the range of the test data was verified using the $log(N-N_0)$-normal and the 3-parameter Weibull distribution functions. This is not fulfilled by the *log(N)*-normal distribution function if the test data indicate a skew distribution. Secondly, extrapolation of the distribution function to very low probabilities of failure remains an uncertain procedure. It means that the distribution function is actually unknown. This type of investigation tries to investigate the suitability of existing statistical distributions to describe specific locations of the *S-N* field, but does not answer the question of the complete *P-S-N* field.

In the literature one may find relevant work trying to model the complete probabilistic *S-N* field. This is the case of the works by Basternaire [82], Spindel and Haibach [83] and Pascual and Meeker [84]. More recently the works by Castillo and Fernández-Canteli, gave new momentum to the analytical probabilistic models for the description of the complete Wohler field, using both physical and statistical conditions. The latter approach will be described in more detail in the next section due to the relevance it represents for the current investigation.

One of the most popular probabilistic approaches adopted in the literature for fatigue analysis in existing deterministic models, consists in incorporating the variability of their individual parameters/properties through adequate probabilistic distributions. The parameters/properties are assumed random variables following specific probabilistic

distributions. The output of the model may be computed using sampling techniques such as Monte Carlo and could be for example the complete *p-S-N* field of a mechanical component or structural detail. This approach allows complex fatigue models to be used, previously validated using deterministic approaches, and permits the derivation of probabilistic outputs of these models to be performed, otherwise impossible to achieve in an analytical explicit form. This has been accomplished for both fatigue crack initiation and fatigue crack propagation problems. For example, Correia et al. [85] and Sanches et al. [86] have proposed this approach for the probabilistic modelling of the fatigue strength of riveted joints from old bridges. These authors adopted the local fatigue approaches for fatigue crack initiation modelling and the fracture mechanics approaches to model the fatigue crack propagation. Uncertainty in the parameters of the models was accounted for assuming random variables following specific statistical distributions and Monte Carlo sampling was used to derive the *P-S-N* field for the riveted joints. In this approach, besides the fatigue parameters uncertainty, uncertainty in mechanical parameters influencing the behaviour of the joint such as friction and clamping stresses was included in the approach. The macroscopic crack definition was also considered as a random variable.

Kandarpa *et al.* [87] applied the strain-life relation by Morrow to assess the fatigue behaviour of notched specimens. The material constants characterizing the strain-life equation are assumed random variables. It is interesting to note that they adopted LogNormal distributions for the ductility and strength fatigue coefficients and normal distributions for the respective exponents and for the stress concentration factor of the notched details. Importance factors for the material constants characterizing the problem are analysed to determine which uncertainties are most significant. The failure probability was computed using a first-order reliability method (FORM), second-order reliability method (SORM) and Monte-Carlo simulation (MCS). Comparison of the results indicated that SORM and MCS provided similar results, whereas the FORM results have over-predicted the failure probabilities.

Concerning the formulation of local strain based probabilistic approaches based on Morrow strain-life relations, Meggiolaro and Castro [88] performed a statistical

assessment of the parameters from the ε-N Coffin-Manson and σ-ε Ramberg-Osgood relation, taking into account a significant database of materials (steels and aluminium alloys). Statistical distributions were tested for each one of the involved parameters.

Ni and Mahadevan [89] proposed a probabilistic approach for fatigue life prediction of spot-welded joints used in automotive industry. They adopted a local approach based on a strain-life relation based on Morrow's equation. This strain-life relation was converted into a probabilistic one, assuming a random nature to the four strength and ductility fatigue constants implied, following statistical distributions based on available experimental data. In this way, they were able to derive the p-ε-N field. In addition, the authors proposed the use of a probabilistic Miner approach to deal with variable amplitude loading data. The following relation was proposed:

$$\sum_i \frac{n_{pi}}{N_{fpi}} = 1 \tag{2.44}$$

where N_{fpi} is obtained from the family of p-ε-N curves.

Zhao *et al.* [90] proposed a framework for a strain-based fatigue reliability analysis. The analysis-related experimental methods and test data are worked out first. The random models, considering the entire material constants as dependent random variables using the Morrow law and the modified Ramberg–Osgood equation, respectively, for random cyclic strain–life and stress–strain relations are then successively proposed with considerations of survival probability and sampling size related confidence. Reliability methods are established on a basic consideration of the random cyclic straining applied and capacity interference. Some deficiencies have been overcome from the assumption of incomplete independent random variables, the lack of consideration of the random cyclic stress–stress relations, and the empirical selections of partial statistical parameters in existent methods.

Williams *et al.* [91] proposed a method for the development of statistical strain–life curves from strain controlled fatigue test data. The method establishes i) a series of selection criteria ensuring that the data used in the statistical analysis are significant and truly representative of the material behaviour; ii) a procedure for the statistical analysis

that ensures that each domain of material behaviour is accurately represented; iii) a method based on the approximate Owen tolerance limit to account for the nature of scatter fatigue data. The approximate Owen Tolerance limit method allows the establishment of reliability/confidence levels as a function of the sample size.

Probabilistic fatigue life prediction based on fracture mechanics approach is a topic that requires a significant development, particularly due to the absence of fully probabilistic analytical models for fatigue crack propagation. However it is recognized that fatigue crack propagation is a stochastic process. The approach to reach probabilistic life predictions, using a fracture mechanics approach consists in adopting a deterministic fatigue crack propagation approach and assuming that its parameters are random variables following specific statistical distributions based on both experimental data and empirical assumptions. This approach was followed by Liu and Mahadevan [92] to derive probabilistic *S-N* fields. They adopted the theory of the equivalent initial flaw size (EIFS) and deterministic fatigue crack propagation. Afterwards, they proposed a distribution for the *EIFS* (lognormal) while for the crack propagation law they fixed the exponent and assumed the coefficient as well as the threshold stress intensity factor as being random variables. Using the Monte Carlo sampling and integrating the crack propagation law, the authors were able to predict the probabilistic *S-N* field.

The analysis of variability on parameters of existing deterministic crack propagation laws was performed by various authors. Virkler et al. [93] analysed the statistical distribution of crack propagation in 2024-T3 aluminium centre cracked plates. Tests were conducted on sixty-eight identical specimens with constant amplitude loading. Experimental results showed large amounts of variability in the crack growth rates. They conclude that the fatigue life to reach a certain crack length was best described by the 3 parameter lognormal distribution. Annis [94] performed a Monte Carlo analysis and compared results to experimental data presented by Virkler et al. [93]. If random variables are selected for both C and m constants in the Paris equation, the Monte Carlo simulation results in a variation more than seven times greater than the variation in the experimental data. He proposed that C cannot be picked independently of m so that a bivariate normal distribution must be used. Multivariate normal distributions could be

considered if more than two constants are correlated. Applying this concept, Annis reduced the error to approximately 1% [95]. Some authors, knowing this conclusion decide to fix one parameter of the Paris relation and assume random the other parameter.

Ellyin and Fakinlede [96] proposed a probabilistic fatigue crack growth model based on a nonlinear damage accumulation criterion. The damage criterion takes awareness of the effect of the loading sequence, and is an energy-based function. This model founds some support on deterministic model proposed by Ellyin and Kujawshi [31]. However, in this case the model considers simultaneous damage on several material elements distributed along the full reversed plastic zone and not only on one element with the size of the process zone (see Figure 2.10). The loading history in each element is accounted for by a non-linear damage accumulation rule supported by an energetic-life relation. The failure of one discretization element positioned at the cyclic plastic zone is dictated by a probabilistic Miner rule, where a unit random variable replaces the deterministic unit value.

2.5.2. Overview of probabilistic models by Castillo and Fernández-Canteli

Castillo and Fernández-Canteli proposed a set of probabilistic models for fatigue damage modelling, based on the Weibull distribution and its limiting Gumbel distribution for $\beta \to \infty$. These models are supported by both physical and statistical assumptions leading to a basic probabilistic *S-N* field as well as a basic probabilistic ε-*N* field. Such fields may be applied to describe the fatigue behaviour of both smooth and sharp notched specimens corresponding to mechanical details and structural components including the consideration of run-outs.

2.5.2.1. Probabilistic S–N field for fixed stress level

Castillo and Fernández-Canteli [18] derived a Weibull regression model for variable stress range and fixed stress level (e.g. stress ratio, mean stress). This model, being formulated in the stress space, is recommended for medium to high or even very high cycle fatigue. The derivation of the model is based on satisfaction of physical conditions (identification

of involved variables, dimensionless analysis) and statistical requirements (weakest link principle, stability, limited range, limit behavior). In addition, ~~a~~ fulfilling of the necessary compatibility condition between lifetime distribution for a give stress range and stress range distribution for a given lifetime leads to a functional equation, the solution of which provides the following distribution, defining the probabilistic S-*N* field [18]:

$$F(\log N;\log\Delta\sigma)=p=1-\exp\left\{-\left[\frac{(\log N-B)(\log\Delta\sigma-C)-\lambda}{\delta}\right]^{\beta}\right\} \qquad (2.45)$$

$$(\log N-B)(\log\Delta\sigma-C)\geq\lambda$$

where: N is the lifetime; $\Delta\sigma$ is the stress level; $F()$ is the cumulative probability distribution function (cfd) of N for given $\Delta\sigma$; $B=\log(N_0)$, N_0 being a threshold value of lifetime; $C=\log(\Delta\sigma_0)$, $\Delta\sigma_0$ being the endurance fatigue limit; and λ, β and δ are nondimensional model parameters (β: Weibull shape parameter; δ: Weibull scale parameter; λ: Weibull location parameter defining the position of the zero-percentile curve). The model defined by Equation (2.45) has been studied and successfully applied to different lifetime assessments [18,97-99]. Equation (2.45) may be rewritten for normalized number of cycles (N^*) and normalized stress range ($\Delta\sigma^*$):

$$F(\log N;\log\Delta\sigma)=p=1-\exp\left\{-\left[\frac{\log N^*\log\Delta\sigma^*-\lambda}{\delta}\right]^{\beta}\right\} \qquad (2.46)$$

$$\log N^*\log\Delta\sigma^*\geq\lambda$$

where: $N^*=N/N_0$ is the normalized number of cycles and $\Delta\sigma^*=\sigma_M^*-\sigma_m^*$ is the normalized stress range; $\sigma_M^*=\sigma_M/\sigma_0$ is the normalized maximum stress and $\sigma_m^*=\sigma_m/\sigma_0$ is the normalized minimum stress; σ_M and σ_m are respectively the maximum and minimum stresses of a cycle; N_0 and σ_0 can be identified, respectively, as $\exp(C)$ and $\exp(B)$ converting the formulas dimensionless. Figure 2.13 represents the Weibull *p-S-N* field, with some representative percentile curves illustrated. The percentile curves are hyperbolas sharing the asymptotes $\log N=B$, representing the fatigue limit (horizontal asymptote) and $\log\Delta\sigma=C$, representing the lifetime threshold (vertical asymptote). The zero percentile curve displays the minimum possible required number of cycles to achieve failure for different values of $\Delta\sigma$.

Both asymptotes of the *S-N* field limit its domain of applicability to specific subdomains of the field. The vertical asymptote is more controversial account given of the plastic effects that appear in the region of low cycle fatigue making the real percentile curves to inflect downwards at this region. The horizontal asymptote is not controversial even for those materials that do not exhibit a clear fatigue limit as is the case of some aluminum alloys, since the model encompasses the case *C*=0.

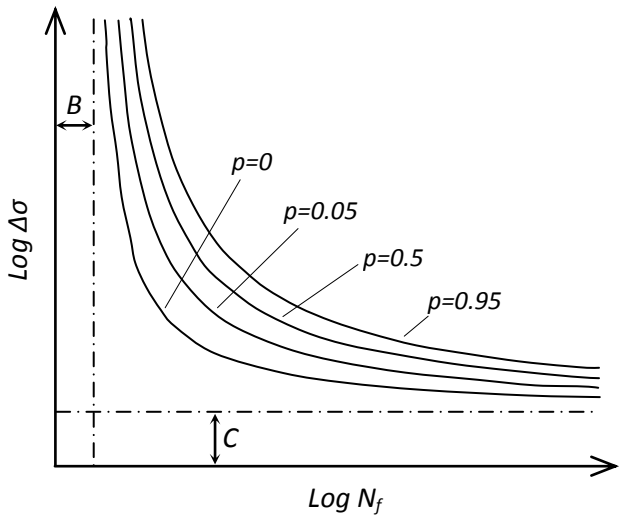

Figure 2.13 – Probabilistic *S-N* field according to the Weibull model proposed by Castillo and Fernández-Canteli.

An alternative for the relations (2.45) and (2.46) were also proposed by authors, using the Gumbel distribution as a limiting case of the Weibull distribution when $\beta \to \infty$, or even for $\beta > 8$:

$$F(\log N;\log \Delta\sigma) = p = 1 - exp\left\{-exp\left[\frac{(\log N - B)(\log \Delta\sigma - C) - \lambda}{\delta}\right]\right\} \tag{2.47}$$

or for non-dimensional variables:

$$F(\log N;\log \Delta\sigma) = p = 1 - \exp\left\{-\exp\left[\frac{\log N^* \log \Delta\sigma^* - \lambda}{\delta}\right]\right\} \tag{2.48}$$

with the same meaning of the symbols as before. Concerning the parameter identification, the process includes two steps: a) estimation of the threshold parameters *B* and *C* using the constrained least square method, and b) estimation of the Weibull parameters, λ, β and δ by the maximum likelihood method [18] once the threshold parameter are known.

In order to illustrate the procedure, let $(\Delta\sigma_i,N_i)|i=1,2,\ldots,n\}$ be a set of pairs, where $\Delta\sigma_i$ is the deterministic stress range of the specimen *i*, and N_i is the resulting experimental random lifetime. The procedure to estimate the threshold parameters is based on a constrained least squares method, from which result the following equation and constraints:

$$\underset{B,C,K_1,K_2,\ldots K_i}{Minimize} \quad Q_{CLS} = \sum_{i=1}^{n} w_i \left(\log N_i - B - \left(\frac{K_i}{\log \Delta\sigma_i - C} \right) \right)^2, \tag{2.49}$$

$$\begin{aligned} C &\le \min_i \left(\log \Delta\sigma_i \right) \\ B &\le \min_i \left(\log N_i \right) \end{aligned} \tag{2.50}$$

where w_i are the weights. The constraints listed by (2.50) are included to guarantee that the values *B* and *C* are valid threshold values for all data points. If the sample contains run-outs, that is, right censored data points, associated with a certain given limit number of cycles, their lifetimes are not known; thus, an iterative process may be used to assign them to the expected final number of cycles [18].

Once *B* and *C* have been estimated, the Weibull constants may be evaluated using a constrained maximum likelihood method. All the data points can be pooled together, in sets of equal lengths, by calculating:

$$v_i = \left(\log N_i - B \right)\left(\log \Delta\sigma_i - C \right) = N_i^* \Delta\sigma_i^* \tag{2.51}$$

The log-likelihood for broken specimens i.e. run-outs that without loss of generality can be assumed to be the first n_1<n specimens, becomes

$$\log f(v) = -\left[\frac{v-\lambda}{\delta} \right]^{\beta} + \log\beta + (\beta - 1)\log\left[\frac{v-\lambda}{\delta} \right] - \log\delta, \quad v \ge \lambda \tag{2.52}$$

and for the run-outs

$$\log(1 - F(v)) = -\left[\frac{v-\lambda}{\delta} \right]^{\beta}, \quad v \ge \lambda \tag{2.53}$$

Finally, an optimization problem is solved,

$$\max_{\lambda,\delta,\beta} Q_l = -\sum_{i=1}^{n}\left[\frac{v_i-\lambda}{\delta_i}\right]^{\beta} + (\beta-1)\sum_{i=1}^{n_1} log\left[\frac{v_i-\lambda}{\delta_i}\right]^{\beta} + n_1 \log\beta - \sum_{i=1}^{n_1}\log\delta_i \tag{2.54}$$

subjected to,

$$\min_i v_i \geq \lambda + \delta_i\left[-\frac{1}{n}log(1-\alpha)\right]^{1/\beta} \tag{2.55}$$

where α can be taken as 0.01. The constraint defined by Equation (2.55) is imposed to avoid data below the threshold value of lifetime, i.e.

$$\min_i v_i \geq \lambda \tag{2.56}$$

The solution of the maximization problem leads to an unbounded likelihood value. It states that the minimum value must be greater than its corresponding α 100 percentile value, that is,

$$F_{\min_i} x = 1 - exp\left[-\left(\frac{x-\lambda}{\delta_i n^{1/\beta}}\right)^{\beta}\right] \geq \alpha \tag{2.57}$$

More details about the parameters identification procedure can be found in reference [18].

2.5.2.2. Probabilistic S–N field for varying stress level

The model parameters *B*, *C*, λ, β and δ described by Equations (2.45) and (2.46) may be identified using experimental data from fatigue tests run according to one of the following test conditions: i) fixed σ_M and varying σ_m; ii) fixed σ_m and varying σ_M, and iii) fixed σ_m/σ_M and varying σ_m and σ_M. Each test condition leads to distinct model parameters. Therefore, the parameters are a function of σ_M for test conditions i) ,~~and~~ a function of σ_m for test conditions ii) and a function of σ_m/σ_M for test conditions iii). The three test conditions must be compatible (see illustration in Fig. 2.14), which means that parameters identified for the three test conditions are not independent. This compatibility condition is the basis for a more general Weibull probabilistic model that accounts for variable stress range and stress level [18, 97, 99-102]:

$$p = 1 - exp\left\{-\left[C_0 + C_1\sigma_m^* + C_2\sigma_M^* + C_3\sigma_m^*\sigma_M^* + (C_4 + C_5\sigma_m^* + C_6\sigma_M^* + C_7\sigma_m^*\sigma_M^*)\log N^*\right]^A\right\} \quad (2.58)$$

The graphs ($log\ N$, $\Delta\sigma$) of the percentiles (Equation (2.48)) for constant σ_M or σ_m are hyperbolas. C_0, C_1, C_2, C_3, C_4, C_5, C_6 and C_7 are dimensionless parameters subject to a number of restrictions [103]:

$$C_4 \geq 0 \quad (2.59)$$

$$C_5 - C_4 \leq 0 \quad (2.60)$$

$$-C_5 - C_4 \leq 0 \quad (2.61)$$

$$-C_4 + C_5 - C_6 + C_7 \leq 0 \quad (2.62)$$

$$-C_4 - C_5 - C_6 - C_7 \leq 0 \quad (2.63)$$

$$C_3C_6 - C_2C_7 \geq 0 \quad (2.64)$$

$$C_3C_5 - C_1C_7 \geq 0 \quad (2.65)$$

$$C_6(C_6(C_0 + \gamma) - C_2C_4) \leq 0 \quad (2.66)$$

$$C_5(C_5(C_0 + \gamma) - C_1C_4) \leq 0 \quad (2.67)$$

where γ=0.57772 is the Euler-Mascheroni number. Constraints (2.59)-(2.67) emerge from the following physical conditions:

i) The asymptotic value of $\Delta\sigma$ for large N and constant σ_m must be non-negative, and, due to physical reasons, must be non-increasing with σ_m; the asymptotic value of Δσ for large N and constant σ_M must be non-negative, and, due to physical reasons, must be non-increasing with σ_M.

ii) The percentile curves defined in Equation (2.58) must be non-decreasing in log N, non-increasing in σ_m and non-decreasing in σ_M.

iii) The curvature of the zero-percentile of (log N, $\Delta\sigma$) for constant σ_m must be non-negative, and, in the case of constant σ_M must be non-negative.

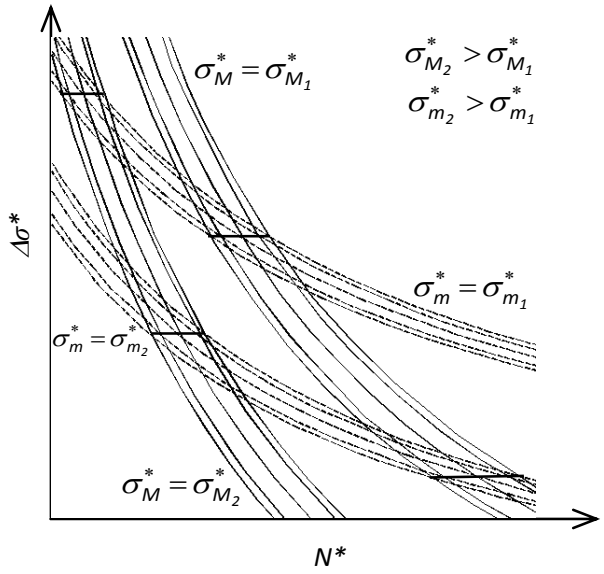

Figure 2.14 – Schematic P-S-N fields for constant σ_{M1}^* and σ_{M2}^*, and constant σ_{m1}^* and σ_{m2}^*, illustrating the compatibility condition. Dashed lines refer to *S-N* curves for constant σ_m^*, and continuous lines refer to *S-N* curves for constant σ_M^* [18].

2.5.2.3. Probabilistic ε–N field

Since the proposed probabilistic fields formulated in stress space are applicable to medium to high or even very high cycle fatigue, Castillo and Fernández-Canteli also proposed the extension of the *p-S-N* field, developed for varying stress range and fixed stress level, to a strain space formulation. The mathematical structure of the model is kept, and only a change of variables is proposed leading to the following relations based on a Weibull distribution:

$$F\left(N^*;\varepsilon_a^*\right)=1-\exp\left\{-\left[\frac{\left(\log(N)-B\right)\left(\log(\varepsilon_a)-C\right)-\lambda}{\delta}\right]^{\beta}\right\}, \quad \log(N)\geq B+\frac{\lambda}{\left(\log(\varepsilon_a)-C\right)} \tag{2.68}$$

or using normalized variables

$$p=F\left(N^*;\varepsilon_a^*\right)=1-\exp\left\{-\left[\frac{\log(N/N_0)\log\left(\varepsilon_a/\varepsilon_{a0}\right)-\lambda}{\delta}\right]^{\beta}\right\}, \quad \log(N/N_0)\log\left(\varepsilon_a/\varepsilon_{a0}\right)\geq\lambda \tag{2.69}$$

where $B=\log(N_0)$, $C=\log(\varepsilon_{a0})$ and λ, δ, β are the Weibull parameters. The percentile

curves are defined as:

$$N_f = exp\left[B + \frac{\lambda + \delta\left(-log\left(1-p\right)\right)^{1/\beta}}{log\left(\varepsilon_a\right) - C} \right] \tag{2.70}$$

When considering the Gumbel distribution, the following relations result for the *p*-ε-*N* field:

$$F\left(N^*;\varepsilon_a^*\right) = 1 - exp\left\{ -exp\left[\frac{\left(log(N) - B\right)\left(log(\varepsilon_a) - C\right) - \lambda}{\delta} \right] \right\} \tag{2.71}$$

or

$$p = F\left(N^*;\varepsilon_a^*\right) = 1 - exp\left\{ -exp\left[\frac{log\left(N/N_0\right) log\left(\varepsilon_a/\varepsilon_{a0}\right) - \lambda}{\delta} \right] \right\} \tag{2.72}$$

Figure 2.15 illustrates the Weibull field, which maintains the same characteristics of the previous referred *p*-*S*-*N* fields.

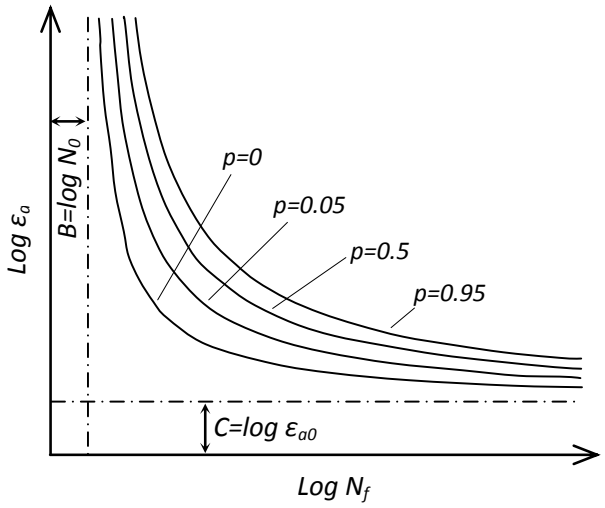

Figure 2.15 – Percentile curves representing the relationship between dimension lifetime, N_f, and the strain amplitude, ε_a, accordingly the *p*-ε_a-*N* Weibull field.

The model proposed by Castillo and Fernández-Canteli for the *p*-ε-*N* field model provides a complete analytical description of the statistical properties of the physical problem being dealt with, including the quantile curves without the need of separating the total strain in its elastic and plastic components but dealing with the total strains directly [18]. This model may be considered a probabilistic counterpart to the Coffin-Manson relation. However, with respect to the classical Coffin-Manson relation, the new probabilistic

model shows some advantages. It arises from sound statistical and physical assumptions and not from an empirical arbitrary assumption; it provides a probabilistic definition of the whole strain-life field; does not need to consider separately the elastic and the plastic strains; the run-outs are also included in the analysis [18], and facilitates the cumulative damage analysis. Nevertheless, one weakness of the proposed *p*-ε-*N* field is the vertical asymptote which does not find physical support. This issue limits the applicability of the probabilistic field to a subdomain excluding the region at the vicinity to this asymptote unless the Gumbel distribution is assumed. Consequently, extrapolations carried out with this model for values out of the domain of experimental data and for a subdomain approaching the vertical asymptote should be performed with care.

The *p*-ε-*N* field opens new opportunities for the local approaches to fatigue, which was not guaranteed by the Coffin-Manson or Morrow relations. In particular, due to its probabilistic formulation it accounts in a convenient way for the scatter in the strain-life data. In fact, the *p*-ε-*N* field has been successfully applied to model fatigue crack initiation in joints [104].

The *p*-ε-*N* field may be transformed into the *p*-σ-*N* field applying a direct replacement of the strains by stresses [105]. This transformation may be explicitly performed for smooth specimens under uniaxial stress states. The strains are related to the stresses using the Ramberg-Osgood relation of the material for cyclic loading. Introducing the Ramberg-Osgood relation for cyclic loading into the Equation (2.69) results the following relation:

$$F\left(N^*;\varepsilon_a^*\right)=1-exp\left\{-\left[\frac{\left(log(N)-B\right)\left(log\left(\frac{\sigma_a}{E}+\left(\frac{\sigma_a}{K'}\right)^{1/n'}\right)-C\right)-\lambda}{\delta}\right]^{\beta}\right\}, \qquad (2.73)$$

$$log(N)\geq B+\frac{\lambda}{\left(log\left(\frac{\sigma_a}{E}+\left(\frac{\sigma_a}{K'}\right)^{1/n'}\right)-C\right)}$$

which represents a *p*-*S*-*N* field. The proposed transformation for the *p*-ε-*N* field leads to a *p*-σ-*N* showing a sigmoidal shape, which result from the Ramberg-Osgood relation that predicts bounded stresses for higher strain amplitudes (see Figure 2.16).

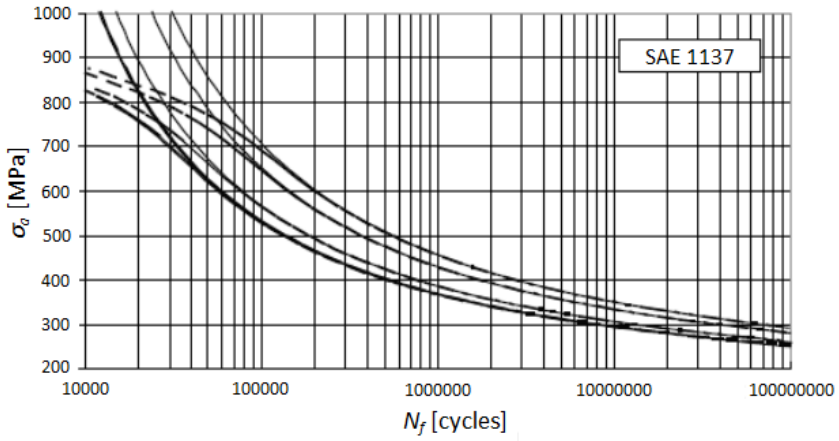

Figure 2.16 – Transformation of the *p*-ε-*N* field into the *p*-σ-*N* field for the SAE 1137 material [18].

2.5.2.4. Relation between damage and probability of failure

Castilo and Fernández-Canteli [18] suggested the use of the percentile curves of the proposed probabilistic fields to represent a damage state. Since the percentile curves of the probabilistic fields represent the number of cycles to failure to be conducted at different stress or strain ranges yielding the same probability of failure, it was suggested that the percentile curves could rather be contemplated as curves representing a determined damage state. Figure 2.17a) shows four different stress histories leading to the same damage (*p* value). In this case the consideration of *p* is equivalent to use *V* as the normalization variable. This normalization variable, for the *p*-*S*-*N* field proposed for fixed stress level (see Equation (2.46)), is defined as:

$$V=\left(\log N^{*}\right)\left(\log\Delta\sigma^{*}\right)=\left(\log N-B\right)\left(\log\Delta\sigma-C\right) \tag{2.74}$$

The normalization variable follows a Weibull distribution, increasing monotonically with the probability of failure:

$$p=1-\exp\left\{-\left[\frac{V-\lambda}{\delta}\right]^{\beta}\right\},V\geq\lambda \tag{2.75}$$

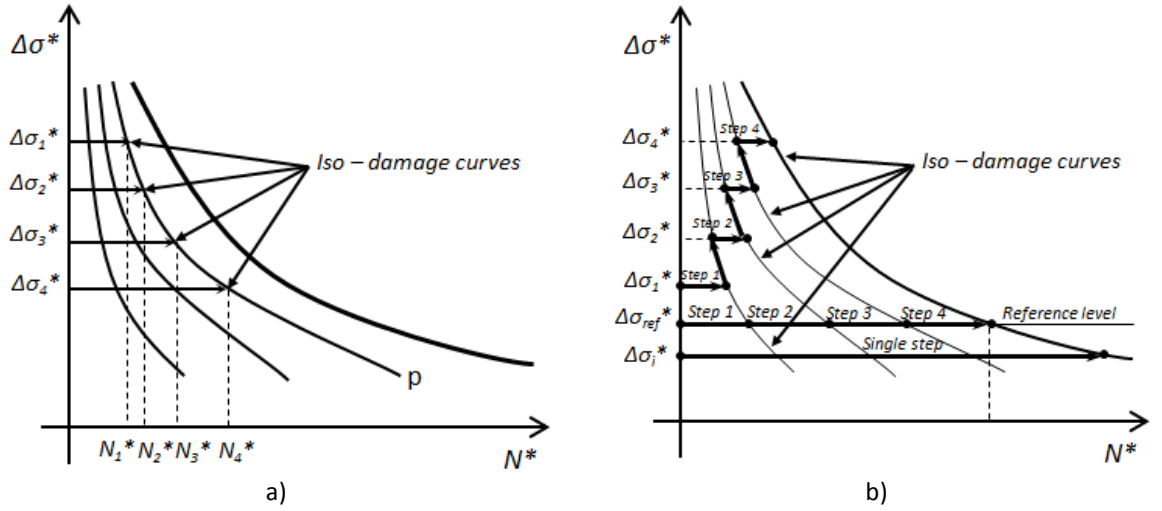

Figure 2.17 – Interpretation of the damage concept using the probabilistic field: a) illustration of four different load histories leading to the same damage (p or V values); b) schematic representation of the conversion process for three load histories to a reference constant amplitude level leading to the same damage [18].

Using the normalizing concept, the case of multi-step loading, i.e., block loading, can be regarded as a simple extension of the one-step or constant load case, provided the number of cycles at a certain stress range can be replaced by an equivalent number of cycles at the onset of the subsequent stress range (see Figure 2.17b)). The four step load produces the same damage as the constant amplitude loads represented. In the representation of the block loading, the evolution in the number of cycles could be interpreted as having apparent sudden decreases, when the stress ranges change to higher levels, but the correct interpretation is that the damage state is kept constant during the stress range changes, and increases continuously during the loading process. This figure only explains how to obtain an equivalent number of cycles, in terms of damage, for two different stress ranges (the larger the stress range, the smaller the lifetime). This is accomplished as long as the damage measure, identified with the normalized variable p or V^* is maintained in each conversion.

The above damage considerations, based on p-S-N fields, are also extendable to the p-ε-N fields.

In order to predict the number of cycles to failure, one must specify a target probability to predict the fatigue failure for the component and follow the procedure depicted in Figure

2.17b) for the variable amplitude loading. The target probability should represent the quality level of the component, a higher damage value should correspond to high quality and a lower damage value should correspond to low quality of the specimens.

2.6. REFERENCES

[1] Schütz W. A History of Fatigue. Eng. Fract. Mech. 1996; 54, pp. 263–300.

[2] Miner MA. Cumulative damage in fatigue. Transactions of The ASME. Series E. J. Appl. Mech., Vol. 12, pp. 159–164, 1945.

[3] Coffin LF. A study of the effects of the cyclic thermal stresses on a ductile metal. Trans ASME 1954;76:931–50.

[4] Manson SS. Behaviour of materials under conditions of thermal stress, NACA TN-2933. National Advisory Committee for Aeronautics; 1954.

[5] Paris PC, Gomez M, Anderson WE. A rational analytic theory of fatigue. Trend Engineering 1961; 13: 9-14.

[6] Beden SM, Abdullah S, Ariffin AK. Review of Fatigue Crack Propagation Models for Metallic Components. European Journal of Scientific Research 2009; 28: 364-397.

[7] Elber W. Fatigue crack closure under cyclic tension. Engineering Fracture Mechanics, 2, PP. 37-45; 1970.

[8] Elber W. The significant of fatigue crack closure. In: Damage tolerance in aircraft structures, ASTM STP 486. Philadelphia, PA: American Society for Testing and Materials 1971, pp. 230-242.

[9] Schijve J. Fatigue of structures and materials. Kluwer Academic Publishers, New York; 2004.

[10] Dowling NE. Mean stress effects in stress-life and strain-life fatigue. Society of Automotive Engineers, Inc. 2004; F2004/51.

[11] Boardman B, Deere and et al. Fatigue resistance of steels. ASM Handbook, Volume 1: Properties and selection: Irons, steels, and high-performance alloys. ASM Handbook Committee, 1990; p. 673-688.

[12] Neuber H. Theory of Notch Stresses: Principles for Exact Calculation of Strength With Reference to Structural Form and Material. Berlin: Springer-Verlag (2nd edition), 1958.

[13] Neuber H. Theory of stress concentration for shear-strained prismatic bodies with arbitrary nonlinear stress–strain law. Trans. ASME Journal of Applied Mechanics, 1961; 28: 544–551.

[14] Peterson RE. Notch Sensitivity. In: Metal Fatigue, G. Sines and J. L. Waisman, eds., McGraw Hill, New York, pp. 293–306, 1959.

[15] Taylor D. The Theory of Critical Distances: A New Perspective in Fracture Mechanics. Oxford: Elsevier, 2007.

[16] Susmel L, Taylor D. Fatigue Design in the Presence of Stress Concentrations. J. Stain Anal., 2008; 38 (5), pp. 443-452.

[17] Bowman MD. Fatigue design and retrofit of steel bridges. Progress in Structural Engineering and Materials, I997 Vol. I (I): 107-114.

[18] Castillo E, Fernández-Canteli A. A Unified Statistical Methodology for Modeling Fatigue Damage. Springer, 2009.

[19] Kulak GL. Fatigue strength of riveted shear splices. Progress in Structural Engineering and Materials, 2000; 2: 110–119.

[20] Branco CM, Fernandes AA, De Catro PMST. Fadiga de Estruturas Soldadas. Fundação Calouste Gulbenkian, 1986.

[21] Weibull W. Fatigue testing and analysis of results. Pergamon Press LTD., London; 1961.

[22] ASTM – American Society for Testing and Materials. ASTM E739-91: standard practice for statistical analysis of linear or linearized stress-life and strain-life fatigue data. In: Annual book of ASTM standards, vol. 03.01; 2004. p. 1–7.

[23] Kühn B, Lukic´ M, Nussbaumer A, Günther H-P, Helmerich R, Herion S, et al. In: Sedlacek G, Bijlaard F, Géradin M, Pinto A, Dimova S, editors. Assessment of existing steel structures: recommendations for estimation of remaining fatigue life – EUR 23252 EN. JRC – ECCS; 2008.

[24] CEN-TC 250. EN 1993-1-9: Eurocode 3, Design of steel structures – Part 1-9: Fatigue. European Committee for Standardization, Brussels; 2003.

[25] British Standards Institution. BS 5400:– Steel, concrete and composite bridges: Part 10: Code of practice for fatigue. London: BSI. 1980.

[26] AASHTO. AASHTO LRFD: bridge design specification; 1995.

[27] APK – Association pour la Promotion de l'Enseignement de la Construction Acier. Construction métallique et mixte acier-béton: Calcul et dimensionnement selon les Eurocodes 3 et 4. Éditions Eyrolles, Paris; 1996.

[28] Åkesson B, Edlund B. Remaining fatigue life of riveted railway bridges. Stahlbau 1996: 65(11): 429–436.

[29] Helmerich R, Brandes K, Herter J. Full scale laboratory fatigue tests on riveted railway bridges. Proceedings IABSE Workshop, Lausanne, 1997. Zurich: IABSE. 1997. 191–200.

[30] Taras A, Greiner R. Statistical Background to the Proposed Fatigue Class Catalogue for Riveted Components. Report: Contribution to WG6.1 – Assessment of Existing Steel Structures, ECCS TC6 – 2010, Spring Meeting – Lausanne – March 22-23, 2010.

[31] Ellyin F. Fatigue damage, crack growth and life prediction. Chapman & Hall, 1997.

[32] Chen H, Grondin GI, Driver RG. Fatigue resistance oh high performance steel. Structural Engineering Report No. 258, University of Alberta, Canada, 2005.

[33] Morrow JD. Cyclic plastic strain energy and fatigue of metals. Int Frict Damp Cyclic Plast ASTM STP 1965; 378: 45–87.

[34] Morrow JD, Socie DF. Evolution of fatigue crack initiation life prediction methods. Materials, experimentation and design in fatigue: Proceedings of Fatigue 1981, Warwick University, England, E. Sherratt and J.B. Sturgeon JB (Editors), Westbury House, Guildford, pp. 3-21.

[35] Dowling NE. Mechanical behaviour of materials: engineering methods for deformation, fracture and fatigue. Second Edition. Prentice Hall, Inc. Upper Saddle River, 1999.

[36] Rice RC, Leis BN, Nelson DV (Editors). Fatigue design handbook. Second Edition. Society of automotive engineers, Warrendale, PA; 1988.

[37] Ramberg W, Osgood WR. Description of stress–strain curves by three parameters. NACA tech. note no. 902; 1943.

[38] Smith KN, Watson P, Topper TH. A Stress-Strain Function for the Fatigue of Metals. Journal of Materials 1970; 5(4): 767-78.

[39] Chan KS, Miller AK. Prediction of fatigue failure in structural alloys: initiation and crack propagation. International Symposium for Testing and Failure Analysis. ASM International, Metals Park, OH, pp. 272-279.

[40] Sarihan V. Energy based methodology for damage and life prediction of solder joints under thermal cycling. IEEE Transactions on Components, Packaging and Manufacturing Technology, Part B, Advanced Packaging, Vol. 17, No. 4, pp. 626-631, 1994.

[41] Kujawski D, Ellyin F. A unified approach to mean stress effect on fatigue threshold conditions. International Journal of Fatigue, Vol. 17, No. 2, pp. 101-106.

[42] Ellyin F, Kujawski D. An energy-based fatigue failure criterion. Microstructure and Mechanical Behaviour of Materials, Vol. II (eds. Gu H, He J), EMAS, West Midlands, UK; 541-600.

[43] Walker EK. The effect of stress ratio during crack propagation and fatigue for 2024-T3 and 7076-T6 aluminum. In: Effect of environment and complex load history on fatigue life, ASTM STP 462. Philadelphia: American Society for Testing and Materials, 1970, pp.1–14.

[44] Dinda S, Kujawski D. Correlation and prediction of fatigue crack growth for different R-ratios using K_{max} and ΔK_C parameters. Eng Fract Mech 2004;71:1779–90.

[45] Donald K, Paris PC. An evaluation of ΔK_{eff} estimation procedure on 6061-T6 and 2024-T3 aluminium alloys. Int J Fatigue 1999;21: S47–S57.

[46] Vasudevan AK, Sadananda K, Louat N. A review of crack closure, fatigue crack threshold and related phenomena. Mater Sci Eng 1994; A188:1–22.

[47] Forman RG. Study of fatigue crack initiation from flaws using fracture mechanics theory. Engineering Fracture Mechanics, 1972; 4(2), PP. 333–345.

[48] Hartman A, Schijve J. The Effects of Environment and Load Frequency on the Crack Propagation law for Macro Fatigue Crack Growth in Aluminum Alloys. Engineering Fracture Mechanics, 1970; 1(4), PP. 615-631.

[49] Dowling NE, Begley JA. Fatigue crack growth during gross plasticity and the Jintegral. Mechanics of Crack Growth. ASTM STP 590, American Society for Testing and Materials, 1976, Philadelphia, PA, pp. 82-105.

[50] Wheeler OE. Spectrum Loading and Crack Growth. Journal of Basic Engineering, March, 1972; 94, PP. 181-186.

[51] Borg J, Engle RM, Wood HA. A crack growth retardation model using an effective stress concept. Air Force Flight Dynamic Laboratory, Dayton, Report AFFDL-TR71-1, 1971.

[52] Varma D. Fatigue Crack Growth. New Age International (P) Ltd., 1990.

[53] Hudson CM. A Root-Mean-Square Approach for Predicting Fatigue Crack Growth under Random Loading, Methods and Models for Predicting Fatigue Crack Growth under Random Loading. ASTM STP 748. Chang JB and Hudson CM, Eds., American Society for Testing and Materials, 1981, pp. 41-52.

[54] Castillo E, Fernández-Canteli A, Siegele D. Obtaining S-N curves from crack growth curves: an alternative to self-similarity, Int. J. Fracture, 2014; Vol. 187, pp. 159-172.

[55] Joint service specification guide aircraft structures, JSSG-2006. United States of America: Department of Defense; 1998.

[56] Gallagher JP, Berens AP, Engle Jr RM. USAF damage tolerant design handbook: guidelines for the analysis and design of damage tolerant aircraft structures, Final report. 1984.

[57] Merati A, Eastaugh G. Determination of fatigue related discontinuity state of 7000 series of aerospace aluminum alloys. Eng Failure Anal 2007; 14(4):673–85.

[58] De Jesus AMP, Da Silva ALL, Correia JAFO. Fatigue of riveted and bolted joints made of puddle iron— A numerical approach. Journal of Constructional Steel Research, Volume 102, November 2014, Pages 164–177.

[59] Krasnowski BR, Rotenberger KM, Spence WW. A damage-tolerance method for helicopter dynamic components. J Am Helicopter Soc 1991;36(2).

[60] Forth SC, Everett Jr RA, Newman JA. A novel approach to rotorcraft damage tolerance. 6th Joint FAA/DoD/NASA aging aircraft conference. 2002.

[61] Liu Y, Sankaran Mahadevan S. Probabilistic fatigue life prediction using an equivalent initial flaw size distribution. International Journal of Fatigue 31 (2009) 476–487.

[62] Yang JN, M.S. Distribution of equivalent initial flaw size. In: Proceedings of the annual reliability and maintainability symposium. San Francisco (CA): 1980.

[63] White P, Molent L, Barter S. Interpreting fatigue test results using a probabilistic fracture approach. Int J Fatigue 2005;27(7):752–67.

[64] Molent L, Sun Q, Green A. Charcterisation of equivalent initial flaw sizes in 7050 aluminium alloy. J Fatigue Fract Eng Mater Struct 2006;29:916–37.

[65] Moreira PMGP, de Matos PFP, de Castro PMST. Fatigue striation spacing and equivalent initial flaw size in Al 2024-T3 riveted specimens. Theor Appl Fract Mech 2005;43(1):89–99.

[66] Fawaz SA. Equivalent initial flaw size testing and analysis; 2000.

[67] Cross R, Makeev A, Armanios E. Simultaneous uncertainty quantification of fracture mechanics based life prediction model parameters. Int J Fatigue 2007;29(8):1510–15.

[68] Makeev A, Nikishkov Y, Armanios E. A concept for quantifying equivalent initial flaw size distribution in fracture mechanics based life prediction models. Int J Fatigue 2007;29(1):141–5.

[69] Savaidis G, Savaidis A, Zerres P, Vormwald M. Mode I fatigue crack growth at notches considering crack closure. International Journal of Fatigue 32 (2010) 1543–1558.

[70] Glinka G. A notch stress-strain analysis approach to fatigue crack growth. Engineering Fracture Mechanics, 1985; Vol. 21, No. 2, pp. 245-261.

[71] Peeker E, Niemi E. Fatigue crack propagation model based on a local strain approach. Journal of Constructional Steel Research, 1999: 49, 139–155.

[72] Noroozi AH, Glinka G, Lambert S. A two parameter driving force for fatigue crack growth analysis. International Journal of Fatigue 2005; 27: 1277-1296.

[73] Noroozi AH, Glinka G, Lambert S. A study of the stress ratio effects on fatigue crack growth using the unified two-parameter fatigue crack growth driving force. International Journal of Fatigue 2007; 29:1616-1633.

[74] Noroozi AH, Glinka G, Lambert S. Prediction of fatigue crack growth under constant amplitude loading and a single overload based on elasto-plastic crack tip stresses and strains. Engineering Fracture Mechanics 2008; 75: 188-206.

[75] Mikheevskiy S, Glinka G. Elastic–plastic fatigue crack growth analysis under variable amplitude loading spectra. International Journal of Fatigue, 2009; 31: 1828–1836.

[76] Hurley PJ, Evans WJ. A methodology for predicting fatigue crack propagation rates in titanium based on damage accumulation. Scripta Materialia 2007; 56: 681–684.

[77] Basquin OH. The exponential law of endurance tests. Proc Am Soc Test Mater 1910;10:625–30.

[78] Molski K, Glinka G. A method of elastic-plastic stress and strain calculation at a notch root. Materials Science and Engineering, 1981; 50: 93-100.

[79] Schijve J. Statistical distribution functions and fatigue of structures. International Journal of Fatigue, 2005; 27, 1031–1039.

[80] ASTM E739-91: Standard Practice for Statistical Analysis of Linear or Linearized Stress-Life (S-N) and Strain Life (ε-N) Fatigue Data. Annual Book of ASTM Standards, American Society for Testing and Materials, 1991, pgs. 597-603.

[81] Zhao YX, Yang B, Feng MF, Wang H. Probabilistic fatigue S–N curves including the super-long life regime of a railway axle steel. International Journal of Fatigue, 2009; 31, 1550–1558.

[82] Basternaire FA. New method for the statistical evaluation of constant stress amplitude fatigue test results. Probabilistic Aspect of Fatigue. American Society for Testing Materials. ASTM STP 511, pages 3–28, 1972.

[83] Spindel JE, Haibach E. Some considerations in the statistical determination of the shape of s − n curves. Statistical Analiysis of Fatigue Data. American Society for Testing Materials. ASTM STP 744, pages 89–113, 1981.

[84] Pascual FG, Meeker WQ. Estimating fatigue curves with the random fatigue-limit model. Technometrics, 41(4):277–290, 1999.

[85] Correia JAFO, De Jesus AMP, Da Silva ALL, Da Silva JFN. A Procedure to derive probabilistic fatigue strength data for riveted joints. In: Proceedings of the 5th International Conference on Bridge Maintenance, Safety, Management and Life-Cycle Optimization – IABMAS'10, Frangopol, Sause & Kusko (Eds.), Philadelphia, PA, USA, July 11-15, 2010.

[86] Sanches RF, De Jesus AMP, Correia JAFO, Da Silva ALL. A Probabilistic Fatigue Approach for Riveted Joints Using Monte Carlo Simulation. Journal of Constructional Steel Research, submitted.

[87] Kandarpa S, Spencer JR BF, Kirkner DJ. Reliability analysis of structural component utilizing the strain-life method. Engineering Fracture Mechanics, 1996; Vol. 53, no. 5, pp. 761-774.

[88] Meggiolaro MA, Castro JTP. Statistical evaluation of strain-life fatigue crack initiation predictions, International Journal of Fatigue 26 (2004) 463–476.

[89] Ni K, Mahadevan S. Strain-based probabilistic fatigue life prediction of spot-welded joints. International Journal of Fatigue 26 (2004) 763–772.

[90] Zhao YX, Yang B, Zhai ZY. The framework for a strain-based fatigue reliability analysis. International Journal of Fatigue 30 (2008) 493–501.

[91] Williams CR, Lee YL, Rilly JT. A practical method for statistical analysis of strain–life fatigue data. International Journal of Fatigue 25 (2003) 427–436.

[92] Liu Y, Sankaran Mahadevan S. Probabilistic fatigue life prediction using an equivalent initial flaw size distribution. International Journal of Fatigue 31 (2009) 476–487.

[93] Virkler D, Hillberry B, Goel P. The Statistical Nature of Fatigue Crack Propagation. Journal of Engineering Materials and Technology, 1979; 101, pp. 148 - 153.

[94] Annis C. Probabilistic Life Prediction Isn't as Easy as It Looks. Journal of ASTM International, 1(2), 2004.

[95] Melson JH. Fatigue Crack Growth Analysis with Finite Element Methods and a Monte Carlo Simulation. MSc. Thesis 2014, Virginia Polytechnic Institute and State University.

[96] Ellyin F, Fakinlede COA. Probabilistic crack growth by nonlinear damage accumulation. International Journal of Fracture, 1988; Volume 36, Issue 2, pp 137-149.

[97] Castillo E, Fernández-Canteli A. A General Regression Model for Lifetime Evaluation and prediction," Int. J. Fract., 2001; 107, pp. 117–137.

[98] Castillo E, López-Aenlle M, Ramos A, Fernández-Canteli A, Kieselbach R, Esslinger V. Specimen Length Effect on Parameter Estimation in Modelling Fatigue Strength by Weibull Distribution. Int. J. Fatigue, 2006; 28, pp. 1047–1058.

[99] Castillo E, Fernández-Canteli A, Ruiz-Ripoll ML. A General Model for Fatigue Damage Due to Any Stress History," Int. J. Fatigue, 2008; 30, pp. 150–164.

[100] Bolotin VV. Mechanics of Fatigue. CRC Press, Boca Raton, 1998.

[101] Castillo E, Fernández-Canteli A, Hadi AS, López-Aenlle M. A Fatigue Model With Local Sensitivity Analysis. Fatigue Fract. Eng. Mater. Struct., 2007; 30, pp. 149–168.

[102] Castillo E, Fernández-Canteli A. A Parametric Lifetime Model for the Prediction of High Cycle Fatigue Based on Stress Level and Amplitude. Fatigue Fract. Eng. Mater. Struct., 2006; 29, pp. 1031–1038.

[103] Castillo E, Fernández-Canteli A, Koller R, Ruiz-Ripoll ML, García A. A Statistical Fatigue Model Covering the Tension and Compression Wöhler Fields. Probab. Eng. Mech., 2007;24, pp. 199–209.

[104] De Jesus AMP, Pinto H, Fernández-Canteli A, Castillo E, Correia JAFO. Fatigue assessment of a riveted shear splice based on a probabilistic model. International Journal of Fatigue 32 (2010), pp. 453–462.

[105] Fernández-Canteli A, Castillo E, Pinto H, López-Aenlle M. Estimating the SN Field From Strain-Lifetime Curves , Strain, Volume 47 (2011), Issue Supplement s1, pages e93–e97.

CHAPTER III

FATIGUE BEHAVIOUR OF MATERIALS AND CONNECTIONS FROM ANCIENT PORTUGUESE RIVETED STEEL BRIDGES

Experimental Characterization

3.1. INTRODUCTION

The maintenance and safety of existing bridges is a major concern of governmental agencies. In particular, the safety of old metallic riveted road and railway bridges fabricated and put into service at the end of the 19th century and beginning of 20th century deserve particular attention, since they were designed taking into account traffic conditions, both in terms of vehicle gross weight and frequency, completely different from those arising nowadays. Also, the current design procedures were not yet fully developed or even did not exist in the 19th century and design engineers were not aware of some important phenomena, such as fatigue. Nevertheless, fatigue was only intensively studied in the 20th century. Fatigue failures are a concern for steel bridges due to the likelihood of the steel to deteriorate under variable stresses [1–3], being recognised as the major cause of failure in metallic bridges [4]. In order to assure high safety levels in old riveted metallic bridges, road and railway authorities have to invest heavily in their maintenance and retrofitting.

Residual life calculations of existing bridges in operation should take into account fatigue as a progressive damaging mechanism. A consistent residual life prediction should be based on actual fatigue data from bridge members being assessed.

The *S–N* approach is widely used to assess the fatigue damage of riveted connections, which is included in design codes of practice (ex: *EC3-1-9* [5], *AASHTO* [6]). This approach is based on detail category *S–N* curves and relates the total number of cycles to failure to the applied stress range. Alternatively, Fracture Mechanics has been applied to assess the residual fatigue life of damaged riveted connections [7]. This approach requires the knowledge of the initial defect, which may be assessed by inspection. In order to turn the Fracture Mechanics in a more versatile design alternative than the *S–N* approach, if should be complemented by another approach to assess the crack initiation [8,9]. Local approaches to fatigue, based on local or notch stresses or strains, are frequently used to assess the fatigue crack initiation [10]. The application of the local approaches to fatigue as well as the Fracture Mechanics requires the knowledge of experimental fatigue data of the plain material, such as strain-life fatigue data as well as fatigue crack propagation data. This data is generally available in the literature for modern construction steels. However, there is a lack of experimental fatigue data for materials used in old metallic riveted bridges. Many of these materials are puddle irons, precursors of modern construction steels, which are not sufficiently studied.

This chapter aims at the characterization of the fatigue behaviour of different materials from a representative group of Portuguese old metallic riveted bridges, namely the Eiffel, Luiz I, Fão, Pinhão and Trezói bridges. Besides the strain-life and the fatigue crack propagation behaviour, the monotonic and cyclic elastoplastic behaviours, the microstructures and the chemical composition of the materials are also characterized [11-18]. In addition to the material characterization, S-N fatigue data from riveted joints is also presented in this chapter. A review of data derived by the author and other data dispersed in the literature is gathered and compiled in this chapter.

A brief description of the riveted bridges from which materials have been characterized, is presented in the next paragraphs. The oldest bridge is the Eiffel bridge that was designed by Gustave Eiffel and inaugurated on 30th of June 1878 (see Fig. 3.1). This 573 m long and 6 m wide bridge, made of a continuous deck composed by nine spans, crosses the Lima river, between Darque and Viana do Castelo, and serves both road and railway traffic. The material used in the experimental program was extracted from a beam of the railway

Darque viaduct, which was removed during the last rehabilitation, occurred between 1st February 2006 and 30st October 2007 [11,18].

The second oldest bridge is the Luiz I bridge (see Fig. 3.2) that was also designed by Gustave Eiffel and commissioned in 31st October 1886. This bridge crosses the Douro river and links the Porto and Gaia cities. The main features of the Luiz I bridge are: double deck supported by an arch; span of 172 meters; arch radius of 45 meters; length of upper deck is 391.25 meters; length of lower deck is 174 meters and width is 8 meters (original design was 6 meters). A diagonal member 1600 mm in length was removed from the Luiz I bridge, that was also rehabilitated some years ago [12,18].

The third oldest bridge included in this study is the Fão road bridge. It was designed by Abel Maria Mota, under the supervision of Reynau, at the end of 19th century and was inaugurated on 7th of August 1892. This bridge, made of a continuous deck with eight spans of 33.5 m each, supported on masonry piers, crosses the Cávado river at Esposende, as illustrated in Fig. 3.3, it was recently rehabilitated and 7 diagonals were replaced. The removed diagonals were used in the fatigue experimental program [13,14,18].

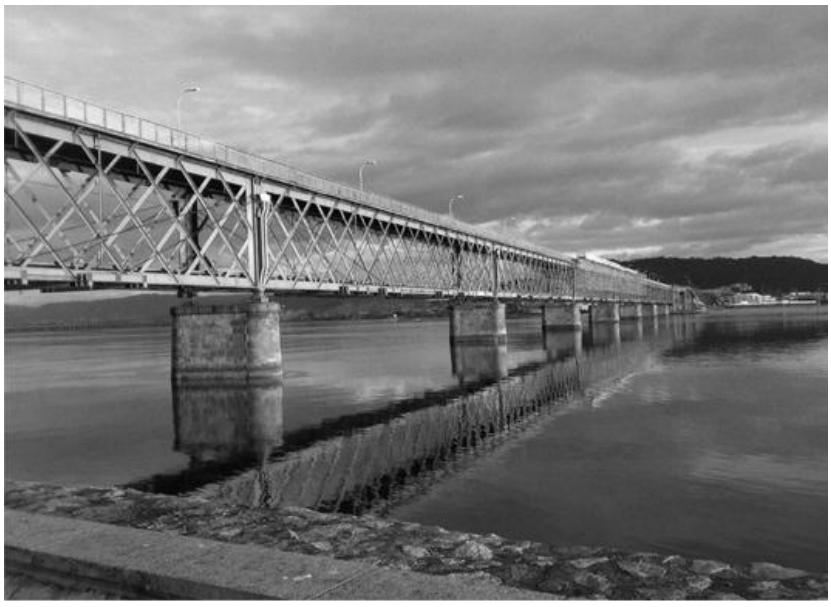

Figure 3.1 – Riveted metallic Eiffel bridge in Viana do Castelo.

Figure 3.2 – Riveted metallic Luiz I bridge in Porto.

Figure 3.3 – Riveted metallic Fão bridge in Esposende.

The fourth oldest bridge considered in this research, illustrated in Fig. 3.4, is the Pinhão road bridge, also designed by Gustave Eiffel at the end of 19th century and built between 1903 and 1906. This bridge crosses the Douro river at Pinhão. Consisting in three spans of 68.8 m each and one span of 10 m; there is only one deck 6 m wide, divided into one traffic lane 4.60 m wide and two sidewalks 0.675 m wide each. A diagonal 1500 mm in length and a bracing 1400 mm in length were removed and replaced by new material [15,18]. The bridge was also rehabilitated few years ago.

Finally, the youngest bridge included in this study is the Trezói railway bridge, illustrated in Fig. 3.5. This bridge makes part of the Beira Alta railway line and was inaugurated on 20th of August 1956. The deck is composed of three continuous spans of 39, 48 and 39 m, totalizing a bridge length of 126 m. The deck width is 4.40 m throughout the bridge length. The Trezói bridge has about half old as the above four referred bridges, which in turn are more than 100 years old. A 3000 mm long bracing was removed from the Trezói bridge only for research purposes, since this bridge was not recently subject to any rehabilitation work [16,18]. While the material used in the Trezói bridge is a construction steel, the materials used in the older bridges are very likely puddle irons. At the end of the XIX century and beginning of the XX century, the qualities of the puddle irons changed appreciably.

Figure 3.4 – Riveted metallic Pinhão bridge.

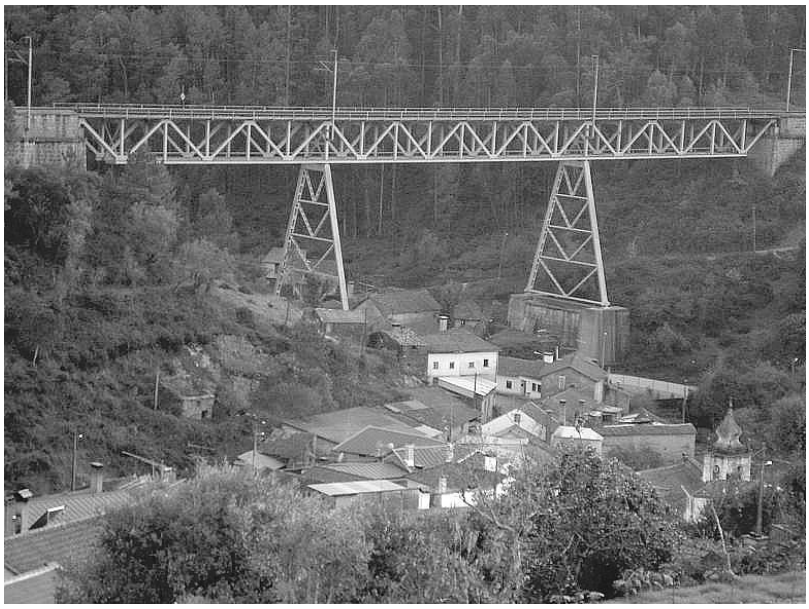

Figure 3.5 – Riveted metallic Trezói bridge.

3.2. MONOTONIC TENSILE STRENGTH PROPERTIES CHARACTERIZATION

All materials from the referred structures were characterized using monotonic tensile tests. According to the Portuguese NP 10002-1 Standard [19], round specimens machined from original members removed from the five bridges under investigation, exhibiting the dimensions listed in the Table 3.1, were subjected to monotonic increasing loading. Distinct diameters were selected since the materials samples extracted from the bridges showed distinct sizes. Besides the strength properties, the elastic properties of the materials were estimated, in particular the Young modulus and Poisson ratio.

Eight specimens were extracted from a south viaduct girder of the Eiffel bridge, in particular from the angle connecting the web and the flange (CT specimens) and from the web (TA specimens); five specimens were extracted from a diagonal of the Luiz I bridge; twenty two specimens were extracted from side diagonals of the Fão bridge; fourteen specimens were machined from a diagonal (CT specimens) and a bracing (BT specimens) from the Pinhão bridge; finally, three specimens of material from Trezói bridge were prepared from the removed upper bracing. Figure 3.6 presents a photo of a typical tensile specimen.

Table 3.1 – Cross-sections of the specimens used in the monotonic tensile tests of the materials from the bridges.

Bridge / *Material*		*Diameter* *mm*	*Cross-section* mm^2
Eiffel	Viaduct	4	12.57
	Viaduct	5	19.63
	Viaduct	6	28.27
Luiz I	Diagonal	6	28.27
	Diagonal	8	50.27
Fão	Diagonal	6	28.27
Pinhão	Diagonal	5	19.63
	Bracing	8	50.27
Trezói	Bracing	8	50.27

Figure 3.6 – Typical specimen used in monotonic tensile tests [16].

Table 3.2 – Summary of results from the monotonic tensile tests for the material from Eiffel bridge [11].

Specimen	f_u	f_y	*A*	*Z*
-	*MPa*	*MPa*	*%*	*%*
TA1	387.0	345.0	6.80	4.70
TA2	376.0	309.0	13.20	14.70
TA3	285.0	282.0	2.00	0.80
TA4	276.0	275.0	0.80	1.60
TC1	424.0	297.0	14.30	35.30
TC2	428.0	295.0	22.00	31.70
TC3	286.0	269.0	3.20	2.00
TC4	272.0	267.0	2.80	2.00

The results from the monotonic tensile tests, for the materials under consideration of the Eiffel, Luiz I, Fão, Pinhão and Trezói bridges are presented in Tables 3.2 to 3.6, respectively, where f_u is the ultimate tensile strength, f_y is the higher yield stress, *A* is the elongation at fracture and *Z* is the reduction in cross-section at failure.

Tables 3.7 to 3.11 show the mean values, standard deviation and coefficient of variation (*COV*) of the various properties evaluated with the monotonic tensile tests for the materials of the Eiffel, Luiz I, Fão and Trezói bridges, respectively.

Table 3.3 – Summary of results from the monotonic tensile tests for the material from Luiz I bridge [12].

Specimen	f_u	f_y	*A*	*Z*
-	*MPa*	*MPa*	*%*	*%*
S1T1	435.0	336.0	14.00	11.00
S2T1	374.0	275.0	13.60	9.70
S3T1	395.0	302.0	29.30	39.20
S3T2	383.0	287.0	25.30	37.70
S3T3	396.0	313.0	23.80	38.30

Table 3.4 – Summary of results from the monotonic tensile tests for the material from Fão bridge [13].

Specimen	f_u	f_y	*A*	*Z*
-	*MPa*	*MPa*	*%*	*%*
1	345.5	209.4	23.43	8.31
2	337.2	198.5	-	12.06
3				
4	423.9	288.8	21.60	13.07
5	317.8	208.0	12.77	7.64
6	425.0	276.8	25.87	13.87
7	371.3	249.0	-	12.81
8				
9	333.8	225.6	-	8.79
10	355.5	216.1	27.00	14.86
11	342.7	195.2	21.47	13.26
12	348.6	223.8	12.97	7.78
13	354.8	210.7	19.03	14.52
14	357.8	239.3	24.07	12.66
15	378.3	237.3	21.67	20.77
16	337.3	200.7	-	15.05
17	396.7	245.6	22.23	17.91
18	352.7	210.2	23.27	16.07
19	369.0	226.4	24.77	18.07
20	343.0	196.2	21.43	9.81
21	361.9	232.7	-	14.23
22	333.8	107.7	45.33	9.58

Table 3.5 – Summary of results from the monotonic tensile tests for the material from Pinhão bridge [15].

Specimen	f_u	f_y	*A*	*Z*
-	*MPa*	*MPa*	*%*	*%*
CT1	372.0	297.0	31.30	69.40
CT2	373.0	274.0	-	69.40
CT3	365.0	289.0	-	72.00
CT4	365.0	275.0	36.00	71.40
CT5	367.3	278.8	34.00	69.80
CT6	365.8	302.1	34.80	69.80
CT7	364.2	274.1	29.00	68.40
BT1	377.0	377.0	-	77.00
BT2	361.0	361.0	-	71.00
BT3	348.0	344.0	-	73.00
BT4	354.0	352.0	-	71.00
BT5	345.0	263.7	33.20	75.00
BT6	348.7	300.7	33.60	68.00
BT7	348.9	294.1	33.60	68.40

Table 3.6 – Summary of results from the monotonic tensile tests for the material from Trezói bridge [16,17].

Specimen	f_u	f_y	*A*	*Z*
-	*MPa*	*MPa*	*%*	*%*
T1	455.0	392.0	22.00	66.00
T2	501.0	401.0	23.00	71.00
T3	464.0	402.0	24.00	62.00

Table 3.7 shows the mean values, standard deviation and *COV* of the properties for the materials extracted from the angle and web of the south viaduct girder of the Eiffel bridge, respectively the TA and TC specimens. The table also presents global mean, standard deviation and *COV* of the properties for all specimens taken from the web and the upper angle of the south viaduct girder of the Eiffel bridge.

The mean tensile, standard deviation and *COV* of the properties of the material extracted from the diagonal and bracing of the Pinhão bridge, referred as CT and BT specimens, respectively, are shown in Table 3.10. Global mean, standard deviation and *COV* of the properties for all specimens, analysed together, taken from the diagonal and bracing of the Pinhão bridge, are also included in Table 3.10.

Table 3.7 – Mean, standard deviation and *COV* of the monotonic tensile properties for the material from Eiffel bridge.

Specimen	*Statistical data*	f_u	f_y	*A*	*Z*
-		*MPa*	*MPa*	*%*	*%*
TA	Mean	331.0	302.8	5.70	5.45
	Standard Deviation	58.6	31.8	5.63	6.39
	COV [%]	17.7	10.5	98.81	117.28
TC	Mean	352.5	282.0	10.58	17.75
	Standard Deviation	85.1	16.2	9.30	18.25
	COV [%]	24.1	5.7	87.91	102.79
TA/TC	Mean	341.8	292.4	8.14	11.60
	Standard Deviation	68.6	25.8	7.58	14.26
	COV [%]	20.1	8.8	93.12	122.95

Table 3.8 – Mean, standard deviation and *COV* of the monotonic tensile properties for the material from Luiz I bridge.

Statistical data	f_u	f_y	*A*	*Z*
	MPa	*MPa*	*%*	*%*
Mean	396.6	302.6	21.20	27.18
Standard Deviation	23.3	23.6	7.05	15.38
COV [%]	5.9	7.8	33.25	56.58

Table 3.9 – Mean, standard deviation and *COV* of the monotonic tensile properties for the material from Fão bridge [13].

Statistical data	f_u	f_y	*A*	*Z*
	MPa	*MPa*	*%*	*%*
Mean	359.3	219.9	23.13	13.06
Standard Deviation	28.5	36.6	7.35	3.63
COV [%]	7.9	16.6	31.80	27.81

Clearly the material from Trezói bridge exhibits the highest strength properties associated with high ductility. The material from the Eiffel bridge – the oldest one – shows the lowest ductility properties. The material from the Pinhão bridge shows the highest ductility properties. When compared with the materials from the other centenary bridges, the material from the Pinhão bridge shows a very good strength/ductility ratio [17]. It is worthwhile mentioning that the Pinhão bridge is the youngest of the centenary bridges and at that time the steel production processes evolved quickly in quality. The material from the Pinhão bridge shows characteristics very similar to the modern construction steels.

Table 3.10 – Mean, standard deviation and *COV* of the monotonic tensile properties for the material from Pinhão bridge.

Specimen	*Statistical data*	f_u	f_y	*A*	*Z*
-		*MPa*	*MPa*	*%*	*%*
CT	Mean	367.5	284.3	33.02	70.03
	Standard Deviation	3.6	11.7	2.83	1.25
	COV [%]	1.0	4.1	8.58	1.78
BT	Mean	354.7	327.5	33.47	71.91
	Standard Deviation	11.2	41.5	0.23	3.31
	COV [%]	3.1	12.7	0.69	4.61
CT/BT	Mean	361.1	305.9	33.19	70.97
	Standard Deviation	10.4	36.9	2.16	2.60
	COV [%]	2.9	12.1	6.50	3.66

Table 3.11 – Mean, standard deviation and *COV* of the monotonic tensile properties for the material from Trezói bridge.

Statistical data	f_u	f_y	*A*	*Z*
	MPa	*MPa*	*%*	*%*
Mean	473.3	398.3	23.00	66.33
Standard Deviation	24.4	5.5	1.00	4.51
COV [%]	5.2	1.4	4.35	6.80

The monotonic stress-strain curves were further correlated each other using the Ramberg-Osgood relation:

$$\varepsilon = \frac{\sigma}{E} + \left(\frac{\sigma}{K}\right)^{1/n} \tag{3.1}$$

where: ε and σ are, respectively, the strain and stress, E is the Young modulus, K and n are the strain hardening coefficient and exponent. The resulting monotonic properties (K and n) are summarized in Table 3.12 for all materials under consideration.

Table 3.12 – Strain hardening coefficients and exponents for the materials from the bridges.

Bridge	*K*	*n*
Material	*MPa*	-
Eiffel	411.07	0.0585
Luiz I	506.20	0.0902
Fão	477.53	0.1300
Pinhão	444.29	0.1166
Trezói	586.86	0.0957

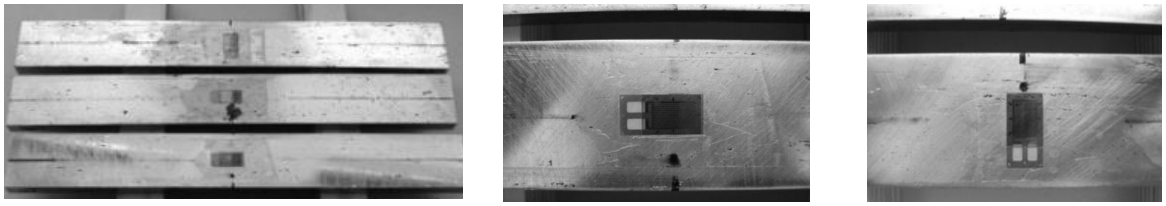

a) b) c)

Figure 3.7 – Specimens used in the assessment of the elasticity modulus and Poisson ratio for the material from the Fão bridge: a) specimens series; b) longitudinal strain gauge and c) transverse strain gauge [13].

Table 3.13 – Elastic properties of the materials from the bridges.

Bridge	*E*	*ν*
Material	*GPa*	-
Eiffel[b]	193.10	0.300
Luiz I[a]	192.70	0.255
Fão[a]	198.70	0.260
Pinhão[c]	210.68	-
Trezói[b]	198.49	0.320

[a] Computed directly from strain gauge measurements.

[b] Computed indirectly from cyclic elastoplastic analysis.

[c] Computed indirectly from monotonic tensile data.

The elastic properties, represented by the Young modulus, E, and Poisson ratio, ν, of the materials from the Luiz I and Fão bridges were computed directly from strain gauge measurements (see Fig. 3.7). The elastic properties of the materials from the Eiffel and Trezói bridges were computed indirectly from cyclic elastoplastic analysis. For the material of the Trezói bridge, the elastic properties were computed indirectly from analysis of the monotonic tensile tests. Table 3.13 summarizes the estimates of the elastic properties for all materials.

3.3. METALLOGRAPHIC ANALYSIS OF THE MATERIALS

3.3.1. Optical microscope observations

Figure 3.8 illustrates typical microstructures of the materials under investigation. In general, the microstructures strengthen the conclusion that materials are mainly composed of a ferrite matrix. For some cases, namely the material from Pinhão and Trezói bridges, perlite is observed. These latter materials show a more homogeneous microstructure of regular grains than the other materials. All materials exhibit lined-up inclusions induced by deformation, the density of them being however is higher in the centenary materials, thus limiting the material ductility and increasing the scatter of mechanical properties [11-13,15-18].

3.3.2. Chemical composition

Table 3.14 summarizes the chemical composition of some material samples from the bridges under investigation [18]. The chemical compositions were assessed using the spark emission spectrometry technique. The material from the Trezói bridge exhibits the lowest sulphur and phosphorus contents, which is consistent with the age of the material. The Trezói material is a ferritic structural steel, since it has a very small amount of carbon. The materials from the centenary bridges show significant variable chemical compositions, due to the typical heterogeneous microstructures of these materials. Due to the low carbon content they should exhibit a ferrite matrix. The samples from Luiz I bridge show higher carbon, silicon and manganese contents than the other materials. This material revealed a significant heterogeneous chemical composition which is consistent with the heterogeneous microstructure of the puddle irons. The higher carbon content measured is due to local segregations. The higher silicon content may be probably due to the use of Si in the metal desoxidation/desulphurization process.

a) Eiffel bridge.

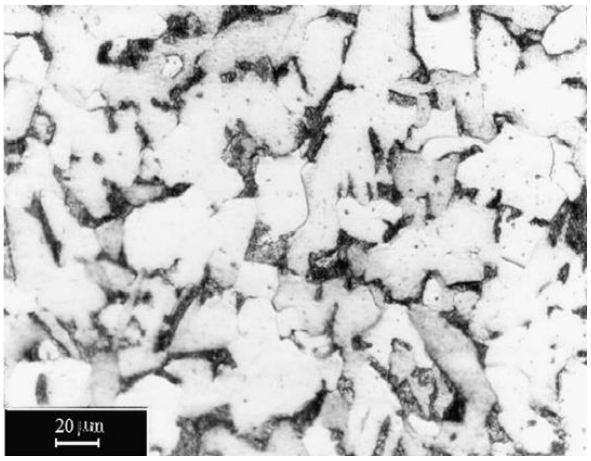

b) Luiz I bridge.

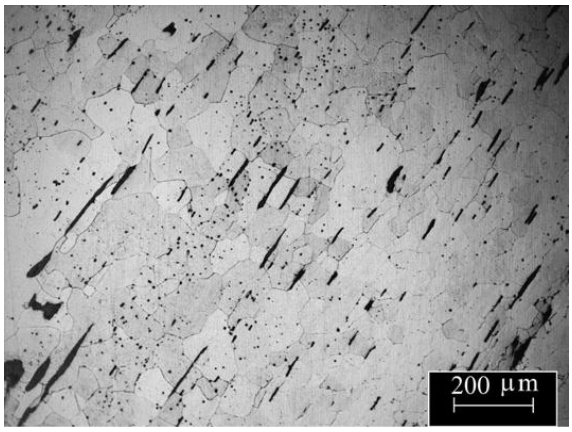

c) Fão bridge.

d) Pinhão bridge.

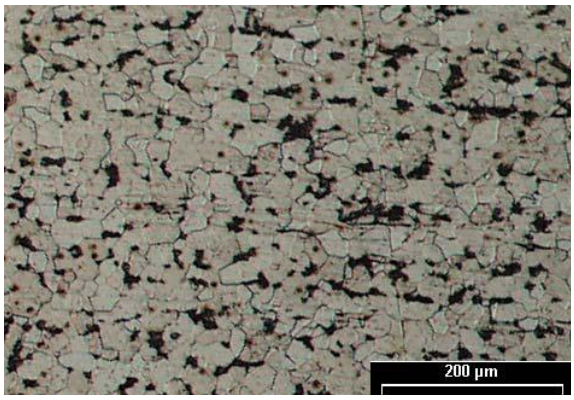

e) Trezói bridge.

Figure 3.8 – Microstructures of the materials from the bridges.

Table 3.14 – Chemical composition for each material of the bridges (wt.%) [18].

Brigde	*Material*	*%C*	*%Si*	*%Mn*	*%P*	*%S*
Eiffel	Darque Viaduct	0.23	0.39	1.78	>0.15	>0.15
	bridge*	0.81	0.24	2.71	>0.15	>0.15
Luiz I	Diagonal	0.72	0.34	2.09	>0.15	>0.15
Fão	Diagonal	0.09	0.06	0.13	0.14	0.007
Pinhão	Diagonal	0.06	<0.01	0.04	0.04	0.03
	Bracing	0.05	<0.01	0.34	0.04	0.04
Trezói	Bracing	0.06	0.03	0.34	0.02	0.02

* determined with a portable emission spectrometry.

3.4. FATIGUE BEHAVIOUR CHARACTERIZATION OF THE MATERIALS

This section presents the strain-life fatigue data obtained for the materials from the bridge under consideration. Besides the fatigue behaviour characterization, the cyclic elastoplastic behaviour of the materials are also presented. Strain-life fatigue data from tests performed on smooth specimens may be used to assess the crack initiation, in the framework of local approaches to fatigue [20].

Smooth specimens with rectangular cross section were machined from material samples from the Eiffel, Luiz I, Fão and Trezói bridges (see Fig. 3.9). These specimens were used to carry out fatigue tests under strain-controlled conditions, according to the ASTM E606 Standard [21]. The specimens were machined according to the rolling (longitudinal) direction of the members removed from the bridges. The dimensions of the specimens were not the same for each material, since the available material thicknesses were not constant. The faces of the specimens were grinded and additionally polished in the central gauge zone.

The tests were performed in an Instron close-loop servo hydraulic machine, model 8801, rated to 100 KN. The deformation was measured using an Instron clip gauge, model 2620-602 with displacement range of ± 2.5 mm. A base gauge length of 12.5 mm was used with specimens from the Luiz I and Eiffel bridges; for materials from Eiffel, Fão and Trezói bridges, a base gauge length of 25 mm was chosen. A sinusoidal waveform was taken as command signal. The fatigue tests, in all series, were conducted at room-temperature in air under constant strain amplitudes at a frequency adjusted to result an average strain rate of 0.008/s. However, that average strain rate was not followed in the tests that

resulting in a very high number of cycles (high cycle fatigue). In these cases, a higher frequency was selected in order to reduce the testing times.

The choice of specimens with rectangular cross-section instead of a circular one was justified by the fact that the structural elements removed from the bridges have reduced thickness to prepare round specimens. Table 3.15 summarizes the nominal dimensions of the smooth dog-bone specimens used in the fatigue tests of the materials from the bridges [13,17,18].

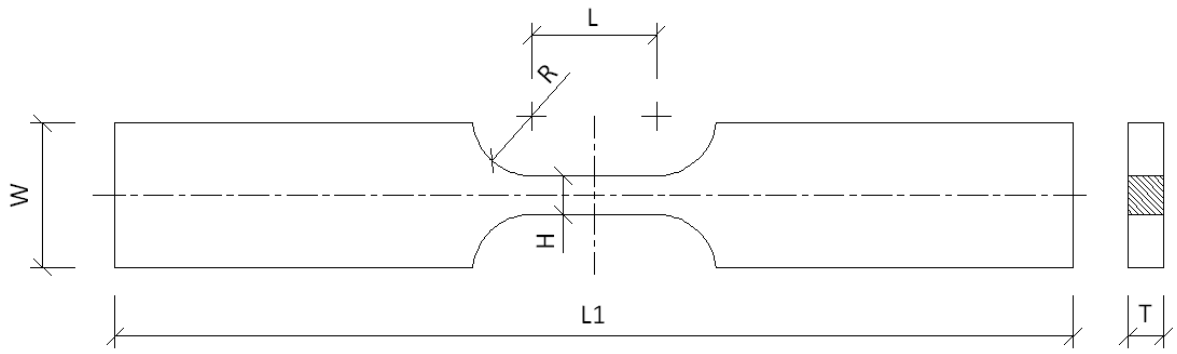

Figure 3.9 – Geometry of the specimens used in fatigue tests under strain-control conditions.

Table 3.15 – Nominal dimensions of the smooth dog-bone specimens used in fatigue tests.

Bridge Material	*No. of specimens*	*W mm*	*T mm*	*L mm*	*L1 mm*	*R mm*	*H mm*
Eiffel	12	22.0	6.0	20.0	150.0	15.0	7.0
	15	20.0	5.0	15.0	150.0	10.0	6.0
Luiz I	15	20.0	5.0	15.0	150.0	10.0	6.0
Fão	35	30.0	7.5	26.0	200.0	12.5	8.0
Trezói	10	30.0	7.5	26.0	200.0	12.5	8.0

The average gauge cross sections were 6.4 × 5.2 mm^2, 4.9 × 6.8 mm^2 and 7.5 × 8.1 mm^2, respectively for the Eiffel (27 specimens), Luiz I (15 specimens) and Trezói (10 specimens) bridges. Regarding the Fão bridge, two test series were prepared with average cross sections of 5.4 × 7.3 mm^2 and 5.3 × 7.5 mm^2, which were tested under strain ratios equal to -1 (14 specimens) and 0 (18 specimens), respectively. For the other bridge materials, only one test series was tested, namely under strain ratio equal to -1. Figures 3.10, 3.11 and 3.12 illustrate some specimens tested respectively for the materials from Eiffel, Fão and Trezói bridges.

Tables 3.16, 3.17, 3.18 and 3.19 summarize the program of strain-controlled fatigue tests performed on smooth specimens of materials from Eiffel, Luiz I, Trezói and Fão bridges, respectively. In the referred tables, L_1 and L_2 represent the length of the central section of the smooth specimens, S_t is the cross-section, R_ε the strain ratio, $\Delta\varepsilon$ the strain range, $d\varepsilon/dt$ the average strain rate and f the frequency used for each test.

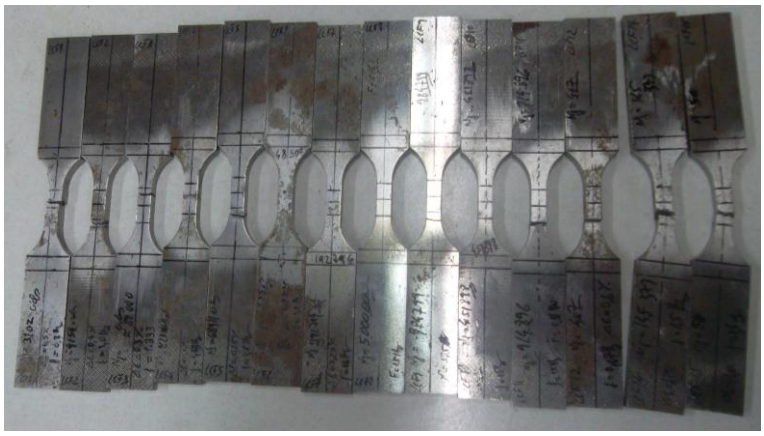

Figure 3.10 – Some smooth specimens of material from Eiffel bridge used in fatigue tests.

Figure 3.11 – Some smooth specimens of material from Fão bridge used in fatigue tests [13].

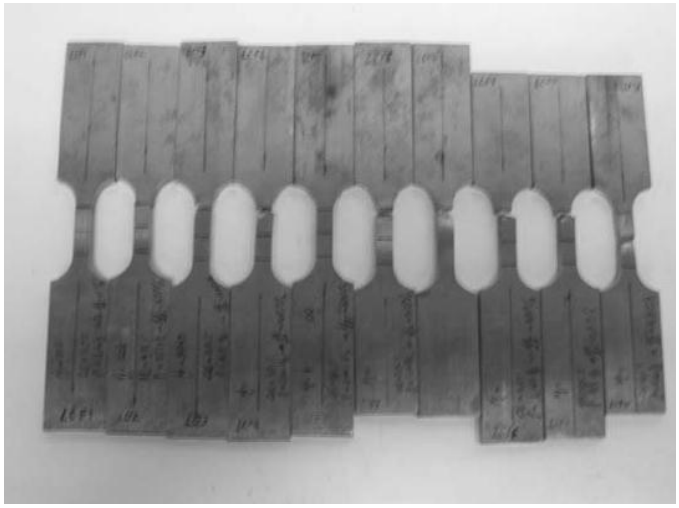

Figure 3.12 – Some smooth specimens of material from Trezói bridge used in fatigue tests.

Table 3.16 – Plan of fatigue tests with smooth specimens of material from the Eiffel bridge.

Specimens	L_1	L_2	S_t	R_ε	$\Delta\varepsilon$	$d\varepsilon/dt$	f
	mm	mm	mm^2		%	%/s	Hz
LCF-viana-050-01	6.77	5.59	37.84		0.500	0.80	0.800
LCF-viana-050-02	6.79	5.59	37.96		0.500	0.80	0.800
LCF-viana-050-03	6.83	5.64	38.52		0.500	0.80	0.800
LCF-viana-040-01	6.80	5.60	38.08		0.400	0.80	1.000
LCF-viana-040-02	6.81	5.63	38.34		0.400	0.80	1.000
LCF-viana-040-03	6.87	5.63	38.68		0.400	0.80	1.000
LCF-viana-030-01	6.82	5.60	38.19		0.300	0.80	1.333
LCF-viana-030-02	6.76	5.60	37.86		0.300	0.80	1.333
LCF-viana-020-01	6.76	5.61	37.92		0.200	0.80	2.000
LCF-viana-020-02	6.78	5.61	38.04		0.200	0.80	2.000
LCF-viana-075-01	6.82	5.63	38.40		0.750	0.80	0.533
LCF-viana-075-02	6.86	5.61	38.48		0.750	0.80	0.533
LCF_050_01	6.16	4.88	30.0608		0.500	0.80	0.800
LCF_040_01	6.18	5.02	31.0236	-1	0.400	0.80	1.000
LCF_030_01	6.11	4.86	29.6946		0.300	0.80	1.333
LCF_030_02	6.23	4.91	30.5893		0.300	0.80	1.333
LCF_025_01	6.18	4.89	30.2202		0.250	0.80	1.600
LCF_007_01	6.12	4.9	29.988		0.256	-	15.000
LCF_006_01	6.21	5.01	31.1121		0.195	-	15.000
LCF_005_01	6.29	4.93	31.0097		0.166	-	15.000
LCF_0055_01	6.06	4.93	29.8758		0.188	-	15.000
LCF_006_02	5.87	4.9	28.763		0.203	-	15.000
LCF_0055_02	6.05	4.92	29.766		0.188	-	15.000
LCF_060_01	5.95	4.97	29.5715		0.600	0.80	0.667
LCF_070_01	6.09	4.9	29.841		0.700	0.80	0.571
LCF_080_01	6.12	4.98	30.4776		0.800	0.80	0.500
LCF_100_01	5.85	4.92	28.782		1.000	0.80	0.400

Table 3.17 – Plan of fatigue tests with smooth specimens of material from the Luiz I bridge.

Specimens	L_1	L_2	S_t	R_ε	$\Delta\varepsilon$	$d\varepsilon/dt$	f
	mm	**mm**	**mm²**		**%**	**%/s**	**Hz**
LCF1	8.00	7.38	59.04	-1	1.000	0.80	0.400
LCF2	7.95	7.48	59.47		0.750	0.80	0.533
LCF3	7.96	7.50	59.70		0.500	0.80	0.800
LCF4	8.08	7.49	60.52		0.300	0.80	1.333
LCF5	8.11	7.53	61.07		0.200	0.80	2.000
LCF6	8.08	7.48	60.44		0.300	0.80	1.333
LCF7	8.04	7.40	59.50		0.500	0.80	0.800
LCF8	8.17	7.44	60.78		1.500	0.80	0.267
LCF9	8.13	7.42	60.32		2.000	0.80	0.200
LCF10	8.29	7.48	62.01		2.500	0.80	0.160

Table 3.18 – Plan of fatigue tests with smooth specimens of material from the Trezói bridge [17].

Specimens	L_1	L_2	S_t	R_ε	$\Delta\varepsilon$	$d\varepsilon/dt$	f
	mm	**mm**	**mm²**		**%**	**%/s**	**Hz**
LCF1	8.00	7.38	59.04	-1	1.000	0.80	0.400
LCF2	7.95	7.48	59.47		0.750	0.80	0.533
LCF3	7.96	7.50	59.70		0.500	0.80	0.800
LCF4	8.08	7.49	60.52		0.300	0.80	1.333
LCF5	8.11	7.53	61.07		0.200	0.80	2.000
LCF6	8.08	7.48	60.44		0.300	0.80	1.333
LCF7	8.04	7.40	59.50		0.500	0.80	0.800
LCF8	8.17	7.44	60.78		1.500	0.80	0.267
LCF9	8.13	7.42	60.32		2.000	0.80	0.200
LCF10	8.29	7.48	62.01		2.500	0.80	0.160

Table 3.19 – Plan of fatigue tests of smooth specimens of material from the Fão bridge [13].

Specimens	L_1	L_2	S_t	R_ε	$\Delta\varepsilon$	$d\varepsilon/dt$	f
	mm	mm	mm^2		%	%/s	Hz
LCF-e020-01	5.88	7.46	43.86	-1	0.400	0.80	1.000
LCF-e020-02	6.01	7.42	44.59		0.400	0.80	1.000
LCF-e020-03	4.72	7.41	34.98		0.400	0.80	1.000
LCF-e015-01	5.09	7.33	37.31		0.300	0.80	1.333
LCF-e015-02	5.31	7.27	38.60		0.300	0.80	1.333
LCF-e015-03	5.70	7.32	41.72		0.300	0.80	1.333
LCF-e040-01	4.72	7.37	34.79		0.800	0.80	0.500
LCF-e040-02	5.12	7.41	37.94		0.800	0.80	0.500
LCF_e025-01	5.87	7.39	43.38		0.500	0.80	0.800
LCF-e025-02	5.37	7.22	38.77		0.500	0.80	0.800
LCF-e025-03	5.38	7.23	38.90		0.500	0.80	0.800
LCF-e010-01	5.90	7.35	43.37		0.200	0.80	2.000
LCF-e010-02	5.93	7.29	43.23		0.200	0.80	2.000
LCF-e010-03	5.23	7.35	38.44		0.200	0.80	2.000
LCF-150-01	5.22	7.38	38.52	0	1.500	0.80	0.267
LCF-100-01	5.24	7.47	39.14		1.000	0.80	0.400
LCF-100-02	5.20	7.79	40.51		1.000	0.80	0.400
LCF-100-03	5.65	7.41	41.87		1.000	0.80	0.400
LCF-075-01	4.99	7.41	36.98		0.750	0.80	0.533
LCF-075-02	5.08	7.44	37.80		0.750	0.80	0.533
LCF-075-03	5.84	7.35	42.92		0.750	0.80	0.533
LCF-050-01	5.76	7.41	42.68		0.500	0.80	0.800
LCF-050-02	5.15	7.44	38.32		0.500	0.80	0.800
LCF-050-03	4.99	7.36	36.73		0.500	0.80	0.800
LCF-030-01	5.02	7.41	37.20		0.300	0.80	1.333
LCF-030-02	5.47	7.50	41.03		0.300	0.80	1.333
LCF-030-03	5.37	7.51	40.33		0.300	0.80	1.333
LCF-025-01	5.45	7.40	40.33		0.250	0.80	1.600
LCF-025-02	5.43	7.38	40.07		0.250	0.80	1.600
LCF-025-03	5.63	7.35	41.38		0.250	0.80	1.600
LCF-020-01	5.16	7.48	38.60		0.200	0.80	5.000
LCF-020-02	5.47	7.49	40.97		0.200	0.80	5.000
LCF-020-03	4.49	7.50	33.68		0.200	0.80	5.000
LCF-020-04	6.02	7.34	44.19		0.200	0.80	5.000
LCF-015-01	4.70	7.46	35.06		0.150	0.80	5.000

Tables 3.20, 3.21, 3.22 and 3.23 summarize the results of the test program of smooth specimens for the materials from the Eiffel, Trezói, Luiz I and Fão bridges, respectively. The tables include the total strain range applied to the specimens, $\Delta\varepsilon$, the resulting elastic strain ranges, $\Delta\varepsilon^E$, the plastic strain ranges, $\Delta\varepsilon^P$, the stress range, $\Delta\sigma$, the number of

cycles to failure, N_f, and the number of reversals to failure, $2N_f$. The plastic strain ranges and the stress ranges were determined based on the stabilized hysteresis loops. The range of the fully-reversed strains (R_ε=-1) varied, respectively, from 0.166% to 1.00%, 0.20% to 1.00% and 0.20% to 2.50%, for the materials from Eiffel, Luiz I and Trezói bridges. Regarding the material from Fão bridge, the range of applied strains varied, respectively, from 0.20% to 0.80% and 0.15% to 1.50%, for R_ε=-1 and R_ε=0.

The presented results will be used in the definition of strain-life relations for the fatigue resistance of the materials of the bridges.

Table 3.20 – Results of fatigue tests performed under strain-control conditions (R_ε = -1) for the material from the Eiffel bridge.

Specimens	$\Delta\varepsilon$	$\Delta\varepsilon^P$	$\Delta\varepsilon^E$	$\Delta\sigma$	σ_{max}	N_f	$2N_f$
	%	**%**	**%**	**MPa**	**MPa**	**cycles**	**reversals**
LCF-viana-050-01	0.500	0.141	0.359	660.37	318.28	2845	5690
LCF-viana-050-02	0.500	0.143	0.357	691.09	344.61	922	1844
LCF-viana-050-03	0.500	0.140	0.360	690.36	338.89	537	1074
LCF-viana-040-01	0.400	0.059	0.341	656.79	324.20	2684	5368
LCF-viana-040-02	0.400	0.073	0.327	632.79	303.50	581	1162
LCF-viana-040-03	0.400	0.065	0.335	637.38	309.97	5697	11394
LCF-viana-030-01	0.300	0.017	0.283	562.65	270.79	80281	160562
LCF-viana-030-02	0.300	0.014	0.286	578.36	293.41	49460	98920
LCF-viana-020-01	0.200	0.002	0.198	408.38	230.90	854096	1708192
LCF-viana-020-02	0.200	0.003	0.197	399.58	269.69	1000000*	2000000*
LCF-viana-075-01	0.750	0.374	0.376	700.35	346.18	164	328
LCF-viana-075-02	0.750	0.362	0.388	726.31	358.49	153	306
LCF_050_01	0.500	0.160	0.340	646.98	309.42	3012	6024
LCF_040_01	0.400	0.060	0.340	639.10	321.99	4154	8308
LCF_030_01	0.300	0.010	0.290	535.88	255.78	80120	160240
LCF_030_02	0.300	0.019	0.281	548.05	275.06	20010	40020
LCF_025_01	0.250	0.007	0.243	463.72	231.61	68911	137822
LCF_007_01	0.256	0.006	0.249	466.70	233.05	68502	137004
LCF_006_01	0.195	0.002	0.194	385.58	193.22	192794	385588
LCF_005_01	0.166	0.00002	0.166	322.59	161.13	5000000*	10000000*
LCF_0055_01	0.188	0.001	0.187	367.51	183.72	984799	1969598
LCF_006_02	0.203	0.00037	0.202	417.24	208.48	684114	1368228
LCF_0055_02	0.188	0.002	0.186	369.31	184.70	914896	1829792
LCF_060_01	0.600	0.236	0.364	700.21	340.76	407	814
LCF_070_01	0.700	0.335	0.365	649.86	305.55	759	1518
LCF_080_01	0.800	0.432	0.368	661.91	316.92	145	290
LCF_100_01	1.000	0.623	0.377	716.16	333.56	50	100

*Run-out

Table 3.21 – Results of fatigue tests performed under strain-control conditions (R_ε = -1) for the material from the Trezói bridge [17].

Specimens	$\Delta\varepsilon$	$\Delta\varepsilon^P$	$\Delta\varepsilon^E$	$\Delta\sigma$	σ_{max}	N_f	$2N_f$
	%	%	%	MPa	MPa	cycles	reversals
LCF1	1.000	0.694	0.306	574.60	287.20	716	1432
LCF2	0.750	0.470	0.280	555.80	277.47	1626	3252
LCF3	0.500	0.251	0.249	485.80	244.46	5749	11498
LCF4	0.300	0.091	0.209	438.20	219.66	20596	41192
LCF5	0.200	0.001	0.199	436.80	167.79	1031126*	2062252*
LCF6	0.300	0.108	0.192	412.00	204.22	15852	31704
LCF7	0.500	0.241	0.259	542.80	271.93	2586	5172
LCF8	1.500	1.141	0.359	667.40	331.89	414	828
LCF9	2.000	1.623	0.377	715.40	356.16	153	306
LCF10	2.500	2.080	0.420	733.00	369.00	199	398

*Run-out

Table 3.22 – Results of fatigue tests performed under strain-control conditions (R_ε = -1) for the material from the Luiz I bridge.

Specimens	$\Delta\varepsilon$	$\Delta\varepsilon^P$	$\Delta\varepsilon^E$	$\Delta\sigma$	σ_{max}	N_f	$2N_f$
	%	%	%	MPa	MPa	cycles	reversals
LCF-Luiz1A-050-01	1.000	0.637	0.363	718.98	356.34	17	34
LCF-Luiz1B-050-02	1.000	0.635	0.365	726.64	356.15	28	56
LCF-Luiz1C-0375-01	0.750	0.386	0.364	695.47	340.85	55	110
LCF-Luiz1D-0375-02	0.750	0.367	0.383	720.63	350.28	94	188
LCF-Luiz1E-025-01	0.500	0.161	0.339	675.60	332.83	325	650
LCF-Luiz1F-025-02	0.500	0.165	0.335	662.99	328.87	465	930
LCF-Luiz1G-020-01	0.400	0.077	0.323	659.87	322.89	888	1776
LCF-Luiz1H-020-02	0.400	0.067	0.333	660.51	342.82	987	1974
LCF-Luiz1I-015-01	0.300	0.012	0.288	583.58	288.03	4950	9900
LCF-Luiz1J-015-02	0.300	0.021	0.279	562.44	288.60	97775	195550
LCF-Luiz1K-015-03	0.300	0.023	0.277	548.43	284.42	8551	17102
LCF-Luiz1L-015-04	0.300	0.013	0.287	575.90	279.77	19332	38664
LCF-Luiz1M-010-01	0.200	0.00029	0.19971	411.24	201.86	788684	1577368
LCF-Luiz1N-010-02	0.200	0.00147	0.19853	414.69	201.52	191591	383182
LCF-Luiz1O-010-03	0.200	0.00128	0.19872	415.58	174.75	567651	1135302

Table 3.23 – Results of fatigue tests performed under strain-control conditions (R_ε=-1 and R_ε=0) for the material from the Fão bridge [13].

Specimens	R_ε	$\Delta\varepsilon$	$\Delta\varepsilon^P$	$\Delta\varepsilon^E$	$\Delta\sigma$	σ_{max}	N_f	$2N_f$
		%	%	%	MPa	MPa	cycles	reversals
LCF-e020-01	-1	0.400	0.101	0.299	561.79	277.43	4416	8832
LCF-e020-02		0.400	0.091	0.309	591.80	287.77	5433	10866
LCF-e020-03		0.400	0.077	0.323	736.84	356.74	8420	16840
LCF-e015-01		0.300	0.027	0.273	507.97	225.52	49300	98600
LCF-e015-02		0.300	0.027	0.273	522.47	230.89	16788	33576
LCF-e015-03		0.300	0.027	0.273	550.33	259.05	27731	55462
LCF-e040-01		0.800	0.441	0.359	657.58	315.05	374	748
LCF-e040-02		0.800	0.355	0.445	730.47	347.96	452	904
LCF_e025-01		0.500	0.192	0.308	631.26	305.33	290	580
LCF-e025-02		0.500	0.171	0.329	623.48	303.19	2108	4216
LCF-e025-03		0.500	0.197	0.303	617.30	297.89	2254	4508
LCF-e010-01		0.200	0.006	0.194	381.34	166.97	530604	1061208
LCF-e010-02		0.200	0.005	0.195	391.23	134.27	663962	1327924
LCF-e010-03		0.200	0.009	0.191	375.88	155.97	74549	149098
LCF-150-01	0	1.500	1.079	0.421	616.59	372.47	143	286
LCF-100-01		1.000	0.554	0.446	824.48	406.74	92	184
LCF-100-02		1.000	0.612	0.388	616.37	305.24	955	1910
LCF-100-03		1.000	0.620	0.380	654.92	324.96	528	1056
LCF-075-01		0.750	0.319	0.431	755.61	361.40	384	768
LCF-075-02		0.750	0.334	0.416	779.19	385.97	250	500
LCF-075-03		0.750	0.373	0.377	699.42	345.92	507	1014
LCF-050-01		0.500	0.169	0.331	572.95	282.58	1106	2212
LCF-050-02		0.500	0.121	0.379	715.77	351.51	3454	6908
LCF-050-03		0.500	0.158	0.342	636.91	331.55	1195	2390
LCF-030-01		0.300	0.074	0.226	531.51	300.39	25560	51120
LCF-030-02		0.300	0.026	0.274	526.50	278.63	22618	45236
LCF-030-03		0.300	0.025	0.275	494.96	272.04	15517	31034
LCF-025-01		0.250	0.069	0.181	467.02	262.92	23878	47756
LCF-025-02		0.250	0.061	0.189	464.76	202.33	76677	153354
LCF-025-03		0.250	0.007	0.243	483.21	237.01	39998	79996
LCF-020-01		0.200	0.050	0.150	372.07	217.32	692177	1384354
LCF-020-02		0.200	0.016	0.184	376.46	214.90	357127	714254
LCF-020-03		0.200	0.019	0.181	385.79	213.07	54116	108232
LCF-020-04		0.200	0.025	0.175	398.56	247.24	306129	612258
LCF-015-01		0.150	0.004	0.146	296.46	158.81	1000000*	2000000*

*Run-out

3.4.1. Cyclic elastoplastic behaviour

Metals when subjected to reversible plastic strains, exhibit a cyclic elastoplastic behaviour which is distinct from its monotonic plastic behaviour. The cyclic elastoplastic behaviour may be characterized by several phenomena, namely: i) cyclic hardening or cyclic softening; ii) cyclic mean stress relaxation; iii) cyclic creep or progressive plastic deformation. In addition to these cyclic behaviours, memory effect and dependency on the strain rate may occur for some materials.

The cyclic curve of the material can be determined connecting the tips of several stabilized hysteresis loops, obtained for different strain amplitudes. The technique for the evaluation of the cyclic curve may be based on a single specimen test for each point of the cyclic curve, which was the case followed to analyse the data available for the bridge materials. The cyclic curve can be described by the relation proposed by Morrow [22]:

$$\frac{\Delta\sigma}{2} = K' \cdot \left(\frac{\Delta\varepsilon^P}{2} \right)^{n'} \tag{3.2}$$

where *K'* and *n'* are the cyclic strain hardening coefficient and exponent, respectively; $\Delta\varepsilon^P$ is plastic strain range; and $\Delta\sigma$ is the stress range. In metals, the cyclic strain hardening exponent, n', varies usually in range of 0.05 to 0.25.

Since for some materials and certain strain rates, the stabilized behaviour was not achieved during the cyclic loading, the stabilized hysteresis loops were extracted using the half-life criterion. Therefore, the stabilized behaviour may correspond, for some cases to a pseudo-stabilized behaviour.

Alternatively, the Ramberg–Osgood mathematical representation of the cyclic curve may be presented in the following form, using the total strain amplitude instead of the plastic strain [23]:

$$\frac{\Delta\varepsilon}{2} = \frac{\Delta\varepsilon^E}{2} + \frac{\Delta\varepsilon^P}{2} = \frac{\Delta\sigma}{2E} + \left(\frac{\Delta\sigma}{2K'} \right)^{1/n'} \tag{3.3}$$

where *E* is the Young modulus; $\Delta\sigma$ and $\Delta\varepsilon$ are, respectively, the stress and strain ranges; $\Delta\varepsilon^E$ and $\Delta\varepsilon^P$ are, respectively, the elastic and plastic strain ranges and *K'* and *n'* are the same constants of Equation (3.2).

3.4.1.1. Eiffel bridge

Figure 3.13 presents the stabilized hysteresis loops together with the cyclic for the sample curve of the material from the Eiffel bridge, obtained for a strain ratio equal to -1 while Figure 3.14 shows, for the sample material, the superposition of several stabilized hysteresis loops, with the lower tips coinciding at the origin of the graph. Besides the cyclic curve, a cyclic curve scaled by a factor of two is plotted in the figure. The analysis of the figure shows some deviation from the Masing behaviour; however, that deviation

may be partly attributed to the scatter in material behaviour due to the high level of heterogeneities found in the microstructures of the material. Taking into account the scatter effects one may conclude that this material fairly follows the Masing behaviour [18].

Figure 3.15 illustrates the evolution of the cyclic stress amplitude with the number of cycles for the tested strain ranges. The analysis of the data reveals that the material from the Eiffel bridge shows some cyclic hardening for higher strain ranges. This hardening reduces progressively with diminishing applied strain range until it stabilizes when elastic behaviour is achieved.

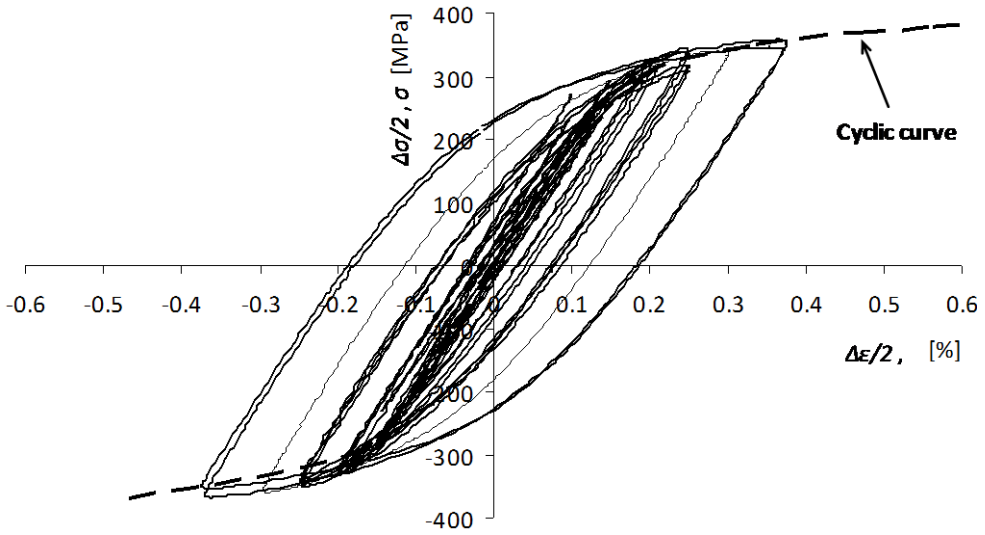

Figure 3.13 – Stabilized hysteresis loops together with the cyclic curve of the Eiffel bridge material, R_ε=-1.

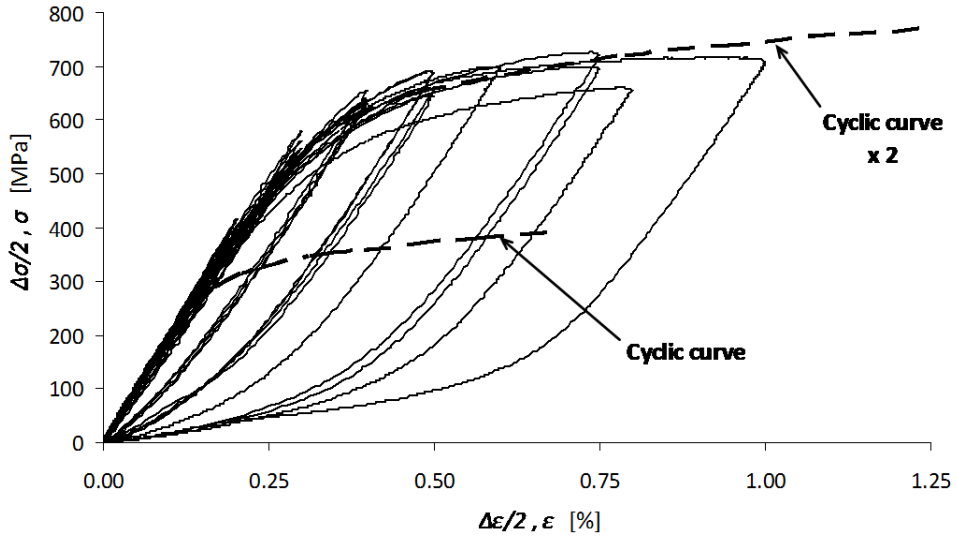

Figure 3.14 – Stabilized hysteresis loops together with the cyclic curve of the Eiffel bridge material, with the lower tips coinciding at the origin, R_ε=-1.

Figure 3.16 shows the cyclic curve of the material in the form of the stress amplitude versus plastic strain amplitude (Equation (3.2)). From the analysis of Figure 3.16 results directly the cyclic strain hardening coefficient (*K'*) and exponent (*n'*) of the material.

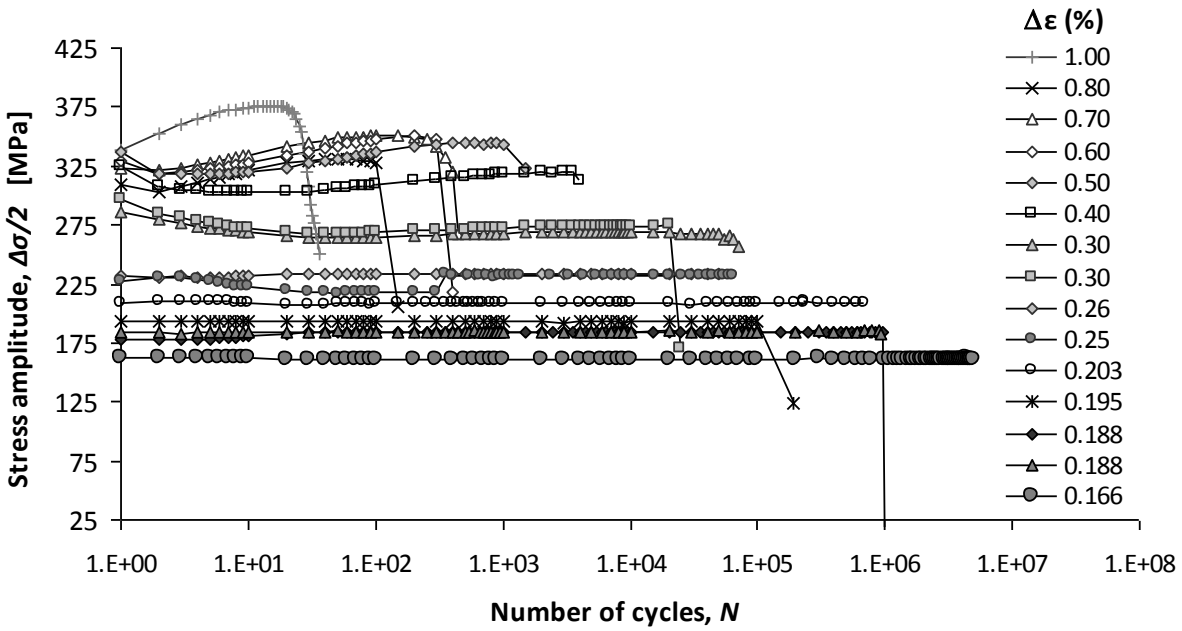

Figure 3.15 – Stress amplitude versus number of cycles for fully-reversed strain-controlled tests, R_ε=-1, of the Eiffel bridge material

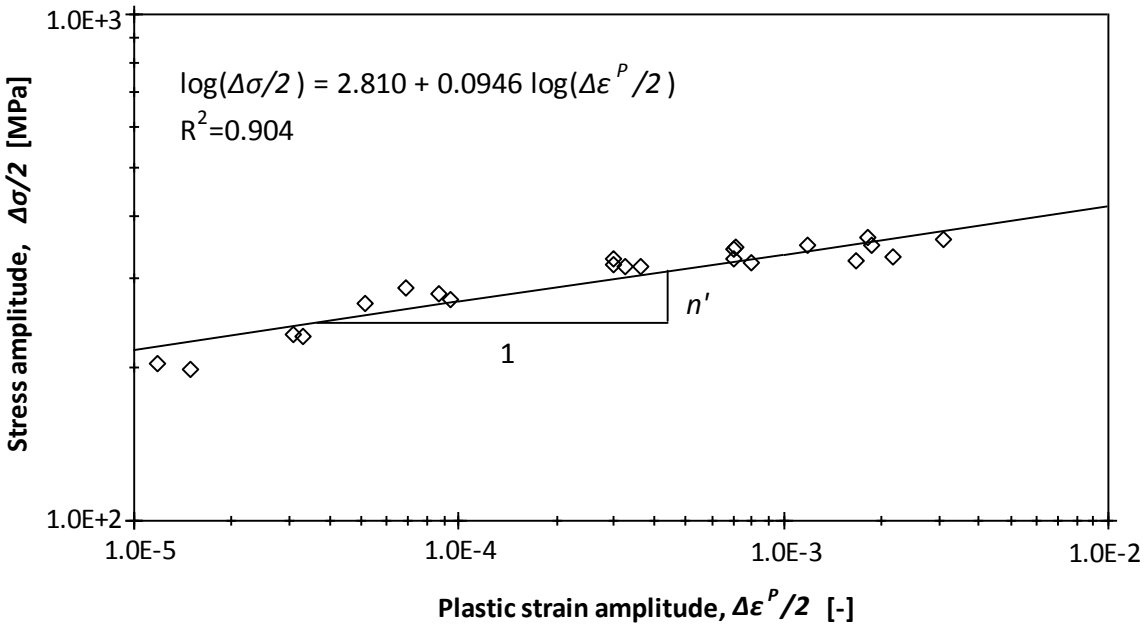

Figure 3.16 – Cyclic curve, $\Delta\sigma/2$ versus $\Delta\varepsilon^P/2$ (R_ε=-1), for the Eiffel bridge material.

3.4.1.2. Luiz I bridge

Figure 3.17 presents the stabilized hysteresis loops together with the cyclic curve for the sample of the material from the Luiz I bridge, obtained for a strain ratio equal to -1 [18] while Figure 3.18 shows, for the same material, the superposition of several stabilized hysteresis loops, with the lower tips coinciding at the origin of the graph. This material from the Luiz I bridge shows some deviation from the Masing behaviour; this deviation may be also partially attributed to the scatter in material behaviour. Therefore, the material from the Luiz I bridge shows a cyclic behaviour that fairly follows the Masing behaviour, similarly to the material of the Eiffel bridge. Figure 3.19 illustrates the evolution of the cyclic stress amplitude with the number of cycles for the tested strain ranges. The analysis of the data reveals that the material from the Luiz I bridge shows some slight cyclic hardening for higher strain ranges. However, this hardening fades with the decrease in the applied strain range, until stabilization is achieved, when the elastic behaviour is attained.

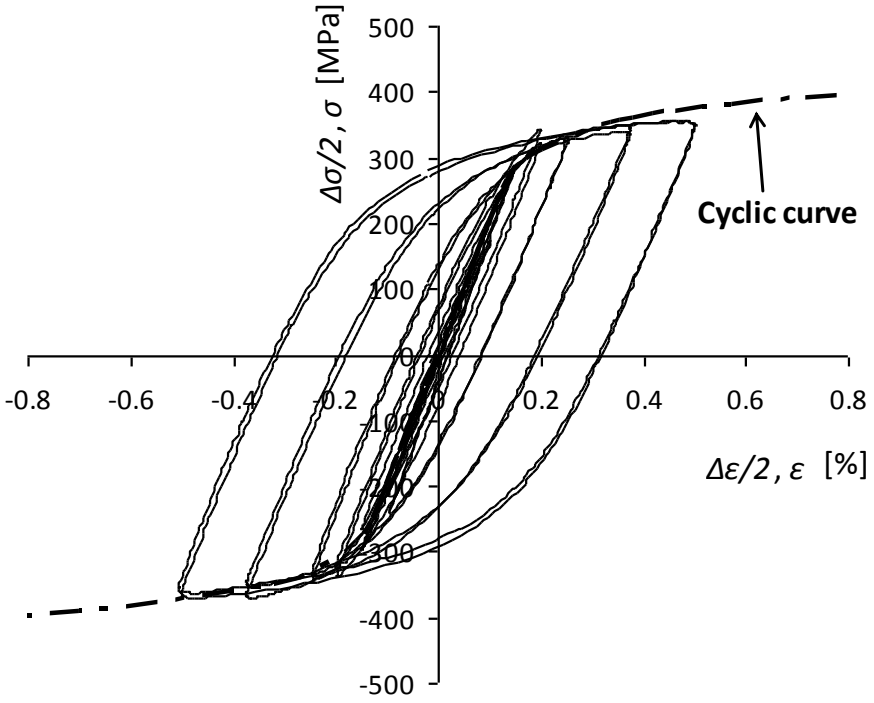

Figure 3.17 – Stabilized hysteresis loops together with the cyclic curve of the Luiz I bridge material, R_ε=-1.

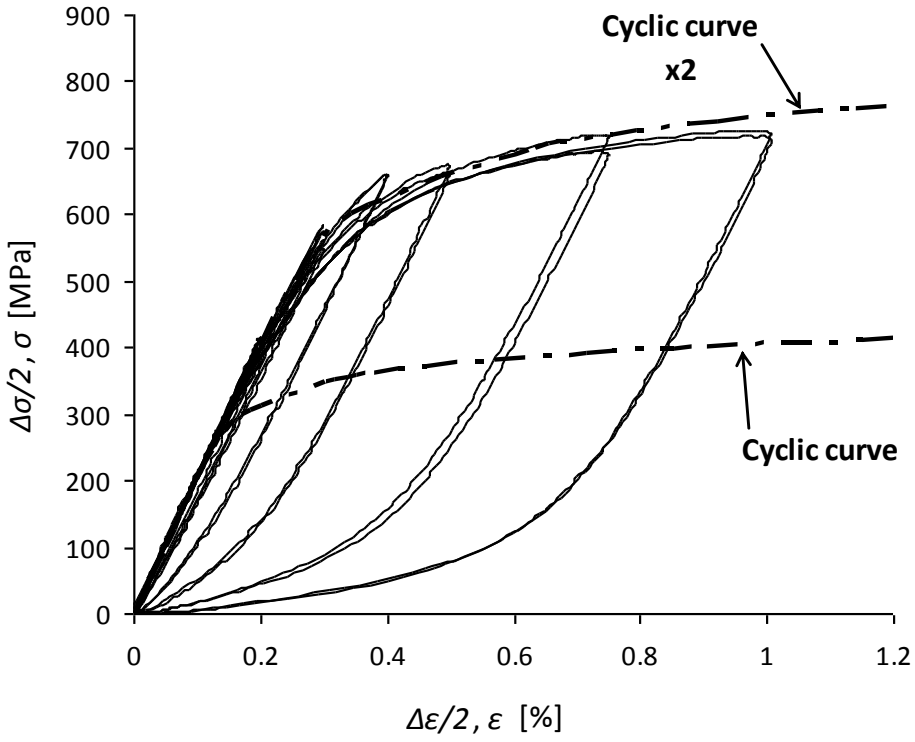

Figure 3.18 – Stabilized hysteresis loops together with the cyclic curve of the Luiz I bridge material, with the lower tips coinciding at the origin, R_ε=-1.

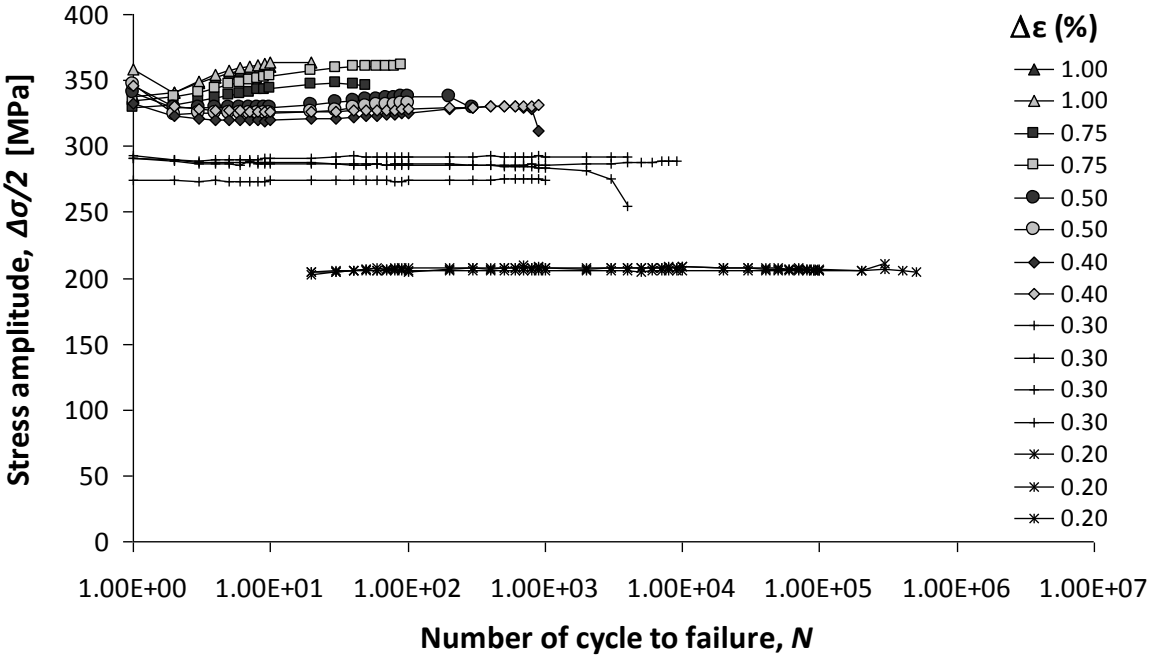

Figure 3.19 – Stress amplitude versus number of cycles for fully-reversed strain-controlled tests , R_ε=-1, of the Luiz I bridge material.

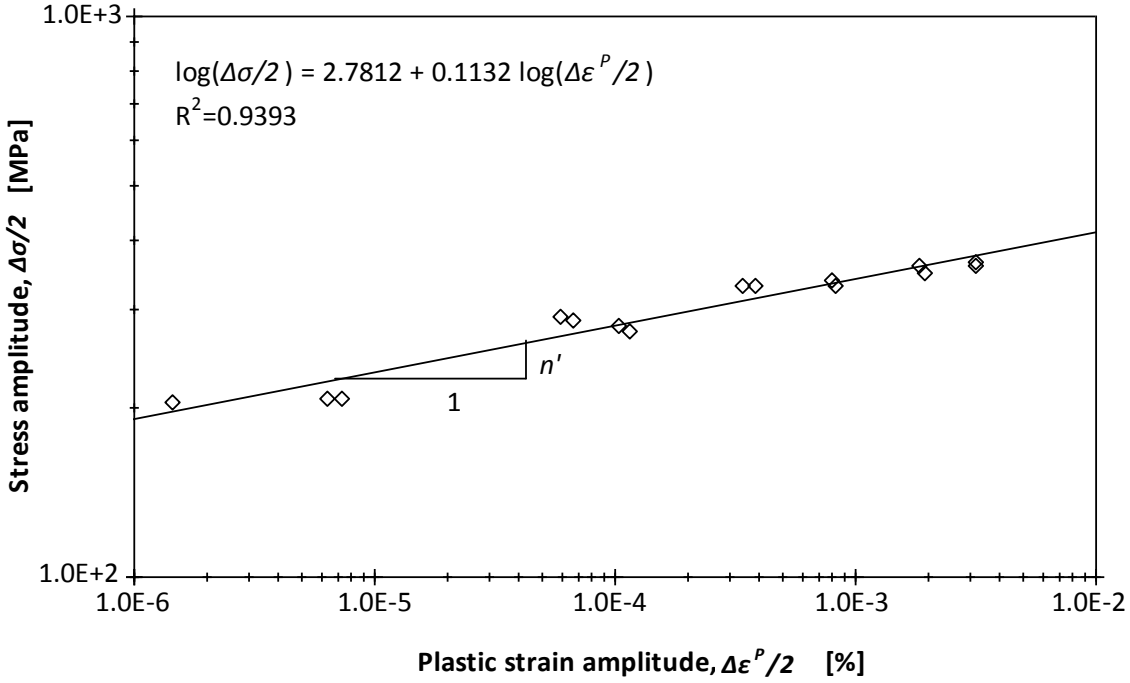

Figure 3.20 – Cyclic curve, $\Delta\sigma/2$ versus $\Delta\varepsilon^P/2$ (R_ε=-1), for the Luiz I bridge material.

Figure 3.20 shows the cyclic curve of the material from the Luiz I bridge in the form of a stress amplitude versus plastic strain amplitude plot, for direct assessment of the hardening constants, namely the cyclic strain hardening coefficient (*K'*) and exponent (*n'*). Taking into account the type of materials under investigation, the determination coefficient is considered very satisfactory.

3.4.1.3. Fão bridge

Figure 3.21 presents the stabilized hysteresis loops together with the cyclic curve for the sample of the material from the Fão bridge, obtained for strain ratios equal to -1 [13,18] while Figures 3.22 and 3.23 show, for the same material, the superposition of several stabilized hysteresis loops, with the lower tips coinciding at the origin of the graph, obtained for strain ratios equal to -1 and 0, respectively. The significant scatter observed in the hysteresis loops hinders the assessment of the Masing behaviour of the material. This scatter is noticeable in the material from the Fão bridge showing two anomalous hysteresis loops, for strain ratio equal -1. Neglecting these two hysteresis loops the material shows Masing behaviour for strain ratio equal -1. For null strain ratio, the material from Fão bridge shows a clear non-Masing behaviour. It seems that hysteresis loops of the material from Fão bridge are sensitive to the strain.

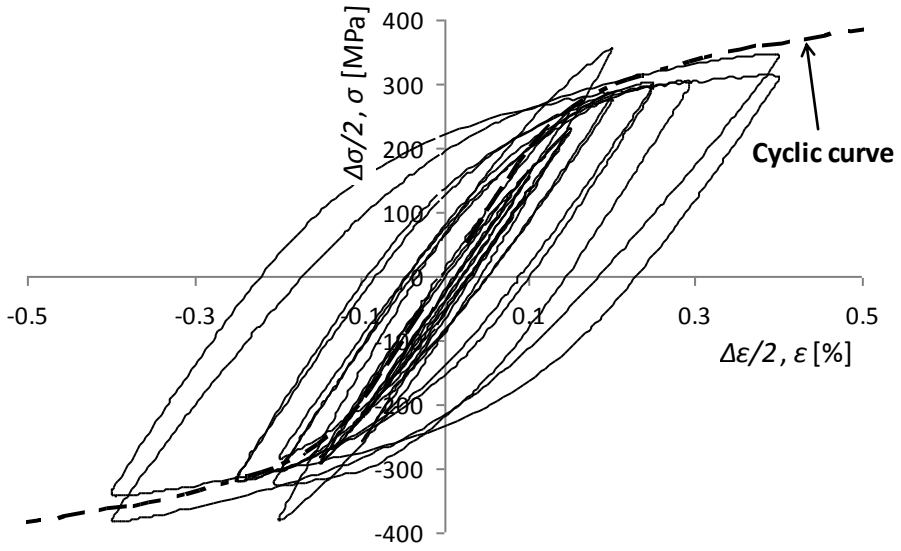

Figure 3.21 – Stabilized hysteresis loops together with the cyclic curve of the Fão bridge material, R_ε=-1.

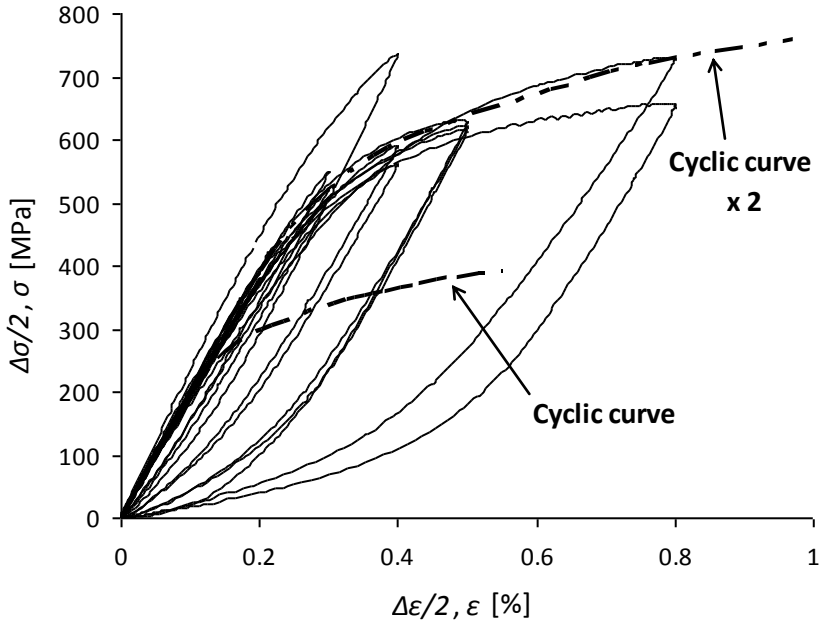

Figure 3.22 – Stabilized hysteresis loops together with the cyclic curve of the Fão bridge material, with the lower tips coinciding at the origin, R_ε=-1.

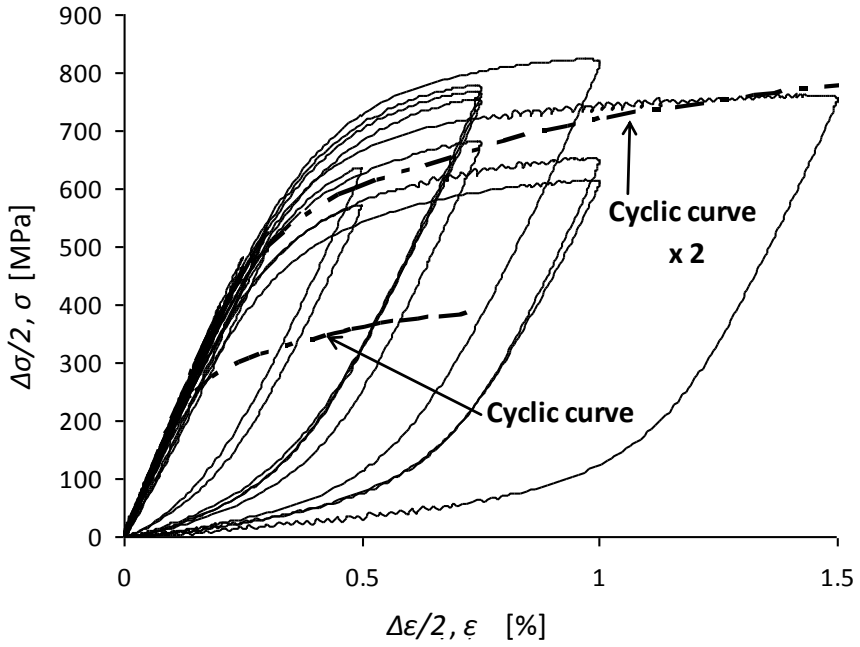

Figure 3.23 – Stabilized hysteresis loops together with the cyclic curve of the Fão bridge material, with the lower tips coinciding at the origin, R_ε=0.

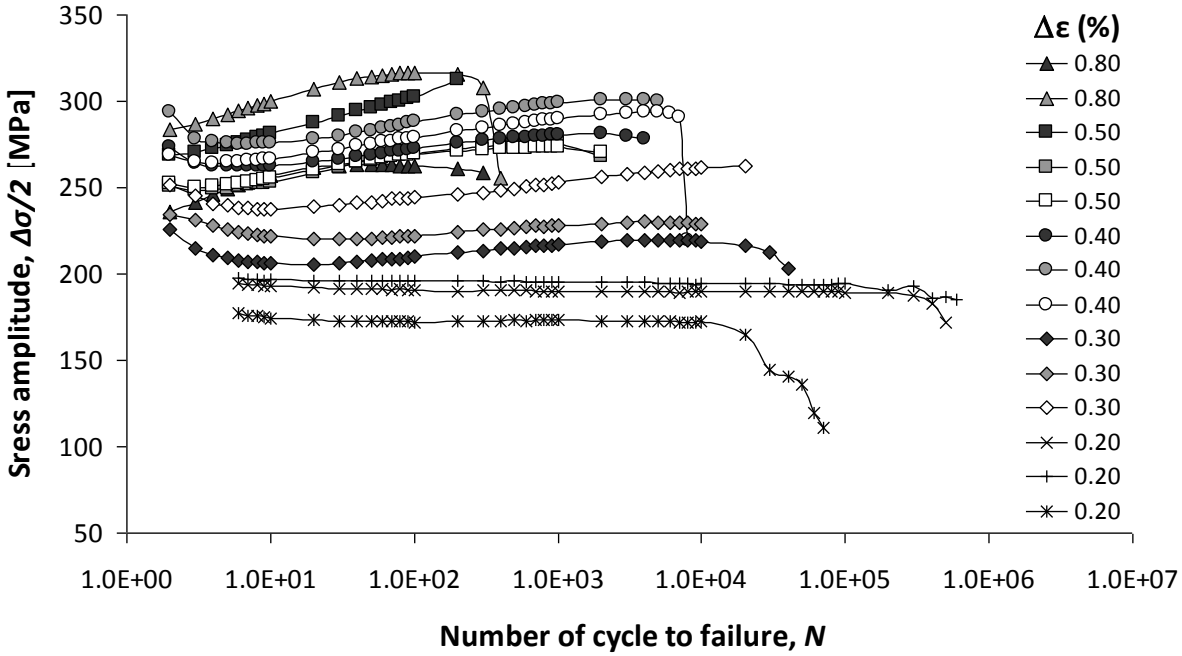

Figure 3.24 – Stress amplitude versus number of cycles for fully-reversed strain-controlled tests, R_ε=-1, of the Fão bridge material.

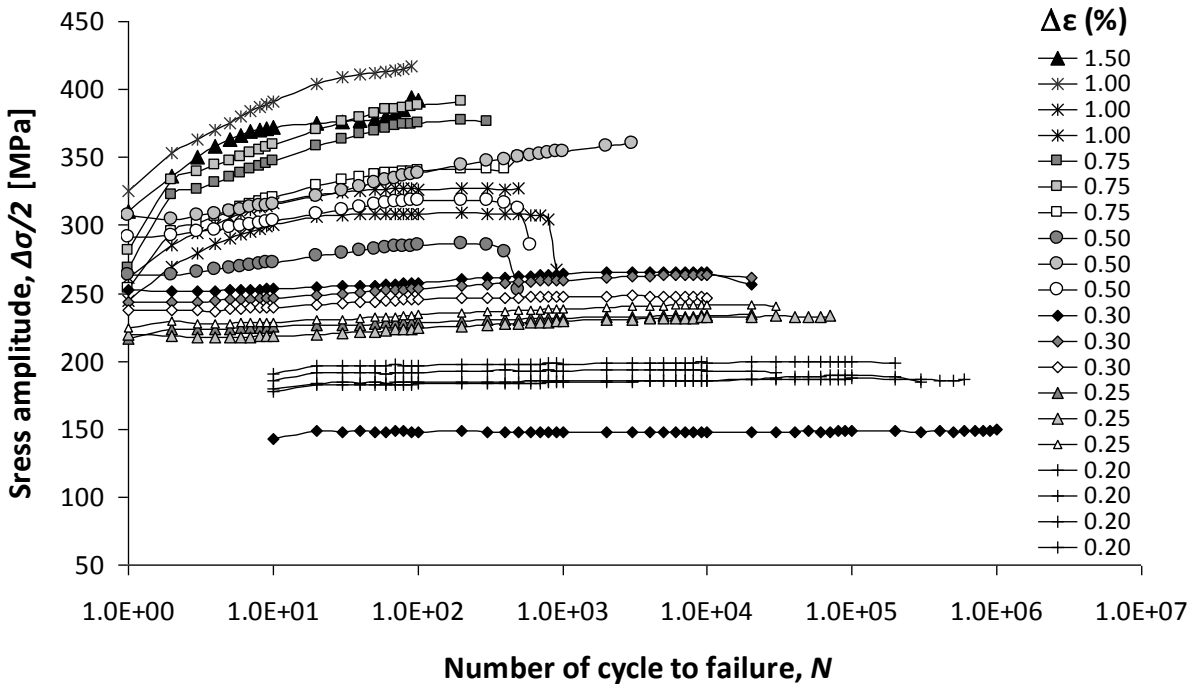

Figure 3.25 – Stress amplitude versus number of cycles for alternate strain-controlled tests, R_ε=0, of the Fão bridge material.

Figures 3.24 and 3.25 illustrate the evolution of the cyclic stress amplitude with the number of cycles for the tested strain ranges, for strain ratios equal to -1 and 0, respectively. The analysis of the data reveals that material from the Fão bridge displays cyclic hardening for higher strain ranges, but this cyclic hardening reduces progressively with decreasing applied strain range until it stabilizes for fully elastic behaviour. This behaviour is similar to the behaviour observed for the materials from the Eiffel and Luiz I bridges. It is interesting to note that the material from the Fão bridge shows higher hardening for null strain ratios than for fully-reverse strain loading conditions.

Figures 3.26, 3.27 and 3.28 show the cyclic curves of the material from the Fão bridge. The stress amplitude is plotted versus plastic strain amplitude, for R_ε=-1, R_ε=0 and R_ε=-1 + R_ε=0, respectively. From the analysis of these figures results directly the cyclic strain hardening constants of the material from the Fão bridge. Comparing with the previous materials, lower determination coefficients in the cyclic curve assessment were observed for this material, which is consistent with the higher scatter observed in hysteresis loops depicted in the Figures 3.22 and 3.23.

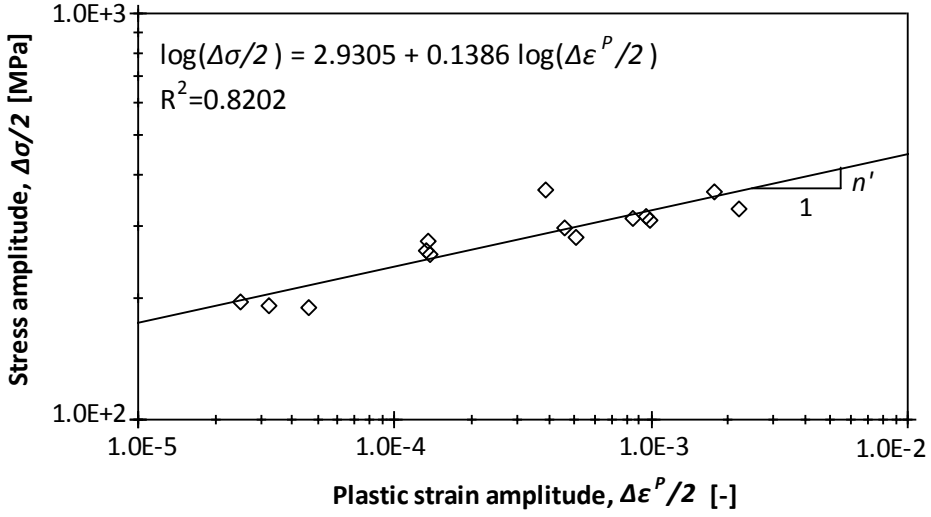

Figure 3.26 – Cyclic curve, $\Delta\sigma/2$ versus $\Delta\varepsilon^P/2$ (R_ε=-1), for the Fão bridge material.

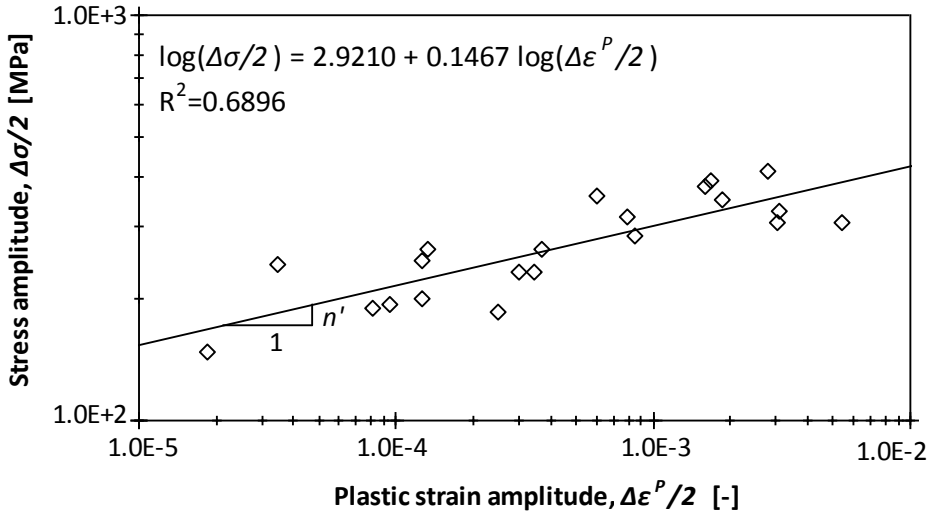

Figure 3.27 – Cyclic curve, $\Delta\sigma/2$ versus $\Delta\varepsilon^P/2$ (R_ε=0), for the Fão bridge material.

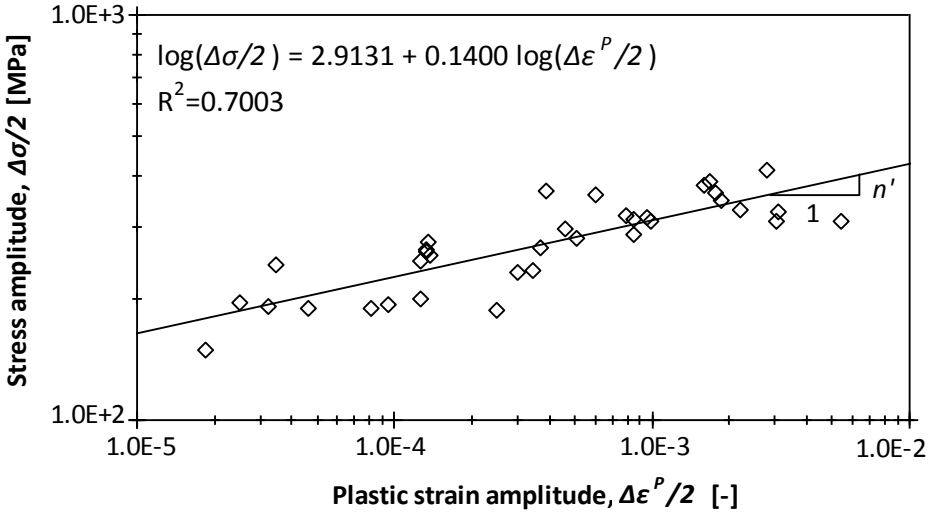

Figure 3.28 – Cyclic curve, $\Delta\sigma/2$ versus $\Delta\varepsilon^P/2$ (R_ε=-1 + R_ε=0), for the Fão bridge material.

3.4.1.4. Trezói bridge

Figure 3.29 presents the stabilized hysteresis loops superimposed with the cyclic curve of the material from the Trezoi bridge [17,18], obtained for a strain ratio equal to -1 while Figure 3.30 shows the superposition of several stabilized hysteresis loops, with the lower tips coinciding at the origin of the graph of the material, together with the cyclic curve magnified by a factor of two. The analysis of this figure shows clearly that the material from the Trezói bridge does not follow the Masing behaviour.

Figure 3.31 illustrates the evolution of the cyclic stress amplitude with the number of cycles for the tested strain ranges and for a strain ratio equal to -1. The material from the Trezói bridge shows a clear cyclic softening for strain ranges below 1.5%. For strain ranges above 1.5%, the cyclic behaviour is not clearly defined since for a strain range of 2.5% a cyclic softening is observed whereas for strain ranges of 2% and 1.5%, a cyclic hardening is verified, after some stabilization. If a comparison between all materials is made only for strain ranges below 1%, but involving plasticity, it is clear that the material from the Trezói bridge shows a cyclic softening while the other materials show cyclic hardening. The material from the Trezói bridge shows higher cyclic hardening values.

Figure 3.32 shows the cyclic curve of the material from the Trezói bridge for a strain ratio equal to -1. From the analysis of Figure 3.32 results directly the cyclic strain hardening coefficient and exponent. Figure 3.33 compares the cyclic curves of the four materials from the Eiffel, Luiz I, Fão and Trezói bridges. The material from the Trezói bridge shows the lowest cyclic yield stress, which means that this material experiences a significant cyclic softening with respect to the others. The other materials show higher cyclic yield stresses. The materials from Eiffel and Fão bridge show similar cyclic behaviours, mainly for lower strain amplitudes. The materials from the Trezói and Luiz I bridges also show similar cyclic behaviours, but in this case for high strain amplitudes.

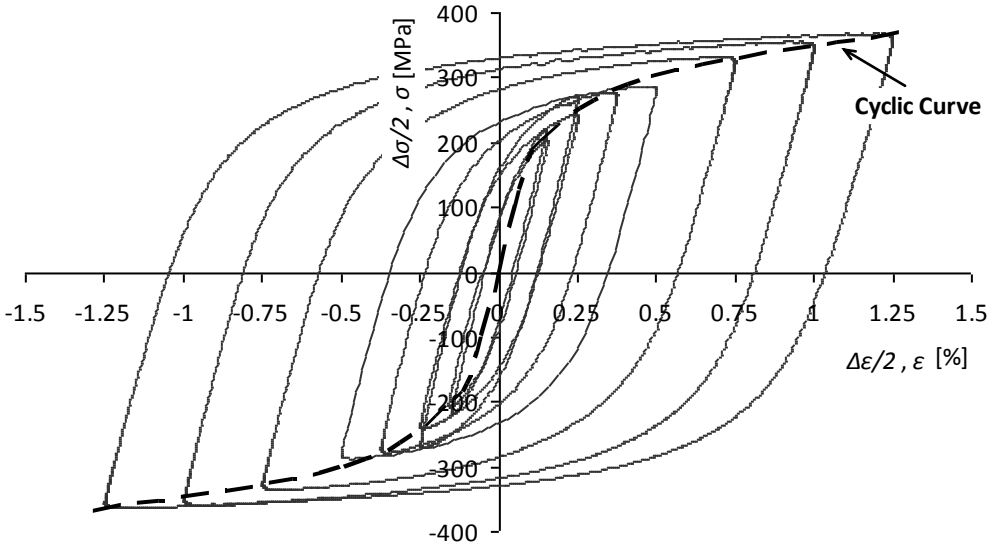

Figure 3.29 – Stabilized hysteresis loops together with the cyclic curve of the Trezói bridge material, R_ε=-1.

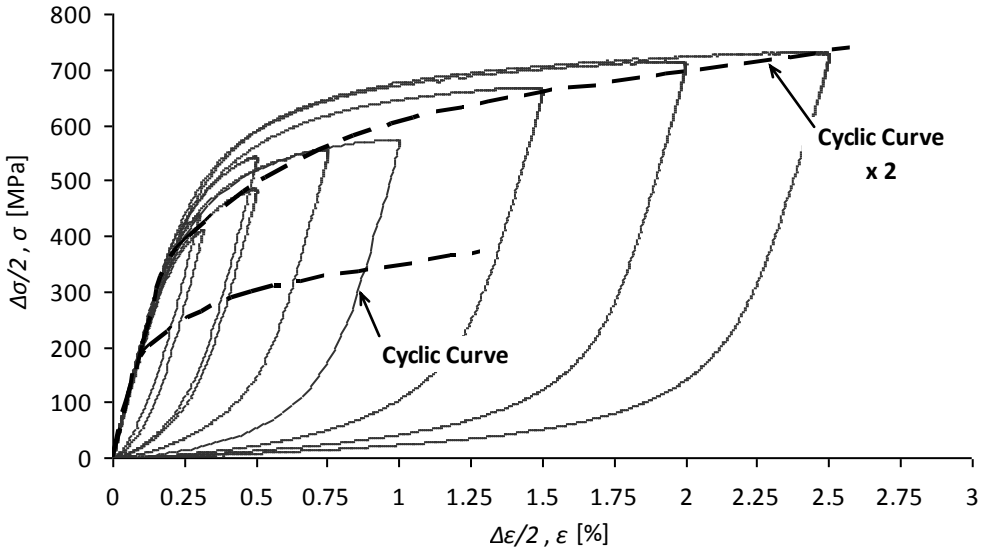

Figure 3.30 – Stabilized hysteresis loops together with the cyclic curve of the Trezói bridge material, with the lower tips coinciding at the origin, R_ε=-1.

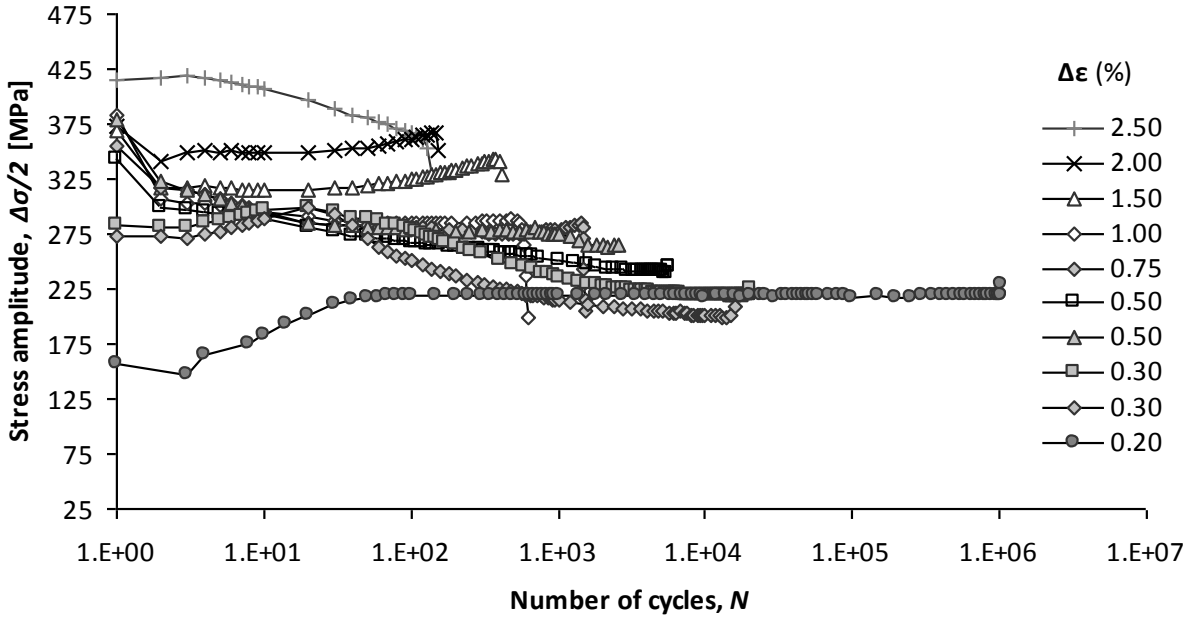

Figure 3.31 – Stress amplitude versus number of cycles for fully-reversed strain-controlled tests, R_ε=-1, of the Trezói bridge material.

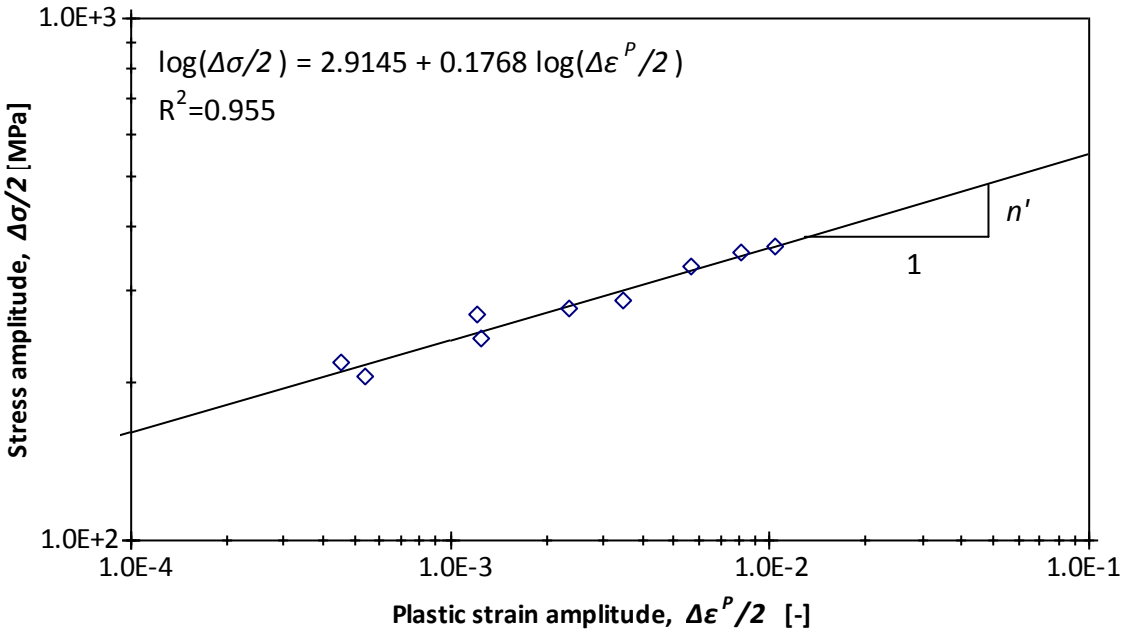

Figure 3.32 – Cyclic curve, $\Delta\sigma/2$ versus $\Delta\varepsilon^P/2$ (R_ε=-1), for the Trezói bridge material.

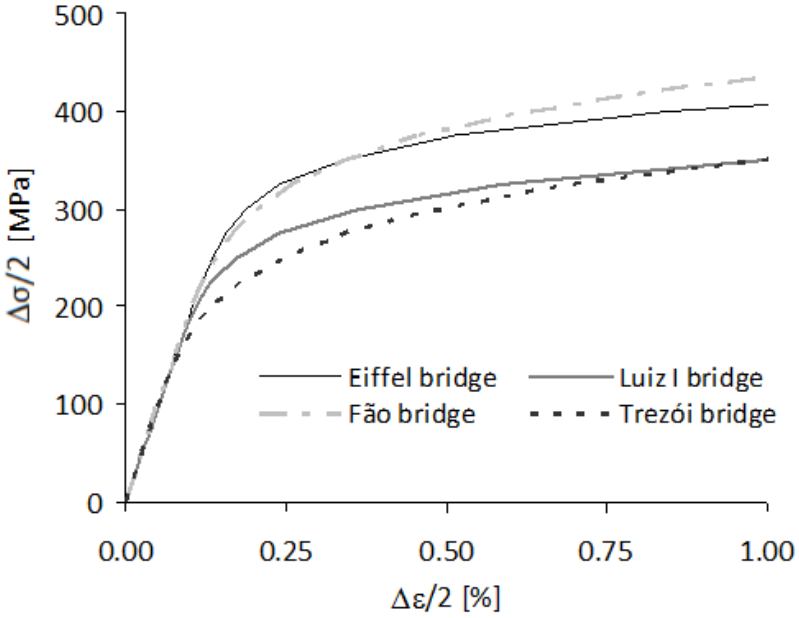

Figure 3.33 – Comparison of the cyclic curves for the materials studied.

3.4.2. Evaluation of fatigue behaviour based on strain-life relations

Low-cycle fatigue results are very often represented using the relation between the strain amplitude and the number of reversals to failure, $2N_f$, usually assumed to correspond to the initiation of a macroscopic crack. The classical way to express the strain-life data is to use the superposition of Coffin [24] and Manson [25] equation with the Basquin [26] equation, usually known as Morrow relation [22]. The Coffin and Manson equation relates the plastic strain amplitude, $\Delta\varepsilon^P/2$, to the number of reversals at crack initiation, $2N_f$:

$$\frac{\Delta\varepsilon^p}{2} = \varepsilon'_f \cdot (2N_f)^c \tag{3.4}$$

where ε'_f and c are, respectively, the fatigue ductility coefficient and fatigue ductility exponent. The Coffin-Manson relation is well suited for the low-cycle fatigue domain whereas the Basquin relation [26] that relates the elastic strain amplitude, $\Delta\varepsilon^E/2$, to the number of reversals to failure $2N_f$, is best suited for high cycle fatigue:

$$\frac{\Delta\varepsilon^E}{2} = \frac{\Delta\sigma}{2E} = \frac{\sigma'_f}{E} \cdot (2N_f)^b \tag{3.5}$$

where σ'_f is the fatigue strength coefficient, b is the fatigue strength exponent and E is the Young modulus. The number of reversals corresponding to the transition between

low and high cycle fatigue regimes is characterized by total strain amplitude composed by equal components of elastic and plastic strain amplitudes. Lives below this transition value are dictated by ductility properties while lives above this transition value are dictated by strength properties. Morrow [22] suggested the superposition of Equations (3.4) and (3.5), resulting in a more general equation, valid for low and high-cycle fatigue regimes:

$$\frac{\Delta\varepsilon}{2}=\frac{\Delta\varepsilon^{E}}{2}+\frac{\Delta\varepsilon^{p}}{2}=\frac{\sigma'_{f}}{E}\cdot\left(2N_{f}\right)^{b}+\varepsilon'_{f}\cdot\left(2N_{f}\right)^{c} \tag{3.6}$$

Alternatively to the Morrow relation, the Smith-Watson-Topper fatigue damage parameter [27] can be used, which shows the following form:

$$\sigma_{max}\cdot\Delta\varepsilon/2=SWT=\left(\sigma'_{f}\right)^{2}\cdot\left(2N_{f}\right)^{2b}/E+\sigma'_{f}\cdot\varepsilon'_{f}\cdot\left(2N_{f}\right)^{b+c} \tag{3.7}$$

where σ_{max} is the maximum stress of the cycle and *SWT* is the damage parameter. Both Morrow and Smith-Watson-Topper models are deterministic models and are used to represent the average fatigue behaviour of the bridge materials based on the available experimental data.

3.4.2.1. Strain-life results and discussion for materials from ancient Portuguese riveted steel bridges

Figures 3.34 to 3.39 present the strain-life data for the materials from the Eiffel, Luiz I, Fão and Trezói bridges. The total strain, i.e. elastic strain plus plastic strain, versus life relations is considered. The data are correlated based on the Coffin-Manson, Basquin and Morrow models. The materials from the centenary bridges shows very low transition lives ($2N_t$), which are bellow the 1×10^3 reversals. The material from the Trezói bridge exhibits a number of transition reversals one order of magnitude higher possibly because the fatigue ductility coefficient is significantly higher in the material from the Trezói bridge than in the materials from the other centenary bridges. The fatigue ductility coefficient increases for younger materials, according to better techniques achieved in the steel production. Regarding the material from the Fão bridge, higher fatigue ductility was verified for the strain ratio equal to -1. For the material from the Fão bridge, two distinct strain-ratios were tested, namely a null-strain ratio and a fully reversible strain history. Besides the individual treatment of the test data for each strain ratio, Figure 3.36

presents the stain-life data for the material from the Fão bridge resulting from the conjunction of both strain ratios, R_ε=-1+R_ε=0 [13].

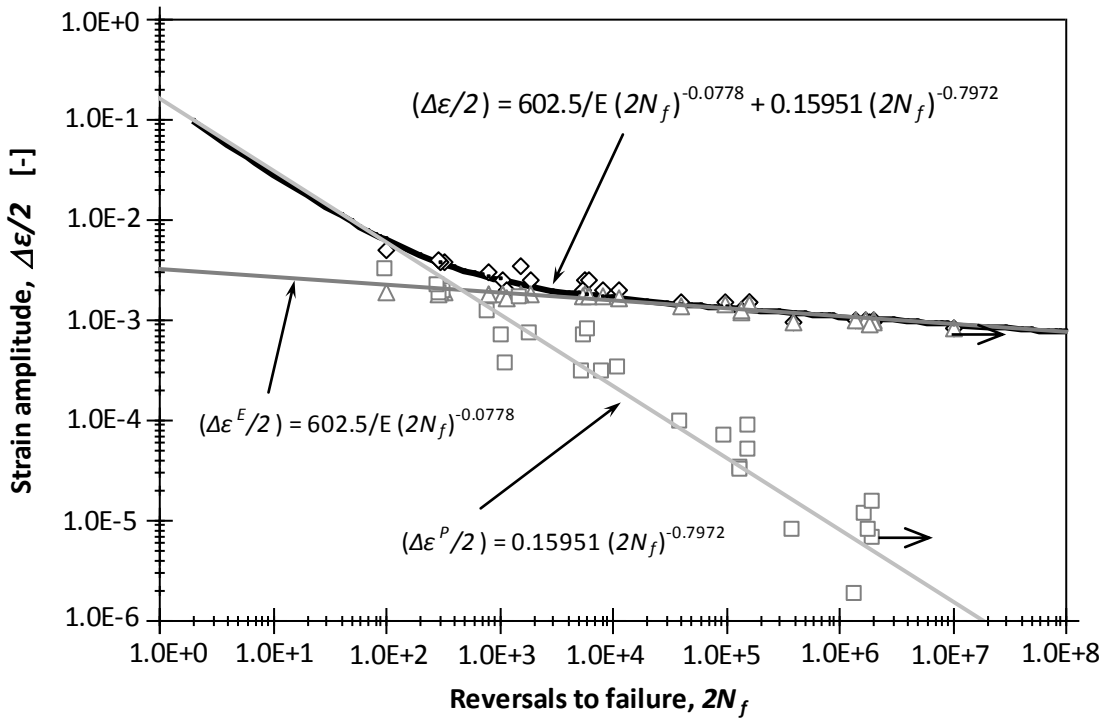

Figure 3.34 – Strain-life curves according to Morrow's model for the material from the Eiffel bridge, R_ε=-1.

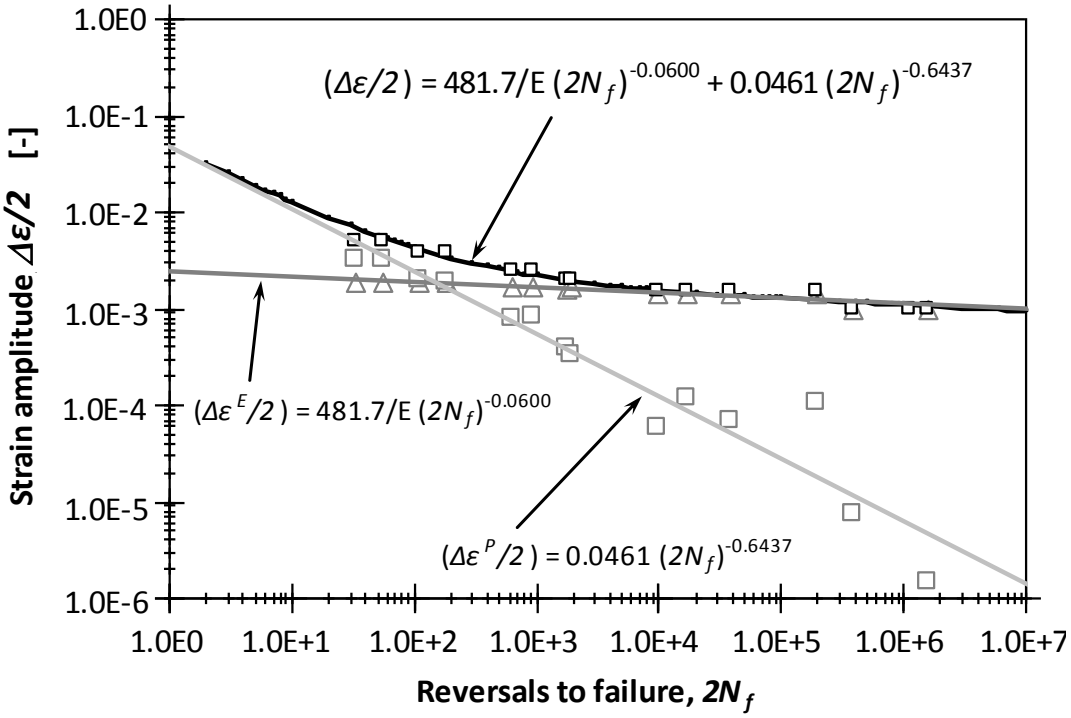

Figure 3.35 – Strain-life curves according to Morrow's model for the material from the Luiz I bridge, R_ε=-1.

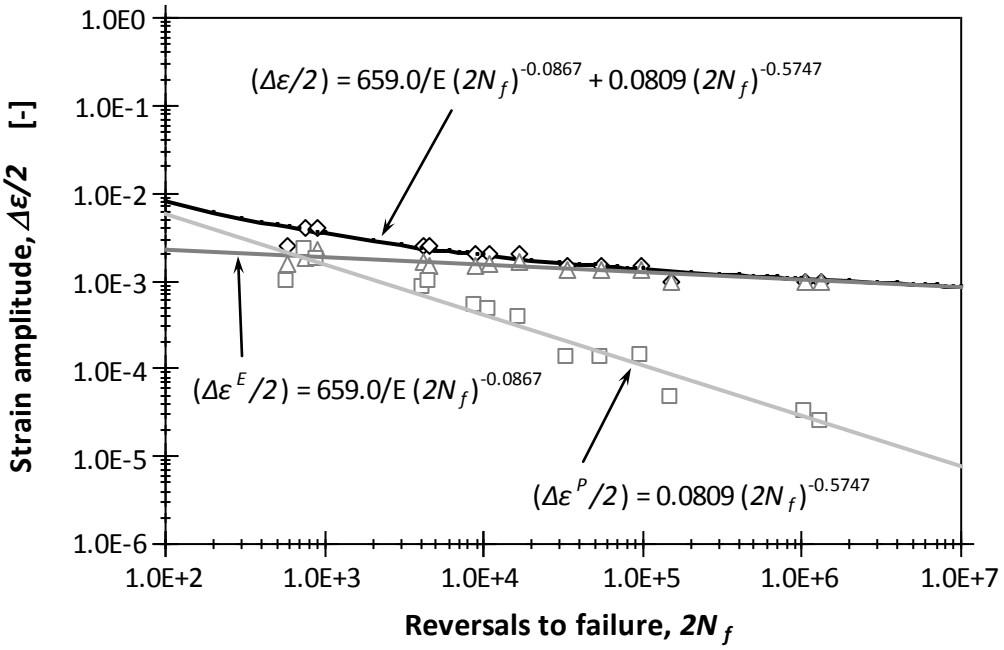

Figure 3.36 – Strain-life curves according to Morrow's model for the material from Fão bridge, R_ε=-1.

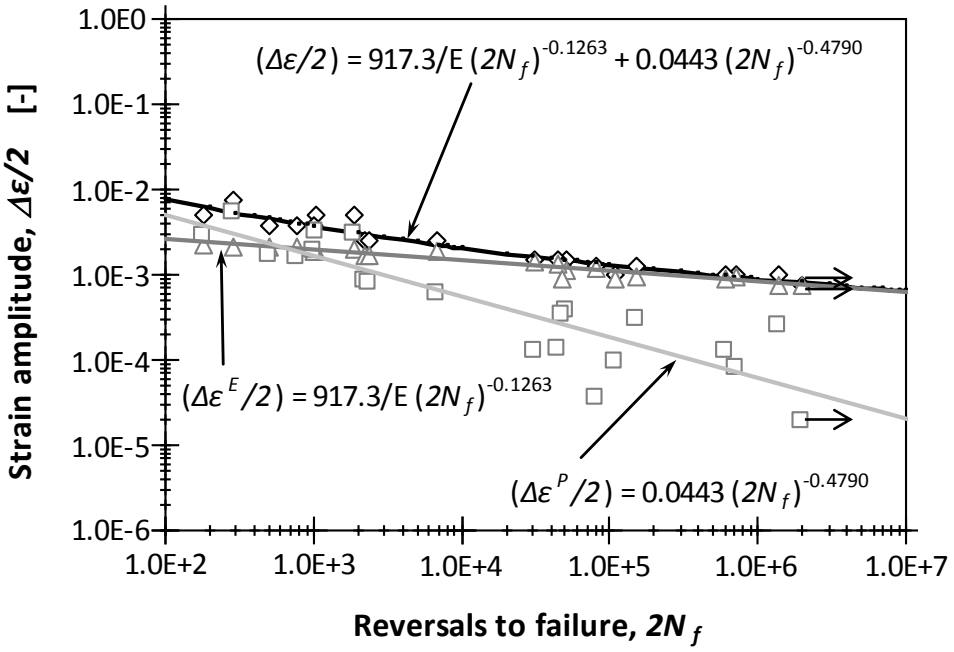

Figure 3.37 – Strain-life curves according to Morrow's model for the material from Fão bridge, R_ε=0.

Tables 3.24 to 3.29 summarize the main parameters derived from the low-cycle fatigue tests, including the constants from the strain-life equation and the cyclic curve of the materials from the Eiffel, Luiz I, Fão and Trezói bridges [13,17,18]. The number of reversals corresponding to the transition from an elastic dominant behaviour to a plastic dominant behaviour is also pointed out in the referred tables.

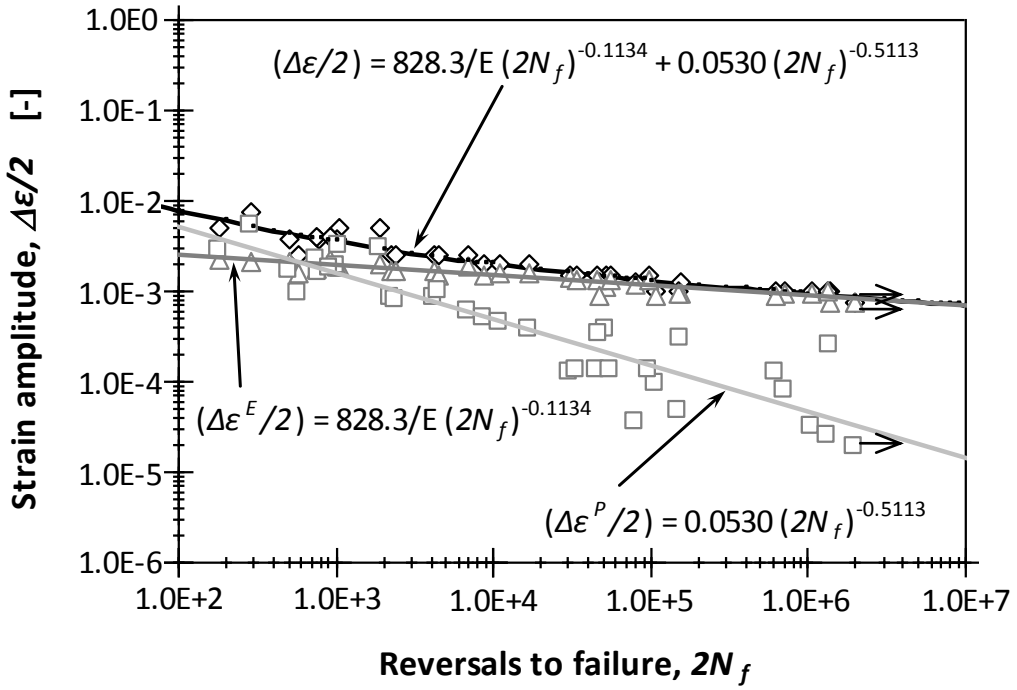

Figure 3.38 – Strain-life curves according to Morrow's model for the material from Fão bridge, R_ε=-1+ R_ε=0.

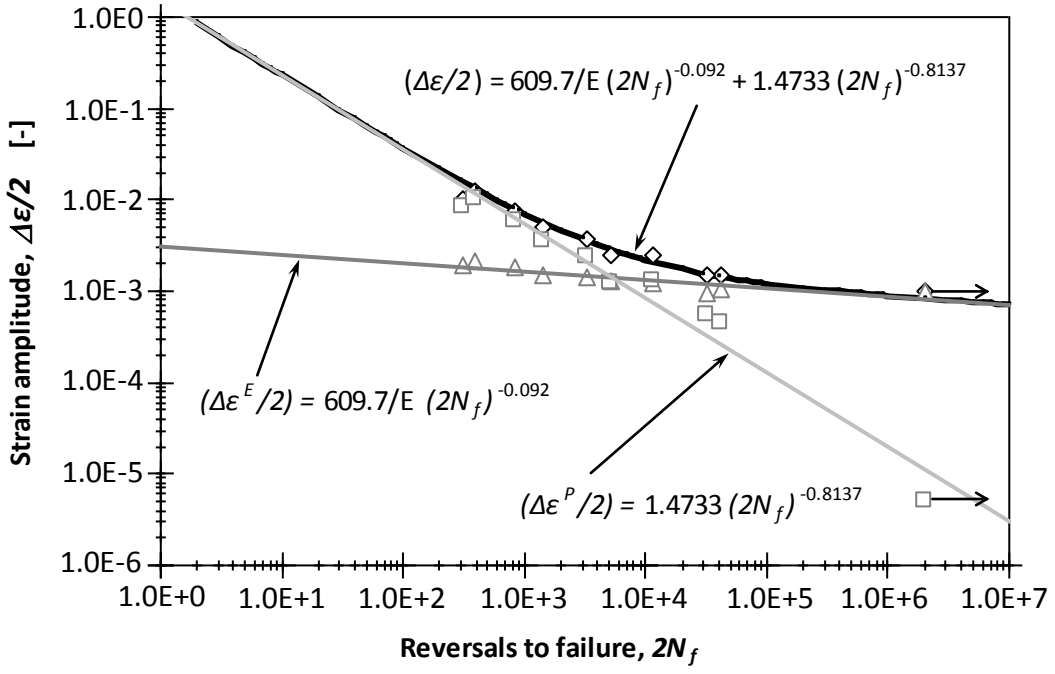

Figure 3.39 – Strain-life curves according to Morrow's model for the material from the Trezói bridge, R_ε=-1.

Table 3.24 – Low-cycle fatigue constants for the material from the Eiffel bridge, R_ε=-1.

Fatigue Strength Coefficient, σ'_f	***Fatigue Strength Exponent, b***	***Determination Coefficient, R^2***
[MPa]	**[-]**	**[-]**
602.5	-0.0778	0.8985
Fatigue Ductility Coefficient, ε'_f	***Fatigue Ductility Exponent, c***	***Determination Coefficient, R^2***
[-]	**[-]**	**[-]**
0.1595	-0.7972	0.9002
Transition Number of Reversals, $2N_f$	***Transition Total Strain Amplitude, $\Delta\varepsilon_t/2$***	***σ'_f / E***
[-]	**[%]**	**[-]**
475	0.3104	0.00312

Table 3.25 – Low-cycle fatigue constants for the material from the Luiz I bridge, R_ε=-1.

Fatigue Strength Coefficient, σ'_f	***Fatigue Strength Exponent, b***	***Determination Coefficient, R^2***
[MPa]	**[-]**	**[-]**
481.7	-0.0600	0.8864
Fatigue Ductility Coefficient, ε'_f	***Fatigue Ductility Exponent, c***	***Determination Coefficient, R^2***
[-]	**[-]**	**[-]**
0.0461	-0.6437	0.9157
Transition Number of Reversals, $2N_f$	***Transition Total Strain Amplitude, $\Delta\varepsilon_t/2$***	***σ'_f / E***
[-]	**[%]**	**[-]**
150	0.3631	0.00243

Table 3.26 – Low-cycle fatigue constants for the material from the Fão bridge, R_ε=-1.

Fatigue Strength Coefficient, σ'_f	***Fatigue Strength Exponent, b***	***Determination Coefficient, R^2***
[MPa]	**[-]**	**[-]**
659.0	-0.0867	0.7836
Fatigue Ductility Coefficient, ε'_f	***Fatigue Ductility Exponent, c***	***Determination Coefficient, R^2***
[-]	**[-]**	**[-]**
0.0809	-0.5747	0.9411
Transition Number of Reversals, $2N_f$	***Transition Total Strain Amplitude, $\Delta\varepsilon_t/2$***	***σ'_f / E***
[-]	**[%]**	**[-]**
695	0.3762	0.00332

Table 3.27 – Low-cycle fatigue constants for the material from the Fão bridge, R_ε=0.

Fatigue Strength Coefficient, σ'_f	***Fatigue Strength Exponent, b***	***Determination Coefficient, R^2***
[MPa]	**[-]**	**[-]**
917.3	-0.1263	0.9226
Fatigue Ductility Coefficient, ε'_f	***Fatigue Ductility Exponent, c***	***Determination Coefficient, R^2***
[-]	**[-]**	**[-]**
0.0443	-0.4790	0.7809
Transition Number of Reversals, $2N_f$	***Transition Total Strain Amplitude, $\Delta\varepsilon_t/2$***	***σ'_f / E***
[-]	**[%]**	**[-]**
609	0.4109	0.00462

Table 3.28 – Low-cycle fatigue constants for the material from the Fão bridge, R_ε=-1+ R_ε=0.

Fatigue Strength Coefficient, σ'_f	***Fatigue Strength Exponent, b***	***Determination Coefficient, R^2***
[MPa]	**[-]**	**[-]**
828.3	-0.1134	0.8645
Fatigue Ductility Coefficient, ε'_f	***Fatigue Ductility Exponent, c***	***Determination Coefficient, R^2***
[-]	**[-]**	**[-]**
0.0530	-0.5113	0.8233
Transition Number of Reversals, $2N_f$	***Transition Total Strain Amplitude, $\Delta\varepsilon_t/2$***	***σ'_f / E***
[-]	**[%]**	**[-]**
334	0.4874	0.00417

Table 3.29 – Low-cycle fatigue constants for the material from the Trezói bridge, R_ε=-1.

Fatigue Strength Coefficient, σ'_f	***Fatigue Strength Exponent, b***	***Determination Coefficient, R^2***
[MPa]	**[-]**	**[-]**
609.7	-0.0920	0.7870
Fatigue Ductility Coefficient, ε'_f	***Fatigue Ductility Exponent, c***	***Determination Coefficient, R^2***
[-]	**[-]**	**[-]**
1.4733	-0.8137	0.9582
Transition Number of Reversals, $2N_f$	***Transition Total Strain Amplitude, $\Delta\varepsilon_t/2$***	***σ'_f / E***
[-]	**[%]**	**[-]**
5184	0.2797	0.00307

Figures 3.40 to 3.45 present the fitting of the fatigue data using the Smith-Watson-Topper damage parameter (=$\sigma_{max}.\varepsilon_a$) resulting in a good correlation with the experimental data. This damage parameter accounts for the mean stress effects, since it depends on the maximum stress of the cycle. The referred figures also include the representation of Equation (3.7).

Figures 3.46 to 3.48 compare the Morrow equation between the materials from the bridges. The analysis of the results confirms that the material from the Trezói bridge shows the highest fatigue resistance for low to high-cycle fatigue regimes. This higher fatigue resistance is mainly due to the higher ductility as illustrates Figure 3.46. All materials show very similar elastic strain-life relations.

Figure 3.49 shows that total strain-life curves for the material from the Fão bridge are not sensitive to the strain ratio. This is the result of the well know behaviour in cyclic plasticity of metals that corresponds to the cyclic mean stress relaxation occuring for non-symmetric strain local conditions.

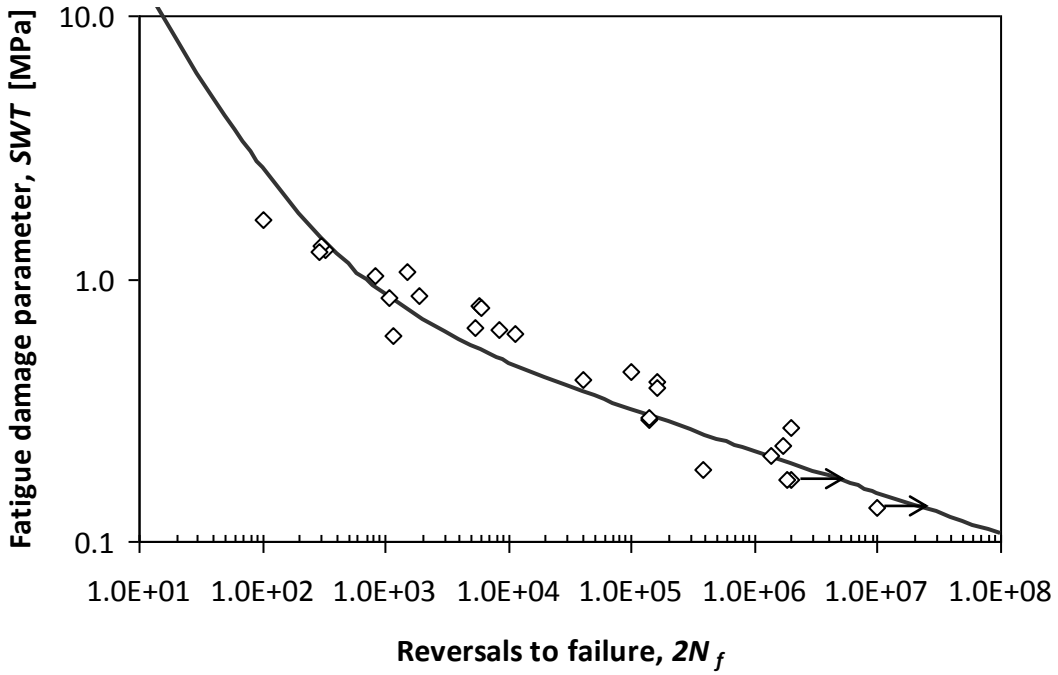

Figure 3.40 – Fitting of the *SWT* model to the lifetime for the material data from Eiffel bridge, R_ε=-1.

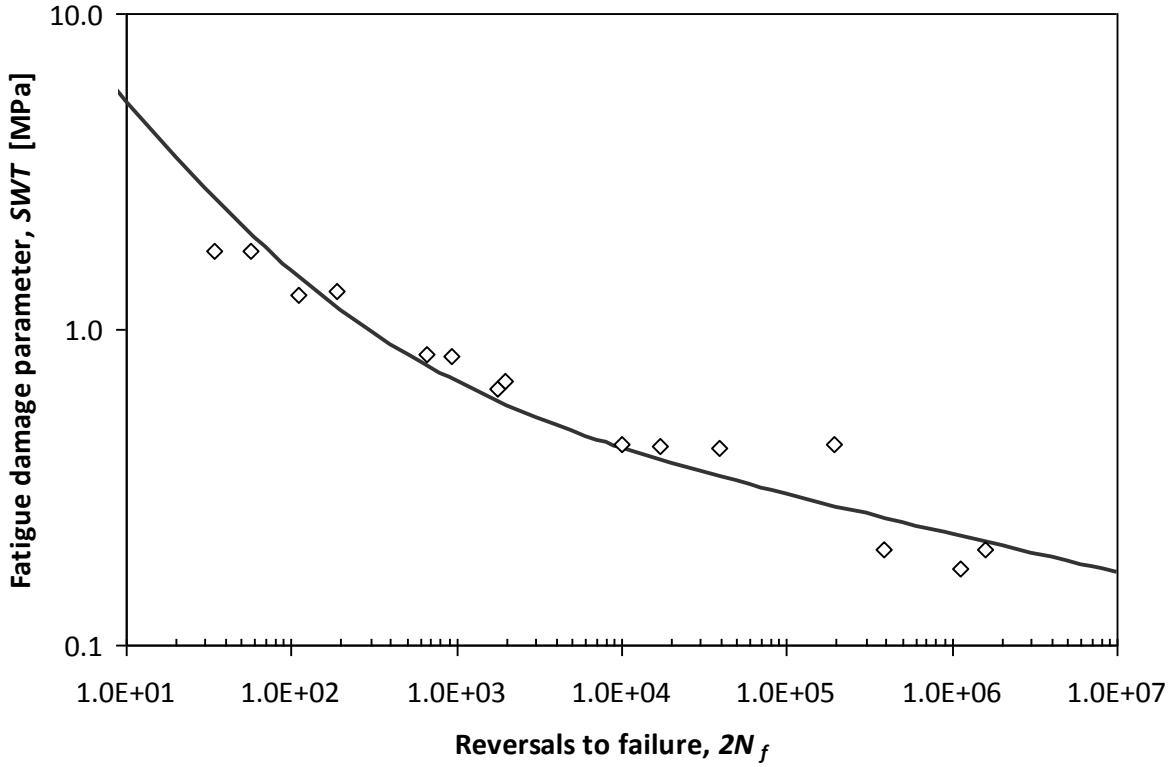

Figure 3.41 – Fitting of the *SWT* model to the lifetime for the material data from Luiz I bridge, R_ε=-1.

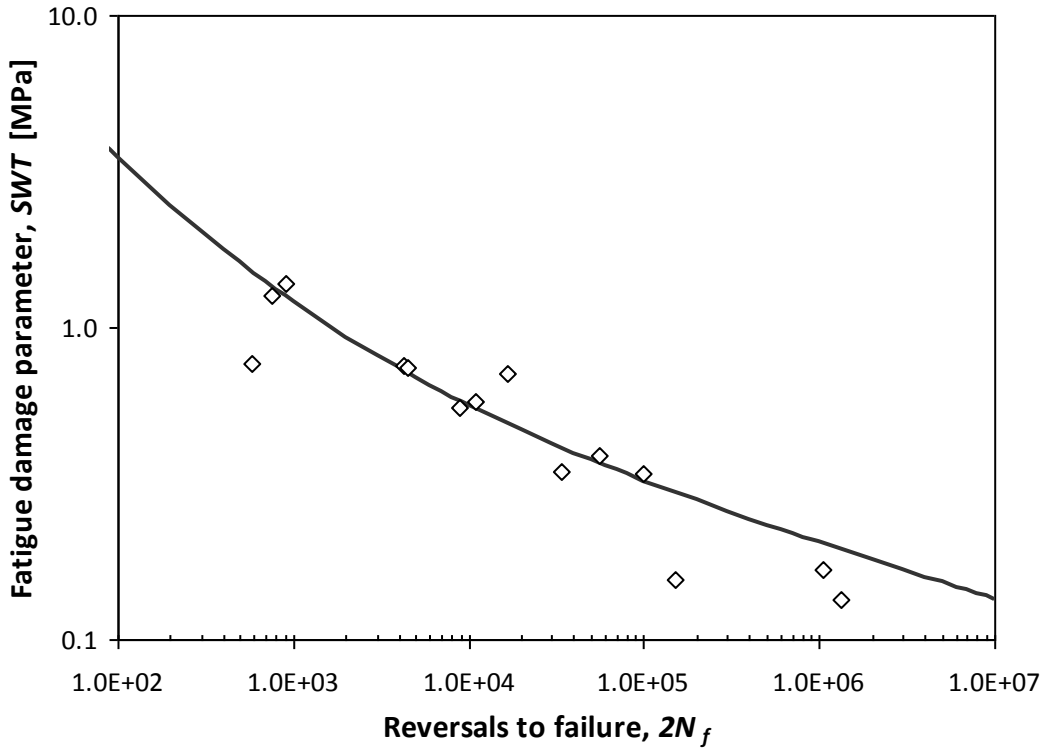

Figure 3.42 – Fitting of the *SWT* model to the lifetime for the material data from Fão bridge, R_ε=-1.

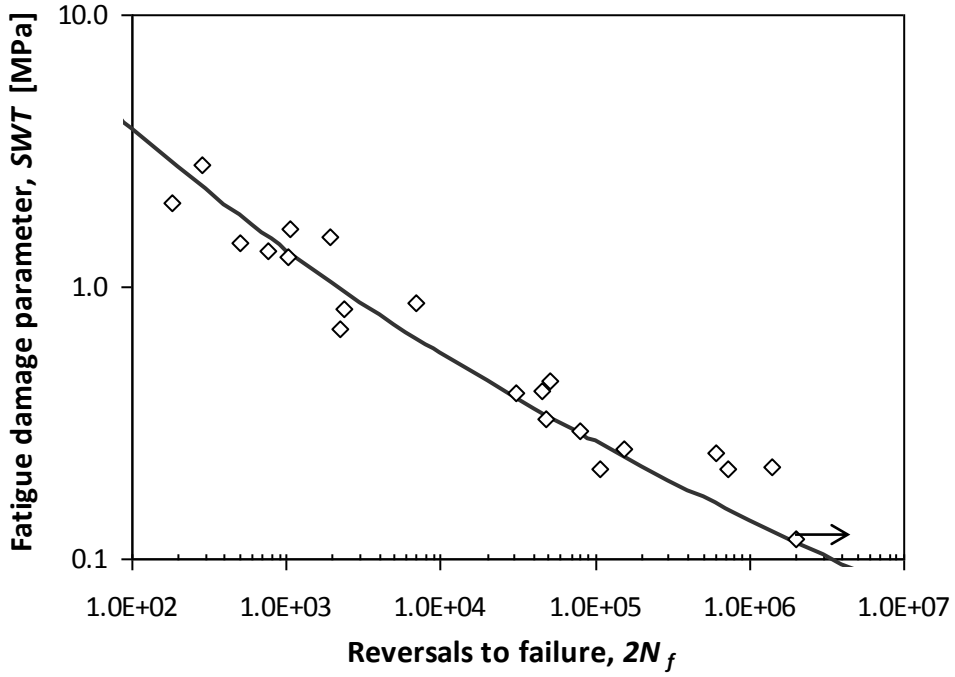

Figure 3.43 – Fitting of the *SWT* model to the lifetime for the material data from Fão bridge, R_ε=0.

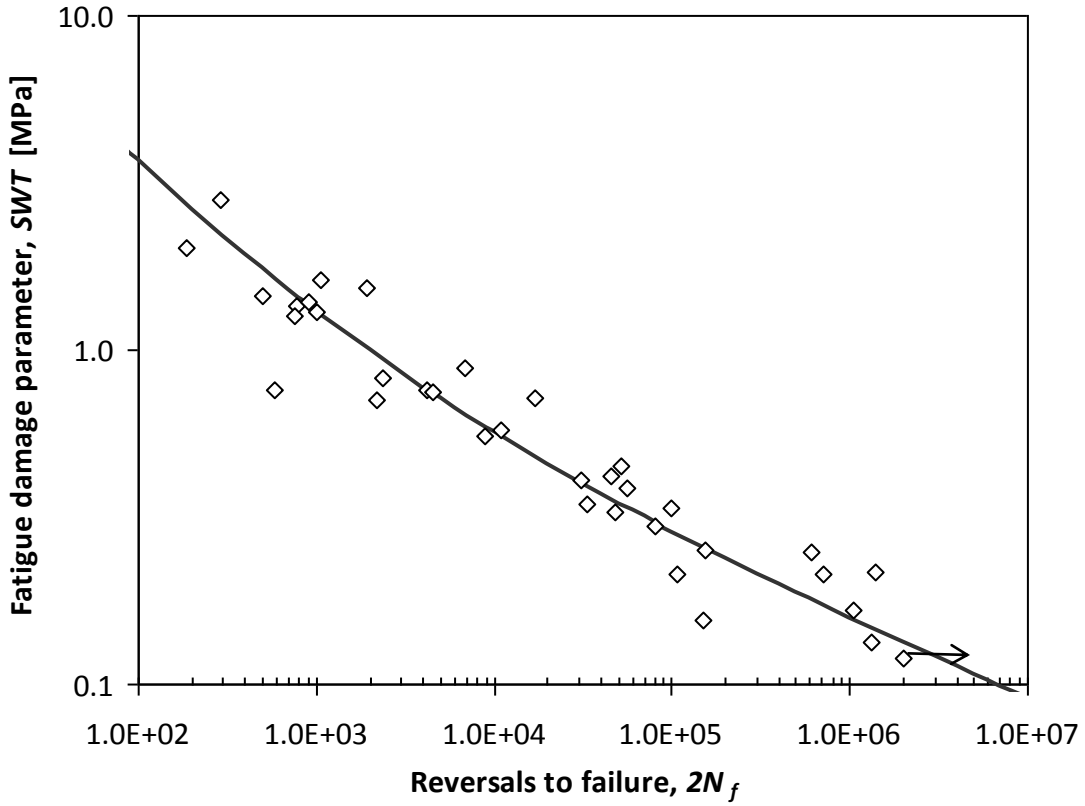

Figure 3.44 – Fitting of the *SWT* model to the lifetime for the material data from the Fão bridge, R_ε=-1+R_ε=0.

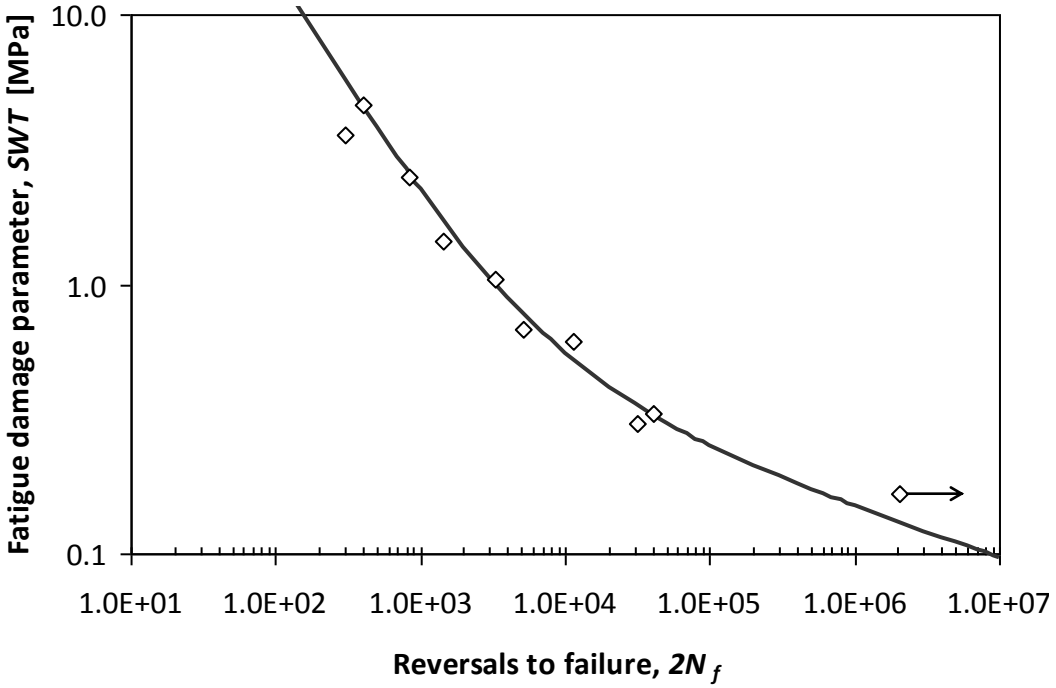

Figure 3.45 – Fitting of the *SWT* model to the lifetime for the material data from the Trezói bridge, R_ε=-1.

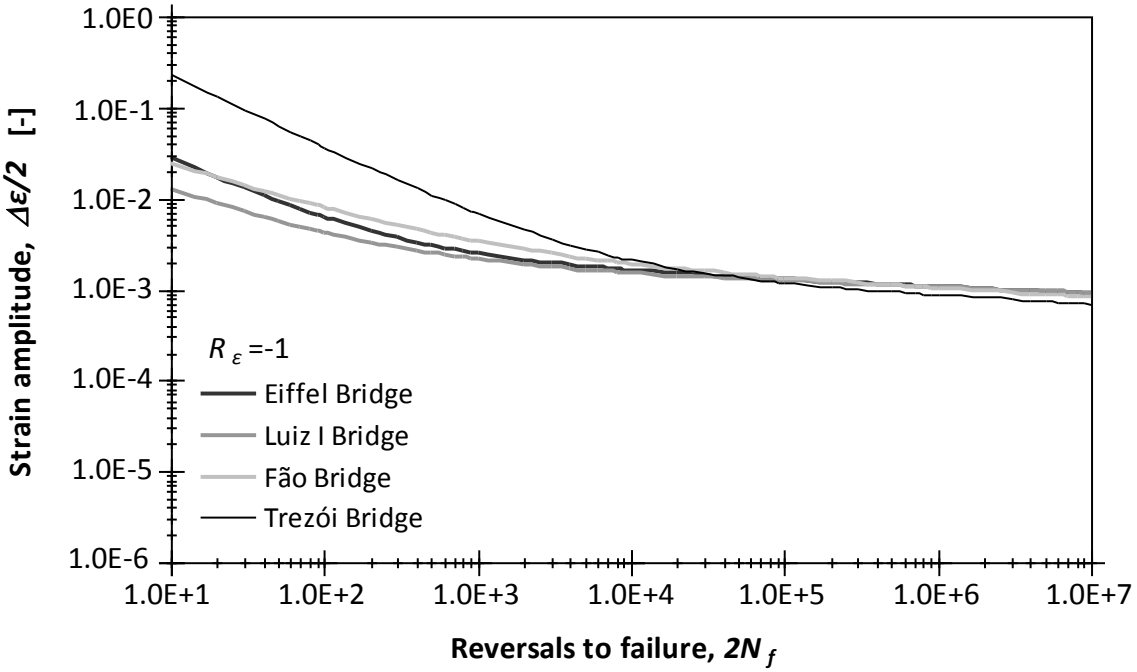

Figure 3.46 – Comparison of the total strain-life using Morrow curves for all materials, R_ε=-1.

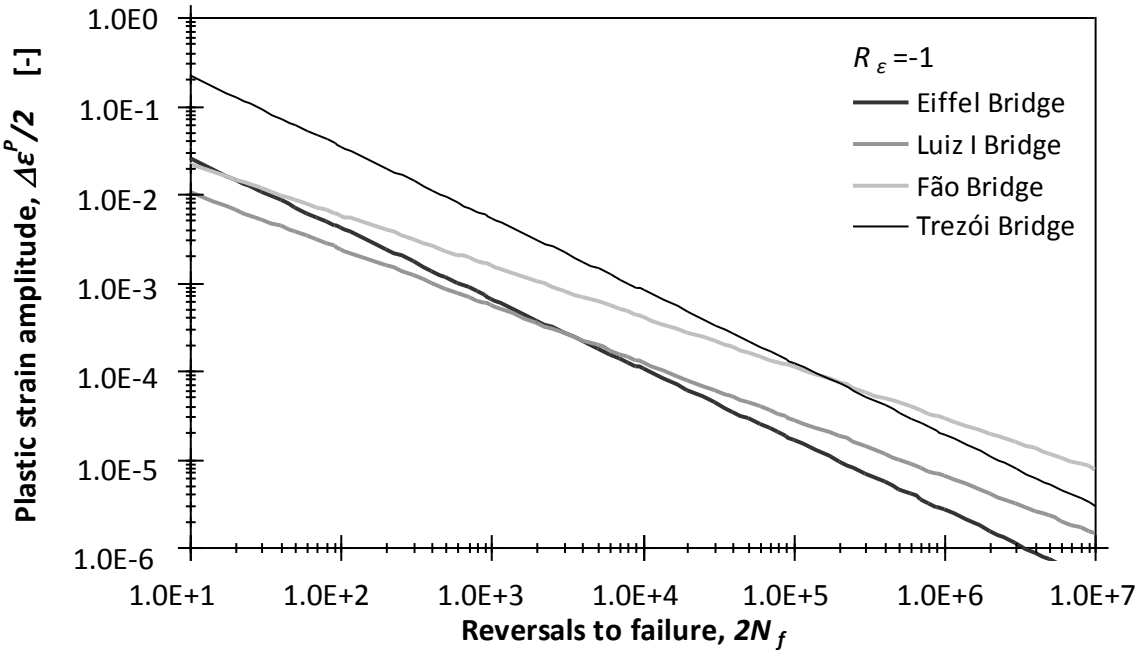

Figure 3.47 – Comparison of the plastic strain-life using Coffin-Manson curves for all materials, R_ε=-1.

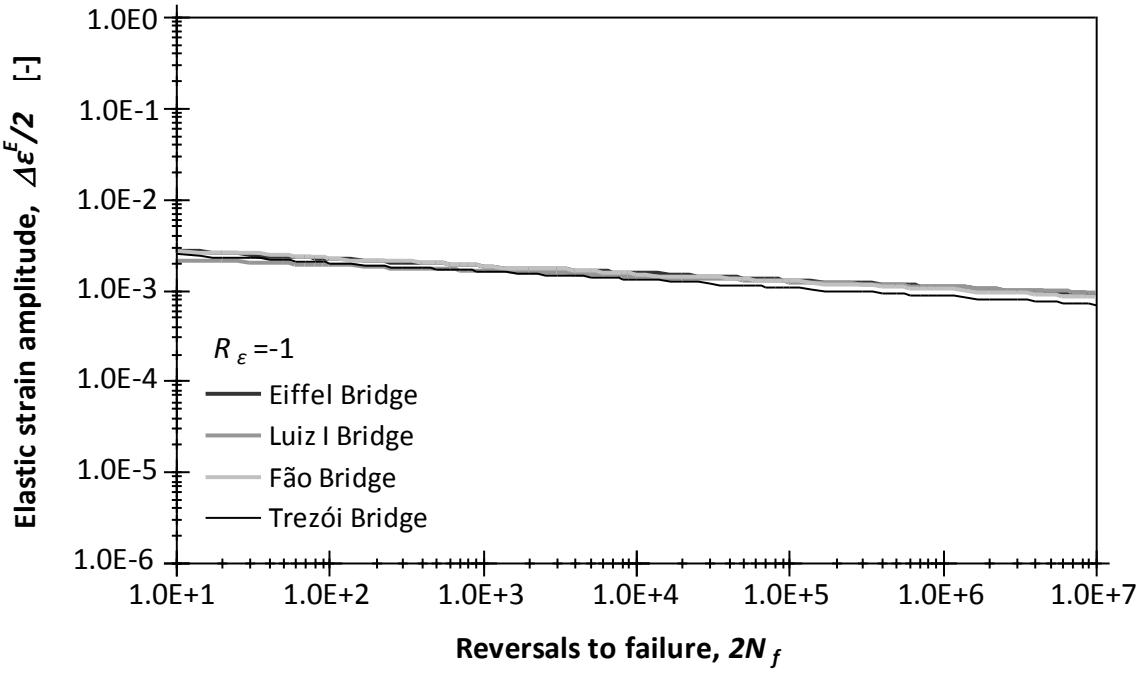

Figure 3.48 – Comparison of the strain-life using Basquin curves for all materials, R_ε=-1.

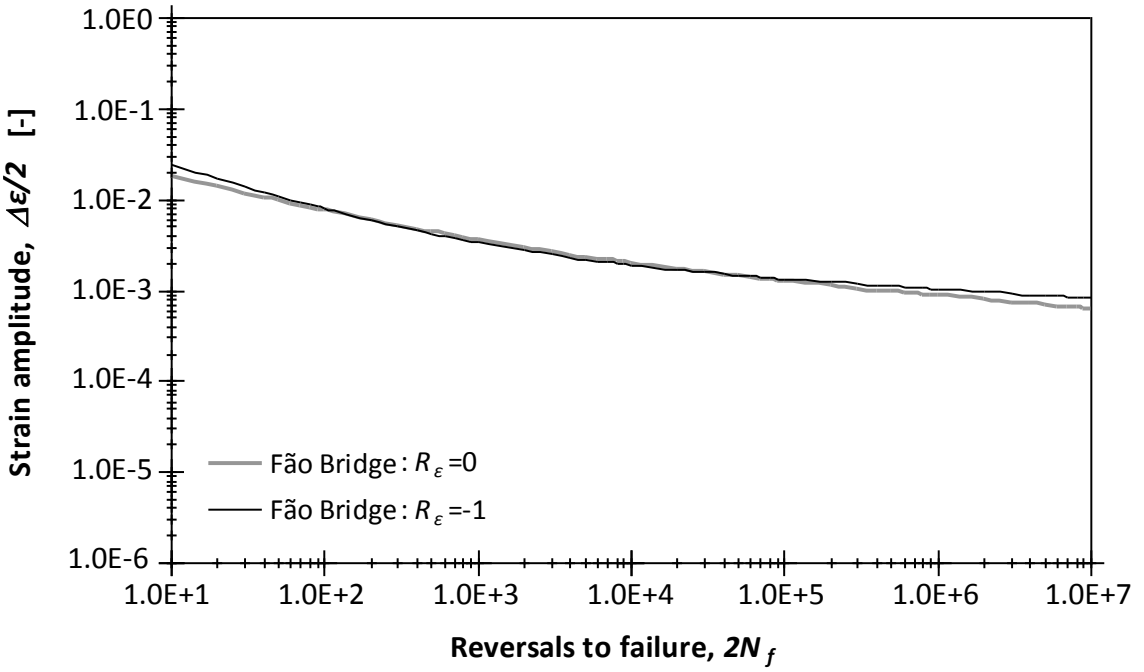

Figure 3.49 – Comparison of the total strain-life using Morrow curves for the material from the Fão bridge.

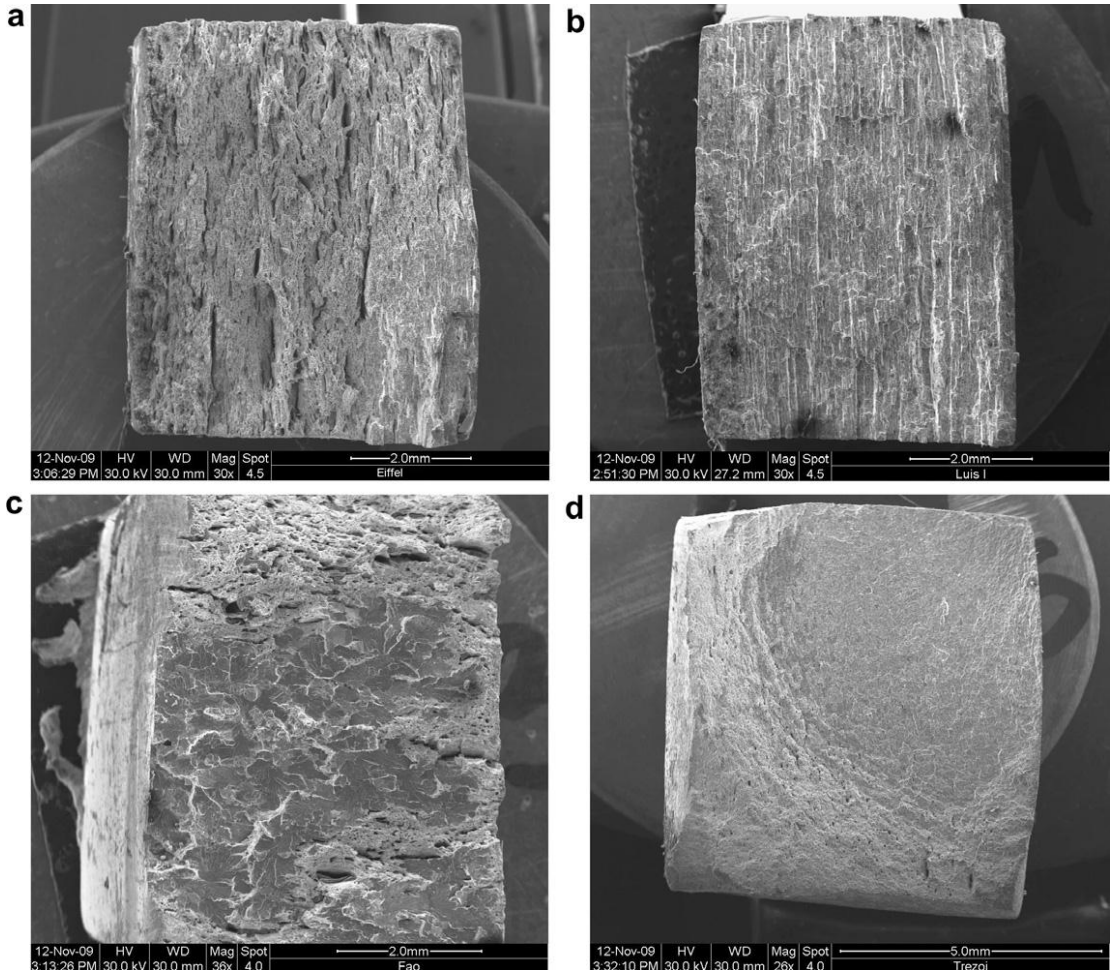

Figure 3.50 – Typical fracture surfaces of the smooth specimens tested under strain control: a) Eiffel; b) Luiz I; c) Fão; d) Trezói bridges [18].

Figure 3.50 exhibits typical fracture surfaces from the smooth specimens used to assess the strain-life fatigue data and the cyclic elastoplastic behaviours of the bridge materials [18]. The fracture surfaces of the material from Luiz I bridge shows clearly a lamellar structure corresponding to lined-up inclusions. Fracture surface of the specimen from the material from the Eiffel bridge also shows some lamellar structure. The fatigue crack propagation surfaces are clearly identified in the specimens from the Fão and Trezói bridges. The fracture surface of the specimen made of material from Trezói bridge shows lower levels of roughness, which is consistent with finer microstructure of the material and higher ductility.

3.5. FATIGUE CRACK PROPAGATION RATES OF THE MATERIALS

3.5.1. Experimental details

Fatigue crack growth tests were conducted on old bridge materials, according to the ASTM 647-99 standard [28], in order to assess the fatigue crack propagation rates for these materials. An experimental program was carried out using samples of the materials from the five bridges [11-13, 15, 17, 18]. Compact tension specimens (*CT specimens*), see Figure 3.51, were prepared with materials from Eiffel, Fão, Pinhão and Trezói bridges. Middle tension specimens were used for the material from Luiz I bridge (W= 40 mm; t = 10 mm). Due to limitations in material availability, distinct dimensions were adopted for the specimens. Table 3.30 shows the dimensions for the compact tension specimens and the total number of specimens tested for each material. All tests were performed in air, at room temperature, under a sinusoidal waveform with a frequency of 20 Hz for all materials with the exception of the material from Luiz I bridge, which was tested under a frequency of 10 Hz. The crack growth was measured on both faces of the specimens by direct visual inspection using two travelling microscopes with accuracy of 0.001 mm (see Figure 3.52). The tests were performed in load control conditions in a Instron close-loop servo hydraulic machine, model 8801, rated to 100 KN (see Figure 3.52).

A total of 42 specimens were tested: five from the Eiffel bridge (one according to the longitudinal direction and four according to the transverse direction); four from the Luiz I bridge; 12 specimens from the Fão bridge; 13 specimens from the Pinhão bridge (six from the diagonal and seven from the bracing) and eight specimens from the Trezói bridge.

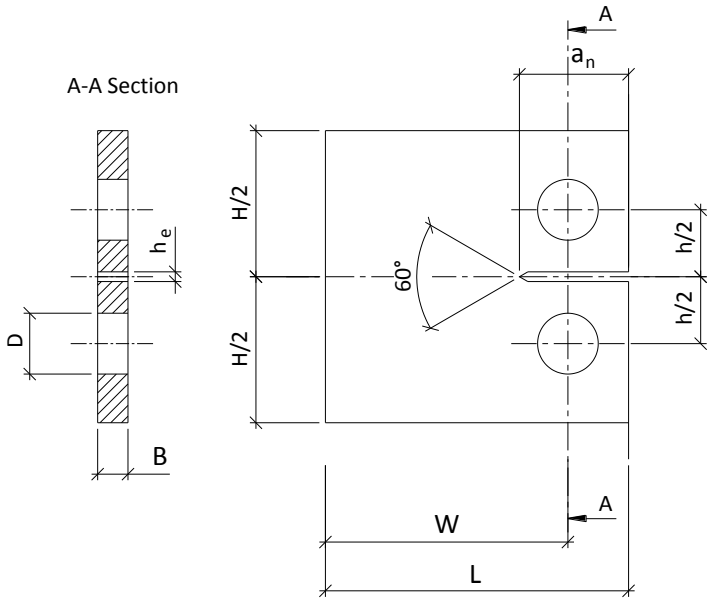

Figure 3.51 – *CT* specimens geometry used in fatigue crack growth tests for materials from Eiffel, Fão, Pinhão and Trezói bridges.

a) b) c)

Figure 3.52 – Experimental fatigue crack growth tests: a) overview of the *CT* specimen test; b) two xy traveling microscopes measuring the crack advance on both faces; c) two magnification microscopes on both faces of the *CT* specimen [17].

Table 3.30 – Nominal dimensions (see Figure 3.51 for reference dimensions) of the compact tension specimens and total number of the specimens used in fatigue tests for each material of the bridges.

Bridge Material	*No. of specimens*	*W* mm	*L* mm	*H/2* mm	*h/2* mm	*B* mm	*D* mm	h_e mm	a_n mm
Eiffel	5	40.0	50.0	24.0	11.00	4.35	10.0	1.6	8.0
Fão	12	50.0	62.5	30.0	13.75	8.00	12.5	3.0	10.0
Pinhão	13	40.0	50.0	24.0	11.00	4.35	10.0	1.6	8.0
Trezói	8	50.0	62.5	30.0	13.75	8.00	12.5	3.0	10.0

The following stress ratios were investigated for each material:

- Eiffel bridge: R_σ=0.1 and R_σ =0.5;
- Luiz I bridge: R_σ =0.1;
- Fão bridge: R_σ =0.0, R_σ =0.25, R_σ =0.5 and R_σ =0.75;

- Pinhão bridge: R_σ =0.0, R_σ =0.1 and R_σ =0.5;
- Trezói bridge: R_σ =0.0, R_σ =0.25 and R_σ =0.5.

The experimental crack propagation data obtained for each material related the crack propagation rate to the stress intensity factor range, using the power law as proposed by Paris and Erdogan [29]:

$$\frac{da}{dN} = C \cdot \Delta K^m \tag{3.8}$$

where *da/dN* is the fatigue crack propagation rate, ΔK represents the stress intensity factor range and *C* and *m* are material constants. The Paris's law can be modified to take into account the stress ratio effect using the Walker's modification [30]:

$$\frac{da}{dN} = C_1 \cdot \left[\frac{\Delta K}{(1-R_\sigma)^{1-\gamma}} \right]^{m_1} \tag{3.9}$$

where C_1, m_1 and γ are constants to be determined from crack propagation data evaluated at distinct stress ratios. Using the equivalent stress intensity range defined as follows:

$$\overline{\Delta K} = \frac{\Delta K}{(1-R_\sigma)^{1-\gamma}} \tag{3.10}$$

a higher correlation will result for the fatigue crack propagation rates for distinct stress ratios.

The formulation to determine the stress intensity factor range, ΔK, for the CT geometry is included in ASTM 647-99 standard [28], according to the following form:

$$\Delta K = \frac{\Delta F}{B \cdot \sqrt{W}} \cdot \frac{(2+\alpha)}{(1-\alpha)^{3/2}} \cdot \left(0.886 + 4.64 \cdot \alpha - 13.32 \cdot \alpha^2 + 14.72 \cdot \alpha^3 - 5.6 \cdot \alpha^4\right) \tag{3.11}$$

where: $\alpha = a/W$; *a* is the corresponding crack size, measured from the line of application of the load; ΔF is the force range; *B* and *W* are the thickness and nominal width of the *CT* specimens, respectively. The relation (3.11) is valid for $a/W \geq 0.2$.

For the MT geometry, the value of stress intensity factor range, ΔK, is obtained using the following expression:

$$\Delta K = \frac{\Delta F}{B} \cdot \sqrt{\frac{\pi \cdot \alpha}{2 \cdot W} \sec \frac{\pi \cdot \alpha}{2}} \tag{3.12}$$

where: α=2a/W. The expression is valid for $2a/W<0.95$.

The main result of the fatigue crack propagation tests, documented in this section, corresponds to the fatigue crack propagation rates as a function of the stress intensity factor ranges. The fatigue crack propagation rates were determined using the incremental polynomial method, as stated in ASTM E647-99 standard [28]. This method is based on the adjustment of 2nd degree polynomials to successive sets of experimental data points which define successive lengths of the crack as a function of the stress intensity factor range. The fatigue crack propagation rate results from the derivative of these 2nd degree polynomials, which are expressed as a function of the stress intensity factor range.

3.5.2. Experimental fatigue crack propagation results

In this section, a series of graphs are presented for various stress ratios [11-13,15,17,18,31], showing the evolution of the fatigue crack propagation rates as a function of the stress intensity factor range, for the materials extracted from the Eiffel, Luiz I, Fão, Pinhão and Tezói bridges. All fatigue crack propagation data was correlated with the Paris's law. Consequently, each graph includes the Paris constants as well as the respective determination coefficient.

3.5.2.1. Material from Eiffel bridge

Figures 3.53 and 3.54 present the fatigue crack propagation rates of the material from the Eiffel bridge, for the two stress ratios tested, namely, R_σ=0.1 and R_σ=0.5 [11,18]. For this bridge, crack propagation rates were measured in the girder longitudinal (L) direction, whereas only one test was carried out in the transverse direction (T). The crack propagation rates in the transverse direction showed a very irregular pattern. Figure 3.55 presents all fatigue crack propagation rates together, for both stress ratios (R_σ=0.1+R_σ=0.5) form the material from the Eiffel bridge. Figure 3.56 compares the Paris mean regression lines for each stress ratio and that resulting from the aggregation of all stress ratios [11,18]. The analysis of the figure reveals a clear stress ratio dependency of

the fatigue crack propagation rate of the material. A significant increase in the fatigue crack growth rate is observed for increasing stress ratio from 0.1 to 0.5.

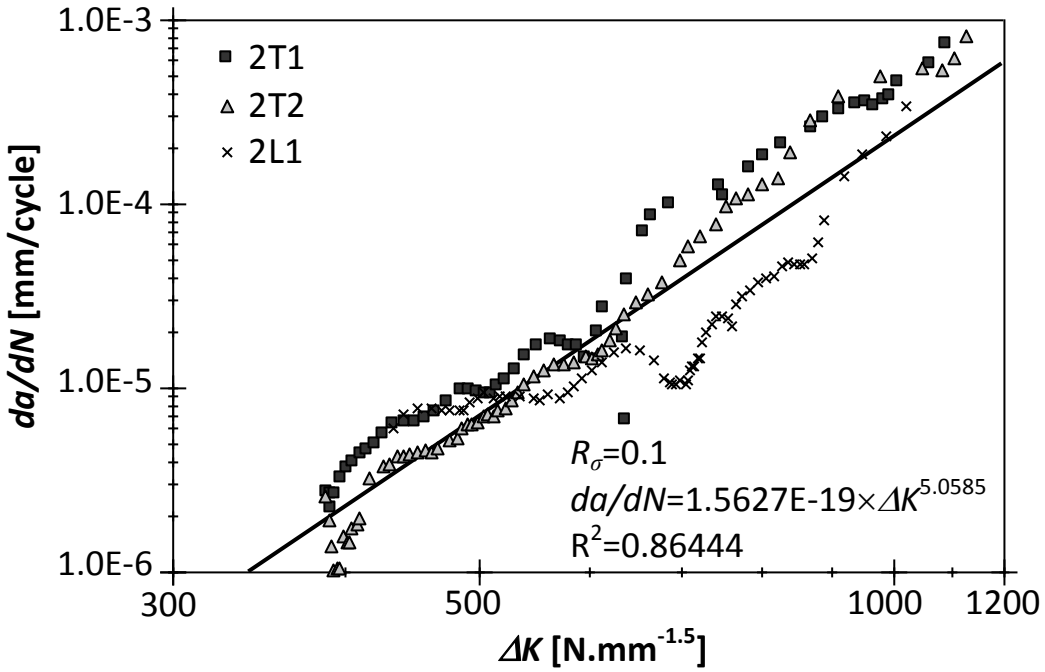

Figure 3.53 – Fatigue crack growth data of the material from the Eiffel bridge, R_σ=0.1.

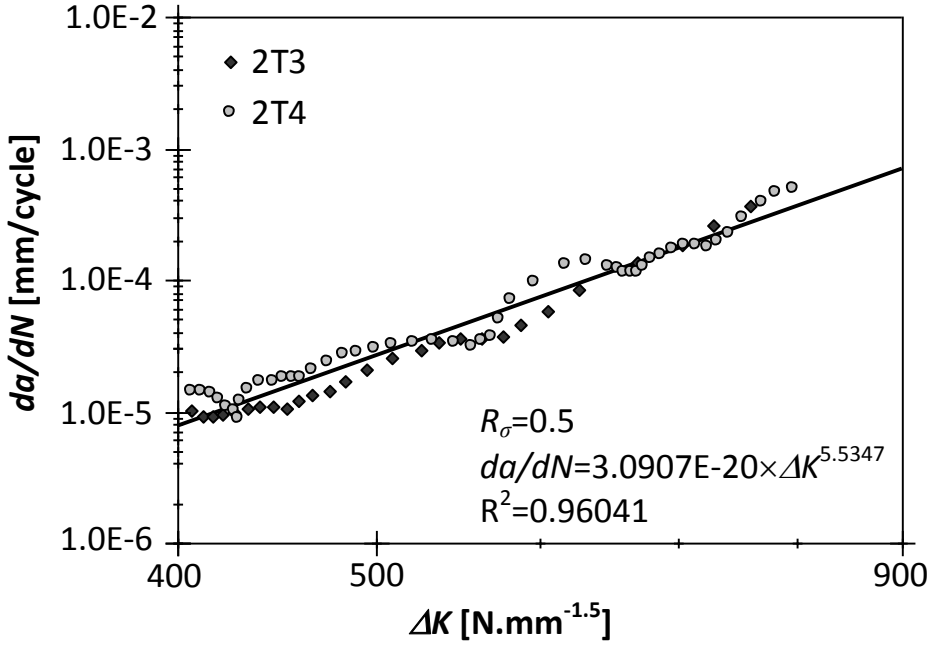

Figure 3.54 – Fatigue crack growth data of the material from the Eiffel bridge, R_σ=0.5.

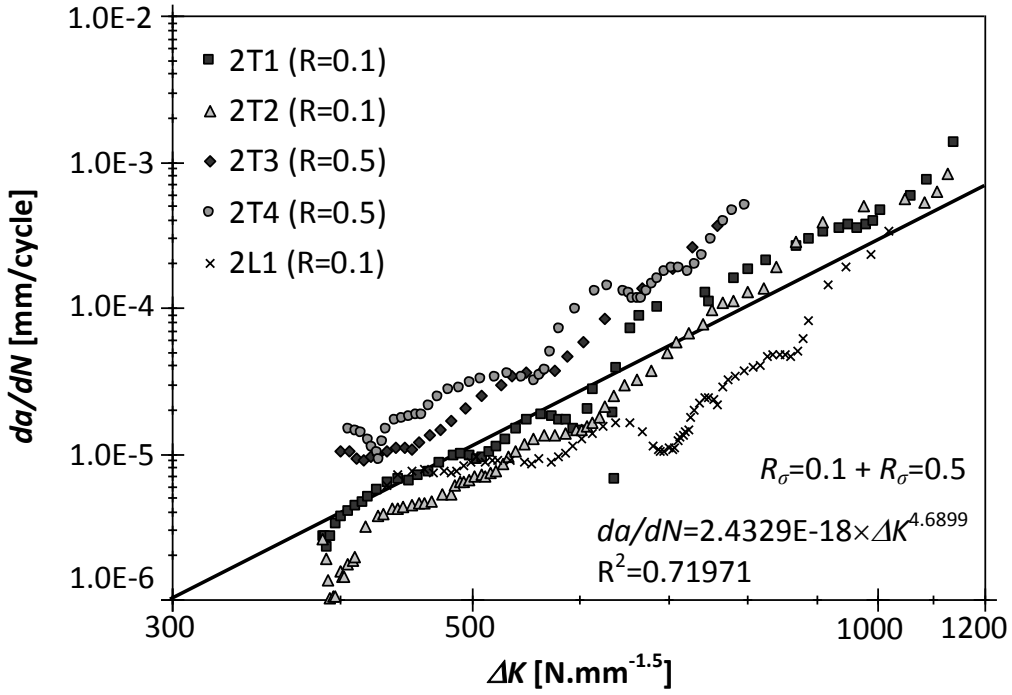

Figure 3.55 – Fatigue crack growth data of the material from the Eiffel bridge, R_σ=0.1+R_σ=0.5.

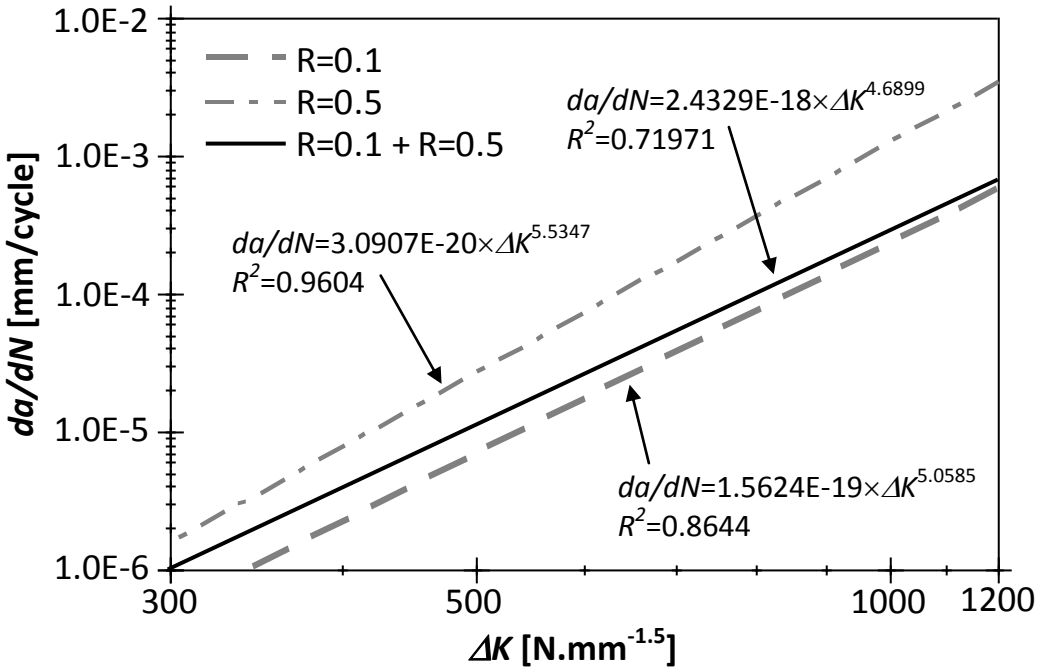

Figure 3.56 – Comparison between the regression lines of the fatigue crack propagation rates for different stress ratios obtained from the material of the Eiffel bridge.

3.5.2.2. Material from Luiz I bridge

Figure 3.57 exhibits the fatigue crack propagation rates of the material from the Luiz I bridge, for the tested stress ratio, R_σ=0.1 [12]. Data for only one stress ratio is available for this material. The scatter level is significant as pointed out by the relative low determination coefficient.

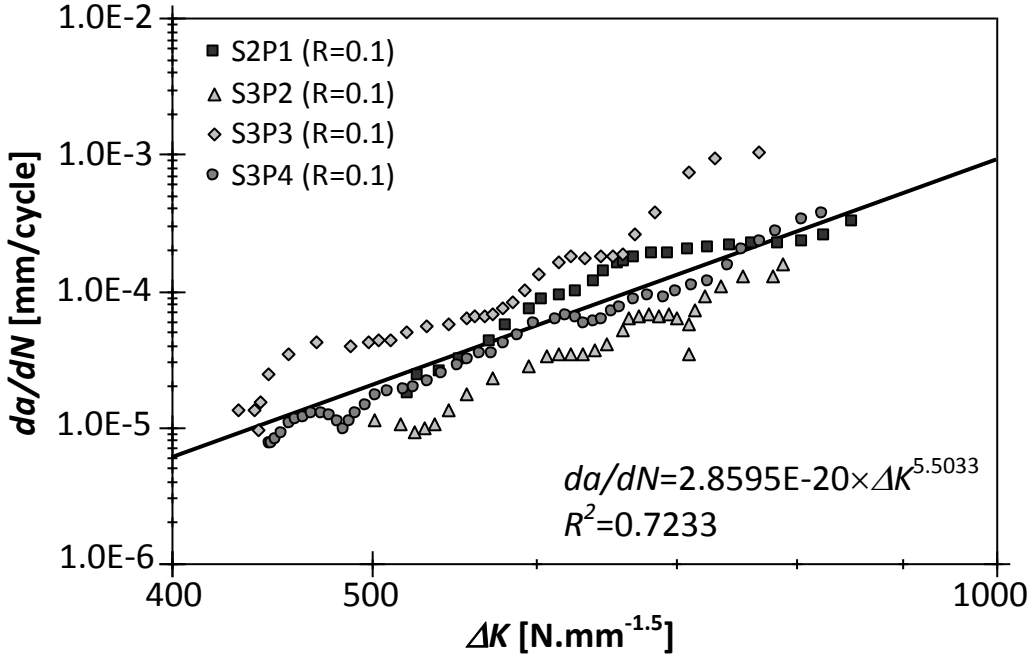

Figure 3.57 – Fatigue crack growth data for the material from the Luiz I bridge, R_σ=0.1.

3.5.2.3. Material from Fão bridge

Figures 3.58 to 3.61 show the fatigue crack propagation rates of the material from the Fão bridge, for the four stress ratios tested, namely, R_σ=0.0, R_σ=0.25, R_σ=0.5 and R_σ=0.75 [13]. Figure 3.62 presents together the fatigue crack propagation rates of the material from the Fão bridge for all stress ratios tested (R_σ=0.0+R_σ=0.25+R_σ=0.5+R_σ=0.75). Comparing the determination coefficient from the global fitting of the Paris law with the determination coefficient of the individual fitting for each stress ratio, we realize a reduction in the determination coefficient, which is attributed to the stress ratio effects not being captured by the Paris relation. Figure 3.63 compares the average fatigue crack propagation rates, given by the Paris relation, for several stress ratios tested. The analysis of the graph reveals that the stress ratio influences the fatigue crack propagation rates. In

general, an increase in the fatigue crack propagation rates is observed for increasing stress ratios [13,18]. This phenomenon may be explained by the crack closure phenomenon occurring for lower stress ratios.

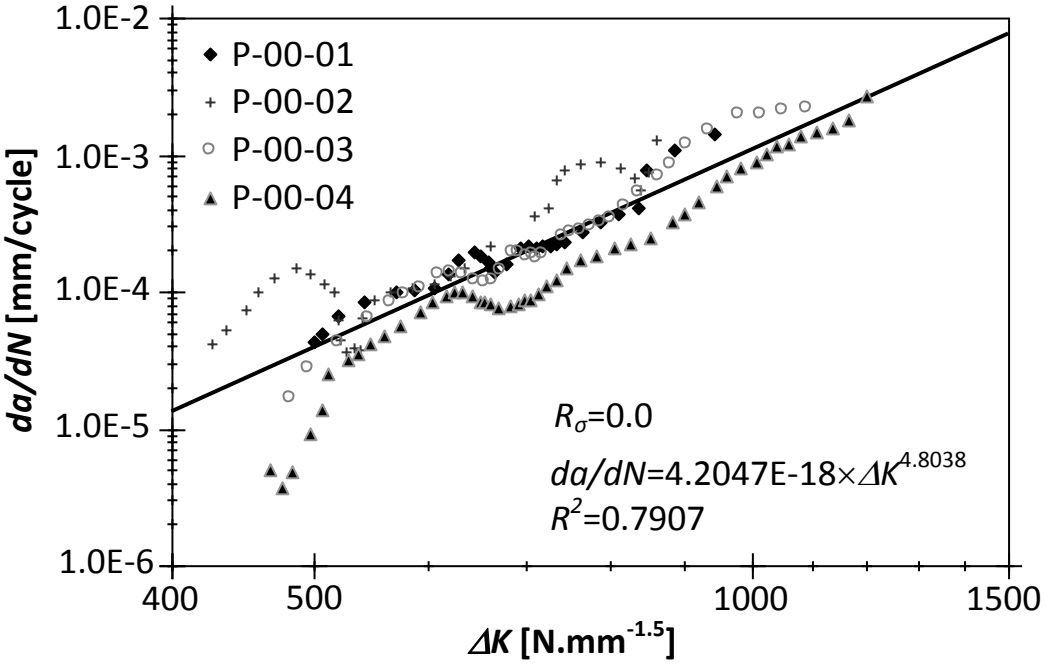

Figure 3.58 – Fatigue crack growth data for the material from the Fão bridge, R_σ=0.0.

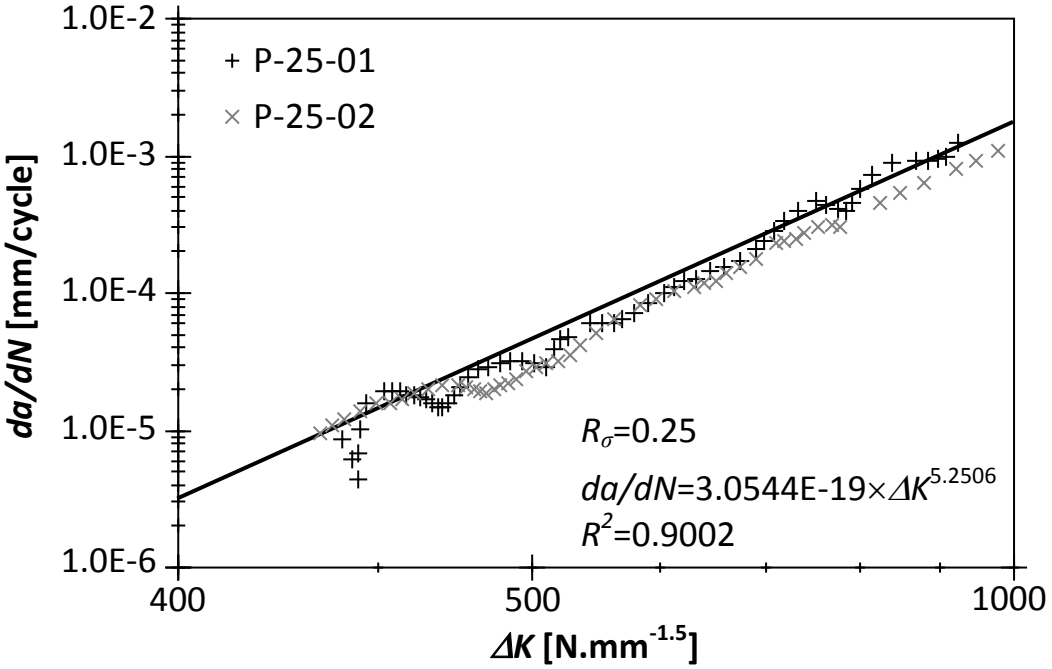

Figure 3.59 – Fatigue crack growth data for the material from the Fão bridge, R_σ=0.25.

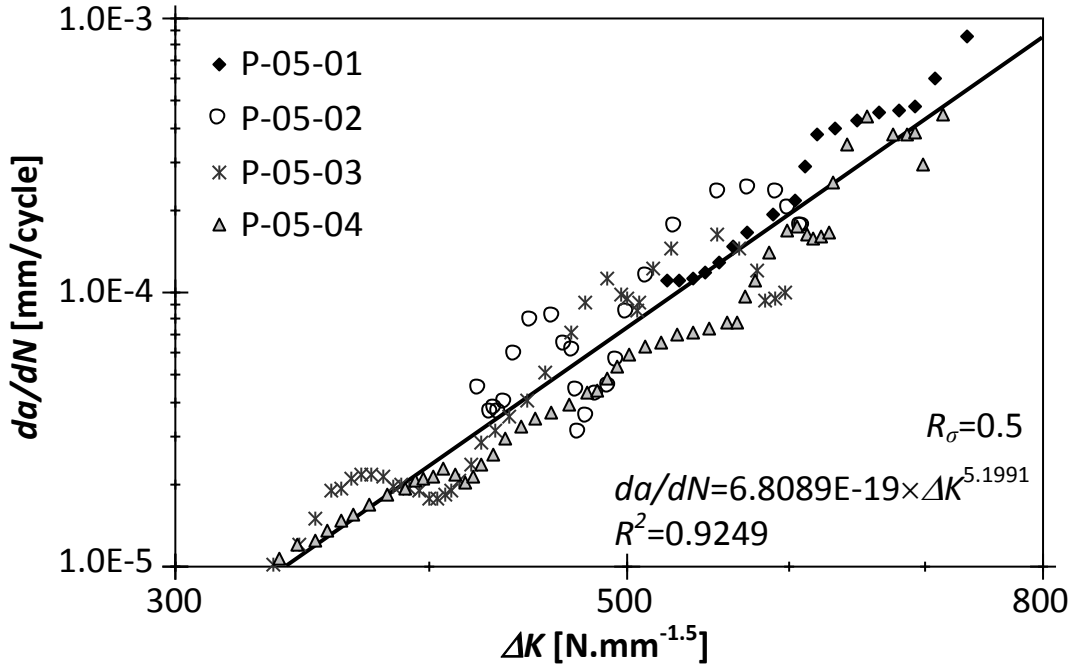

Figure 3.60 – Fatigue crack growth data for the material from the Fão bridge, R_σ=0.5.

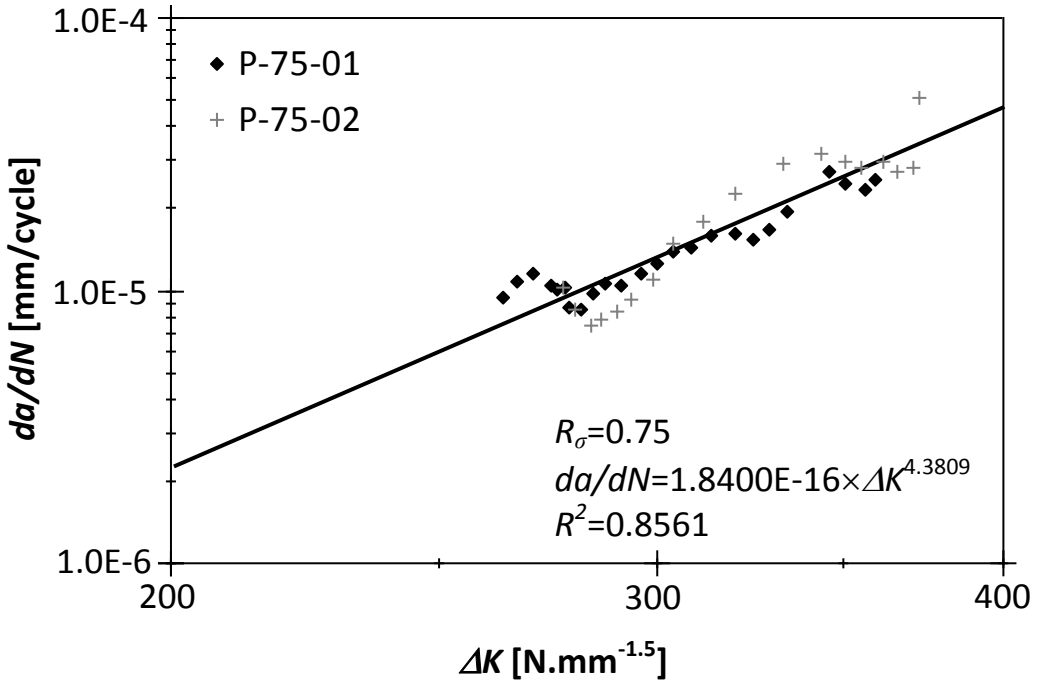

Figure 3.61 – Fatigue crack growth data for the material from the Fão bridge, R_σ=0.75.

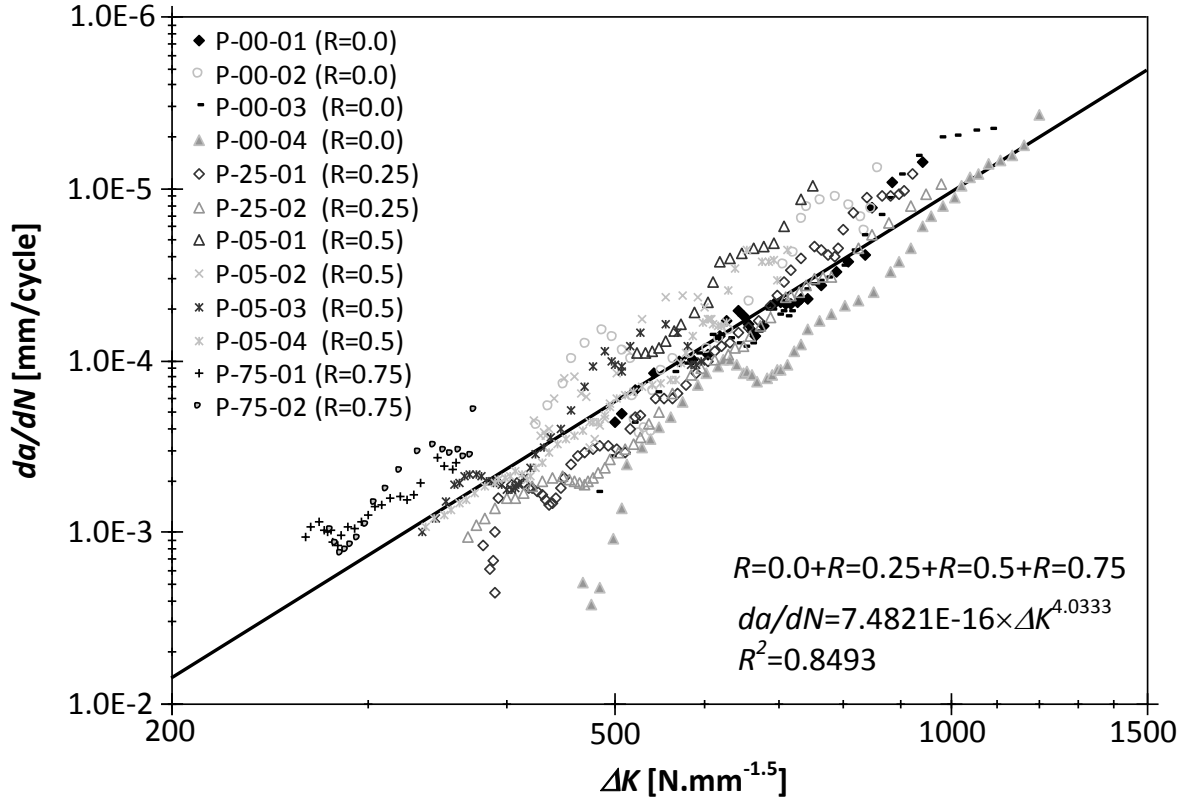

Figure 3.62 – Fatigue crack growth data for the material from the Fão bridge, R_σ=0+R_σ=0.25+R_σ=0.5+R_σ=0.75.

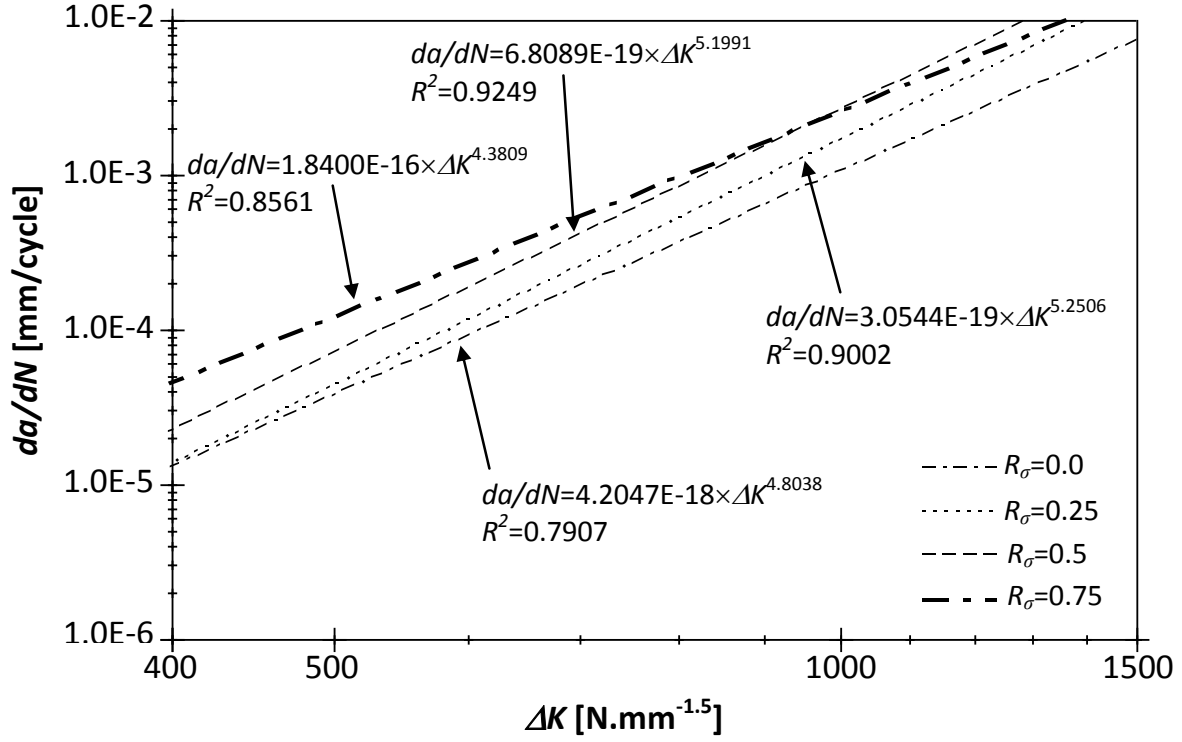

Figure 3.63 – Comparison among the regression lines of the fatigue crack propagation rates for different stress ratios obtained from the material of the Fão bridge.

3.5.2.4. Material from Pinhão bridge

Figures 3.64 to 3.66 present the fatigue crack propagation rates for the material from the Pinhão bridge, for three stress ratios, namely, R_σ=0.0, R_σ=0.1 and R_σ=0.5 [15,18]. Figure 3.67 shows the fatigue crack propagation data for all the stress ratios considered (R_σ=0.0+R_σ=0.1+R_σ=0.5). Figure 3.68 compares the trend lines of the fatigue crack propagation rates for each stress ratio. The analysis of the figure proves an increase of the fatigue crack propagation rates for increasing stress ratio, mainly for lower stress intensity factor ranges while for higher stress intensity factor ranges, the fatigue crack propagation rates tend to be less sensitive to the stress ratio.

The two samples from the material of the Pinhão bridge, namely those from the bracing (B) and the diagonal (C), exhibit slightly distinct crack growth rates for R_σ=0.0; however, for the other stress ratios no differences for the crack growth rates have been found between these two material samples.

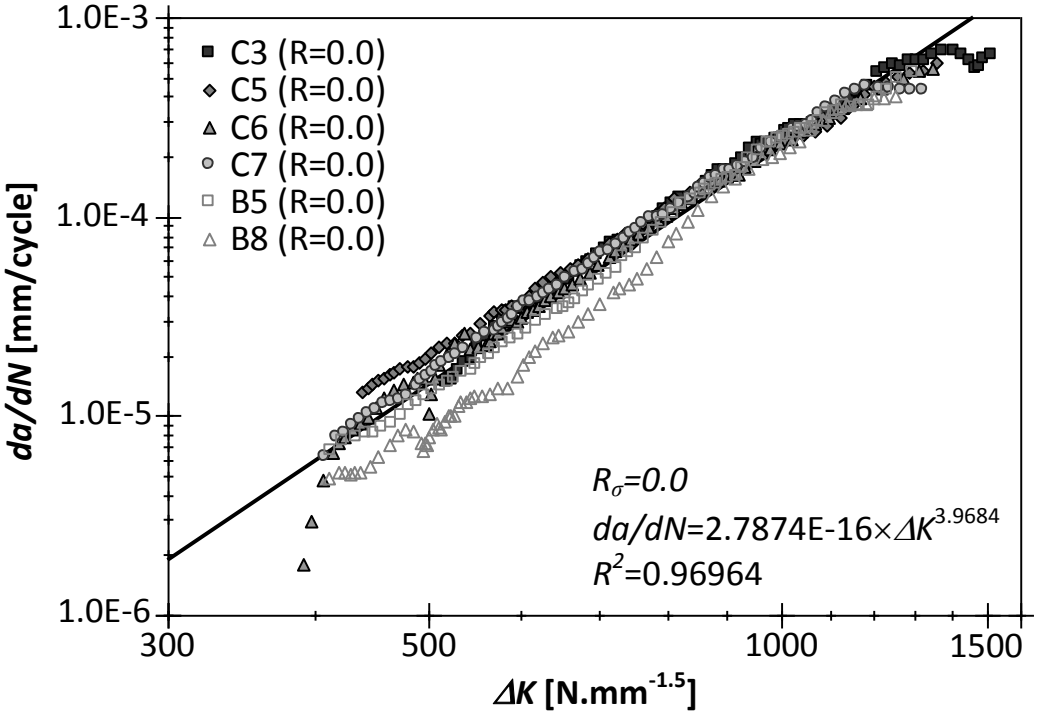

Figure 3.64 – Fatigue crack growth data for the material from the Pinhão bridge, R_σ=0.0.

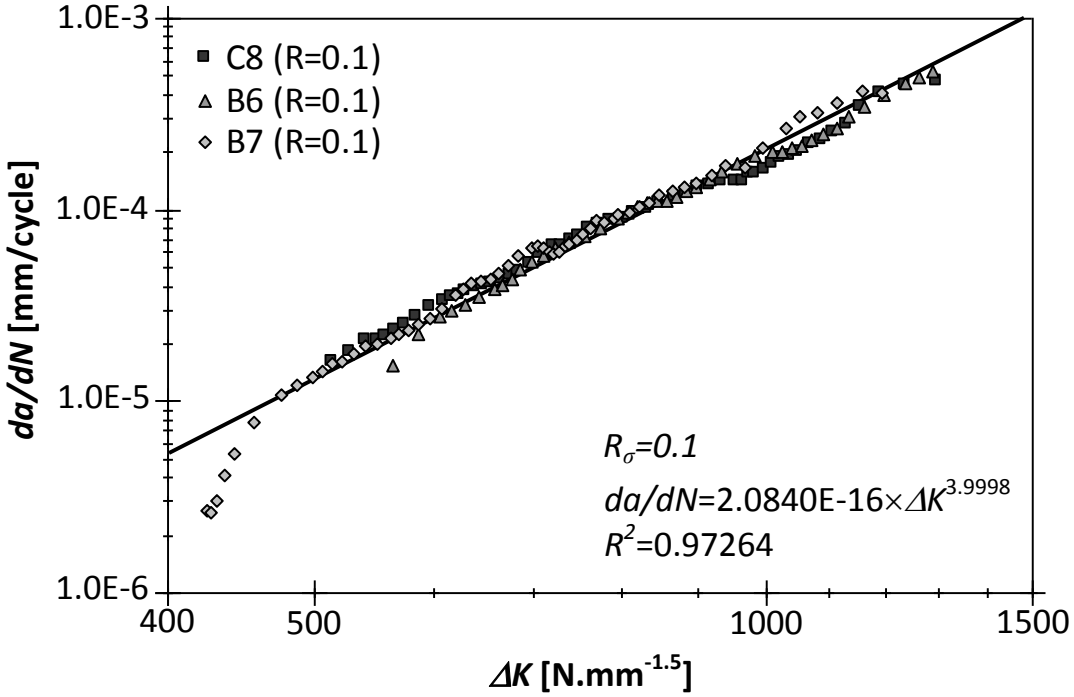

Figure 3.65 – Fatigue crack growth data for the material from the Pinhão bridge, R_σ=0.1.

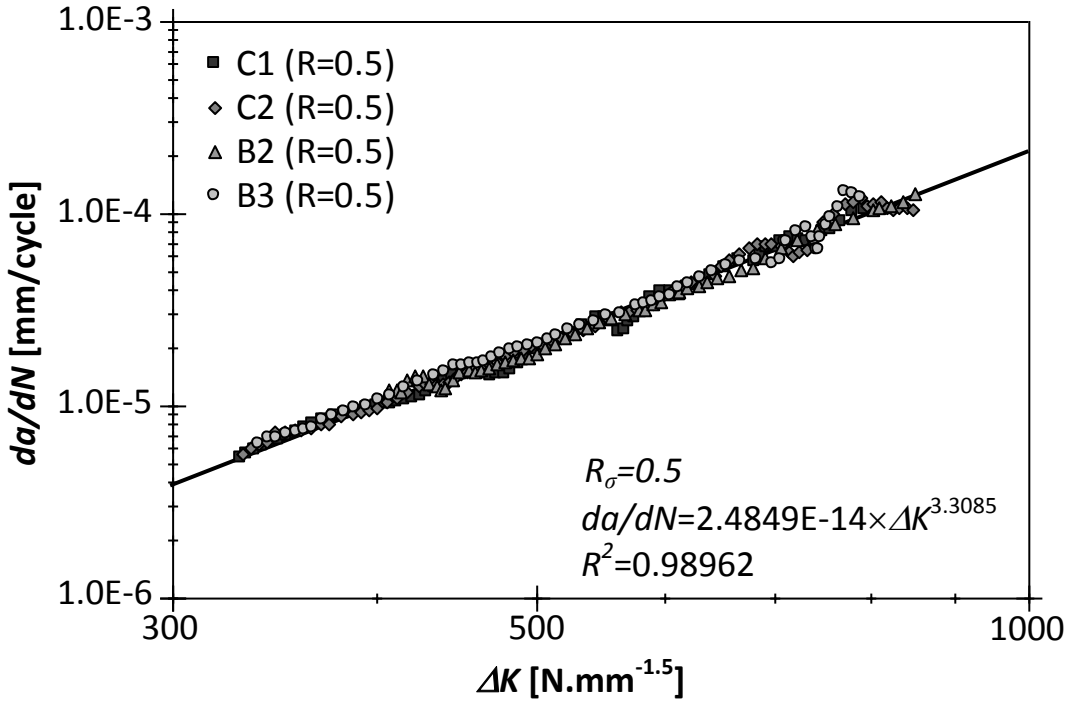

Figure 3.66 – Fatigue crack growth data for the material from the Pinhão bridge, R_σ=0.5.

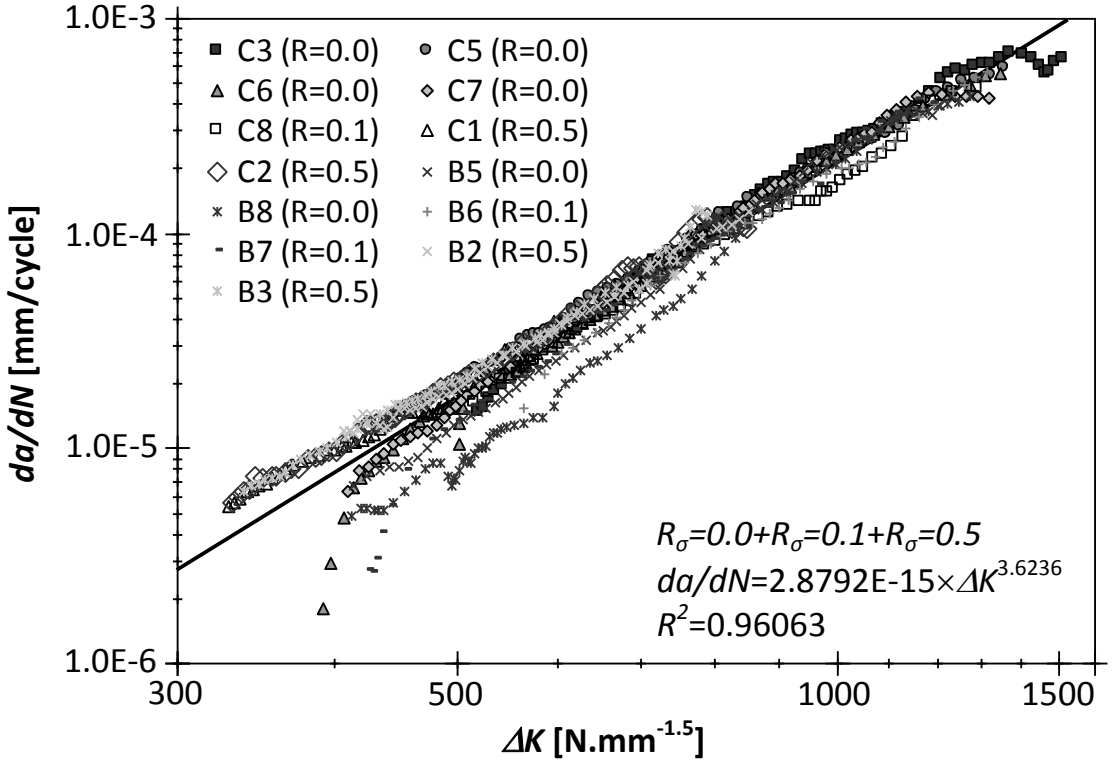

Figure 3.67 – Fatigue crack growth data for the material from the Pinhão bridge, R_σ=0+R_σ=0.1+R_σ=0.5.

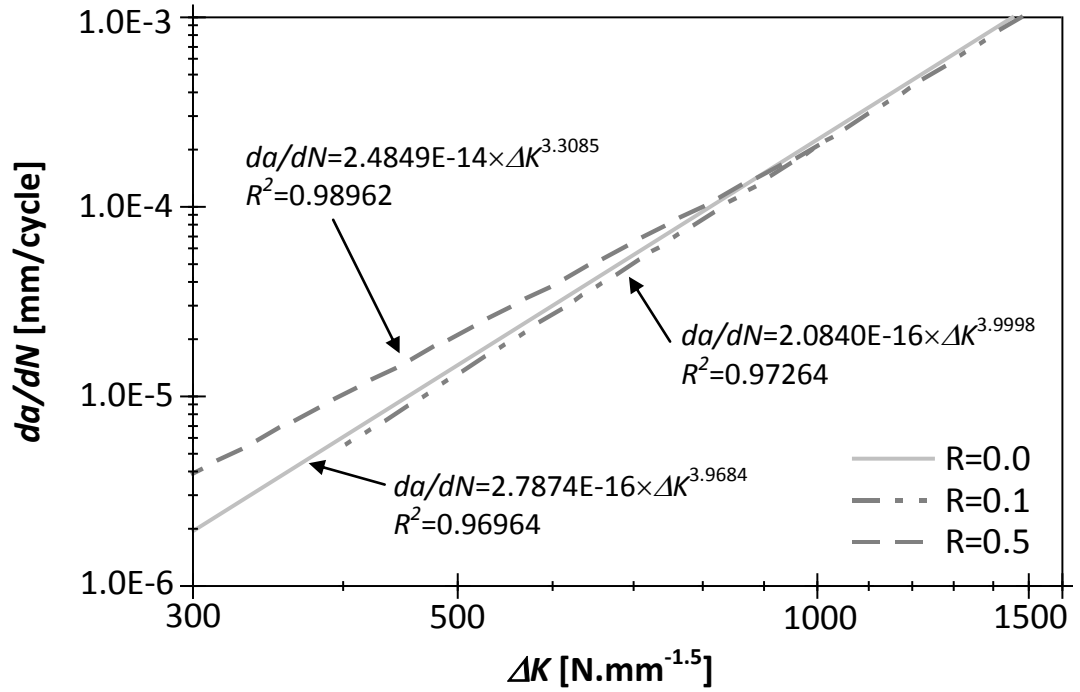

Figure 3.68 – Comparison between the regression lines of the fatigue crack propagation rates for different stress ratios obtained from the material of the Pinhão bridge.

3.5.2.5. Material from Trezói bridge

Figures 3.69 to 3.71 present the fatigue crack propagation rates of the material from the Trezói bridge, for three tested stress ratios, namely R_σ=0.0, R_σ=0.25 and R_σ=0.5 [17,18]. Figure 3.72 illustrates the fatigue crack propagation rates for the material from the Trezói bridge for all stress ratios joined together. This material shows clearly a reduced scatter in the crack propagation rates. This material is a modern construction steel and therefore, shows less scatter in mechanical properties than old puddle irons. Figure 3.73 compares the trends in the fatigue crack propagation rates of the material for the stress ratios tested. It is visible that this material also shows some dependency with the stress ratio, mainly when stress ratio changes between R_σ=0.0 and R_σ=0.25 on the contrary, for stress ratios changing between R_σ=0.25 and R_σ=0.5, no significant variation of the fatigue crack growth rates are observed. This means that any possible crack closure that may occur will vanish above R_σ=0.25.

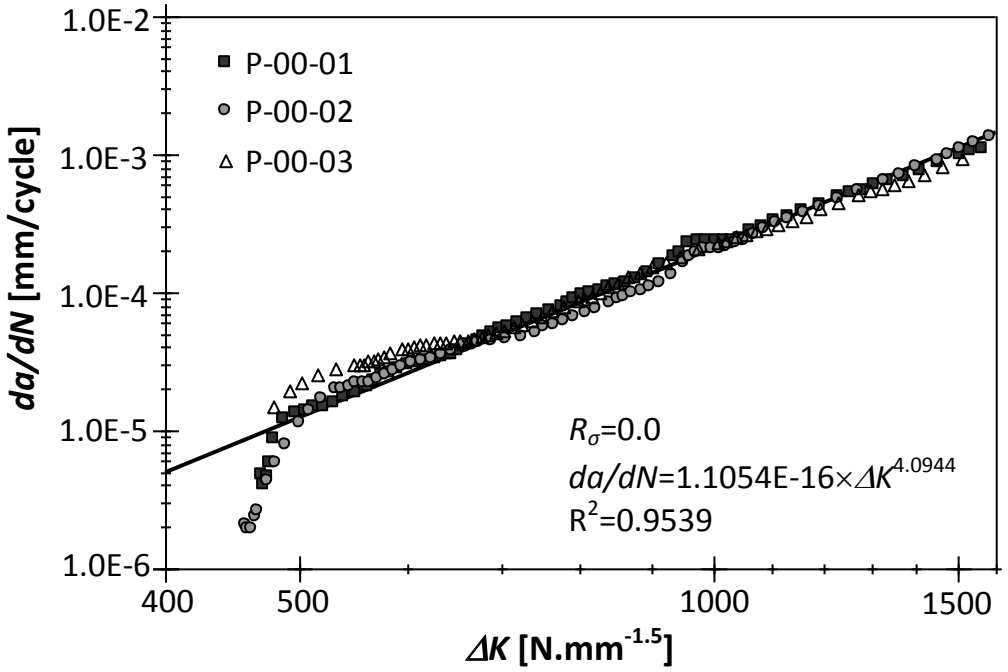

Figure 3.69 – Fatigue crack growth data for the material from the Trezói bridge, R_σ=0.0.

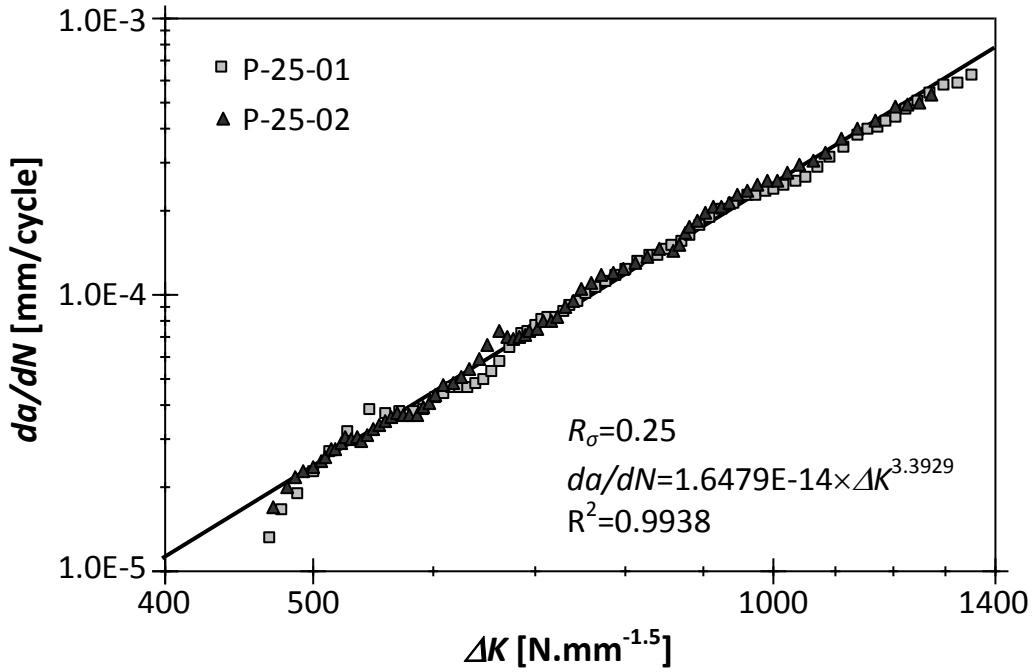

Figure 3.70 – Fatigue crack growth data for the material from the Trezói bridge, R_σ=0.25.

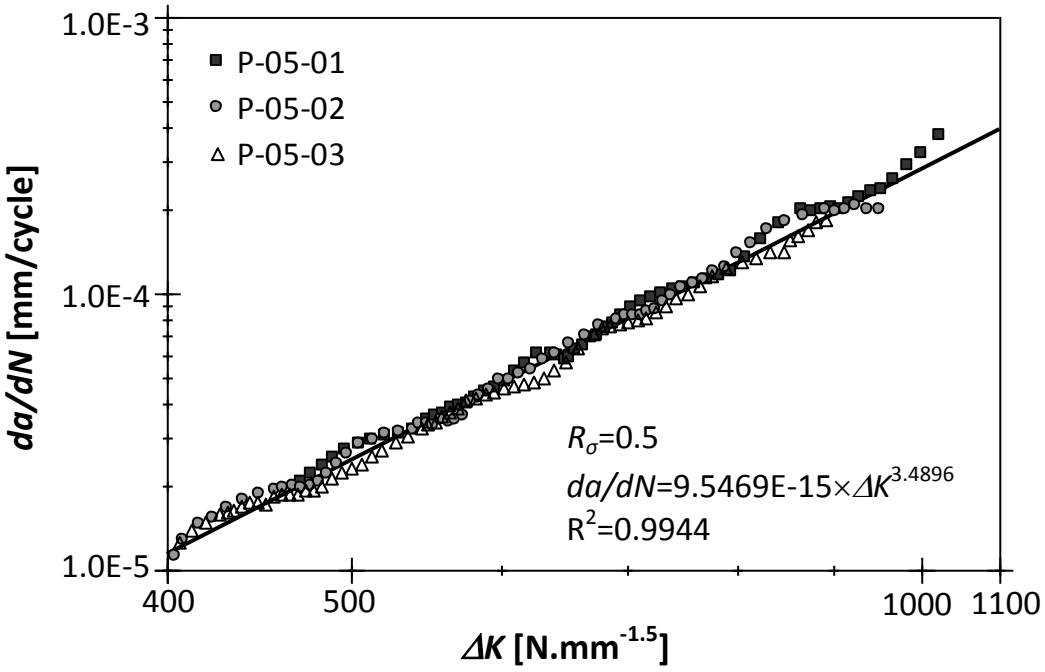

Figure 3.71 – Fatigue crack growth data for the material from the Trezói bridge, R_σ=0.5.

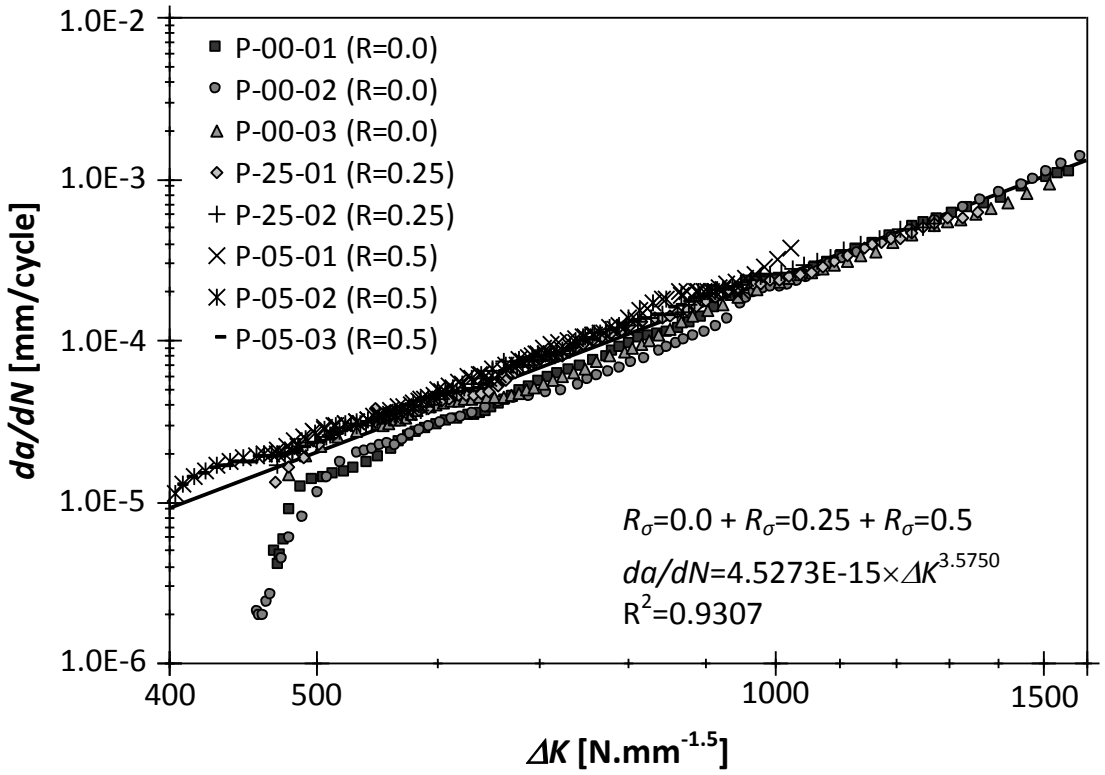

Figure 3.72 – Fatigue crack growth data for the material from the Trezói bridge, R_σ=0+R_σ=0.25+R_σ=0.5.

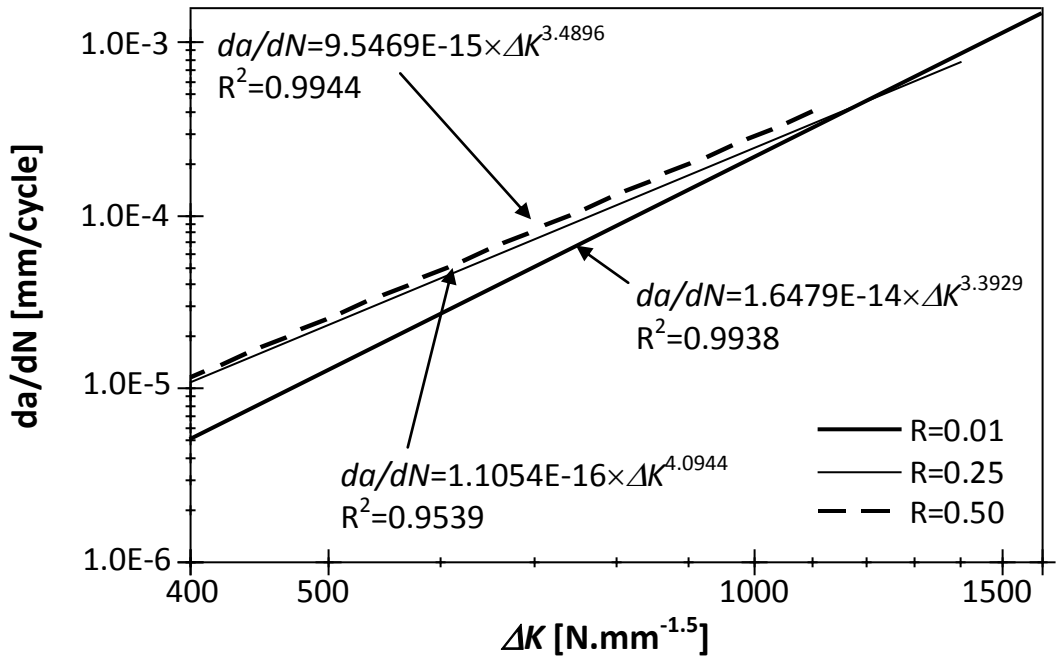

Figure 3.73 – Comparison between fatigue crack propagation rate trends for different stress ratios obtained for the material of the Trezói bridge.

3.5.2.6. Discussion of the results

The greatest scatter in fatigue crack propagation data was found for the materials from Eiffel, Luiz I and Fão bridges which is consistent with the fact that these bridges are the oldest ones and the respective materials present important heterogeneities. The data from Pinhão bridge reveals a relative low scatter; this material being about 25 years younger than the previous, one revealing good homogeneity, similar to modern steels. Finally, the material from the Trezoi bridge exhibits very low scatter, as expected, due to the relative low age of the material. However, there is one exception with the material from the Trezói bridge, which shows lower determination coefficient than that from the Pinhão bridge. This apparent exception may be justified by the fact that data from the Trezói bridge for R_σ=0 covers the near threshold crack propagation, which is not reproduced by the Paris's law.

For the material from the Eiffel bridge (Figures 3.53 to 3.56), it is clear that crack propagation increases for increasing stress ratio effect, which may be justified by the reduction of the crack closure effect. The crack propagation rate of the material from the Eiffel bridge was the most sensitive to the stress ratio. Regarding the material from the Luiz I bridge (Figure 3.57), only one stress ratio was tested (R_σ=0.1), so that it was not possible to assess the stress ratio effects on the fatigue crack propagation for this material. Four stress ratios were tested for the sample of material from the Fão bridge (Figures 3.58 to 3.63), namely R_σ=0, R_σ=0.25, R_σ=0.5 and R_σ=0.75. For this material a slight increase of the fatigue crack propagation rate is also observed for increasing stress ratio. Finally, the materials from the Pinhão (Figures 3.64 to 3.68) and Trezói (Figures 3.69 to 3.73) bridges showed a slight acceleration in the crack propagation for increasing stress ratio.

It is interesting to note that the exponent of the Paris's law [29], *m*, is always higher than 3 (value adopted in design codes) and falls in the range 3.6–5.5. The coefficient *C* is within the range $2.9\text{x}10^{-15}$–$2.9\text{x}10^{-20}$ (*da/dN* in *mm/cycle* and ΔK in $Nmm^{-1.5}$). Table 3.31 summarizes the material constants, *C* and *m*, of the Paris´s model for each bridge material.

Table 3.31 – Constants of the Paris´s model for each material of the bridges.

Material	R_σ	*Specimens*	*C*	*m*	R^2
	-	*n.º*	*	-	-
Eiffel	0.1	3	1.5627E-19	5.0585	0.8644
	0.50	2	3.0907E-20	5.5347	0.9604
	0.1; 0.5	5	2.4329E-18	4.6899	0.7197
Luiz I	0.1	4	2.8595E-20	5.5033	0.7233
Fão	0.0	4	4.2047E-18	4.8038	0.7907
	0.25	2	3.0544E-19	5.2506	0.9002
	0.5	4	6.8089E-19	5.1991	0.9249
	0.75	2	1.8400E-16	4.3809	0.8561
	0.0; 0.25; 0.5; 0.75	12	7.4821E-16	4.0333	0.8493
Pinhão	0.0	6	2.7874E-16	3.9684	0.9694
	0.1	3	2.0840E-16	3.9998	0.9726
	0.5	4	2.4849E-14	3.3085	0.9896
	0.0; 0.1; 0.5	13	2.8792E-15	3.6236	0.9606
Trezói	0.0	3	1.1054E-15	4.0944	0.9539
	0.25	2	1.6479E-14	3.3929	0.9938
	0.5	3	9.5469E-15	3.4896	0.9944
	0.0; 0.25; 0.5	8	4.5273E-15	3.5750	0.9307

**da/dN [mm/cycle] and ΔK [N.mm$^{-1.5}$]*

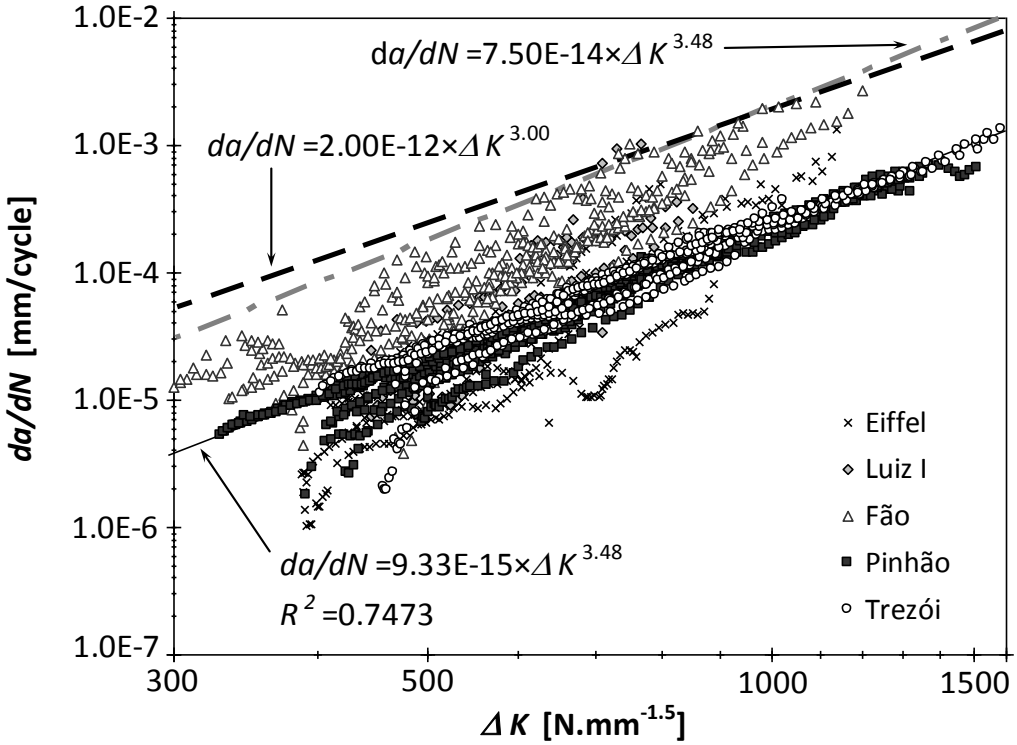

Figure 3.74 – Correlation among all fatigue crack propagation data using the Paris model.

A tentative is done to derive a unique relation for the fatigue crack propagation data from all bridge materials, joined together. Figure 3.74 plots the fatigue crack propagation data obtained for all materials. The best fit of the Paris relation provides a determination coefficient, R^2=0.75, which is relatively high, taking into account the different origins of the materials investigated. It can be verified that fatigue data of the materials from Fão and Luiz I bridges diverge from the mean values, presenting higher fatigue crack propagation values. One specimen from Eiffel bridge exhibits markedly lower fatigue crack propagation rates for intermediate stress intensity factor ranges. The constant *m* from the Paris's law obtained for all data together, is higher than 3.0, this being the latter value usually adopted in current design codes of practice [5,32], indirectly defined as the slope of the *S–N curves* of structural details. The constant *C* is significantly lower than the usual values recommended in the literature for modern steels [32]: $1.2\text{x}10^{-13} \leq C \leq 5\text{x}10^{-13}$. Figure 3.74 also includes an upper bound, parallel to the linear regression line, which can be used for design purposes. Another upper bound was established based on a slope of 3. For this latter case, the *C* constant happens to be higher than the values referred in literature for modern steels [32].

Figures 3.75 to 3.78 plot again the fatigue crack propagation data for the materials from the bridges investigated, but in these graphs the data is plotted by considering the effective stress intensity factor range, as proposed by Walker [18]. The material from the Luiz I bridge is excluded from this analysis since only data for R_o=0.1 is available. The application of the Walker model to correlate the fatigue crack propagation data resulted in higher determination coefficients, when compared with those resulting when applying the Paris law. Figure 3.79 plots all data together, using the transformation proposed by Equation (3.10). The data is correlated using a power relation, and an increase of the determination coefficient is again verified [18].

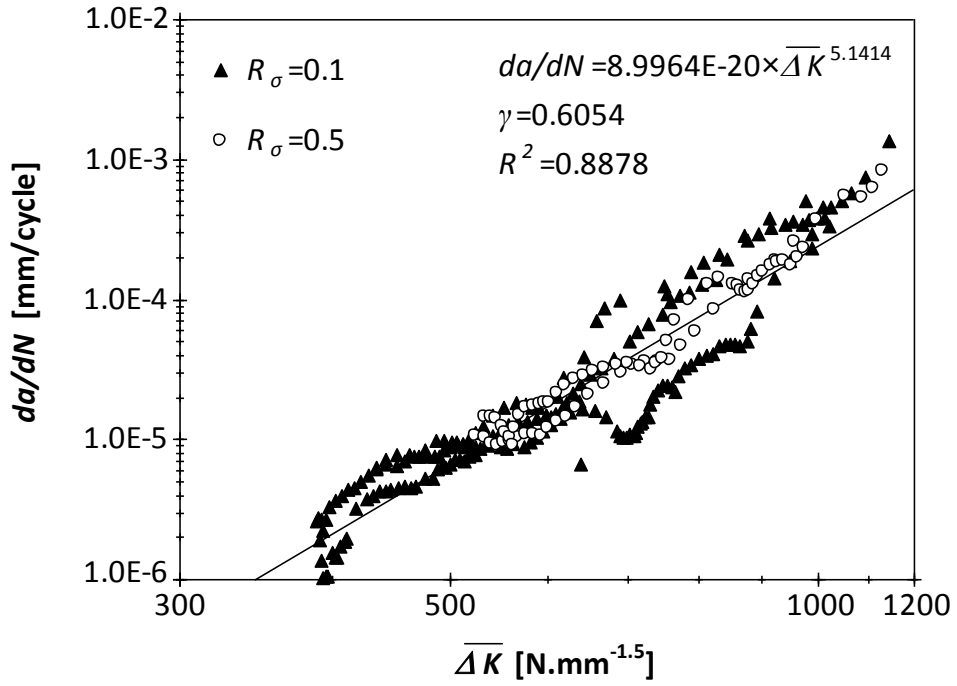

Figure 3.75 – Correlation between the fatigue crack propagation data from the material of the Eiffel bridge using Walker's model.

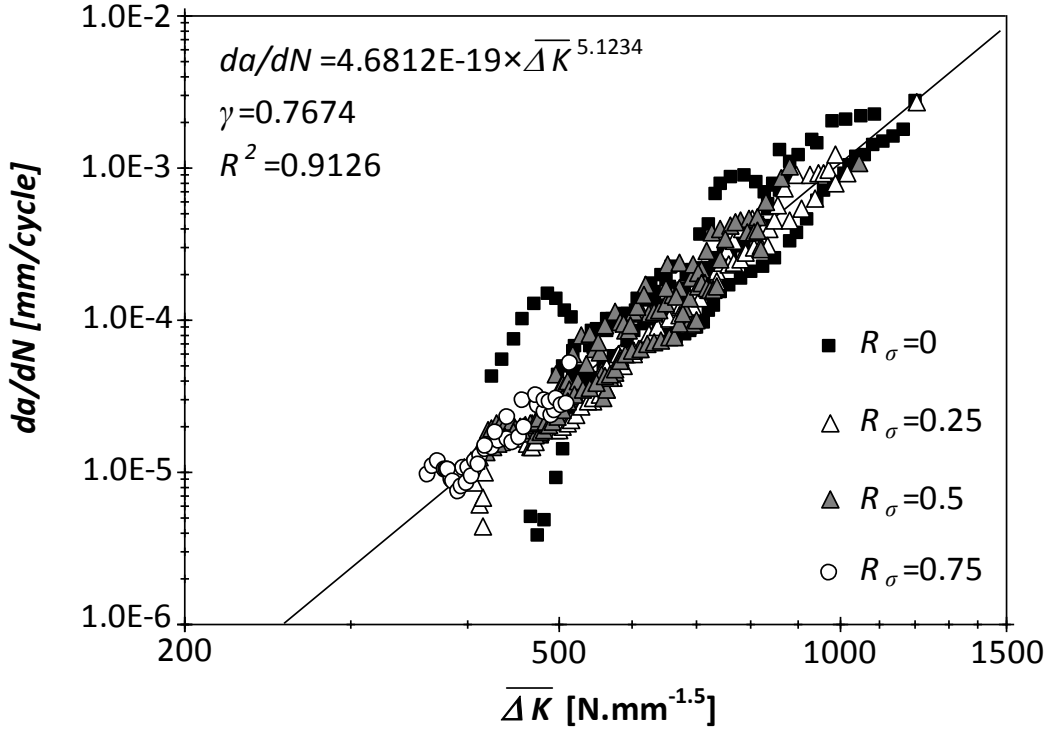

Figure 3.76 – Correlation between the fatigue crack propagation data from the material of the Fão bridge using Walker's model.

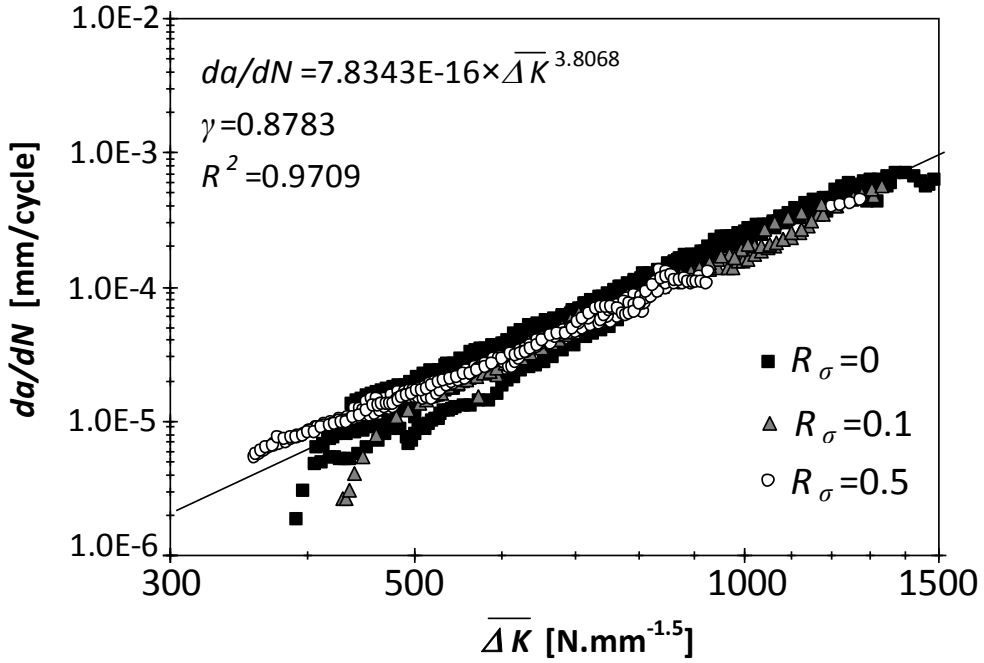

Figure 3.77 – Correlation for the fatigue crack propagation data from the material of the Pinhão bridge using Walker's model.

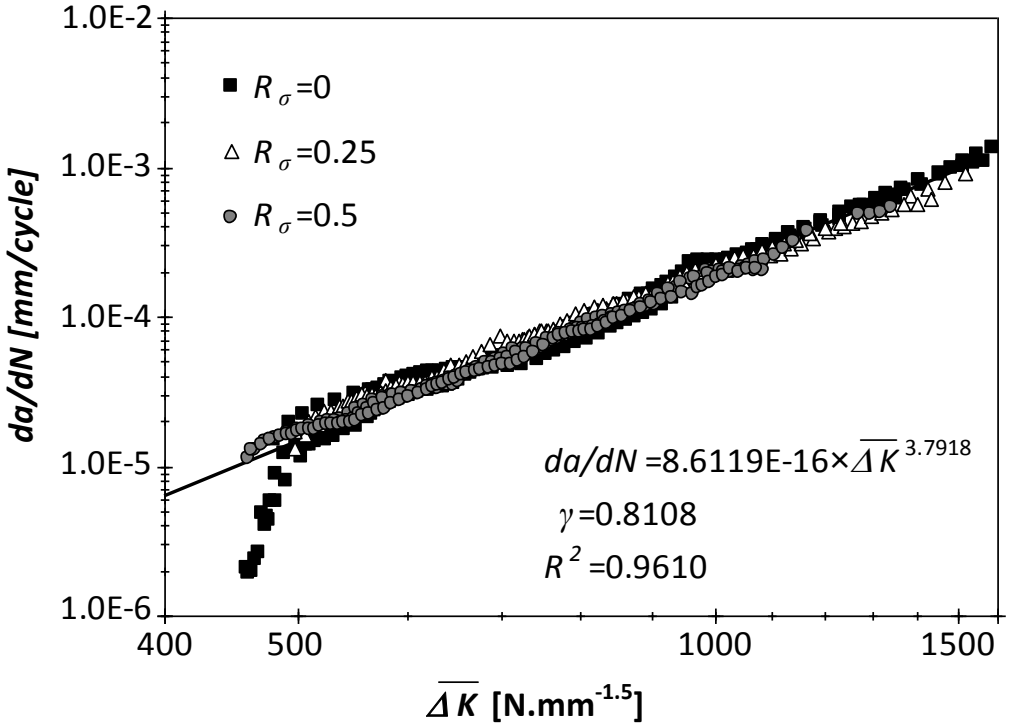

Figure 3.78 – Correlation between the fatigue crack propagation data from the material of the Trezói bridge using Walker's model.

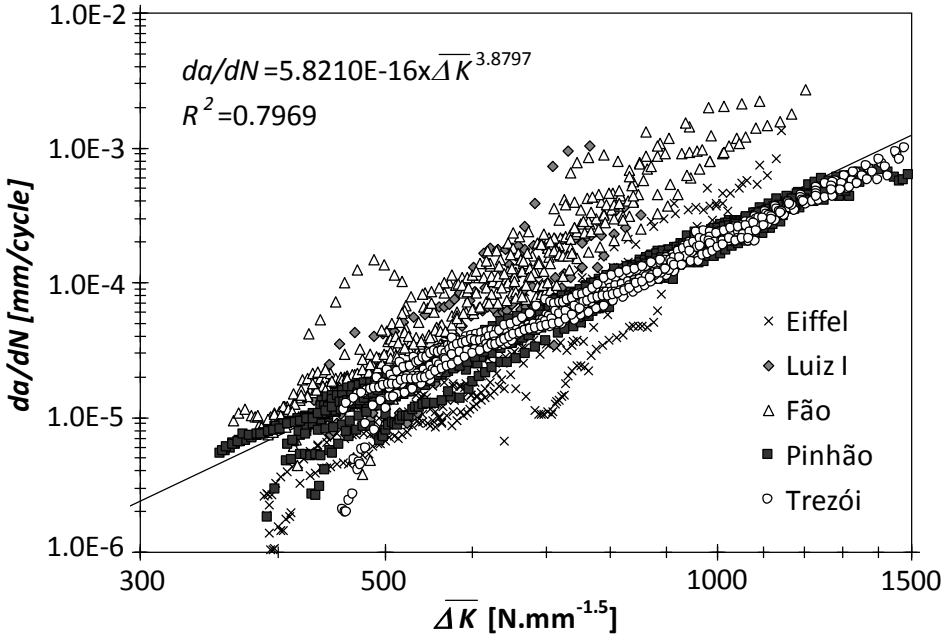

Figure 3.79 – Correlation between the fatigue crack propagation rates for all bridge materials using Walker's model.

3.6. FATIGUE STRENGTH OF RIVETED CONNECTIONS

The fatigue resistance of riveted joints made of original materials from the Portuguese bridges has been evaluated by means of fatigue tests [12,14,15,16,17]. Riveted joints with original rivets were extracted from the Eiffel, Luiz I, Pinhão and Trezói bridges. In addition, riveted joints were manufactured using original material from the Fão bridge, but applying new rivets. In this section, a summary of available S-N fatigue data, from riveted connections representative of old metallic riveted Portuguese bridges, is presented.

The results of the fatigue tests of riveted joints are presented in the form of *S-N* or Wöhler curves, which shows a power relationship between the applied stress range ($\Delta\sigma$) and the corresponding number of cycles to failure (N_f) for the finite life domain and excluding low-cycle fatigue regimes. Design codes of practice [33] adopt the following form for the S-N curves:

$$\Delta\sigma^m N_f = C \tag{3.13}$$

where C and m are constants. Alternatively, the mean S-N curves may be represented using the following linear model [34,35], which is more suitable for parameter identification using linear regression analysis:

$$Y = A + B \cdot X \tag{3.14}$$

where Y is the dependent variable defined as $Log(N_f)$, X is the independent variable defined as $Log(\Delta\sigma)$, A and B are linear regression parameters. Consequently, it is possible to rewrite the *S-N* curve in the following forms [34,35]:

$$\begin{cases} Log(N_f) = A + B \cdot Log(\Delta\sigma) \\ Log(\Delta\sigma) = -\dfrac{A}{B} + \dfrac{1}{B} \cdot Log(N_f) \end{cases} \tag{3.15}$$

where A and B parameters are related to the C and m constants:

$$\begin{cases} C = 10^A \\ m = -B \end{cases} \tag{3.16}$$

The S-N results presented in this section, were obtained using fatigue tests of specimens, performed on servo-hydraulic machines rated to 100kN or 250kN and subjected to load control conditions. The results of the fatigue tests of riveted connections for the materials under consideration from the Eiffel, Luiz I, Fão, Pinhão and Trezói bridges are summarized, respectively in Tables 3.32, 3.33, 3.34, 3.35 and 3.36, where S_{gross} is the gross cross-section, S_{net} is the net cross-section, R_σ is the stress ratio, F_{max} is the maximum testing force, ΔF is the test load range, f is the test frequency, $\Delta\sigma_{gross}$ is the stress range computed on the gross cross-section, $\Delta\sigma_{net}$ is the stress range calculated in the net cross-section and N_f is the number of cycles to failure [12,14-17,31]. The gross cross-section corresponds to the remote section of the joint, while the net cross-section corresponds to the section excluding the rivet hole.

3.6.1. Riveted connections from the Eiffel bridge

Double shear riveted connections were cut out from the web of a girder from the Darque south viaduct of the Eiffel bridge. The specimens were cut along the longitudinal direction and the respective mid plates showed an average thickness of 6.7mm. Figure 3.80 illustrates the complete test series of the riveted specimens extracted from the Eiffel bridge. A total of 14 specimens were tested under a stress R-ratio equal to 0.1 and frequencies, f, ranged between 5 and 7.5Hz. Each specimen exhibits a single row of four rivets, aligned in the loading direction. The results of these fatigue tests are summarized in Table 3.32.

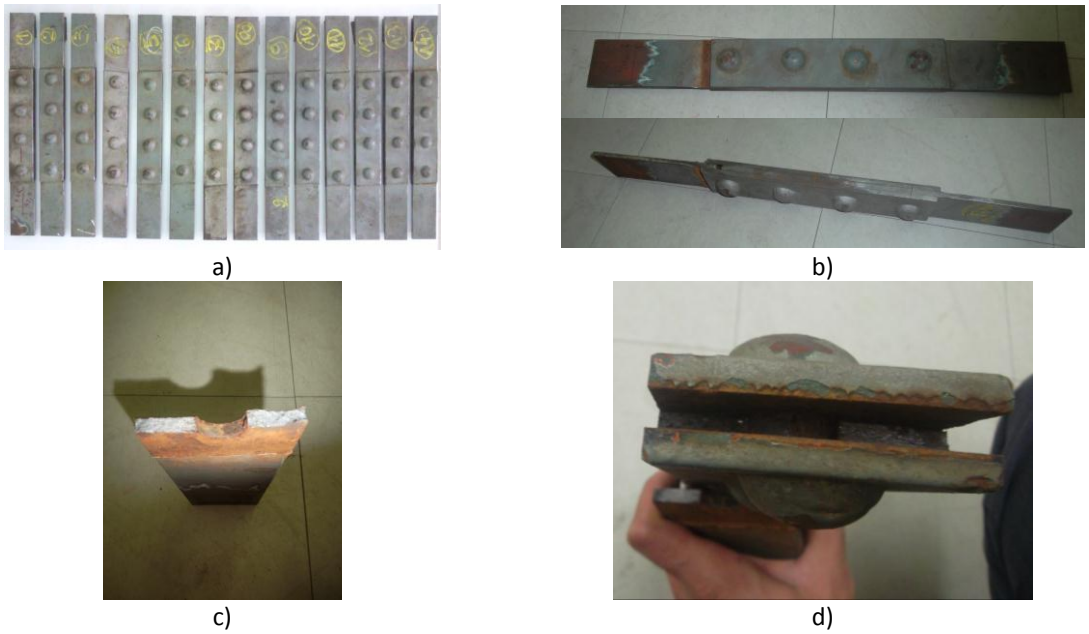

a) b) c) d)

Figure 3.80 – Riveted specimens extracted from the Eiffel bridge: a) complete test series; b), c) and d) illustration of the specimen, before and after fatigue failure.

Table 3.32 – Results of the fatigue tests of the riveted joints from the Eiffel bridge.

Specimen	S_{gross}	S_{net}	R_σ	F_{max}	ΔF	f	$\Delta\sigma_{gross}$	$\Delta\sigma_{net}$	N_f
-	mm^2	mm^2	-	N	N	Hz	MPa	MPa	cycles
V1	430.1	296.8	0.1	55533	49980	5.0	116.2	168.4	1513265
V2	427.3	293.5		54939	49445	7.5	115.7	168.4	1500331
V3	445.3	278.7		57538	51784	7.5	116.3	185.8	240383
V4	432.0	299.6		55640	50076	7.5	115.9	167.1	149378
V5	433.7	303.3		67551	60796	5.0	140.2	200.5	61456
V6	442.2	301.2		69239	62315	5.0	140.9	206.9	149879
V7	427.9	280.4		66115	59504	5.0	139.1	212.2	19768
V8	437.8	308.1		68511	61660	5.0	140.8	200.2	12195
V9	431.2	304.3		61121	55009	5.0	127.6	180.8	31954
V10	438.1	306.9		62122	55910	5.0	127.6	182.1	53638
V11	441.4	285.9		63062	56756	5.0	128.6	198.5	114510
V12	452.8	311.2		64352	57917	5.0	127.9	186.1	23196
V13	428.5	259.0		54480	49032	5.0	114.4	189.3	91069
V14	431.1	309.3		66909	60218	5.0	139.7	194.7	12950

3.6.2. Riveted connections from the Luiz I bridge

Original single shear riveted specimens with single rivets were tested from the Luiz I bridge, the geometry of which is illustrated in Figure 3.80 [12]. Due to limitations imposed by the available material, only single lap joints were tested. A total of 7 specimens were tested under R_σ=0.1 and test frequencies, f, ranged between 6 and 8Hz. The respective results are summarized in Table 3.33 [12].

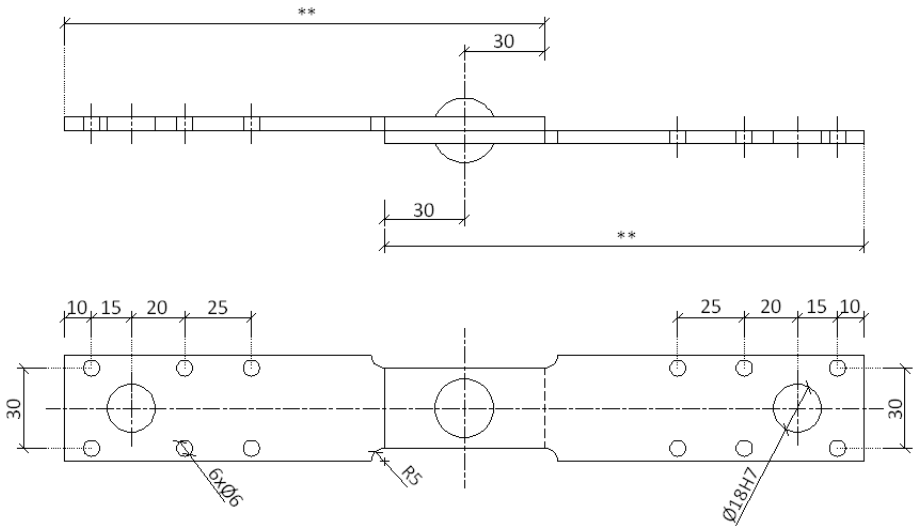

** Maximum dimension allowing equal dimension of side plates.

Figure 3.81 – Nominal geometry of the riveted joint from the Luiz I bridge [12].

Table 3.33 – Results of the fatigue tests of the riveted joints from the Luiz I bridge [12].

Specimen	S_{gross}	S_{net}	R_σ	F_{max}	ΔF	f	$\Delta\sigma_{gross}$	$\Delta\sigma_{net}$	N_f
-	mm^2	mm^2	-	N	N	Hz	MPa	MPa	cycles
S5R1	350.0	210.0		31500	28350	8.0	81.0	135.0	164985
S5R2	350.0	210.0		31500	28350	6.0	81.0	135.0	426259
S5R3	350.0	210.0		26600	23940	7.0	68.4	114.0	161801
S5R4	350.0	210.0	0.1	22600	20340	7.0	58.1	96.9	999453
S5R5	350.0	210.0		19200	17280	7.0	49.4	82.3	514569
S5R6	350.0	210.0		16330	14697	8.0	42.0	70.0	1586560
S5R7	350.0	210.0		14000	12600	8.0	36.0	60.0	904586

3.6.3. Riveted connections from the Fão bridge

Specimens manufactured with the original material from the Fão bridge were also of double shear type, as shown in Figure 3.82. In this case, only two rivets were applied and the plate thickness ranged between 5 and 8 mm. New holes were drilled with a diameter of 24mm and rivets with a diameter of 22mm were used to assemble the plates. The clearance between rivets and holes were filled due to the expansion of the rivets. A total of 15 specimens were tested under stress ratio R_σ=0.0 and test frequencies, f, ranging between 2.5 and 12Hz. Table 3.34 summarizes the results of the fatigue tests [14] obtained for these riveted specimens.

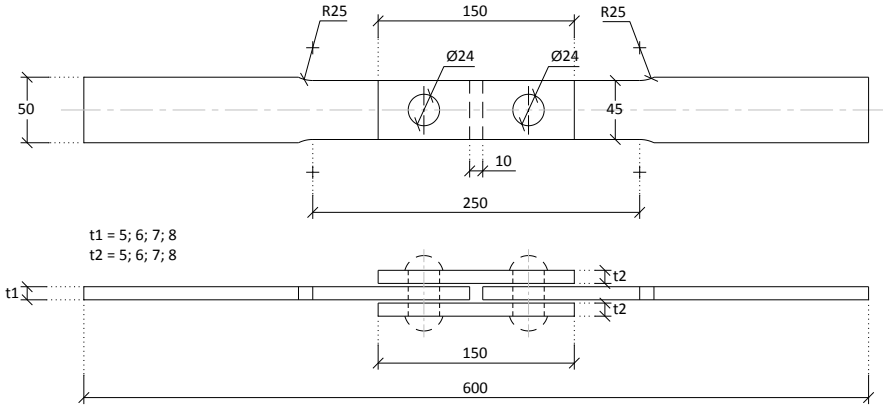

a)

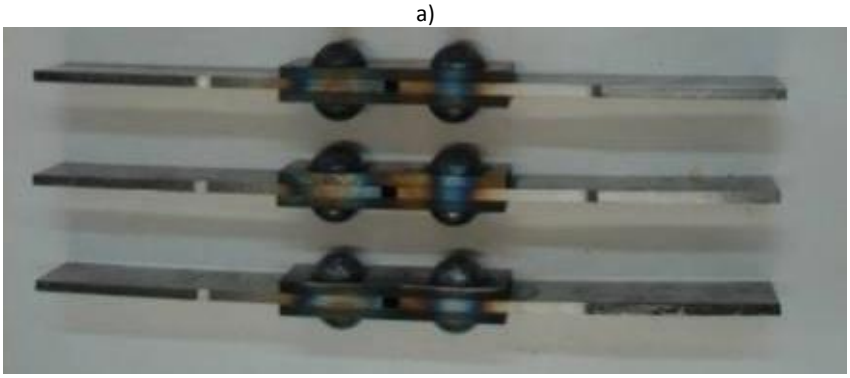

b)

Figure 3.82 – Riveted joint prepared with the material from the Fão bridge: a) geometry of the riveted joint (dimensions in mm); b) views of the riveted specimens [14].

Table 3.34 – Results of the fatigue tests for riveted joints from the Fão bridge [14].

Specimen	S_{gross}	S_{net}	R_σ	F_{max}	ΔF	f	$\Delta\sigma_{gross}$	$\Delta\sigma_{net}$	N_f
-	mm^2	mm^2	-	N	N	Hz	MPa	MPa	cycles
FA1	342.2	160.2		56940	56370.6	2.5	164.7	351.9	9744
FA2	345.7	163.8		58210	57627.9	2.5	166.7	351.9	5285
FA3	342.9	162.3		57690	57113.1	2.5	166.5	351.9	24357
FA4	340.9	160.3		56960	56390.4	5.0	165.4	351.9	3458
FA5	333.6	157.8		49300	48807	2.5	146.3	309.3	141330
FA6	329.4	155.5		48570	48084.3	5.0	146.0	309.3	52879
FA7	349.2	165.6		51730	51212.7	5.0	146.6	309.3	6644
FA8	345.6	163.8	0.01	51160	50648.4	5.0	146.5	309.2	21050
FA9	344.3	163.1		47430	46955.7	5.0	136.4	287.9	38242
FA10	344.0	163.4		47530	47054.7	5.0	136.8	287.9	103809
FA11	345.9	163.1		47430	46955.7	5.0	135.8	287.9	75749
FA12	343.7	163.0		35120	34768.8	5.0	101.2	213.3	210995
FA13	327.7	155.3		26770	26502.3	5.0	80.9	170.7	699161
FA14	347.2	160.8		27700	27423	10.0	79.0	170.6	4000000→
FA15	338.7	159.7		27520	27244.8	5.0	80.5	170.6	1439414

3.6.4. Riveted connections from the Pinhão bridge

Figure 3.83 illustrates the geometry of the original riveted specimens extracted from the Pinhão bridge, which was similar to that of the specimens extracted from the Luiz I bridge. An approximate thickness of the plates between 10 and 11mm was measured for those specimens. The observation of a macrograph of the rivet longitudinal section allow us the estimation of the hole diameter (Ø21mm) and the rivet diameter (Ø20mm). A total of seven specimens were tested under load control, with stress *R*-ratio, R_σ=0.1. The number of specimens was limited by the amount of available material. The results of the fatigue tests are summarized in Table 3.35 [15]. The fracture surfaces of specimens CF1, CF4 and CF5 show that the fatigue cracks initiated at existing flaws as illustrated in Figure 3.84 [15].

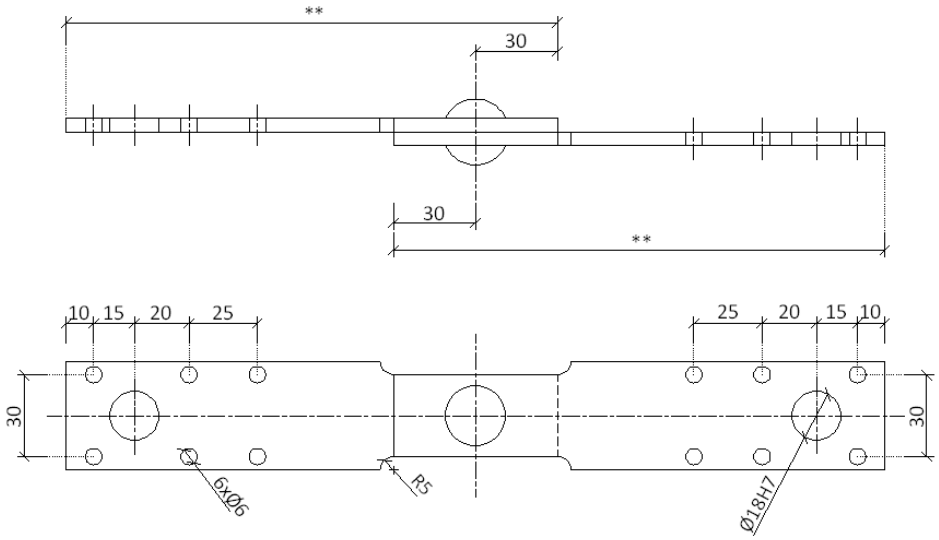

**Maximum dimension allowing equal length of side plates.

a)

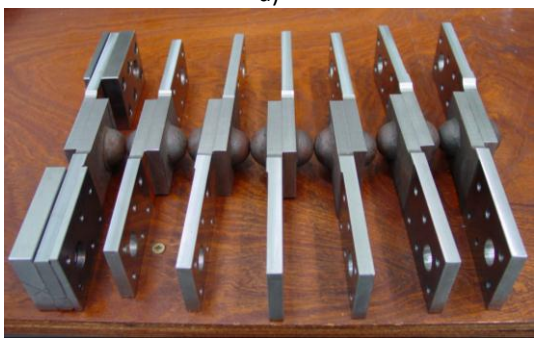

b)

Figure 3.83 – Riveted joint specimens prepared with the material from the Pinhão bridge: a) geometry of the riveted joint (dimensions in mm); b) view of the riveted specimens [15].

Table 3.35 – Results of the fatigue tests of riveted joints from the Pinhão bridge [15].

Specimen	S_{gross}	S_{net}	R_σ	F_{max}	ΔF	f	$\Delta\sigma_{gross}$	$\Delta\sigma_{net}$	N_f
-	mm^2	mm^2	-	N	N	Hz	MPa	MPa	cycles
CF1	460.3	269.3		25000	22500	6.0	48.9	83.5	1922024
CF2	458.4	267.4		50000	45000	6.0	98.2	168.3	86140
CF3	459.4	268.4		37000	33300	6.0	72.5	124.1	635172
CF4	460.3	269.3	0.1	31000	27900	6.0	60.6	103.6	574452
CF5	460.3	269.3		18500	16650	6.0	36.2	61.8	1450789
CF6	460.3	269.3		25000	22500	6.0	48.9	83.5	2243676
CF7	460.3	269.3		18500	16650	6.0	36.2	61.8	10000000→

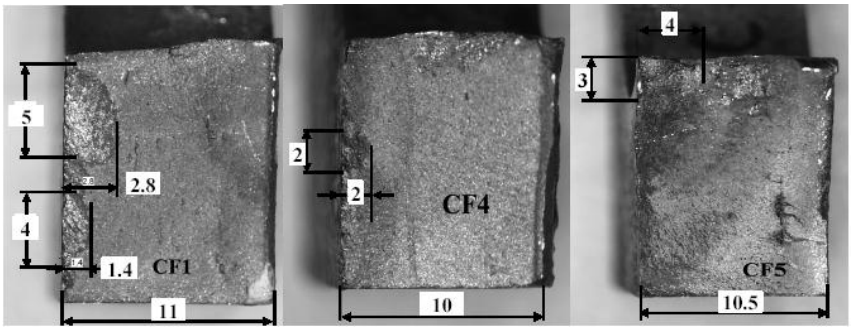

Figure 3.84 – Initial crack-like flaws observed in some tested riveted specimens from the Pinhão bridge [15].

3.6.5. Riveted connections from the Trezói bridge

Riveted joints, with a single rivet and one shear plane, were machined from an original bracing member removed from the Trezói bridge. The final dimensions of the riveted joints are illustrated in Figure 3.85 [16]. The original rivets of the connections were preserved. The riveted joints were fatigue tested under a stress *R*-ratio equal to 0.1 and test frequencies, *f*, ranging between 4 and 10Hz. The *S–N* data is summarized in Table 3.36 [16,17]. Some failures were generated at cracks that initiated at the rivet hole and propagated through the net cross section; other failures were due to cracks initiated and propagated outside the net cross section, motivated by important clamping forces on the rivets. The true value of the clamping forces in the rivets is, in general, difficult to assess and in this particular case were not measured.

3.6.6. Results and discussion

A linear regression analysis was performed on the *S-N* experimental data available for the riveted joints from the old Portuguese metallic bridges. Figures 3.86 and 3.87 show the experimental S-N data and the respective *S-N* curves. The riveted joints were categorized

into single and double shear joints. Relatively low coefficients resulted from the regression analysis, the lowest determination coefficient being obtained for the riveted joints from the Eiffel bridge. The parameters of the mean *S-N* curves are presented in Table 3.37, together with the stress range, $\Delta\sigma_c$, for a number of cycles to failure of 2×10^6 cycles. Besides the parameters of the individual *S-N* curves, corresponding to each tested riveted joint, the parameters for the single and double shear joints are also proposed for the S-N data analysed. Clearly, the single shear joints show lower fatigue strength than the double shear joints, which may be in part attributed to bending effects acting on the specimen. The slope of the double shear joints is also significantly higher than the slope of the single shear joints.

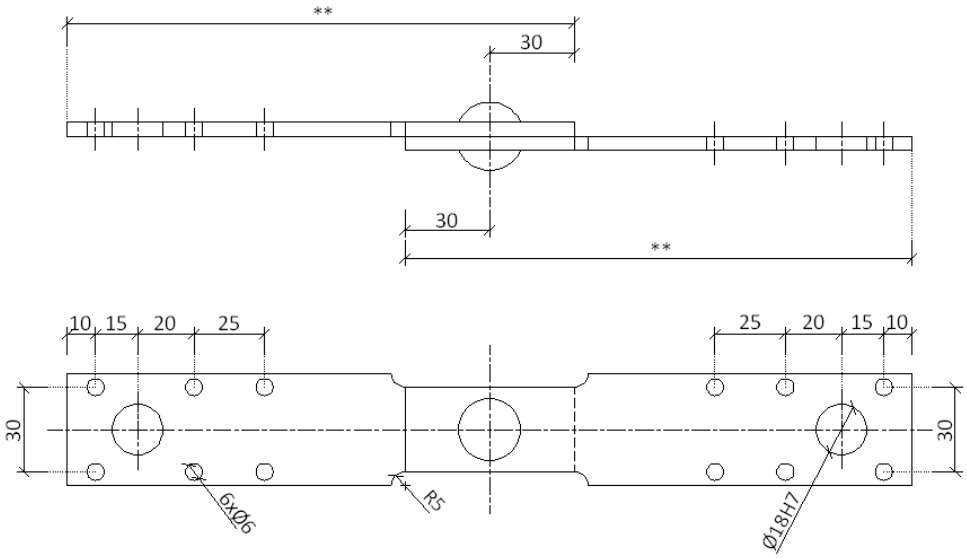

** Maximum dimension allowing equal length of side plates.

a)

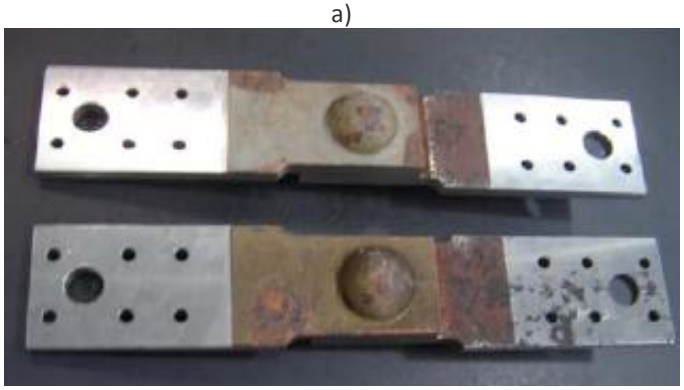

b)

Figure 3.85 – Riveted joint prepared with material from the Trezói bridge: a) geometry of the riveted joint (dimensions in mm); b) view of the riveted specimens [16].

Table 3.36 – Results of the fatigue tests for riveted joints from the Trezói bridge [16,17].

Specimen	S_{gross}	S_{net}	R_σ	F_{max}	ΔF	f	$\Delta\sigma_{gross}$	$\Delta\sigma_{net}$	N_f
-	mm^2	mm^2	-	N	N	Hz	MPa	MPa	cylces
F1	591.3	328.5	0.1	71000	63900	4.0	108.1	194.5	50771
F2	580.5	322.5		47500	42750	6.0	73.6	132.6	605387
F3	585.9	325.5		47500	42750	6.0	73.0	131.3	566477
F4	495.8	235.4		30000	27000	10.0	54.5	114.7	2518224
F5	540.0	280.8		33000	29700	10.0	55.0	105.8	1202674
F6	498.1	236.5		36200	32580	8.0	65.4	137.8	846982
F7	499.1	239.7		29000	26100	10.0	52.3	108.9	4901965
F8	540.0	280.8		33000	29700	10.0	55.0	105.8	3473620

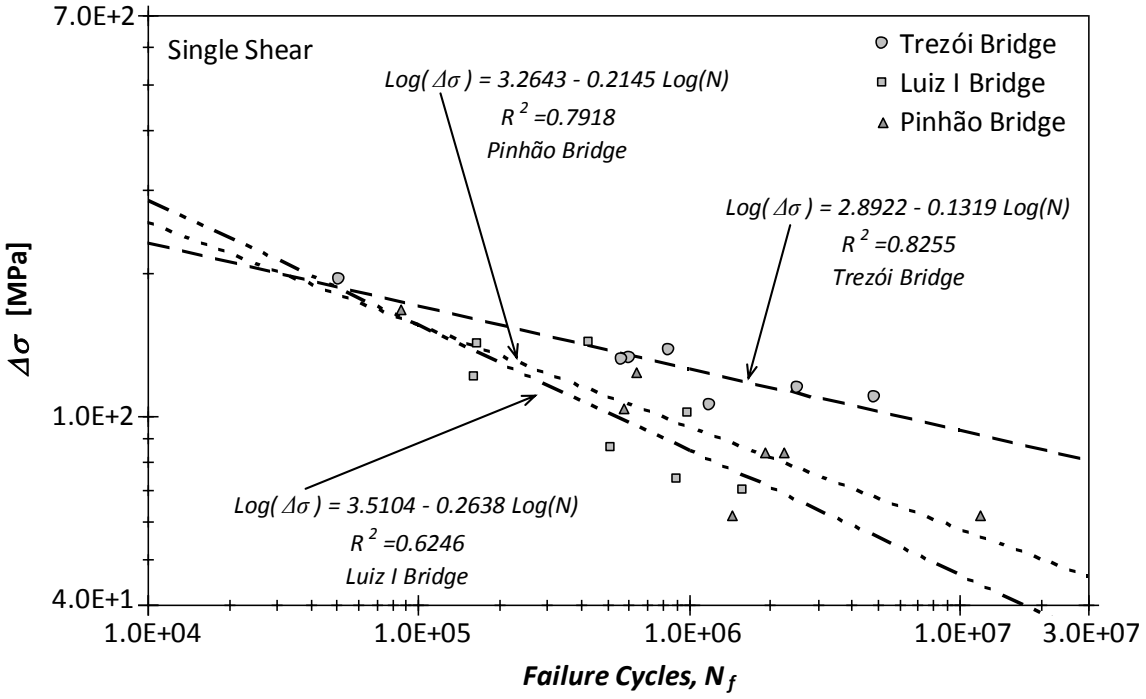

Figure 3.86 – *S-N* fatigue data for single shear riveted connections from Portuguese metallic bridges.

Table 3.37 – *S-N* curve parameters resulting from the experimental data.

Bridge	***Riveted***	***C***	***m***	$\Delta\sigma_c$
-	**joints**	MPa	-	MPa
Trezói	Single shear	8.4570E+21	7.5815	115.1
Pinhão		1.6527E+15	4.6620	81.8
Luiz I		2.0279E+13	3.7908	70.5
Fão	Double Shear	1.6401E+25	8.3612	182.9
Eiffel		6.6637E+77	32.0513	170.4
Trezói, Pinhão and Luiz I	Single Shear	1.2770E+17	5.5310	89.9
Fão and Eiffel	Double Shear	9.4512E+28	10.2145	165.9

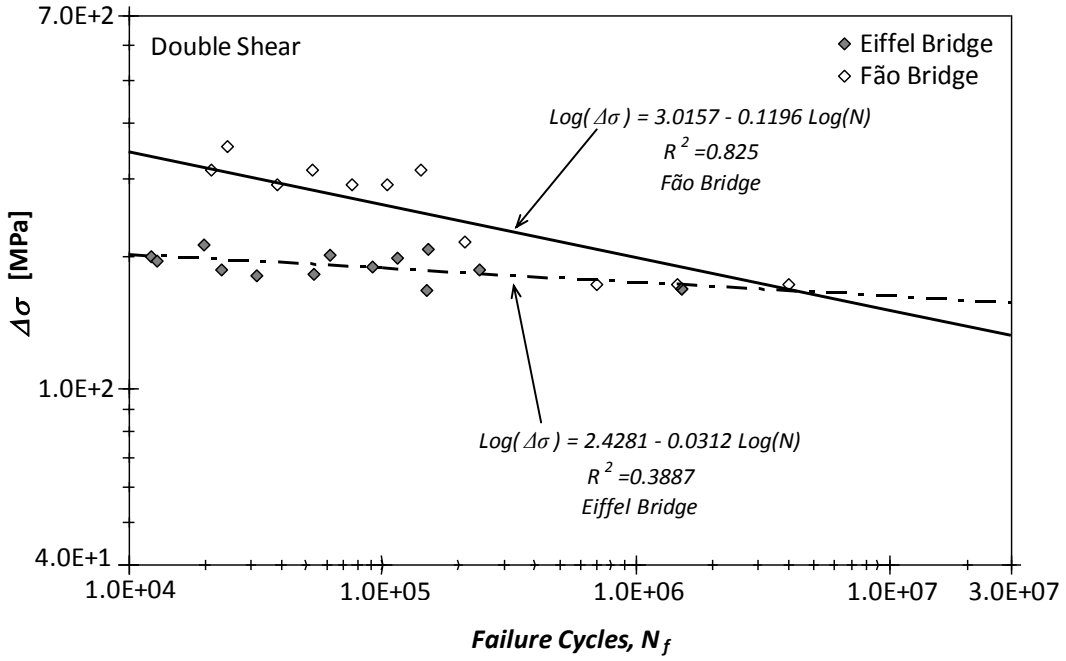

Figure 3.87 – *S-N* fatigue data for double shear riveted connections from Portuguese metallic bridges.

Taras and Greiner [36] have performed a statistical analysis of a significant amount of experimental fatigue data available in literature for riveted joints from old bridges. These authors suggested the categorization of the riveted joints into five categories. Two of the categories are the single and double shear splices under tensile loading. They also suggested the use of a slope, *m*=5 for the design curve, instead of the *m*=3 proposed in the design codes for the joints, EC3-1-9 [5]. In addition, they refer that mean stress effects must be accounted for riveted joints and suggested the use of a normalized stress range to allow the comparison of experimental fatigue data for distinct mean stresses to be made [36]:

$$\Delta\sigma_{norm} = \frac{\Delta\sigma}{f(R_\sigma)} \tag{3.17}$$

where $\Delta\sigma_{norm}$ is the normalized stress range, $\Delta\sigma$ is the tested stress range, $f(R_\sigma)$ is a normalization function to account for stress ratio effects, defined as a function of the material.

For wrought iron and mild steel manufactured before 1900, $f(R_\sigma)$ is defined as [36]:

$$\begin{aligned} f(R_\sigma) &= \frac{1-R_\sigma}{1-0.70\cdot R_\sigma} \Leftarrow -1 \le R_\sigma \le 0 \\ f(R_\sigma) &= \frac{1-R_\sigma}{1-0.75\cdot R_\sigma} \Leftarrow R_\sigma > 0 \end{aligned} \tag{3.18}$$

For mild steel after 1900 (St37, St48, St52, etc.) the following normalization function is proposed [36]:

$$f(R_\sigma)=\frac{1-R_\sigma}{1-0.40\cdot R_\sigma} \Leftarrow -1 \le R_\sigma \le 0$$
$$f(R_\sigma)=\frac{1-R_\sigma}{1-0.60\cdot R_\sigma} \Leftarrow R_\sigma > 0 \quad (3.19)$$

Figures 3.88 and 3.89 compare the *S-N* data from riveted joints of Portuguese bridges with *S-N* data from Taras and Greiner investigation [36], with details categorization, respectively, into single and double joints. Also, the Eurocode 3, class 71 *S-N* curve is presented [5]. The *S-N* data is represented using the normalized stress function, as defined in Equation (3.17). For double shear riveted joints, Taras and Greiner [36] proposed a design *S-N* curve with a slope, *m*=5 and a fatigue strength of 90MPa at 2×10^6 cycles, while for single shear riveted joints, a design *S-N* curve with a slope, *m*=5 and a fatigue strength of 71MPa at 2×10^6 cycles was proposed by these authors. Only very few points from Portuguese riveted bridges fall below these design *S-N* curves, namely corresponding to riveted connections from Eiffel (double shear), Luiz I and Pinhão bridges (single shear). This result may be justified by the high damage levels experienced by the riveted joints, due to the long bridge operation time. A higher slope, *m*, of the *S-N* curve ($\Delta\sigma^m N_f = C$) is suggested by the experimental data, when a comparison is made with the class 71 *S-N* curve of the Eurocode EC3-1-9 [5]. Therefore, the proposition of new S-N curves based on a slope m=5 seems to be an appropriate decision for riveted joints.

3.7. CONCLUDING REMARKS

In this chapter, strain-life and fatigue crack propagation data for samples of original materials removed from five Portuguese ancient riveted metallic bridges, namely from the Eiffel, Luiz I, Fão, Pinhão and Trezói bridges was compiled. Also, S-N fatigue resistance data from riveted joints made of original materials from the Portuguese bridges was gathered. The strain-life fatigue data was correlated using deterministic models. The fatigue crack propagation data was correlated using both the Paris model and the Walker model, the latter allowing the description of stress ratio effects.

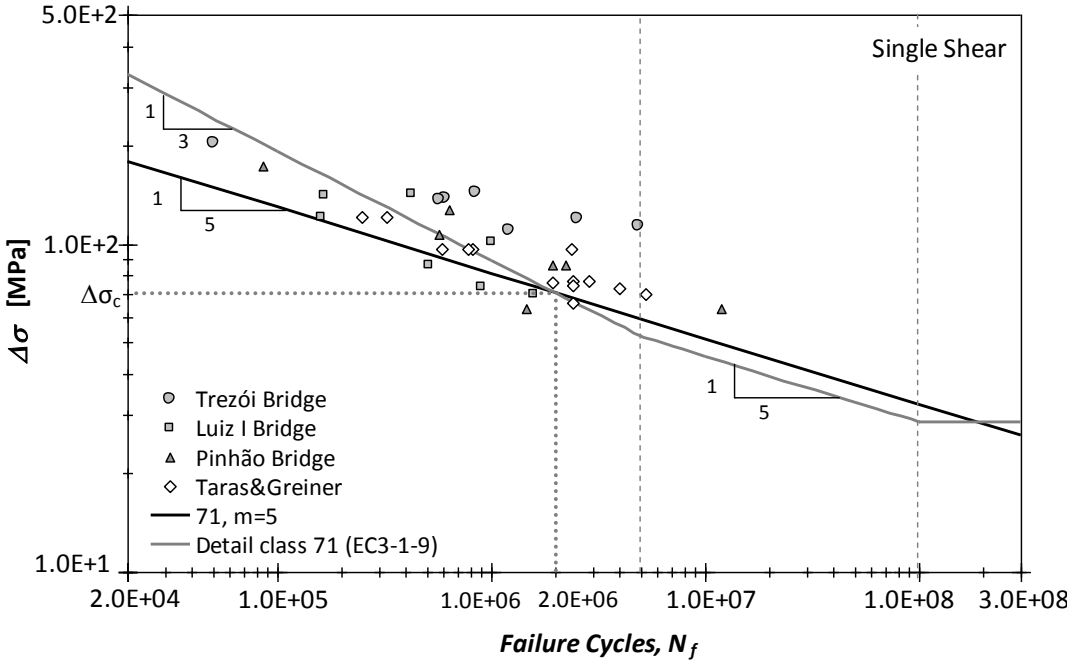

Figure 3.88 – Comparison of *S-N* data between Portuguese and international bridges details and proposal of a design *S-N* curve for single shear joints.

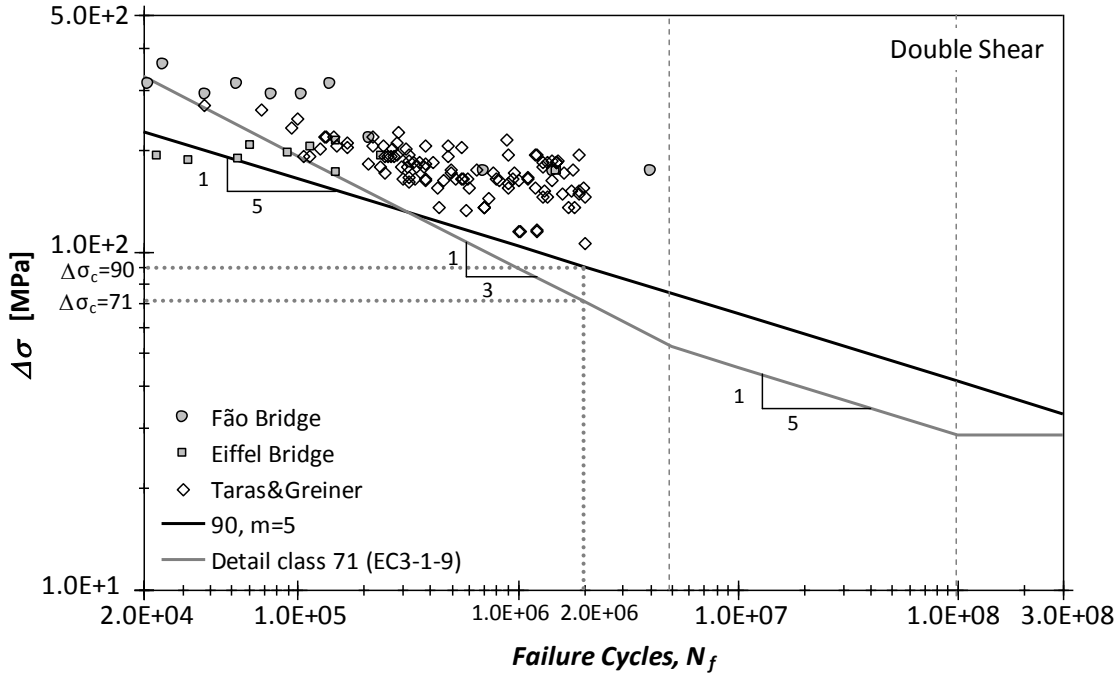

Figure 3.89 – Comparison of *S-N* data between Portuguese and international bridges details and proposal of a design *S-N* curve for double shear joints.

Materials from the Eiffel, Luiz I, Fão and Pinhão bridges are very likely puddle irons account give of their age, the high microstructural heterogeneities and the low ductility properties. The material from the Trezói bridge is a low carbon structural steel. In general,

there is a significant correlation between the mechanical performance, including fatigue, and the age of the materials.

Regarding the cyclic elastoplastic behaviour, the material from Trezói bridge does not follow the Masing behaviour while the materials from Eiffel and Luiz I bridge may be satisfactorily described by the Masing model, since some apparent deviation from the Masing behaviour may be justified by scatter in material properties. The material from Fão bridge shows a cyclic elastoplastic behaviour dependent on strain ratio, while the material from the Trezói bridge shows cyclic softening for strain ranges below 1%, the older materials show cyclic hardening.

Regarding the strain-life behaviour of the materials investigated, the number of transition reversals decreases with increasing age of the materials. The older materials show a transition life between low- and high-cycle fatigue regimes that is considered very low. Only the material from the Trezói bridge shows a transition life in the usual range for low carbon steels. Therefore, fatigue strength properties should play an important role on fatigue assessment of these old metallic bridges.

The fatigue crack propagation tests showed that the Paris law gives a good description of the fatigue crack growth data, for each stress ratio. The exponent of the Paris law resulted always greater than the value suggested by codes of practice (m=3). The C coefficient was in order of magnitude lower than that recommended in literature for modern construction steels. A fatigue crack propagation design curve was proposed taking into account 42 fatigue crack propagation tests on original samples of the material from five distinct bridges. The Walker model improved the correlation of the fatigue crack propagation rates with the stress ratio effects.

S-N fatigue data from original riveted joints was compared with existing design curves. This comparison shows some data falling below the design *S-N* curves that corroborates the presence of cracks originated by the prior operation of the bridge or material degradation. The comparison performed with literature *S-N* data suggests the need of a riveted joint categorization, in particular the consideration of single and symmetric double shear splices. Also, a slope m=5 seems to be more appropriate for riveted joints,

rather than *m*=3, as suggested by the current design codes. The influence of the stress *R*-ratio on *S*-*N* data for riveted joints has also to be accounted for in a convenient way.

Fracture mechanics and *S*-*N* based fatigue approaches have been used to assess riveted details, consisting on more classical approaches. Recent research suggests the use of local approaches to fatigue, supported on detailed finite element models [37,38,39]. The availability of adequate material properties is crucial. This issue is a limitation of the local approaches when materials under consideration are not fully investigated, and their fatigue properties are, consequently, not available.

3.8. REFERENCES

[1] Akesson B. Fatigue life of riveted railway bridges. PhD thesis, Chalmers University of Technology, Sweden; 1994.

[2] Crocetti R. On some fatigue problems related to steel bridges. PhD thesis, Chalmers University of Technology, Sweden; 2001.

[3] Mohammad AE. Fatigue in riveted railway bridges. PhD thesis, Chalmers University of Technology, Sweden; 2002.

[4] Kühn B, Lukic´ M, Nussbaumer A, Günther H-P, Helmerich R, Herion S, et al. In: Sedlacek G, Bijlaard F, Géradin M, Pinto A, Dimova S, editors. Assessment of existing steel structures: recommendations for estimation of remaining fatigue life – EUR 23252 EN. JRC – ECCS; 2008.

[5] CEN-TC 250. EN 1993-1-9: Eurocode 3, Design of steel structures – Part 1-9: Fatigue. European Committee for Standardization, Brussels; 2003.

[6] AASHTO. AASHTO LRFD: bridge design specification; 1995.

[7] De Jesus AMP, Figueiredo MAV, Ribeiro AS, de Castro PMST, Fernandes AA. Residual lifetime assessment of an ancient riveted steel road bridge. Strain. doi:10.1111/j.1475-1305.2008.00596.x.

[8] De Jesus AMP, Correia JAFO. Fatigue assessment of riveted railway bridge connections. Part II: numerical investigations. In: 7th international conference on steel bridges steel bridges, Guimarães; 2008. p. II:339–48.

[9] Correia JAFO, de Jesus AMP, da Silva ALL, da Silva JFN. A procedure to derive probabilistic fatigue strength data for riveted joints. In: The fifth international conference on bridge maintenance, safety and management (IABMAS2010), Philadelphia, Pennsylvania, USA; 11–15 July 15 2010.

[10] De Jesus AMP, Pinto H, Fernández-Canteli A, Castillo E, Correia JAFO. Fatigue assessment of a riveted shear splice based on a probabilistic model. International Journal Fatigue 2010;32:453–62.

[11] Jorge RN, Ribeiro A, De Jesus AMP, Figueiredo M, Castro PT, Fernandes AA. Ponte Eiffel – Viana do Castelo, Avaliação de resultados de programa experimental (in Portuguese). Research Report,

IDMEC/FEUP, 2006.

[12] Fernandes AA, Castro PT, Figueiredo M, Oliveira F. Structural integrity evaluation of highway riveted bridges. In Watanabe E. et al. (eds.), Bridge Maintenance, Safety and Management (IABMAS'04); Proc. intern. conf., Kyoto, 18-22 October 2004.

[13] Silva ALL. Fatigue behaviour of a typical material from ancient metallic riveted bridges, under constant and variable amplitude loading. MSc. Thesis, University of Trás-os-Montes and Alto Douro, Portugal (in Portuguese), 2009. 271 p.

[14] Silva JFN. Comparison of the fatigue behavior between riveted and bolted connections. MSc. Thesis, University of Trás-os-Montes and Alto Douro, Portugal (in Portuguese), 2009. 249 p.

[15] Figueiredo M, De Jesus AMP, Pereira H, Ribeiro A, Natal R, Moreira P, Castro PT, Fernandes AA. Avaliação da integridade estrutural da Ponte do Pinhão (in Portuguese). Research Report, IDMEC/FEUP, 2004.

[16] Silva T, Fernandes AA. Ponte Trezói – Estudo do comportamento à fadiga de ligações rebitadas em pontes metálicas antigas (in Portuguese). Research Report, FEUP/DEMEGI, 2006.

[17] Correia JAFO. Development of procedures for fatigue life prediction of riveted connections. MSc. Thesis, University of Trás-os-Montes and Alto Douro, Portugal (in Portuguese), 2008. 143 p.

[18] De Jesus AMP, Silva ALL, Figueiredo MV, Correia JAFO, Ribeiro AS, Fernandes AA. Strain-life and crack propagation fatigue data from several Portuguese old metallic riveted bridges. Engineering Failure Analysis, 2010, Vol. 17, pp. 1495–1499.

[19] NP EN 10002-1: Materiais metálicos. Ensaio de tracção. Parte 1: Método de ensaio à temperatura ambiente. Instituto Português da Qualidade (IPQ), Lisboa, 2006.

[20] Chen H, Grondin GI, Driver RG. Fatigue resistance oh high performance steel. Structural Engineering Report No. 258, University of Alberta, Canada, 2005.

[21] ASTM – American Society for Testing and Materials. ASTM E606-92: standard practice for strain controlled fatigue testing. In: Annual book of ASTM standards, part 10; 1998. p. 557–71.

[22] Morrow JD. Cyclic plastic strain energy and fatigue of metals. Int Frict Damp Cyclic Plast ASTM STP 1965;378:45–87.

[23] Ramberg W, Osgood WR. Description of stress–strain curves by three parameters. NACA tech. note no. 902; 1943.

[24] Coffin LF. A study of the effects of the cyclic thermal stresses on a ductile metal. Trans ASME 1954;76:931–50.

[25] Manson SS. Behaviour of materials under conditions of thermal stress, NACA TN-2933. National Advisory Committee for Aeronautics; 1954.

[26] Basquin OH. The exponential law of endurance tests. Proc Am Soc Test Mater 1910;10:625–30.

[27] Smith KN, Watson P, Topper TH. A Stress-Strain Function for the Fatigue of Metals. Journal of Materials 1970; 5(4): 767-78.

[28] ASTM – American Society for Testing and Materials. ASTM E647: standard test method for measurement of fatigue crack growth rates. In: Annual book of ASTM standards, vol. 03.01. West

Conshohocken, PA: ASTM – American Society for Testing and Materials; 1999. p. 591–630.

[29] Paris PC, Erdogan F. A critical analysis of crack propagation laws. Trans ASME Ser E: J Basic Eng 1963;85:528–34.

[30] Walker K. The effect of stress ratio during crack propagation and fatigue for 2024-T3 and 7075-T6 aluminum, effects of environment and complex load histories on fatigue life, ASTM STP 462. American Society for Testing and Materials; 1970.

[31] Fernandes AA, De Jesus AMP, Silva ALL, Correia JAFO. Retrofitting of old riveted Portuguese bridges. Past and current remnant life assessment research. 15th International Conference on Experimental Mechanics (ICEM15); Proc. intern. conf., Porto – Portugal, 22-27 July 2012.

[32] APK – Association pour la Promotion de l'Enseignement de la Construction Acier. Construction métallique et mixte acier-béton: Calcul et dimensionnement selon les Eurocodes 3 et 4. Éditions Eyrolles, Paris; 1996.

[33] Branco CM, Fernandes AA, De Catro PMST. Fadiga de Estruturas Soldadas. Fundação Calouste Gulbenkian, 1986.

[34] Weibull W. Fatigue testing and analysis of results. Pergamon Press LTD., London; 1961.

[35] ASTM – American Society for Testing and Materials. ASTM E739-91: standard practice for statistical analysis of linear or linearized stress-life and strain-life fatigue data. In: Annual book of ASTM standards, vol. 03.01; 2004. p. 1–7.

[36] Taras A, Greiner R. Statistical Background to the Proposed Fatigue Class Catalogue for Riveted Components. Report: Contribution to WG6.1 – Assessment of Existing Steel Structures, ECCS TC6 – 2010, Spring Meeting – Lausanne – March 22-23, 2010.

[37] Glinka G. A notch stress-strain analysis approach to fatigue crack growth. Engineering Fracture Mechanics 1985; 21: 245-261.

[38] Peeker E, Niemi E. Fatigue crack propagation model based on a local strain approach. Journal of Constructional Steel Research 1999; 49: 139–155.

[39] Noroozi AH, Glinka G, Lambert S. A two parameter driving force for fatigue crack growth analysis. International Journal of Fatigue 2005; 27: 1277-1296.

CHAPTER IV

A PROPOSAL FOR GENERALIZATION OF EXISTING PROBABILISTIC FATIGUE DAMAGE MODELS

4.1. INTRODUCTION

Probabilistic fatigue models are required to account conveniently for the different sources of uncertainty arising in the prediction procedures, such as the scatter inherent to material behaviour. Most of the fatigue models currently used has essentially a deterministic basis. However, their application for design purposes requires subsequently additional statistical arguments in order to establish appropriate safety margins, not always based on sound criteria, and consequent assumptions of the statistical distributions implied. Also, to carry out reliability analyses the fatigue resistance must be established in an appropriate probabilistic form. As a consequence, failure prediction, engineering design and risk analysis in fatigue are not possible without the support of probabilistic fatigue models.

A generalization of the basic probabilistic model proposed by Castillo and Fernández-Canteli [1] to describe the S–N and ε_a–N fields is proposed in this chapter. In the development of the original model, the referred authors assumed simple variables, namely the stress and strain amplitudes (or ranges) as governing fatigue damage variables. With this original model, it is possible to correlate the stress or strain based fatigue data obtained for simple loading conditions (e.g. uniaxial stress/strain states) using a hyperbolic field derived from Weibull or Gumbel distributions (see Figure 4.1).

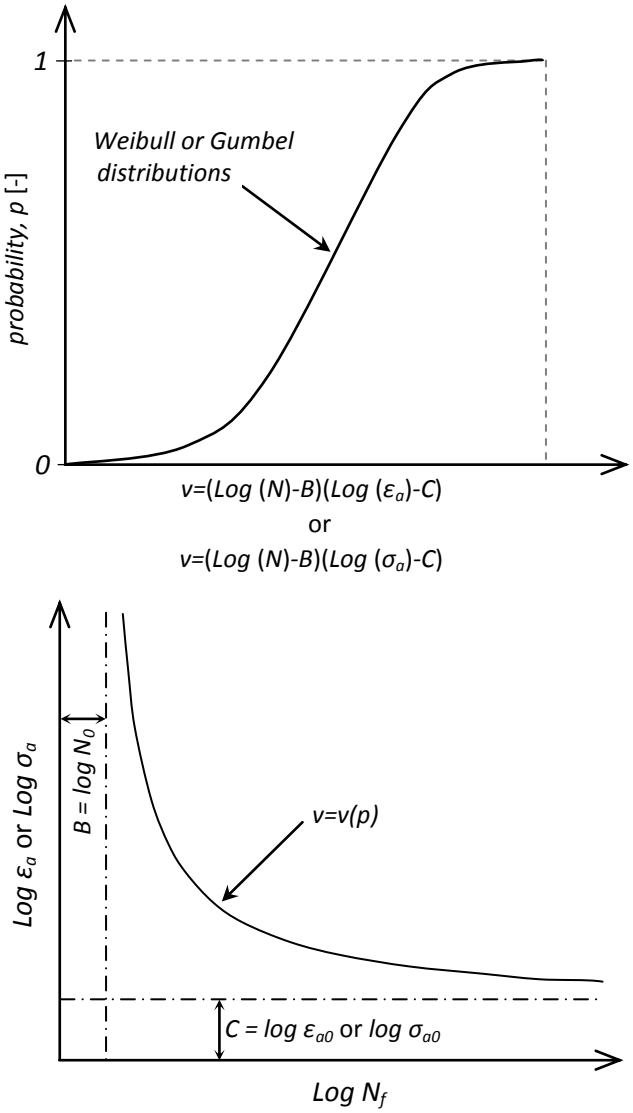

Figure 4.1 – Relation between the hyperbolic probabilistic fatigue and the Weibull/Gumbel distributions.

However, the use of the referred simple variables to model the fatigue phenomena proves to be an apparent limitation of the proposed basic model. On effect, literature demonstrates that fatigue damage is very often governed by more complex damage parameters in order to cover many aspects concerning the fatigue phenomenon. In particular, the mean stress effects on *S-N* fields may be accounted by a convenient change of damage variables, such as that proposed by the empirical model of Smith-Watson-Topper [2]. For this particular case of mean stress effects, Castillo and Fernández-Canteli [1] also proposed a analytical, probabilistic model to describe the mean stress effects on *S-N* fields, but the resulting model, despite very accurate representation of experimental data [1], implies a significant number of constants that requires a

complex identification procedure. The availability of a model with a simpler structure is attractive, for it to be used for the design of structural components.

Despite not formal, the Smith-Watson-Topper damage parameter may be assumed as an energetic parameter. A number of energetic parameters are suggested in the literature, some of which are considered in this chapter to demonstrate the capability, of the proposed generalization concept based on the basic probabilistic model [3].

Another possible generalization of the basic probabilistic model consists in its application to multiaxial fatigue damage parameters. Many of the existing works on multiaxial fatigue deal with deterministic models [3]. Therefore, this generalization proposal will open new possibilities for experimental data analysis in multiaxial fatigue.

In this chapter, the basic probabilistic model is introduced and its generalization described. Thereafter, the fatigue damage parameters are introduced, most of them based on literature. Finally, the capability, of the new fatigue damage parameters combined with the basic probabilistic model is demonstrated based on existing experimental data.

4.2. PROPOSAL FOR THE GENERALIZATION OF AN EXISTING PROBABILISTIC MODEL

In the original contributions of Castillo and Fernández-Canteli [1], a probabilistic field for the stress amplitude *versus* life is proposed based on Weibull or Gumbel distributions as represented in Equations (4.1) and (4.2):

$$p = F(N_f^*;\varepsilon_a^{\,*}) = 1 - \exp\left\{-\left[\frac{\log\left(N_f/N_0\right)\log\left(\varepsilon_a/\varepsilon_{a0}\right)-\lambda}{\delta}\right]^{\beta}\right\} \qquad (4.1)$$

$$\log\left(N_f/N_0\right)\log\left(\varepsilon_a/\varepsilon_{a0}\right) \geq \lambda$$

$$p = F(N_f^*;\varepsilon_a^{\,*}) = 1 - \exp\left\{-\exp\left[\frac{\log\left(N_f/N_0\right)\log\left(\varepsilon_a/\varepsilon_{a0}\right)-\lambda}{\delta}\right]\right\} \qquad (4.2)$$

Similar fields but referred to strain amplitude are also proposed by the those authors as given in Equations (4.3) and (4.4):

$$p = F(N_f^*;\sigma_a^*) = 1 - \exp\left\{-\left[\frac{\log(N_f/N_0)\log(\sigma_a/\sigma_{a0}) - \lambda}{\delta}\right]^{\beta}\right\} \qquad (4.3)$$

$$\log(N_f/N_0)\log(\sigma_a/\sigma_{a0}) \geq \lambda$$

$$p = F(N_f^*;\sigma_a^*) = 1 - \exp\left\{-\exp\left[\frac{\log(N_f/N_0)\log(\sigma_a/\sigma_{a0}) - \lambda}{\delta}\right]\right\} \qquad (4.4)$$

The Gumbel field is a limiting case of the Weibull field, when $\beta \to \infty$ or even for values of β higher than, say, 6. It is interesting to note that authors by applying the same model to describe the probabilistic stress and strain fields, implicitly assumed the possibility of generalization of the model. In any case, they propose the use of two simple damage variables: the uniaxial stress or strain amplitudes.

Figure 4.2 illustrates the p-ε_a-N Weibull field, which is characterized by percentile curves showing hyperbolic shape with two asymptotes: the horizontal one, having a clear physical meaning, represents the fatigue limit; the vertical one, denoted threshold value of lifetime, has a more controversial meaning as a limiting number of cycles.

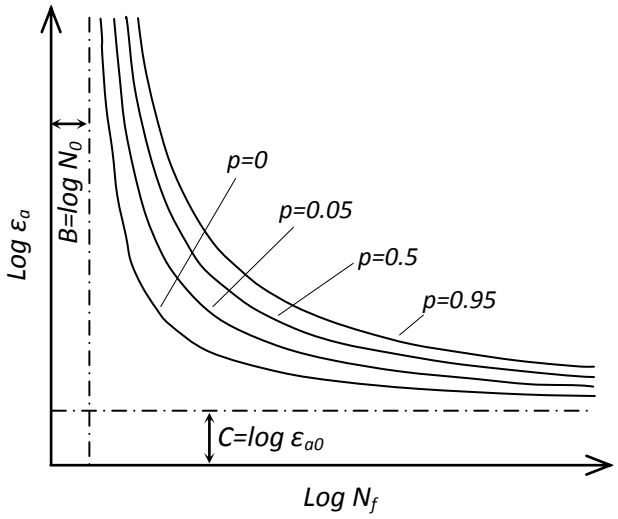

Figure 4.2- Probabilistic ε_a -N field.

Some authors [3] proposing deterministic fatigue models have shown that a power function between the damage parameter and the fatigue life gives a good description of

the fatigue data in the assessment of many practical cases. Figure 4.3 illustrates such generic damage power relation, which has the following mathematical form:

$$\psi = \kappa(t)^{\alpha} + \psi_0 \tag{4.5}$$

where ψ represents a fatigue damage parameter, ψ_0 is a fatigue damage threshold, κ and α are material constants. A comparison between the generic power damage relation and the hyperbolic percentile curves shows that the power damage relation may be approached by a subdomain of the hyperbolic curves. The main differences resides in the lower part of the fatigue lives, where the hyperbolic field fails to represent adequately the material behaviour. Therefore, the hyperbolic field should be used with precaution to perform extrapolations of the fatigue behaviour to lower fatigue lives than covered by the existing experimental data. Also, the referred power relation is clearly not appropriate to represent fatigue data in very low fatigue life regimes, where a sigmoidal function between the damage parameter and the number of cycles would be required, in general, required to cover experimental results.

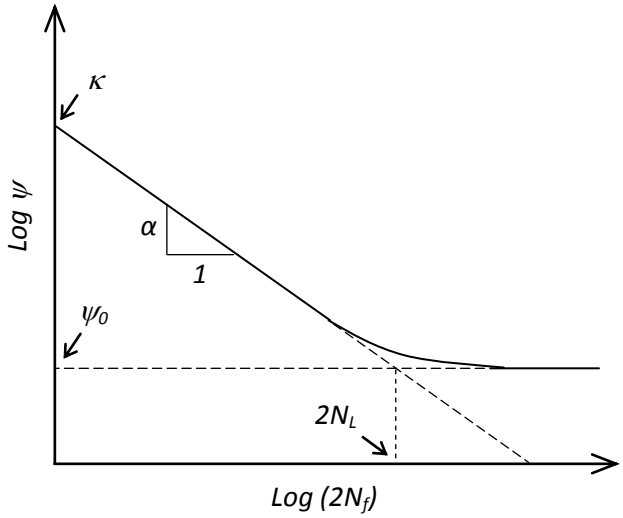

Figure 4.3 - Schematic representation of the power relation between the fatigue life and a generic damage parameter, ψ, showing a damage threshold.

Taking into account the aforementioned arguments, it is proposed a generalization of the probabilistic models developed by Castillo and Fernández-Canteli [1] by considering other damage parameters. The selection of the damage variables involved in the derivation of the original model needs therefore to be updated accordingly:

$$r\left(N_f, N_0, \psi, \psi_0, p\right) = 0 \tag{4.6}$$

where ψ, ψ_0 are, respectively, generalized fatigue damage and threshold fatigue damage parameters. The same mathematical representation of the probabilistic fields as previously referred in Equations (4.1)-(4.4) arise by performing dimensional analysis and applying the statistical assumptions proposed by those authors. If only the Weibull distribution is considered hereafter, the generalized damage probabilistic field is defined as:

$$p = F(N_f^*; \psi^*) = 1 - \exp\left\{-\left[\frac{\log\left(N_f/N_0\right)\log\left(\psi/\psi_0\right) - \lambda}{\delta}\right]^{\beta}\right\} \tag{4.7}$$
$$\log\left(N_f/N_0\right)\log\left(\psi/\psi_0\right) \geq \lambda$$

where p is the probability of failure, N_0 and ψ_0 are normalizing values and λ, δ and β are the non-dimensional Weibull model parameters. The physical meaning of the parameters involved in Equation (4.7) is (see illustration in Figure 4.4):

N_0: Threshold value of lifetime;

ψ_0 : Damage threshold expressed in terms of the general damage parameter;

λ : Parameter defining the position of the corresponding zero-percentile curve;

δ : Scale parameter;

β : Shape parameter.

Equation (4.7) has a dimensionless form and reveals that the probability of failure p depends only on the product $N_f^*\psi^*$, according to a Weibull distribution:

$$N_f^*\psi^* \sim W(\lambda, \delta, \beta) \Leftrightarrow N_f^* \sim W\left(\frac{\lambda}{\psi^*}, \frac{\delta}{\psi^*}, \beta\right) \tag{4.8}$$

where $N_f^* = \log\left(N_f/N_0\right)$ and $\psi^* = \log\left(\psi/\psi_0\right)$.

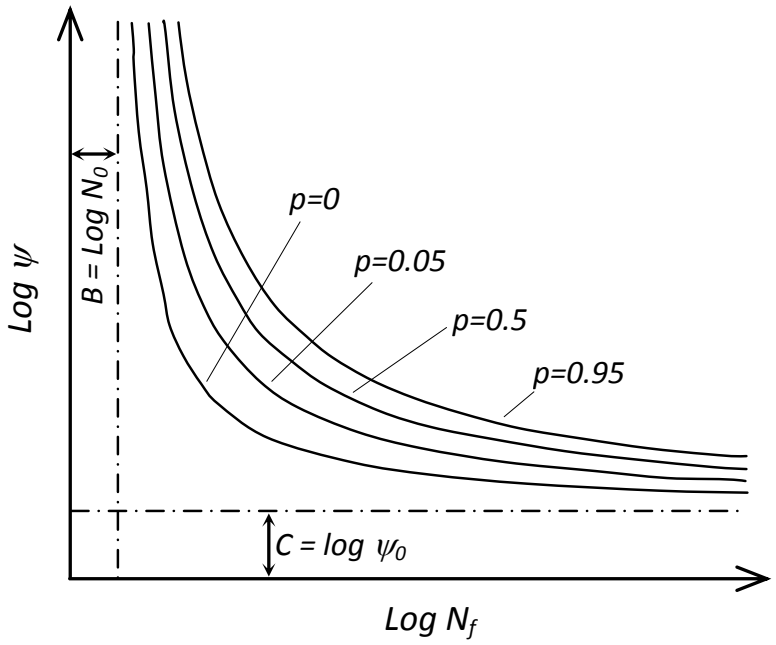

Figure 4.4- Generalized probabilistic ψ-N field.

4.3. SELECTION AND ANALYSIS OF SOME REPRESENTATIVE DAMAGE PARAMETERS

In this section, a selection of fatigue damage parameters that could be considered as the reference driving force by the Weibull probabilistic representation, will be presented thus covering distinct aspects of the fatigue modelling. The proposed damage parameters will be selected from existing deterministic fatigue damage approaches that may be represented with the following functional forms:

$$f(\psi,\psi_0)=g(N_f) \tag{4.9}$$

or

$$f_1(\psi)=g(N_f)+f_2(\psi_0) \tag{4.10}$$

where f, f_1 and f_2 are not functions of the number of cycles to failure and g is not a function of the damage parameters what implies the separation of the variables, damage and cycles to failure, in Equations (4.9) and (4.10). For example, the Morrow equation with mean stress correction (see Equation (2.6)) does not fulfill the requirements of equations (4.9) or (4.10).

4.3.1. Smith-Watson-Topper damage parameter and counterpart parameter for uniaxial loading conditions

Smith *et al.* [2] proposed a damage parameter, known as *SWT* parameter, to account for mean stress effects updating existing strain-based fatigue models. This parameter is defined as:

$$SWT = \sigma_{\max} \cdot \varepsilon_a \tag{4.11}$$

where $\sigma_{\max}$ is the maximum stress during the cycle and $\varepsilon_a = \Delta\varepsilon/2$ is the strain amplitude. According to Smith *et al.* [2], a specimen subjected to any loading condition representing different combinations of $\sigma_{\max}$ *and* ε_a but resulting in the same *SWT* damage parameter, i.e. the same product $\sigma_{\max} \cdot \varepsilon_a$ should exhibit the same fatigue life. Also, for any fixed strain amplitude, an increase of the maximum stress (which also implies an increase of the mean stress) leads, obviously, to an increment of the *SWT* damage parameter, which entails a reduction of the fatigue life. The *SWT* damage parameter was originally related to the fatigue life by means of the following equation that results from the combination of the Morrow [4] and Basquin [5] relations:

$$\sigma_{\max} \cdot \Delta\varepsilon/2 = SWT = \left(\sigma'_f\right)^2 \cdot \left(2N_f\right)^{2b} / E + \sigma'_f \cdot \varepsilon'_f \cdot \left(2N_f\right)^{b+c} \tag{4.12}$$

where σ_{max} is the maximum stress and *SWT* is the fatigue damage parameter. In Figure 4.5, the *SWT* parameter is plotted against fatigue life obtained for the material from Eiffel bridge using data from smooth specimens tested under strain-controlled conditions (R_ε=–1). The figure also includes the deterministic line fitted by Equation (4.12), which shows a good correlation with the experimental data. From the analysis of the data one can realize that the experimental data can be approximated by an hyperbolic field as will be demonstrated later in this chapter.

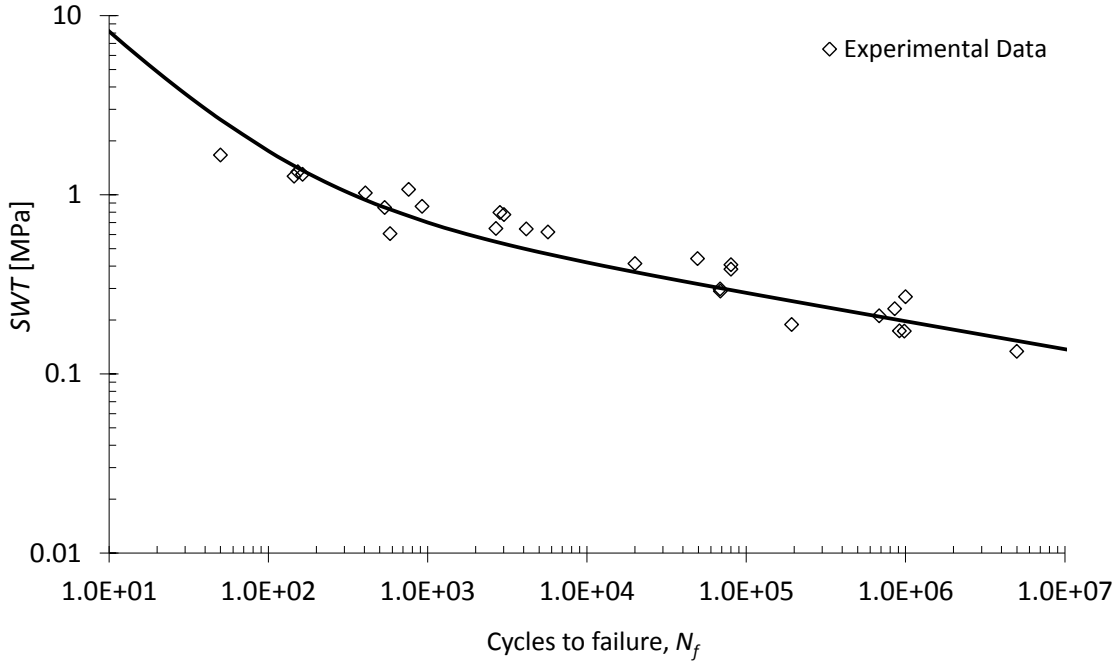

Figure 4.5 - Fitting of fatigue data for material available from Eiffel bridge (R_ε=-1) using the *SWT* damage parameter and a deterministic relation (Eq. (4.12)).

The *SWT* parameter may be considered an informal energetic damage parameter. A counterpart of the *SWT* damage parameter can be stated as the product $\varepsilon_{\max}\cdot\Delta\sigma/2$ as suggested in reference [6]. For fully-elastic conditions both parameters are coincident:

$$\sigma_{\max}\cdot\frac{\Delta\varepsilon}{2}=\frac{\Delta\sigma}{1-R_\sigma}\cdot\frac{1}{2}\cdot\Delta\varepsilon=\frac{1}{1-R_\sigma}\cdot\frac{\Delta\sigma^2}{2E}$$

$$\varepsilon_{\max}\cdot\frac{\Delta\sigma}{2}=\frac{\sigma_{\max}}{E}\cdot\frac{\Delta\sigma}{2}=\frac{\Delta\sigma}{E\left(1-R_\sigma\right)}\cdot\frac{\Delta\sigma}{2}=\frac{1}{1-R_\sigma}\cdot\frac{\Delta\sigma^2}{2E} \quad (4.13)$$

Even for elastoplastic conditions, the $\sigma_{\max}\cdot\Delta\varepsilon/2$ and the $\varepsilon_{\max}\cdot\Delta\sigma/2$ damage parameters also coincide, if fully-reversible elastoplastic conditions are ensured. For fully-reversible elastoplastic conditions the following conditions are met:

$$\sigma_{\max}=\frac{\Delta\sigma}{2}\Rightarrow\sigma_{\max}\frac{\Delta\varepsilon}{2}=\frac{\Delta\sigma\cdot\Delta\varepsilon}{4}$$

$$\varepsilon_{\max}=\frac{\Delta\varepsilon}{2}\Rightarrow\varepsilon_{\max}\frac{\Delta\sigma}{2}=\frac{\Delta\sigma\cdot\Delta\varepsilon}{4} \quad (4.14)$$

For general non-symmetrical elastoplastic conditions, the referred damage parameters differ from each other. Depending on plastic conditions, the maximum cyclic elastoplastic

stress and strain may not be constant throughout the loading history. For non-symmetrical stress controlled data, the maximum plastic strains may increase progressively due to progressive plastic deformation (ratcheting). In this condition, the maximum plastic strain may not achieve a stable state, and so that the identification of the $\varepsilon_{max} \cdot \Delta\sigma/2$ parameter is not apparent, and the $\sigma_{max} \cdot \Delta\varepsilon/2$ parameter happens to be more adequate as a reference. On the other hand, for non-symmetrical strain controlled elastoplastic conditions, the material experiences mean stress relaxation, with a relaxation rate depending on the amount of cyclic plasticity. In this case, the identification of the *SWT* parameter is not straightforward, since the maximum stress is not stable, and the $\varepsilon_{max} \cdot \Delta\sigma/2$ parameter becomes now the suitable one.

In general, the stress and strain amplitudes under cyclic elastoplastic conditions may be related using the cyclic *σ-ε* curve of the material, which may be expressed by the non-linear Ramberg-Osgood relation [7] as:

$$\frac{\Delta\varepsilon}{2} = \frac{\Delta\sigma}{2E} + \left(\frac{\Delta\sigma}{2K'}\right)^{1/n'} \tag{4.15}$$

Accordingly, for non-symmetrical stress-controlled elastoplastic conditions, the *SWT* damage parameter may be transformed into the following stress based-damage parameter:

$$\sigma_{max} \cdot \Delta\varepsilon/2 = \frac{\Delta\sigma}{1-R_\sigma}\left[\frac{\Delta\sigma}{2E} + \left(\frac{\Delta\sigma}{2K'}\right)^{1/n'}\right] \tag{4.16}$$

Using the previous stress-based damage parameter, one can describe the *S-N-*R_σ field of the material.

On its turn, for non-symmetrical strain-controlled elastoplastic conditions, the $\varepsilon_{max} \cdot \Delta\sigma/2$ damage parameter may be transformed into the following stress based-damage parameter:

$$\varepsilon_{max} \cdot \Delta\sigma/2 = \frac{\Delta\varepsilon}{1-R_\varepsilon} \cdot \frac{\Delta\sigma}{2} = \frac{\Delta\sigma}{1-R_\varepsilon}\left[\frac{\Delta\sigma}{2E} + \left(\frac{\Delta\sigma}{2K'}\right)^{1/n'}\right] \tag{4.17}$$

Equations (4.16) and (4.17) only differ in the stress and strain ratio parameters whereas these parameters coincide only for elastic conditions and fully-reversible elastoplastic conditions. Under other elastoplastic conditions, they differ from each other and does not exist a simple analytical relation between them.

Since the aforementioned damage parameters are coincident for elastic conditions they are both adequate to fit fatigue data in the high cycle region where elastic stresses are dominant. The shape of the cyclic *σ–ε* curve suggests the consideration of $\varepsilon_{\max} \cdot \Delta\sigma/2$ as the new parameter representing the driving force. Instead of being considered a simple opportunistic variant to the *SWT* parameter, it tries to take allowance of the markedly increasing values for ε_{max} compared to those of σ_{max}, when the elastic limit stress is exceeded, maintaining the energy character of any product of stress and strain in the search of a general fatigue parameter capable to reproduce elastic-plastic effects, just like does the *SWT* parameter.

Figure 4.6 represents again the experimental fatigue data obtained for the material of the Eiffel bridge, this time using $\varepsilon_{\max} \cdot \Delta\sigma/2$ as damage parameter. Since the fatigue data were derived from fatigue tests performed under strain controlled conditions with R_ε=-1, it is expected both parameter to be coincident and thus leading to the same representation. However, both strains and stresses were independently measured during tests, thus leading to small variations between the two damage parameters due to results scatter. In Figure 4.6 it was decided to fit the data using a simple power relation, since no explicit relation was found between the damage parameter $\varepsilon_{\max} \cdot \Delta\sigma/2$ and the number of cycles. Again, those experimental data will be correlated later in this chapter using the proposed generalized probabilistic model.

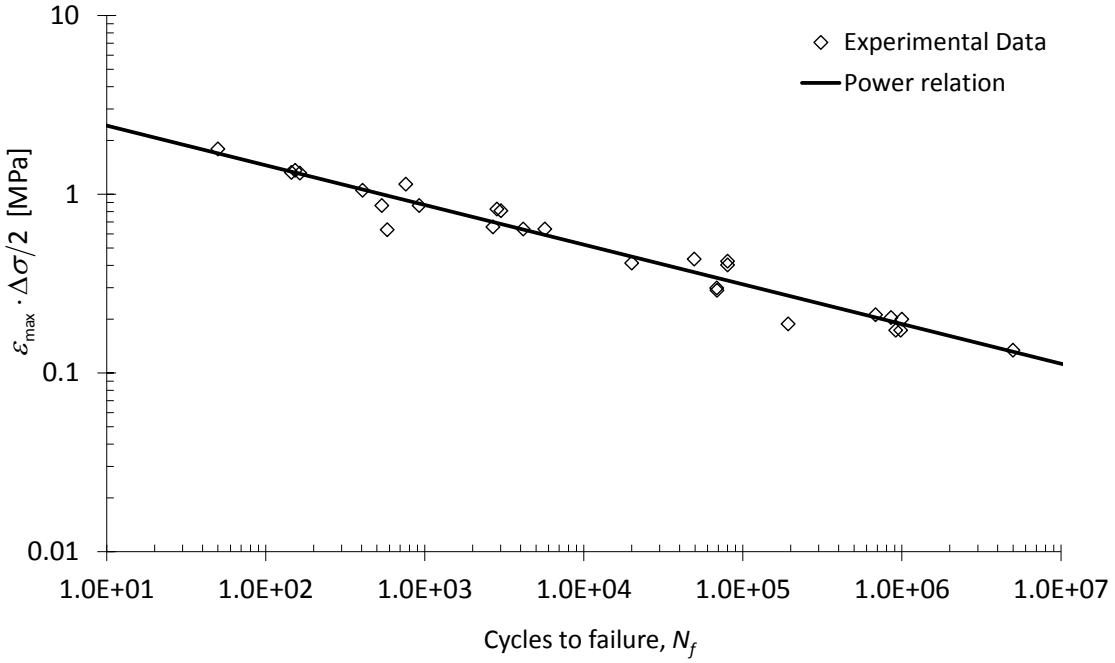

Figure 4.6 – Deterministic fitting of fatigue data for material available from Eiffel bridge (R_ε=-1) using the $\Delta\sigma \cdot \varepsilon_{max}$ damage parameter and power relation.

4.3.2. Energetic parameters for uniaxial fatigue loading conditions

In the previous section, two damage parameters were described, which may be considered energetic type damage parameters. However, some more formal energetic damage parameter formulations are found in the literature [3], which may be tested in the proposed generalization of the probabilistic model. These energetic damage formulations are developed for elastoplastic stress-strain conditions, using the strain energy associated to stress-strain hysteresis loops. Energy-based criteria can be classified into two categories depending upon which one of the following hypotheses is used:

- The total absorbed energy to fracture is constant and independent of the number of cycles to failure;

- The total absorbed energy to fracture depends on the number of cycles to failure.

Halford [8] observed for a wide variety of materials that the total absorbed energy at the moment of fracture was dependent on the numbers of cycles. Assuming the hypothesis of a total energy of fracture being dependent of the total number of cycles, the energy-life relationships can be presented under the generic deterministic form given by Equation

(4.5) or using the hyperbolic generalised probabilistic Weibull field given by Equation (4.7).

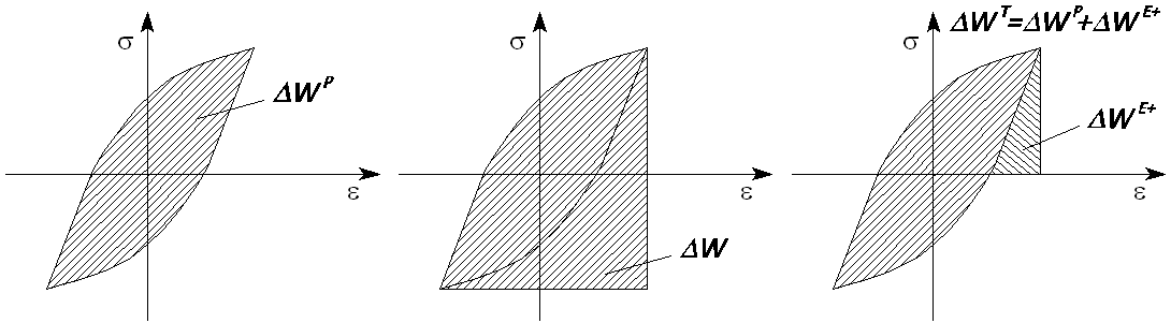

Figure 4.7 - Cyclic energetic parameters: a) plastic strain energy range; b) total strain energy range; c) modified total strain energy range taking into account the mean stress effects.

Different energetic parameters have been proposed, among which the plastic strain energy range, ΔW^P deserves to be stated as a reference magnitude. The plastic strain energy range, ΔW^P, associated to a load cycle, is given by the area of the stress-strain hysteresis loop (see Figure 4.7a)) and, for a Masing type material may be defined by the following relation:

$$\Delta W^p = \frac{1-n'}{1+n'}\Delta\sigma\Delta\varepsilon^P \tag{4.18}$$

where $\Delta\varepsilon^P$ is the plastic strain range, $\Delta\sigma$ is the stress range and n' is the cyclic strain-hardening exponent. For a non-Masing material, the Equation (4.18) may not be accurate. The procedure for calculating the plastic strain energy range for a non-Masing material is outlined in references [9,10], using the master curve concept, and is given by:

$$\Delta W^p = \frac{1-n^*}{1+n^*}\Delta\sigma\Delta\varepsilon^P + \frac{2n^*}{1+n^*}\delta\sigma_0\Delta\varepsilon^P \tag{4.19}$$

where $\delta\sigma_0$ is the increase of the proportional limit stress.

Using the plastic strain energy range, ΔW^P, as a damage energetic parameter, Equation (4.5) can be rewritten as follows:

$$\Delta W^P = \kappa_P\left(2N_f\right)^{\alpha_P} + \Delta W_0^P \tag{4.20}$$

where α_P<0 and κ_P>0 are constants and ΔW_0^P is the plastic strain energy range corresponding to the fatigue limit. For most materials the plastic strain energy range at the fatigue limit, ΔW_0^P, is very small and, therefore, can be neglected. Equation (4.20) is more adequate to describe the behaviour for the low-cycle fatigue region.

Ellyin and Kujawski [11] suggested the use of the total strain energy range per reversal, ΔW, which includes both the elastic and plastic strain energy components (see Figure 4.7b)), to unify the description of the low- and high-cycle fatigue behaviours. The strain energy range per reversal, i.e. the area of Figure 4.7 b), can be written as:

$$\Delta W = \tfrac{1}{2}\Delta W^P + \tfrac{1}{2}\Delta\sigma\Delta\varepsilon \tag{4.21}$$

where ΔW^p is the hysteresis energy given by Equation (4.18). Substituting ΔW in Equation (4.5), the fatigue failure criterion in terms of the total strain energy range for low- and high-cycle fatigue is given by the following expression:

$$\Delta W = \kappa\left(2N_f\right)^{\alpha} + \Delta W_0 \tag{4.22}$$

where α<0 and κ>0 are constants of materials and ΔW_0 is the plastic strain energy range corresponding to the fatigue limit, which is defined by the following equation:

$$\Delta W_0 = \left(\Delta W_0^P + \frac{\Delta\sigma_f^2}{2E}\right) \approx \frac{\Delta\sigma_f^2}{2E} \tag{4.23}$$

where $\Delta\sigma_f$ is the stress range fatigue limit. The energy-life relations defined by Equations (4.20) and (4.22) have certain limitations regarding their range of applicability because they are not sensitive to the mean stress. Thus, these relationships are generally adequate to describe the fatigue behaviour for alternating or almost alternating loads (R_σ≈-1). Golos and Ellyin [12,13] suggested an alternative energetic parameter sensitive to the mean stress. These authors proposed another version of the total strain energy range, ΔW^t, resulting from the superposition of the plastic strain energy range, ΔW^P, with the elastic strain energy range associated with the tensile stress, ΔW^{E+} (see Figure 4.7c)):

$$\Delta W^t = \Delta W^P + \Delta W^{E+} \tag{4.24}$$

The plastic strain energy range, ΔW^P, is defined by Equation (4.18) whereas the elastic strain energy range associated with the tensile stress, ΔW^{E+} is determined by:

$$\Delta W^{E+} = \frac{1}{2E}\left(\frac{\Delta\sigma}{2}+\sigma_m\right)^2 = \frac{\sigma_{\max}^2}{2E} \quad for\ \sigma_{\min} \le 0 \tag{4.25}$$

Substituting ΔW^t in Equation (4.5) results in the following energy-life relation, sensitive to the mean stress:

$$\Delta W^t = \kappa_t \left(2N_f\right)^{\alpha_t} + \Delta W_0^t \tag{4.26}$$

where α_t<0 and κ_t>0 are constants and ΔW_0^t is the total strain energy range, ΔW^t, corresponding to fatigue limit, defined by the following expression:

$$\Delta W_0^t \approx \frac{\sigma_{\max}^2}{2E} \quad for\ \sigma_{\min} \le 0 \tag{4.27}$$

Figure 4.8 plots the fatigue data obtained for the material from Eiffel bridge using the relation given by Equation (4.26). A high determination coefficient was achieved for the resulting fitting using Equation (4.26). Inspired in Morrow relation, it is also possible to use a superposition of two power relations to correlate the ΔW^t according to:

$$\Delta W^t = \Delta W^P + \Delta W^{E+} = \kappa_p \left(2N_f\right)^{\alpha P} + \kappa_E \left(2N_f\right)^{\alpha E} \tag{4.28}$$

Figure 4.9 represents the previous equation for the material from the Eiffel bridge. Lower determination coefficients were observed in this regression analysis, but global fitting is still very satisfactory. In a later Section the performance of the proposed generalized probabilistic fatigue model will be assessed using this particular damage parameter.

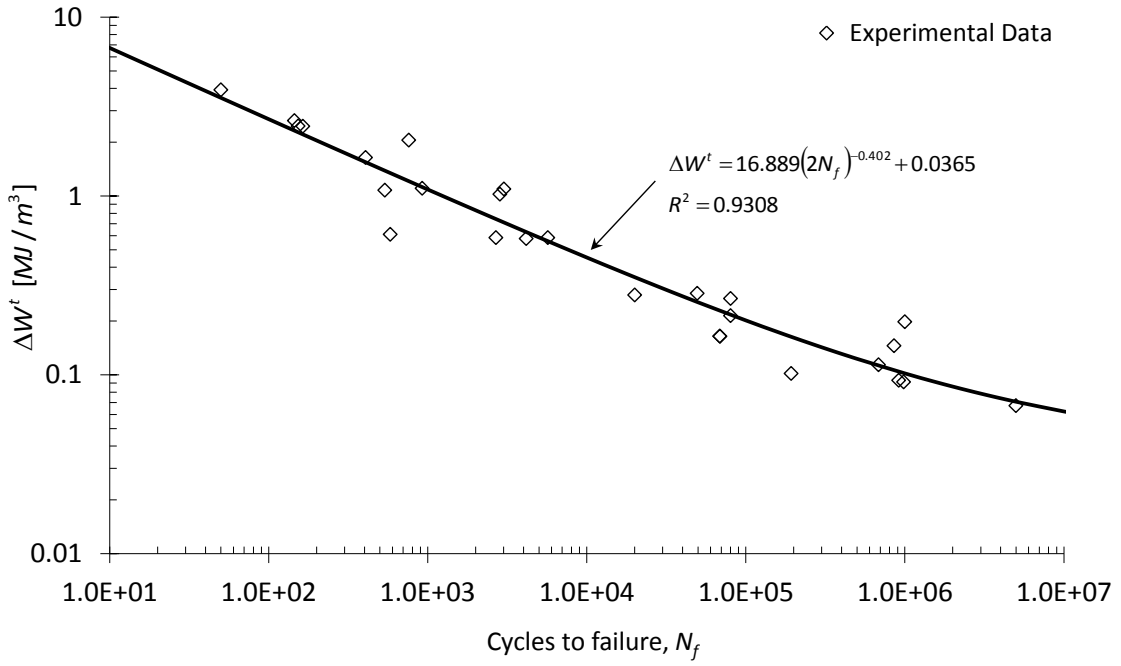

Figure 4.8 – Fitting of fatigue data for material available from Eiffel bridge (R_ε=-1) using the energetic damage parameter, ΔW^t, and a power relation.

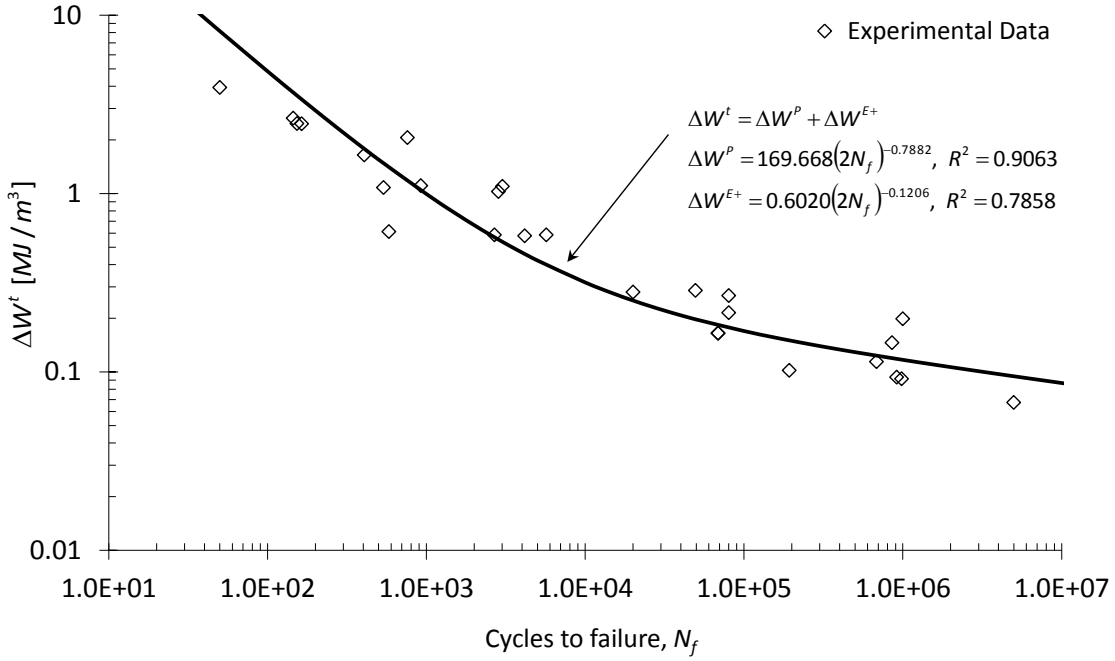

Figure 4.9 – Fitting of fatigue data for material available from Eiffel bridge (R_ε=-1) using the energetic damage parameter, ΔW^t, and a superposition of two power functions.

4.3.3. Fatigue damage parameters for multiaxial loading conditions

The proposed generalization of the probabilistic Weibull model of Castillo and Fernández-Canteli could represent also an important advantage to correlate multiaxial fatigue data. This model could be a valuable probabilistic tool to account for the scatter of multiaxial fatigue results. There are a number of multiaxial damage parameters being proposed in the literature covering low-cycle fatigue, high-cycle fatigue, proportional and non-proportional loading conditions [3,14]. Many of these damage parameters are approximately correlated with the number of cycles to failure, by means of a power relation with the general form illustrated in Figure 4.3. Depending on the fatigue regime, a trend to a horizontal asymptote representing the damage threshold could also be noticeable. This type of representation could be properly approximated by a subdomain of a hyperbolic function as given by the proposed probabilistic model. In the next subsections, some multiaxial damage parameters are presented that will illustrate a proper generalization of the Weibull field to correlate multiaxial fatigue. It is not the aim of this thesis to describe all possible damage parameters for multiaxial fatigue but instead to present some representative ones, for which experimental data has been found in the literature.

4.3.3.1. Energetic damage parameters

Energetic approaches constitute an important means to derive multiaxial fatigue models. Ellyin [3] proposed a model based on the energy density associated to each cycle, ΔW^t, which is composed by two parts: plastic strain energy, ΔW^P, and the positive elastic strain energy, ΔW^{E+}. These two quantities were illustrated in Figure 4.7 for uniaxial loading conditions. The ΔW^{E+} term allows the inclusion of mean stress effects into the energy-based criterion. In the case of proportional or biaxial non-proportional loading, the total energy density associated to a cycle may be computed as:

$$\Delta W^t = \Delta W^P + \Delta W^{E+} = \int_t^{t+T} \sigma_{ij} d\varepsilon_{ij}^P + \int_t^{t+T} H(\sigma_i) H\left(d\varepsilon_i^e\right) \sigma_i d\varepsilon_i^e \tag{4.29}$$

where σ_{ij} and ε_{ij}^{P} are the stress and plastic strain tensors, σ_i and ε_i^e are the principal stresses and the principal elastic strains, T is the period of one cycle and $H(x)$ is the Heaviside function ($H(x)=1$ for $x\geq 0$ and $H(x)=0$ for $x<0$).

The fatigue failure criterion is defined according to the following expression:

$$\psi = \Delta W^t = \frac{\Delta W^P}{\bar{\rho}} + \Delta W^{E+} = \kappa\left(2N_f\right)^{\alpha} + C \tag{4.30}$$

where κ, α and C are material parameters to be determined from appropriate tests and $2N_f$ is the number of reversals to failure. The multiaxial constraint ratio, $\bar{\rho}$, can be determined using the following expression:

$$\bar{\rho} = \left(1+\bar{\nu}\right)\frac{\hat{\varepsilon}_{\max}}{\hat{\gamma}_{\max}} \tag{4.31}$$

with

$$\hat{\varepsilon}_{\max} = \max\left[\varepsilon_a, \varepsilon_t\right] \tag{4.32}$$

$$\hat{\gamma}_{\max} = \max\left[\left|\varepsilon_a - \varepsilon_r\right|, \left|\varepsilon_t - \varepsilon_r\right|\right] \tag{4.33}$$

where $\bar{\nu}$ is an effective Poisson's ratio calculated from:

$$\bar{\nu} = \frac{\nu_p\left(1-\nu_e\right)\left(\varepsilon_a+\varepsilon_t\right)+\left(\nu_e-\nu_p\right)\left(\varepsilon_a^e+\varepsilon_t^e\right)}{\left(1-\nu_e\right)\left(\varepsilon_a+\varepsilon_t\right)+\left(\nu_e-\nu_p\right)\left(\varepsilon_a^e+\varepsilon_t^e\right)};\ \ \varepsilon_a \neq -\varepsilon_t \tag{4.34}$$

where ε_a and ε_t are principal in-plane strain (axial and transversal) parallel to the free surface, and ε_r is the radial strain (perpendicular to the free surface), given by the following expression:

$$\varepsilon_r = \frac{-\bar{\nu}}{\left(1-\bar{\nu}\right)}\left(\varepsilon_a+\varepsilon_t\right) \tag{4.35}$$

The multiaxial constraint ratio, $\bar{\rho}$, defined by Equation (4.21), demonstrates the importance of the orientation of the free surface with respect to the imposed principal strains, and has an important physical interpretation regarding the fatigue damage process:

$$\begin{aligned} &\textit{Torsion}: \ \varepsilon_a = -\varepsilon_t \ ; \ \overline{\rho} = 1 + \overline{\nu} \\ &\textit{Uniaxial}: \ \varepsilon_t = \varepsilon_r = -\overline{\nu}\varepsilon_a \ ; \ \overline{\rho} = 1 \\ &\textit{Equi-biaxial}: \ \varepsilon_a = \varepsilon_t \ ; \ \overline{\rho} = 1 - \overline{\nu} \end{aligned} \tag{4.36}$$

Figure 4.10 represents a correlation between the energetic multiaxial fatigue parameter proposed by Ellyin [3] (see Equation 4.29) and the number of cycles obtained for proportional multiaxial fatigue data covering several multiaxial constraint factors, for the ASTM A-516 Gr. 70 steel. The plotted line was fitted to uniaxial tensile data. The good agreement of the multiaxial fatigue data to this line shows the suitability of the proposed multiaxial damage parameter.

The application of the energetic parameter proposed by Ellyin to non-proportional loading requires a modification in the multiaxial constraint factor, $\overline{\rho}$ [3]. The multiaxial constraint factor proposed for multiaxial loading does not work conveniently for non-proportional loading since it is not constant during the cycle. The following alternative form was proposed for non-proportional loading:

$$\overline{\rho} = (1 + \overline{\nu}) \left(\frac{\hat{\varepsilon}(t)}{\hat{\gamma}(t)} \right)_{\hat{\gamma} = \hat{\gamma}_{\max}} \tag{4.37}$$

This means that the $\overline{\rho}$ parameter is evaluated using a ratio $\hat{\varepsilon}/\hat{\gamma}$ taken at the instant when the shear strain in the direction 45° to the surface reaches its maximum value. Figure 4.11 represents a correlation between the energetic multiaxial fatigue parameter proposed for proportional and non-proportional multiaxial fatigue data, where ϕ represents the phase angle between ε_a and ε_t, obtained for ASTM A516 Gr. 70 steel. The proportional fatigue data is the same as Figure 4.10.

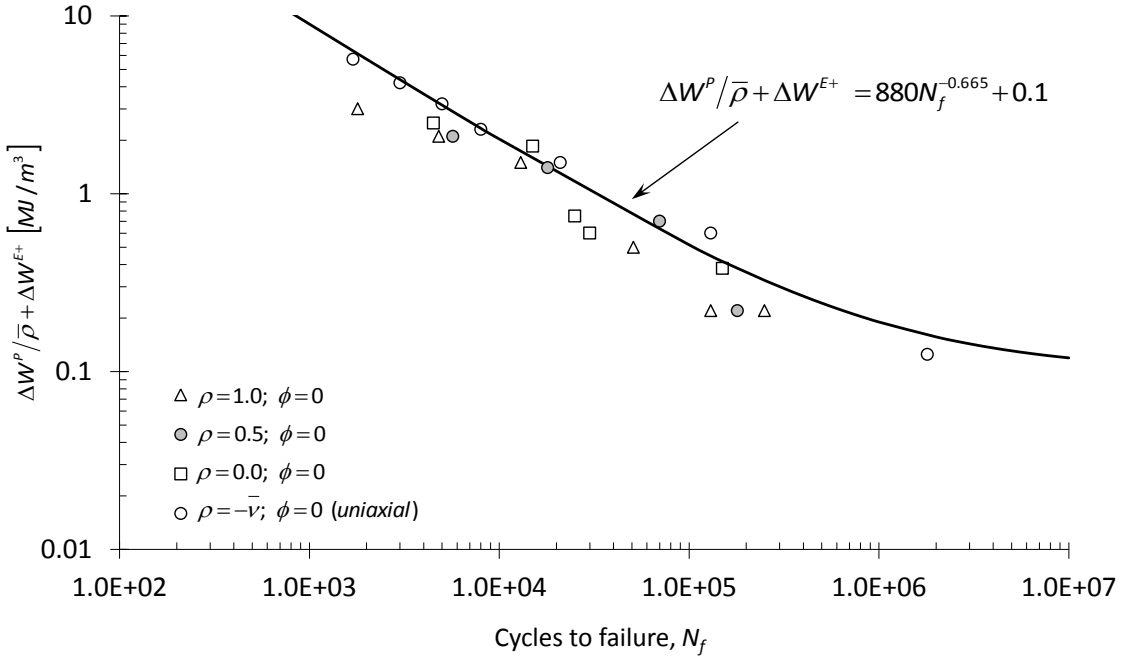

Figure 4.10 – Fitting of multiaxial proportional data to lifetime using the energetic parameter by Ellyin [3].

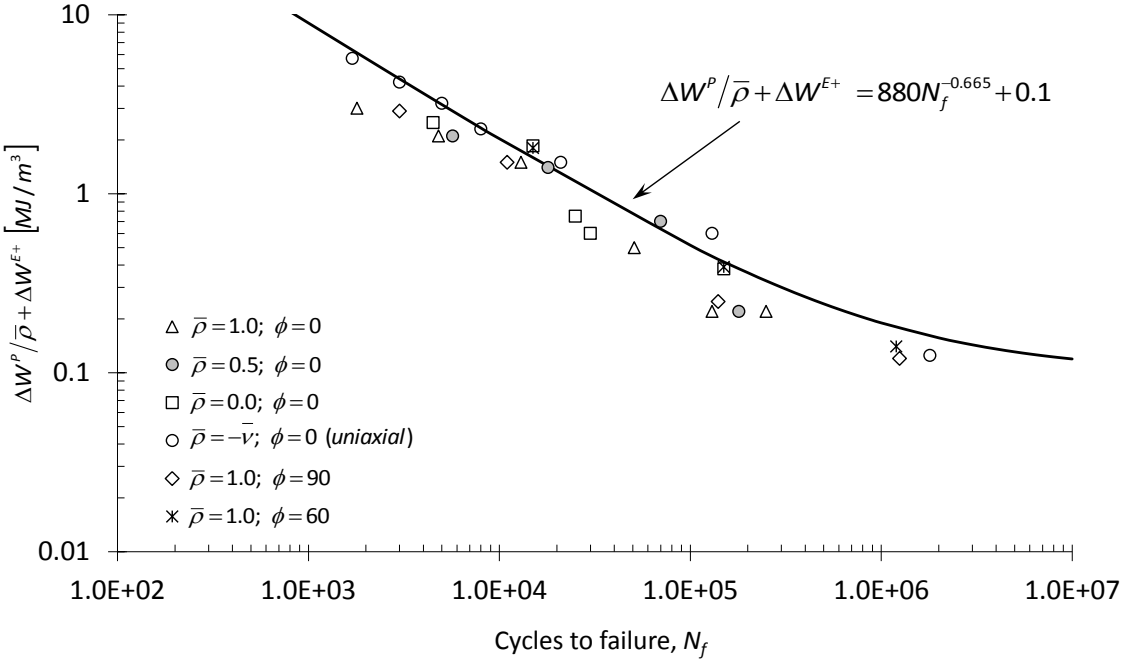

Figure 4.11 – Correlation between multiaxial proportional and non-proportional data using the energetic parameter by Ellyin [3].

4.3.3.2. Critical plane based damage parameters

Another group of damage parameters for multiaxial fatigue is represented by the critical plane based damage parameters, among which those of Fatemi and Socie [15] and Fatemi and Kurath [16], improved by Jiang *et al.* [17] are presented in this Section. Fatemi and

Socie [15] and Fatemi and Kurath [16] proposed a shear-strain based multiaxial fatigue criterion that can be expressed by the following mathematical form:

$$FP = \frac{\Delta\gamma}{2}\left(1 + K\frac{\sigma_{n,\max}}{\sigma_y}\right) \tag{4.38}$$

where FP is the fatigue parameter, $\Delta\gamma/2$ is the shear strain amplitude, $\sigma_{n,\max}$ is the maximum normal stress on the critical plane, σ_y is the yield stress of the material and K is a material constant. The original fatigue criterion proposed by Fatemi and Socie [15] and Fatemi and Kurath [16] defined the critical plane as the plane associated with the maximum shear strain amplitude. However Jiang *et al.* [17] defined the critical plane as the material plane where the fatigue parameter (FP) expressed by Eq. (4.38) reaches a maximum. Using data available from tubular specimens made of S460 steel tested under pure tension-compression and pure torsion Jiang *et al.* [17] were able to identify the K constant and to correlate the fatigue parameter with the number of cycles to failure using a power relation. Figure 4.12 illustrates such correlation, which was obtained by a trial and error procedure for parameters estimation ($K = 0.98, \sigma_y = 500MPa$). The resulting power relation has the following form:

$$\begin{cases} \left(FP - 0.00225\right)^{0.2} N_f = 0.20 \\ FP = \dfrac{\Delta\gamma}{2}\left(1 + 0.98\dfrac{\sigma_{n,\max}}{500}\right) \end{cases} \tag{4.39}$$

Jiang *et al.* [17] demonstrated the suitability of relation (4.39) to predict multiaxial proportional and non-proportional multiaxial loading paths.

The analysis of Figure 4.12 reveals that the referred fatigue parameter is a good candidate to be correlated with the number of cycles to failure using the Weibull probabilistic model.

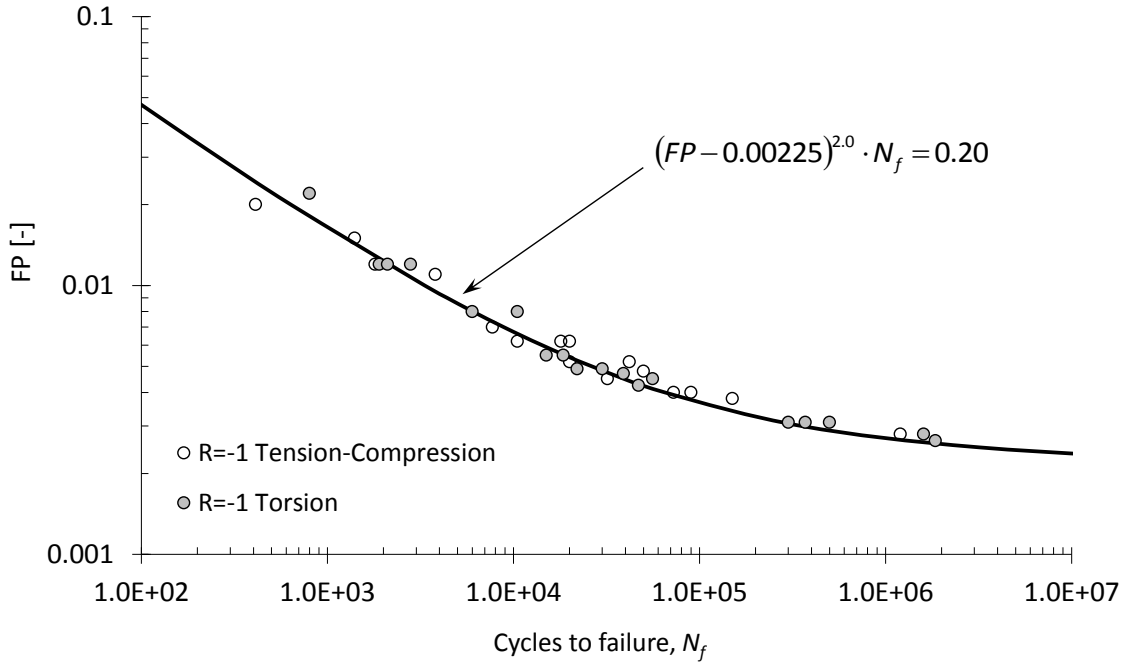

Figure 4.12 – Fitting of multiaxial proportional data to lifetime using a critical plane parameter [17].

4.4. APPLICATION OF THE PROBABILISTIC FATIGUE DAMAGE MODEL TO DIFFERENT FATIGUE DAMAGE PARAMETERS

In this section the probabilistic fatigue model originally proposed by Castillo and Fernández-Canteli [1] will be applied to a diversity of fatigue damage models selected and described in the previous section. The aim of this section is to demonstrate the suitability of the probabilistic model to correlate distinct types of fatigue parameters with lifetime, covering uniaxial and multiaxial fatigue loading.

The parameters of the probabilistic ψ–N fields (B,C, β, λ, δ) are estimated using the procedures proposed by Castillo and Fernández-Canteli [1], namely the constrained least square method (B,C) and the maximum likelihood method (β, λ, δ) (see chapter II for more details).

The quality of the fitted model is assessed through P-P plots, where the resulting goodness of fit of the 45° line gives a measure of the difference between the test data set (sample) and the theoretical proposed field.

For each damage parameter, the respective probabilistic field is presented using the percentile curves corresponding to probability of failures of 1%, 5%, 50%, 95% and 99%. In addition to these percentile curves, the deterministic fitting curves given in the previous Section are included for comparison purposes with the 50% percentile curve.

4.4.1. Smith-Watson-Topper damage parameter and counterpart parameter for uniaxial loading conditions

Figures 4.13 and 4.14 illustrate the probabilistic fields correlating, respectively, the $\sigma_{max} \cdot \Delta\varepsilon/2$ and $\varepsilon_{max} \cdot \Delta\sigma/2$ parameters with the number of cycles to failure, using the experimental data obtained from the Eiffel bridge material. Figures 4.15 and 4.16 illustrate the goodness of the fittings using P-P plots. In general, the correlation of the experimental data using the probabilistic field is satisfactory. The comparison between the 50% percentile curve and the deterministic lines referred in Section 4.2 show the major deviations for the extrapolation in the very-low cycle fatigue region. Nevertheless, concerning the $\varepsilon_{max} \cdot \Delta\sigma/2$ parameter, a very good agreement between the regression line and the 50% percentile is observed. For the $\sigma_{max} \cdot \Delta\varepsilon/2$ parameter, the main deviation between the 50% percentile and the deterministic fitted line occurs for an extrapolated domain, where no experimental data is found. Therefore, a comparison in this region should be not overvalued.

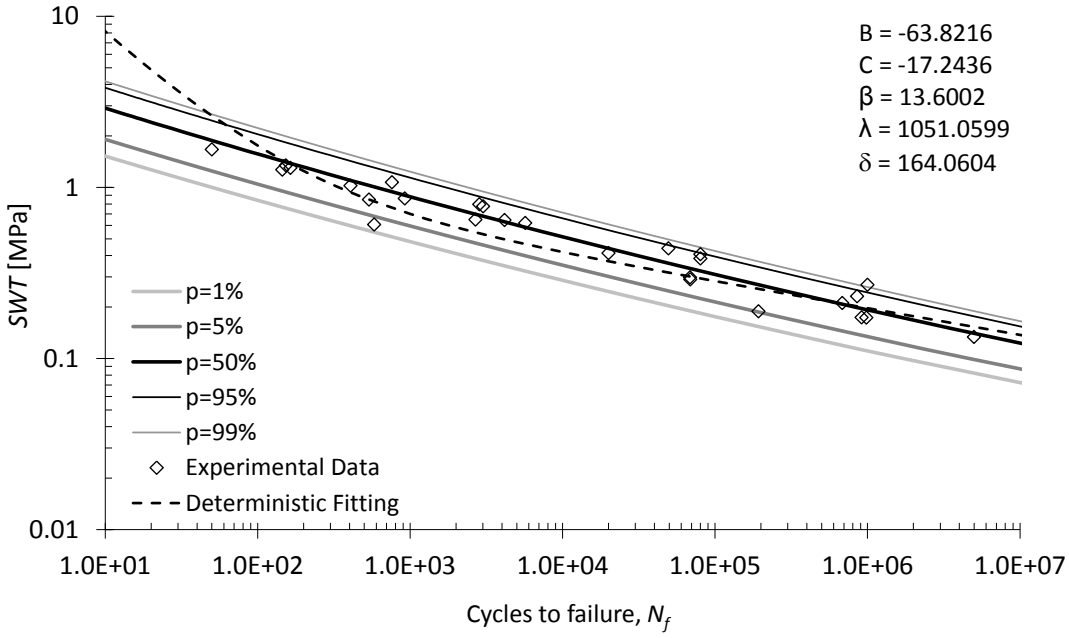

Figure 4.13 – *p-SWT-N* field for the puddle iron from the Eiffel bridge.

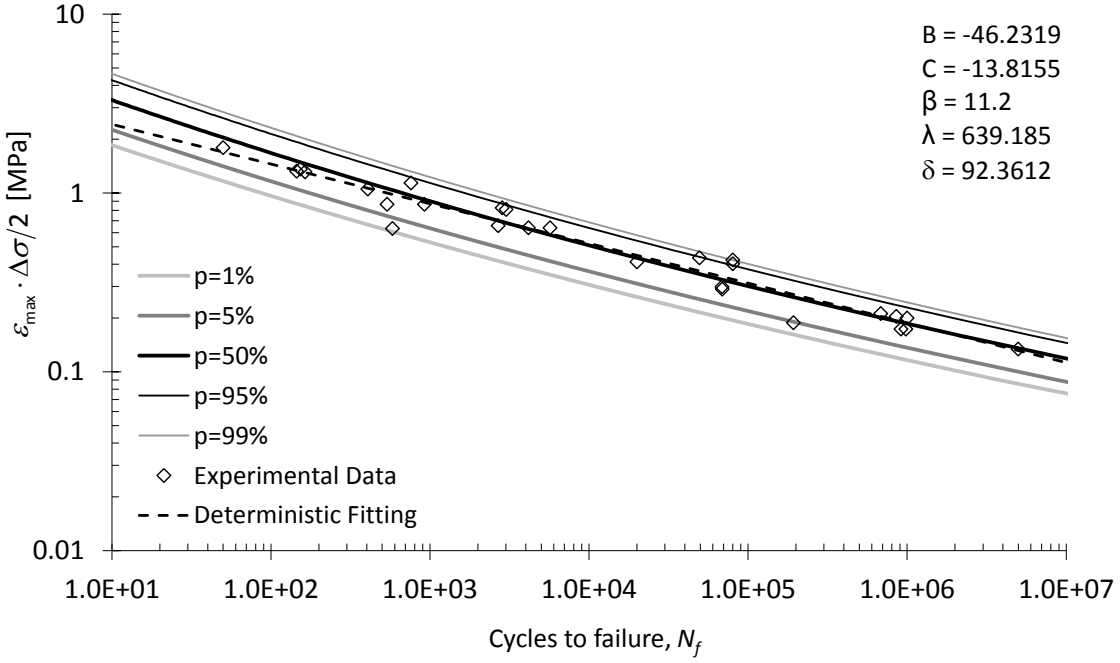

Figure 4.14 – p-$\varepsilon_{max}.\Delta\sigma/2$-$N$ field for the puddle iron from the Eiffel bridge.

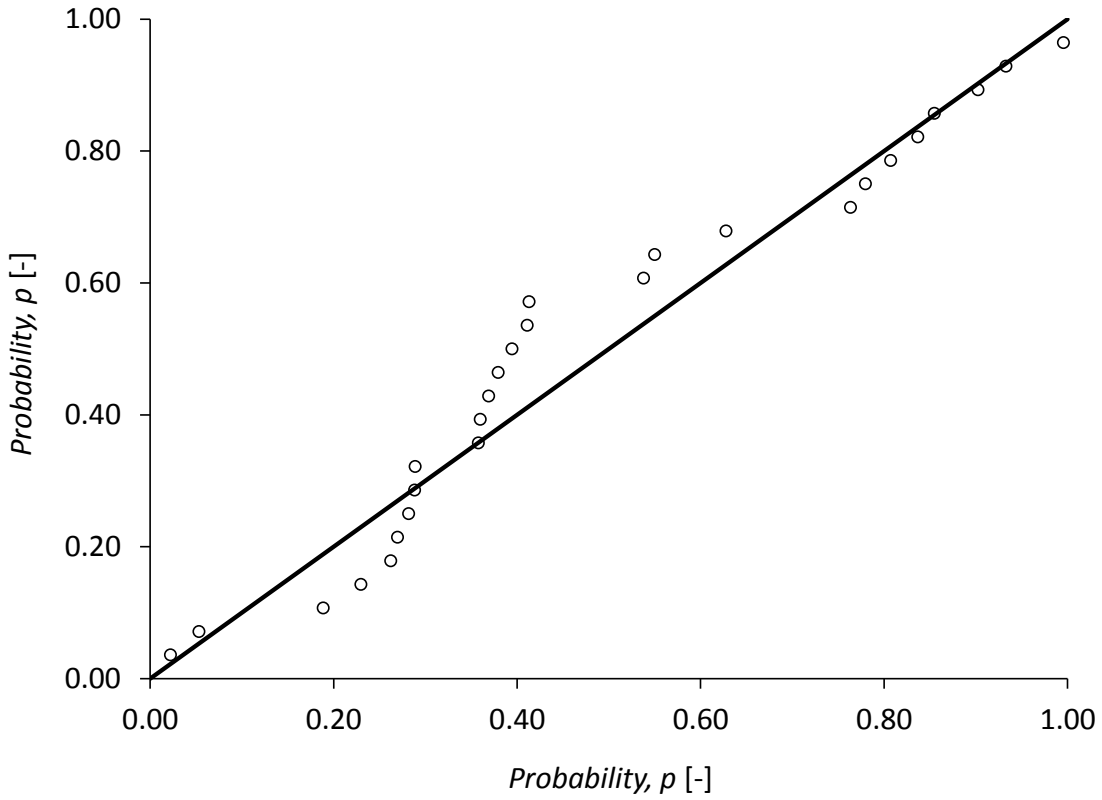

Figure 4.15 – P-P plot showing the quality of the fitted probabilistic fatigue model based on the *SWT* parameter, proposed for the material from Eiffel bridge.

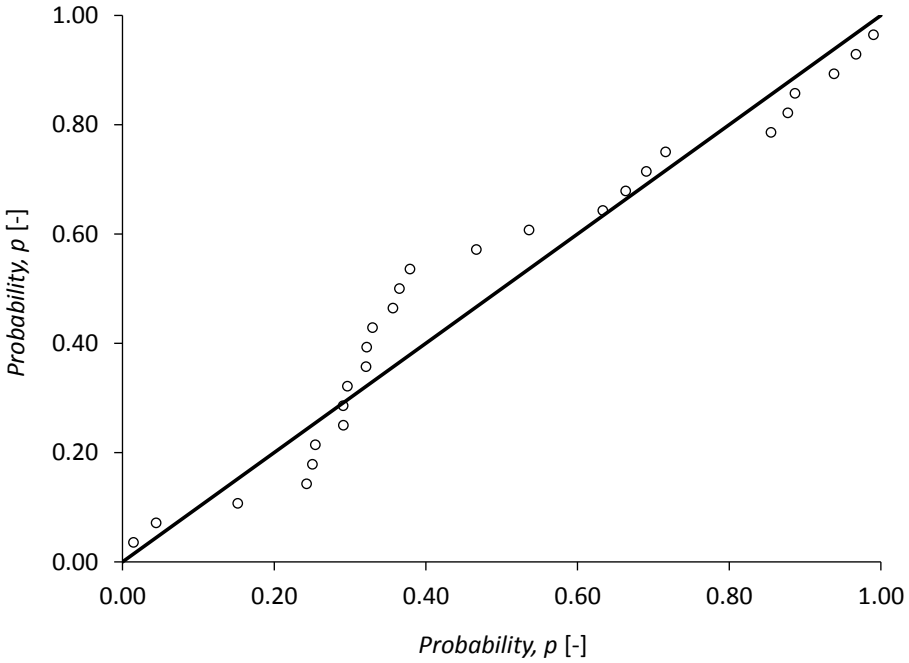

Figure 4.16 – P-P plot showing the quality of the fitted probabilistic fatigue model based on the $\varepsilon_{max}.\Delta\sigma/2$ parameter, proposed for the material from Eiffel bridge.

4.4.2. Energetic parameters for uniaxial loading conditions

Figure 4.17 shows the probabilistic field correlating the ΔW^t energetic fatigue damage parameter with the number of cycles to failure, using the experimental data obtained for the Eiffel bridge material. The P-P plot shown in Figure 4.18 illustrates the good fitting given by the proposed probabilistic field. The comparison between the 50% percentile curve and the two deterministic lines referred in Section 4.2 for this data show better agreement for the deterministic combined power relation. The original deterministic relation proposed by Ellyin [3] underestimates the fatigue lives in the medium region and overestimates fatigue lives for the low and high cycle regimes. It is interesting to note that the 50% percentile curve fits in between the two deterministic lines for very-low cycle fatigue. For very high cycle fatigue the 50% percentile curve falls below the two deterministic fitted lines, apparently suggesting a lower fatigue limit. However, this probabilistic model is able to correlate this fatigue limit region if adequate data is available for this region, including run-outs. In addition the probabilistic model gives the complete probabilistic field and one can realize that all experimental data fall inside the 98% failure probability. Only one data points falls outside this band, giving a high indication of the accuracy of the probabilistic model.

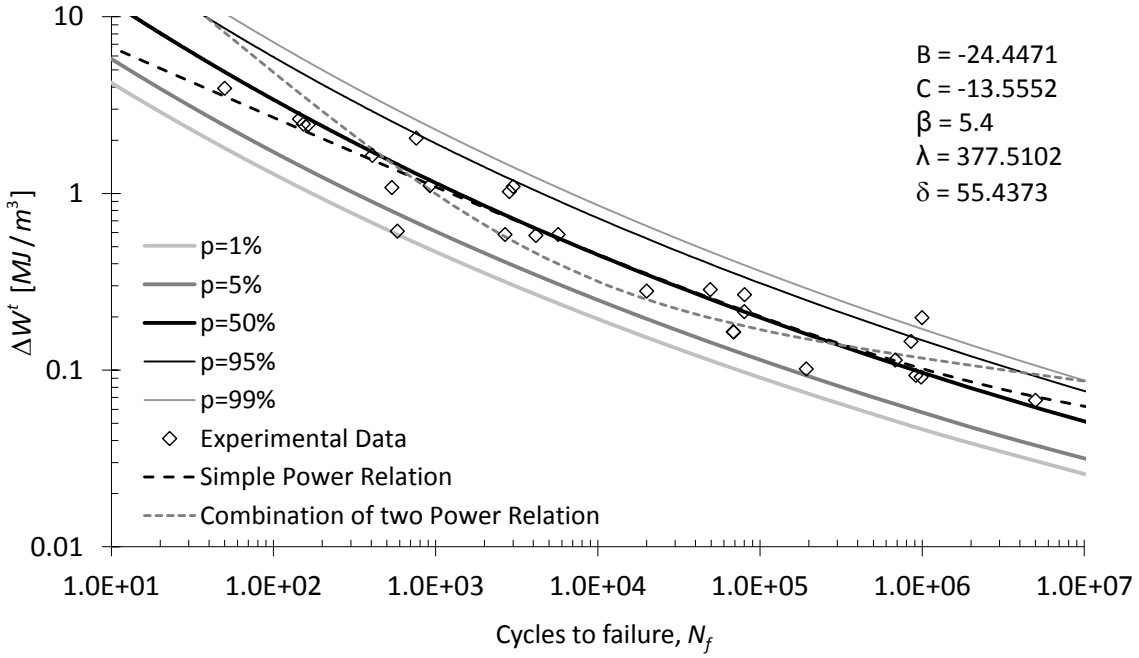

Figure 4.17 – p-ΔW^t -N field for the puddle iron from the Eiffel bridge.

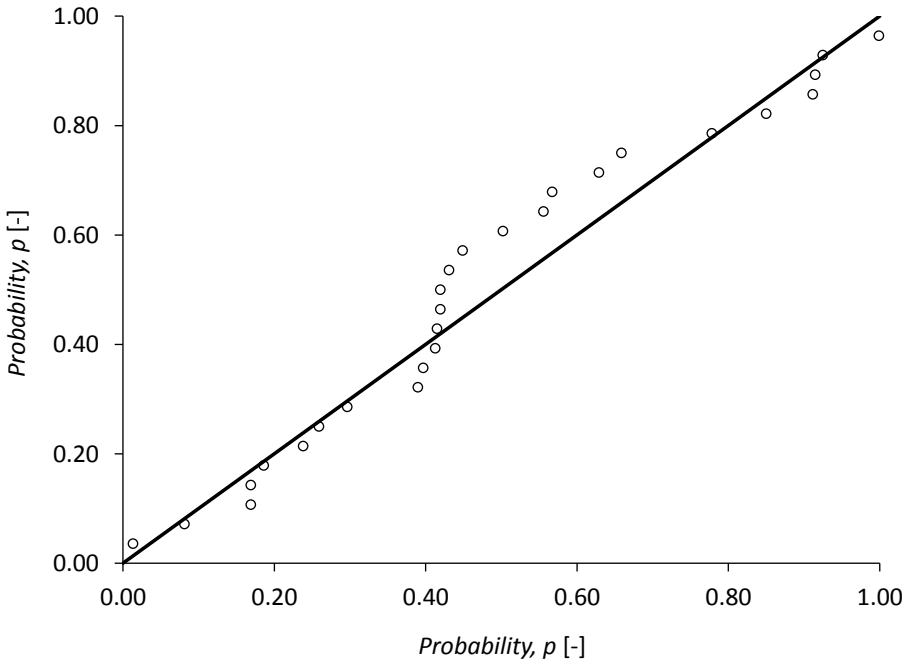

Figure 4.18 – P-P plot showing the quality of the fitted probabilistic fatigue model based on the ΔW^t parameter, proposed for the material from Eiffel bridge.

4.4.3. Energetic fatigue damage parameters for multiaxial loading conditions

Figures 4.19 and 4.20 represent the probabilistic fields correlating the $\Delta W^P / \overline{\rho} + \Delta W^{E+}$ energetic fatigue damage parameter and the number of cycles to failure, using the

multiaxial experimental data available from the ASTM A516 Gr. 70. According to the respective P-P plots, shown in Figures 4.21 and 4.22, an excellent fitting of the experimental data was obtained using the proposed probabilistic field. The comparison between the 50% percentile curve and the deterministic lines referred in Section 4.2 for this data show some agreement below $1x10^6$ cycles. However, a major deviation is observed above this fatigue life, with the 50% percentile curve falling below the deterministic line. In the identification process of the probabilistic field, no run-outs were assumed, so that the model was not able to define this domain. Apparently, the deterministic regression line is suggesting a fatigue limit plateau no supported by the experimental data since the available experimental data for lives above $1x10^6$ cycles are not highlighted as run-outs.

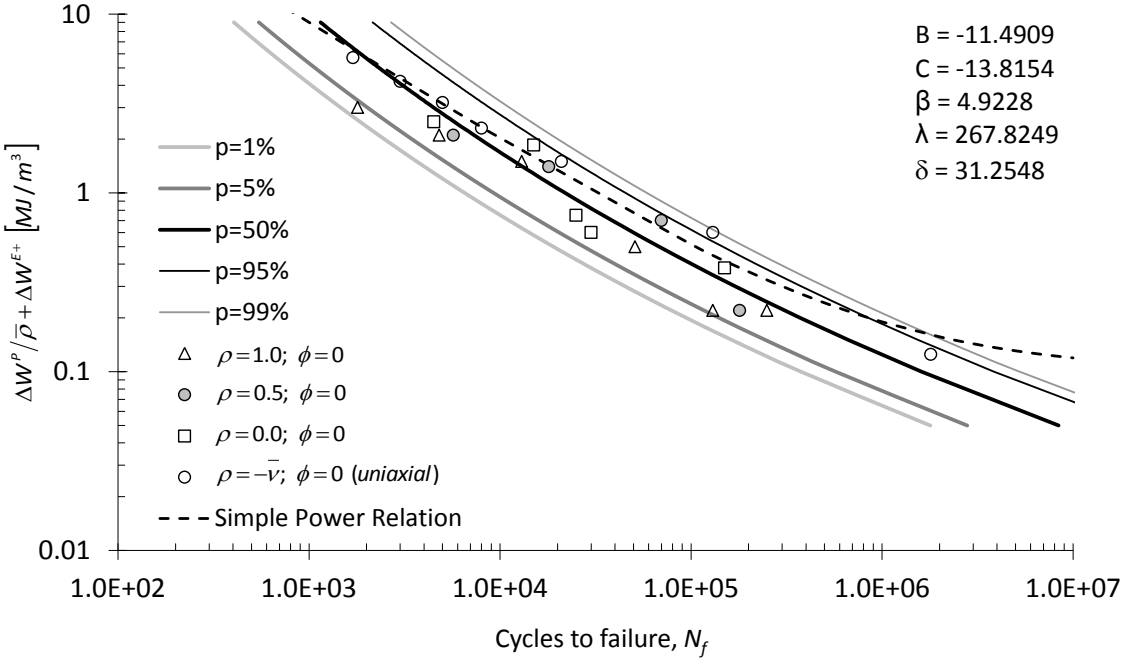

Figure 4.19 – *p*- $\Delta W^P/\overline{\rho}+\Delta W^{E+}$ -*N* field proposed for the A516 Gr. 70.

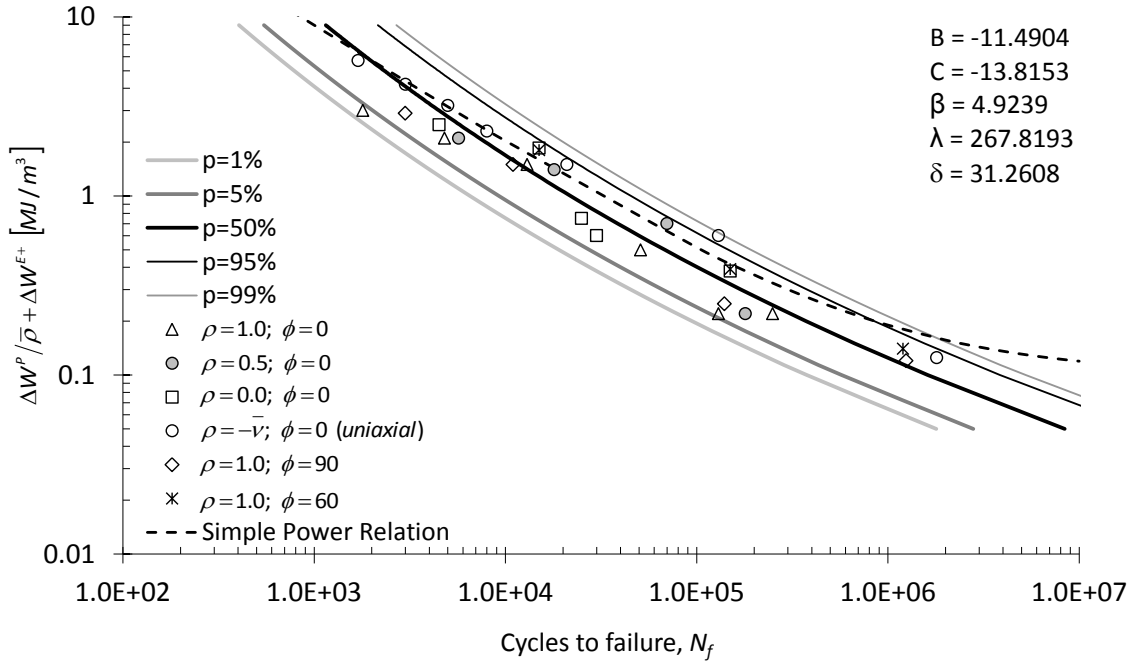

Figure 4.20 – *p*- $\Delta W^P/\overline{\rho}+\Delta W^{E+}$ -*N* field proposed for the A516 Gr. 70 (including non-proportional loading data).

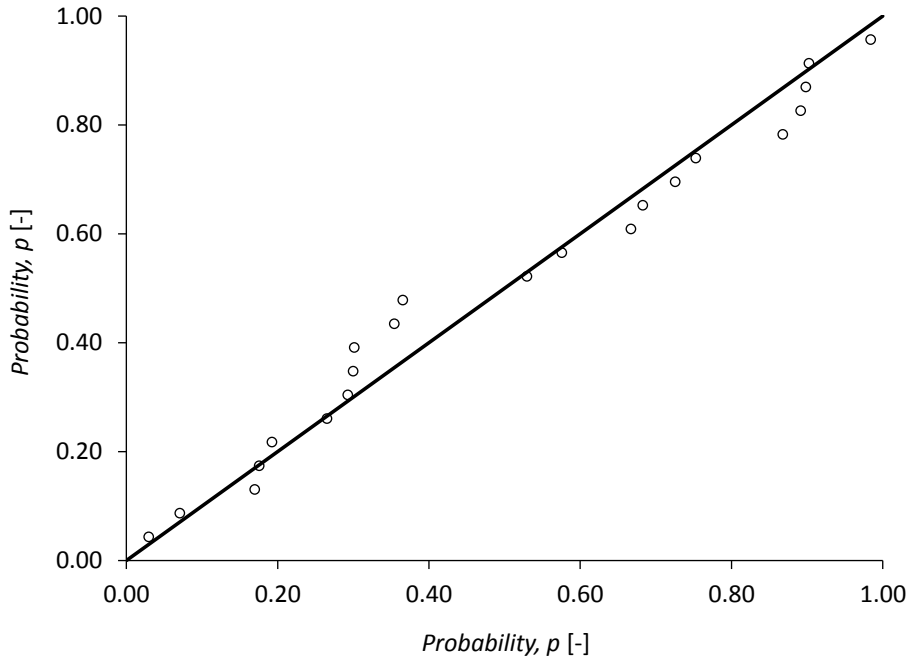

Figure 4.21 – P-P plot showing the quality of the fitted probabilistic fatigue model based on the $\Delta W^P/\overline{\rho}+\Delta W^{E+}$ parameter, proposed for the A516 Gr. 70.

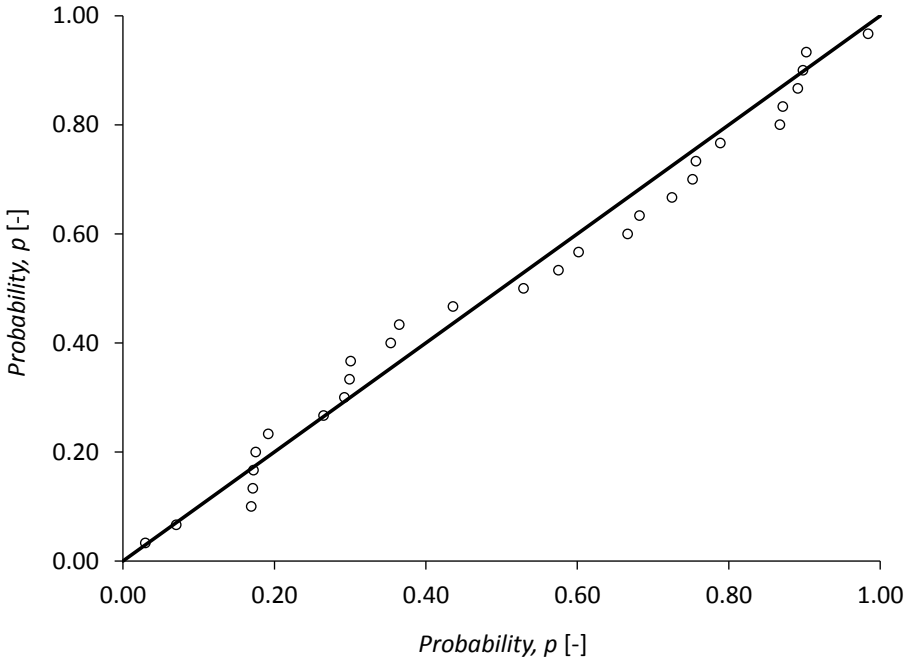

Figure 4.22 – P-P plot showing the quality of the fitted probabilistic fatigue model based on the $\Delta W^P / \overline{\rho} + \Delta W^{E+}$ parameter, proposed for the A516 Gr. 70 (including non-proportional loafing data).

4.4.4. Critical plane based fatigue damage parameter for multiaxial loading conditions

Figure 4.23 represents the probabilistic field correlating the critical plane fatigue parameter proposed by Fatemi *et al.* [15,16] for multiaxial fatigue and the number of cycles to failure obtained for the S460N structural steel grade. Despite the global satisfactory agreement between the probabilistic field and the experimental fatigue data, the respective P-P plots, shown in Figure 4.24, points out some deviation for low probabilities of failure. This is mainly justified by a very narrow scatter band of the experimental data with one exception point corresponding to the lowest fatigue life. The experimental data fitting below the 50% percentile is very close to this line with the referred data point. Censoring the lowest lifetime data point, the probabilistic field of Figure 4.25 is obtained for which the P-P plot (see Figure 4.26) becomes very satisfactory. The comparison between the 50% percentile line and the deterministic simple power relation only shows significant deviation for lives below $1x10^3$ cycles that would be even more amplified if eventual extrapolations should be performed for lower fatigue lives. It is important to note that due to the asymptotic behaviour of the probabilistic field for very

low number of cycles to failure, its use for extrapolations in this fatigue regime should be performed with care.

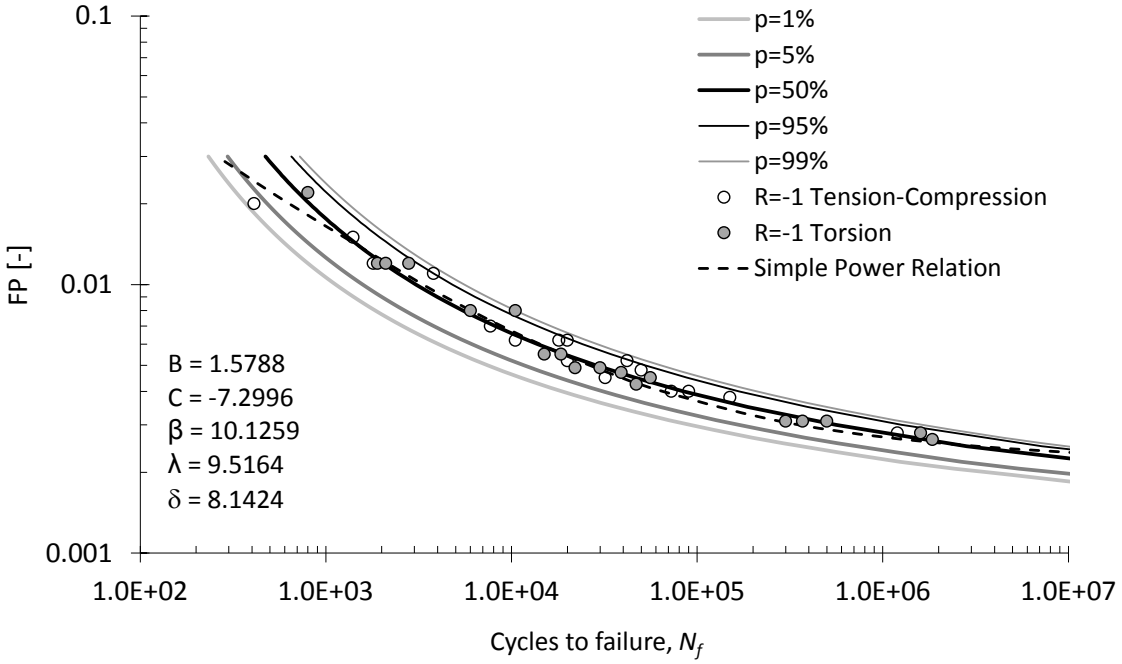

Figure 4.23 – *p-FP-N* field proposed for the S460N.

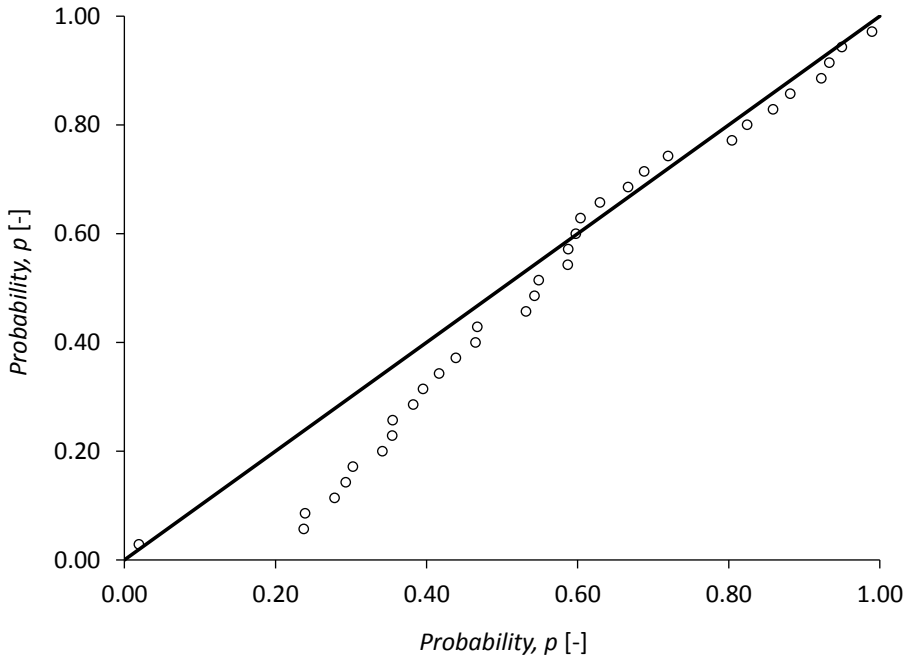

Figure 4.24 – P-P plot showing the quality of the fitted probabilistic fatigue model based on the *FP* parameter, proposed for the S460N.

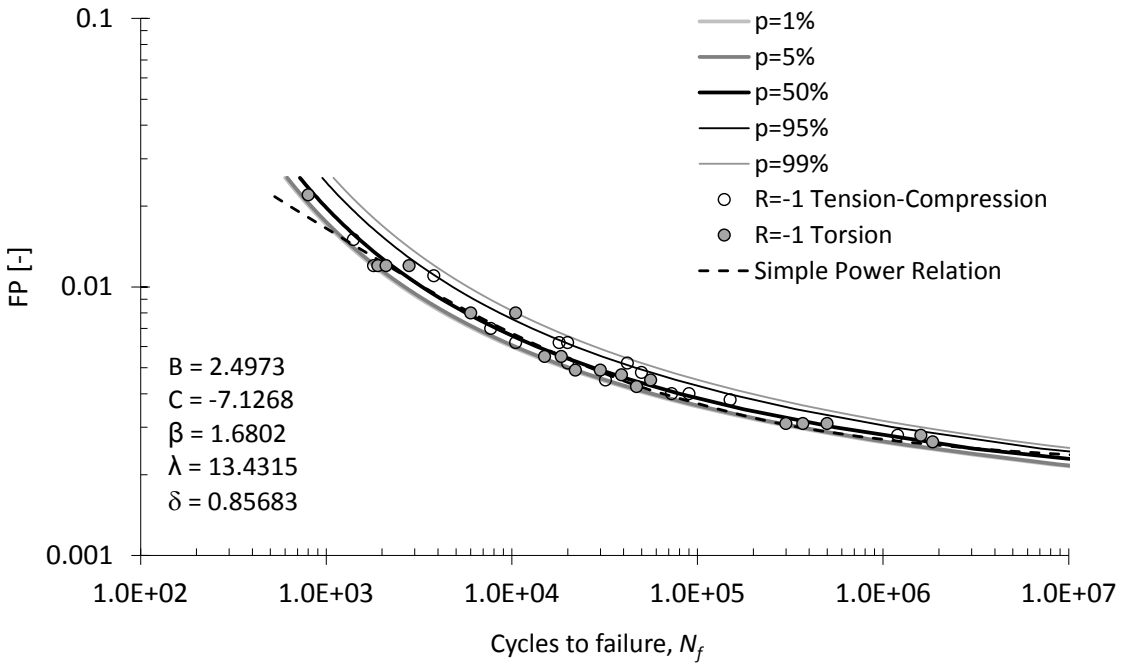

Figure 4.25 – *p-FP-N* field proposed for the S460N (one experimental data point censored).

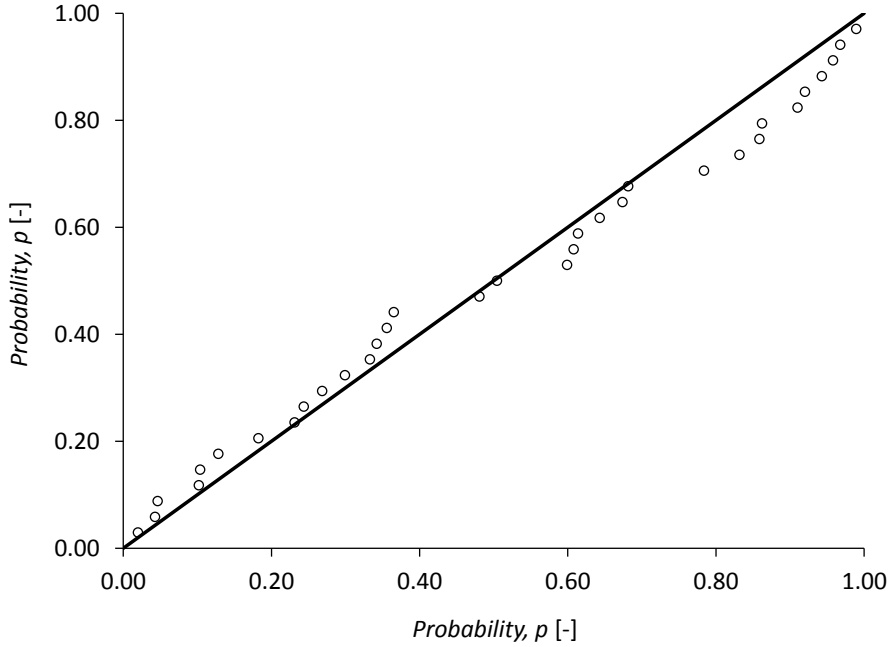

Figure 4.26 – P-P plot showing the quality of the fitted probabilistic fatigue model based on the *FP* parameter, proposed for the S460N (one experimental data point censored).

The comparison between the 50% percentile curve and the deterministic lines referred to in Section 4.2 for this data show good agreement below $1x10^6$ cycles.

4.5. CONCLUSIONS

A generalization of the probabilistic model originally proposed by Castillo and Fernández-Canteli is proposed in this chapter by introducing conventional and new fatigue damage variables. This proposal opens new perspectives for the application of the probabilistic model to a number of very general problems of lifetime involving fatigue modelling. In particular, the proposed probabilistic model can be used as an suitable alternative to replace existing deterministic approaches to fatigue relating explicitly a damage parameter with the number of cycles.

Energetic parameters as reference for fatigue damage for both uniaxial and multiaxial fatigue are considered and adequately estimated using the probabilistic model. Concerning multiaxial fatigue, both proportional and non-proportional fatigue data are satisfactory related to probabilistic using the approach proposed.

4.6. REFERENCES

[1] Castillo E, Fernández-Canteli A. A Unified Statistical Methodology for Modeling Fatigue Damage. Springer, 2009.

[2] Smith KN, Watson P, Topper TH. A Stress-Strain Function for the Fatigue of Metals. Journal of Materials 1970; 5(4): 767-78.

[3] Ellyin F. Fatigue damage, crack growth and life prediction. Chapman & Hall, 1997.

[4] Morrow JD. Cyclic plastic strain energy and fatigue of metals. Int Frict Damp Cyclic Plast ASTM STP 1965; 378: 45–87.

[5] Basquin OH. The exponential law of endurance tests. Proc Am Soc Test Mater 1910;10:625–30.

[6] Fernández-Canteli A, Castillo E, Correia JAFO, De Jesus AMP, Przybilla C. Extending the applicability of probabilistic S-N models to the LCF region using energetic damage parameters. XVI International Colloquium Mechanical Fatigue of Metals. Brno – Czech Republic, 2012.

[7] Ramberg W, Osgood WR. Description of stress–strain curves by three parameters. NACA tech. note no. 902; 1943.

[8] Halford GR. The energy required for fatigue. Journal Materials 1966; 1: 3-18.

[9] Lefebvre D, Ellyin F. Cyclic response and inelastic strain energy in low-cyclic fatigue. International Journal of fatigue 1984; 6(1): 9-15.

[10] Ellyin F, Kujawski D. Plastic strain energy in fatigue failure. Journal Pressure Vessel Technology, Trans. ASME 1984; 106, 342-7.

[11] Ellyin F, Kujawski D. An energy-based fatigue failure criterion. Microstructure and Mechanical Behaviour of Materials, Vol. II (eds. Gu H, He J), EMAS, West Midlands, UK; 541-600.

[12] Golos K, Ellyin F. Generalization of cumulative damage multilevel cyclic loading. Theor. Appl. Fract. Mech. 1987; 7, 169-76.

[13] Golos K, Ellyin F. A total strain energy density theory live damage. J. Pressure Vessel Technol, Trans. ASME 1988; 110, 36-41.

[14] Socie DF, Marquis GB. Multiaxial Fatigue. Society of Automotive Engineers, Inc, 2000.

[15] Fatemi A, Socie DF. A Critical plane approach to multiaxial fatigue damage including out of phase loading. Fatigue Fract Eng Mater Struct 1988; 11: 149–165.

[16] Fatemi A, Kurath P. Multiaxial fatigue life predictions under the influence of mean stresses. ASME J Eng Mater Technol 1988; 110: 380–388.

[17] Jiang Y, Hertel O, Vormwald M. An experimental evaluation of three critical plane multiaxial fatigue criteria. International Journal of Structural Integrity, 2009; No. 29: 15–183.

CHAPTER V

PROCEDURE TO DERIVE PROBABILISTIC FATIGUE CRACK PROPAGATION FIELDS (p-da/dN-ΔK-R)

5.1. INTRODUCTION

The research on fatigue of materials and structures has deserved great interest both by academia and industry. Fatigue has been investigated for more than 150 years and still is a hot topic in research [1]. In particular, the investigation on fatigue crack propagation is not fully accomplished, despite the great achievements of the last decades.

Paris et al. [2] were the first ones to establish a direct correlation between the fatigue crack propagation and a Fracture Mechanics parameter – the stress intensity factor, leading to the so-called Paris's law. Since then, the Paris's law has been used extensively to model fatigue crack growth under constant amplitude loading. However, Paris' law shows several limitations, namely it only models the stable crack propagation, excluding near threshold and near unstable fatigue crack propagation regimes. Also, the stress ratio effects are not accounted for by the Paris' law. Many other fatigue crack propagation laws have been proposed to overcome the limitations of the Paris' law and also to deal with variable amplitude loading [3]. The proposed fatigue models differ on the number of variables and parameters involved.

Local strain-based approaches to fatigue [4-7] represents an alternative to Fracture Mechanics based fatigue crack propagation models. Local strain-based approaches to fatigue are often applied to model the crack initiation on notched components [8].

Some authors, such as Glinka [9], Peeker and Niemi [10], Noroozi et al. [11,13,14], Hurley and Evans [12] have developed relations between the local strain-based approaches to fatigue and the Fracture Mechanics based fatigue crack propagation models. Glinka was one of the first researchers to propose the application of the local strain-based approaches to model fatigue crack propagation [9].

The original idea of Glinka was latter followed and developed by his collaborators, such as Noroozi et al. [11,13,14], using residual stress concepts. Peeker and Niemi [10], based on the original idea of Glinka, made also independent contributions, using crack closure concepts to explain stress *R*-ratio and load interaction effects. In general, elastoplastic stress analysis at the crack vicinity is performed using analytical approaches though Hurley and Evans [12] proposed the use of elastoplastic finite element analysis.

The fatigue crack propagation is assumed a process of continuous crack re-initializations (failure of consecutive representative materials elements). The resulting crack propagation models have demonstrated to correlate fatigue crack propagation data from several sources, including the stress ratio effects. The crack tip stress-strain fields are computed using elastoplastic analysis, which are applied together with a fatigue damage law to predict the failure of the representative material elements. The simplified method of Neuber [15] or Moftakhar et al. [16] may be used to compute the elastoplastic stress field at the crack tip vicinity using the elastic stress distribution given by the Linear Elastic Fracture Mechanics [11,16,17].

This chapter proposes an evaluation and extension of the model proposed by Noroozi et al. [11,13,14] to predict the fatigue crack propagation rates, based on a local strain-based approach to fatigue. This model has been denoted *UniGrow* model and classed as a residual stress-based crack propagation model [18]. The model is applied in this chapter to derive probabilistic fatigue crack propagation fields (*p−da/dN−ΔK−R fields*) for two materials representative of old Portuguese metallic riveted bridges (Eiffel and Fão bridges), and for a current steel, the S355 construction steel, covering distinct stress *R*−ratios. In addition, the modified *UniGrow* model is applied to compute the fatigue crack propagation rates for the P355NL1 steel (a pressure vessel steel), for distinct stress *R*-ratios. Results are compared with available experimental data [19,20,21]. The required

strain-life data was experimentally evaluated and can be found in the literature [19,20,21]. The material representative element size, ρ^*, a central parameter in the *UniGrow* model, is assessed by means of a try and error procedure. Also, the residual stress field is analyzed for distinct crack sizes and stress R−ratios. The elastoplastic stresses at the vicinity of the crack tip, computed using simplified formulae, are compared with the stresses calculated using an elastoplastic finite element analyses of the specimens considered in the experimental program to derive the fatigue crack propagation data.

The deterministic strain-life relations proposed in the *UniGrow* model are replaced by the probabilistic strain-life fields (p−ε_a−N) proposed by Castillo and Fernández-Canteli [22]. This probabilistic model is also extended by considering a damage parameter able to account for mean stress effects. In particular, a probabilistic Smith-Watson-Topper field (p−SWT−N) is proposed alternatively to the p−ε_a−N and applied to derive the probabilistic crack propagation fields.

5.2. THEORETICAL BACKGROUND

In this section, an overview of the *UniGrow* model, which has been proposed to predict the fatigue crack growth by means of a local approach to fatigue, is presented. An isotropic elastoplastic constitutive model based on von Mises yield criterion, was adopted to obtain the residual stress field ahead of the crack tip. Afterwards, a recently proposed probabilistic strain-life model is presented. An extension of the probabilistic strain-life approach, to account for mean stress effects, is proposed which will be applied latter in this chapter to predict probabilistic fatigue crack propagation data.

5.2.1. Overview of the deterministic UniGrow model

The *UniGrow* model was proposed by Noroozi et al. [11] supported on the following assumptions:

- The material is composed of elementary particles of a finite dimension ρ^*. It represents a material representative element, below which the material cannot be regarded as a continuum, Figure 5.1.a).

- The fatigue crack tip is considered equivalent to a notch with radius equal to ρ^*, Figure 5.1.b).

- The fatigue crack growth is considered a process of successive crack increments due to crack re-initializations over the distance ρ^*.

- The fatigue crack growth rate can be determined as:

$$\frac{da}{dN} = \frac{\rho^*}{N_f} \tag{5.1}$$

where N_f is the number of cycles required to fail the material representative element, which can be computed using a strain-life relation.

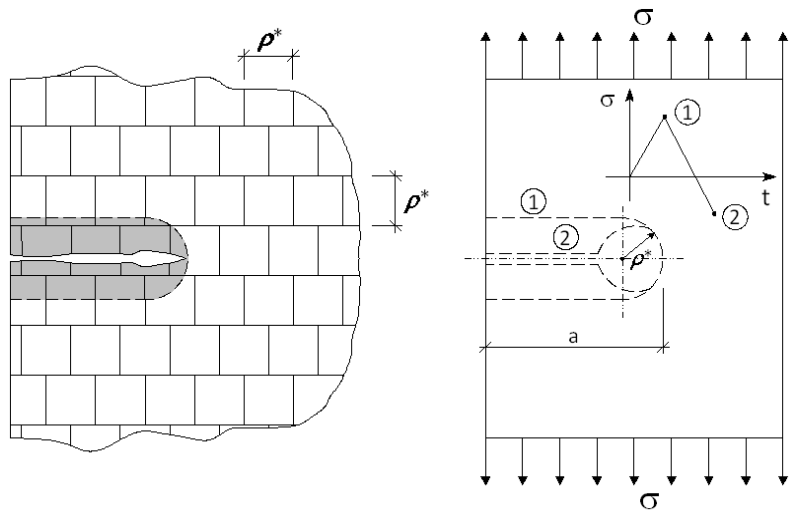

Figure 5.1 – Crack configuration according to the *UniGrow* model: a) crack and the discrete elementary material blocks; b) crack shape at the tensile maximum and compressive minimum loads [11].

Noroozi et al. [11] suggested the use of a strain-life relation based on the Smith, Watson and Topper fatigue damage parameter (SWT damage parameter) [7]:

$$\sigma_{max} \cdot \Delta\varepsilon/2 = SWT = \left(\sigma'_f\right)^2 \cdot \left(2N_f\right)^{2b} / E + \sigma'_f \cdot \varepsilon'_f \cdot \left(2N_f\right)^{b+c} \tag{5.2}$$

Peeker and Niemi [10] suggested, alternatively, the use of the Morrow's equation [6] to compute the failure of the material representative element:

$$\frac{\Delta\varepsilon}{2} = \frac{\sigma'_f - \sigma_m}{E} \cdot \left(2N_f\right)^b + \varepsilon'_f \cdot \left(2N_f\right)^c \tag{5.3}$$

The Morrow's equation was derived from the following Coffin-Manson relation [4,5] of the material, in order to include mean stress effects:

$$\frac{\Delta\varepsilon}{2}=\frac{\sigma'_f}{E}\cdot\left(2N_f\right)^b+\varepsilon'_f\cdot\left(2N_f\right)^c \tag{5.4}$$

In particular, Equation (5.2) was derived as multiplication of the Coffin-Manson Equation (5.4) by the Basquin relation [23], for a stress *R*-ratio equal to −1:

$$\frac{\Delta\sigma}{2}=\sigma_{max}=\sigma'_f\cdot\left(2N_f\right)^b \tag{5.5}$$

In the previous two equations, σ'_f and *b* represents, respectively, the fatigue strength coefficient and exponent; ε'_f and *c* represents, respectively, the fatigue ductility coefficient and exponent and *E* is the Young modulus. The maximum stress, σ_{max}, mean stress, σ_m, and the strain range, $\Delta\varepsilon$, have to be evaluated as the average values at the elementary material block size, ρ^*, taking into account an elastoplastic analysis.

To compute the elastoplastic stresses and strains at the elementary material blocks ahead of the crack tip, Noroozi et al. [11,13] proposed the following procedure:

i) The elastic stresses are computed ahead of the crack tip, using the Creager-Paris solution [24] for a crack with a tip radius ρ^*, using the applied stress intensity factors:

$$\begin{cases}\sigma_x=-\dfrac{K}{\sqrt{2\pi r}}\dfrac{\rho^*}{2r}\cos\dfrac{3\theta}{2}+\dfrac{K}{\sqrt{2\pi r}}\cos\dfrac{\theta}{2}\left[1-\sin\dfrac{\theta}{2}\sin\dfrac{3\theta}{2}\right]+\ldots\\ \sigma_y=\dfrac{K}{\sqrt{2\pi r}}\dfrac{\rho^*}{2r}\cos\dfrac{3\theta}{2}+\dfrac{K}{\sqrt{2\pi r}}\cos\dfrac{\theta}{2}\left[1+\sin\dfrac{\theta}{2}\sin\dfrac{3\theta}{2}\right]+\ldots\\ \tau_{xy}=-\dfrac{K}{\sqrt{2\pi r}}\dfrac{\rho^*}{2r}\sin\dfrac{3\theta}{2}+\dfrac{K}{\sqrt{2\pi r}}\sin\dfrac{\theta}{2}\cos\dfrac{\theta}{2}\cos\dfrac{3\theta}{2}+\ldots\end{cases} \tag{5.6}$$

In the previous equation, *r* and θ are crack tip polar coordinates. The elastic stress distribution along the crack line (θ=0 and *r*=*x*) is given by:

$$\begin{cases} \sigma_x = \dfrac{K}{\sqrt{2\pi x}}\left(1-\dfrac{\rho^*}{2x}\right)+\ldots \\ \sigma_y = \dfrac{K}{\sqrt{2\pi x}}\left(1+\dfrac{\rho^*}{2x}\right)+\ldots \\ \tau_{xy} = 0 \end{cases} \tag{5.7}$$

Average stresses have to be computed over each material elementary block using the following equations:

$$\begin{cases} \tilde{\sigma}^e_{x,i} = \dfrac{1}{x_{i+1}-x_i}\displaystyle\int_{x_i}^{x_{i+1}} \dfrac{K}{\sqrt{2\pi x}}\left(1-\dfrac{\rho^*}{2x}\right)dx \\ \tilde{\sigma}^e_{y,i} = \dfrac{1}{x_{i+1}-x_i}\displaystyle\int_{x_i}^{x_{i+1}} \dfrac{K}{\sqrt{2\pi x}}\left(1+\dfrac{\rho^*}{2x}\right)dx \end{cases} \tag{5.8}$$

where $\tilde{\sigma}^e_{x,i}$ and $\tilde{\sigma}^e_{y,i}$ are the average elastic stresses at the elementary block *i*.

ii) The actual elastoplastic stresses and strains, ahead of the crack tip, are computed using the Neuber's [15] or Glinka's approaches [25]. Multiaxial approaches may be adopted using the procedures presented by Moftakhar et al. [16] and Reinhard et al. [17]. This multiaxial approach together with Neuber's approach, result in the following set of simultaneous equations:

$$\begin{cases} \tilde{\varepsilon}^{ep}_{x,i} = \dfrac{1}{E}\left(\tilde{\sigma}^{ep}_{x,i}-\nu\tilde{\sigma}^{ep}_{y,i}\right)+\dfrac{f\left(\tilde{\sigma}^{ep}_{eq,i}\right)}{\tilde{\sigma}^{ep}_{eq,i}}\left(\tilde{\sigma}^{ep}_{x,i}-\dfrac{1}{2}\tilde{\sigma}^{ep}_{y,i}\right) \\ \tilde{\varepsilon}^{ep}_{y,i} = \dfrac{1}{E}\left(\tilde{\sigma}^{ep}_{y,i}-\nu\tilde{\sigma}^{ep}_{x,i}\right)+\dfrac{f\left(\tilde{\sigma}^{ep}_{eq,i}\right)}{\tilde{\sigma}^{ep}_{eq,j}}\left(\tilde{\sigma}^{ep}_{y,i}-\dfrac{1}{2}\tilde{\sigma}^{ep}_{x,i}\right) \\ \tilde{\varepsilon}^{ep}_{z,i} = \dfrac{1}{E}\left[-\nu\left(\tilde{\sigma}^{ep}_{x,i}+\tilde{\sigma}^{ep}_{y,i}\right)\right]+\dfrac{f\left(\tilde{\sigma}^{ep}_{eq,i}\right)}{\tilde{\sigma}^{ep}_{eq,i}}\left[-\dfrac{1}{2}\left(\tilde{\sigma}^{ep}_{x,i}+\tilde{\sigma}^{ep}_{y,i}\right)\right] \\ \tilde{\sigma}^e_{x,i}\tilde{\varepsilon}^e_{x,i} = \tilde{\sigma}^{ep}_{x,i}\tilde{\varepsilon}^{ep}_{x,i} \\ \tilde{\sigma}^e_{y,i}\tilde{\varepsilon}^e_{y,i} = \tilde{\sigma}^{ep}_{y,i}\tilde{\varepsilon}^{ep}_{y,i} \\ \tilde{\sigma}^{ep}_{eq,i} = \sqrt{\left(\tilde{\sigma}^{ep}_{x,i}\right)^2-\tilde{\sigma}^{ep}_{x,i}\tilde{\sigma}^{ep}_{y,i}+\left(\tilde{\sigma}^{ep}_{y,i}\right)^2} \\ f\left(\tilde{\sigma}^{ep}_{eq,i}\right) = \left(\dfrac{\tilde{\sigma}^{ep}_{eq,i}}{K'}\right)^{1/n'} \end{cases} \tag{5.9}$$

where $\tilde{\sigma}_{x,i}^{ep}$ and $\tilde{\sigma}_{y,i}^{ep}$ are the average elastoplastic stresses at the elementary material block *i*, $\tilde{\varepsilon}_{x,i}^{ep}$ and $\tilde{\varepsilon}_{y,i}^{ep}$ are the average elastoplastic strains at the elementary material block *i*, $\tilde{\sigma}_{eq,i}^{ep}$ is the average equivalent elastoplastic stress at the elementary material block *i*, ν is the Poisson's ratio, *E* is the Young's modulus, K' and n' are, respectively, the cyclic strain hardening coefficient and exponent.

iii) The residual stress distribution, ahead of the crack tip, along the *y* direction is computed using the actual elastoplastic stresses computed at the end of the first load reversal and subsequent cyclic elastoplastic stress range:

$$\sigma_r = \sigma_{max} - \Delta\sigma \tag{5.10}$$

iv) The residual stress distribution computed ahead of the crack tip is assumed to be applied on the crack faces, behind the crack tip, in a symmetric way with respect to the crack tip. The loading process generates a plastic zone at the crack tip that does not vanish completely during unloading, leading to a cyclic plastic zone, which is controlled by compressive stresses ahead of the crack tip, and to some amount of crack opening displacement just behind the crack tip (crack faces does not close completely just behind the crack tip). One possibility to model crack opening is assuming that the compressive residual stress field acting ahead of the crack tip is applied in a symmetrical way, behind the crack tip, directly on crack faces. This compressive stress distribution, acting on crack faces, is equivalent to a residual stress intensity factor which is used to correct the applied stress intensity factor range leading to a total (effective) stress intensity factor range, which excludes the effects of the compressive stresses. The residual stress intensity factor, K_r, is computed using the weight function method [26]:

$$K_r = \int_0^a \sigma_r(x) m(x,a) dx \tag{5.11}$$

where $m(x,a)$ is the weight function.

v) The applied stress intensity factors (maximum and range values) are corrected using the residual stress intensity value, resulting the total $K_{max,tot}$ and ΔK_{tot} values

[11,13]. For positive stress *R*-ratios, which is the range covered by the experimental data used in this research, $K_{max,tot}$ and ΔK_{tot} may be computed as follows:

$$K_{max,tot} = K_{max,applied} + K_r$$
$$\Delta K_{tot} = \Delta K_{applied} + K_r \quad (5.12)$$

where K_r takes a negative value corresponding to the compressive stress field. For high stress *R*-ratios, the compressive stresses ahead of the crack tip may be neglected and the applied stress intensity factor range is assumed fully effective; for low stress R-ratios the compressive stresses increases and the effectiveness of the applied stress intensity factor range decreases.

vi) Using the total values of the stress intensity factors, the first and second steps before (i, ii) are repeated to determine the corrected values for the maximum actual stress and actual strain range at the material representative elements. Then, Equation (5.2) is applied together with Equation (5.1) to compute the fatigue crack growth rates, in the original *UniGrow* model proposition.

The described methodology does not allow close-form solutions for the crack propagation rates. However, introducing some simplified assumptions on elastoplastic conditions, such as predominantly elastic behaviour of the material at the crack tip or predominantly plastic behaviour of the material at the crack tip, it is possible to derive close-form solutions for the stress-strain histories at the crack tip and for the number of cycles to failure of the material representative element. Consequently, close-form solutions for the fatigue crack propagation rates are possible, leading to two-parameters crack driving force relations [11,13]:

$$\frac{da}{dN} = C\left[\left(K_{max,tot}\right)^p \left(\Delta K_{tot}\right)^q\right]^\gamma \quad (5.13)$$

where *C*, *p*, *q* and γ are constants to be correlated with the cyclic constants of the material in a form depending on the elastoplastic conditions at the crack tip. The dependency of the crack propagation rates with both K_{max} and ΔK allows mean stress effects on fatigue crack propagation rates to be properly modelled. The crack propagation

models based on a two parameters crack driving force has been proposed recently by several authors [27,28].

In this chapter, the full solution of the methodology proposed by Noroozi et al. [11] is followed. Besides the cyclic elastoplastic and fatigue properties of the material, the *UniGrow* model requires the definition of the elementary material block size, ρ^*. An iterative process is used to compute ρ^*. This parameter is computed using a try and error procedure in order a good correlation of the experimental fatigue crack growth data to be obtained. The simplified elastoplastic analysis, based on Creager-Paris [24] and multiaxial Neuber's approach [15,16,17] is exclusively applied to compute the elastoplastic stress-strain field in the first elementary material block size ahead of the crack tip. The residual stress distribution ahead of the crack tip is computed using an elastoplastic finite element analysis, since inconsistencies were found in the analytical residual stress distributions, as will be demonstrated latter.

5.2.2. Cyclic elastoplastic constitutive modelling

In this section, an elastoplastic constitutive model based on von Mises yield criterion, with associative flow rule and multilinear kinematic hardening was adopted to model the residual stress field ahead of the crack tip. According to the von Mises yield criterion, the yield function, *f*, is defined as follows:

$$f = \left[\frac{3}{2}\left(S_{ij} - X_{ij}\right)\left(S_{ij} - X_{ij}\right)\right]^{\frac{1}{2}} - \sigma_k \leq 0 \tag{5.14}$$

where S_{ij} is the deviatoric stress tensor defined as:

$$S_{ij} = \sigma_{ij} - \sigma_h \delta_{ij} \tag{5.15}$$

X_{ij} is the back stress tensor defining the centre of the yield surface, σ_k is the material yield parameter, σ_{ij} is the stress tensor, σ_h is the hydrostatic stress and δ_{ij} is the Kronecker delta. The associative flow rule defines the plastic strain increment according to the following relation:

$$\dot{\varepsilon}_{ij}^{P} = \lambda \frac{\partial f}{\partial \sigma_{ij}} \tag{5.16}$$

where λ is the plastic multiplier which determines the amount of plastic straining. The hardening rule adopted was of kinematic type, which is adequate for cyclic plasticity description, in particular for the Bauschinger effect description. The kinematic hardening describes the translation of the yield surface. The Besseling model, also called sublayer or overlay model [29] was used to characterize the material behaviour. The material behaviour is assumed to be composed of various portions (or subvolumes), all subjected to the same total strain, but each subvolume having a different yield strength. Each subvolume has a simple stress-strain response but when combined, the model can represent multilinear stress-strain curves, representation that exhibits the Bauschinger (kinematic hardening) effect. The following steps are performed in the plasticity calculations [30]:

i) The portion of total volume (the weighting factor) for each subvolume and its corresponding yield strength are determined.

ii) The increment in plastic strain is determined for each subvolume assuming each subvolume is subjected to the same total strain.

iii) The individual increments in plastic strain are summed using the weighting factors determined in step i) to compute the overall or apparent increment in plastic strain.

iv) The plastic strain is updated and the elastic strain is computed.

The weighting factor and yield stress for each subvolume are determined by matching the material response to the uniaxial stress-strain curve. A perfectly plastic von Mises material is assumed, with a weighting factor for subvolume *k* given by:

$$w_k = \frac{E - E_{Tk}}{E - \frac{1-2\nu}{3}E_{Tk}} - \sum_{i=1}^{k-1} w_i \tag{5.17}$$

where w_k is the weighting factor for subvolume *k* and is evaluated sequentially from 1 to the number of subvolumes, N_{sv}; E_{Tk} is the slope of the k_{th} segment of the uniaxial cyclic stress-strain curve. The yield stress for each subvolume is given by:

$$\sigma_{yk} = \frac{1}{2(1-\nu)}\left(3E\varepsilon_k - (1-2\nu)\sigma_k\right) \tag{5.18}$$

where (ε_k , σ_k) is the breakpoint in the uniaxial cyclic stress-strain curve. The number of subvolumes corresponds to the number of breakpoints specified. Each subvolume follows the von Mises yield criterion with the associative flow rule. The plastic strain increment for the entire volume is computed as follows:

$$\Delta\varepsilon_{ij}^{p} = \sum_{k=1}^{N_{sv}} w_k \Delta\varepsilon_{ij,k}^{p} \tag{5.19}$$

If the equivalent stress computed using elastic properties exceeds the material yield, then plastic straining occurs. Plastic strains reduce the stress state so that it satisfies the yield criterion. The integration of the constitutive equations may be performed following the elastic trial and return mapping procedures as proposed by Simo and Taylor [31]. The proposed cyclic elastoplastic model is available in ANSYS commercial code [30]. The model parameters were identified using the stabilized cyclic stress-strain curves of the materials under consideration in this study.

5.2.3. Probabilistic ε_a–N and SWT–N fields

The *UniGrow* model requires a fatigue damage relation to compute the number of cycles to fail the elementary material blocks. In this chapter, probabilistic fatigue damage models are proposed rather than the deterministic *SWT–N*, Coffin-Manson or Morrow models. In particular the probabilistic ε_a–*N* model proposed by Castillo and Fernández-Canteli [22] is used. This model is described in Section 2.5.2.3. of Chapter II. However, and since the probabilistic ε_a–*N* model does not account for mean stress effects, a new probabilistic *SWT–N* field is also proposed, as an extension of the *p*–ε_a–*N* field suggested by Castillo and Fernández-Canteli [22], to account for mean stress effects. This new probabilistic field using the *SWT* damage parameter is based on the proposal for generalization of existing probabilistic fatigue damage model, as found in the Section 4.2. of Chapter IV.

The threshold and Weibull parameters of the *p-SWT-N* model can be estimated by constrained least square or maximum likelihood methods, respectively, present in the Section 2.5.2.1. of Chapter II.

5.3. PROCEDURE TO GENERATE PROBABILISTIC FATIGUE CRACK PROPAGATION FIELDS

The procedure proposed to derive probabilistic fatigue crack propagation fields may be summarized into three steps, as follows:

1) Estimation of the Weibull parameters for the $p–SWT–N$ or $p–\varepsilon_a–N$ models, described in section 2.5.2.3. of Chapter II, using experimental $\varepsilon_a–N$ or $SWT–N$ data from smooth specimens;

2) Application of the *UniGrow* model with probabilistic fatigue damage models;

3) Computation of the $p–da/dN–\Delta K–R$ field.

The *UniGrow* model was implemented in a worksheet, supported on VBA programming, specifically developed for the *CT* geometry. The input data are the material properties, loads, dimensions of the *CT* specimen, including the initial and final crack size to be simulated. Additionally, the elementary material block size, ρ^*, is required. This parameter may be evaluated by a try and error procedure in order the numerical results to fit satisfactorily the experimental data. Figure 5.2 gives a general overview of the procedure.

Two possibilities for the elastoplastic analysis at the crack vicinity are envisaged, namely based, respectively, on the Neuber and Glinka's approaches [15,25]. The multiaxial elastoplastic approach as proposed by Moftakhar *et al*. [16] and Reinhard *et al*. [17] were considered. This approach is based on Hencky's total deformation equations, and has been demonstrated to provide accurate predictions for the stress-strain field at notch roots, under proportional loading. However, the *UniGrow* model requires not only the evaluation of the elastoplastic stress-strain response at the crack tip but the assessment of the elastoplastic stress-strain response along the crack path, in order to allow the residual stress to be computed. Since the analytical multiaxial elastoplastic approach does not model the stress redistribution due to yielding, this approach may lead to inconsistent predictions of the residual stress distribution. Therefore, in this research the residual stress distribution is computed using a finite element approach, whereby the results are compared with those from the analytical approach. Since the *UniGrow* model is a residual

stress based crack propagation model, the accuracy of the residual stress distribution plays a significant role on predictions.

The probabilistic fatigue crack propagation fields were evaluated using, alternatively, the probabilistic ε_a–*N* and *SWT*–*N* fields. For each fatigue damage modelling approach, an independent elementary material block size, ρ^*, identification is performed.

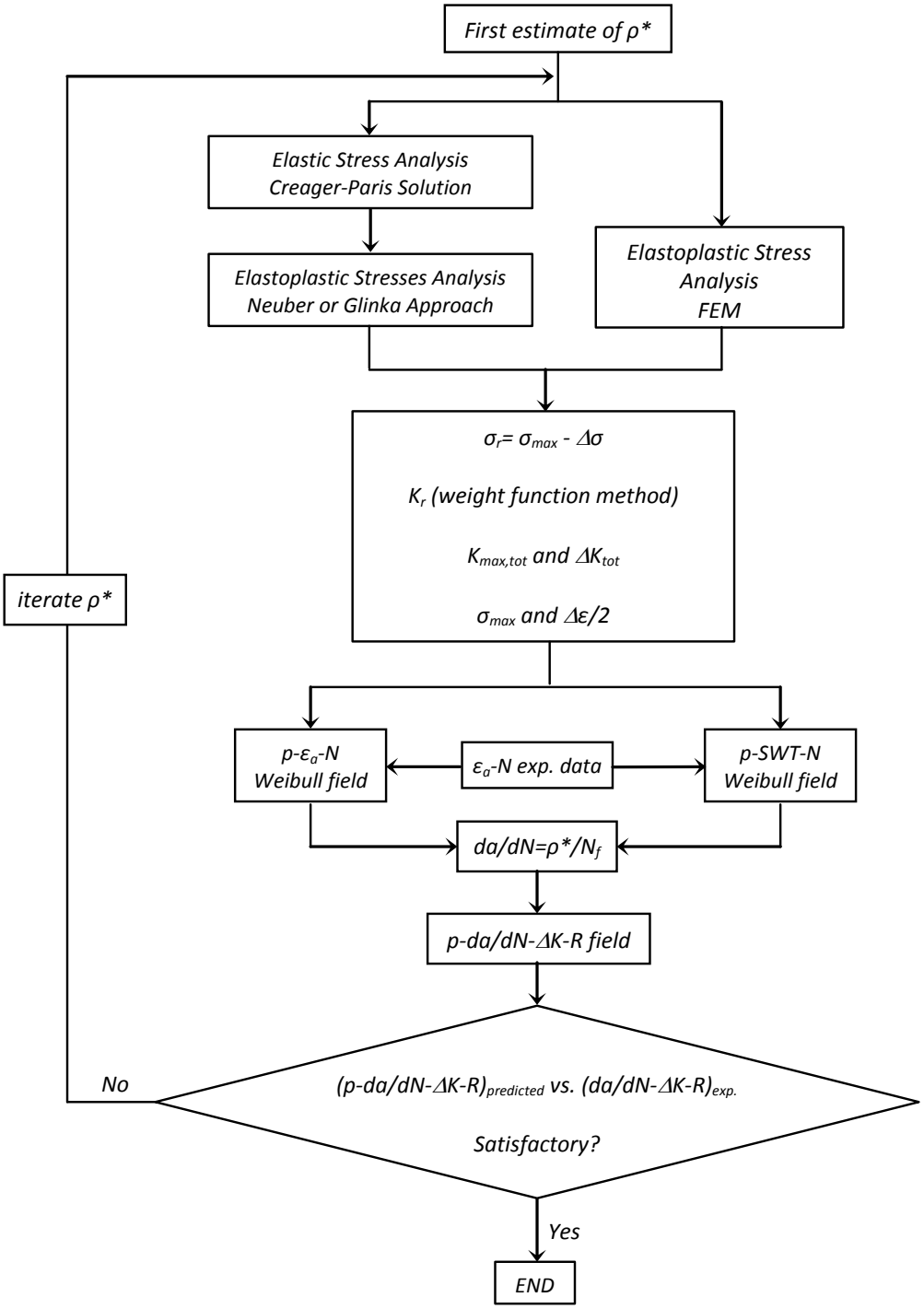

Figure 5.2 – Procedure to generate probabilistic fatigue crack propagation fields.

5.4. BASIC FATIGUE DATA OF THE INVESTIGATED MATERIALS

Four materials are considered in this research, namely two puddle irons from the Portuguese Fão and Eiffel bridges, the S355 construction steel and P355NL1 pressure vessel steel. The fatigue behaviours of these materials were evaluated, based on experimental fatigue tests of smooth specimens as well fatigue crack propagation tests [19,20,21]. In this section, the probabilistic *SWT-N* and ε_a-*N* fields for the materials under consideration are evaluated. In addition, the deterministic models – *SWT-N*, Coffin-Manson and Morrow's relation are also illustrated.

5.4.1. Strain-life behaviour

The strain-life behaviours of the materials were evaluated through fatigue tests of smooth specimens, carried out under strain control conditions, according to the ASTM E606 standard [33]. The strain-life data was firstly correlated using the Morrow's equation (Equation (3.2), Chapter III). The Ramberg and Osgood [34] relation, Equation (5.20), was fitted to the stabilized cyclic stress–strain data:

$$\frac{\Delta\varepsilon}{2}=\frac{\Delta\varepsilon^{E}}{2}+\frac{\Delta\varepsilon^{P}}{2}=\frac{\Delta\sigma}{2E}+\left(\frac{\Delta\sigma}{2K'}\right)^{1/n'} \tag{5.20}$$

where *K'* and *n'* are the cyclic strain hardening coefficient and exponent, respectively; $\Delta\varepsilon^{P}$ is plastic strain range; and $\Delta\sigma$ is the stress range.

The cyclic Ramberg-Osgood and Morrow strain-life parameters of these four materials are summarized in Table 5.1 whereas Table 5.2 presents the elastic and monotonic tensile properties of these materials under investigation.

Table 5.1 – Cyclic elastoplastic and strain-life properties of the materials.

Material	σ'_f	b	ε'_f	c	K'	n'
	MPa	-	-	-	*MPa*	-
Eiffel bridge*	602.50	-0.0778	0.1595	-0.7972	645.95	0.0946
Fão bridge**	828.30	-0.1134	0.0530	-0.5113	818.50	0.1400
S355*	952.20	-0.0890	0.7371	-0.6640	595.85	0.0757
P355NL1**	1005.50	-0.1033	0.3678	-0.5475	948.35	0.1533

** R_ε=-1; **R_ε=-1+R_ε=0*

More details about the fatigue and monotonic properties evaluation, concerning the materials from the Eiffel and Fão bridges, can be found in Chapter III. Figures 5.3 and 5.4 illustrate the deterministic strain-life curves according to the Morrow model, for the materials from the Eiffel and Fão bridges, respectively.

The results of the strain-life fatigue tests, for the S355 mid structural steel, were presented in reference [20]. One series of 10 smooth specimens were tested under a strain ratio, R_ε, equal to -1. Figure 5.5 illustrates the resulting experimental strain-life fatigue data.

Table 5.2 – Elastic and tensile properties of the materials.

Material	E	ν	f_u	f_y	A	Z
	GPa	-	*MPa*	*MPa*	*%*	*%*
Eiffel bridge	193.10	0.300	341.80	292.40	8.14	11.60
Fão bridge	198.70	0.260	359.30	219.90	23.13	13.06
S355	211.60	0.300	744.80	422.00	-	-
P355NL1	205.20	0.275	568.11	418.06	-	-

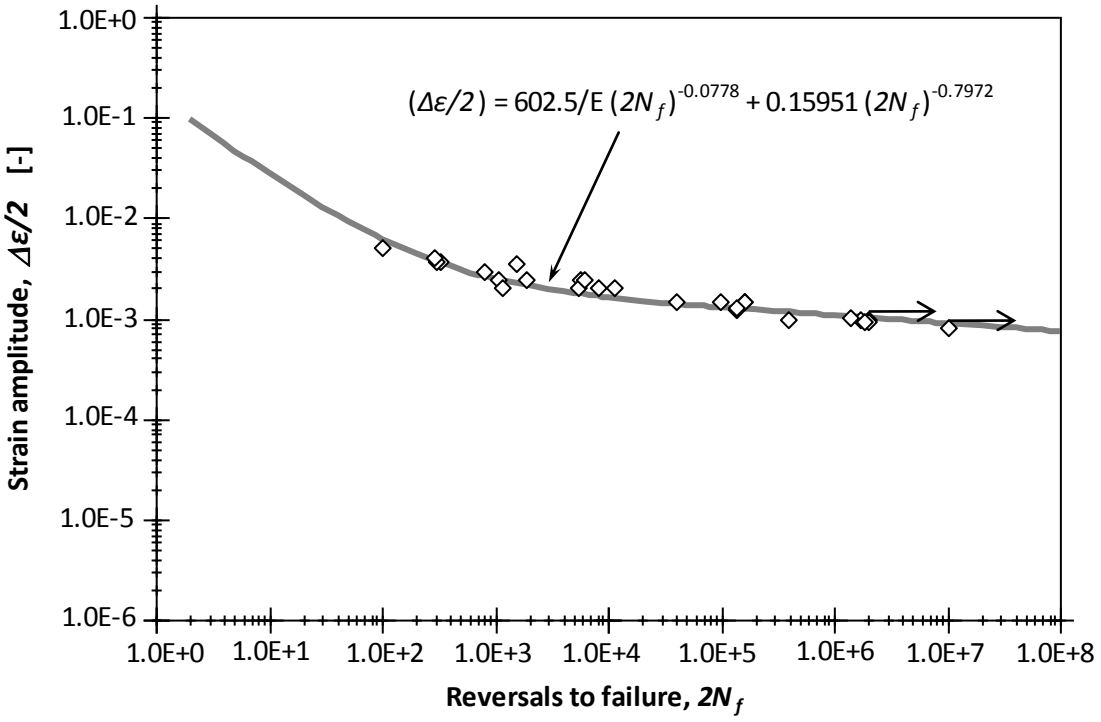

Figure 5.3 – Strain-life curves for the material from the Eiffel bridge, R_ε=-1.

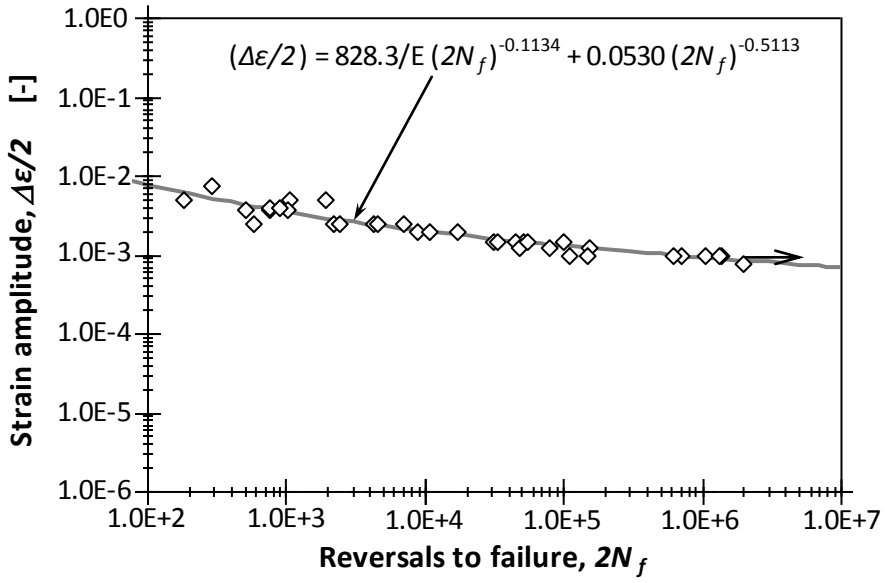

Figure 5.4 – Strain-life curves for the material from the Fão bridge, R_ε=-1+R_ε=0.

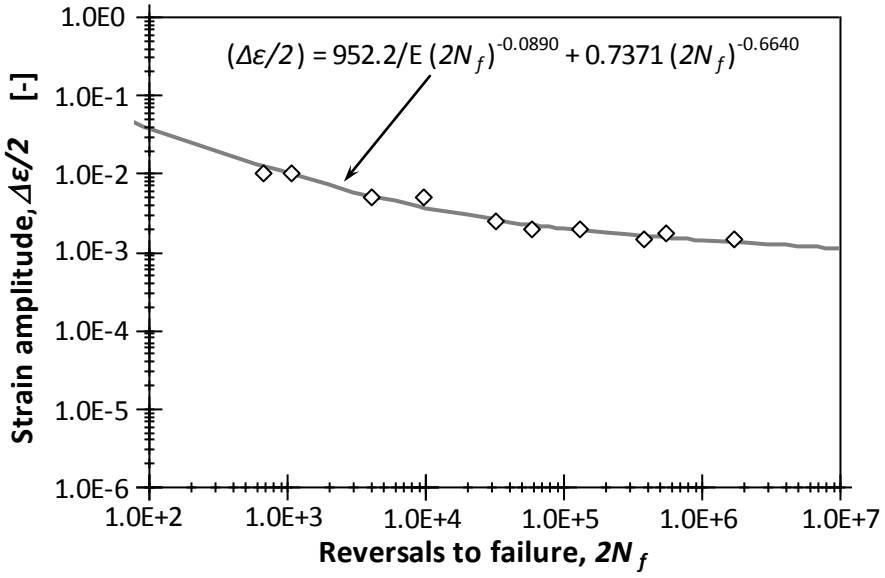

Figure 5.5 – Strain-life curves for the S355 steel, R_ε=-1.

The P355NL1 steel, which is a low carbon pressure vessel steel, has been investigated regarding its fatigue characterization [21]. Two series of specimens were tested under distinct strain ratios (R_ε=0: 19 specimens; R_ε=-1: 24 specimens). Figure 5.6 shows a plot of the experimental strain-life fatigue data, for the two strain ratios. Figure 5.6 also plots the Morrow relation, for each strain ratio and the conjunction of both strain ratios, R_ε=-1+R_ε=0 [21]. Table 5.1 summarizes the resulting properties that were obtained for the conjunction of both strain ratios [21]. This research adopted the values obtained by combining the results of the two test series together.

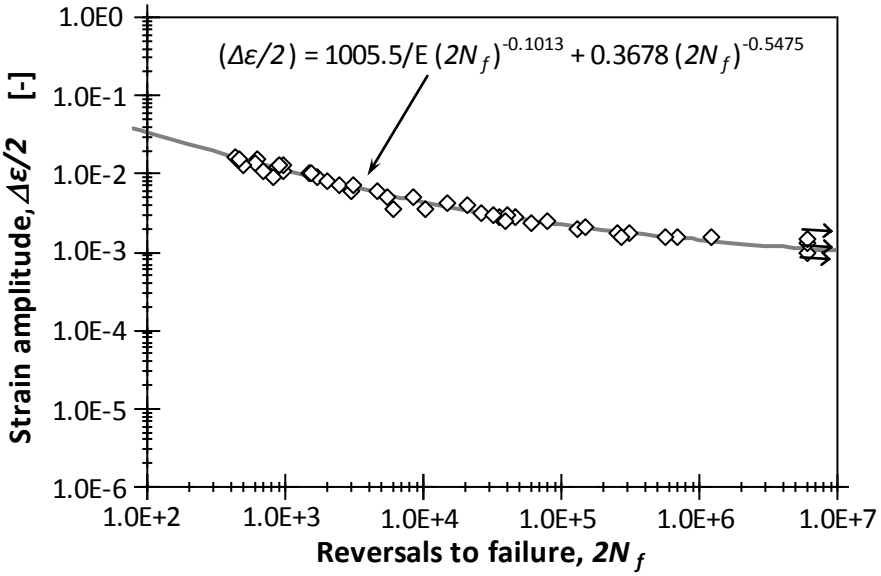

Figure 5.6 – Strain-life curves for the P355Nl1 steel, R_ε=-1+R_ε=0.

5.4.2. Fatigue crack propagation rates

Fatigue crack growth rates of the investigated materials were also evaluated, for several stress *R*-ratios, using compact tension (CT) specimens, following the recommendations of the ASTM E647 standard [35]. The CT specimens of material from the Fão bridge and of S355 steel were defined with a width, W=50mm, and a thickness, B=8mm; specimens from material of the Eiffel bridge and of P355NL1 steel were defined with a width, W=40mm and a thickness, B=4.5mm [19,20,21]. All tests were performed in air, at room temperature, under a sinusoidal waveform at a maximum frequency of 20 Hz. The crack growth was measured on both faces of the specimens by visual inspection, using two travelling microscopes with an accuracy of 0.001mm.

Figures 5.7 to 5.10 exhibit the fatigue crack propagation data for the four materials under consideration. With respect to the material from the Eiffel bridge, crack propagation data for the stress *R*-ratios, R_σ=0.1 and R_σ=0.5 was included in Figure 5.7. Regarding the material from the Fão bridge, crack propagation data for the stress *R*-ratios, R_σ=0.0, R_σ=0.25, R_σ=0.5 and R_σ=0.75 was included in Figure 5.8. Figure 5.9 presents the fatigue crack propagation rates of the S355 steel, for the three tested stress ratios, R_σ=0.0, R_σ=0.25 and R_σ=0.5. Figure 5.10 illustrates the crack growth data derived for the P355NL1 steel, for the three tested stress ratios, R_σ=0.0, R_σ=0.5 and R_σ=0.7.

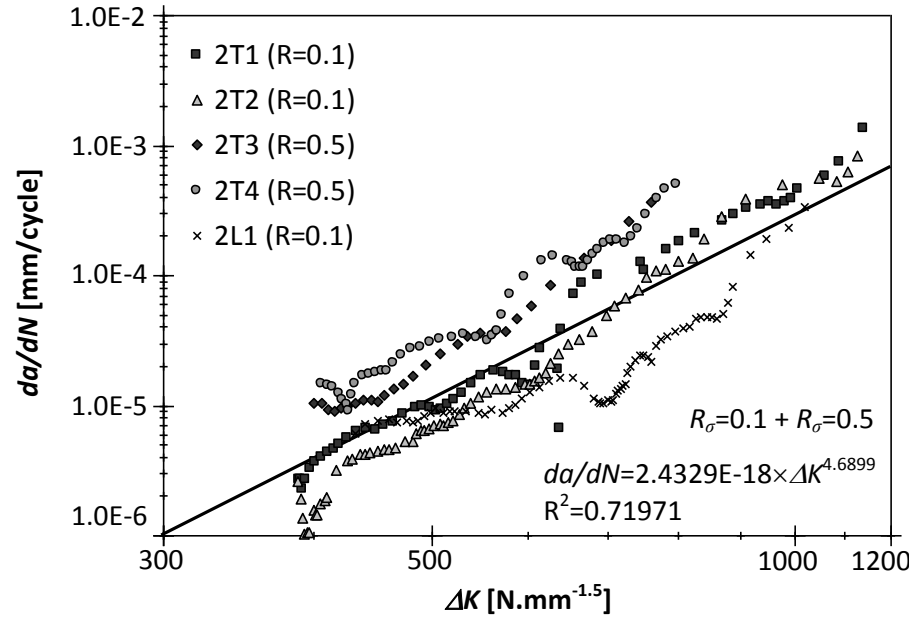

a)

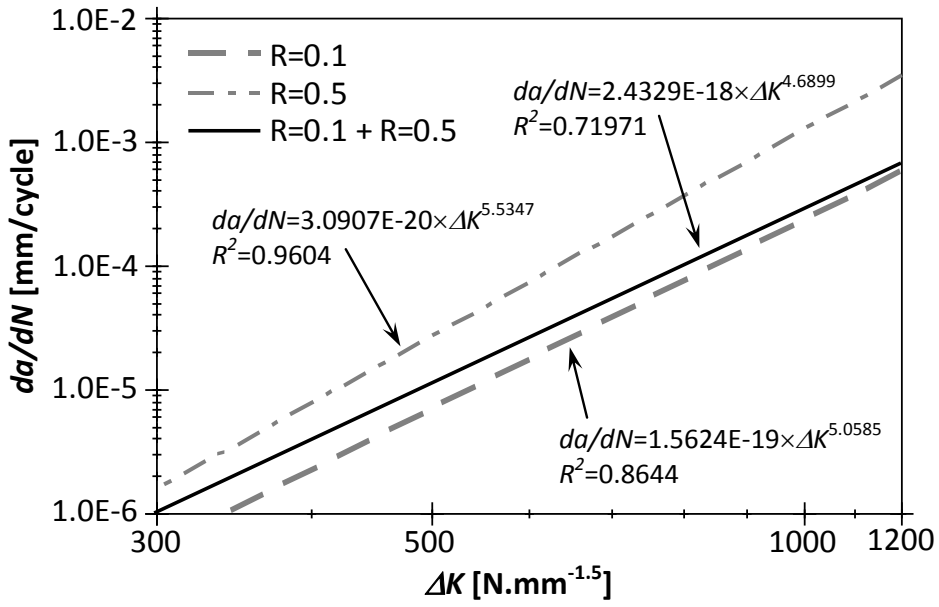

b)

Figure 5.7 – Fatigue crack propagation data obtained for the material from the Eiffel bridge:
a) Experimental data; b) Paris correlations for each stress R_σ-ratio.

Besides the experimental data, Figures 5.7 to 5.10 also present regression lines, for each stress *R*-ratio, which were defined according to the Paris law [2]:

$$\frac{da}{dN} = C(\Delta K)^m \tag{5.21}$$

where *C* and *m* are constants resulting from the linear regression analysis.

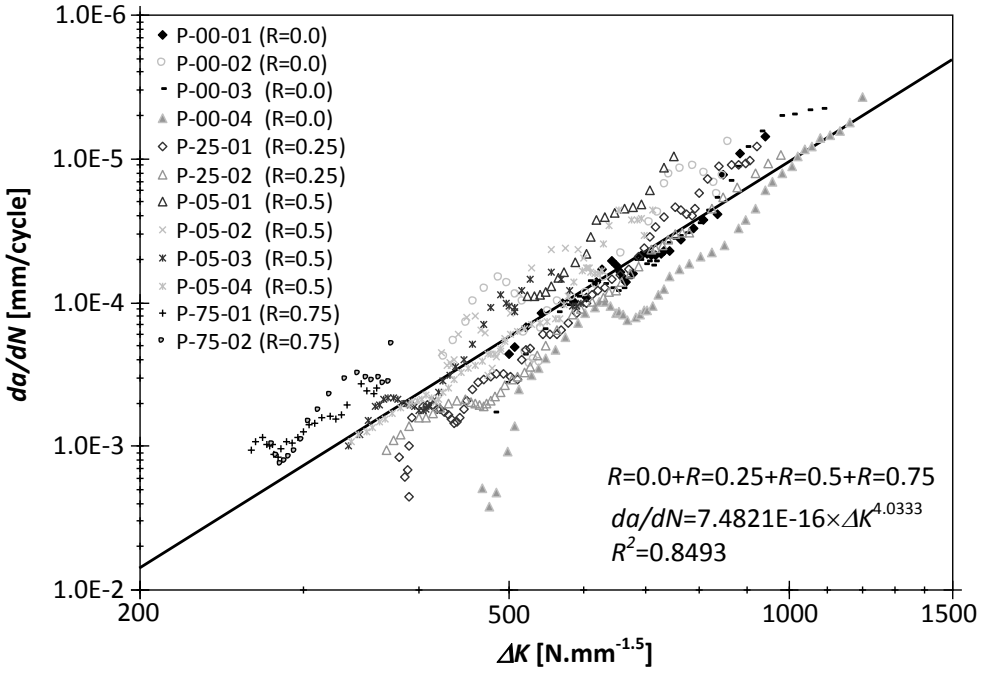

a)

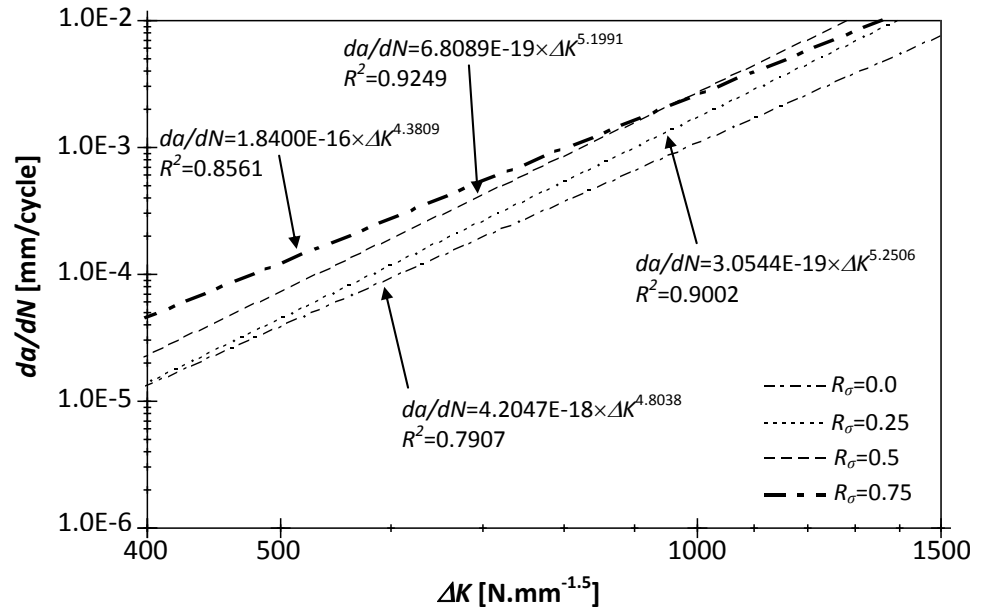

b)

Figure 5.8 – Fatigue crack propagation data obtained for the material from the Fão bridge: a) Experimental data; b) Paris correlations for each stress R_σ-ratio.

The fatigue crack propagation data of the materials from Fão and Eiffel bridges shows important scatter due to the significant amount of heterogeneities that characterizes the puddle irons.

More details about the fatigue properties evaluation, concerning materials from the Eiffel and Fão bridges, are given in Chapter III and reference [19].

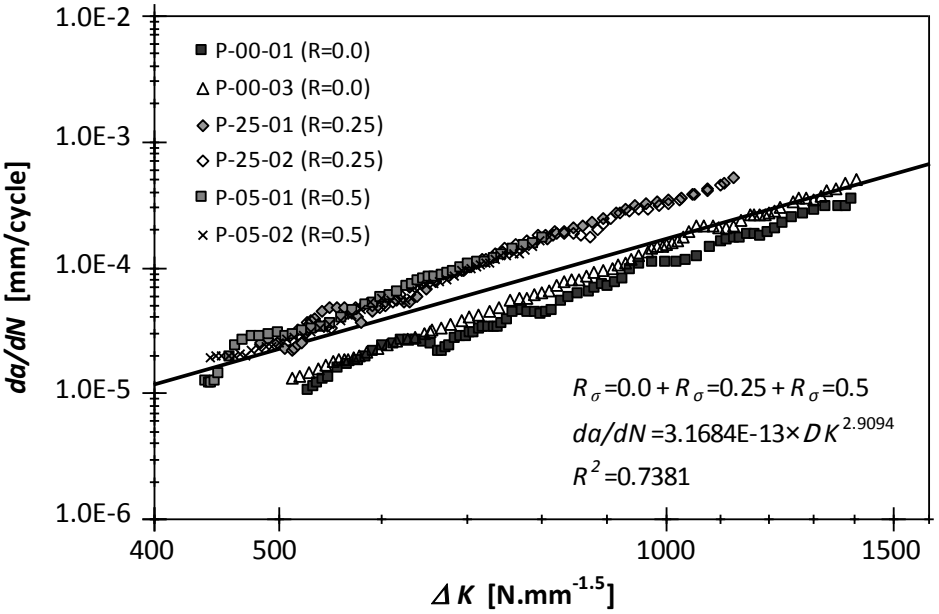

a)

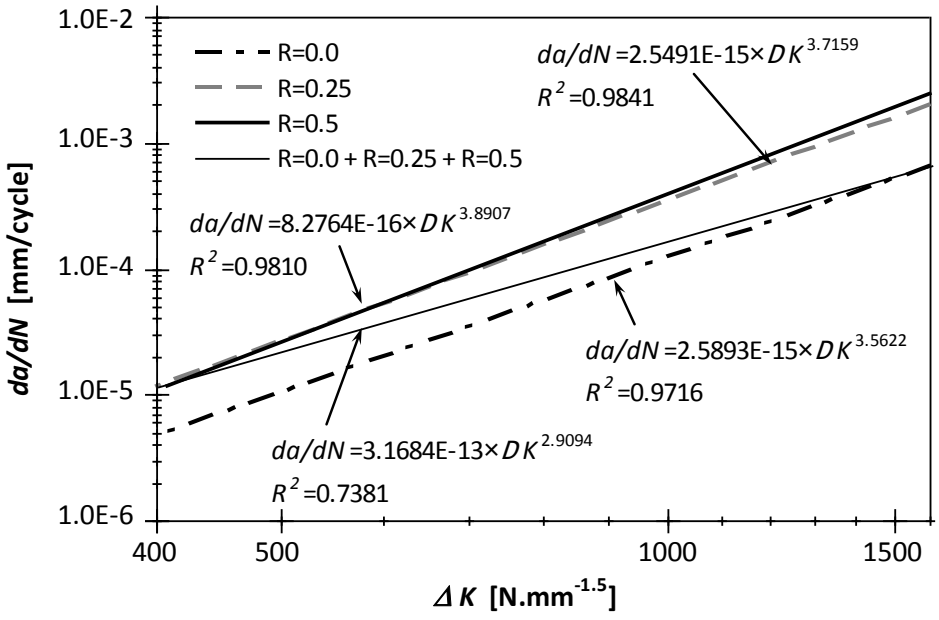

b)

Figure 5.9 – Fatigue crack propagation data obtained for the S355 steel:
a) Experimental data; b) Paris correlations for each stress R_σ-ratio.

Figure 5.9 illustrates the effects of the stress ratio on fatigue crack propagation rates, for the S355 steel grade. An increase in fatigue crack propagation rates is clear, when the stress ratio changes from 0 to any of the positive stress ratios considered in the experimental program. Also, it is clear that all the positive stress ratios resulted in similar

crack propagation rates. This behaviour is consistent with a crack closure effect that occurs in between R_σ=0.0 and R_σ=0.25. For R_σ=0.0 there is some crack closure, so that the applied stress intensity factor range is not fully effective. On the contrary, for R_σ=0.25 and higher, no crack closure occurs and the applied stress intensity factor range is fully effective. Details about the properties evaluation can be found in reference [20].

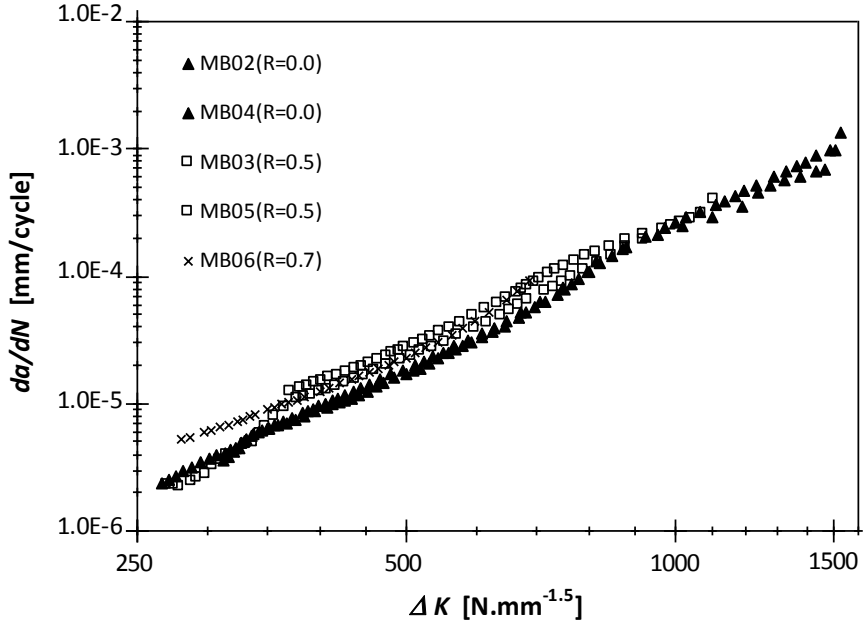

a)

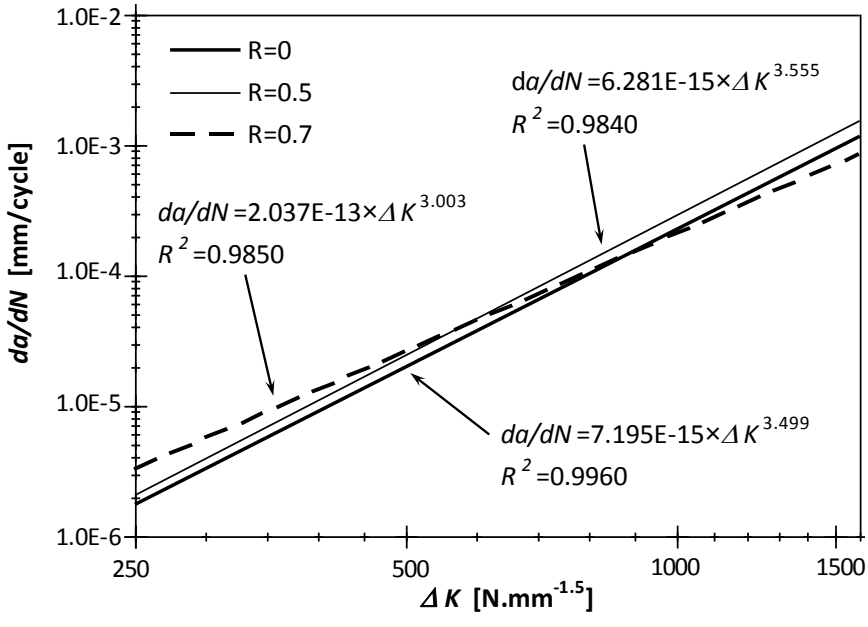

b)

Figure 5.10 – Fatigue crack propagation data obtained for the P355NL1 steel:

a) Experimental data; b) Paris correlations for each stress R_σ-ratio.

Figures 5.10a) and 5.10b) represent the experimental data and the Paris law correlations for each stress ratio of the P355NL1 steel, respectively. The crack propagation rates are only slightly influenced by the stress ratio. Higher stress ratios result in higher crack growth rates. The lines representing the Paris law, for R_σ=0.0 and R_σ=0.5, are approximately parallel to each other.

On the other hand, the line representing the Paris law for R_σ=0.7 converges to the other lines as the stress intensity ranges increases. However, the crack propagation rates for R_σ=0.7 could never be considered lower than the crack propagation rates for the other stress ratios, as suggested by Fig. 5.10b), since the failure of the CT specimen will occur before that can happen [21]. In general, the stress ratio effects are more noticeable for lower ranges of the stress intensity factors. For higher stress intensity factor ranges, the stress ratio effect tends to vanish.

5.4.3. p-SWT-N and p-ε_a-N fields

The probabilistic *SWT-N* and *p-ε_a-N* models [22,37] are presented in section 5.2.3 to describe the strain-life field of the materials, based on Weibull distribution.

Figures 5.11 to 5.14 show the *p-SWT-N* and *p-ε_a-N* fields that are identified for the materials from Fão and Eiffel bridges, the S355 construction steel and the P355NL1 pressure vessel steel, using the experimental data from the fatigue tests of smooth specimens. These tests were performed for strain ratios, R_ε=-1, for the S355 steel and the material from the Eiffel bridge, and for the strain ratios R_ε=0 and R_ε=-1, for the P355NL1 steel and the material from the Fão bridge. The constants of the Weibull fields are also included in the figures, in particular the threshold constants (B and C) and the Weibull parameters (β, λ and δ). The Weibull fields show a hyperbolic behaviour with vertical and horizontal asymptotes. Although the horizontal asymptote has a physical background as fatigue limit, the meaning of the vertical asymptote may be questionable, which requires care for extrapolations to lives lower than those of the experimental data used in the identification process.

Both *p-SWT-N* and *p-ε_a-N* fields produce a good fitting of the experimental data. The *SWT* experimental parameter was identified through the analysis of the stabilized or half-life

pseudo-stabilized hysteresis loops of the materials, for each performed test. The maximum stress and strain ranges of the hysteresis cycles were used to compute the *SWT* parameter. The statistical confidence intervals of the input parameters of the probabilistic model are not possible to be estimated analytically due to the complexity of the Weibull description of the complete ε_a-*N* field. However, and despite not included in this chapter, there is the possibility of using the bootstrap technique to compute estimates of the confidence intervals for the input parameters [36].

The number of cycles to failure, N_f, reported in Figures 5.11 to 5.14, corresponds to the macroscopic crack initiation in tested specimens. The fatigue crack propagation was excluded through the analysis of the changes verified in the cyclic stress-strain histories, which are not likely due to cyclic strain hardening/softening. This concern in the analysis of the experimental strain–life data seeks the increasing of the representativeness of the *p*-*SWT*-*N* and *p*-ε_a-*N* fields for the fatigue behaviour of crack tip elements, with smaller size than specimens used in the testing program.

The *p*-ε_a-*N* and *p*-*SWT*-*N* fields of the material from the Eiffel and Fão bridges are presented in the Figures 5.11 and 5.12, respectively, and the constants of the Weibull fields included.

Consequently, both *p*-ε_a-*N* and *p*-*SWT*-*N* fields of the S355 and P355NL1 steels are presented in Figures 5.13 and 5.14. The extrapolations using the Weibull field should be avoided for high and essentially low fatigue lives. Since the number of cycles to fail the representative volume element, in the crack propagation regime, may be low, it was decided to postulate some fatigue data at the low to very low-cycle fatigue domain, using the deterministic Morrow equation of the material for that purpose. The Morrow equation may be considered more reliable to perform extrapolations for very low number of cycles than the Weibull field. In this way, the Weibull fields presented in the Figures 5.13 and 5.14 may be used for a wider range of fatigue lives, for the S355 steel and P355NL1, respectively [38]. The constants of the Weibull fields are also pointed out in these figures.

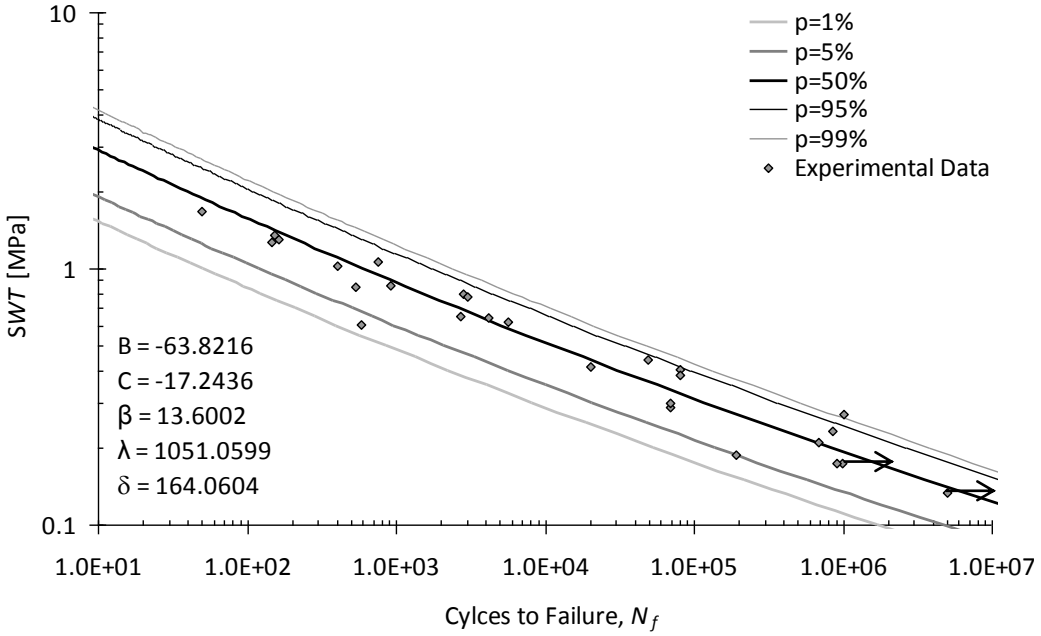

a)

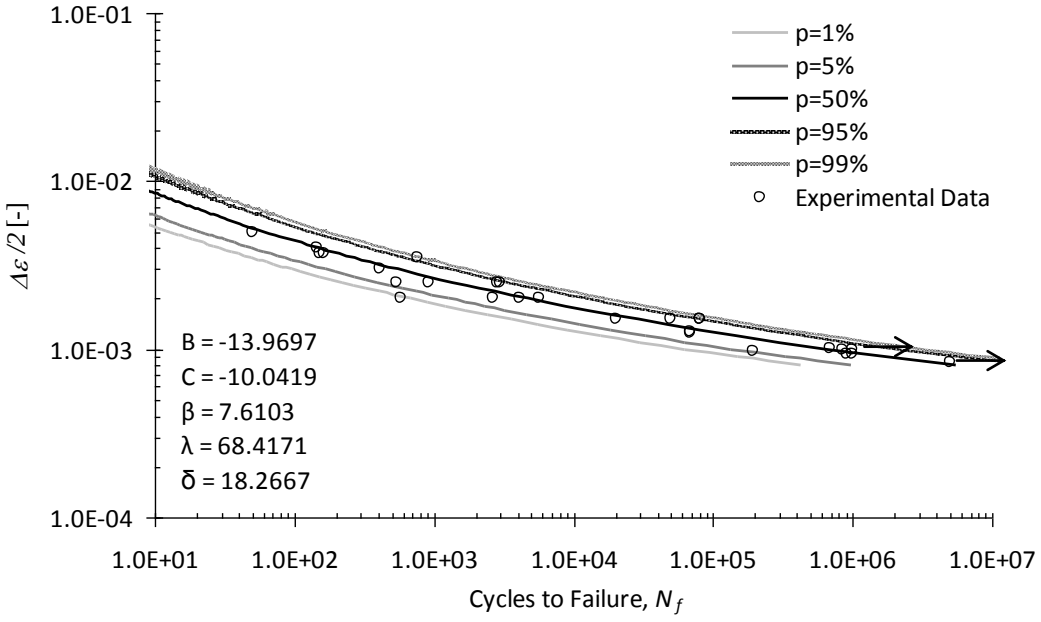

b)

Figure 5.11 – Probabilistic fatigue field of the material from the Eiffel bridge:

a) *p-SWT-N* field; b) *p-*ε_a*-N* field.

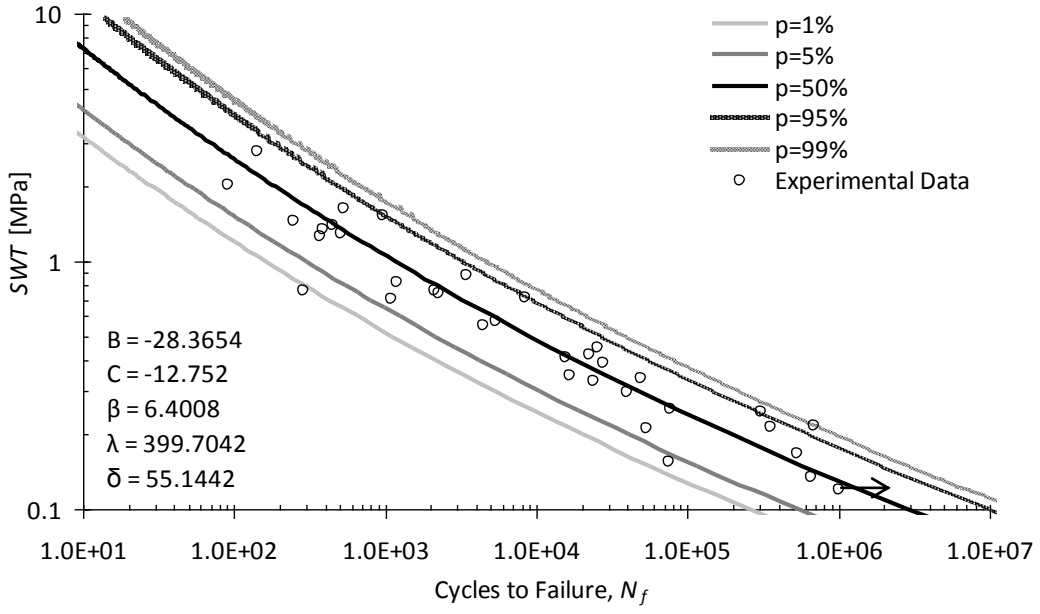

a)

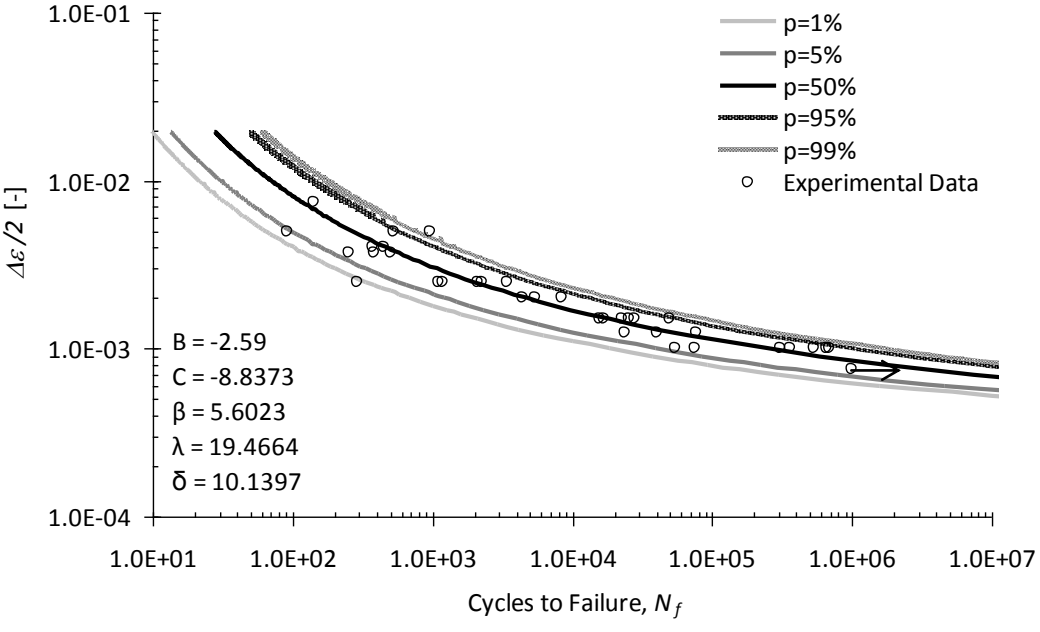

b)

Figure 5.12 – Probabilistic fatigue field of the material from the Fão bridge:

a) *p-SWT-N* field; b) *p-*ε_a*-N* field.

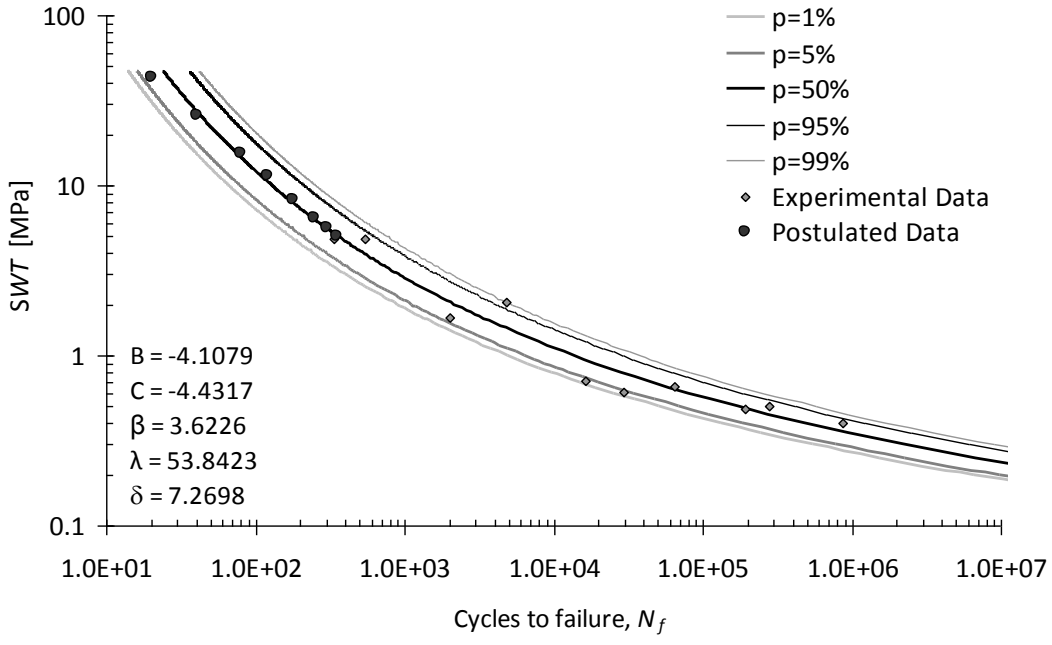

a)

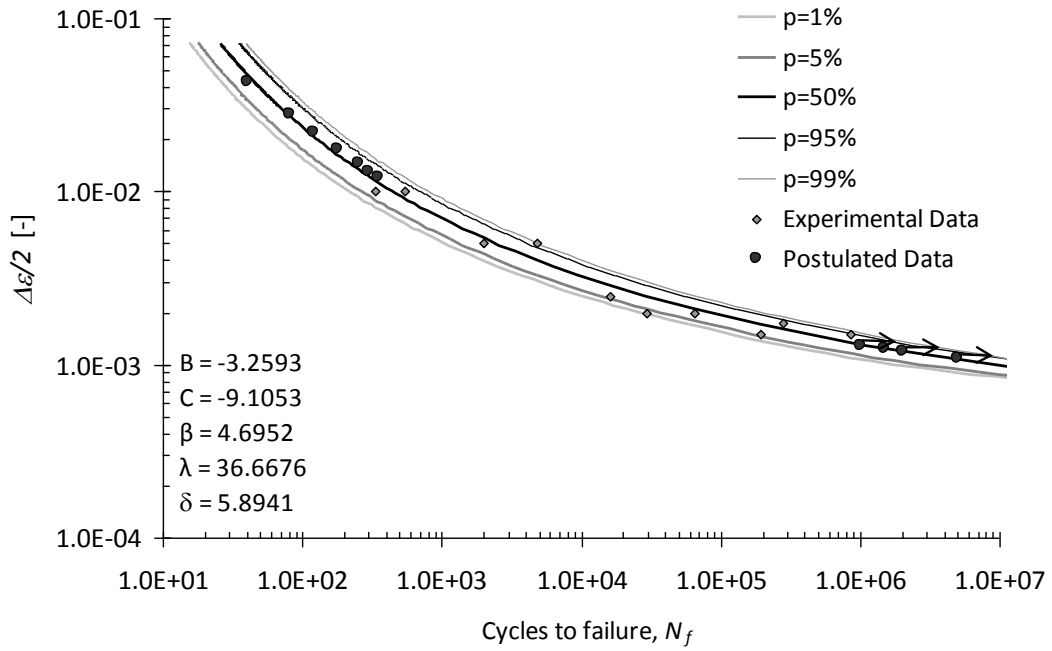

b)

Figure 5.13 – Probabilistic fatigue field for the S355 steel: a) *p-SWT-N* field; b) *p-*ε_a*-N* field.

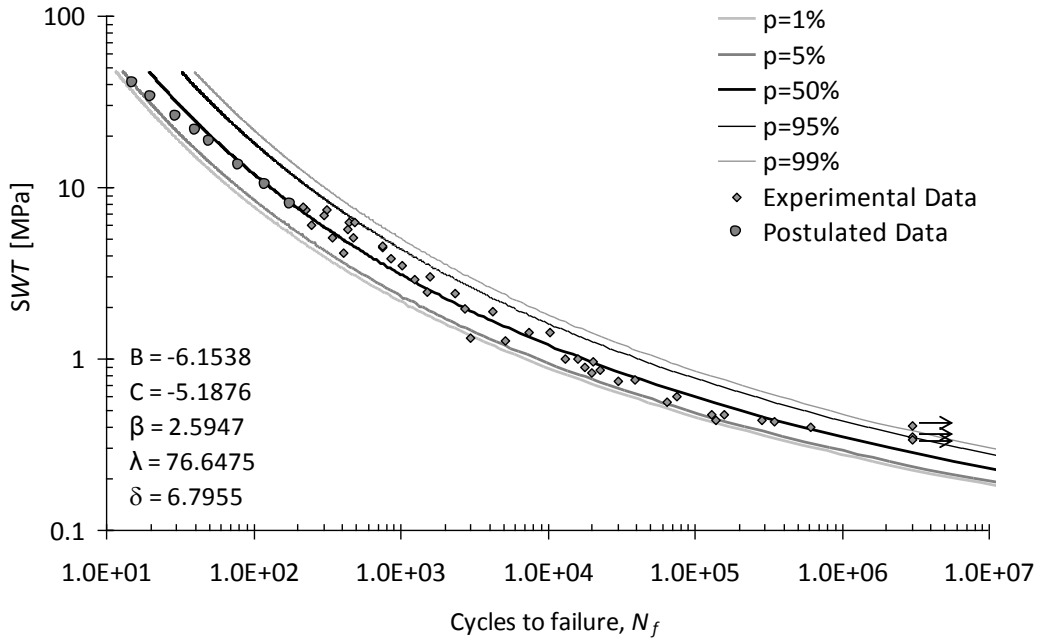

a)

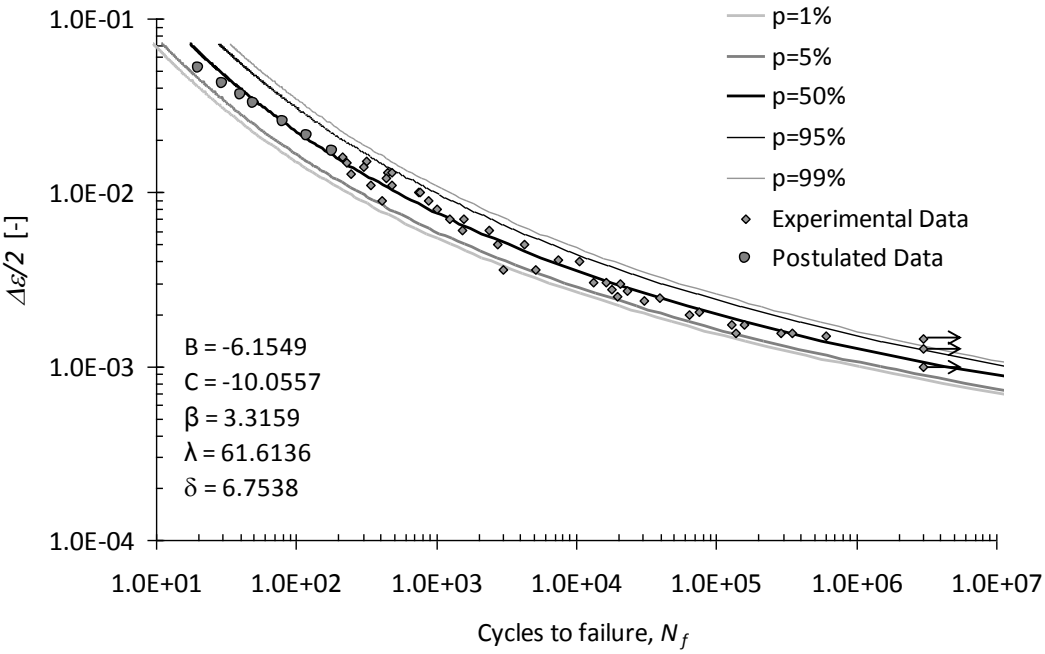

b)

Figure 5.14 – Probabilistic fatigue field for the P355NL1 steel: a) *p-SWT-N* field; b) *p-*ε_a*-N* field.

5.5. PROBABILISTIC FATIGUE CRACK PROPAGATION RATE PREDICTIONS

The prediction of the probabilistic fatigue crack propagation fields is performed through the application of the *UniGrow* model for the CT geometry. Additionally, the elementary material block size, ρ^*, is required, and was evaluated by a trial and error procedure in order to result a good agreement between the predicted and experimental *da/dN vs.* ΔK data, for the materials under consideration. The probabilistic fatigue crack propagation fields are evaluated using, alternatively, the probabilistic material ε_a–*N* and *SWT*–*N* fields. The procedure to generate probabilistic fatigue crack propagation fields was described in section 5.3.

5.5.1. Finite element analysis of the CT geometry

In order to assess the accuracy of the simplified elastoplastic analysis, for the residual stress estimation, a bi-dimensional finite element model of the CT specimen was built and used in an elastoplastic finite analysis. A very refined mesh at the crack tip region is required, in order to model the crack tip notch radius, ρ^* (refer to Figure 5.1b) for geometric details). Figure 5.17 illustrates the typical finite element mesh of the CT geometry with the respective boundary conditions. Only the half of the geometry is modelled, taking into account the existing plane of symmetry. Plane stress conditions were assumed since the thickness of specimens is relatively reduced (B=4.5mm for the material from Eiffel bridge and the 355NL1 steel and B=8mm for the material from the Fão bridge and the S355 steel). Plane stress quadratic triangular elements (6-noded elements) were used in the analysis with full integration. In order to simulate the pin loading, rigid-to-flexible frictionless contact was selected. The pin was modelled as a rigid circle controlled by a pilot node.

All numerical simulations were carried out using the ANSYS® 12.0 code [30]. The 6-noded plane element adopted in the FE analyses was the PLANE181 element available in the ANSYS® library. The contact and target elements used in the pin-loading simulation were, respectively, the CONTA172 and TARGE169 elements available in ANSYS® [30]. A parametric model was built using the APDL language. The surface of the holes was modelled as flexible, using CONTA172 elements. The Augmented Lagrange contact

algorithm was used. The associative Von Mises (J2) yield criterion with multilinear kinematic hardening was used to model the plastic behaviour. The multilinear kinematic hardening uses the Besseling model, also called the sublayer or overlay model, so that the Bauschinger effect is included. The plasticity model was fitted to the stabilized or half-life pseudo stabilized cyclic curve of the materials. The von Mises yield criterion with multilinear kinematic hardening was adopted to model the plastic behaviour. The plasticity model was fitted to the cyclic curve of the material.

The finite element model allowed the variation of the crack length, the crack tip radius and the mesh density, for the various case studies. A very refined mesh was created at crack tip region, with average element sizes about one order of magnitude below the crack tip radius, in order to allow a good representation of the crack tip radius. The mesh size was progressively coarsened with increasing distance to the crack tip. More refined meshes at the crack vicinity region and very long time consuming elastoplastic simulations were tested but they did not result in significant changes in elastic stress, being consequently avoided.

The residual stresses were computed from the stress field at the end of the unloading step, in case of the finite element analysis, and from the subtraction of the cyclic stress range to the maximum stress, in case of the analytical analysis. The multiaxial Neuber's approach [15] was implemented in the analytical one.

The finite element model was initially applied to perform elastic and elastoplastic stress analyses in order to allow the comparison of the elastic and elastoplastic stress distributions by the Creager-Paris solution [24] and multiaxial Neuber approach [15], respectively.

According to the UniGrow model, the compressive residual stresses computed ahead of the crack tip are assumed to be applied symmetrically, in the crack faces. Using the weight function method [26], the residual stress intensity factor, K_r, was computed for the stress R-ratios considered in the experimental program.

5.5.1.1. Material from Eiffel bridge

Figure 5.15 shows the CT geometry of the material from the Eiffel bridge adopted in the finite element analysis [37,39]. Figure 5.16 shows the superposition of the Ramberg-Osgood relation [34] with the response of a elastoplastic finite element model reproducing a uniaxial stress state, for the material from the Eiffel bridge. Table 5.3 presents the maximum elastic stresses (σ_x and σ_y) ahead of the crack tip, resulting from distinct mesh densities, for the material from the Eiffel bridge. The mesh densities are illustrated in Figure 5.17. Mesh 1 was adopted in this investigation. Table 5.3 also compares the maximum stress values obtained with distinct meshes.

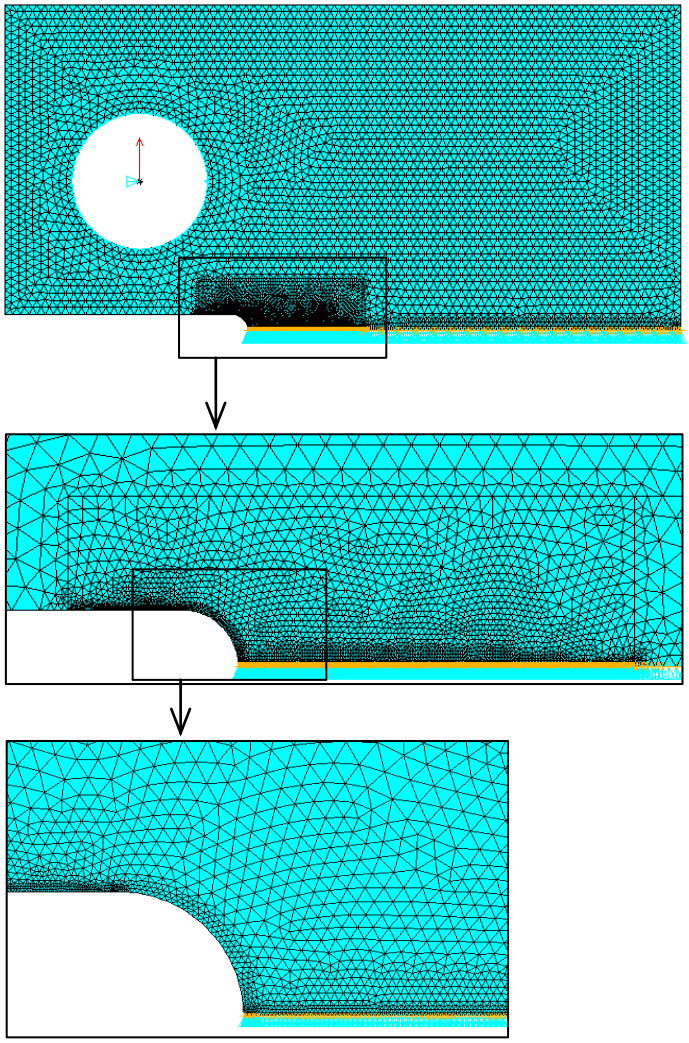

Figure 5.15 – Finite element meshes of a CT specimen, consisting in six-noded quadratic triangular plane stress elements, used to model the material from the Eiffel bridge.

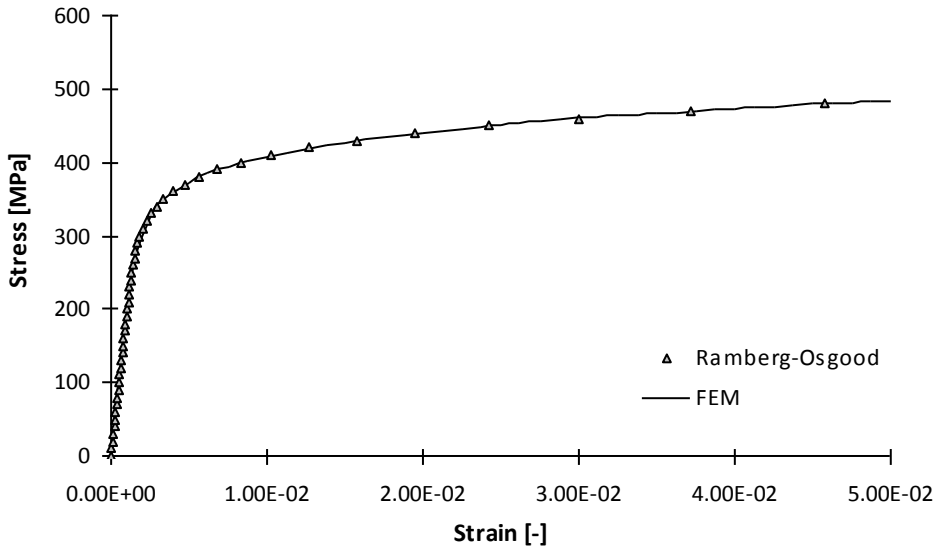

Figure 5.16 – Cyclic stress-strain relation obtained for the material from the Eiffel bridge: Ramberg-Osgood representation vs. finite element response based on multilinear kinematic hardening [37,39].

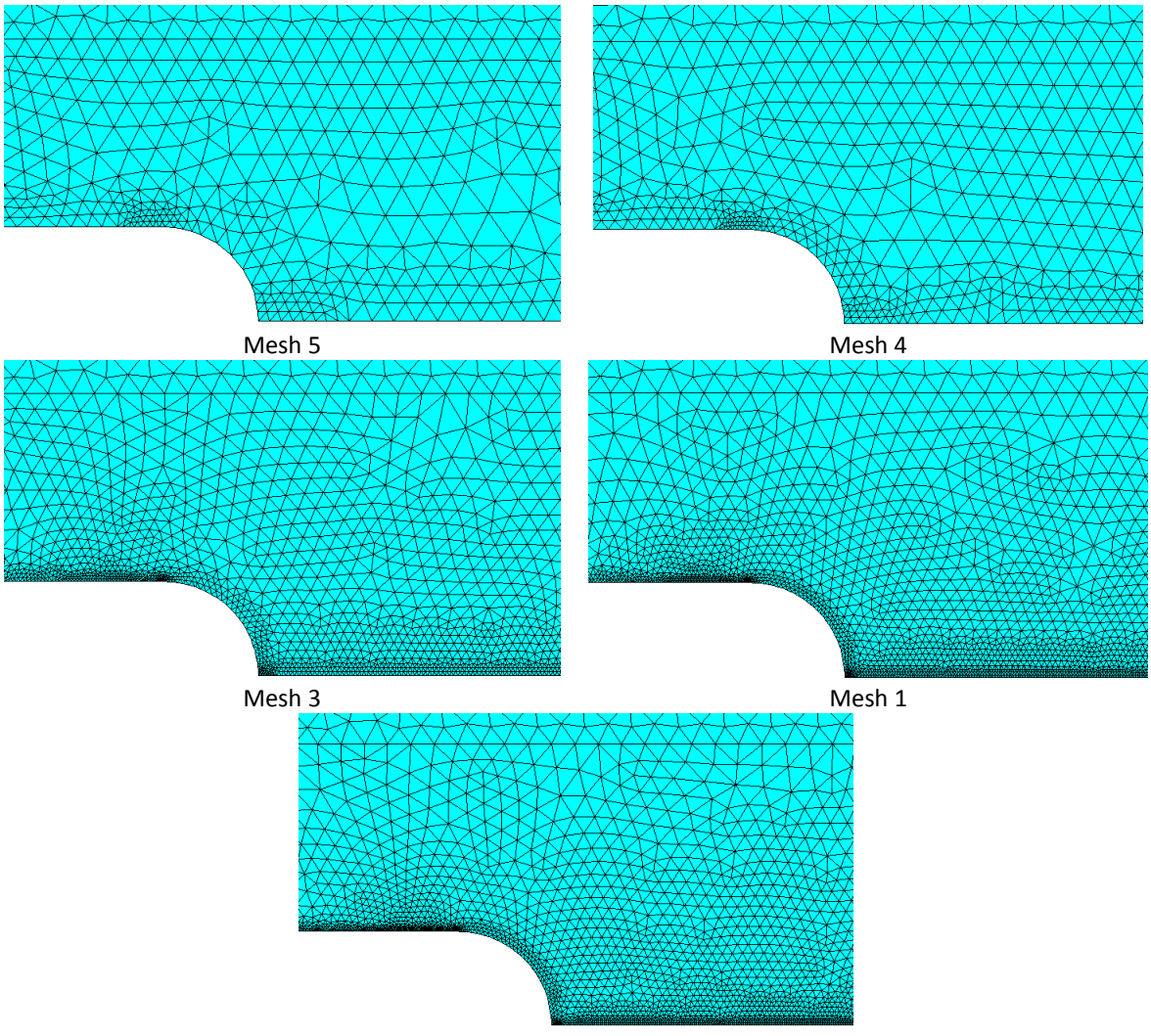

Figure 5.17 – Finite element meshes used in the convergence study performed for the CT specimen made of material from the Eiffel bridge.

Table 5.3 – Maximum elastic stresses for distinct finite element mesh densities for the material from the Eiffel bridge (F_{max}=2882.7N, a=8mm, ρ^*=1200µm).

Maximum stresses	mesh 5	mesh 4	mesh 3	mesh 1	mesh 2
σ_y [MPa]	457.7	458.4	459.4	459.4	459.4
Dev. [%]	-0.37	-0.22	0.00	-	0.00
σ_x [MPa]	97.7	97.5	97.6	97.5	97.5
Dev. [%]	0.14	0.00	0.01	-	0.00

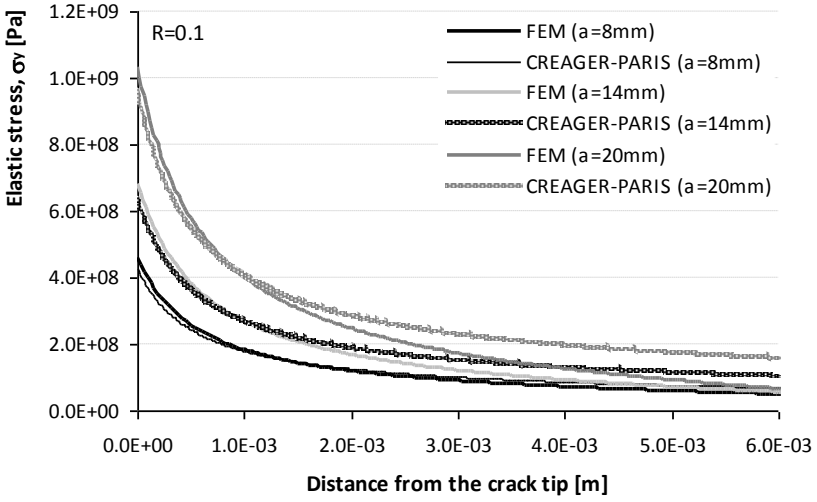

a)

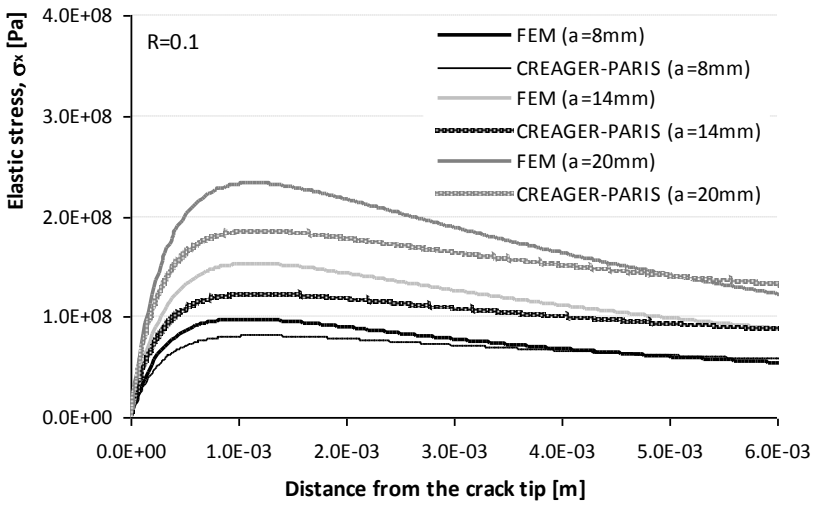

b)

Figure 5.18 – Comparison between analytical and numerical results of the elastic stress distribution ahead of the crack tip and along the crack line (y=0) for CT specimens made of material from the Eiffel bridge: a) σ_y stress distribution (F_{max}=2882.7N, ρ^*=1200µm); b) σ_x stress distribution (F_{max}=2882.7N, ρ^*=1200µm).

Figure 5.18 compares the elastic stress distributions from the numerical and analytical solutions for the CT specimens made of material from the Eiffel bridge. The results were computed for a crack tip radius, $\rho^*=12\times10^{-4}$m=1200µm, which was found to be the best

value for the material from the Eiffel bridge – it gives the best predictions for the crack growth rates, based on *SWT* damage parameter, as will be verified hereafter.

Figure 5.19 represents the elastoplastic stress distribution ahead of the crack tip, along the line aligned with the crack faces (y=0). The same conditions of Figure 5.18 were used.

The residual stress distributions were computed by means of the analytical and numerical solutions and are compared in Figure 5.20, for distinct crack sizes and stress R-ratios, for the material from the Eiffel bridge. An elementary material block size, $\rho^*=12\times10^{-4}$m was selected.

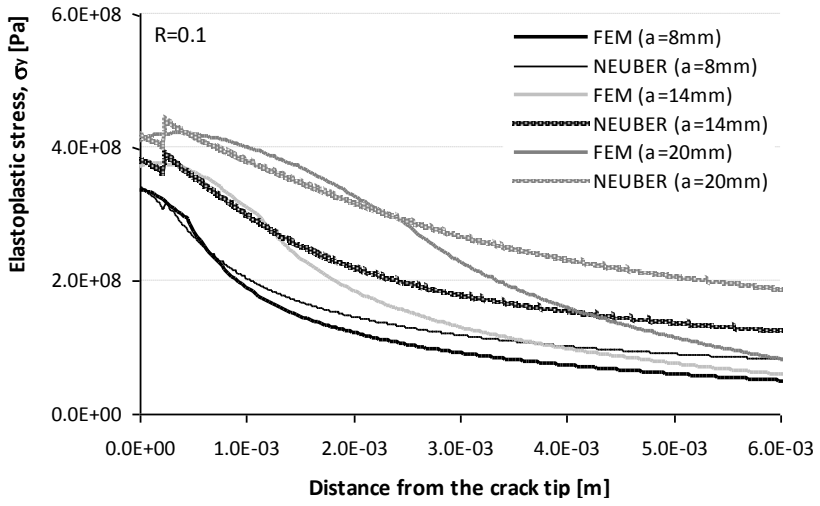

a)

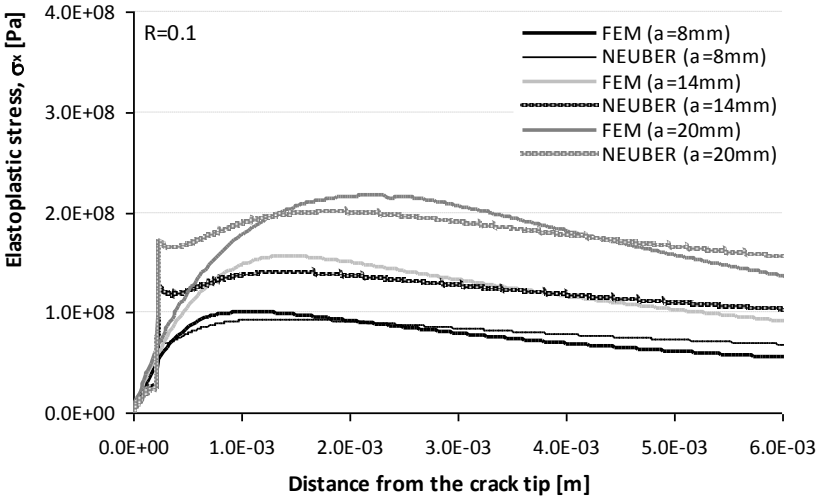

b)

Figure 5.19 – Comparison between analytical and numerical results of the elastoplastic stress distribution ahead of the crack tip in the crack line (y=0) for CT specimens made of material from the Eiffel bridge: a) σ_y stress distribution (F_{max}=2882.7N, ρ^*=1200μm); b) σ_x stress distribution (F_{max}=2882.7N, ρ^*=1200μm).

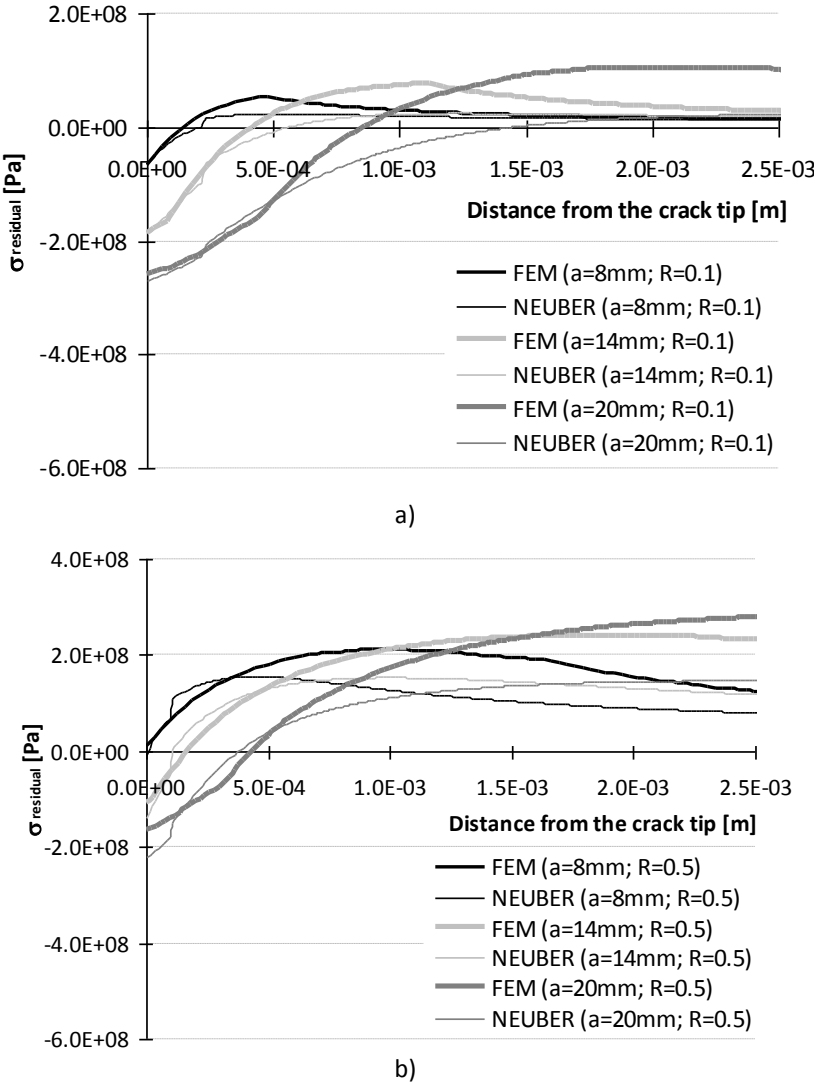

Figure 5.20 – Comparison between analytical and numerical results of the residual stress distribution ahead of the crack tip in the crack line (y=0) for CT specimens made of material from the Eiffel bridge: a) R_σ=0.1 (F_{max}=2882.7N, ρ^*=1200µm); b) R_σ=0.5 (F_{max}=4815.2N, ρ^*=1200µm).

Figure 5.21 illustrates the stress and strain fields along the y (load) direction, obtained for the CT specimens using the elastoplastic finite element analysis. The results were obtained using the properties of the material from the Eiffel bridge and assuming a material representative element of ρ^*=1200µm, a crack size a=14mm, a maximum load F_{max}=2882.7N, and a stress R-ratio, R_σ=0.1. The stress and strain fields are shown at the end of the first loading reversal and at the end of the unloading reversal. In Figure 5.21, the compressive stress field at the crack tip vicinity and also at some extension of the crack wake can be clearly distinguished.

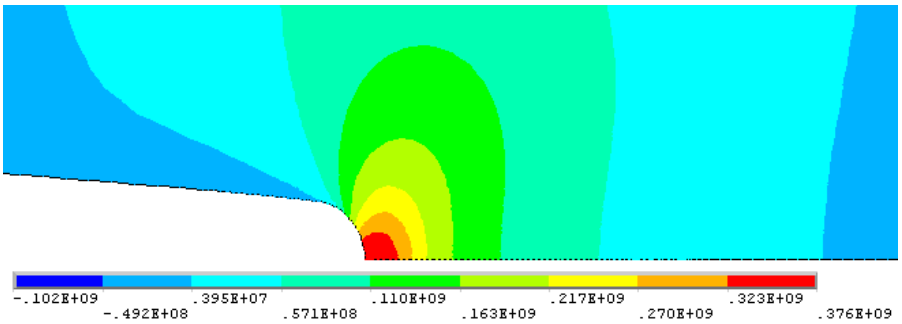

a) Stress field, in MPa, at the end of the loading reversal.

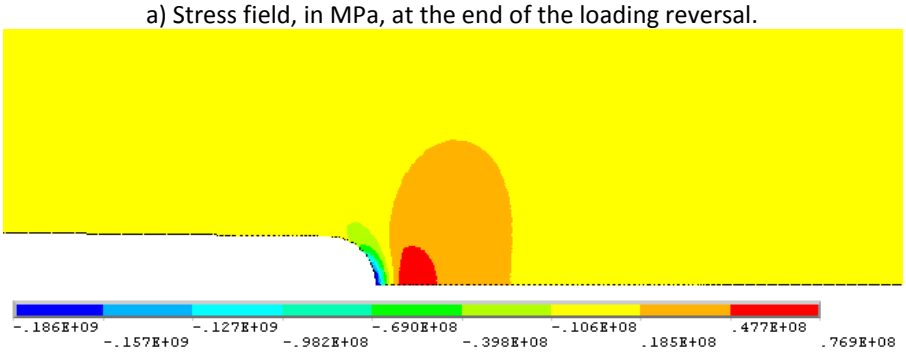

b) Stress field, in MPa, at the end of the first unloading reversal.

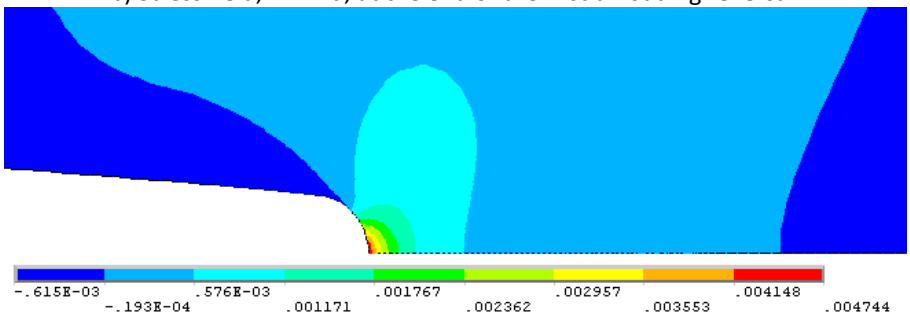

c) Strain field at the end of the loading reversal.

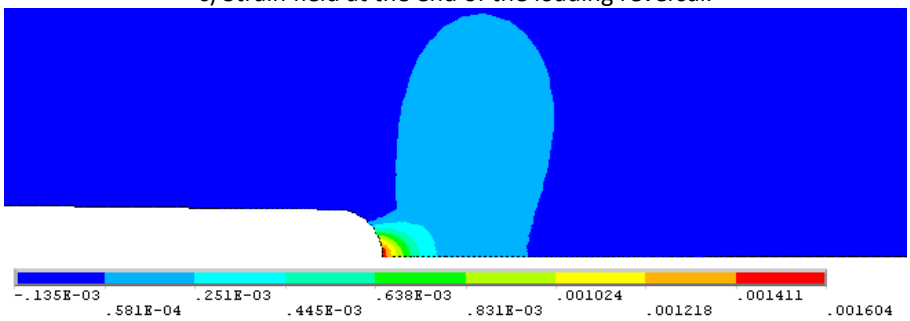

d) Strain field at the end of the first unloading reversal.

Figure 5.21 – Stress and strain fields, along the load direction, obtained for the CT specimens of the material from the Eiffel bridge, resulting from elastoplastic finite element analysis (F_{max}=2882.7N, ρ^*=1200µm, a=14mm, R_σ=0.1).

The compressive residual stress distributions from the numerical analysis were used to compute the residual stress intensity factor. The resulting stress intensity factors are presented in terms of the applied stress intensity factor range, instead of the crack size, as presented in Figure 5.22, for two distinct elementary material block sizes, and stress ratios, for the material from the Eiffel bridge.

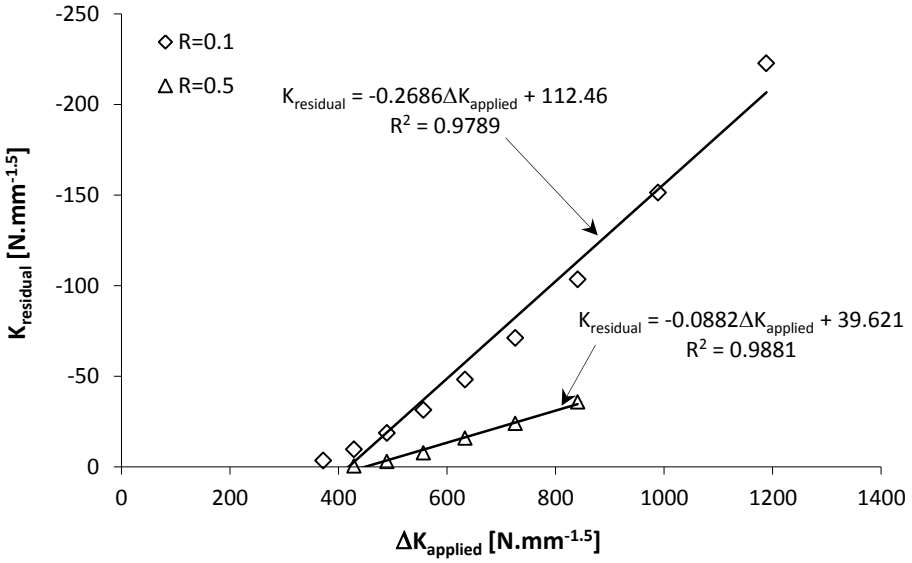

a)

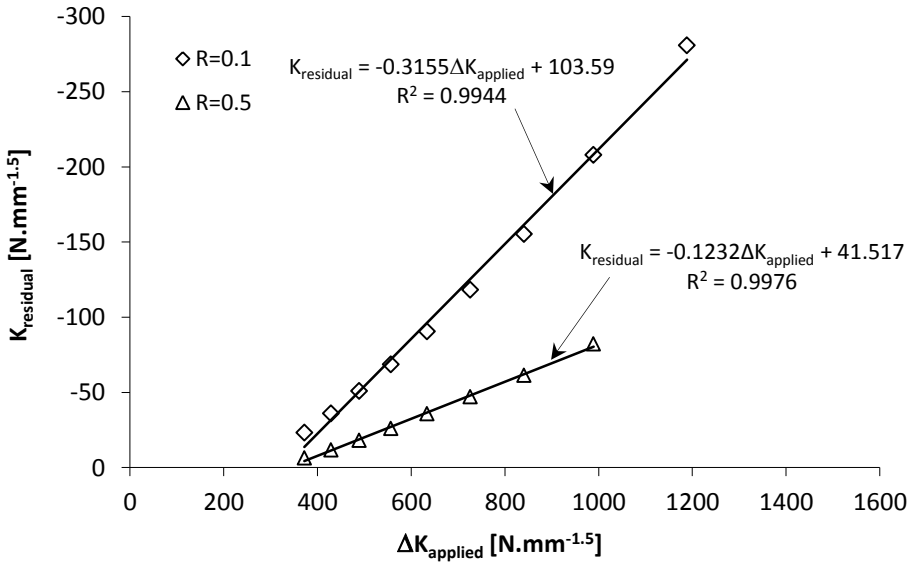

b)

Figure 5.22 – Residual stress intensity factor as a function of the applied stress intensity factor range obtained for the material from the Eiffel bridge: a) ρ^*=1200µm; b) ρ^*=400µm.

5.5.1.2. Material from Fão bridge

Figure 5.23 shows the finite element mesh of the CT geometry of the material from the Fão bridge adopted in the finite elements analysis [37]. A plasticity model for the material from the Eiffel bridge was adopted and Figure 5.24 compares the Ramberg-Osgood relation [34] with the response of a finite element model, reproducing a uniaxial stress state. Table 5.4 presents the maximum elastic stresses (σ_x and σ_y) ahead of the crack tip, resulting from distinct mesh densities, for the material from the Fão bridge. The mesh

densities are illustrated in Figure 5.25 and the Mesh 1 was selected for the numerical analysis. The results of the maximum stress values are compared between the mesh 1 and the other meshes, and given in Table 5.4.

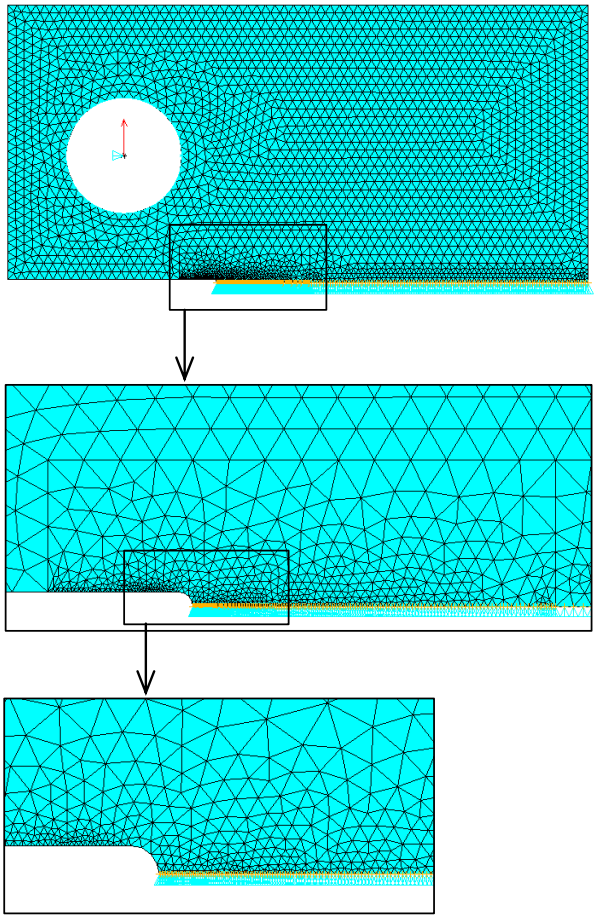

Figure 5.23 – Finite element meshes of a CT specimen, consisting in six-noded quadratic triangular plane stress elements, used to model the material from the Fão bridge.

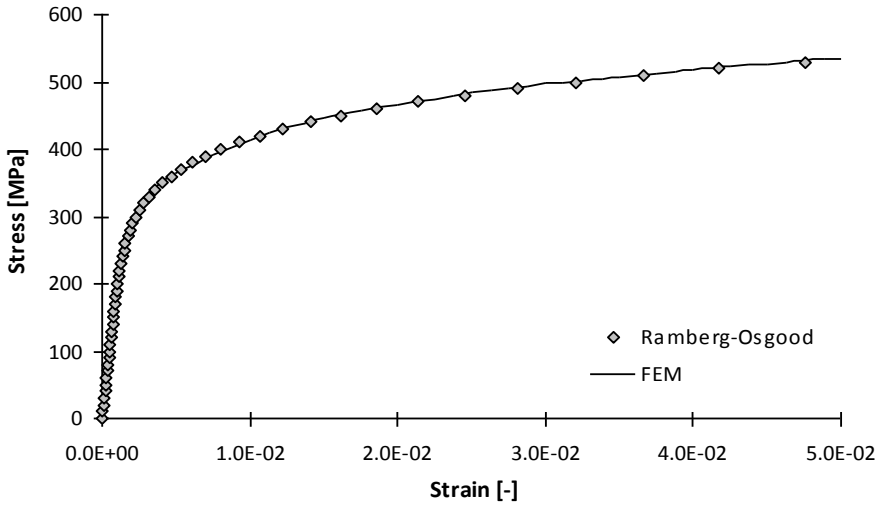

Figure 5.24 – Cyclic stress-strain relation obtained for the material from the Fão bridge: Ramberg-Osgood representation vs. finite element response based on multilinear kinematic hardening [37].

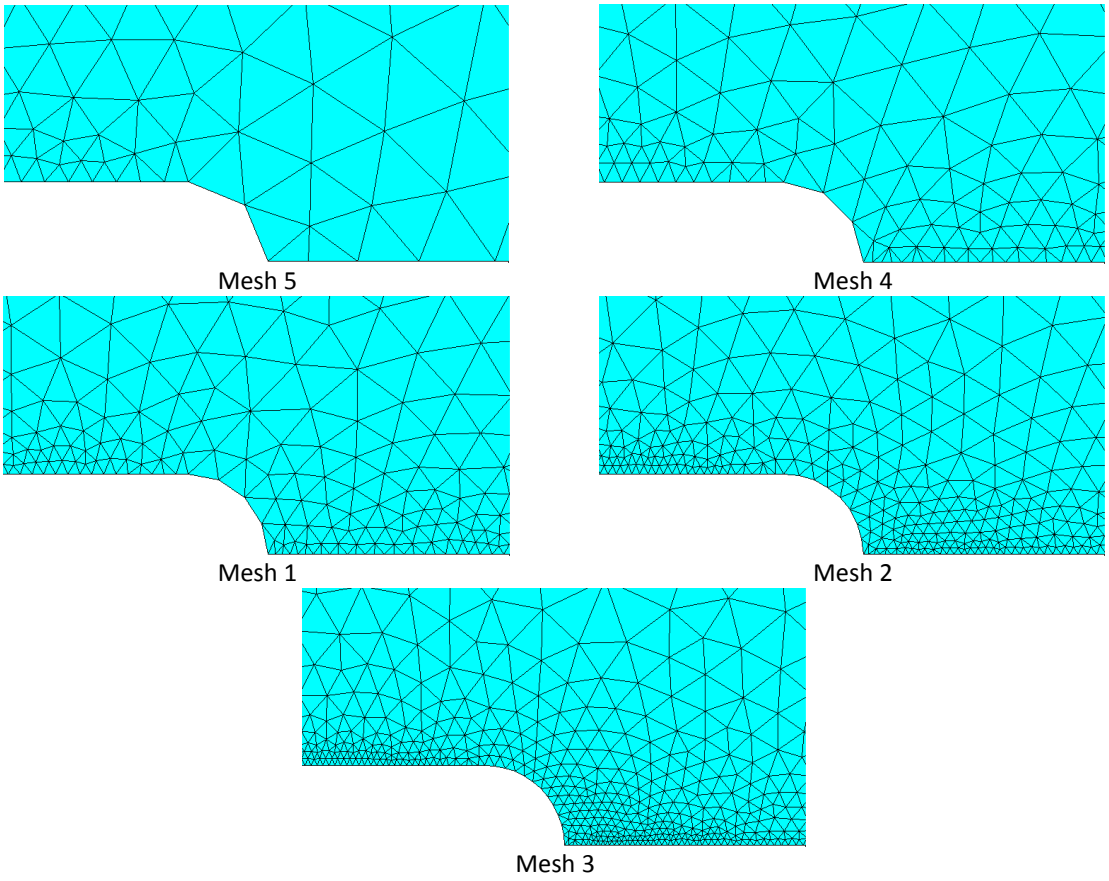

Figure 5.25 – Finite element meshes used in the convergence study performed for the CT specimen made of material from the Fão bridge.

Table 5.4 – Maximum elastic stresses for distinct finite element mesh densities for the material from the Fão bridge (F_{max}=4972.2N, a=10mm, ρ^*=400µm).

Maximum stresses	mesh 5	mesh 4	mesh 1	mesh 2	mesh 3
σ_y [MPa]	609.2	667.6	661.7	656.6	654.9
Dev. [%]	-7.94	0.88	-	-0.77	-1.03
σ_x [MPa]	147.8	145.1	144.6	144.6	144.6
Dev. [%]	2.17	0.34	-	0.01	-0.01

Figures 5.26 and 5.27 compare the elastic and elastoplastic stress distributions from the numerical and analytical solutions for the CT specimens, made of material from the Fão bridge, respectively. The results were computed for a crack tip radius, ρ^*=400 µm, which was found to be the best value for the material of the Fão bridge. This ρ^* parameter gives the best predictions for the crack growth rates, based on the *SWT* damage parameter, as will be verified hereafter [37].

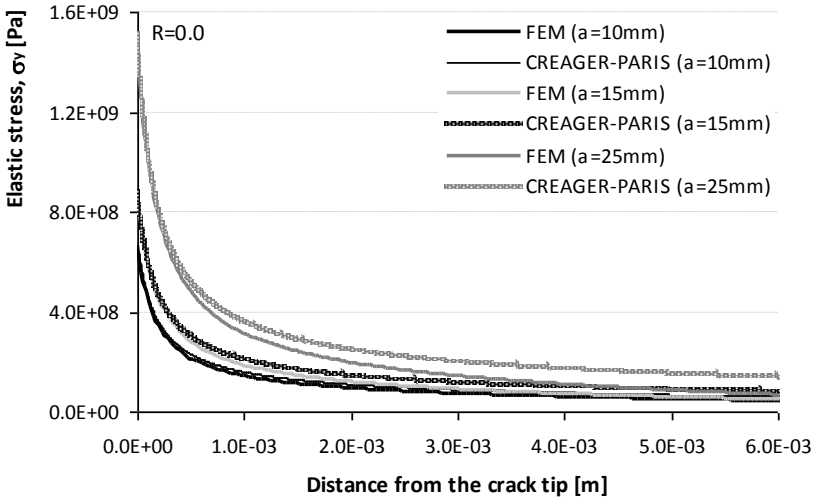

a)

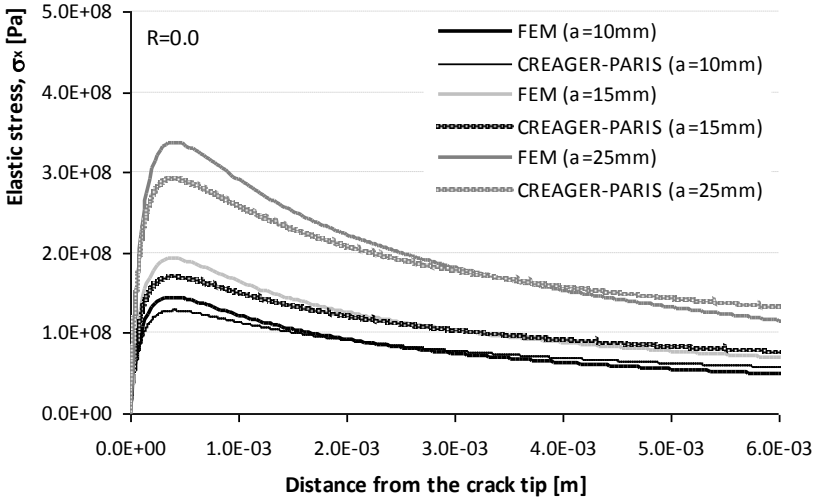

b)

Figure 5.26 – Comparison between analytical and numerical results of the elastic stress distribution ahead of the crack tip and along the crack line (y=0) for CT specimens made of material from the Fão bridge: a) σ_y stress distribution (F_{max}=4972.2N, ρ^*=400μm); b) σ_x stress distribution (F_{max}=4972.2N, ρ^*=400μm).

Figure 5.28 shows the residual stress distributions for distinct crack sizes and stress *R*-ratios, for the material from the Fão bridge, as computed by means of the analytical and numerical solutions, using an elementary material block size, ρ^*=400 μm.

Figure 5.29 illustrates the stress and strain fields along the y (load) direction and assuming a material representative element of ρ^*=400 μm, a crack size a=15mm, a maximum load F_{max}=4972.2N, and a stress *R*-ratio, R_σ=0.0, obtained for the CT specimens using the elastoplastic finite element analysis. The stress and strain fields are shown at the end of the first loading reversal and at the end of the first unloading reversal. In Figure 5.29, the

compressive stress field at the crack tip vicinity and also to some extension of the crack wake can be clearly distinguished.

Using the results of the numerical analysis, particularly the compressive residual stress distribution, the residual stress intensity factor was computed and presented in Figure 5.30 as a function of the applied intensity factor range. This figure presents the results for two distinct elementary material block sizes for the material from the Fão bridge [37], and for three distinct stress ratios.

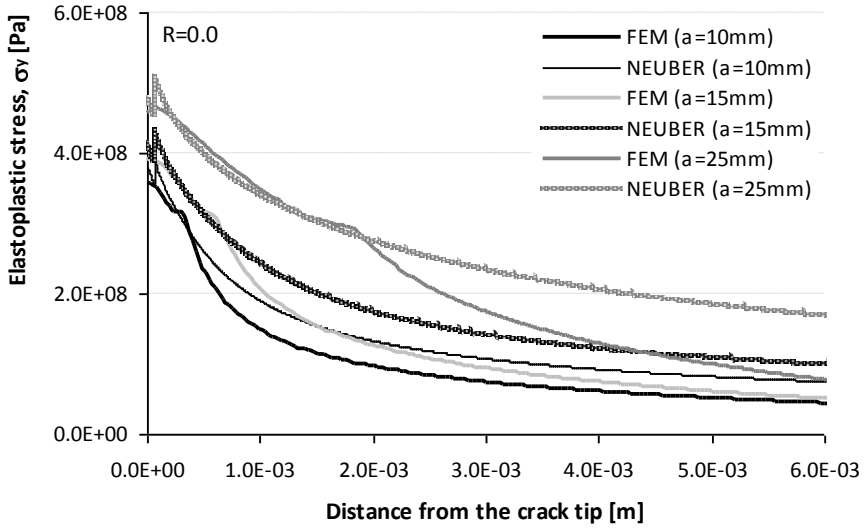

a)

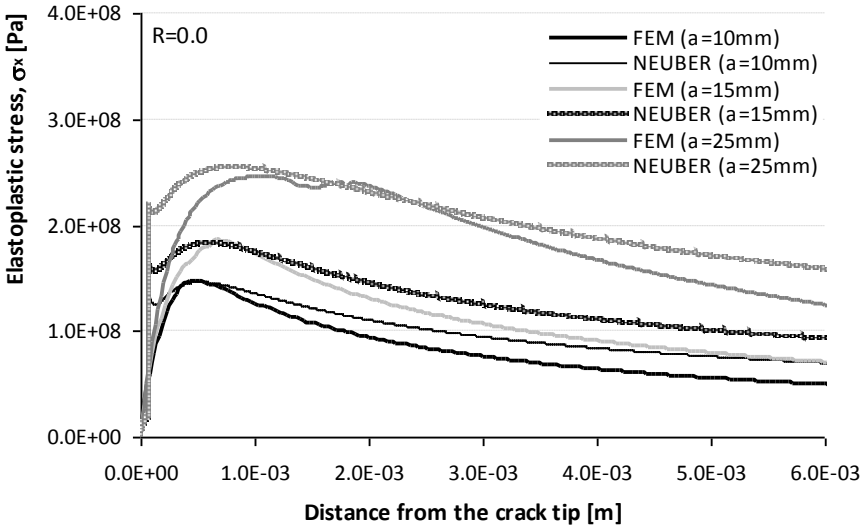

b)

Figure 5.27 – Comparison between analytical and numerical results of the elastoplastic stress distribution ahead of the crack tip in the crack line (y=0) for CT specimens made of material from the Fão bridge: a) σ_y stress distribution (F_{max}=4972.2N, ρ*=400μm); b) σ_x stress distribution (F_{max}=4972.2N, ρ*=400μm).

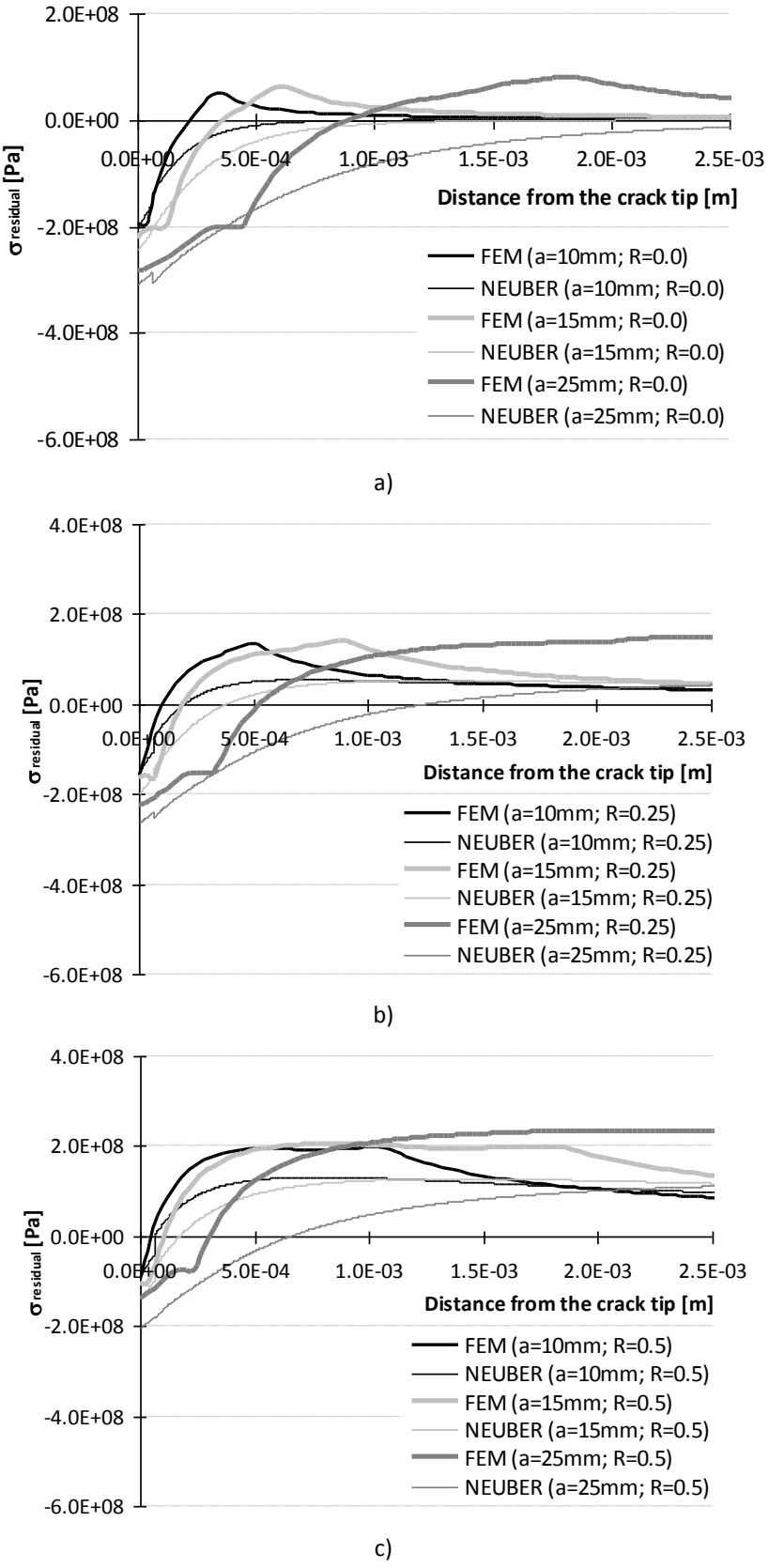

Figure 5.28 – Comparison between analytical and numerical results of the residual stress distribution ahead of the crack tip in the crack line (y=0) for CT specimens made of material from the Fão bridge: a) R_σ=0.0 (F_{max}=4972.2N, ρ^*=400μm); b) R_σ=0.25 (F_{max}=6031.7N, ρ^*=400μm); c) R_σ=0.5 (F_{max}=8455.2N, ρ^*=400μm).

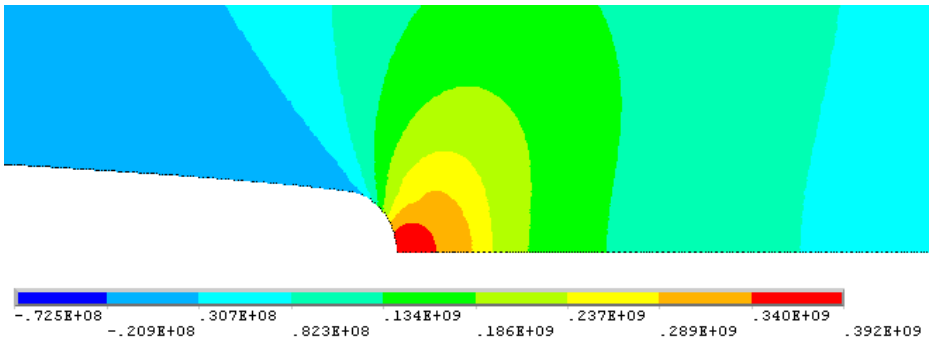

a) Stress field, in MPa, at the end of the loading reversal.

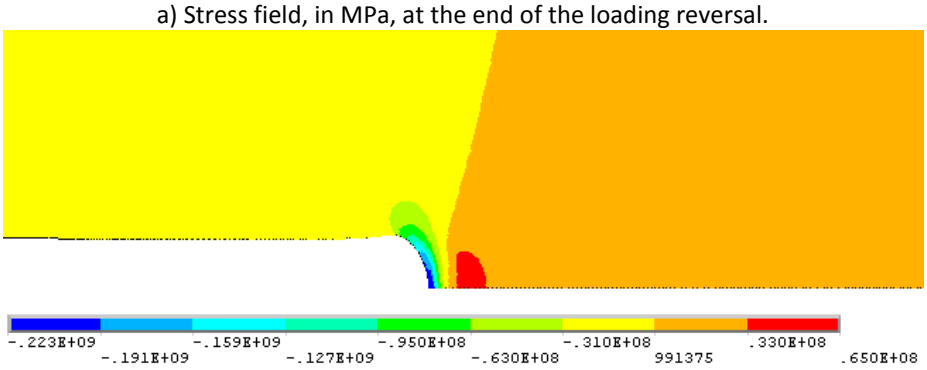

b) Stress field, in MPa, at the end of the first unloading reversal.

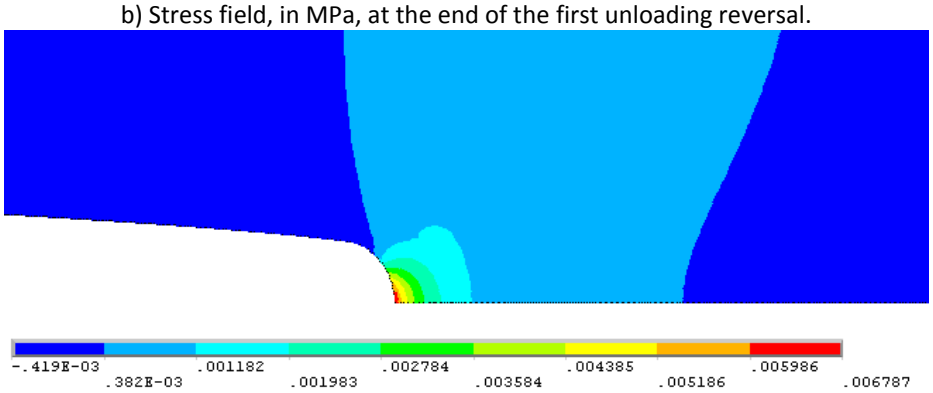

c) Strain field at the end of the loading reversal.

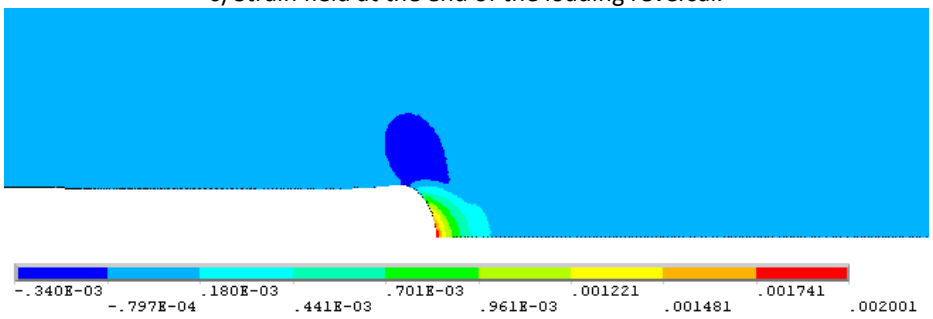

d) Strain field at the end of the first unloading reversal.

Figure 5.29 – Stress and strain fields, along the load direction, obtained for the CT specimens of the material from the Fão bridge, resulting from elastoplastic finite element analysis (F_{max}=4972.2N, ρ^*=400μm, a=15mm, R_σ=0.0).

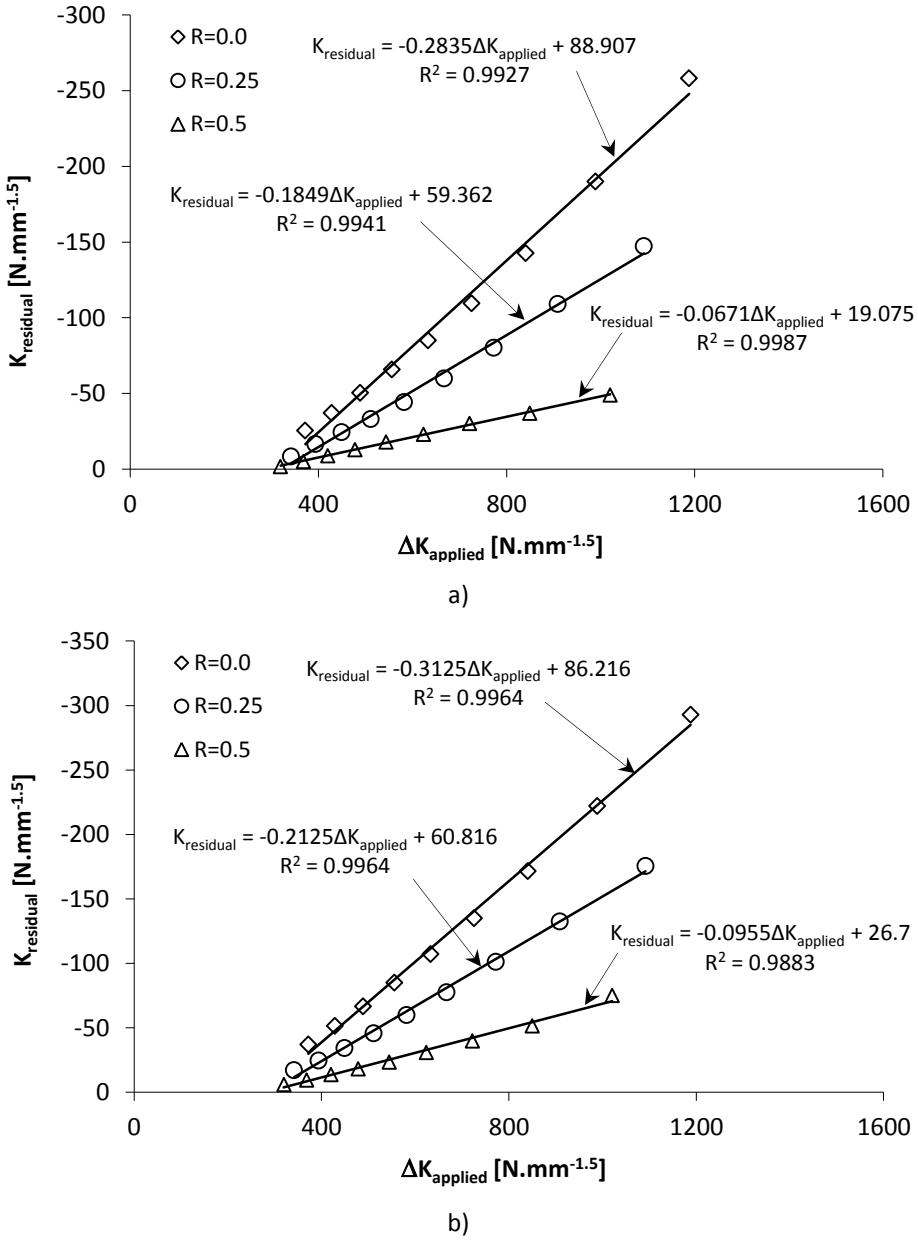

Figure 5.30 – Residual stress intensity factor as a function of the applied stress intensity factor range obtained for the material from the Fão bridge: a) ρ^*=400μm; b) ρ^*=200μm.

5.5.1.3. S355 structural steel

The finite element mesh of the CT geometry made S355 steel adopted in the finite element analysis is presented in Figure 5.31 [40]. Figure 5.32 compares the Ramberg-Osgood relation of the S355 steel with the elastoplastic response of a finite element model reproducing a uniaxial stress state.

After some mesh densities were analysed, as illustrated in Figure 5.33 the Mesh 2 was adopted in this study. Table 5.4 presents the maximum elastic stresses (σ_x and σ_y) ahead

of the crack tip, resulting from distinct mesh densities, for the S355 steel. The maximum stress results are compared between the mesh 2 and other meshes.

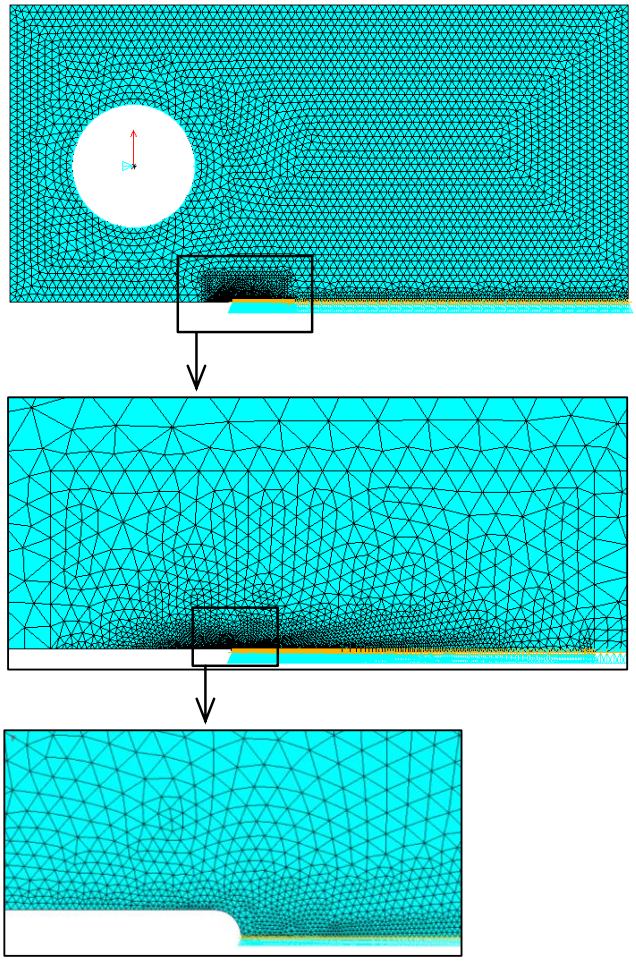

Figure 5.31 – Finite element meshes of a CT specimen, consisting in six-noded quadratic triangular plane stress elements, used to model the S355 steel.

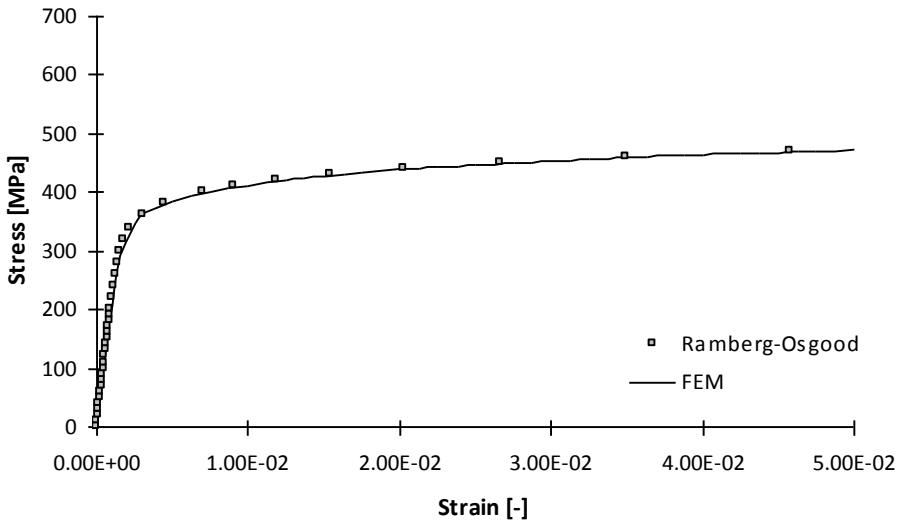

Figure 5.32 – Cyclic stress-strain relation obtained for the S355 steel: Ramberg-Osgood representation vs. finite element response based on multilinear kinematic hardening.

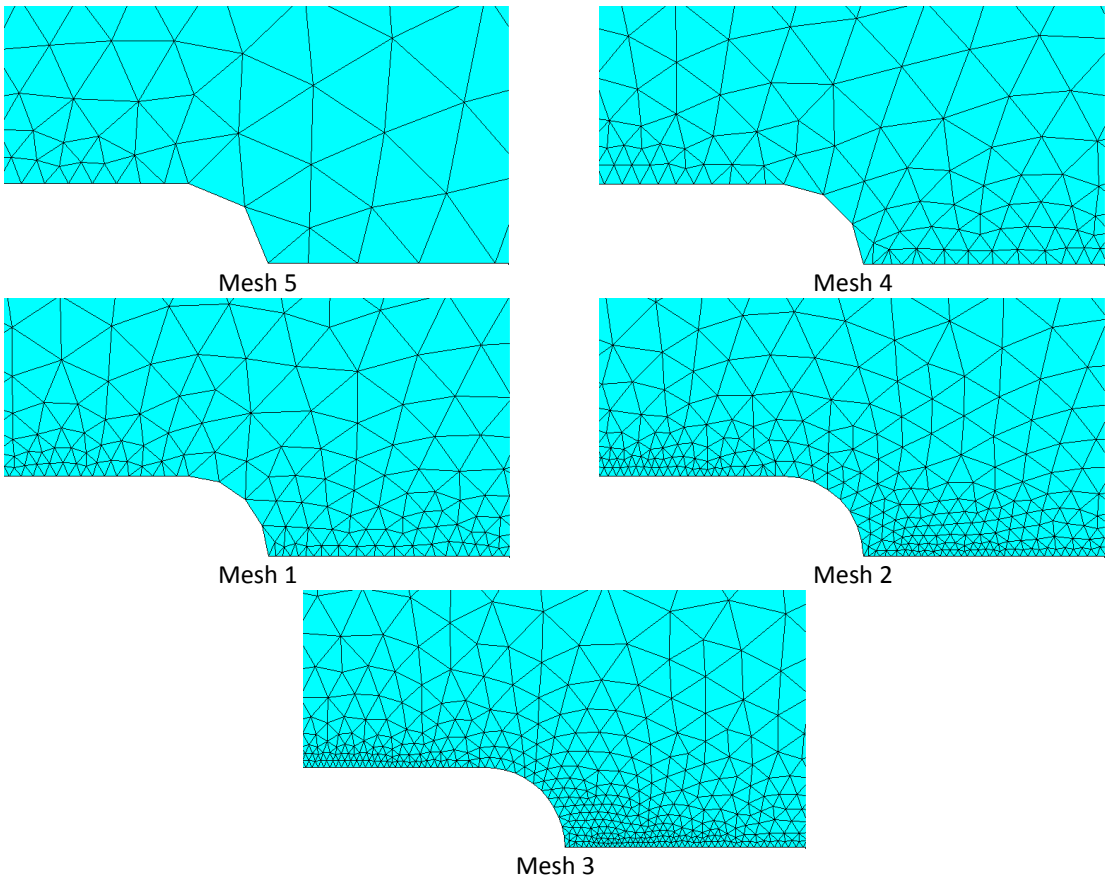

Figure 5.33 – Finite element meshes used in the convergence study performed for the CT specimen made of the S355 steel.

Table 5.5 – Maximum elastic stresses for distinct finite element mesh densities for the S355 steel (F_{max}=5443.5N, a=10mm, ρ^*=55µm).

Maximum stresses	**mesh 5**	**mesh 4**	**mesh 1**	**mesh 2**	**mesh 3**
σ_y **[MPa]**	1637.0	1772.0	1797.6	1926.9	1928.8
***Dev.* [%]**	-15.04	-8.04	-6.71	-	0.10
σ_x **[MPa]**	429.7	423.8	416.7	417.9	417.8
***Dev.* [%]**	2.83	1.42	-0.29	-	-0.03

The elastic stress distributions obtained from the numerical and analytical solutions for the CT specimens made of S355 steel are compared in Figure 5.34. Figure 5.35 compares the elastoplastic stress distributions between the numerical and analytical solutions, for the same CT specimens. The results were computed for a crack tip radius, ρ^*=55µm, which was found to be the best value for the S355 steel; it gives the best predictions for the crack growth rates, based on the *SWT* damage parameter [40].

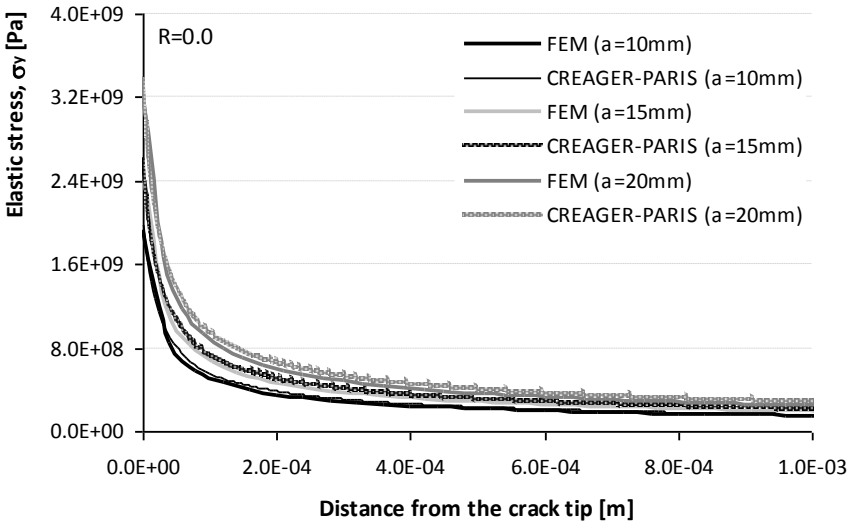

a)

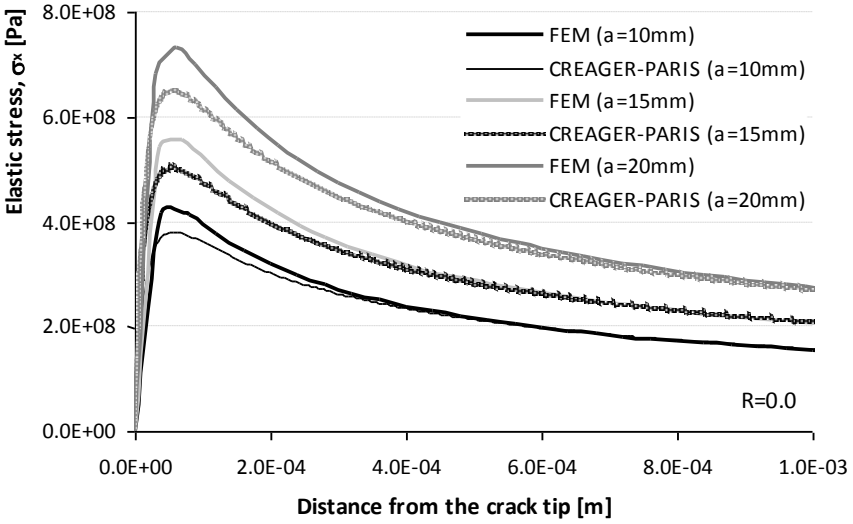

b)

Figure 5.34 – Comparison between analytical and numerical results of the elastic stress distribution ahead of the crack tip and along the crack line (y=0) for CT specimens made of the S355 steel: a) σ_y stress distribution (F_{max}=5443.5N, ρ^*=55µm); b) σ_x stress distribution (F_{max}=5443.5N, ρ^*=55µm).

The residual stress distributions for the S355 steel, shown in Figure 5.36 for distinct crack sizes and stress *R*-ratios, were computed by means of the analytical and numerical solutions, using an elementary material block size, ρ^*=55µm.

The stress and strain fields along the y (load) direction, obtained for the CT specimens using the elastoplastic finite element analysis, are illustrated in Figure 5.37, assuming a material representative element of ρ^*=55µm, a crack size a=15mm, a maximum load F_{max}=5443.5N, and a stress *R*-ratio, R_σ=0.0. The results were obtained using the properties of the S355 steel. In this figure, the compressive stress field at the crack tip vicinity and at

some extension of the crack wake can be clearly distinguished. The stress and strain fields are shown at the end of the first loading reversal and at the end of the unloading reversal.

Figure 5.38 presents the residual stress intensity factor as a function of the applied stress intensity factor range, obtained for the S355 steel, using the numerical elastoplastic compressive stress distribution and the weight function method.

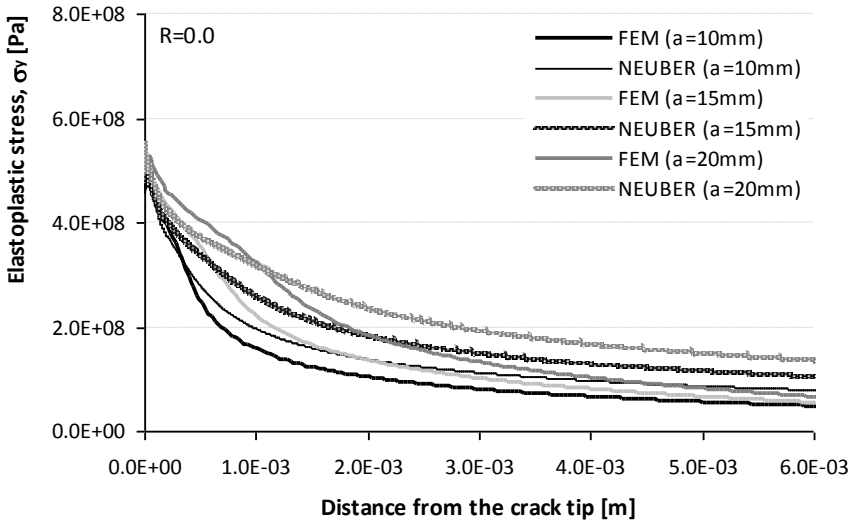

a)

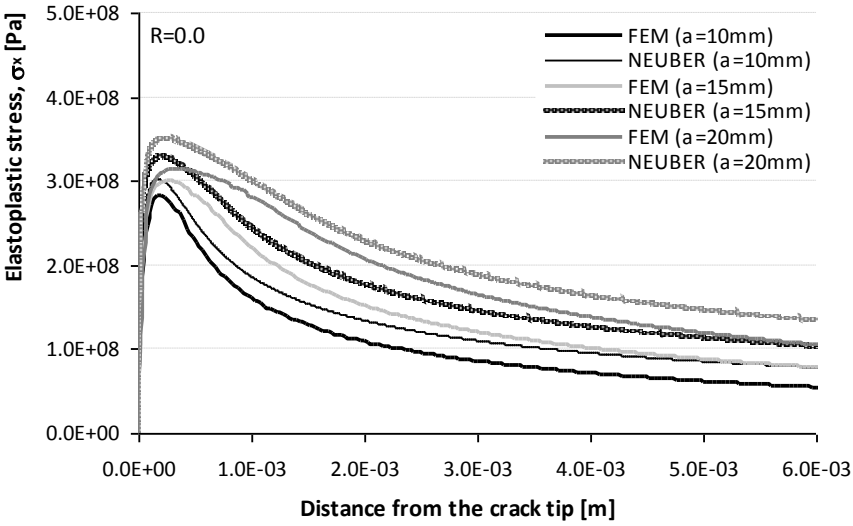

b)

Figure 5.35 – Comparison between analytical and numerical results of the elastoplastic stress distribution ahead of the crack tip in the crack line (y=0) for CT specimens made of the S355 steel: a) σ_y stress distribution (F_{max}=5443.5N, ρ^*=55µm); b) σ_x stress distribution (F_{max}=5443.5N, ρ^*=55µm).

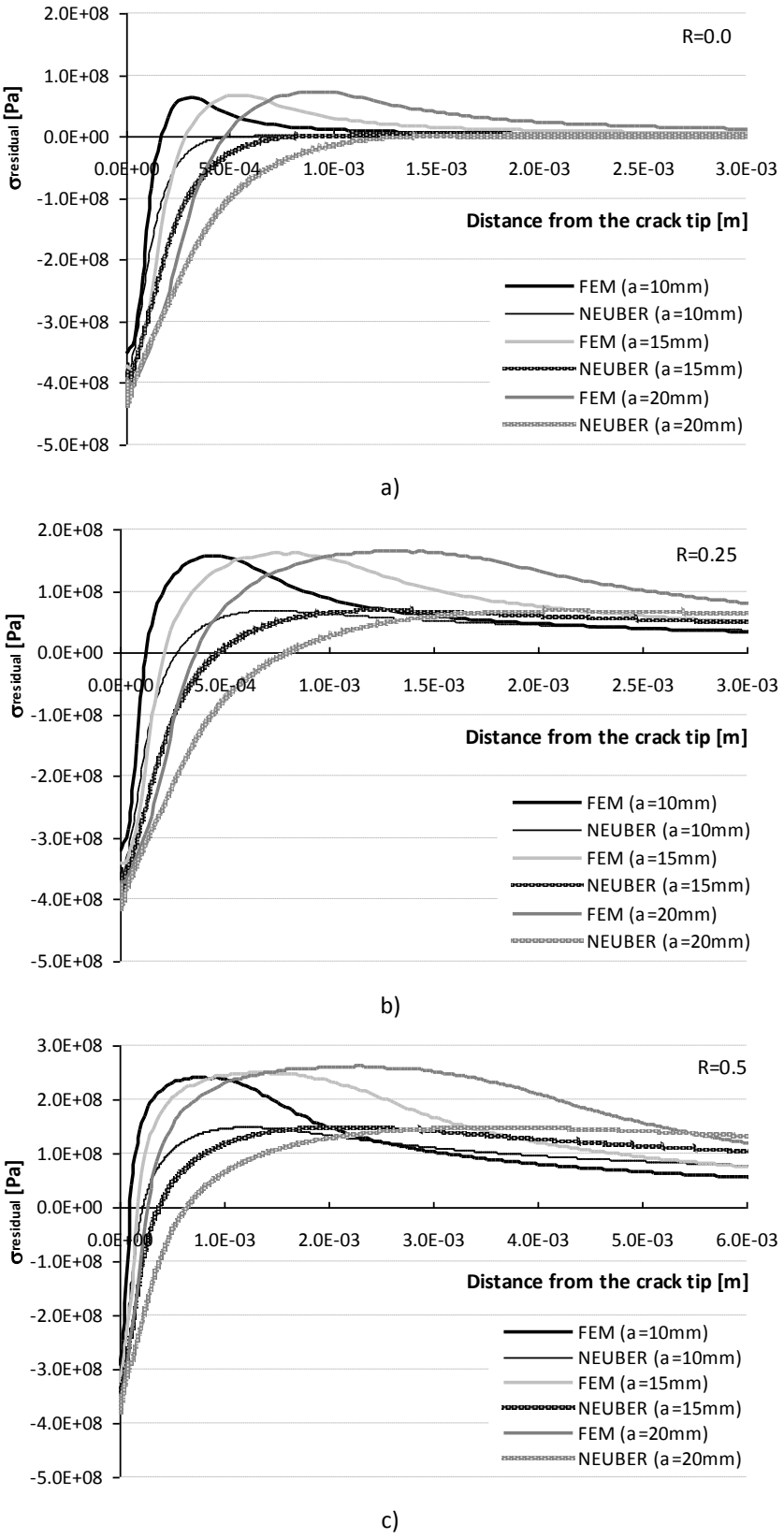

Figure 5.36 – Comparison between analytical and numerical results of the residual stress distribution ahead of the crack tip in the crack line (y=0) for CT specimens made of the S355 steel: a) R_σ=0.0 (F_{max}=5443.5N, ρ^*=55µm); b) R_σ=0.25 (F_{max}=7185.5N, ρ^*=55µm); c) R_σ=0.5 (F_{max}=10778.2N, ρ^*=55µm).

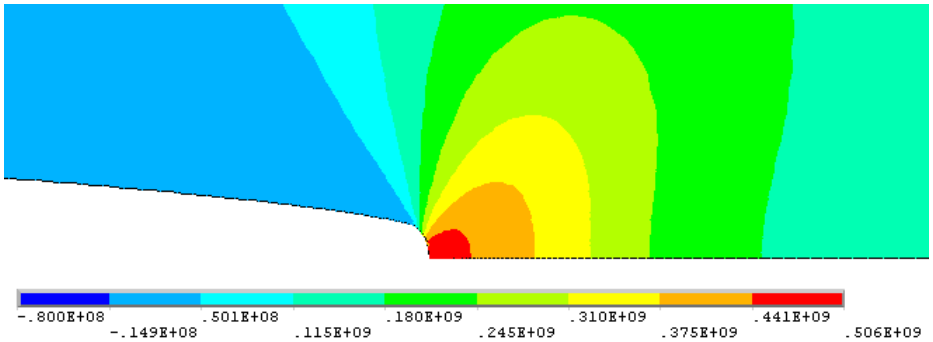

a) Stress field, in MPa, at the end of the loading reversal.

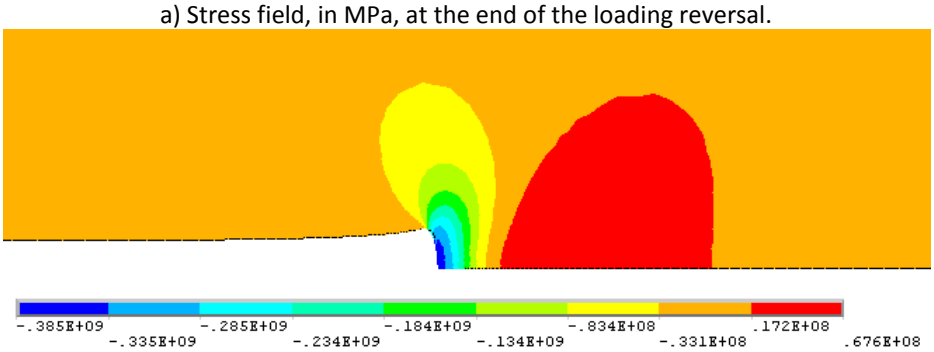

b) Stress field, in MPa, at the end of the first unloading reversal.

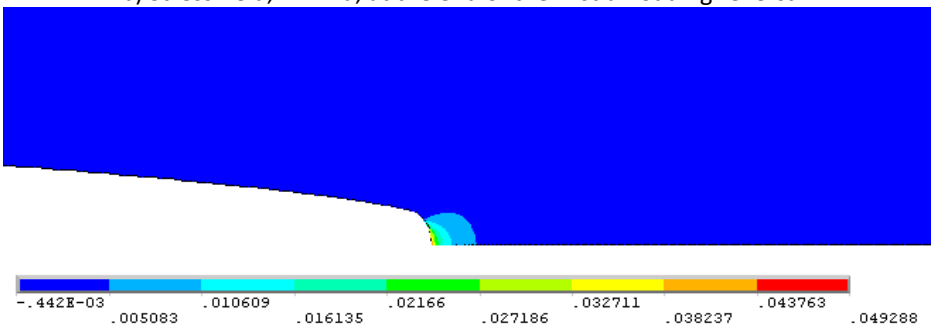

c) Strain field at the end of the loading reversal.

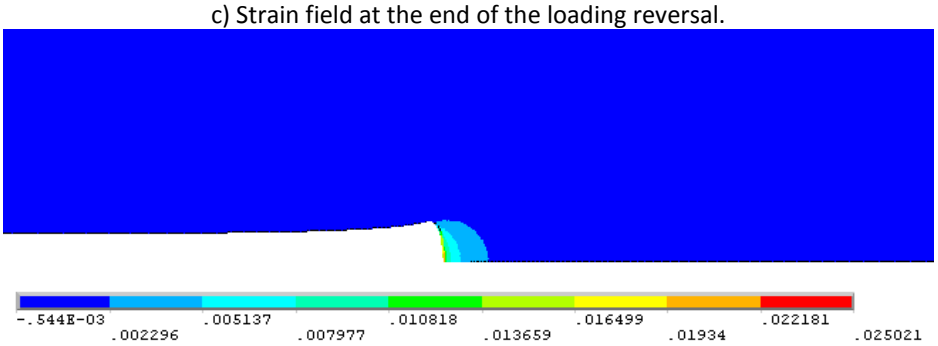

d) Strain field at the end of the first unloading reversal.

Figure 5.37 – Stress and strain fields, along the load direction, obtained for the CT specimes of the S355 steel, resulting from elastoplastic finite element analysis (F_{max}=5443.5N, ρ^*=55µm, a=15mm, R_σ=0.0).

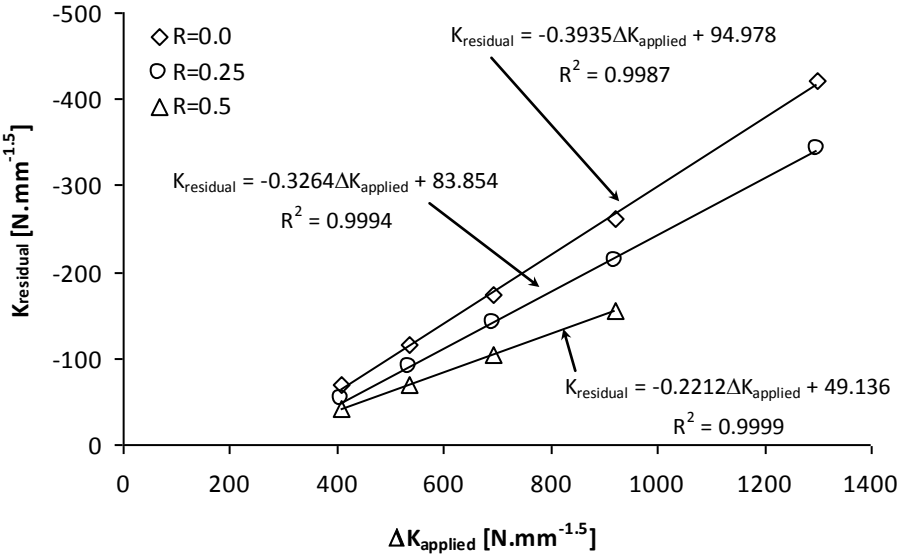

Figure 5.38 – Residual stress intensity factor as a function of the applied stress intensity factor range, obtained for CT specimens made of S355 steel (ρ^*=55µm).

5.5.1.4. P355NL1 pressure vessel steel

Figures 5.39 and 5.40 show the finite element mesh of the CT geometry and the cyclic stress-strain curves adopted in the plasticity model of the P355NL1 steel, respectively [41]. The Ramberg-Osgood relation [34] is compared with the response of the finite element model reproducing a uniaxial stress state in Figure 5.40. Table 5.6 presents the maximum elastic stresses (σ_x and σ_y) ahead of the crack tip, resulting from distinct mesh densities illustrated in Figure 5.41. The mesh 2 was adopted for residual stress computation. Results presented in Table 5.6 compare the mesh 2 with the other meshes.

Figures 5.42 and 5.43 illustrate the elastic and elastoplastic stress distributions for the P355NL1 steel, respectively. In these figures, the numerical and analytical solutions for the CT specimens are computed for a crack tip radius, ρ^*=30µm, which was found to be the best value for the P355NL1 steel. This ρ^* parameter gives the best predictions of the fatigue crack growth rates, using the Morrow relation as referred in [6].

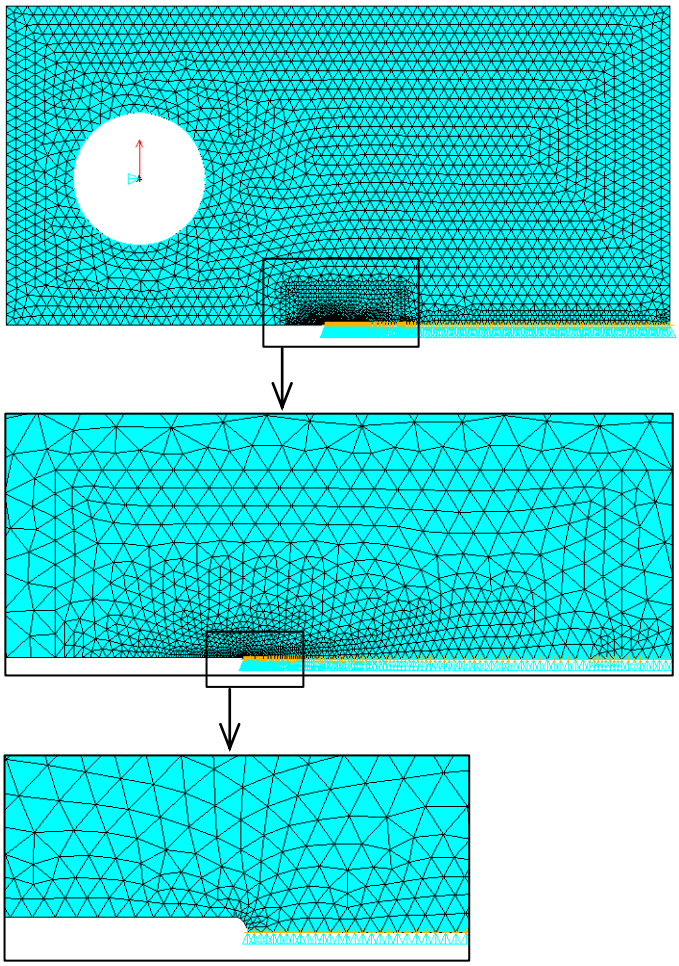

Figure 5.39 – Finite element meshes of the CT specimen, consisting in six-noded quadratic triangular plane stress elements, for the P355NL1 steel.

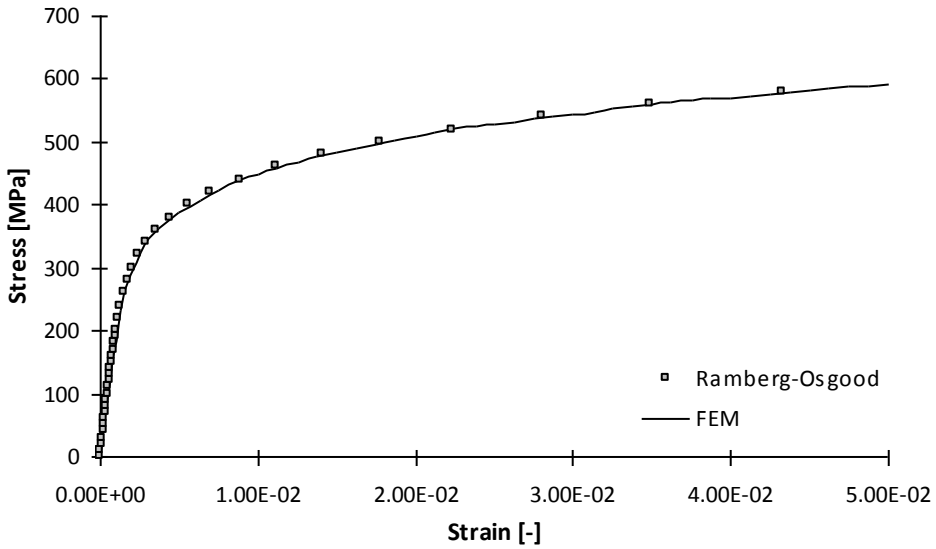

Figure 5.40 – Cyclic stress-strain relation obtained for the P355NL1 steel: Ramberg-Osgood representation vs. finite element response based on multilinear kinematic hardening [41].

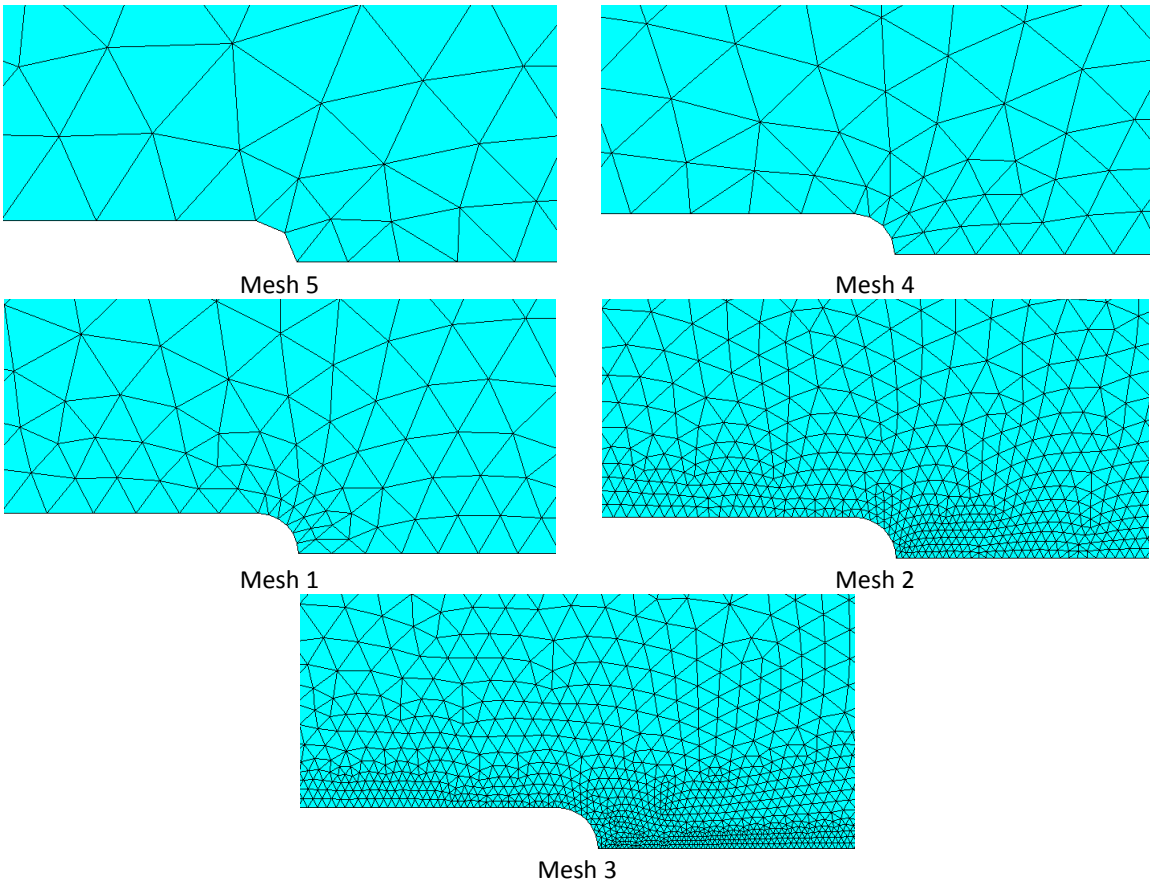

Figure 5.41 – Finite element meshes used in the convergence study performed for the CT specimen made for the P355NL1 steel.

Table 5.6 – Maximum elastic stresses for distinct finite element mesh densities for the P355NL1 steel (F_{max}=1634.1N, ρ^*=30μm).

Maximum stresses	mesh 5	mesh 4	mesh 1	mesh 2	mesh 3
σ_y [MPa]	1367.9	1420.1	1495.8	1605.3	1606.7
Dev. [%]	-14.79	-11.54	-6.82	-	0.09
σ_x [MPa]	347.4	370.3	363.9	354.2	354.1
Dev. [%]	-1.93	4.57	2.74	-	-0.03

Figure 5.44 shows the residual stress distributions for the P355NL1 steel for distinct crack sizes and stress *R*-ratios. The residual stress distributions were computed by means of the analytical and numerical solutions using an elementary material block size, ρ^*=30μm [41].

Figure 5.45 illustrates the stress and strain fields along the y (load) direction obtained for the CT specimens using the elastoplastic finite element analysis and the properties of the P355NL1 steel, for a material representative element, ρ^*=30μm, a crack size a=14mm, a maximum load F_{max}=1634.1N, and a stress *R*-ratio, R_σ=0.0. The stress and strain fields are

shown at the end of the first loading reversal and at the end of the first unloading reversal.

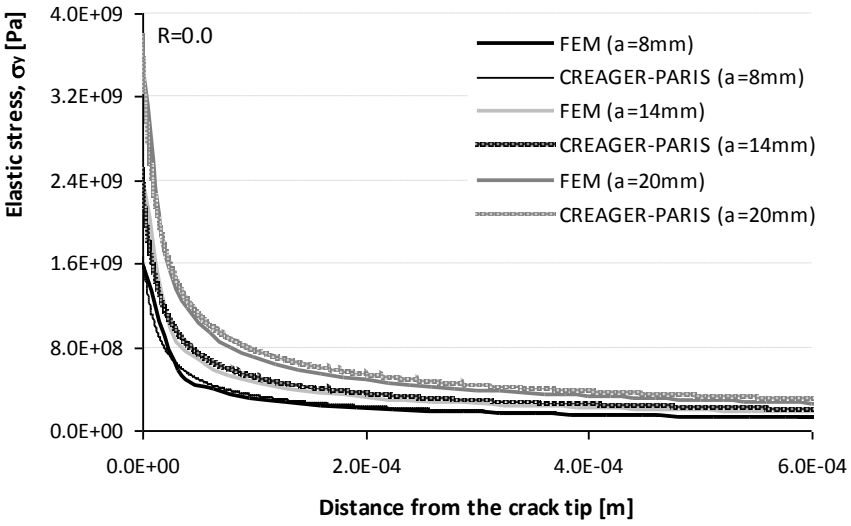

a)

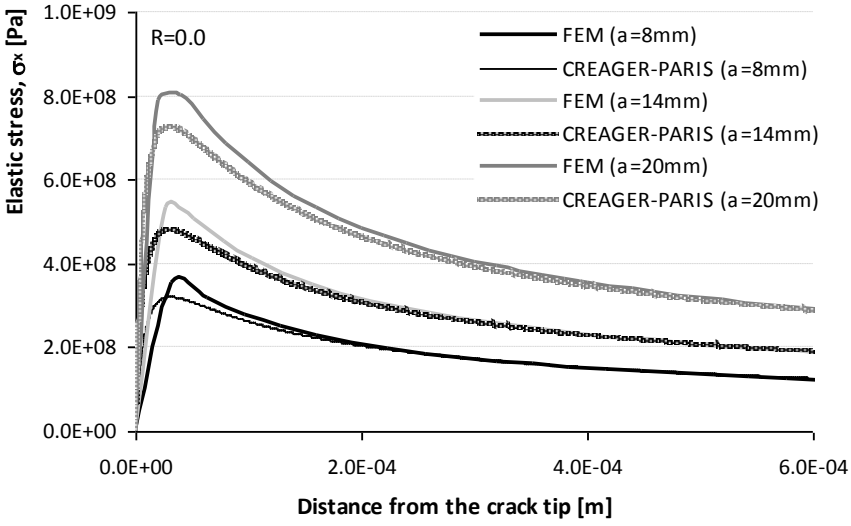

b)

Figure 5.42 – Comparison between analytical and numerical results of the elastic stress distribution ahead of the crack tip and along the crack line (y=0) for CT specimens made of the P355NL1 steel: a) σ_y stress distribution (F_{max}=1634.1N, ρ^*=30μm); b) σ_x stress distribution (F_{max}=1634.1N, ρ^*=30μm).

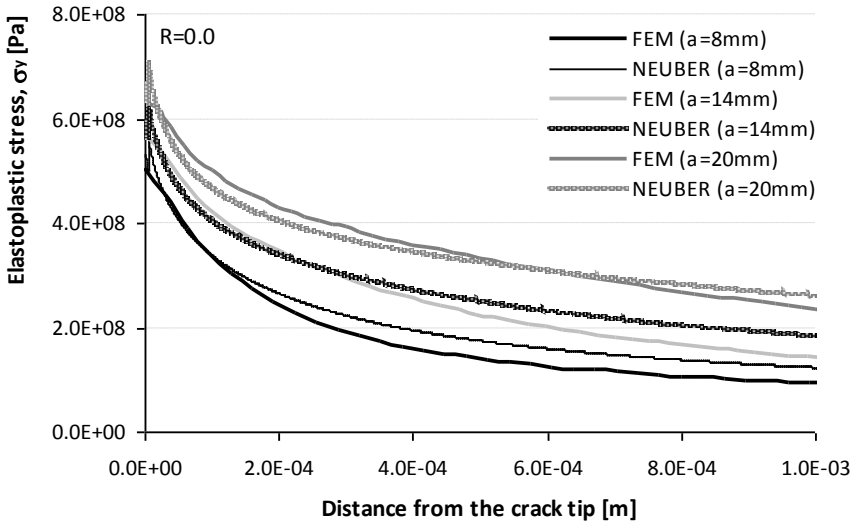

a)

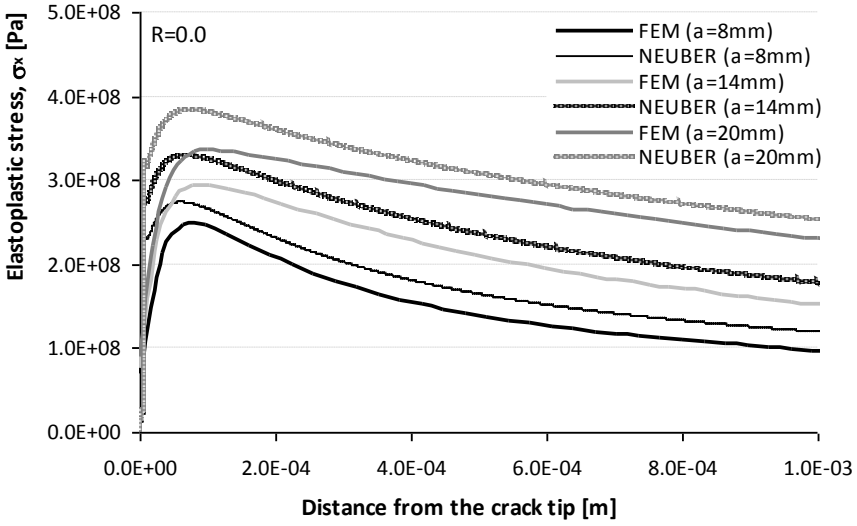

b)

Figure 5.43 – Comparison between analytical and numerical results of the elastoplastic stress distribution ahead of the crack tip and along the crack line (y=0) for CT specimens made of the P355NL1 steel: a) σ_y stress distribution (F_{max}=1643.1N, ρ^*=30μm); b) σ_x stress distribution (F_{max}=1643.1N, ρ^*=30μm).

Figure 5.46 presents the residual stress intensity factor range for an elementary material blok size ρ^*=30μm [41] as a function of the applied stress intensity factor range, obtained with the numerical analysis.

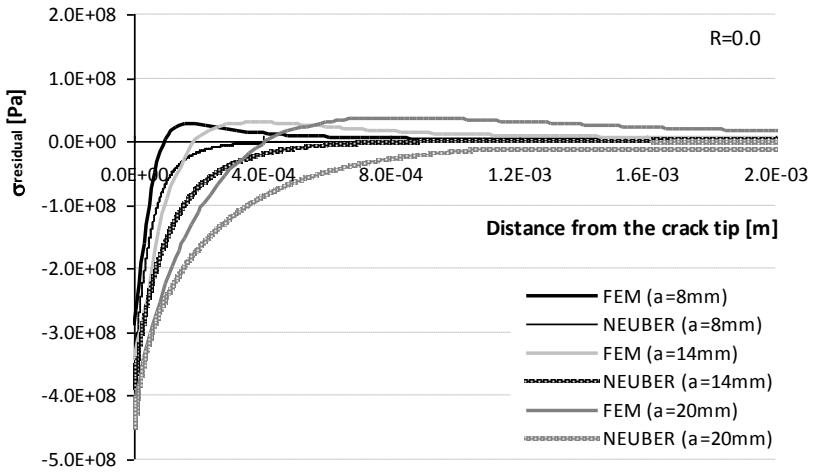

a)

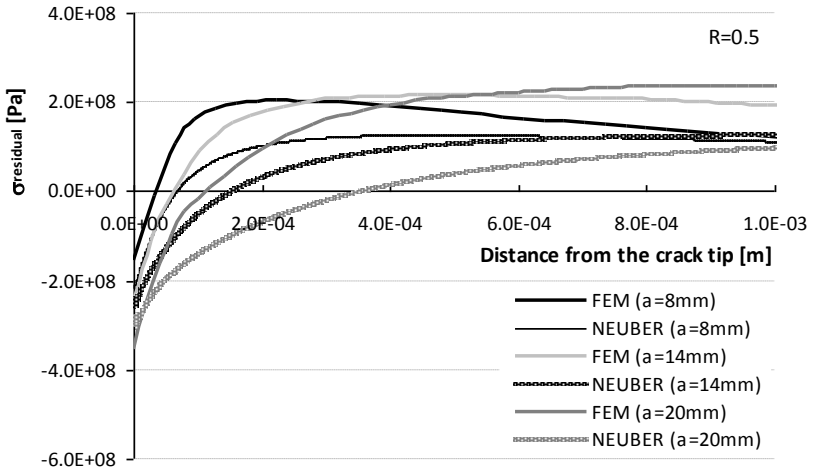

b)

Figure 5.44 – Comparison between analytical and numerical results of the residual stress distribution ahead of the crack tip and along the crack line (y=0) for CT specimens made of the P355NL1 steel: a) R_σ=0.0 (F_{max}=1643.1N, ρ*=30µm); b) R_σ=0.5 (F_{max}=3235.5N, ρ*=30µm).

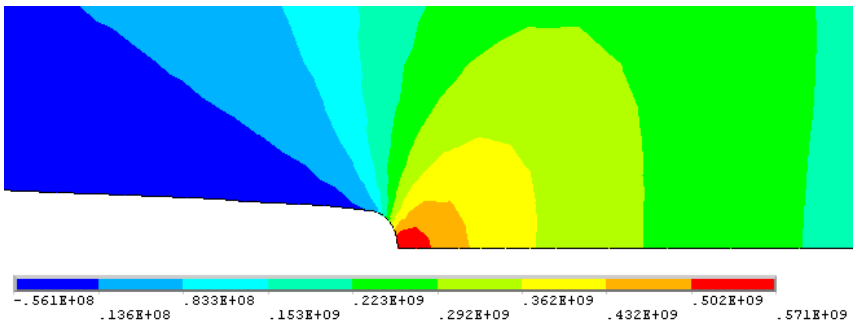

a) Stress field, in MPa, at the end of the loading reversal.

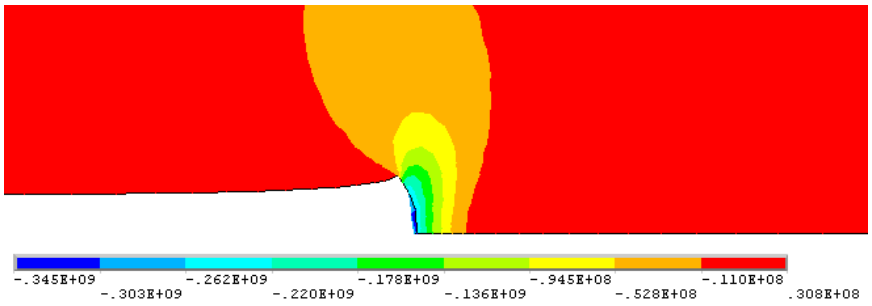

b) Stress field, in MPa, at the end of the first unloading reversal.

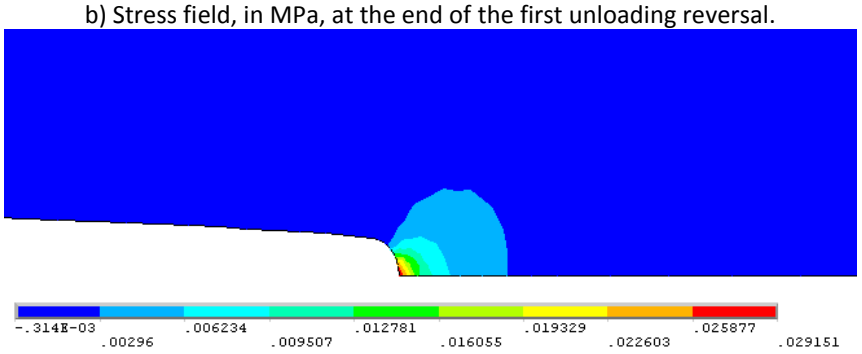

c) Strain field at the end of the loading reversal.

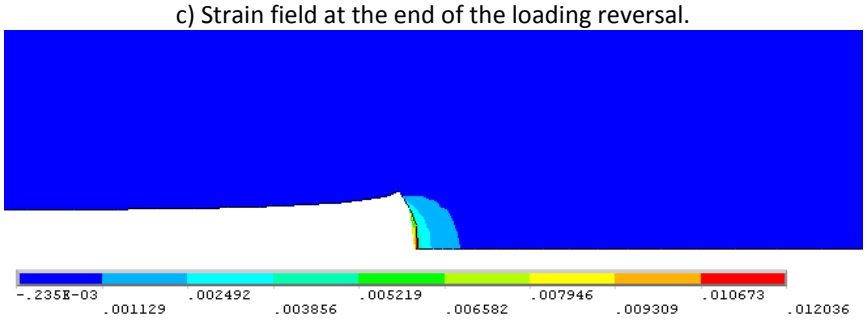

d) Strain field at the end of the first unloading reversal.

Figure 5.45 – Stress and strain fields, along the load direction, obtained for the CT specimens of the P355NL1 steel, resulting from elastoplastic finite element analysis (F_{max}=1634.1N, ρ^*=30µm, a=14mm, R_σ=0.0).

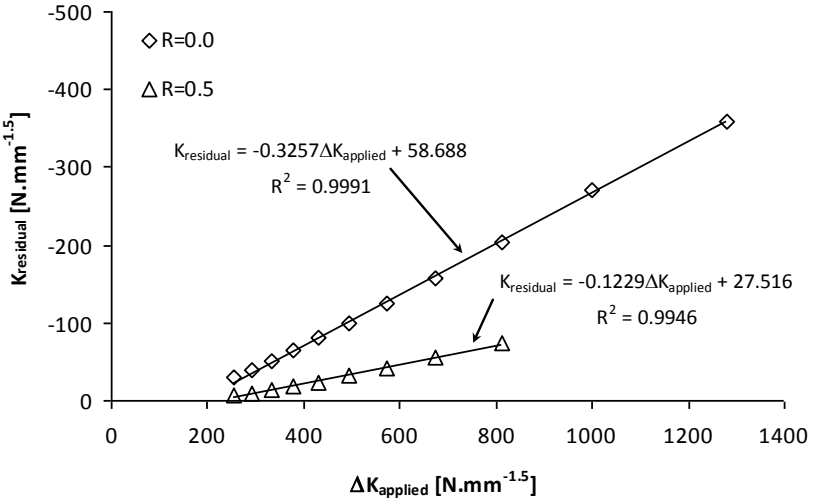

Figure 5.46 – Residual stress intensity factor as a function of the applied stress intensity factor range obtained for the P355NL1 steel.

5.5.1.5. Analysis of the simulation results

This sub-section presents the discussion of the results of the non-linear elastoplastic analysis for the materials and CT geometries under consideration. The discussion is extensible to all materials [37-41].

The elastic stress distribution presents a very good agreement between the analytical and numerical results, for several crack sizes, within a small distance from the crack tip. For higher distances, slight deviations are found for σ_y stresses. For σ_x stresses, the maximum deviation is found to be around the maximum absolute value. For small and high distances from the crack tip, the deviations on σ_x stresses are minimal. Additional simulations with further mesh refinements relative to the selected mesh did not produce noticeable changes in the elastic stress distributions, demonstrating a good mesh refinement.

Besides the numerical solution of the elastoplastic analysis, results from the multiaxial Neuber analysis are also plotted. Despite the same global trends are observed for the σ_y and σ_x stress distributions, deviations in maximum absolute values are verified in the plastic stress distributions. In general, the analytical solutions lead to higher maximum absolute stresses than the elastoplastic FE analysis. σ_x stresses are more stepped than the corresponding numerical stresses near the crack tip. Also, the analytical solution shows some instability near the crack tip. The analysis of the σ_y stress distribution shows an inflection point which is related to the size of the plastic zone. The analytical solution does not show this behaviour, which is a clear limitation of the analytical approach.

The compressive residual stresses decrease progressively with increasing stress ratio, making the applied stress intensity range more effective. The extension of the compressive residual stresses increases with the crack size. The numerical model always predicts a compressive stress region which is lower than that predicted using the analytical model. The comparison between the numerical and analytical results highlight some inconsistencies in the analytical results. The analytical procedure produces reliable results at the crack notch root, but the residual stress distribution along the crack front path (away from the crack notch root) seems to be inconsistent, which is in part justified by the incapacity of the analytical model to handle the stress redistribution due to

yielding. Therefore, the numerical solution, for the residual stresses, was adopted in the crack propagation prediction, based on the UniGrow model.

A very high linear correlation between the residual stress intensity factor and the applied stress range is verified, for each stress *R*-ratio. This linear relation agrees with the proposition by Noroozi et al. [13], based on analytical analysis.

5.5.2. p-da/dN-ΔK-R: results and discussion

The UniGrow model was applied to compute the fatigue crack propagation rates for the same conditions used to derive the experimental fatigue crack propagation data described previously (see section 5.4). The residual stress intensity factor was computed based on compressive residual stress distribution from the finite element analysis, and using the weight function method [26], as proposed in the UniGrow model. The strain range and maximum stress, required by the probabilistic strain-life or SWT-life models, were assessed using the analytical approach, applied to the first elementary material block, keeping the original structure of the UniGrow model. Average strain and stress values, along the first elementary material block, were used instead of peak values. The analytical solution produces reliable results at the crack tip notch root as verified in previous section. The original structure of the UniGrow model presents some advantages: i) provides a direct correspondence with fracture mechanics based analyses, which facilitates the physical understanding of the process; ii) allows close form solutions for fatigue crack propagation laws to be achieved in the same format as that of existing fracture mechanics approaches; iii) requires inexpensive computations.

The probabilistic ε_a–*N* and *SWT*–*N* fields were used to derive the probabilistic fatigue crack propagation fields (*p-da/dN-ΔK-R* fields). For each case, an independent identification of the elementary material block size, ρ^*, was performed.

Figures 5.47 to 5.50 show the probabilistic fatigue crack propagation fields obtained, respectively for the materials from Eiffel and Fão bridges, for the S355 steel and the P355NL1 steel, using the *p-SWT-N* material fields. Figures 5.51 and 5.54 illustrate the probabilistic fatigue crack propagation fields predicted, respectively for the materials

from Eiffel and Fão bridges, for the S355 steel and for the P355NL1 steel, resulting from the *p*- ε_a-*N* material fields.

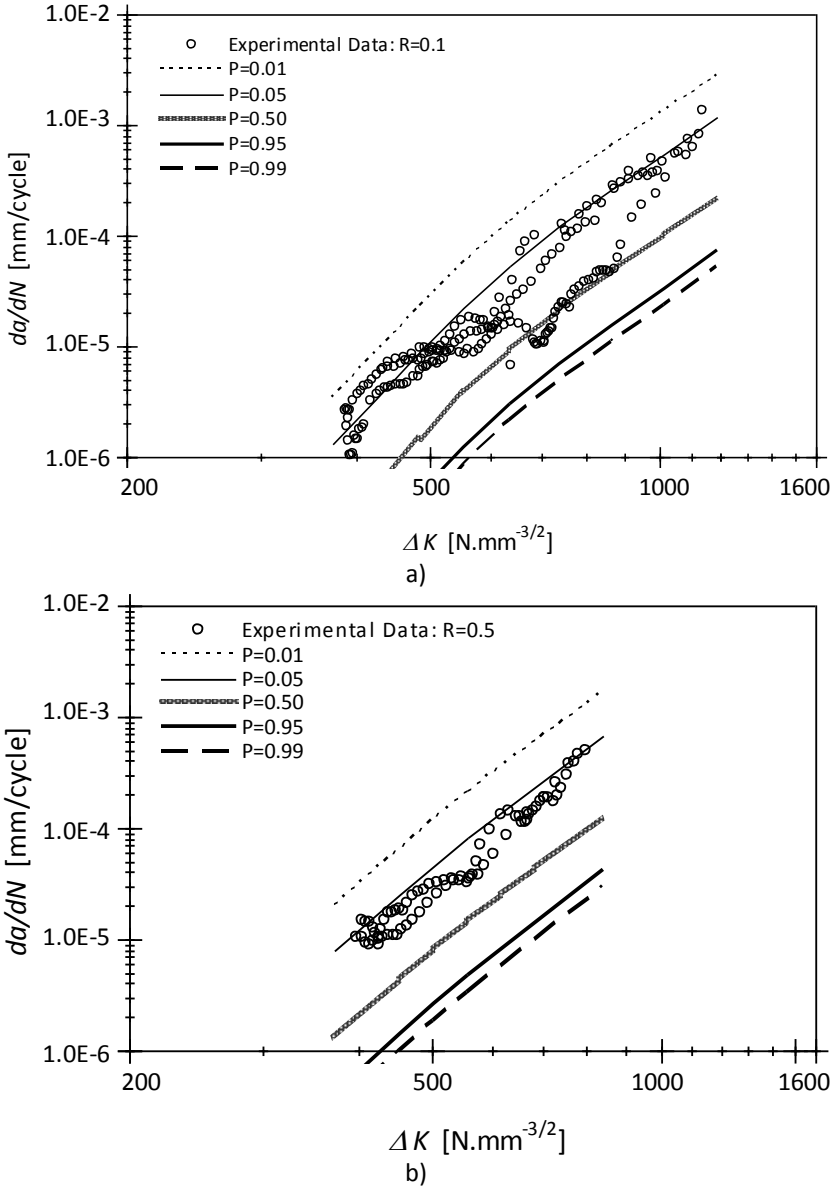

Figure 5.47 – Probabilistic prediction of the fatigue crack propagation based on the *p-SWT-N* field, for the material from the Eiffel bridge (ρ^*=12×10^{-4}m): a) R_σ=0.1; b) R_σ=0.5.

Elementary material block sizes of 12×10^{-4}m and 4×10^{-4}m were found suitable for the material from Eiffel bridge if the *p-SWT-N* or the *p*- ε_a-*N* fields are, respectively, applied. For the material from the Fão bridge, elementary material block sizes of 4×10^{-4}m and 2×10^{-4}m were found suitable, if the *p-SWT-N* or the *p*- ε_a-*N* fields are, respectively, used. An elementary material block size of 5.5×10^{-5}m was found adequate for the S355 steel, when both *p-SWT-N* or *p-ε-N* fields are used. Finally, for the P355NL1 steel, a ρ^*=3×10^{-5}m was found suitable, resulting from the application of the *p-ε-N* fields.

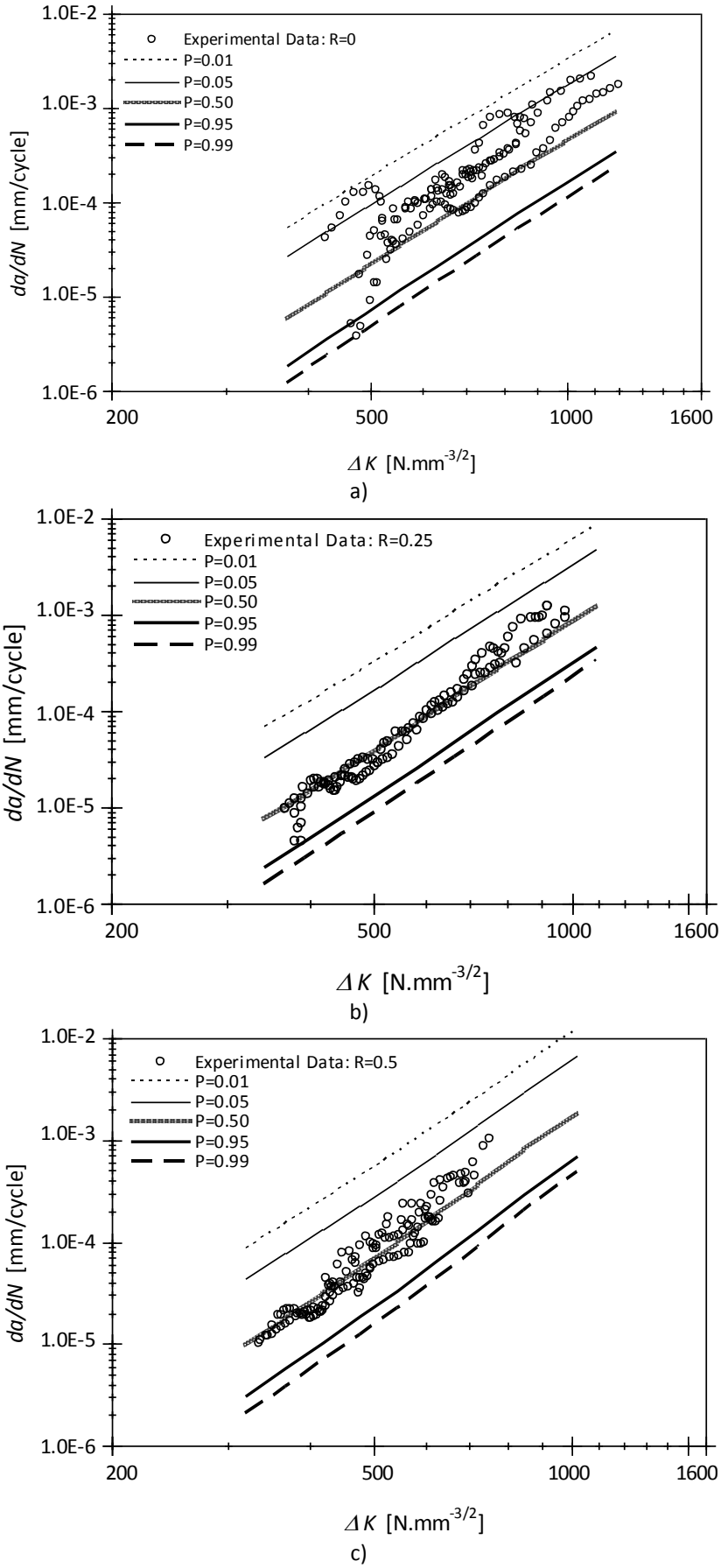

Figure 5.48 – Probabilistic prediction of the fatigue crack propagation based on the *p-SWT-N* field, for the material from the Fão bridge (ρ^*=4×10^{-4}m): a) R_σ=0.0; b) R_σ=0.25; c) R_σ=0.5.

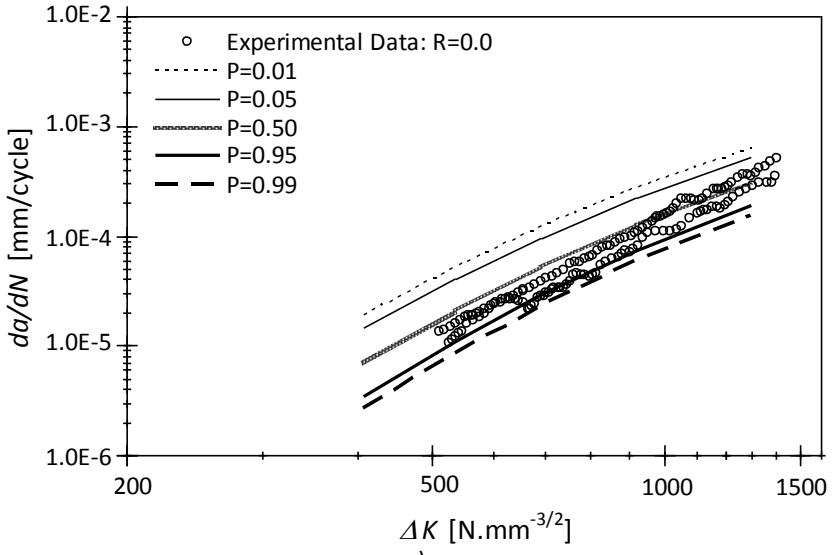

a)

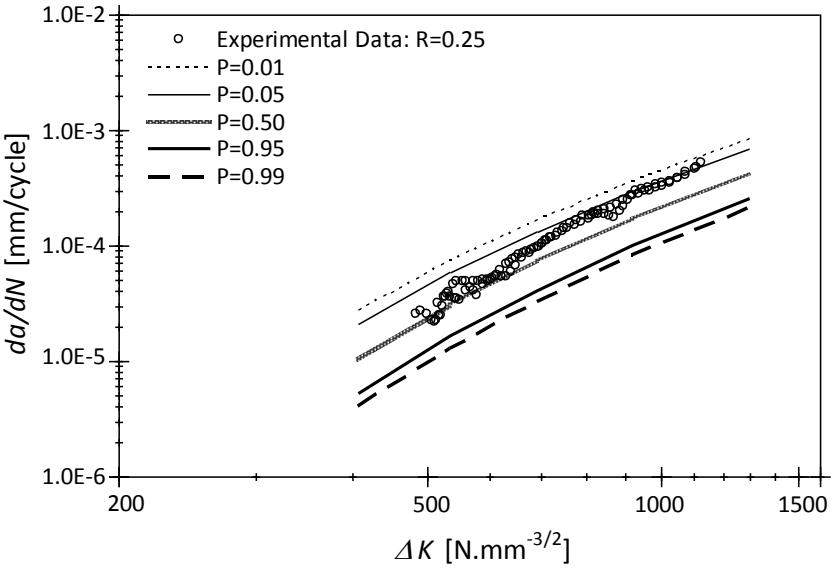

b)

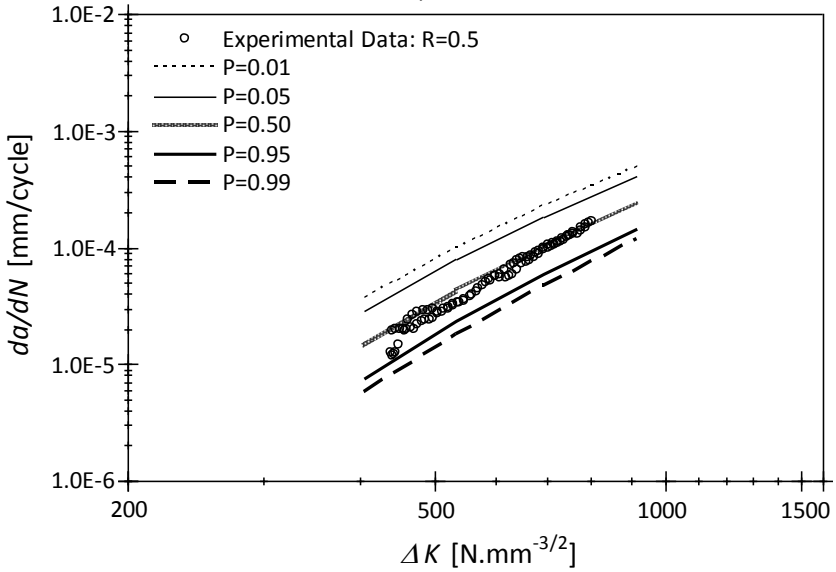

c)

Figure 5.49 – Probabilistic prediction of the fatigue crack propagation based on the *p-SWT-N* field, for the S355 steel (ρ^*=5.5×10^{-5}m): a) R_σ=0.0; b) R_σ=0.25; c) R_σ=0.5.

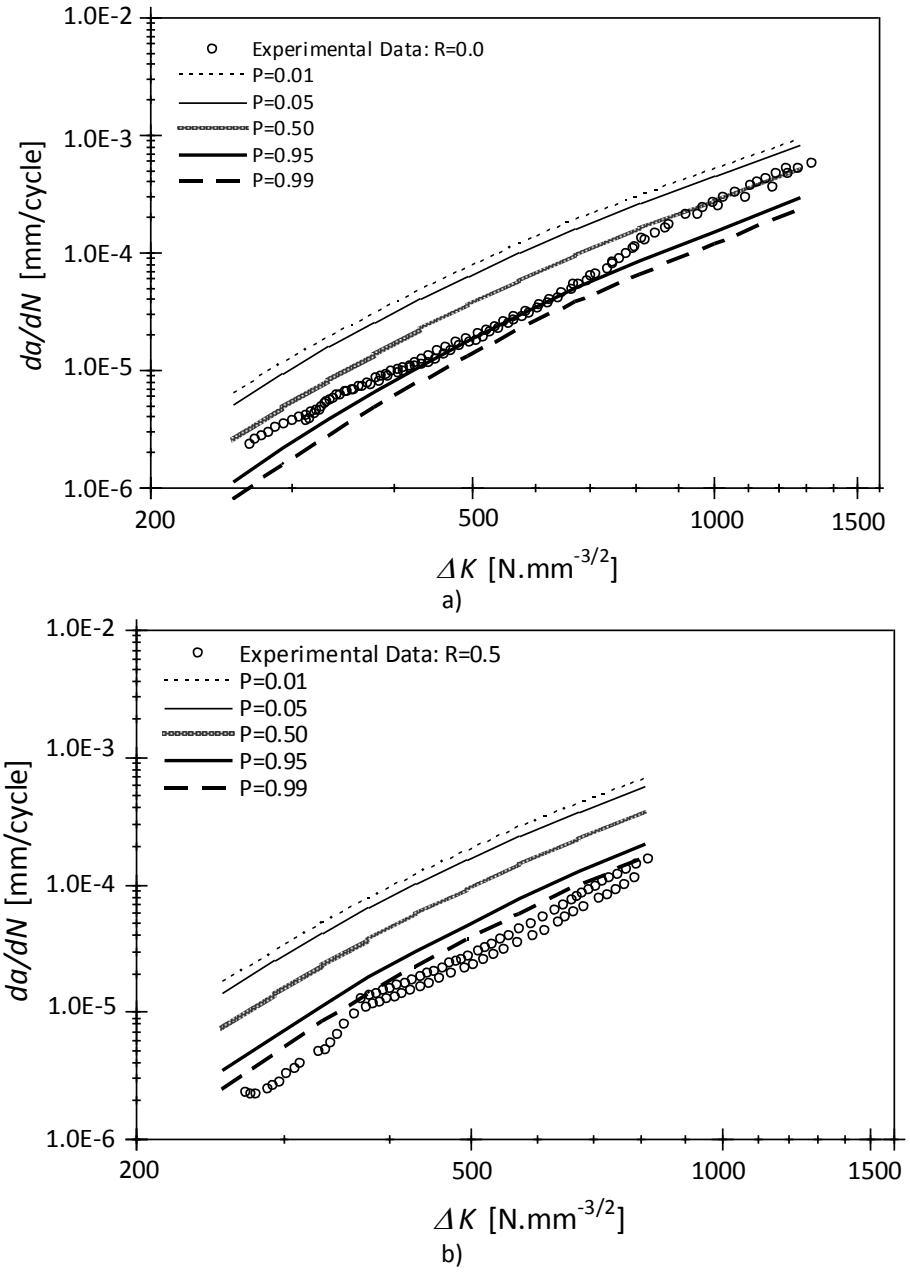

Figure 5.50 – Probabilistic prediction of the fatigue crack propagation based on the *p-SWT-N* field, for the P355NL1 steel (ρ^*=3×10^{-5}m): a) R_σ=0.0; b) R_σ=0.5.

The elementary material block sizes found for materials from the Fão and Eiffel bridges are significantly higher than those proposed by Noroozi et al. [14] for the 4340 steel (ρ^*=2×10^{-6}m), the former being about one order of magnitude higher compared with the S355 and P355NL1 steels. The materials from the Fão and Eiffel bridges are puddle irons, exhibiting higher grain sizes than modern steels. They also show significant amount of heterogeneities which may influence the crack propagation behaviour. The values of ρ^* are consistent for the S355 and P355NL1 steels, as these are modern steels. So far, there are no conclusive studies relating the microstructural grain sizes with the elementary

material block sizes. Nevertheless, it can be anticipated that ρ^* can be indirectly dependent on the micro-structural features of the analysed material (e.g. grain size) but it cannot be uniquely associated with any specific micro-structural particle size. Therefore, the material grain size may be considered just one of the possible microstructural features affecting the definition of ρ^*.

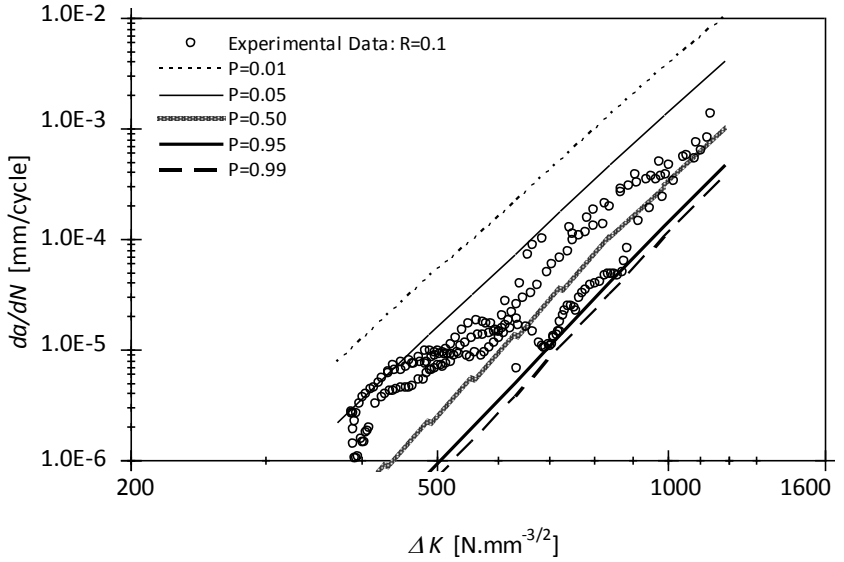

a)

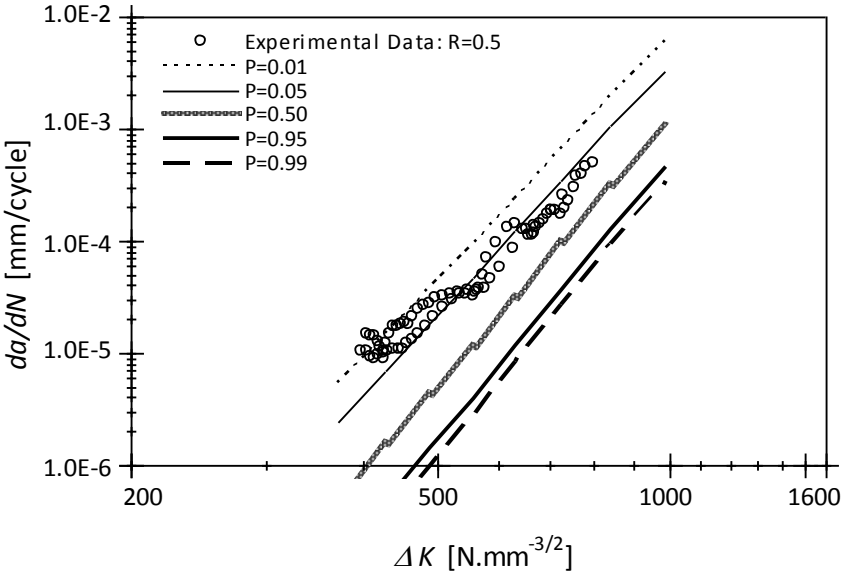

b)

Figure 5.51 – Probabilistic prediction of the fatigue crack propagation based on the p-ε_σ-N field, for the material from the Eiffel bridge (ρ^*=4×10^{-4}m): a) R_σ=0.1; b) R_σ=0.5.

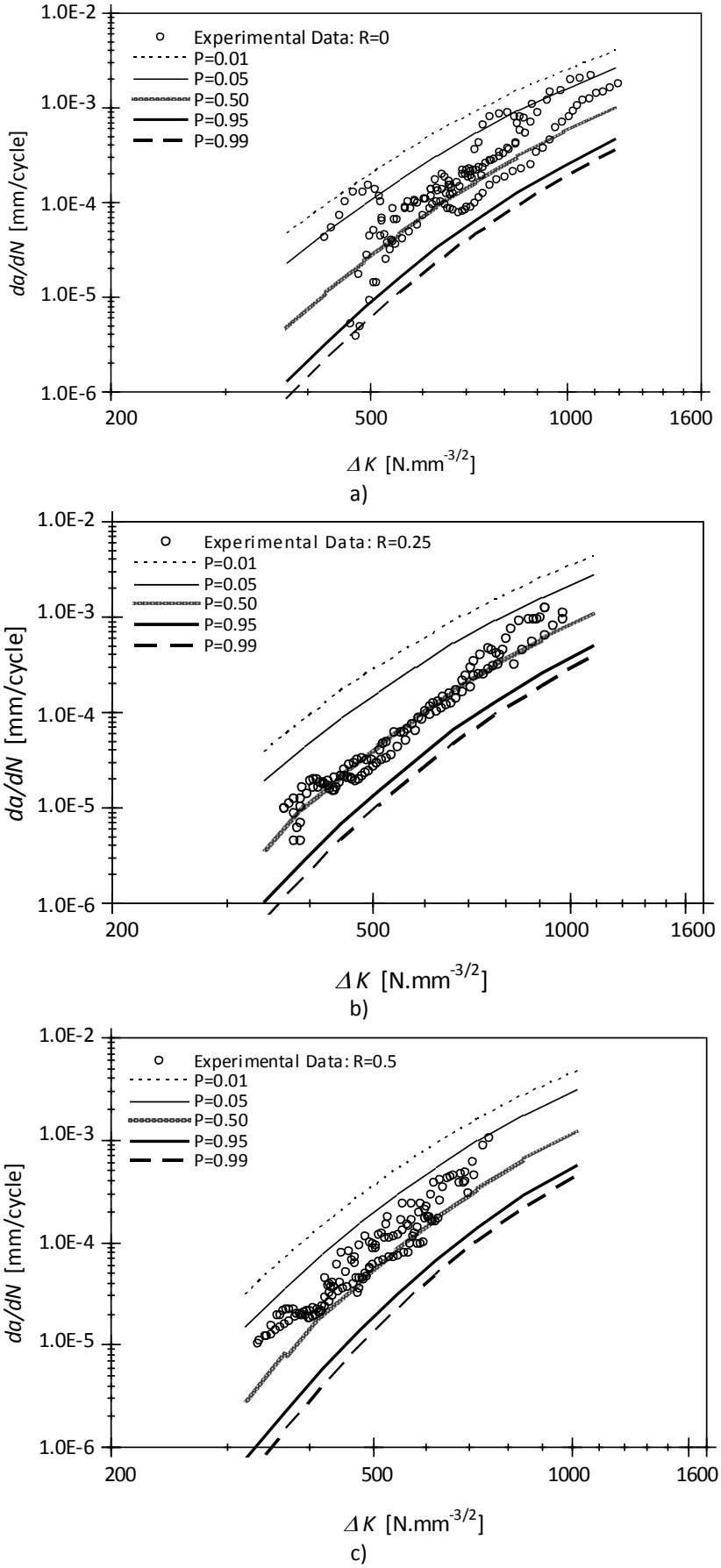

Figure 5.52 – Probabilistic prediction of the fatigue crack propagation based on the p-ε_a-N field, for the material from the Fão bridge (ρ^*=2×10^{-4}m): a) R_σ=0.0; b) R_σ=0.25; c) R_σ=0.5.

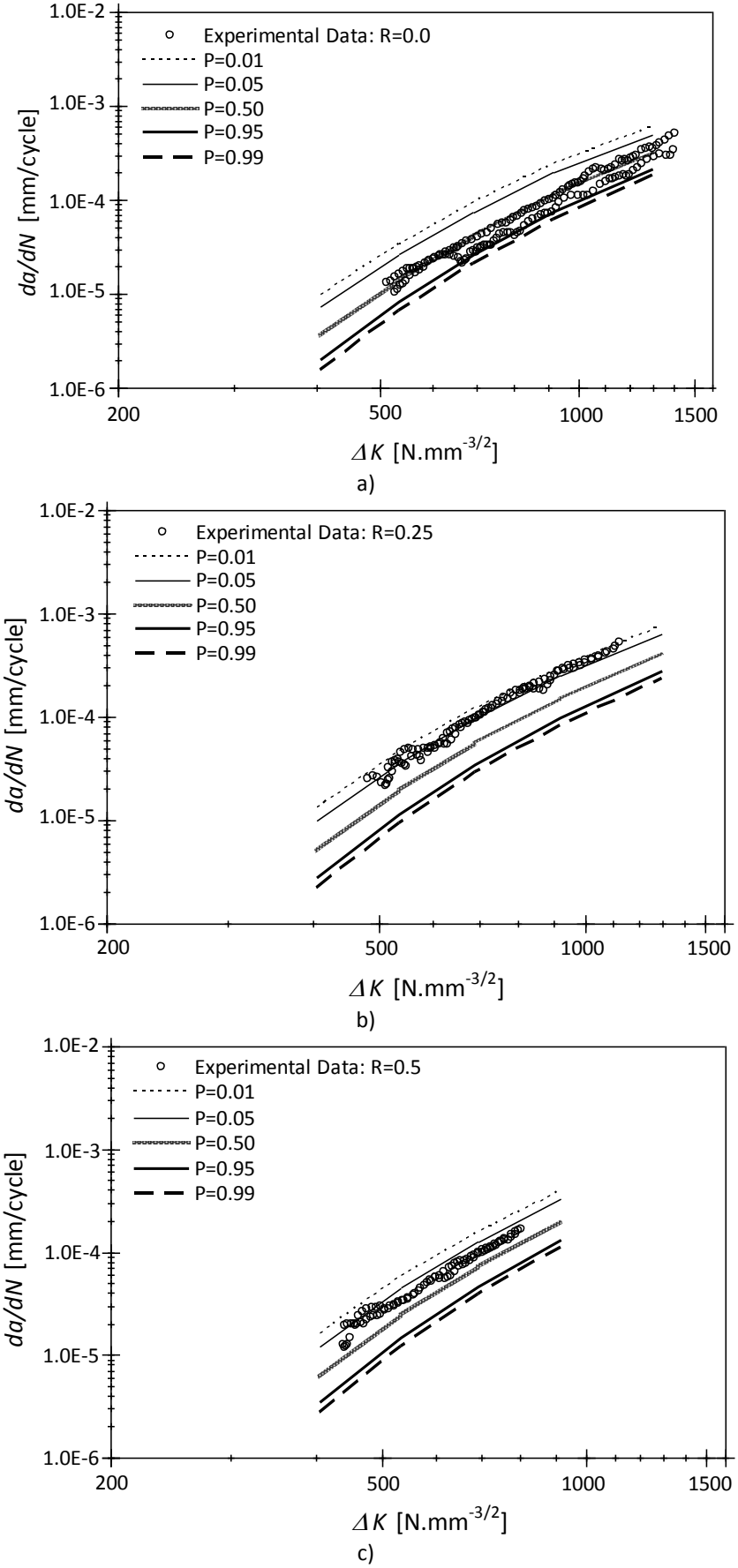

Figure 5.53 – Probabilistic prediction of the fatigue crack propagation based on the p-ε_σ-N field, for the S355 steel (ρ^*=5.5×10^{-5}m): a) R_σ=0; b) R_σ=0.25; c) R_σ=0.5.

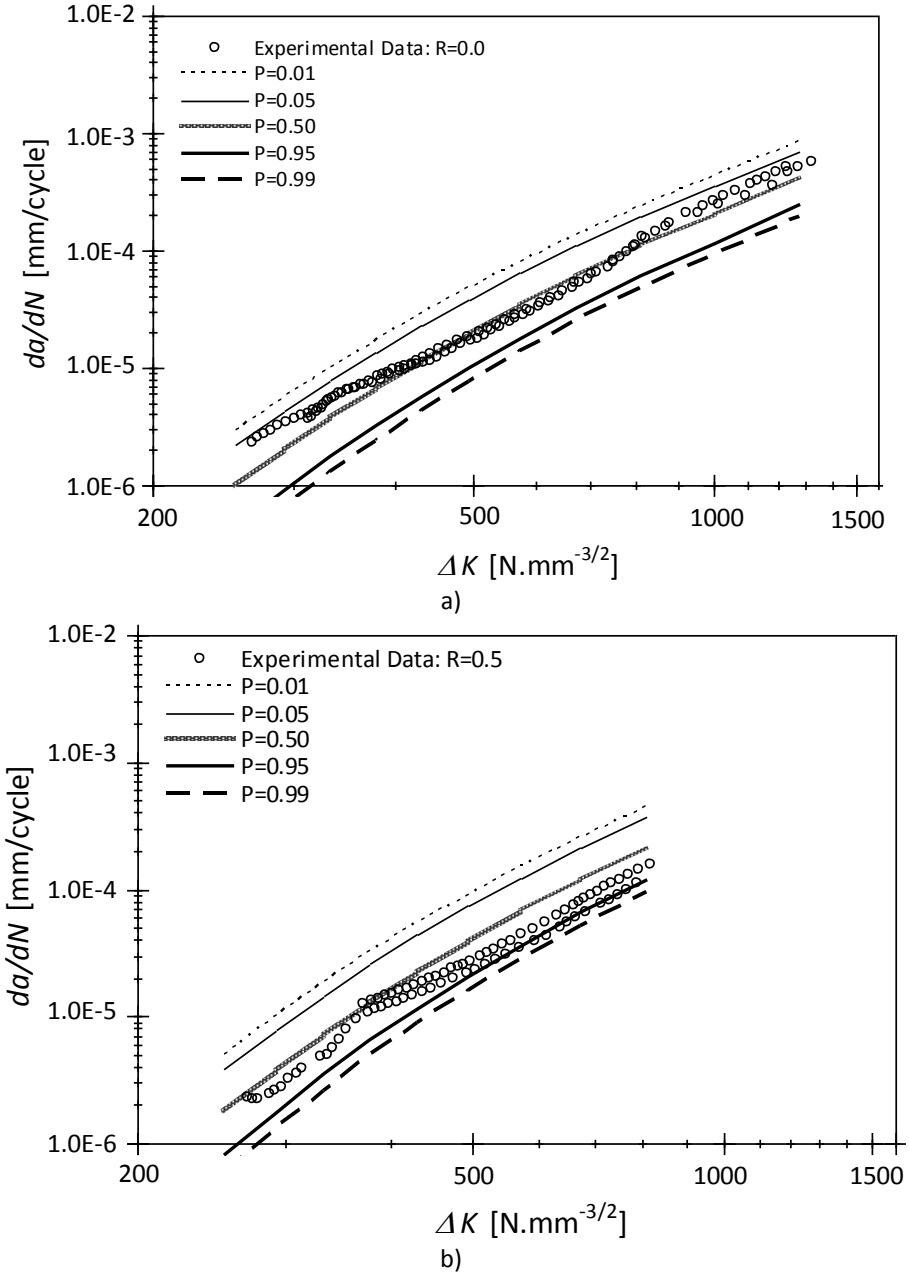

Figure 5.54 – Probabilistic prediction of the fatigue crack propagation based on the p-ε_a-N field, for the P355NL1 steel (ρ^*=3×10^{-5}m): a) R_σ=0.0; b) R_σ=0.5.

The p-da/dN-ΔK-R field predicted for the material of Fão bridge show a satisfactory agreement with the experimental data, using both p-SWT-N and p-ε_a-N fields. Nevertheless, the predictions based on p-ε_a-N fields seems better, which is justified by the fact that the material from the Fão bridge shows only a relative small influence of stress ratio on fatigue crack propagation rates. Also, the curvature of the p-da/dN-ΔK-R field that resulted from the p-ε_a-N field is more consistent with the existence of the propagation threshold. Both fatigue crack propagation regimes, I and II, may be modelled using the strain-life approach. The crack propagation threshold, ΔK_{th}, should correspond

to the fatigue limit given by the *p*- ε_a-*N* or the *p*-*SWT*-*N* fields. The correct description of the fatigue crack growth in the propagation regime I depends on a convenient characterization of the fatigue limit of the material. An inaccurate fatigue limit definition leads to an underestimation or overestimation of the ΔK_{th}. The proposed model is not able to reproduce the acceleration of the crack propagation near unstable propagation, since this damage process (ductile damage) is not accounted for conveniently by the proposed *p*-*SWT*-*N* and *p*-ε_a-*N* fields.

Concerning the *p*-*da/dN*-Δ*K*-*R* fields predicted for the materials from the Eiffel bridge and of the S355 steel, only the field resulting from the *p*-*SWT*-*N* model produces satisfactory results. On effect, the material from the Fão bridge and the S355 steel show a markedly stress ratio influence, requiring a fatigue damage model that is able to account for the mean stress effects.

Concerning the probabilistic fatigue crack propagation rates fields of the P355NL1 steel, it is clear that the use of the *p*-*SWT*-*N* model overestimates the effects of the stress *R*-ratio. Using the probabilistic *SWT*-*N* model, the stress ratio effect is accounted for twice through the residual stress intensity factor and through the mean stress of the cycle. However, the number of cycles to fail the elementary material block fits from the very low-cycle to low-cycle fatigue regimes (number of cycles lower than 5×10^4 cycles) at which the mean stress effects are generally negligible due to a rapid cyclic mean stress relaxation. The plasticity model with multilinear kinematic hardening, used in the current research, is not able to model the cyclic mean stress relaxation. The predictions based on the *p*-ε_a-*N* model are very satisfactory. Firstly, they define lower and upper bounds for the available experimental data. Secondly, the major influence of the stress ratio is verified when it changes from 0 to 0.5.

In the damage computations presented in the chapter, the prior loading history on crack tip elements was not considered. Preliminary calculations performed considering the prior loading history on a set of elements ahead of the crack tip, forming a process zone, showed only a marginal influence on *da/dN* predictions, mainly in the propagation regimes I and II. On the other hand, the computational costs associated to simultaneous damaged elements increases very significantly.

5.6. CONCLUSIONS

An assessment of the UniGrow model was presented in this section, based on available experimental data for the materials under consideration. The UniGrow model was also extended to predict probabilistic fatigue crack propagation fields, replacing the deterministic *SWT-N* relation proposed in the original UniGrow model by the *p-SWT-N* or *p-*ε_a*-N* fields. The *p-SWT-N* field was firstly proposed in the present chapter, as a generalization of the *p-*ε_a*-N* field, in order to take into account the mean stress effects. Both *p-SWT-N* and *p-*ε_a*-N* fields led to satisfactory correlations of the experimental data available for the materials under investigation. Nevertheless, the percentile lines resulting from the *p-SWT-N* field show an approximate linear shape (for bi-logarithm representations); for the *p-*ε_a*-N* field, some curvature is observed in the respective percentile lines.

The multiaxial analytical Neuber elastoplastic analysis proposed in the UniGrow model to compute the residual stress distribution was assessed using elastoplastic finite element analysis. Inconsistent compressive residual stress distributions, mainly for R_σ=0, were found using this approach. The multiaxial Neuber model does not account for stress redistribution due to yielding, and therefore does not provide the dimensions of the plastic zone. Consequently, the dimensions of the residual compressive stress zone, are not accurately evaluated. The residual compressive stress intensity factor, computed with the compressive residual stress field from the finite element analysis, exhibits a linear relation with the applied stress intensity factor range, which confirms the typical trend documented in literature of linear increase of the residual stress intensity factor with the applied stress intensity factor range, for a specific stress *R*-ratio. The K_r vs. $\Delta K_{applied}$ relation depends on stress *R*-ratio, the K_r being negligible for stress *R*-ratios higher than 0.5 and the applied ΔK, $\Delta K_{applied}$, becoming fully effective. The knowledge of the K_r vs. $\Delta K_{applied}$ relation is important to avoid the necessity of time consuming elastoplastic analysis for every crack increments.

The *p-da/dN-*Δ*K-R* fields predicted for the investigated materials, based on the material *p-SWT-N* field showed a satisfactory agreement with the experimental data available for both materials. The proposed *p-da/dN-*Δ*K-R* fields were able to model conveniently the

stress *R*-ratio effects on crack propagation rates as well as to represent the scatter on these fatigue crack propagation rates, which are significant on this type of materials. Predictions based on material p-ε_a-N field also produced satisfactory results for the materials from the Fão bridge and the P355NL1 steel, since these materials show crack propagation rates with relative small sensitivity to the stress *R*-ratio. The p-da/dN-ΔK-R fields, for the materials from the Eiffel bridge and the S355 steel, the use of the p-SWT-N model was justified since these material are clearly influenced by the mean stress effects.

The elementary material block sizes found for the materials from the Eiffel and Fão bridges are within the same order of magnitude, which is consistent with the fact that they are puddle irons of about same age. However, these elementary material block sizes are two orders of magnitude higher than those proposed in the literature for the 4340 steel, which is a material with smaller grain sizes and significant lower level of heterogeneities. This parameter, for the S355 and P355NL1 steels, was found to be about one order of magnitude higher than the value proposed by Noroozi et al. [12] for the 4340 steel. The ρ^* can be indirectly dependent on the micro-structural features of the analysed material (e.g. grain size) but it cannot be uniquely associated with any specific micro-structural particle size.

5.7. REFERENCES

[1] Schütz W. A History of Fatigue. Eng. Fract. Mech. 1996; 54, pp. 263–300.

[2] Paris PC, Gomez M, Anderson WE. A rational analytic theory of fatigue. Trend Engineering 1961; 13: 9-14.

[3] Beden SM, Abdullah S, Ariffin AK. Review of Fatigue Crack Propagation Models for Metallic Components. European Journal of Scientific Research 2009; 28: 364-397.

[4] Coffin LF. A study of the effects of the cyclic thermal stresses on a ductile metal. Trans ASME 1954;76:931–50.

[5] Manson SS. Behaviour of materials under conditions of thermal stress, NACA TN-2933. National Advisory Committee for Aeronautics; 1954.

[6] Morrow JD. Cyclic plastic strain energy and fatigue of metals. Int Frict Damp Cyclic Plast ASTM STP 1965; 378:45–87.

[7] Smith KN, Watson P, Topper TH. A Stress-Strain Function for the Fatigue of Metals. Journal of Materials 1970; 5(4): 767-778.

[8] Shang D-G, Wang D-K, Li M, Yao W-X. Local stress–strain field intensity approach to fatigue life prediction under random cyclic loading. International Journal of Fatigue 2001; 23: 903–910.

[9] Glinka G. A notch stress-strain analysis approach to fatigue crack growth. Engineering Fracture Mechanics 1985; 21: 245-261.

[10] Peeker E, Niemi E. Fatigue crack propagation model based on a local strain approach. Journal of Constructional Steel Research 1999; 49: 139–155.

[11] Noroozi AH, Glinka G, Lambert S. A two parameter driving force for fatigue crack growth analysis. International Journal of Fatigue 2005; 27: 1277-1296.

[12] Hurley PJ, Evans WJ. A methodology for predicting fatigue crack propagation rates in titanium based on damage accumulation. Scripta Materialia 2007; 56: 681–684.

[13] Noroozi AH, Glinka G, Lambert S. A study of the stress ratio effects on fatigue crack growth using the unified two-parameter fatigue crack growth driving force. International Journal of Fatigue 2007; 29:1616-1633.

[14] Noroozi AH, Glinka G, Lambert S. Prediction of fatigue crack growth under constant amplitude loading and a single overload based on elasto-plastic crack tip stresses and strains. Engineering Fracture Mechanics 2008; 75: 188-206.

[15] Neuber H. Theory of stress concentration for shear-strained prismatic bodies with arbitrary nonlinear stress–strain law. Trans. ASME Journal of Applied Mechanics, 1961; 28: 544–551.

[16] Moftakhar A, Buczynski A, Glinka G. Calculation of elasto-plastic strains and stresses in notches under multiaxial loading. International Journal of Fracture, 1995; 70: 357-373.

[17] Reinhard W, Moftakhar A, Glinka G. An Efficient Method for Calculating Multiaxial Elasto-Plastic Notch Tip Strains and Stresses under Proportional Loading. Fatigue and Fracture Mechanics, Vol. 27, ASTM STP 1296, R.S. Piascik, J.C. Newman, N.E. Dowling, Eds., American Society for Testing and Materials, 1997; pp. 613-629.

[18] Mikheevskiy S, Glinka G. Elastic–plastic fatigue crack growth analysis under variable amplitude loading spectra. International Journal of Fatigue, 2009; 31: 1828–1836.

[19] De Jesus AMP, Silva ALL, Figueiredo MV, Correia JAFO, Ribeiro AS, Fernandes AA. Strain-life and crack propagation fatigue data from several Portuguese old metallic riveted bridges. Engineering Failure Analysis, 2010; 17: 1495–1499.

[20] De Jesus AMP, Matos R, Fontoura BFC, Rebelo C, Simões da Silva L, Veljkovic M. A comparison of the fatigue behaviour between S355 and S690 steel grades. Journal of Constructional Steel Research 79 ,2012; 140–150.

[21] De Jesus AMP, Ribeiro AS, Fernandes AA. Influence of the Submerged Arc Welding in the Mechanical Behaviour of the P355NL1 Steel—Part II: Analysis of the Low/High Cycle Fatigue Behaviours. J. Mater. Sci., 42, 2007, pp. 5973–5981.

[22] Castillo E, Fernández-Canteli A. A Unified Statistical Methodology for Modeling Fatigue Damage. Springer, 2009.

[23] Basquin OH. The exponential law of endurance tests. Proc. Annual Meeting American Society for

Testing Materials, 1910; 10: 625-630.

[24] Creager M, Paris PC. Elastic field equations for blunt cracks with reference to stress corrosion cracking. International Journal of Fracture Mechanics, 1967; 3: 247–252.

[25] Molski K, Glinka G. A method of elastic-plastic stress and strain calculation at a notch root. Materials Science and Engineering, 1981; 50: 93-100.

[26] Glinka G. Development of weight functions and computer integration procedures for calculating stress intensity factors around cracks subjected to complex stress fields. Progress Report No.1: Stress and Fatigue-Fracture Design, Petersburg Ontario, Canada, 1996.

[27] Sadananda K, Vasudevan AK, Kang IW. Effect of Superimposed Monotonic Fracture Modes on the ΔK and K_{max} Parameters of Fatigue Crack Propagation. Acta Materialia, 2003, 51(22): 3399-3414.

[28] Kajawski D. A new $(\Delta K^{+} K_{max})^{0.5}$ driving force parameter for crack growth in aluminium alloys. International Journal of Fatigue, 2001, 23(8): 733-740.

[29] Schiffner K. Overlay Models for Structural Analysis under Cyclic Loading. Computers and Structures, Vol. 56, No. 2/3, 1995, pp. 321-328.

[30] SAS, 2011, ANSYS, Swanson Analysis Systems, Inc., Houston, Version 12.0.

[31] Simo JC, Taylor RL. Consistent Tangent Operators for Rate-Independent Elastoplasticity. Computer Methods in Applied Mechanics and Engineering, Vol. 48, 1985, pp. 101-118.

[32] Castillo E, Galambos J. Lifetime Regression Models Based on a Functional Equation of Physical Nature. Journal of Applied Probability, 1987, 24: 160-169.

[33] ASTM – American Society for Testing and Materials. ASTM E606-92: standard practice for strain controlled fatigue testing. In: Annual book of ASTM standards, part 10; 1998. p. 557–71.

[34] Ramberg W, Osgood WR. Description of the stress-strain curves by the three parameters. NACA TN-902, National Advisory Committee for Aeronautics, 1943.

[35] ASTM – American Society for Testing and Materials. ASTM E647: standard test method for measurement of fatigue crack growth rates. In: Annual book of ASTM standards, vol. 03.01. West Conshohocken, PA: ASTM – American Society for Testing and Materials; 2000. p. 591–630.

[36] Castillo E, Fernández-Canteli A, Hadi AS, López-Anelle M. A Fatigue Model with Local Sensitivity Analysis. Fatigue and Fracture of Engineering Material and Structure, 2006, 30: 149–168.

[37] Correia JAFO, De Jesus AMP, Fernández-Canteli A. A procedure to derive probabilistic fatigue crack propagation data. International Journal of Structural Integrity, 2012; Vol. 3, No. 2: 158–183.

[38] Correia JAFO, De Jesus AMP, Fernández-Canteli A. Critical assessment of a local strain-based fatigue crack growth model using experimental data available for the P355NL1 steel. Engineering Structures, 2013; Vol. 52: 394–407.

[39] Hafezi MH, Abdullah NN, Correia JAFO, De Jesus AMP. An assessment of a strain-life approach for fatigue crack growth. International Journal of Structural Integrity, 2012; Vol. 3, No. 2: 344–376.

[40] Correia JAFO, De Jesus AMP, Fernández-Canteli A, Calçada RAB. Modelling probabilistic fatigue crack propagation rates of mild strength steels. Proceedings of the 3.º Congresso de Segurança e Conservação de Pontes (ASCP'13), 2013.

[41] De Jesus AMP, Correia JAFO. Critical assessment of a local strain-based fatigue crack growth model using experimental data available for the P355NL1 steel. Journal of Pressure Vessel Technology, 2013; Vol. 135, No. 1: 011404-1–0114041-9.

CHAPTER VI

PROCEDURE TO DERIVE PROBABILISTIC S-N FIELDS FOR STRUCTURAL DETAILS (p-S-N_f-R)

6.1. INTRODUCTION

Probabilistic fatigue models are required to account conveniently for several sources of uncertainty arising in the prediction procedures for structural details, such as the scatter in material behaviour. In this chapter, an approach is proposed to generate probabilistic *S*–*N* fields for distinct stress *R*-ratios, based on the local approaches supported by the probabilistic ε_a–*N* or Smith–Watson–Topper (*SWT*)–*N* fields [1,2]. Both fatigue crack initiation and fatigue crack propagation mechanisms are accounted for in the proposed approach, which is applied to two notched geometries, one made of P355NL1 steel and the other made of puddle iron from the Eiffel bridge.

This chapter suggests an extension of the fatigue crack propagation model proposed by Noroozi et al. [3,4] to structural details, in order to cover both the fatigue crack initiation and fatigue crack propagation, based on local strain approaches to fatigue. The model proposed by Noroozi et al. [3,4], commonly denoted *UniGrow* model, has been classed as a residual stress based crack propagation model [5]. This model is applied in this chapter to derive probabilistic fatigue crack propagation fields for notched details, for distinct stress R-ratios (*p*–*S*–N_p–*R* fields). The material representative element size, ρ^*, required by *UniGrow* model was previously introduced in the Chapter V using exclusively fatigue crack propagation data obtained from compact tension (CT) specimens. The same procedure was followed to compute the *p*–*S*–N_p–*R* field for the notched component,

considering an initial crack of ρ^* size. The probabilistic fatigue crack initiation field was evaluated using the material $p–\varepsilon_a–N$ *or* $p–SWT–N$ fields applied to calculate the fatigue damage of the first elementary material block, ahead of the notch root. Consequently, an unified approach for the global prediction (crack initiation and propagation) of the probabilistic $S–N_f–R$ fields is proposed. The predictions are compared with available experimental $S–N$ fatigue data available for two notched details under consideration [6,7].

6.2. GENERAL PROCEDURE TO GENERATE P–S–N_f–R FIELDS FOR STRUCUTRAL DETAILS

6.2.1. Description of the procedure

The procedure proposed to derive the probabilistic $S–N–R$ fields for structural details or mechanical components is applied according to the following steps:

1. Estimation of the parameters of the $p–SWT–N$ or $p–\varepsilon_a–N$ material fields, as described in Section 5.4.3. of Chapter V, using experimental fatigue data from smooth specimens. These probabilistic fields will be the basis for the probabilistic $S–N$ fields of the structural details. They will be used to model both crack initiation and crack propagation. The selection of the damage parameter will depend on material/detail sensitivity to the stress ratio.

2. Estimation of the elementary material block size, ρ^*, using crack propagation data, following the procedure by Noroozi et al. [3,4]. The elementary material block size is estimated using a trial and error procedure in order the fatigue crack propagation field prediction to fit the experimental fatigue crack propagation data, for several stress ratios. This step should be performed using fatigue crack propagation data from cracked specimens in order to avoid the need to model the fatigue crack initiation. This step was implemented in the Chapter V, using fatigue crack propagation data from CT specimens.

3. Fulfilment of elastoplastic analysis to the uncracked structural detail in order to evaluate the average local stresses and strains at the first element block size ahead of the notch root. This step was performed in this chapter, using the finite element method.

4. Application of the *p–SWT–N* or *p–*ε_a*–N* models to derive the *p–S–*N_i*–R* fields representative of the macroscopic crack initiation, in the structural detail/mechanical component.

5. Application of the adapted *UniGrow* model to evaluate the fatigue crack propagation in the structural detail, using the elementary material block size computed previously on step 2. The residual stress field required in the *UniGrow* model is computed in this chapter using elastoplastic finite element analysis.

6. Computation of the *p–S–*N_p*–R* fields corresponding to the fatigue crack propagation in the structural detail/mechanical component.

7. Combination of probabilistic fields from steps 4 and 6 to evaluate the global *p–S–*N_f*–R* field for the structural detail/mechanical component.

Based on these arguments, the structural detail resisting section can be represented as a sum of elementary material blocks of length ρ^*, placed along the crack propagation path (see Figure 6.1). The procedures adopted to compute the probabilistic *S–*N_i*–R* and *S–*N_p*–R* fields, for structural details are illustrated in Figure 6.2 and Figure 6.3, respectively [8].

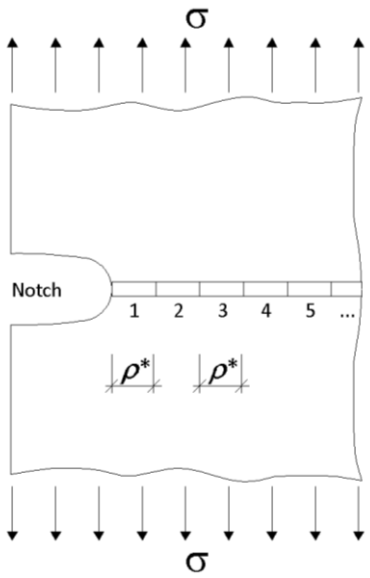

Figure 6.1 – Representative material blocks along the crack propagation path of a notched geometry.

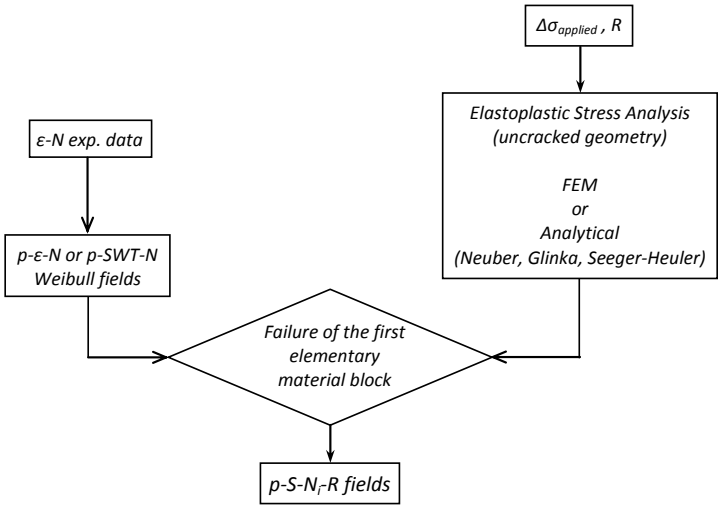

Figure 6.2 – Procedure for the estimation of the probabilistic fatigue crack initiation field for notched geometries.

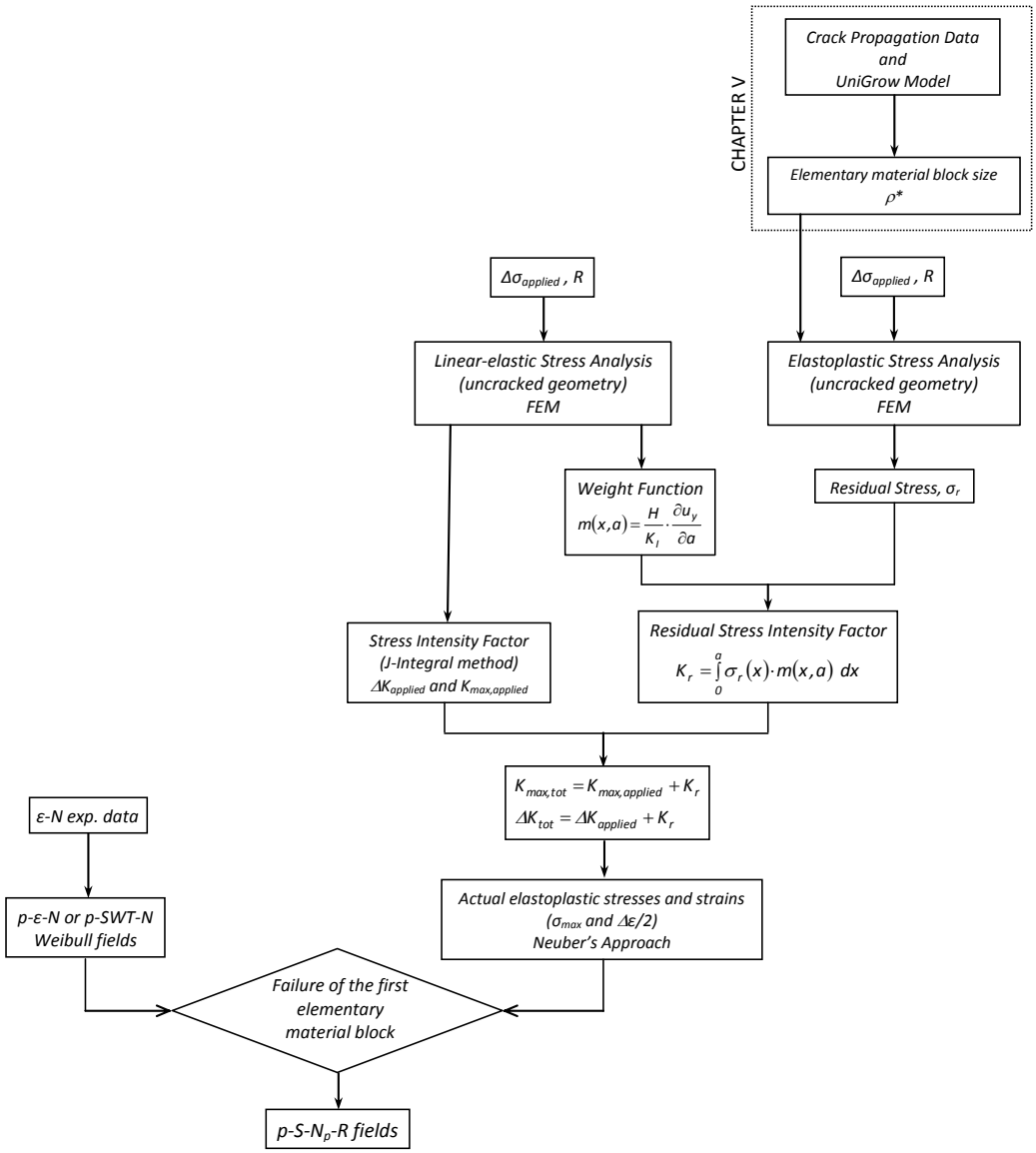

Figure 6.3 – Procedure for the estimation of the probabilistic fatigue crack propagation field for the notched geometries [8].

6.2.2. Additional considerations on the application of the UniGrow model

The *UniGrow* model was proposed by Noroozi et al. [3] based on the assumptions described in Section 5.2.1. of Chapter V.

The procedure proposed by Noroozi et al. [3] to compute the elastoplastic stresses and strains at the elementary material blocks ahead of the crack tip, is developed in the current discussion, particularly in what concerns the determination of the number of cycles to failure of the elementary material blocks, in the fatigue crack propagation regime, according to the following procedure:

i) The stress intensity factors are determined for the detail under investigation using linear elastic finite element analysis with the J-integral method.

ii) The original procedure for the computations of the residual stress distribution consisted in the following actions:

a) The elastic stress fields ahead of the crack tip are estimated using analytical solutions for a crack with a tip radius, ρ^*, and determining the stress intensity factors.

b) The actual elastoplastic stresses and strains, ahead of the crack tip, are computed using Neuber's or Glinka's approach [9,10].

c) The residual stress distribution ahead of the crack tip is computed using the maximum actual elastoplastic stresses resulting at the end of the first load reversal and, subsequently, the cyclic elastoplastic stress range, $\sigma_r = \sigma_{max} - \Delta\sigma$.

In this study, steps a), b) and c) were replaced by an elastoplastic finite element analysis in order to allow the direct computation of the residual stress fields to be performed. A loading-unloading load step sequence was simulated and the residual stresses resulted as the stresses at the end of the unloading step.

iii) The residual stress distribution computed ahead of the crack tip is assumed to be applied on the crack faces, behind the crack tip, in a symmetric way with respect to the crack tip. The residual stress intensity factor, K_r, is computed using the weight function method according to the following general expression [11]:

$$K_r = \int_0^a \sigma_r(x) \cdot m(x,a)\, dx \tag{6.1}$$

To this purpose, the weight function $m(x,a)$ was computed for the cracked detail under consideration using the following expression [11]:

$$m(x,a) = \frac{H}{K_I} \cdot \frac{\partial u_y}{\partial a} \tag{6.2}$$

where $H=E$ (Young's modulus) for generalized plane stress, and $H=E/(1-\nu^2)$ for plane strain, ν being the Poisson's ratio, K_I is the stress intensity factor and u_y is the corresponding crack opening displacement. In this research the weight functions were computed using a linear elastic finite element model for the cracked geometries. The displacements, u_y and the stress intensity factors, K_I, were computed as a function of the crack size, a, allowing the application of Equation (6.2).

iv) The applied stress intensity factor (maximum and range values) is corrected using the residual stress intensity value, resulting in the total values, $K_{max,tot}$ and ΔK_{tot} [3,4]. For positive applied stress ratios, $K_{max,tot}$ and ΔK_{tot} may be computed as follows:

$$\begin{aligned} K_{max,tot} &= K_{max,applied} + K_r \\ \Delta K_{tot} &= \Delta K_{applied} + K_r \end{aligned} \tag{6.3}$$

where K_r takes a negative value corresponding to the compressive stress field. This residual stress correction makes the crack propagation model sensitive to the stress ratio effects. In fact, the compressive stresses decrease with increasing stress ratio. Consequently, the total stress intensity factors tend to the corresponding applied stress intensity factor. For lower stress ratios, the total stress intensity factors will be lower than the applied ones. This step, corresponds to the original proposal of Noroozi et al. [3] that was followed in this study.

v) Using the total values of the stress intensity factors, the above steps 2a) and 2b) are applied to determine the updated values of the actual maximum stress and actual strain range for the material representative elements. Then, Smith-Watson-Topper (*SWT*)-N [2] or Morrow's relations [1] are applied to compute the number of cycles required for the material representative element to fail. For materials with higher sensitivity of the stress propagation rates to the stress ratio, Smith-Watson-Topper (*SWT*)-N [2] should be used;

otherwise, Morrow's relations [1] may be adequate. The Morrow equation referred here corresponds to the superposition of Basquin [12] and Coffin-Manson relations [13,14] without any mean stress correction.

The *UniGrow* crack propagation model will be applied to compute the number of cycles required to propagate an initial crack at the notch root of a component until its critical dimension, responsible for the collapse of the component, is achieved. In this research, it is postulated that the crack initiation corresponds to the development of a crack with a size equal to the elementary material block dimension, ρ^*. In addition to the number of cycles required to propagate the crack, the number of cycles required to initiate a crack of a size, ρ^*, equal to the elementary material block, will be also computed using a local approach. For this purpose, an elastoplastic stress/strain analysis will be carried out for the uncracked geometry to derive the average stress/strains at the first elementary material block ahead of the notch root.

6.3. EXPERIMENTAL FATIGUE DATA OF THE NOTCHED GEOMETRIES UNDER CONSIDERATION

In this section, the experimental fatigue data of the basic materials and notched details under consideration in this study are presented. Two materials are considered in this research, namely the puddle iron from the Portuguese Eiffel bridge and P355NL1 steel (pressure vessel steel). The experimental fatigue data of these materials are presented in detail in Chapter III and Section 5.4. of Chapter V.

6.3.1. Notched detail made of P355NL1 steel

The P355NL1 steel is used for pressure vessels manufacturing proposes. The monotonic, cyclic and strain-life properties of this material are obtained from the references [6] and [15] and summarized in Tables 6.1 and 6.2.

Table 6.1 – Monotonic and cyclic elastoplastic properties of the P355NL1 steel [6,15].

E	ν	f_u	f_y	K'	n'
GPa	-	*MPa*	*MPa*	*MPa*	-
205.20	0.275	568.11	418.06	948.35	0.1533

Table 6.2 – Morrow constants of the P355NL1 steel [6,15].

σ'_f	b	ε'_f	c
MPa	-	-	-
1005.50	-0.1033	0.3678	-0.5475

Fatigue crack propagation curves (*da/dN versus ΔK* curves) were determined for the P355NL1 steel using compact tension (CT) specimens. A total of five specimens were tested under load control: two specimens under load stress *R*-ratio equal to 0 (MB02 & MB04); two specimens under R_σ=0.5 (MB03 & MB05) and one specimen under R_σ=0.7 (MB06). The respective fatigue crack growth data can be found in sub-section 5.4.2 of Chapter V and is reproduced in Figure 6.4 [16].

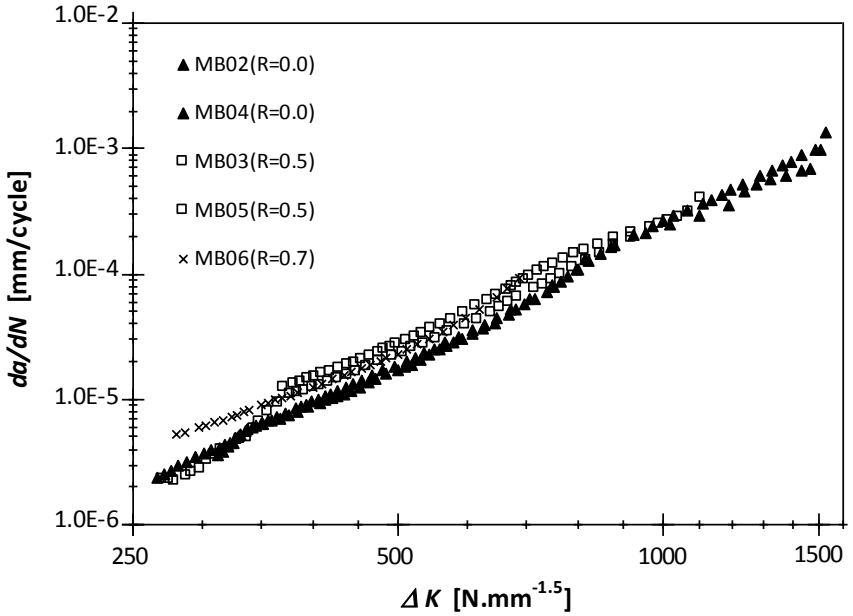

Figure 6.4 – Fatigue crack propagation data of the P355NL1 steel for distinct stress ratios.

More details about the fatigue properties evaluation, concerning P355NL1 steel, are given in Section 5.4. of Chapter V and in reference [16].

A notched detail made of P355NL1 steel, consisting of a double side notched rectangular plate, as illustrated in Figure 6.5 (L1=L2=35mm, L=25mm), was considered in this investigation. This geometry was fatigue tested under remote stress controlled conditions, for three distinct stress ratios, namely R_σ=0, R_σ=0.15 and R_σ=0.3. The respective fatigue data can be found in literature [6] and is illustrated in Figure 6.6. The stress range plotted in Figure 6.6 corresponds to the nominal stress range applied to the

plate. The analysis of the results shows a significant sensitivity of the *S-N* data to the stress ratio.

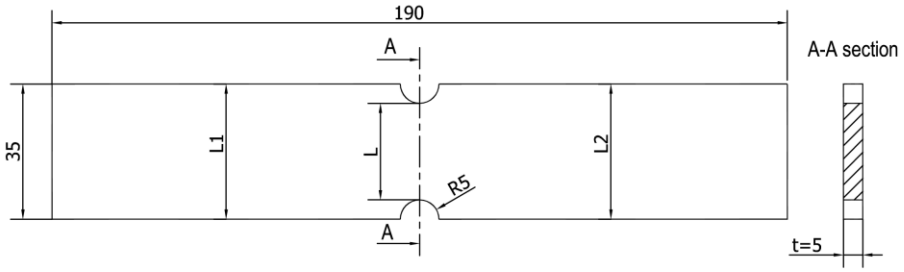

Figure 6.5 – Rectangular notched plate of P355NL1 steel (dimensions in mm).

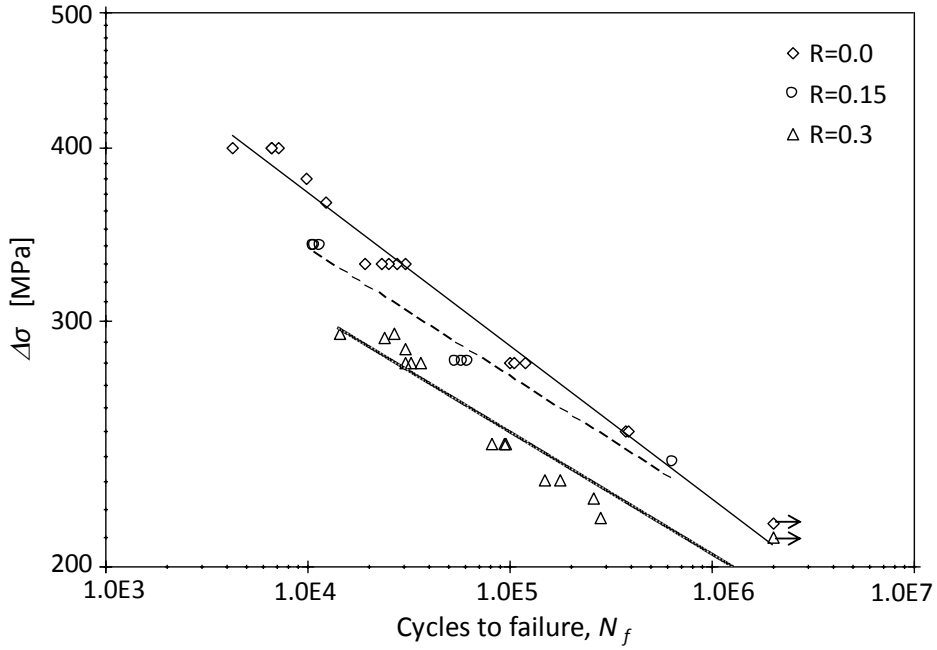

Figure 6.6 – *S-N* data of the notched plate of P355NL1 steel.

The probabilistic *SWT-N* and *p-*ε_a*-N* fields for the P355NL1 steel are presented in Section 5.4.3. of Chapter V to describe the strain-life field of the material, based on the Weibull distribution. The *p-*ε_a*-N* field will be latter used in this chapter to model the fatigue crack propagation field for the notched detail; the *p-SWT-N* field will be used to model the fatigue crack initiation field for the notched detail. Both probabilistic fields will be used with adopted *UniGrow* model to obtain the probabilistic *S-N-R* field.

6.3.2. Notched geometry made of puddle iron from the Eiffel bridge

The puddle iron from the Portuguese Eiffel bridge was also considered in this study. The fatigue behaviour of this material was determined based on fatigue tests of smooth

specimens and fatigue crack propagation tests. The fatigue tests of smooth specimens were carried out according to the ASTME606 standard [17], under strain controlled conditions and the respective results are summarized in Tables 6.3 and 6.4 [18].

Table 6.3 – Monotonic and cyclic elastoplastic properties of the material from the Eiffel bridge [18].

E	ν	f_u	f_y	K'	n'
GPa	-	*MPa*	*MPa*	*MPa*	-
193.11	0.300	342	292	645.95	0.0946

Table 6.4 – Morrow constants of the material from the Eiffel bridge [18].

σ'_f	b	ε'_f	c
MPa	-	-	-
602.50	-0.0778	0.1595	-0.7972

The fatigue crack propagation tests were performed under load controlled conditions, using CT specimens, in accordance with the procedures of the ASTM E647 standard [19]. CT specimens from the Eiffel bridge were defined with a width, W=40mm, and a thickness, B=4.5mm. The fatigue crack propagation tests were performed for stress *R*-ratios, R_σ=0.1 and R_σ=0.5, as illustrated in Figure 6.7 [18].

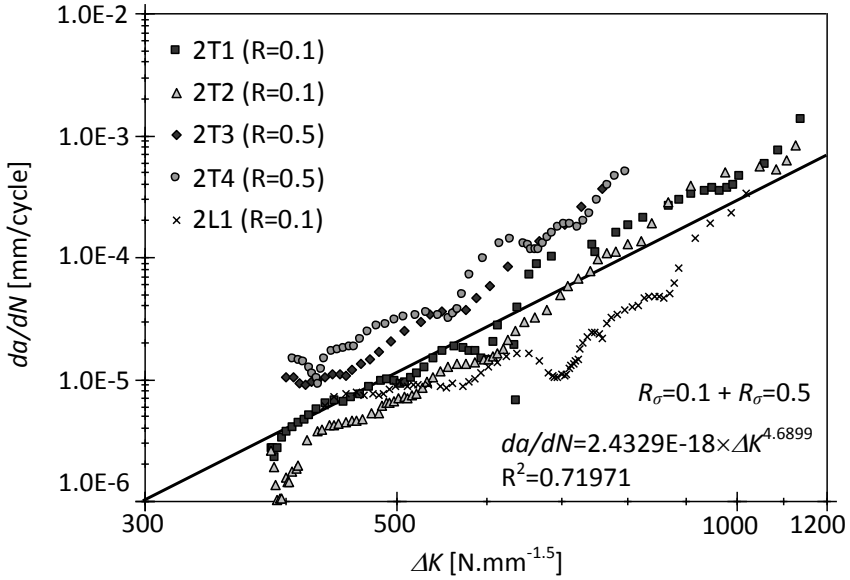

Figure 6.7 – Fatigue crack propagation data of the material from the Eiffel bridge for distinct stress ratios.

Due to the relatively high sensitivity of the fatigue propagation rates to the stress R-ratio, the fatigue crack propagation rates for this material were modelled using the *UniGrow* model based on the *SWT* damage parameter (see Section 5.5.1.1. of Chapter V).

More details about the fatigue properties evaluation, concerning material from Eiffel bridge, are given in Chapter III, and Section 5.4. of Chapter V and reference [18].

A plate with a circular hole, made of puddle iron from the Eiffel bridge, as illustrated in Figure 6.8, was considered in this investigation. The *S-N* results presented in this sub-section were obtained using fatigue tests of specimens subjected to load control conditions, for stress R-ratio equal to 0, and performed on a servo-hydraulic machine rated to 100kN at test frequencies, *f*, ranging between 5 and 10Hz. A total of 15 specimens were tested. Figure 6.9 illustrates the complete test series of the structural detail made of material extracted from Eiffel bridge. The results of these fatigue tests are summarized in Table 6.5. The respective fatigue data can be found in Figure 6.10 [7]. The stress range plotted in Figure 6.10 corresponds to the nominal/net stress range applied to the plate.

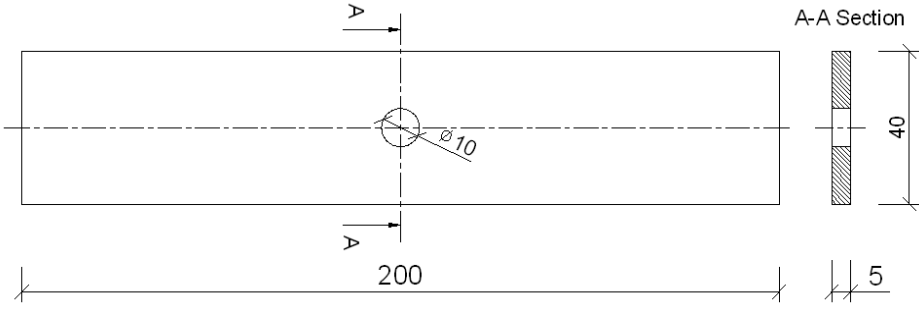

Figure 6.8 – Plate made of puddle iron from the Eiffel bridge with a circular hole (dimensions in mm).

Table 6.5 – Complete test series of the component detail made of material extracted from Eiffel bridge.

Specimen	S_{gross}	S_{net}	R_σ	F_{max}	ΔF	f	$\Delta\sigma_{gross}$	$\Delta\sigma_{net}$	N_f
-	mm^2	mm^2	-	N	N	Hz	MPa	MPa	cylces
C1	199.4	139.5		28173	27891	10.0	139.9	200.0	251736
C2	199.2	139.4		38031	37651	10.0	189.1	270.0	41000
C3	197.8	139.1		41162	40750	10.0	206.0	293.0	6002
C4	195.1	137.0		27687	27410	10.0	140.5	200.0	804145
C5	203.3	142.1		28705	28418	10.0	139.8	200.0	607464
C6	198.4	138.8		41069	40658	5.0	204.9	293.0	12650
C7	195.7	137.0		33905	33566	7.5	171.6	245.0	91668
C8	201.6	141.1	0.01	34929	34580	7.5	171.5	245.0	112741
C9	197.5	138.1		37652	37275	10.0	188.7	270.0	28730
C10	201.2	141.0		38444	38060	10.0	189.2	270.0	20922
C11	203.1	142.4		32357	32033	10.0	157.7	225.0	325192
C12	198.8	138.8		31556	31240	10.0	157.1	225.0	196119
C13	193.9	135.4		24610	24364	10.0	125.7	180.0	911186
C14	198.1	138.5		27987	27707	10.0	139.9	200.0	584230
C15	212.1	148.2		33683	33346	10.0	157.2	225.0	345328

Figure 6.9 – Specimen plates made of puddle iron from the Eiffel bridge with a circular hole (dimensions in mm).

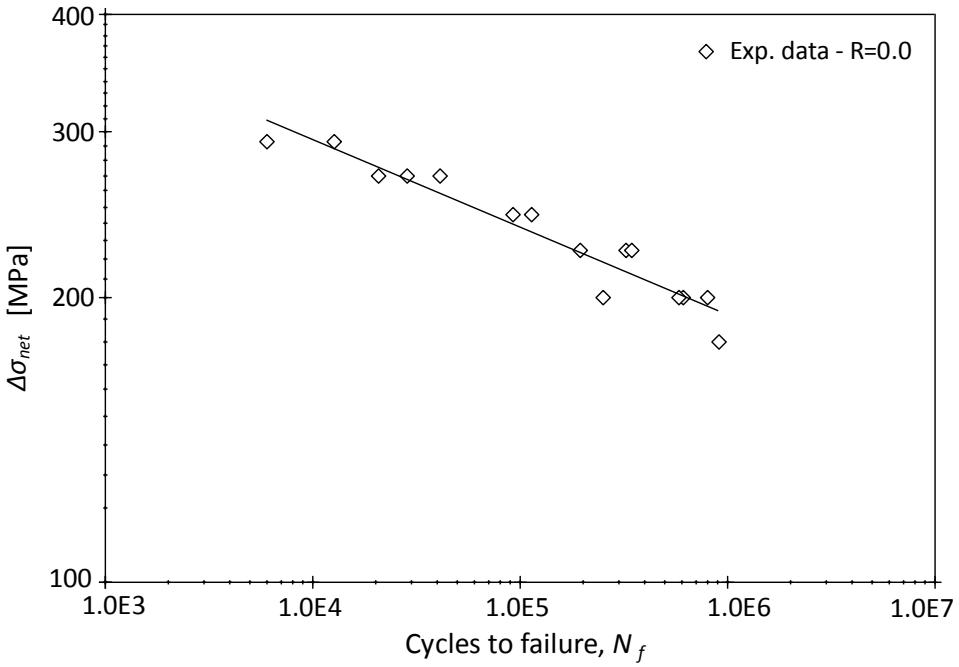

Figure 6.10 – *S-N* data of the plate made of puddle iron from the Eiffel bridge with a circular hole.

The probabilistic *SWT-N* and ε_a-*N* fields for the material from the Eiffel bridge are presented in Section 5.4.3. of Chapter V where the strain-life fields of several materials are presented based on the Weibull distribution. The *p-SWT-N* field will be used to model the fatigue crack initiation and propagation fields for the notched structural detail.

6.4. PREDICTION OF THE PROBABILISTIC S-N FIELDS FOR THE STRUCTURAL DETAILS

In this section the probabilistic *S-N* fields for the structural details are computed. These probabilistic fields will result from the superposition of the crack initiation and crack

propagation probabilistic fields. The number of cycles to failure is assumed to follow the relation:

$$N_f = N_i + N_p \tag{6.4}$$

The crack initiation corresponds to the initiation of a crack size equal to the elementary material block size, ρ^*. The number of crack propagation cycles will correspond to the number of cycles required to propagate the initial crack size of the elementary material block size until failure, i.e., unstable crack propagation.

6.4.1. Notched detail made of P355NL1 steel

The crack initiation will be modelled using the *p-SWT-N* field, due to the sensitivity of the detail to the stress ratio, which is not visible on the fatigue crack propagation rates. Elastoplastic analysis is performed on the uncracked geometry to compute the local/notch stress-strain response needed to compute the *SWT* parameter. The crack propagation will be performed using the denoted *UniGrow* model, using probabilistic fatigue damage fields.

The elementary material block size, ρ^*, equal to 3×10^{-5}m, was estimated in the Section 5.5.1.4. of Chapter V, using fatigue crack propagation data from CT specimens. The value of this parameter will be used in the prediction of the probabilistic *S-N* field for the notched detail represented in Figure 6.5.

6.4.1.1. Finite element analysis of notched detail

In order to assess the accuracy of the simplified elastoplastic analysis, for the residual stress estimation, a bi-dimensional finite element model of the notched detail was proposed, using ANSYS® 12.0 commercial code [20]. Figure 6.11 illustrates a typical finite element mesh of the detail. This mesh exhibits a crack on the left notch. In the practice, cracks started at one side notch root and propagated asymmetrically in the plate. Taking into account the existing symmetry plane, only half of the geometry is modelled. Plane stress 6-noded quadratic triangular elements (PLANE 181) were used in the analysis due to the limited specimen thickness. A parametric model was built using the APDL language.

Concerning the residual elastoplastic stress computation, a highly refined mesh at the crack tip region was used in order to model the crack tip notch radius, ρ^* (see magnification in Figure 6.11). A von Mises yield model, with multilinear kinematic hardening, was used in the simulations with ANSYS® 12.0 code [20]. The plasticity model was fitted to the stabilized cyclic curve of the material (see Section 5.5.1.4. of Chapter V or references [6,15,16]).

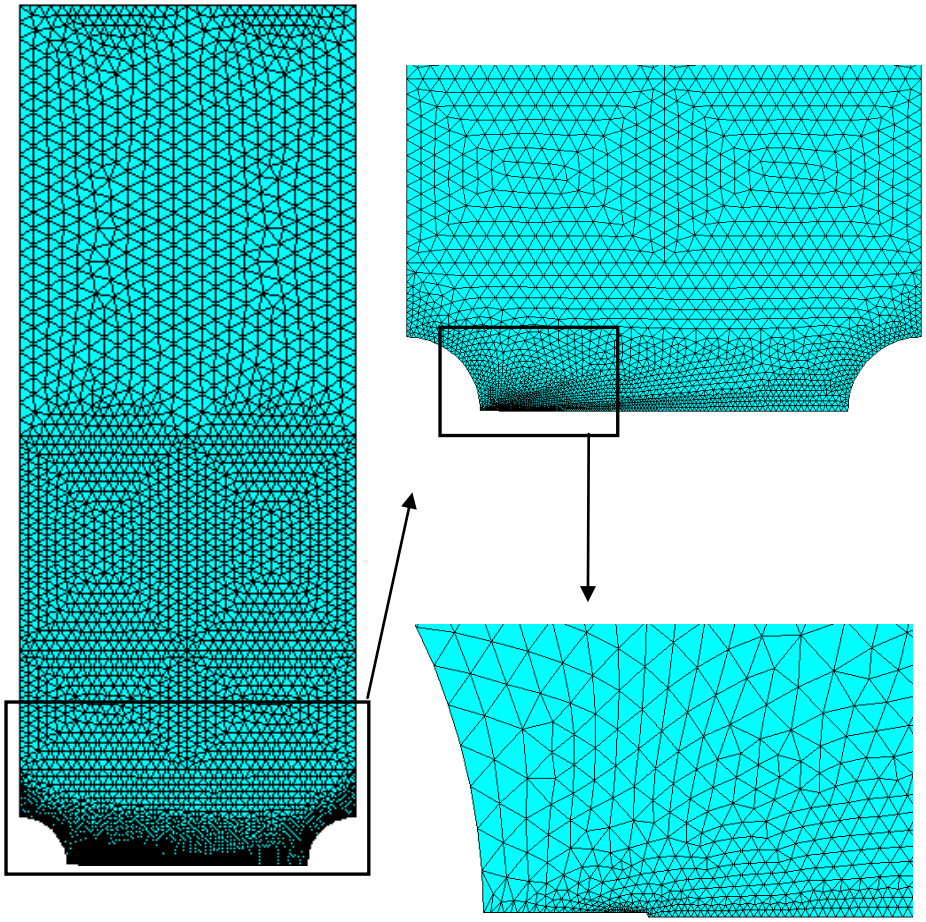

Figure 6.11 – Finite element mesh of the rectangular notched plate with a side crack.

6.4.1.2. Prediction of the probabilistic S-N_i-R field

The *p-SWT-N* model is used to predict the fatigue crack initiation (failure of the first elementary material block) at the notch root of the detail – the procedure is illustrated in the Figure 6.2. An elastoplastic finite element analysis was used to compute the stress/strain history at the notch root. The same material model as used for the CT specimen simulation was adopted for the detail. In order to allow the strain amplitude

computation, loading followed by unloading steps were simulated, using a plasticity model identified with the stabilised cyclic stress-strain curve of the material.

Figures 6.12 and 6.13 show the elastoplastic stress distributions along the *x* and *y* directions for the notched detail made of P355NL1 steel, respectively, assuming applied nominal stress of 200MPa, 275MPa and 350MPa, and computed along the minimum cross section line.

Figures 6.14 and 6.15 show the residual elastoplastic stress and strain range distributions for the notched detail made of P355NL1 steel, respectively, assuming nominal stress ranges of 200MPa, 275MPa and 350MPa (R_σ=0).

Figures 6.16 and 6.17 show, respectively, the stress and strain fields from the left notch root obtained for the structural detail under consideration using the elastoplastic finite element analysis. The results were obtained using the properties of the P355NL1 steel and assuming a nominal stress of 275MPa.

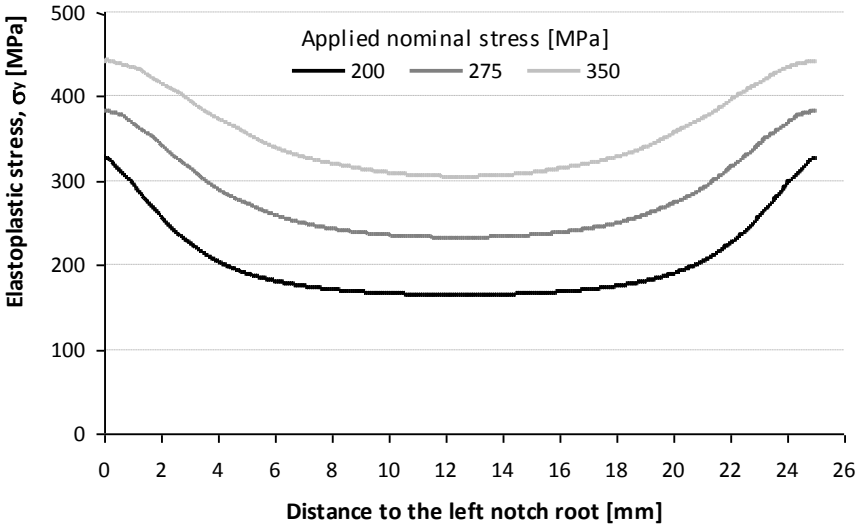

Figure 6.12 – Elastoplastic stress distribution, σ_y, as a function of the distance to the left notch root.

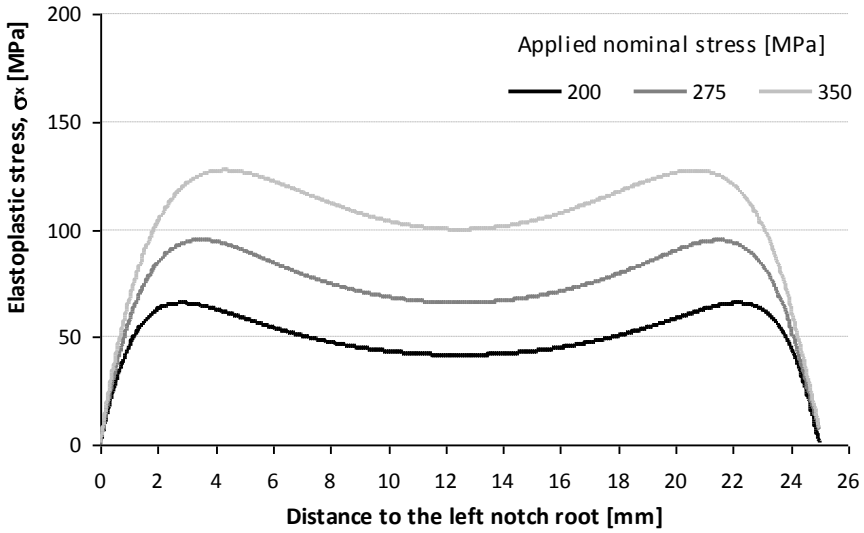

Figure 6.13 – Elastoplastic stress distribution, σ_x, as a function of the distance to the left notch root.

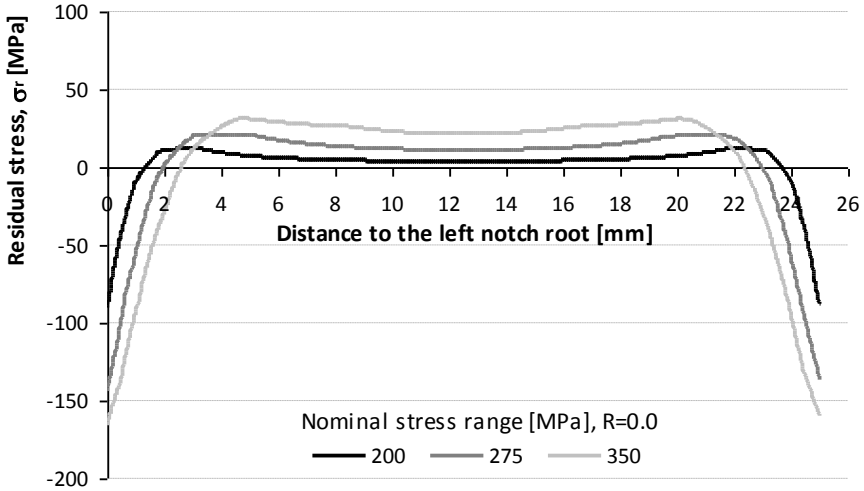

Figure 6.14 – Residual elastoplastic stress distribution, σ_r, as a function of the distance to the left notch root.

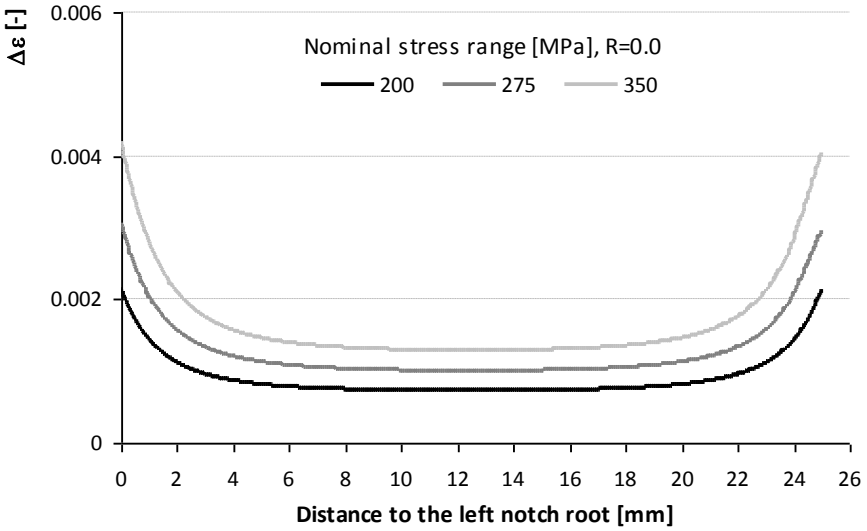

Figure 6.15 – Strain range, $\Delta\varepsilon$, as a function of the distance to the left notch root (R_σ=0).

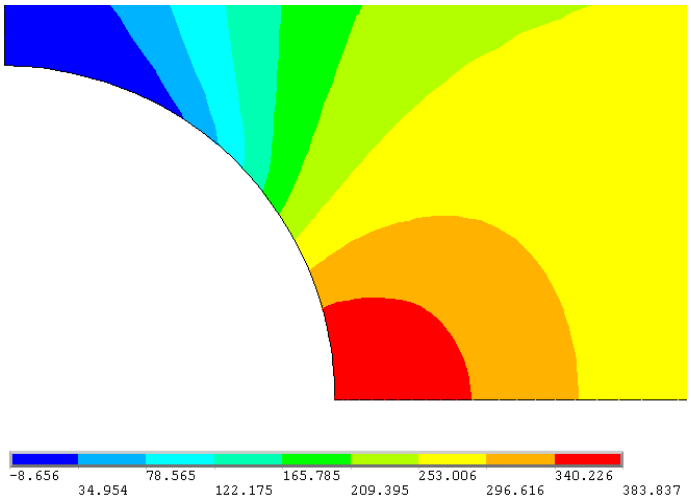

a)

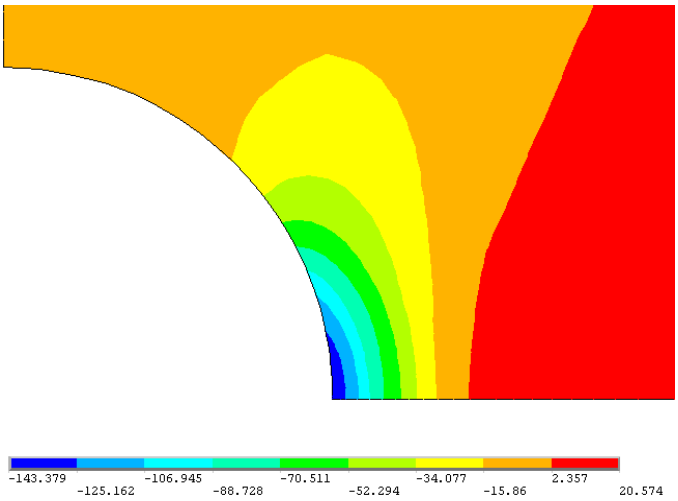

b)

Figure 6.16 – Stress fields from the left notch root, obtained for the structural detail of the P355NL1 steel, resulting from elastoplastic finite element analysis ($\Delta\sigma$ = 275MPa and R_σ=0.0): a) Stress field, σ_y, in MPa, at the end of the first loading reversal; b) Stress field, σ_y, in MPa, at the end of the first unloading reversal.

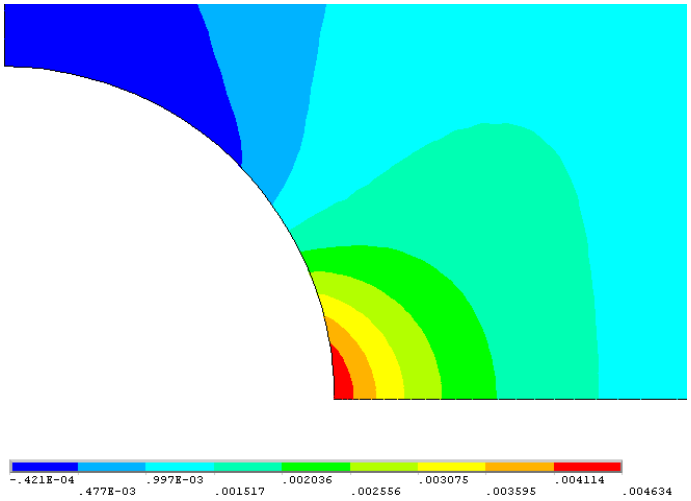

a)

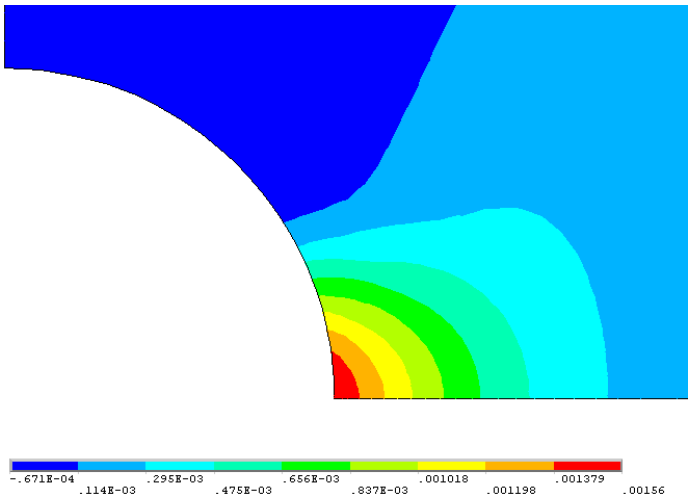

b)

Figure 6.17 – Strain fields from the left notch root, obtained for the structural detail of the P355NL1 steel, resulting from elastoplastic finite element analysis ($\Delta\sigma$ = 275MPa and R_σ=0.0): a) Strain field at the end of the first loading reversal; b) Strain field at the end of the first unloading reversal.

Figure 6.18 shows the *p*-*S*-N_i fields corresponding to the fatigue crack initiation for the notched detail, for R_σ=0.0, R_σ=0.15 and R_σ=0.3. The analysis of the graphs demonstrates that fatigue crack initiation is dominant, since the proposed *p*-*S*-N_i fields already produces a good description of the *S*-*N* fatigue data of the detail [8].

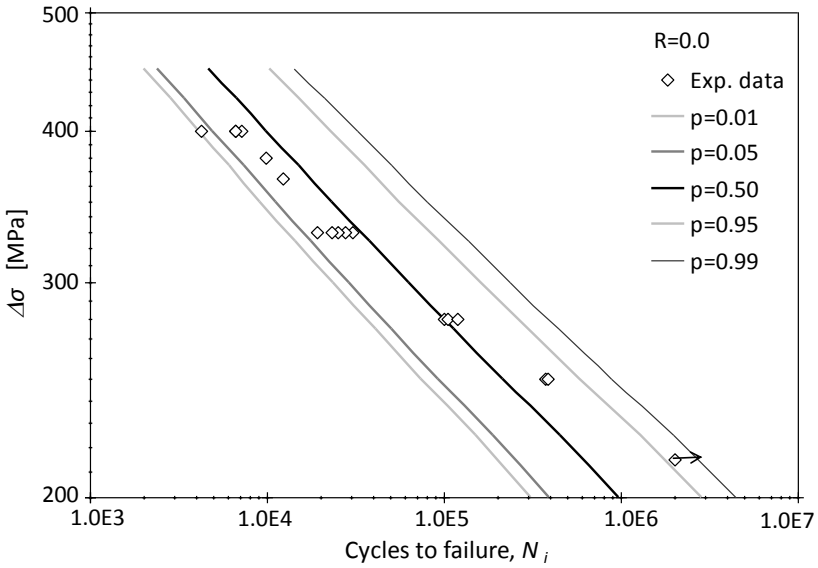

a)

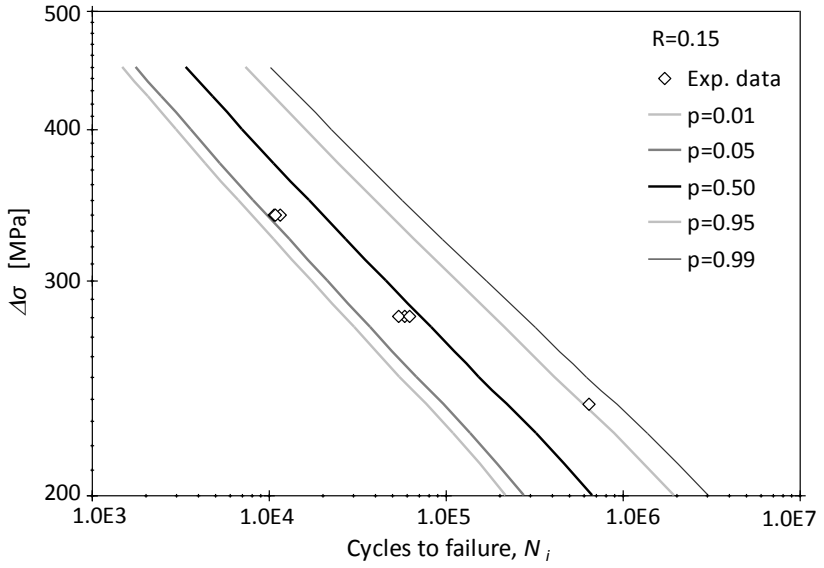

b)

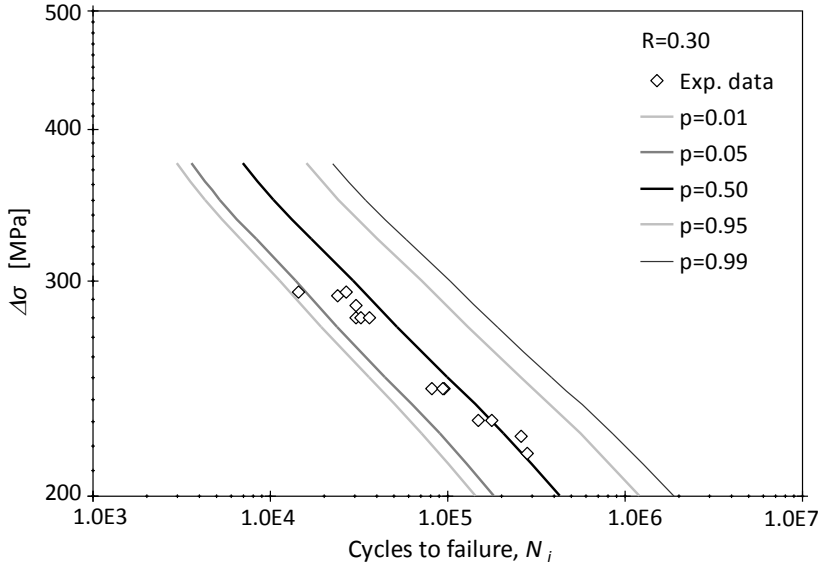

c)

Figure 6.18 – *p-S-N$_i$-R* fields for the notched detail made of P355NL1 steel: a) R_σ=0.0; b) R_σ=0.15; c) R_σ=0.30.

6.4.1.3. Prediction of the probabilistic S-N$_p$-R field

The procedure adopted to compute the probabilistic *S-N$_p$-R* fields for the notched plate is illustrated in Fig. 6.3. The elementary material block size, ρ^*, equal to 3×10^{-5}m, was previously estimated using an independent identification based on pure fatigue crack propagation data (see Section 5.5.1.4. of Chapter V or reference [16]). Finite element models of the detail were used to perform elastoplastic stress analysis for the computation of the residual stresses. In addition, linear elastic finite element models were used to compute the weight functions required for the residual stress intensity

factor computation as well as the stress intensity factor solutions for the notched geometry.

The stress intensity factors were determined based on a linear-elastic finite element analysis using the J-integral method. Figure 6.19 presents the stress intensity evolution with the crack length, for a unitary remote stress used to determine the $\Delta K_{applied}$.

The residual elastoplastic stress computation was based on a elastoplastic finite element analysis using the von Mises yield model, with multilinear kinematic hardening. Figure 6.20 presents the residual stress distribution ahead of the crack tip, from the elastoplastic finite element analysis. These residual stresses were computed after loading/unloading steps. Very high compressive stresses are observed at the vicinity of the crack tip.

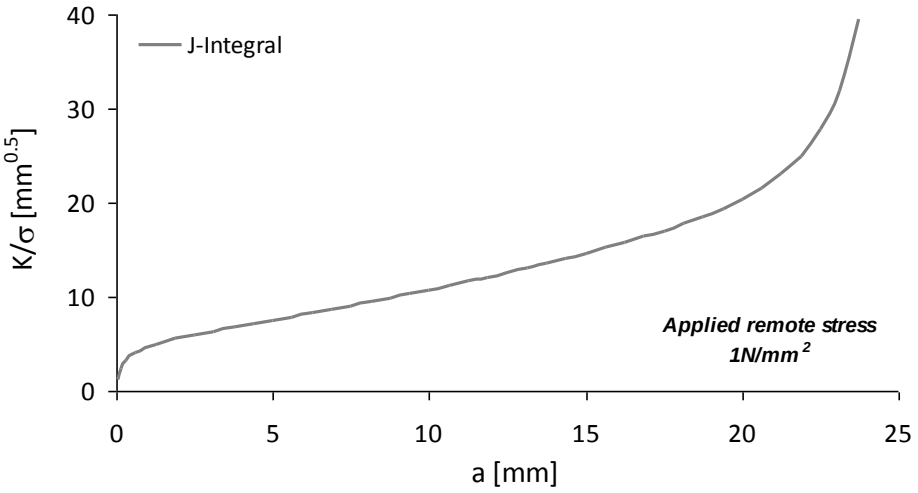

Figure 6.19 – Stress intensity factors as a function of the crack length, for a unit load.

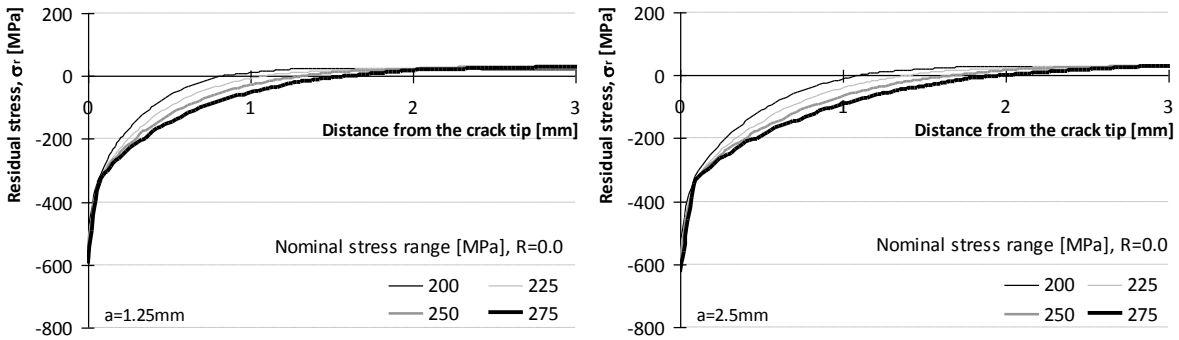

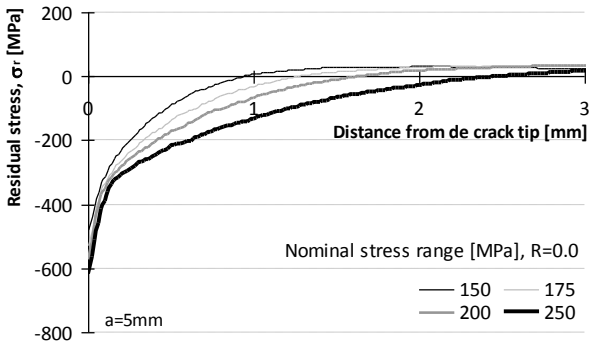

Figure 6.20 – Residual stress distributions for the notched plate for several crack sizes.

Figures 6.21 and 6.22 present the elastoplastic stress distribution in *y* and *x* directions, ahead of the crack tip for the first loading reversal, respectively, from the elastoplastic finite element analysis.

Figures 6.23 and 6.24 show the residual and maximum elastoplastic stress fields along the *y* (load) direction from the left notch root, respectively, obtained for the structural detail under consideration using an elastoplastic finite element analysis. The results were obtained using the properties of the P355NL1 steel and assuming a nominal stress range $\Delta\sigma$ = 275MPa, a = 2.5mm and a stress R-ratio, R_σ=0.0.

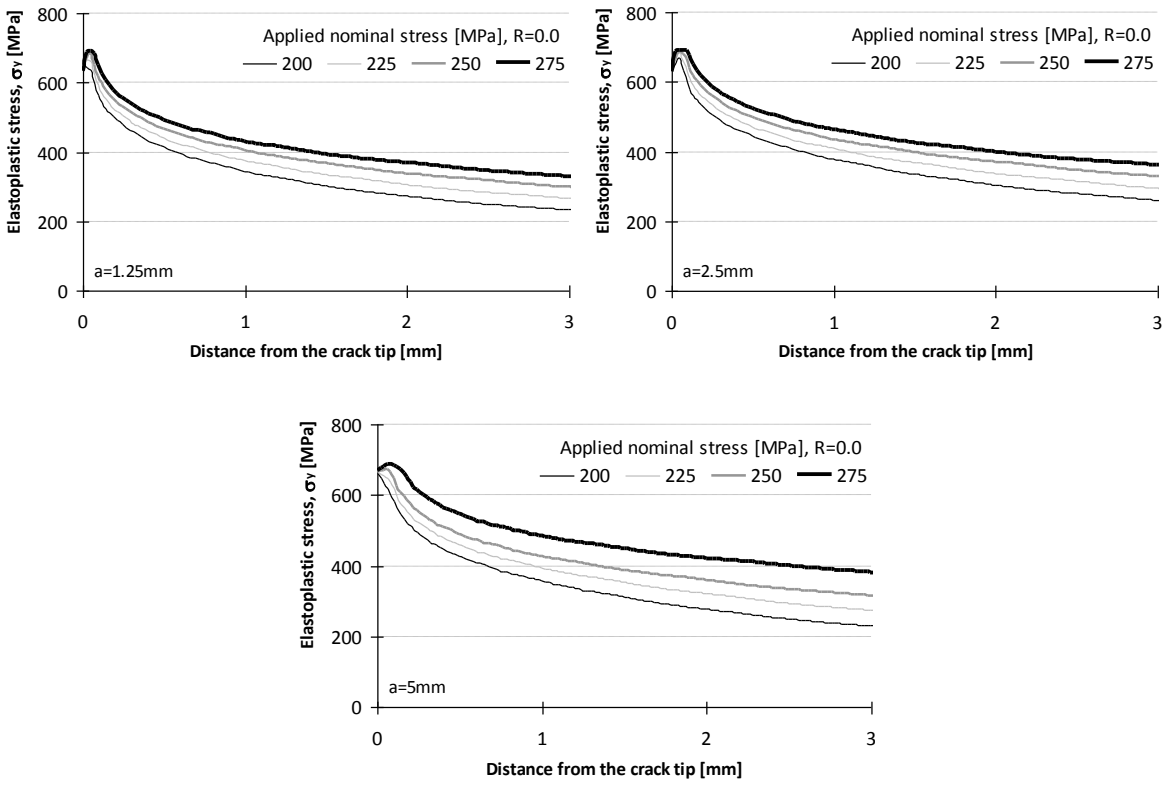

Figure 6.21 – Elastoplastic stress distributions in *y* direction for a notched plate with several crack sizes.

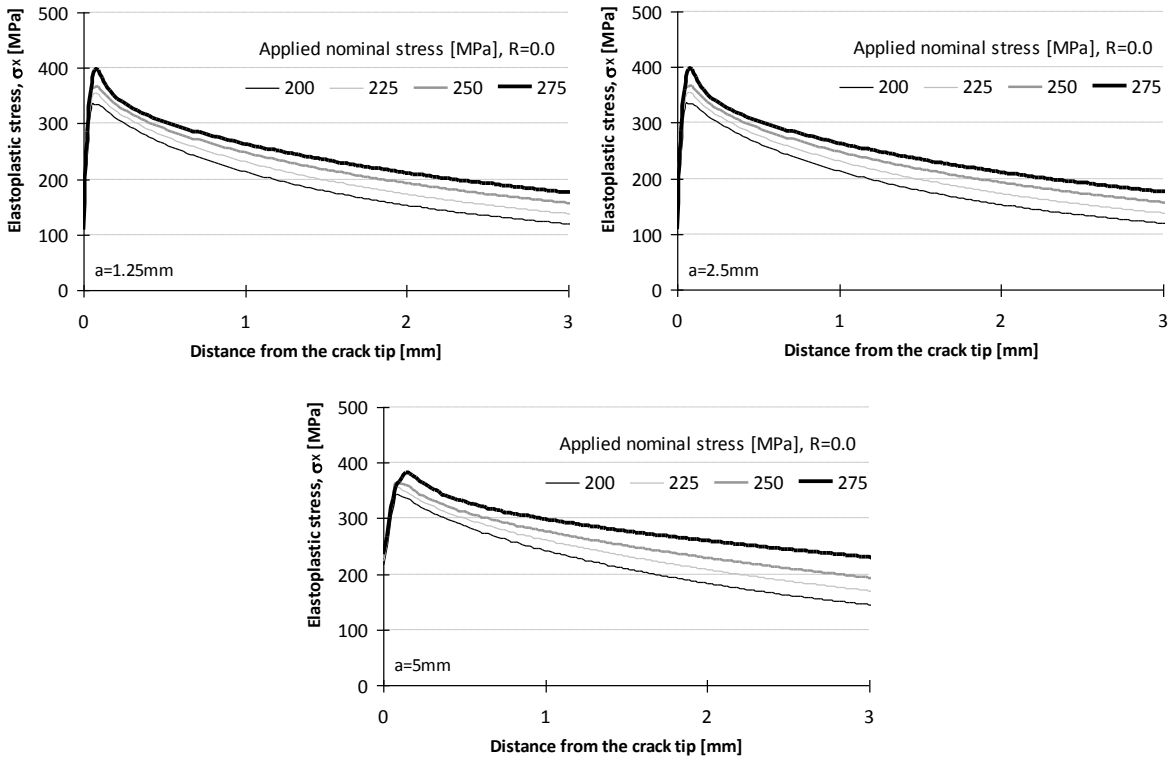

Figure 6.22 – Elastoplastic stress distributions in *x* direction for a notched plate with several crack sizes.

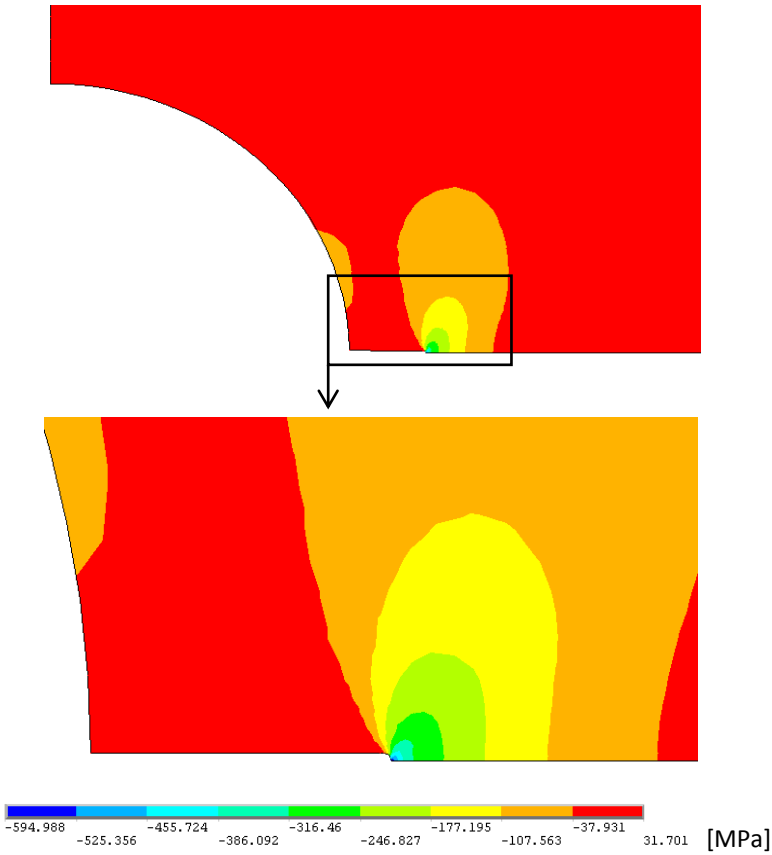

Figure 6.23 – Residual stress field along the *y* (load) direction around the left notch root, obtained for the structural detail made of P355NL1 steel, resulting from an elastoplastic finite element analysis ($\Delta\sigma$=275MPa, R_σ=0.0 and a=2.5mm).

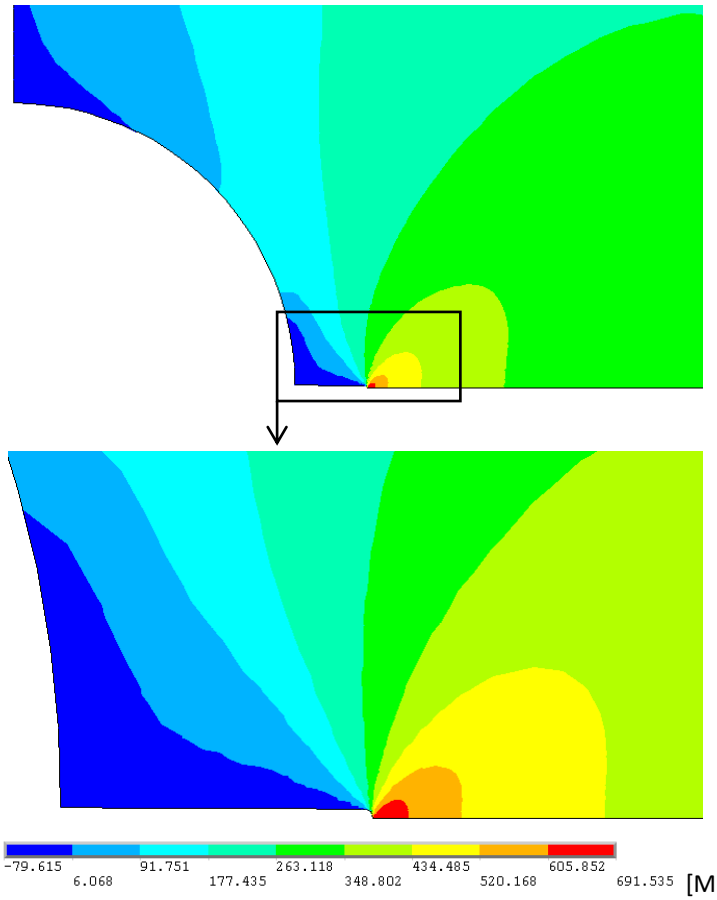

Figure 6.24 – Maximum stress field along the *y* (load) direction around the left notch root, obtained for the structural detail made of P355NL1 steel, resulting from an elastoplastic finite element analysis ($\Delta\sigma$=275MPa, R_σ=0.0 and a=2.5mm).

The residual stress intensity factor, K_r, was determined using the weight functions technique as proposed by Equation (6.1). The weight functions were evaluated using the Equation (6.2) and results from the linear elastic finite element analysis. Figure 6.25 represents the weight functions used to determine the K_r of the notched detail, for distinct crack lengths. The weight functions were determined for specific crack sizes [8]. The following equations present the weight functions for three distinct crack sizes depicted in Figure 6.25, using six order polynomials:

$$m(x,a)=\frac{2}{\sqrt{2\pi(a-x)}}\cdot f(x,a) \tag{6.5}$$

$$f(x,1.25)=-24.2398634250x^6+95.4603270858x^5-141.9796698750x^4+ \\ +98.7550466273x^3-31.8779779164x^2+3.4727307523x+1.4104700095 \tag{6.6}$$

$$f(x,2.5) = -0.4574412613x^6 + 3.473273316x^5 - 9.9856519086x^4 + \\ + 13.4676159667x^3 - 8.4781948571x^2 + 1.7958720636x + 1.5313583469 \quad (6.7)$$

$$f(x,5) = -0.0087492453x^6 + 0.1297015441x^5 - 0.7253925177x^4 + \\ + 1.8943583481x^3 - 2.2956388873x^2 + 0.8061412203x + 2.1542501863 \quad (6.8)$$

Those weight functions allow the residual stress intensity factor, K_r, to be computed. In this case, K_r was calculated for R_σ=0, R_σ=0.15 and R_σ=0.3 [8]. Figure 6.26 shows the evolution of K_r with the applied stress intensity factor range. The resulting data shows good linear correlation. This result confirms the same conclusion pointed out in reference [4], which supports the use of the finite element model as an effective tool for residual stress evaluation.

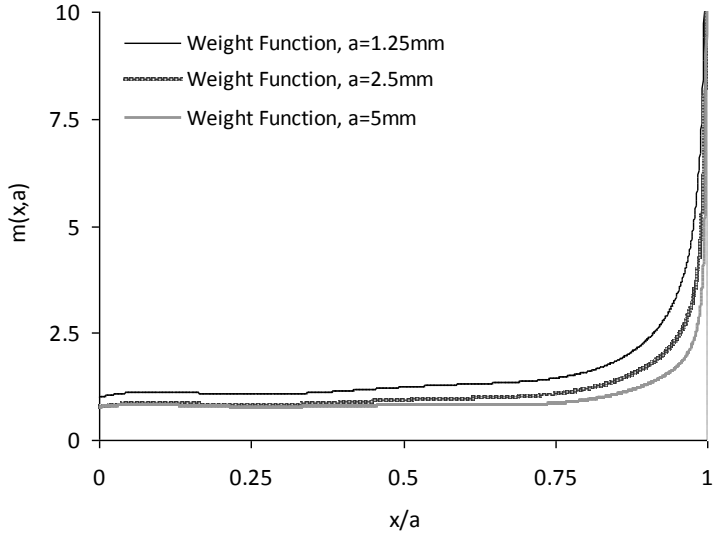

Figure 6.25 – Weight functions of the notched detail, for different crack lengths.

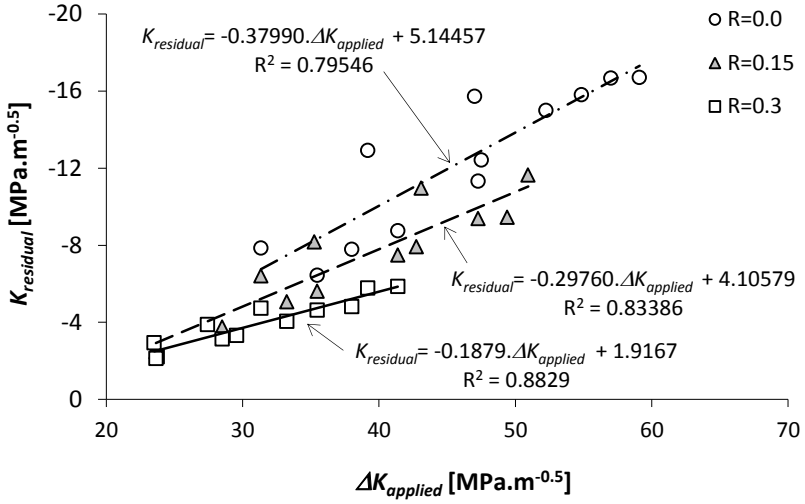

Figure 6.26 – Residual stress intensity factor as a function of the applied stress intensity factor range for the notched plate.

The p-S-N_p field of the notched plate was calculated for R_σ=0, R_σ=0.15 and R_σ=0.3 using the p-ε_a-N field of the P355NL1 steel together with the *UniGrow* model proposed by Noroozi et al. [3], and taking ρ^*=3×10^{-5}m (see Section 5.4.3. and 5.5.1.4. of Chapter V or reference [16]). The use of the p-ε_a-N field of the P355NL1 steel to model the fatigue crack propagation is justified by the fact that the material showed a crack propagation rate with low sensitivity to the stress ratio effects as argued in Section 5.5.1.4. of Chapter V. Figure 6.27 illustrates the p-S-N_p fields obtained for the notched detail. Figure 6.27 also includes the experimental fatigue data, which represents the total fatigue life of the detail. The comparison of the experimental fatigue data with the crack propagation fields shows that the crack propagation, despite not negligible, is not the dominant damage process, at least for low stress ranges/ high fatigue lives. In general, the fatigue crack propagation becomes dominant for larger structural details [8].

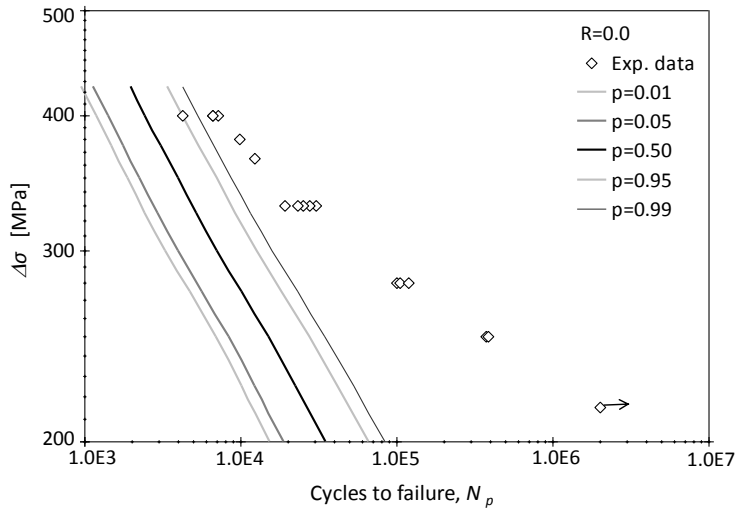

a)

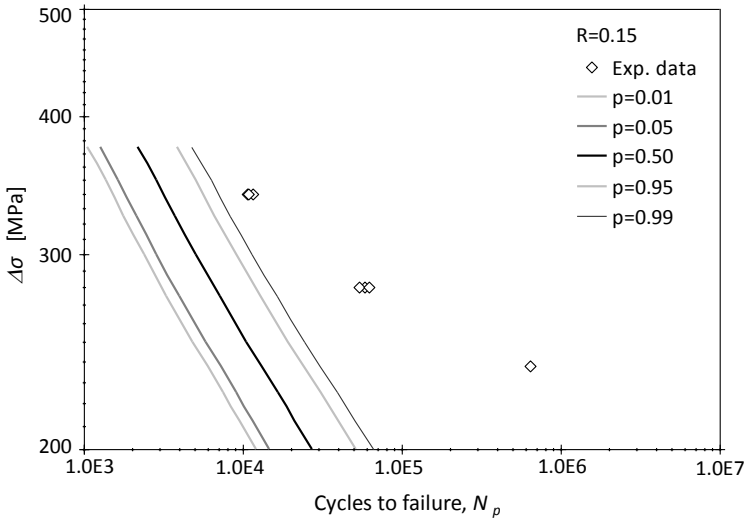

b)

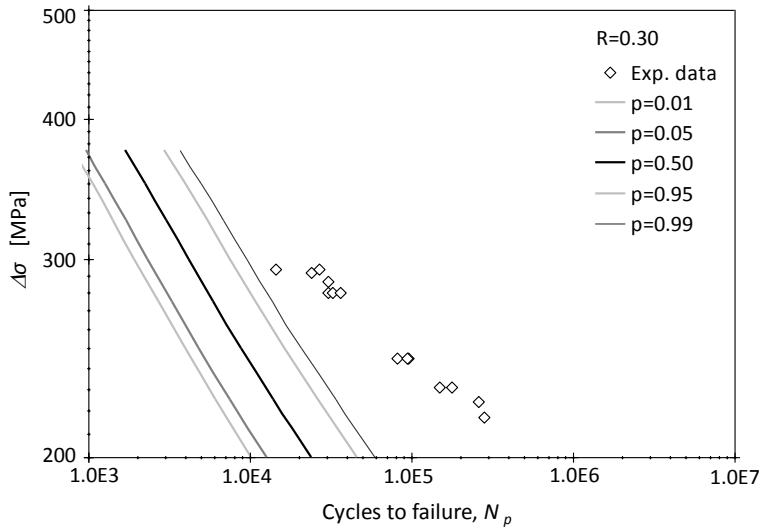

c)

Figure 6.27 – *p-S-N*$_p$ fields for the notched detail made of P355NL1 steel: a) R_σ=0.0; b) R_σ=0.15; c) R_σ=0.30.

6.4.1.4. Prediction of the probabilistic S-N$_f$*-R field*

The combined crack initiation and crack propagation *S-N*$_f$ fields were computed for the notched plate using Equation (6.4). Figure 6.28 presents the combined results. The analysis of the resulting *S-N*$_f$ fields highlights the accuracy of the proposed methodology. The experimental fatigue data falls inside the 1%-99% failure probability band, with a unique exception for R_σ=0 and R_σ=0.3. The proposed unified approach seems to give fairly promising predictions [8].

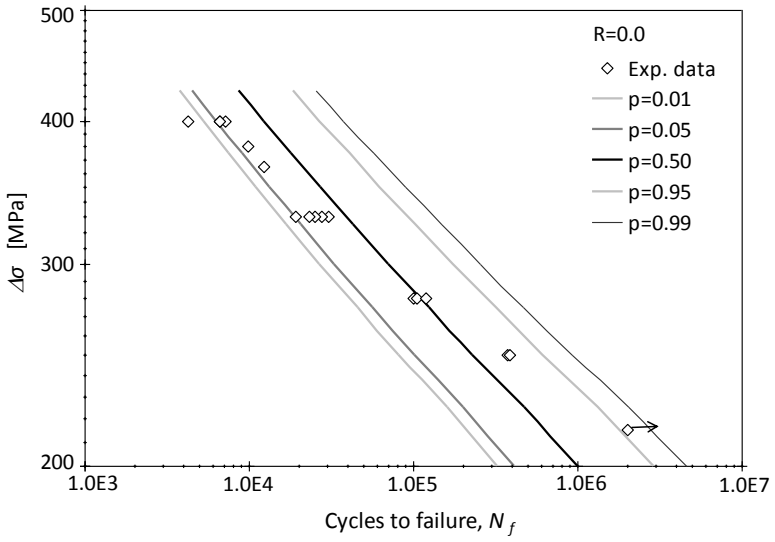

a)

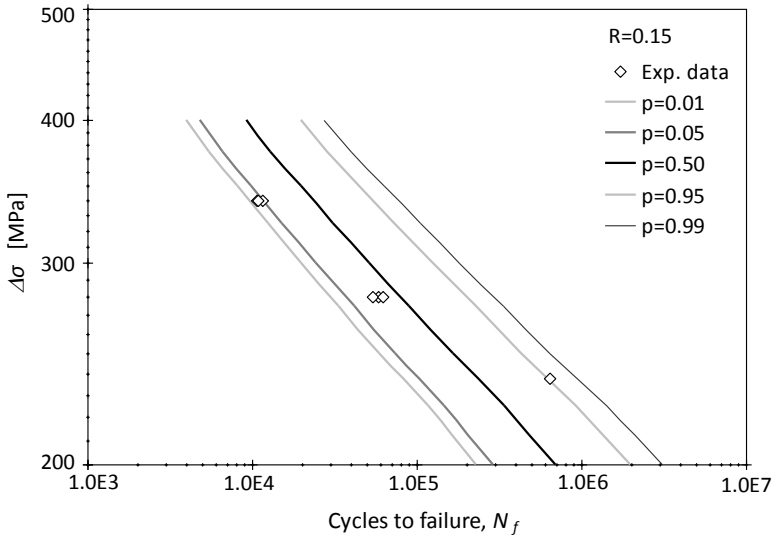

b)

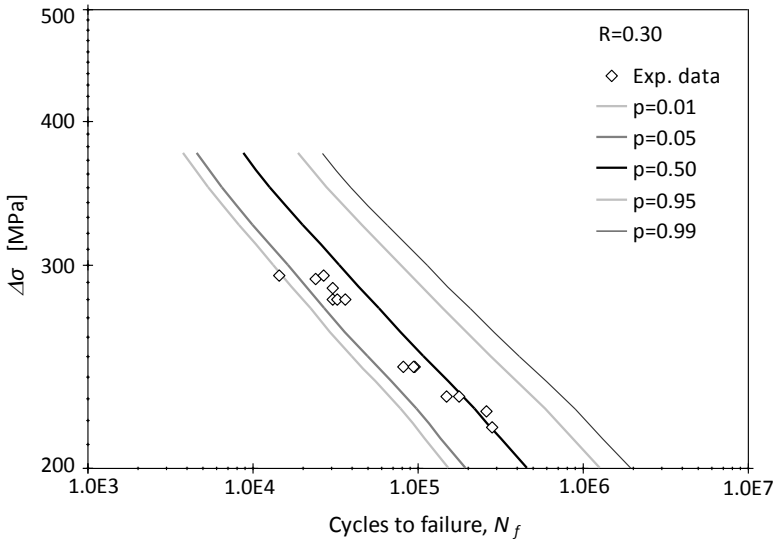

c)

Figure 6.28 – *p-S-N*$_f$ fields for the notched detail made of P355NL1 steel: a) R_σ=0.0; b) R_σ=0.15; c) R_σ=0.30.

6.4.2. Structural detail made of puddle iron from the Eiffel bridge

The crack initiation is modelled using the *p-SWT-N* field, due to the sensitivity of the detail to the stress ratio, which is not visible on the fatigue crack propagation rates. Elastoplastic analysis is performed on the uncracked geometry to compute the local/notch stress-strain response needed to determine the *SWT* parameter. The crack propagation will be performed using the so-called *UniGrow* model, using probabilistic fatigue damage fields.

The value of the elementary material block size, ρ^*=12×10^{-4}m, was estimated in the Section 5.5.1.1. of Chapter V, using fatigue crack propagation data from CT specimens. It

will be used in the prediction of the probabilistic *S-N* field for the structural detail made of material from the Eiffel bridge (see Figure 6.8).

6.4.2.1. Finite element analysis of structural detail

A bi-dimensional finite element model of the structural detail was proposed, using ANSYS® 12.0 commercial code [17]. Figure 6.29 illustrates a typical finite element mesh of the detail, with and without a side crack. This mesh exhibits a crack on the left side of the notch. In the practice, cracks started at both sides of the notch root and propagated symmetrically in the plate. Taking into account the existing symmetry planes, only ¼ of the geometry is modelled. Plane stress quadratic triangular elements were used in the analysis due to the limited specimen thickness. The same PLANE 181 elements used in the analysis of the P355NL1 plate, were also applied to build this plate.

A highly refined mesh at the crack tip region was used in order to model the crack tip notch radius, ρ^* (see magnification in Figure 6.29). The von Mises yield criterion with multilinear kinematic hardening, was used in simulations aiming at an estimation of the residual stress. The plasticity model was fitted to the stabilized cyclic curve of the material (Section 5.5.1.1. of Chapter V).

6.4.2.2. Prediction of the probabilistic S-N_i-R field

The *p-SWT-N* model is used to predict the fatigue crack initiation (failure of the first elementary material block) at the notch root of the detail – according to the procedure illustrated in Figure 6.2. An elastoplastic finite element analysis was used to compute the stress/strain history at the notch root. The same material model as applied for the CT specimen simulation was adopted for the detail. In order to facilitate the strain amplitude computation, loading followed by unloading steps were simulated using a plasticity model identified with the stabilised cyclic stress-strain curve of the material.

Figures 6.30 and 6.31 show the elastoplastic stress distributions in *x* and *y* directions, respectively, for the structural detail made of material from the Eiffel bridge, assuming applied nominal stresses of 175MPa, 250MPa and 325MPa.

Figures 6.32 and 6.33 show the residual elastoplastic stress distributions and strain range for the notched detail made of material from the Eiffel bridge, respectively, assuming applied nominal stress ranges of 175MPa, 250MPa and 325MPa (R_σ=0).

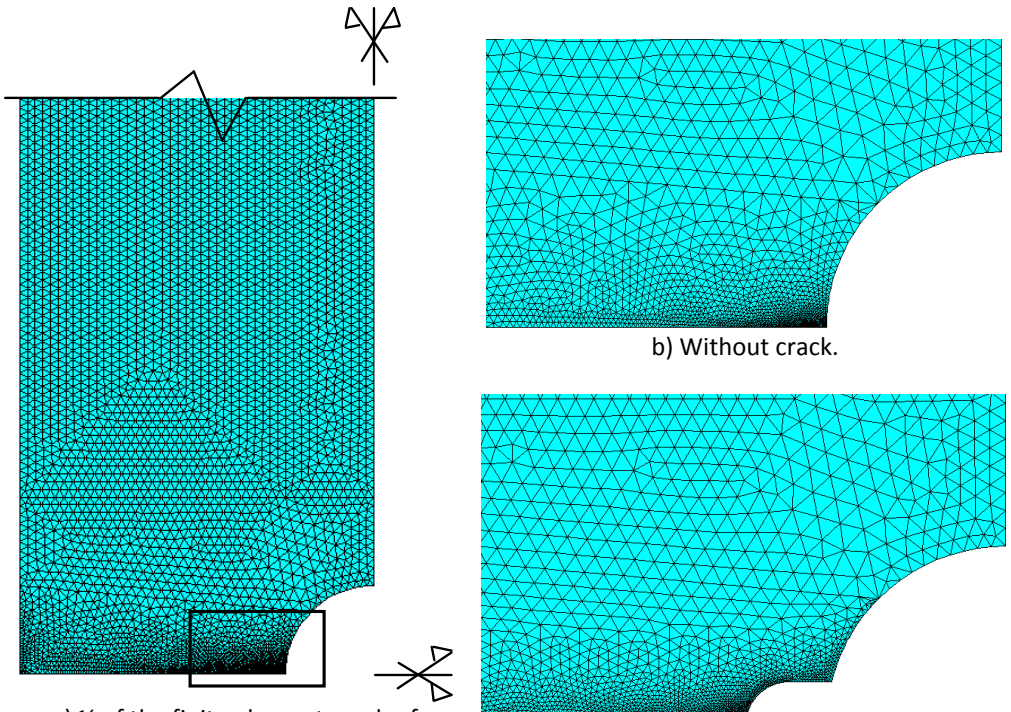

a) ¼ of the finite element mesh of the structural retail.

b) Without crack.

c) With a side crack and tip notch radius of 1200µm.

Figure 6.29 – Finite element mesh of the plate with a circular hole.

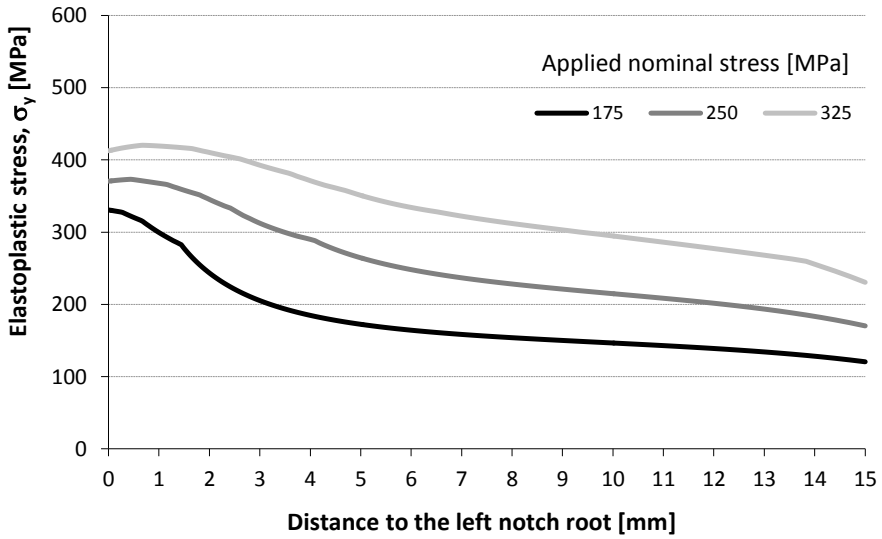

Figure 6.30 – Elastoplastic stress distribution, σ_y, as a function of the distance to the left notch root.

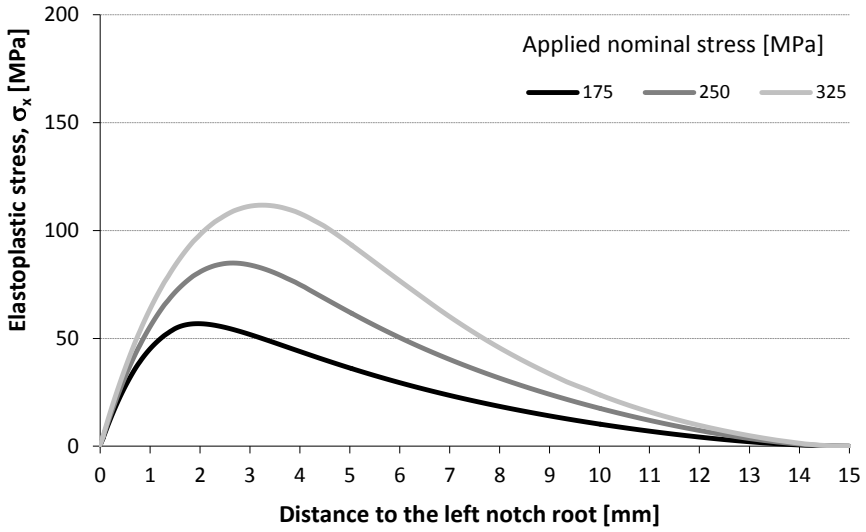

Figure 6.31 – Elastoplastic stress distribution, σ_x, as a function of the distance to the left notch root.

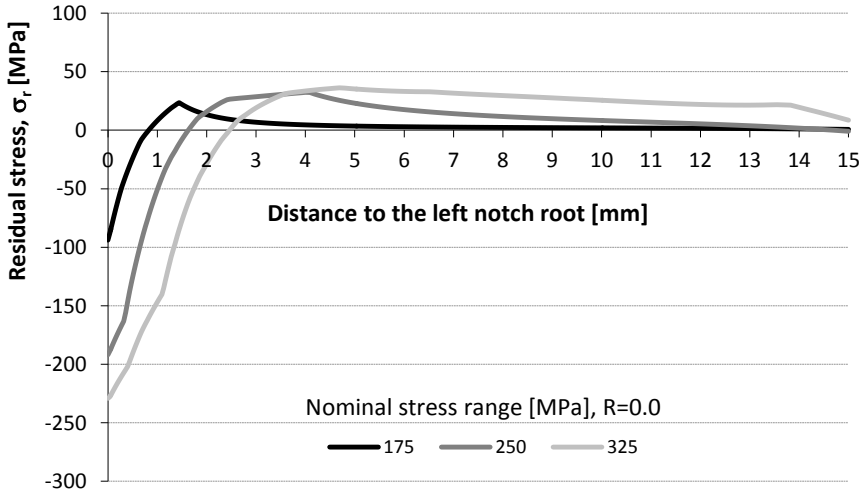

Figure 6.32 – Residual elastoplastic stress distribution, σ_r, as a function of the distance to the left notch root.

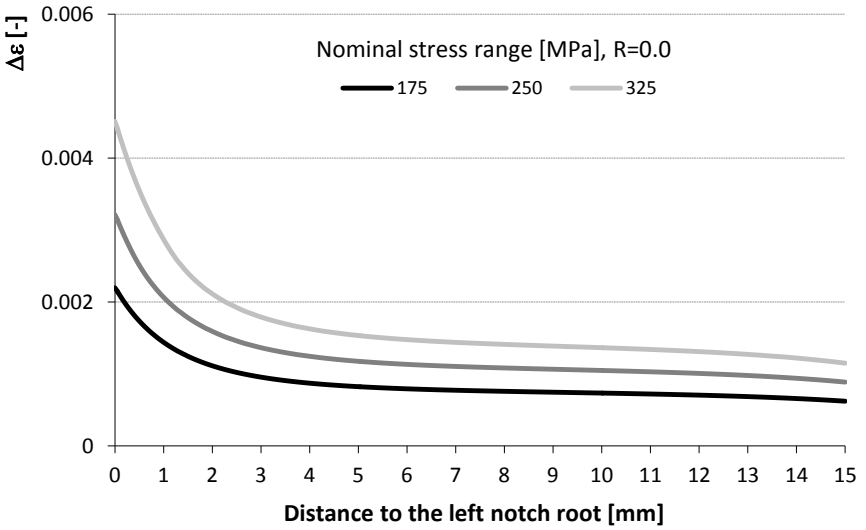

Figure 6.33 – Strain range, $\Delta\varepsilon$, as a function of the distance to the left notch root (R=0).

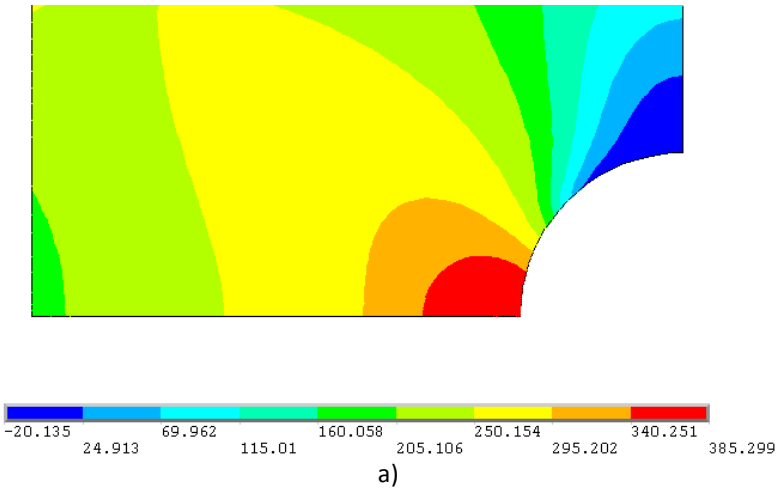

Figure 6.34 – Stress fields from the left notch root, obtained for the structural detail made of material from the Eiffel bridge, resulting from an elastoplastic finite element analysis ($\Delta\sigma$ = 275MPa and R_σ=0.0): a) Stress field, σ_y, in MPa, at the end of the first loading reversal; b) Stress field, σ_y, in MPa, at the end of the first unloading reversal.

Figures 6.34 and 6.35 show, respectively, the stress and strain fields around the left notch root of the structural detail, using the elastoplastic finite element analysis. The results were obtained for a nominal stress range of $\Delta\sigma$=275MPa, and a stress *R*-ratio, R_σ=0.0 [7].

Figure 6.36 shows the *p*-*S*-N_i fields corresponding to the fatigue crack initiation for the structural detail, for R_σ=0.0, in which is possible to observe that fatigue crack initiation is dominant, since it gives already a good description of the *S*-*N* fatigue data of the detail.

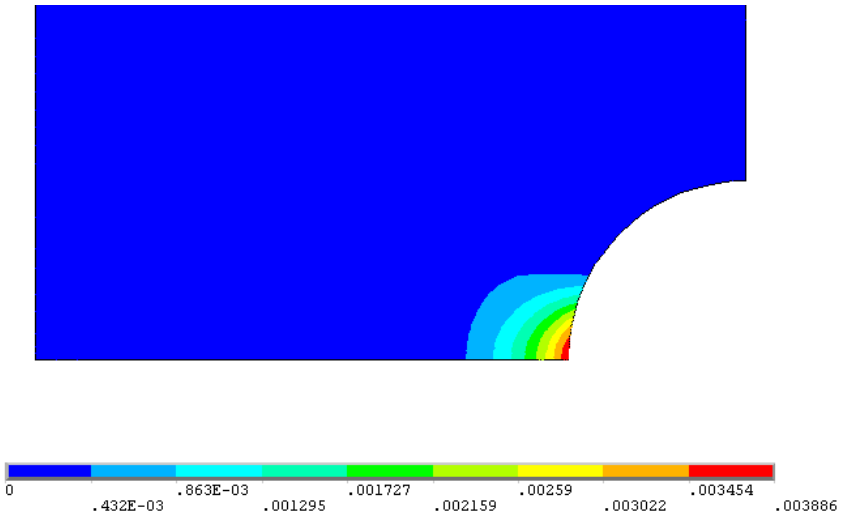

a)

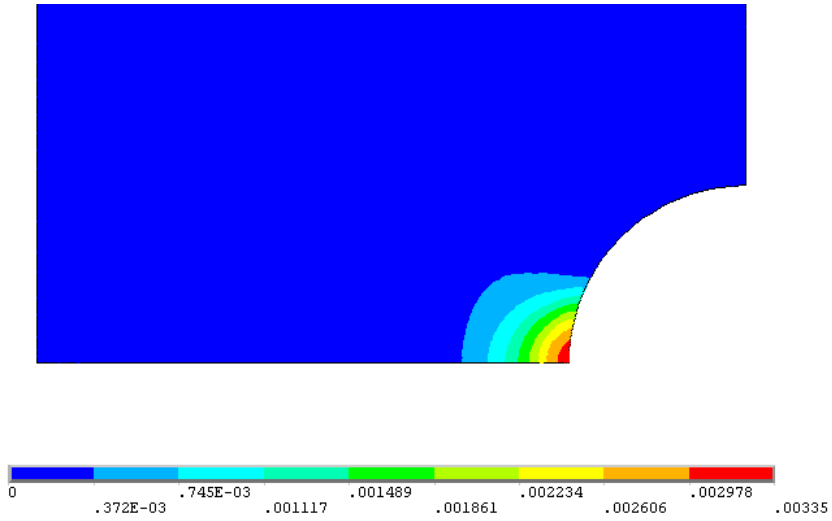

b)

Figure 6.35 – Strain fields around the left notch root, obtained for the structural detail made of material from the Eiffel bridge, resulting from an elastoplastic finite element analysis ($\Delta\sigma$ = 275MPa and R_σ=0.0): a) Strain field at the end of the first loading reversal; b) Strain field at the end of the first unloading reversal.

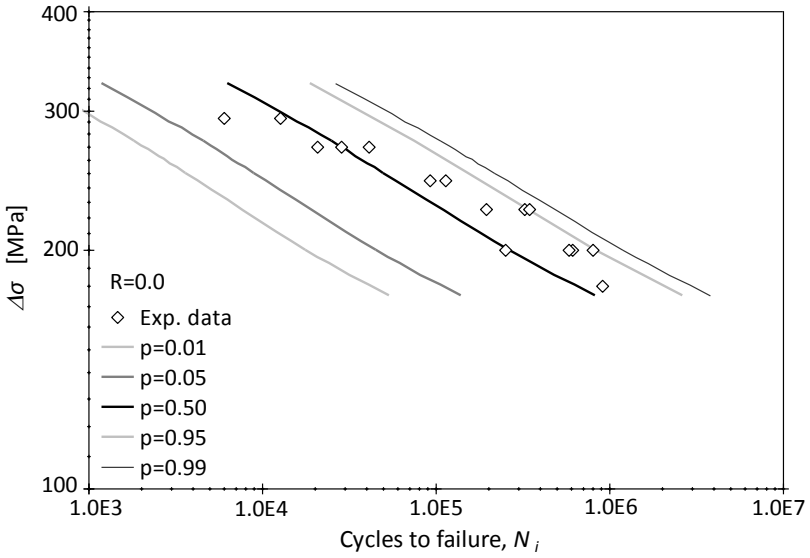

Figure 6.36 – *p-S-N$_i$* field for the structural detail made of material from the Eiffel bridge.

6.4.2.3. Prediction of the probabilistic S-N$_p$-R field

The procedure adopted to compute the probabilistic *S-N$_p$* field for the notched plate is illustrated in the Figure 6.3 (see Section 6.2.). A value of the elementary material block size, ρ^*=12×10^{-4}m, was previously estimated using an independent identification based on pure fatigue crack propagation data (see Section 5.5.1.1.). Finite element models of the detail were used to perform elastoplastic stress analysis for the computation of the residual stresses. In addition, linear elastic finite element models were used to compute the weight functions required for the residual stress intensity factor computation as well as the stress intensity factor solutions for the notched geometry.

The stress intensity factors were determined based on a linear-elastic finite element analysis using the J-integral method. Figure 6.37 presents the stress intensity evolution with the crack length for a unit remote stress, which was used to determine the $\Delta K_{applied}$.

Figure 6.38 presents the residual stress distribution along the *y* direction ahead of the crack tip, resulting from the elastoplastic finite element analysis. These residual stresses were computed after loading followed by unloading steps. High compressive stresses are observed at the vicinity of the crack tip.

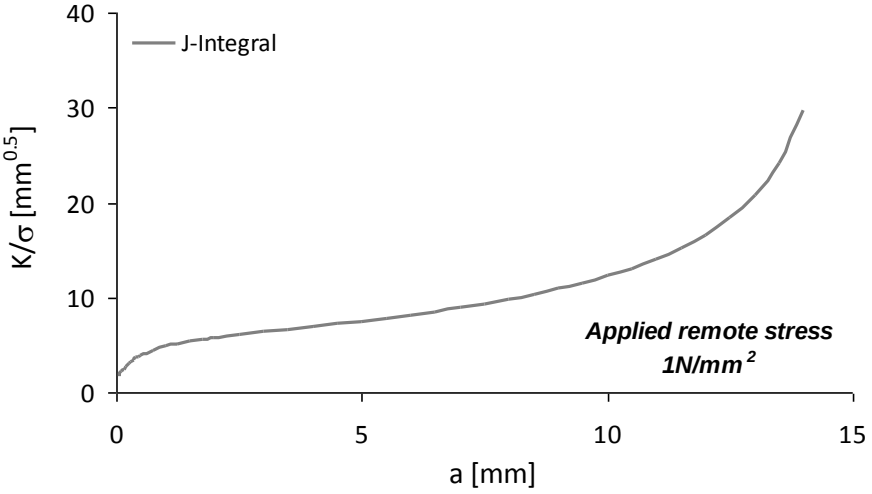

Figure 6.37 – Stress intensity factors as a function of the crack length, for a unit load.

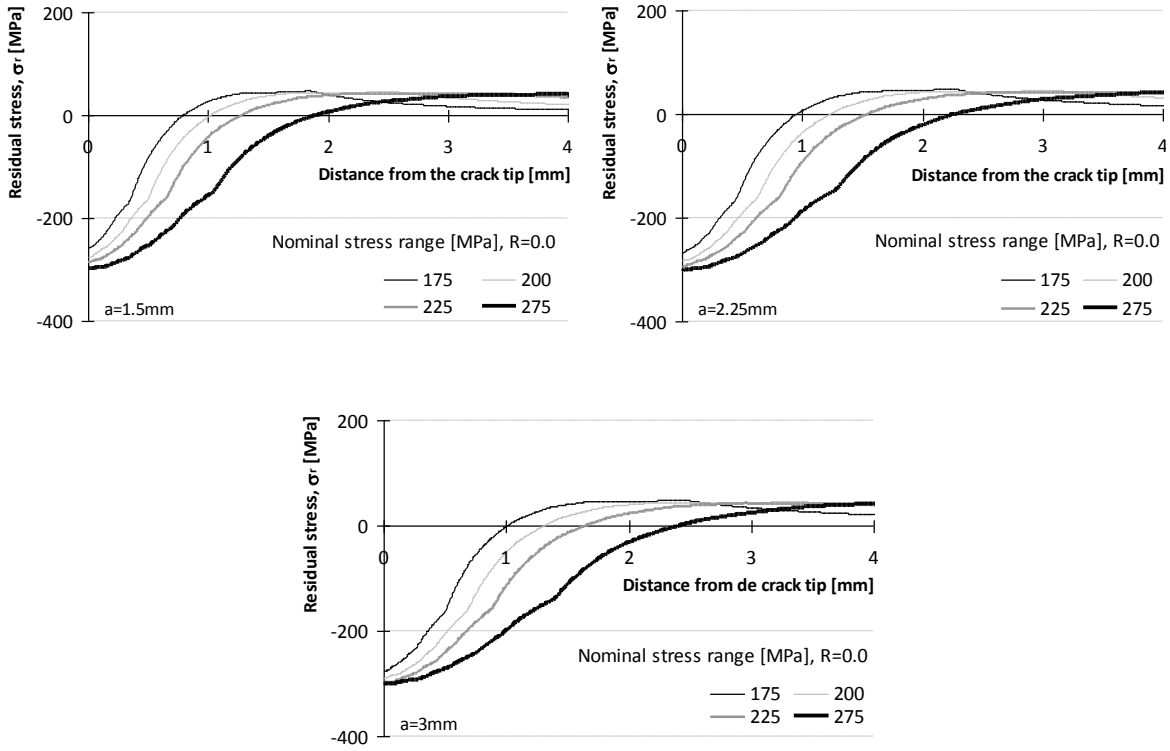

Figure 6.38 – Residual stress distributions for the notched plate for several crack sizes.

Figures 6.39 and 6.40 present the elastoplastic stress distribution in *y* and *x* directions, respectively, ahead of the crack tip, and obtained at the end of the first load reversal using an elastoplastic finite element analysis.

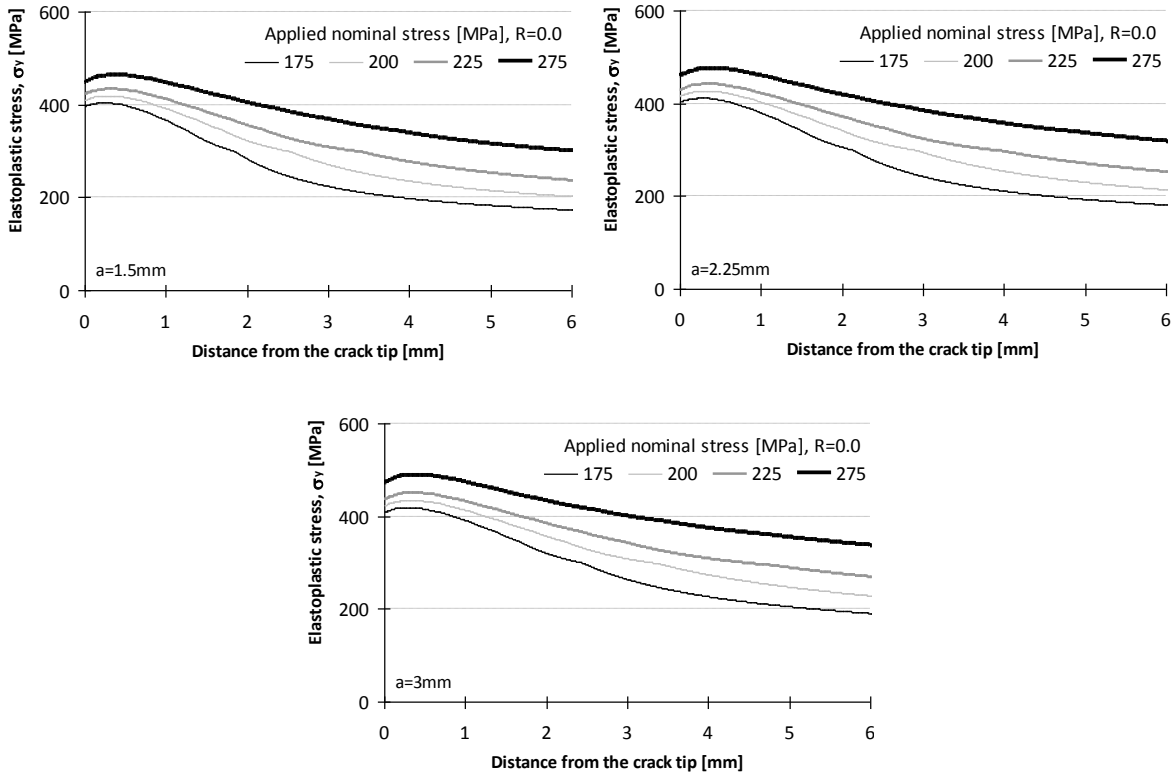

Figure 6.39 – Elastoplastic stress distributions in *y* direction for the notched plate, for several crack sizes.

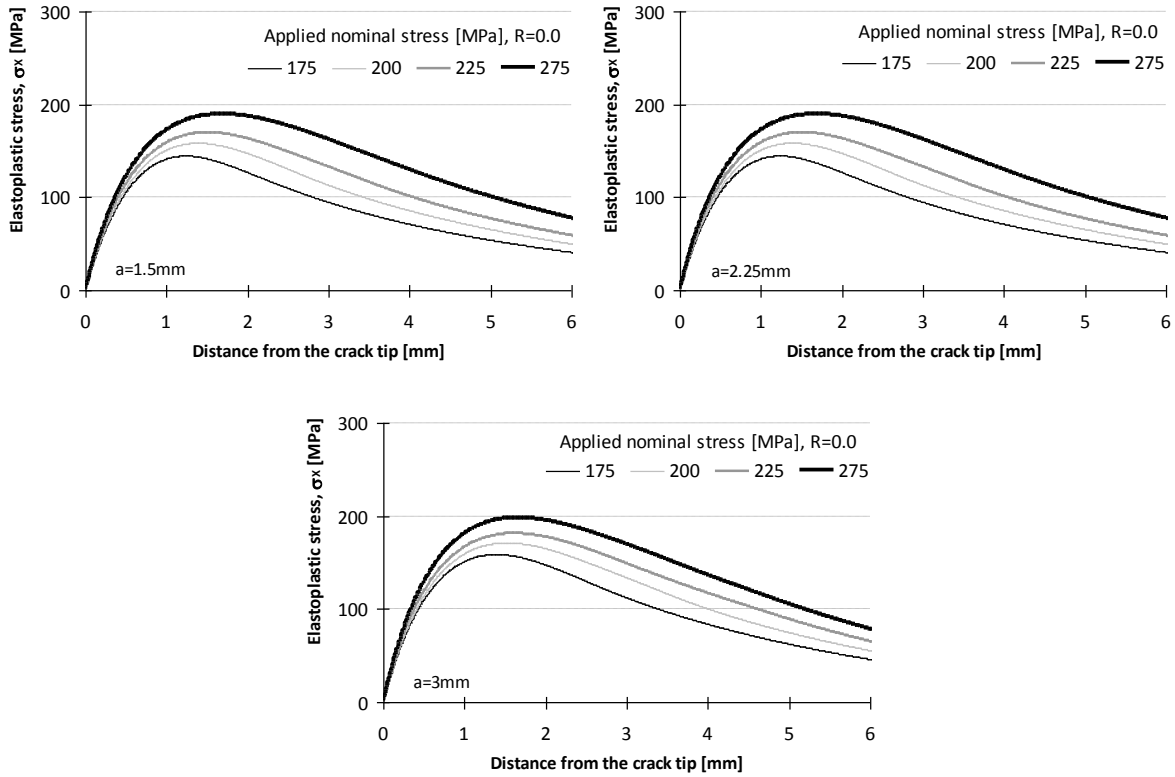

Figure 6.40 – Elastoplastic stress distributions in *x* direction for the notched plate, for several crack sizes.

Figures 6.41 and 6.42 show, respectively, the maximum and residual elastoplastic stress fields along the *y* (load) direction around the left notch root obtained for the structural

detail under consideration, using the elastoplastic finite element analysis. The results were obtained with a nominal stress range $\Delta\sigma$=275MPa, a stress R-ratio, R_σ=0.0 and a=2.25mm.

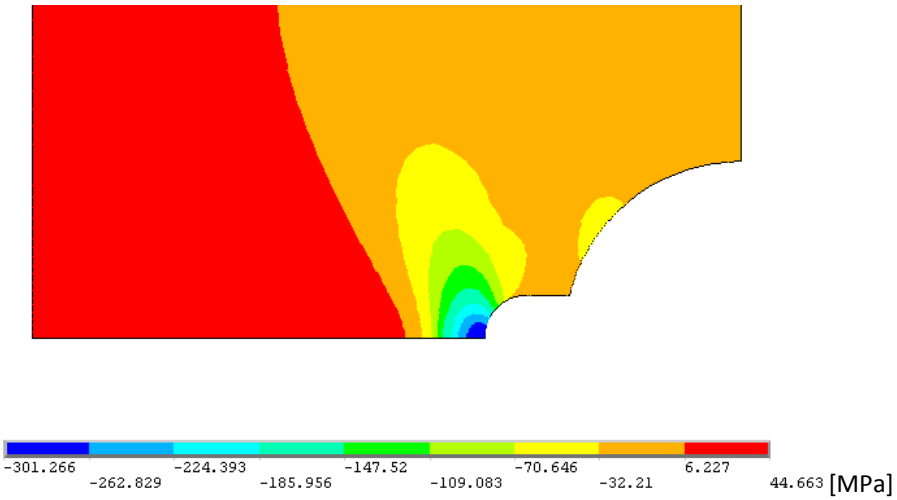

Figure 6.41 – Residual stress field along the y (load) direction around the left notch root, obtained for the structural detail made of material from the Eiffel bridge, resulting from an elastoplastic finite element analysis ($\Delta\sigma$ = 275MPa, R_σ=0.0 and a = 2.25mm).

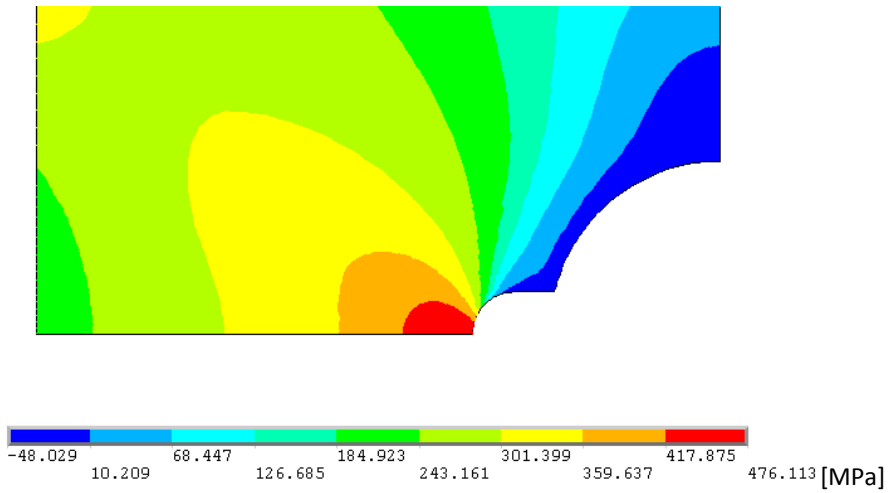

Figure 6.42 – Maximum stress field along the y (load) direction around the left notch root, obtained for the structural detail made of material from the Eiffel bridge, resulting from an elastoplastic finite element analysis ($\Delta\sigma$ = 275MPa, R_σ=0.0 and a = 2.25mm).

The residual stress intensity factor, K_r, was determined using the weight functions technique as proposed by Equations (6.1) and Equation (6.2) and using results from linear elastic finite element analysis. Figure 6.43 represents the weight functions used to determine the K_r of the detail, for different crack lengths. The weight functions were

determined for specific crack sizes [7]. The following equations present the weight functions for three distinct crack sizes:

$$m(x,a)=\frac{2}{\sqrt{2\pi(a-x)}}\cdot f(x,a) \tag{6.9}$$

$$f(x,1.5)=-12.455050852x^6+55.709309060x^5-93.965309722x^4 +73.967342376x^3-27.012555511x^2+3.493488735x+1.294649295 \tag{6.10}$$

$$f(x,2.25)=-1.1098432087x^6+7.4448889819x^5-18.8456078334x^4 +22.2852620795x^3-12.2502954304x^2+2.4146544567x+1.27004076 \tag{6.11}$$

$$f(x,3)=-0.1904681338x^6+1.6804383185x^5-5.5947936452x^4 +8.6988850940x^3-6.2801710788x^2+1.5946251077x+1.32861399 \tag{6.12}$$

Those weight functions allow the residual stress intensity factor, K_r, to be computed. In this case, K_r was computed for R_σ=0. Figure 6.44 shows the evolution of K_r with the applied stress intensity factor range. The resulting data shows a good linear correlation.

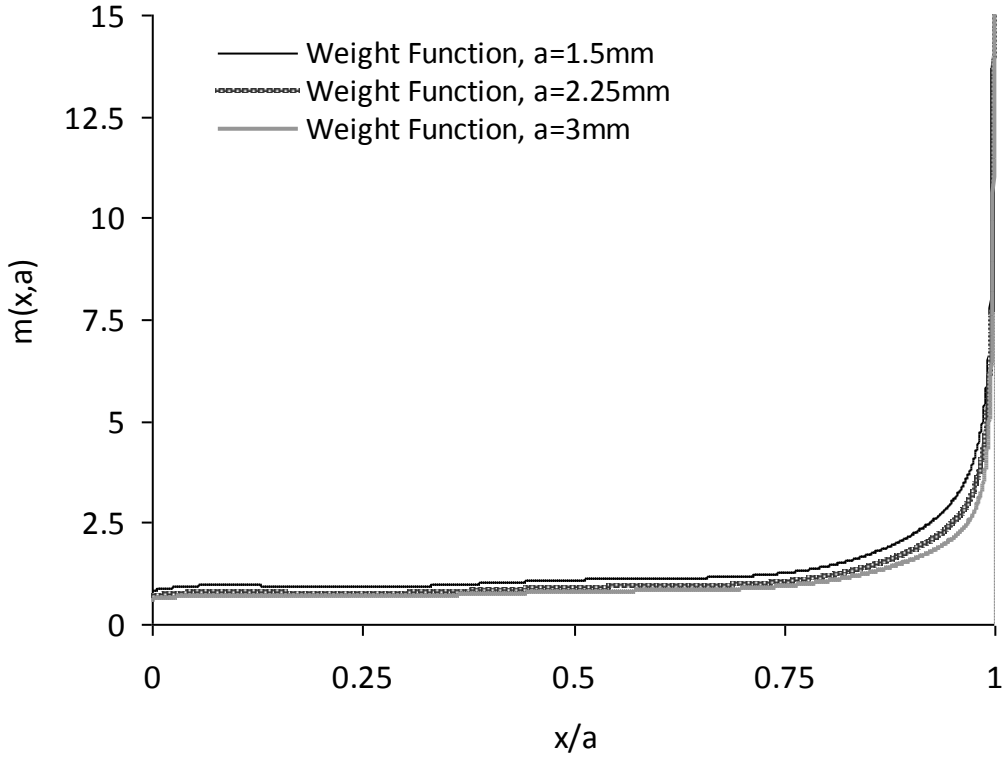

Figure 6.43 – Weight functions of the notched detail for different crack lengths.

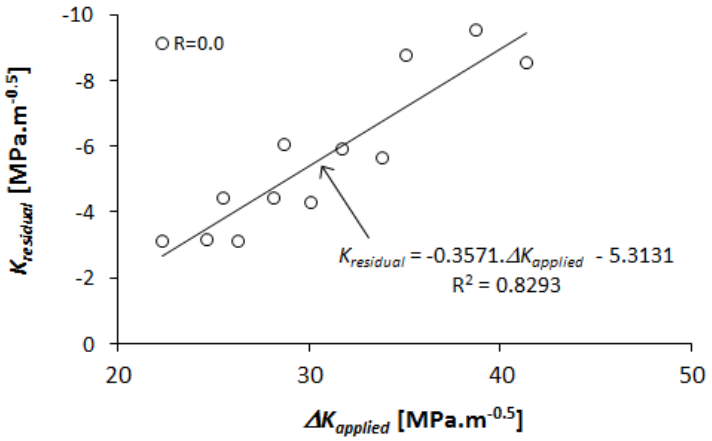

Figure 6.44 – Residual stress intensity factor as a function of the applied stress intensity factor range for the notched plate.

The *p-S-N*$_p$ field of the structural detail was calculated for R=0 using the *p-SWT-N* field of the material from the Eiffel bridge together with the *UniGrow* model proposed by Noroozi et al. [3], and assuming ρ^*=12×10^{-4}m (see Sections 5.4.3. and 5.5.1.1. of Chapter V). The use of the *p-SWT-N* field of the material from the Eiffel bridge to model the fatigue crack propagation is justified by the fact that the material showed a crack propagation rate sensitivity to stress ratio effects as argued in Section 5.5.1.1. of Chapter V. Figure 6.45 illustrates the *p-S-N*$_p$ fields obtained for the structural detail under consideration. Figure 6.45 also includes the experimental fatigue data, which represents the total fatigue life of the detail. The comparison of the experimental fatigue data with the crack propagation fields shows that the crack propagation, despite not negligible, is not the dominant damage process, at least for low stress ranges/ high fatigue lives.

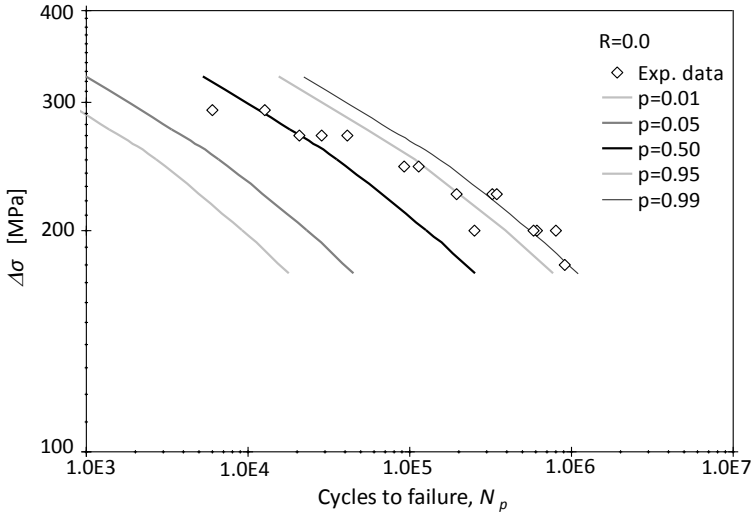

Figure 6.45 – *p-S-N*$_p$ field obtained for the notched plate made of material from the Eiffel bridge.

6.4.2.4. Prediction of the probabilistic S-N_f-R field

The combined crack initiation and crack propagation *S-N* fields were computed for the notched plate, using Equation (6.4). Figure 6.46 presents the combined results. The analysis of the resulting *S-N* field highlights the accuracy of the proposed methodology. The experimental fatigue data falls inside the 5%-95% failure probability band. The proposed unified approach seems to give fairly promising predictions for notched components [7].

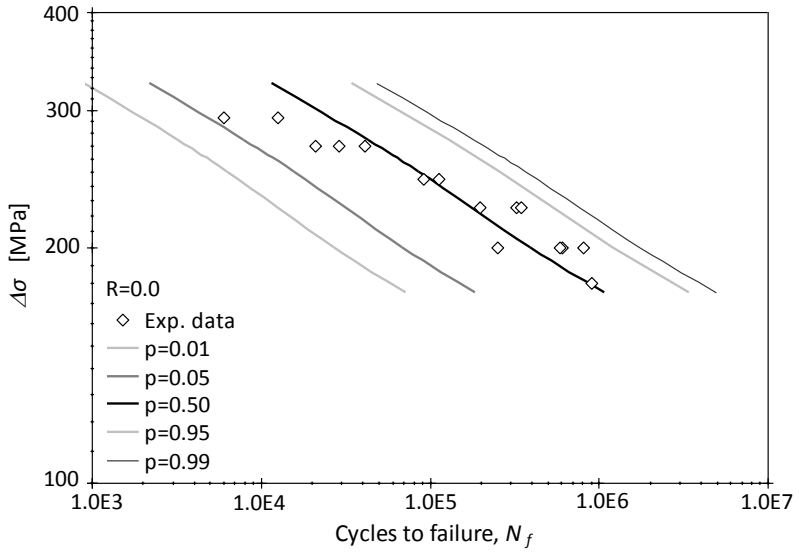

Figure 6.46 – *p-S-*N_f field obtained for the notched plate made of material from Eiffel bridge.

6.5. CONCLUSIONS

A unified approach to derive probabilistic *S-N* fields for notched structural details taking into account both crack initiation and crack propagation was proposed. This approach combines finite element analyses with the *UniGrow* model and probabilistic fatigue damage fields of the base material. One key parameter in this approach is represented by the elementary material block size, which was identified using an independent procedure and pure fatigue crack propagation data.

The predicted *p-S-*N_i field for the notched detail made of P355NL1 steel, based on the *p-SWT-N* model and the elastoplastic finite element analysis provides a good agreement with the experimental results, respectively for R_σ=0, R_σ=0.15 and R_σ=0.3. The same occurred with structural detail made in puddle iron from the Eiffel bridge. The adaptation

of the *UniGrow* model allows us to reproduce satisfactorily crack propagation prediction using residual compressive stress estimation, based on elastoplastic finite element analysis of the structural details. This was demonstrated for two materials/components, one based on P355NL1 steel and another in puddle iron from the Eiffel bridge. The p-ε_a-N and p-SWT-N damage models were used respectively for the P355NL1 steel and puddle iron form the Eiffel bridge. The residual stress intensity factor, computed from the compressive residual stress field, using a finite element analysis, linearly related to the applied stress intensity factor range, thus confirming the typical trend documented in the literature.

The global P-S-N field prediction for the structural details, one made of P355NL1 steel (R_σ=0, R_σ=0.15 and R_σ=0.3) and another made of puddle iron from the Eiffel bridge (R=0), taking into account the fatigue crack initiation and propagation, shows satisfactory results. In this study, crack initiation is the dominant fatigue damaging process, while the fatigue crack propagation exerts a small influence on global predictions of the P-S-N field, mainly in the high-cycle fatigue regime. The procedure proposed to derive the probabilistic S-N curves for structural details proved to be efficient, and can be used to reduce the need for extensive testing.

6.6. REFERENCES

[1] Morrow JD. Cyclic plastic strain energy and fatigue of metals. Int Frict Damp Cyclic Plast ASTM STP 1965; 378:45–87.

[2] Smith KN, Watson P, Topper TH. A Stress-Strain Function for the Fatigue of Metals. Journal of Materials 1970; 5(4): 767-778.

[3] Noroozi AH, Glinka G, Lambert S. A two parameter driving force for fatigue crack growth analysis. International Journal of Fatigue 2005; 27: 1277-1296.

[4] Noroozi AH, Glinka G, Lambert S. A study of the stress ratio effects on fatigue crack growth using the unified two-parameter fatigue crack growth driving force. International Journal of Fatigue 2007; 29:1616-1633.

[5] Mikheevskiy S, Glinka G. Elastic–plastic fatigue crack growth analysis under variable amplitude loading spectra. International Journal of Fatigue, 2009; 31: 1828–1836.

[6] Pereira HFSG, De Jesus AMP, Ribeiro AS, Fernandes AA. Fatigue damage behaviour of a structural component made of P355NL1 steel under block loading. J Press Ves Technol 2009;131:021407.

[7] Correia JAFO, De Jesus AMP, Fernández-Canteli A, Calçada RAB. Probabilistic fatifue behaviour of a

structural detail of puddle iron from the Eiffel bridge. Proceedings of the 3.º Congresso de Segurança e Conservação de Pontes (ASCP'13), 2013.

[8] Correia JAFO, De Jesus AMP, Fernández-Canteli A. A procedure to derive probabilistic fatigue crack propagation data. International Journal of Structural Integrity, 2012; Vol. 3, No. 2: 158–183.

[9] Neuber H. Theory of stress concentration for shear-strained prismatic bodies with arbitrary nonlinear stress–strain law. Trans. ASME Journal of Applied Mechanics, 1961; 28: 544–551.

[10] Molski K, Glinka G. A method of elastic-plastic stress and strain calculation at a notch root. Materials Science and Engineering, 1981; 50: 93-100.

[11] Shang D-G, Wang D-K, Li M, Yao W-X. Local stress–strain field intensity approach to fatigue life prediction under random cyclic loading. International Journal of Fatigue 2001; 23: 903–910.

[12] Basquin OH. The exponential law of endurance tests. Proc. Annual Meeting American Society for Testing Materials, 1910; 10: 625-630.

[13] Coffin LF. A study of the effects of the cyclic thermal stresses on a ductile metal. Trans ASME 1954;76:931–50.

[14] Manson SS. Behaviour of materials under conditions of thermal stress, NACA TN-2933. National Advisory Committee for Aeronautics; 1954.

[15] De Jesus AMP, Ribeiro AS, Fernandes AA. Influence of the Submerged Arc Welding in the Mechanical Behaviour of the P355NL1 Steel—Part II: Analysis of the Low/High Cycle Fatigue Behaviours. J. Mater. Sci., 42, 2007, pp. 5973–5981.

[16] De Jesus AMP, Correia JAFO. Critical assessment of a local strain-based fatigue crack growth model using experimental data available for the P355NL1 steel. Journal of Pressure Vessel Technology, 2013; Vol. 135, No. 1: 011404-1–0114041-9.

[17] ASTM – American Society for Testing and Materials. ASTM E606-92: standard practice for strain controlled fatigue testing. In: Annual book of ASTM standards, part 10; 1998. p. 557–71.

[18] De Jesus AMP, Silva ALL, Figueiredo MV, Correia JAFO, Ribeiro AS, Fernandes AA. Strain-life and crack propagation fatigue data from several Portuguese old metallic riveted bridges. Engineering Failure Analysis, 2010; 17: 1495–1499.

[19] ASTM – American Society for Testing and Materials. ASTM E647: standard test method for measurement of fatigue crack growth rates. In: Annual book of ASTM standards, vol. 03.01. West Conshohocken, PA: ASTM – American Society for Testing and Materials; 2000. p. 591–630.

[20] SAS, 2011, ANSYS, Swanson Analysis Systems, Inc., Houston, Version 12.0.

CHAPTER VII

A PROBABILISTIC INTERPRETATION OF FATIGUE DAMAGE UNDER VARIABLE AMPLITUDE LOADING

7.1. INTRODUCTION

The cumulative concept proposed by Palmgren and Miner [1] maintains that the damage level can be expressed in terms of the number of cycles applied at a given stress range divided by the number of cycles needed to produce failure for the same stress range. Failure occurs when the summation of these damage increments at several stress ranges becomes unity. After this formulation, this rule is repeatedly tested for different materials under multi-step and variable amplitude loading programs [2-4]. Though its applicability has been often questioned, it has been practically adopted by all design codes related to structural and mechanical fatigue design [5-7].

While Birnbaum and Saunders [8] tried to find a relation of the probabilistic distribution of the Miner number to the crack growth, Van Leeuwen and Siemes [9,10] conducted series of tests on plain concrete and interpreted directly the scatter of the Miner number M by obtaining theoretical expressions for the mean and standard deviation values of M from the Wöhler curve. These formulae, initially derived for the simple case of constant amplitude cycling were then extended to the case of general loading. They showed that the Miner number (M) at failure is a stochastic variable with an approximate log-normal distribution and emphasized the importance of the study of the scatter of the Wöhler curve for constant amplitude cycling. Based on Holmen's investigation on concrete [11], Fernández-Canteli [12] justified a generalization of the Van Leeuwen and Siemes work by considering a probabilistic S-N field providing a statistical distribution of the Miner

number although based on a log-normal distribution. Some theoretical advances were performed in [13] and [14].

From this, it follows that the Miner number can be used to ascertain the probability of failure, as a more suitable design criterion, rather than as a measure of a problematic and abstract “degree of damage”. It can then be taken as a basis for a consistent life prediction in fatigue design, in accordance with the consideration of fatigue failure as limit state.

In this chapter, an approach for a probabilistic interpretation of fatigue damage under variable amplitude data, based on the probabilistic model by Castillo and Fernández-Canteli [13] is discussed and applied to existing experimental data. One advantage of this approach is the possibility of associating a failure probability to the classical Miner number without the need of performing extensive variable amplitude testing aiming the identification of the cumulative distribution by direct ranking of data.

In this chapter variable amplitude fatigue test data available for the P355NL1 steel (smooth specimens) [2-4] and for a riveted joint made of a puddle iron original from the Fão bridge [15-16] is explored.

The following discussion will be limited to variable amplitude loading data, for which sequential effects are not determinant in fatigue damage accumulation. It is well-known that the classical Miner damage approach is not well suited to model sequential effects such as those arising from two-blocks loading (e.g. High-Low or Low-High sequences) or to consider single or periodic overloads superimposed to constant amplitude loading. In these cases, the variation of the Miner number from expected value (e.g. 1) may not only be attributed to the scatter in fatigue data but also to such sequential effects.

The proposed approach, aiming at to associate a failure probability to the Miner number, only accounts for the scatter in fatigue data.

7.2. PROPOSAL TO ASSOCIATE FAILURE PROBABILITIES TO (LOG)MINER NUMBERS

The proposed approach, relating to associate failure probabilities to the Miner number, is supported by the probabilistic model proposed by Castillo and Fernández-Canteli [13]. This model allows the definition of probabilistic *S-N* or ε-*N* fields (see Figures 2.13 and 2.15 respectively), where percentile curves, representing constant probability of failure are established. This model proves that the normalized variable $V=(\log N-B)(\log\Delta\sigma-C)$ follows Weibull (see Equation 2.75, see Figure 7.1) or Gumbel distributions. Therefore, the normalized variable resulting from the product of an applied stress or strain ranges with a load duration *N*, is directly related to the probability of failure. The probability of failure is a monotonic increasing function of the normalizing variable, *V*, and consequently of the number of cycles and stress/strain range/amplitudes. For a fixed stress/strain range/amplitude, the probability of failure increases with the number of cycles; in the same way, for a fixed number of cycles, the probability of failure increases the increasing stress/strain ranges/amplitudes. By considering this normalized variable, equivalent loading conditions are established, as those leading to the same probability of failure. Considering the S-N field of Figure 7.2, the loading conditions ($\Delta\sigma_A$, N_A) and ($\Delta\sigma_B$, N_B) are equivalent since they lead to the same failure as a result of showing the same normalizing variable, $V_A=V_B$:

$$V_A = V_B \Rightarrow (\log N_A - B)(\log \Delta\sigma_A - C) = (\log N_B - B)(\log \Delta\sigma_B - C) \tag{7.1}$$

For a given loading condition ($\Delta\sigma_A$, N_A) one can compute the equivalent start point given, respectively, by the stress range $\Delta\sigma_B$ and the number of cycles N_B, representing the same damage state (same probability of failure) for proceeding to compute damage caused by the new loading step at the stress range $\Delta\sigma_B$:

$$\Delta\sigma_B = exp\left[\frac{(\log N_A - B)(\log \Delta\sigma_A - C)}{(\log N_B - B)} + C\right] = exp\left[\frac{V_A}{(\log N_B - B)} + C\right] \tag{7.2}$$

$$N_B = exp\left[\frac{(\log N_A - B)(\log \Delta\sigma_A - C)}{(\log \Delta\sigma_B - C)} + B\right] = exp\left[\frac{V_A}{(\log \Delta\sigma_B - C)} + B\right] \tag{7.3}$$

The equivalence between two loading conditions is established based on percentile (isoprobability) curves. These isoprobability curves may be interpreted as isodamage

curves, and the probability of failure, *p*, represented by the normalizing variable, *V*, may be understood as alternative damage measures [13]. The adoption of the probability of failure associated to the classical deterministic Miner number could be considered advantageous for design purposes, namely to establish safety margins.

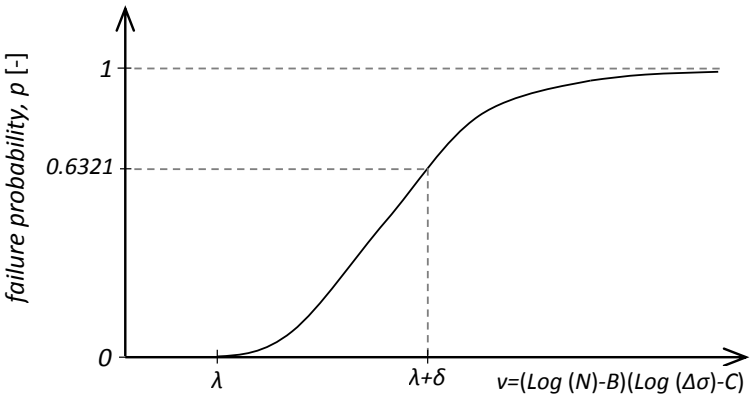

Figure 7.1 – Cumulative Weibull distribution function of the normalized variable *V*.

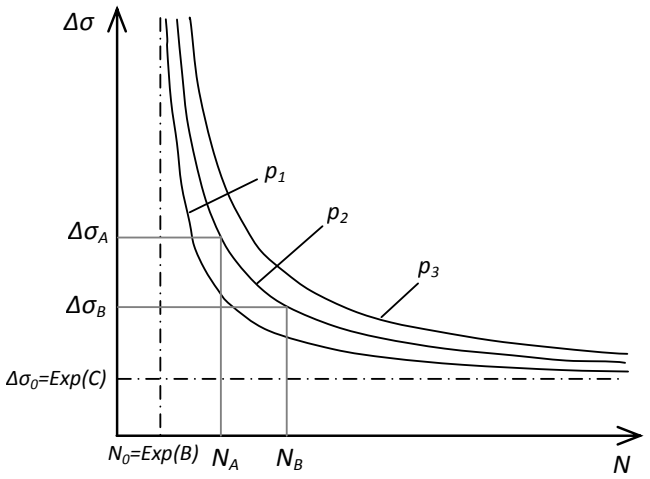

Figure 7.2 – Probabilistic Weibull *S-N* field representation with two equivalent (same probability of failure and damage) loading conditions.

Given a variable amplitude loading, it is possible to compute the evolution of the normalizing variable, cycle-by-cycle or, in case of blocks of constant amplitude loading, block-by-block. At the same time, the probability of failure may be computed using for example the Weibull distribution of the material or mechanical/structural component. With this process one can compute the failure probability associated to any variable amplitude loading history using exclusively the information of the probabilistic S-N field derived by constant amplitude fatigue data. These failure probabilities may be contrasted with the classical Miner numbers computed using, for example, the mean *S-N* curve of the

material or mechanical/structural component. This mean *S-N* curve can also be obtained from the probabilistic *S-N* field proposed by Castillo and Fernández-Canteli [13], considering a probability of failure of 50%. With this process one can derive the cumulative distribution function for the (Log)Miner number values proving that is possible to relate any value of the Miner number to the corresponding probability of failure.

The process proposed to associate a failure probability to the Miner number can be summarized as follows:

i) A probabilistic *S-N* or ε-*N* field must be derived for the material or mechanical/structural component under consideration from constant amplitude stress or strain-based fatigue data. For this purpose the probabilistic model by Castillo and Fernández-Canteli [13] is used. Both Weibull and Gumbel distributions are possible candidates.

ii) For available variable amplitude data, the Miner number (*M*) is computed using the experimental observed lives and the mean *S-N* curve derived using constant amplitude data in the previous step i). Alternatively to the natural Miner number, a logarithmic Miner number (*LM*) can also be computed. Both numbers are respectively defined as follows:

$$M = \sum_{i=1}^{n} \frac{N_i}{N_{fi}} \tag{7.4}$$

$$LM = \sum_{i=1}^{n} \frac{log N_i}{log N_{fi}} \tag{7.5}$$

where N_i corresponds to the number of cycles applied with stress range, $\Delta\sigma_i$ and N_{fi} corresponds to the number of cycles to failure by application of the stress range $\Delta\sigma_i$, computed using the 50% percentile of the *P-S-N* field evaluated in step i). In this step, the *P-S-N* field is presumed, but the process is similar for other probabilistic fields, such as the *P-*ε*-N* fields.

iii) For the same variable amplitude loading of previous step ii), the evolution of the normalized variable, *V*, along the referred loading history is computed. This process can be performed according the workflow given in Figure 7.3, for a block loading $\{(\Delta\sigma_i, N_i), i=1,n\}$.

iv) A direct relation between the Miner or Logarithmic Miner numbers computed in step ii) and the probability of failures computed in step iii) is established. From this relation a cumulative distribution function for the Miner number can be accomplished. This step may be implemented in distinct phases, starting with the V *vs*. *p* relation, then the *M* vs. *V*, or *LM* vs. *V*, relations may be computed and finally *M* vs. *p* or *LM* vs. *p* relations may be evaluated.

v) Finally, the experimental cumulative distribution functions of the Miner number may be computed assigning probabilities to the experimental data by a plotting point position rule. In this way, a comparison between the theoretical and the experimental distribution, derived in step iv), can be established. For limited amount of experimental data under variable amplitude loading, the referred experimental distribution could be far from the expected one.

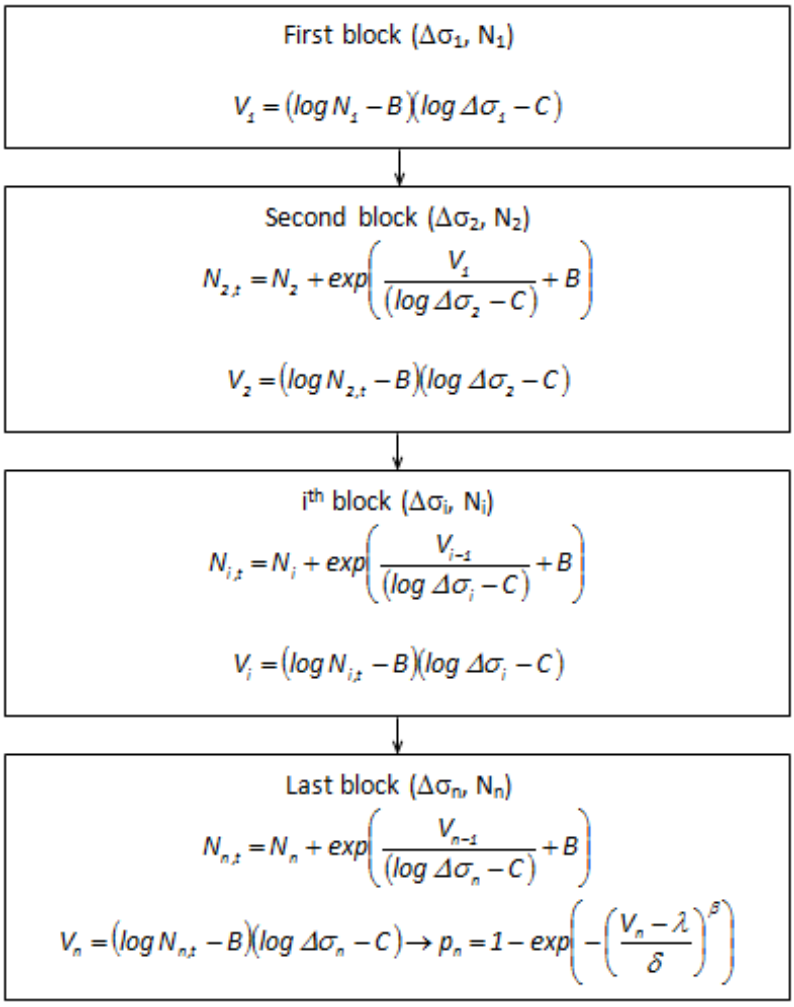

Figure 7.3 – Procedure to compute the failure probability for a block loading (stress based formulation and Weibull distribution assumption).

7.3. APPLICATIONS

7.3.1 Strain controlled smooth test data available for the P355NL1 steel

In this section, the process described above to associate a failure probability to Miner numbers will be applied to existing experimental data available in the literature [2-4] for smooth specimens made of P355NL1 steel tested under strain controlled conditions (see Figure 7.4). Both constant and variable amplitude fatigue data is available for this material. Figure 7.5 represents the *P-ε-N* field obtained for the P355NL1 steel using constant amplitude data. This probabilistic field is defined using the Weibull distribution. Figure 7.6 represents the cumulative distribution function resulting for the normalized variable *V*, which was derived from the Weibull theoretical distribution, using constant amplitude fatigue data.

The smooth specimens represented in Figure 7.4 were subjected to variable amplitude loading histories. Blocks of variable amplitude loading were repeatedly applied until failure. Four types of blocks were defined, each one composed of individual strain cycles, with null strain ratio, the same used for the constant amplitude tests. Figure 7.7 represents the four block types. The H-L, L-H and random blocks were composed of 100 individual cycles; the L-H-L block was composed of 200 cycles. Blocks of Figure 7.7 were applied with a maximum strain of 2.1%, but similar blocks with maximum strains of 1.05% were also applied. Table 7.1 summarizes the specimens that were tested under variable amplitude block loading with respective fatigue lives in terms of blocks or individual cycles to failure.

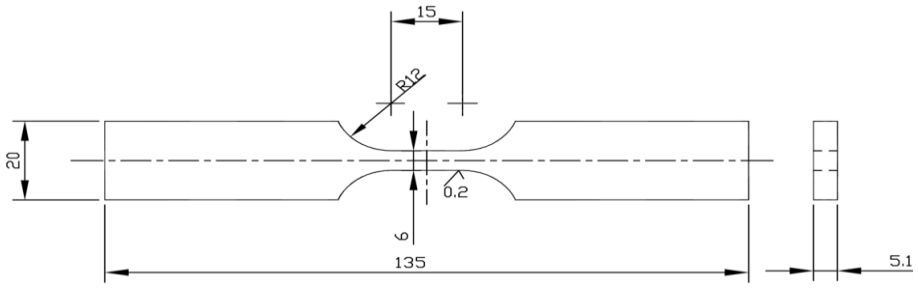

Figure 7.4 – Smooth specimen of P355NL1 steel tested under constant and variable amplitude data (dimensions in mm) [2-4].

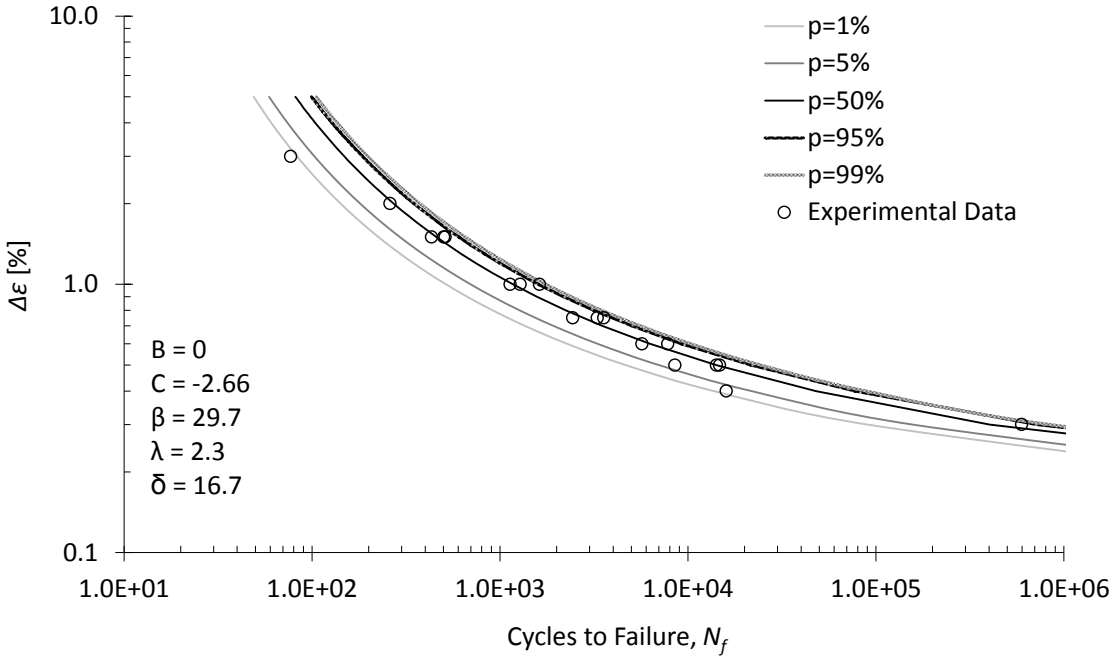

Figure 7.5 – *P-ε-N* field obtained for the P355NL1 steel using constant amplitude data.

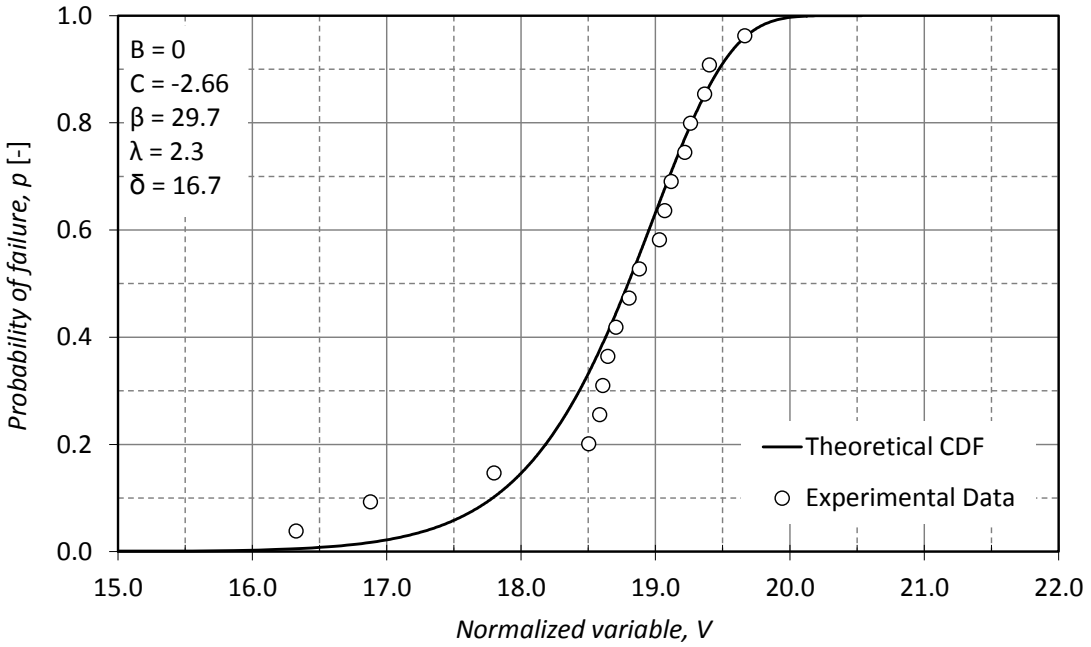

Figure 7.6 – Cumulative distribution function obtained for normalized variable *V* of the P355NL1 steel.

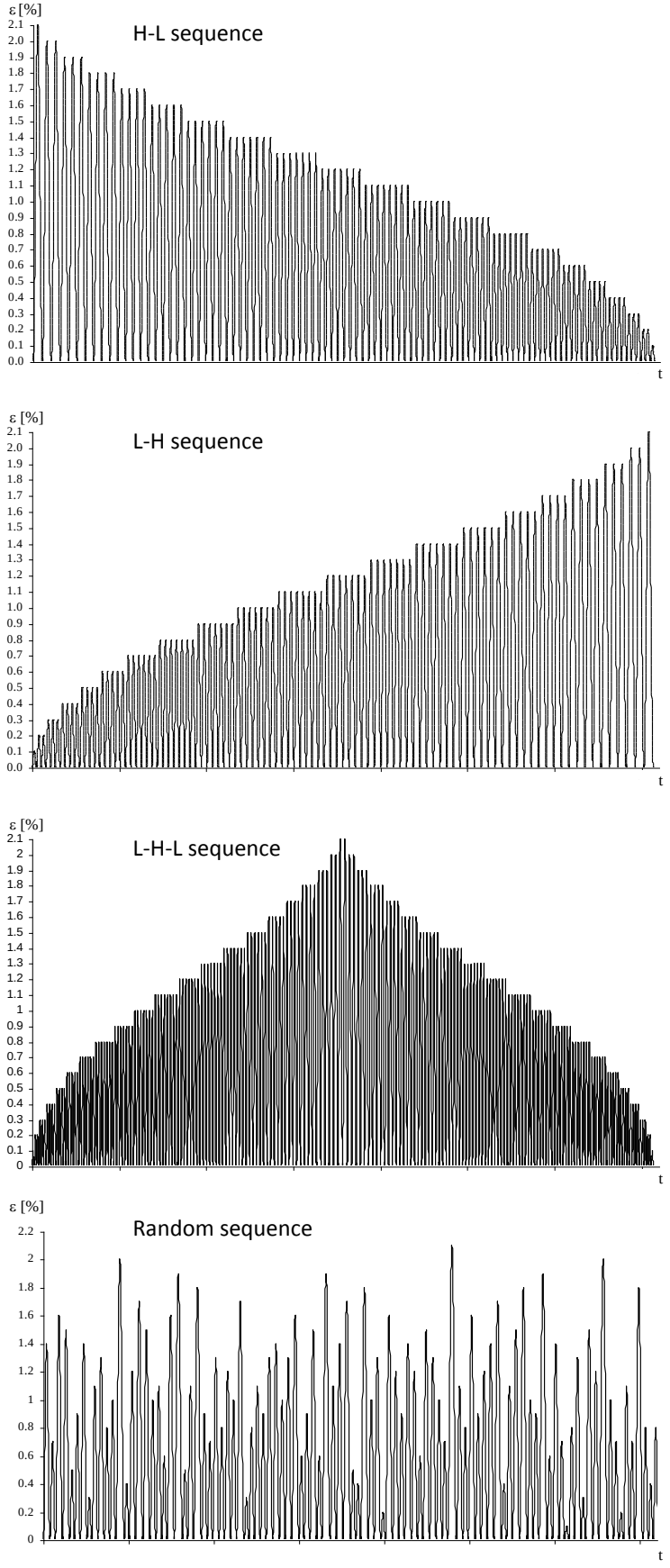

Figure 7.7 – Variable amplitude blocks applied to the smooth specimens made of P355NL1 steel [2-4].

Table 7.1 – Experimental programme of variable amplitude tests performed on P355NL1 steel using smooth specimens [2-4].

Specimens	Block Type	Maximum Strain (%)	No. of Blocks to Failure	Cycles to Failure
D1001	H-L	2.1	6	614
D1002	H-L	2.1	11	1100
D1003	H-L	2.1	14	1400
D1601	L-H	2.1	11	1100
D1602	L-H	2.1	11	1100
D1603	L-H	2.1	8	819
D1701	L-H-L	2.1	6	1200
D1702	L-H-L	2.1	5	1100
D1703	L-H-L	2.1	4	900
D1401	Random	2.1	11	1100
D1402	Random	2.1	8	800
D1101	H-L	1.05	47	4719
D1102	H-L	1.05	42	4200
D1103	H-L	1.05	51	5100
D1501	L-H	1.05	88	8800
D1502	L-H	1.05	40	4000
D1503	L-H	1.05	70	7000
D1201	L-H-L	1.05	30	6100
D1202	L-H-L	1.05	32	6500
D1203	L-H-L	1.05	34	6800
D1301	Random	1.05	44	4400
D1302	Random	1.05	49	4900
D1303	Random	1.05	53	5300

Figure 7.8 represents the distribution of the normalized variable *V* for each specimen, computed from the experimental values of this parameter, taking into account the full loading history until failure (results of Table 7.1) and the theoretical cumulative distribution of Figure 7.6. This figure also compares the results from constant and variable amplitude fatigue data confirming the assumed correlation of both data sources.

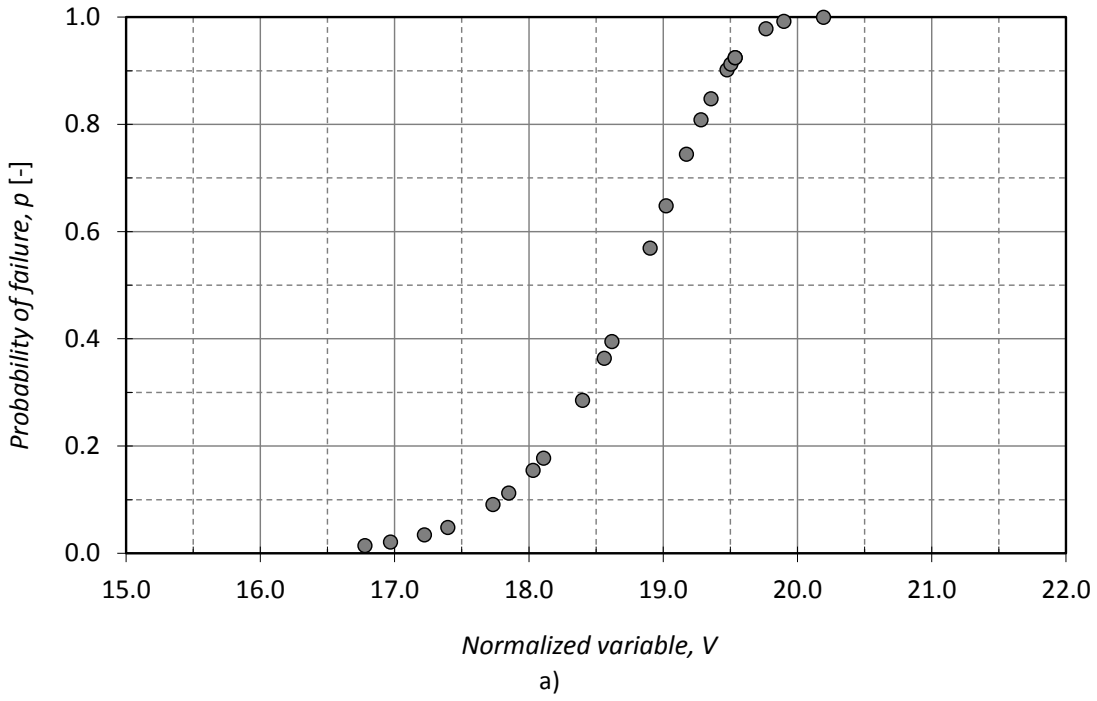

a)

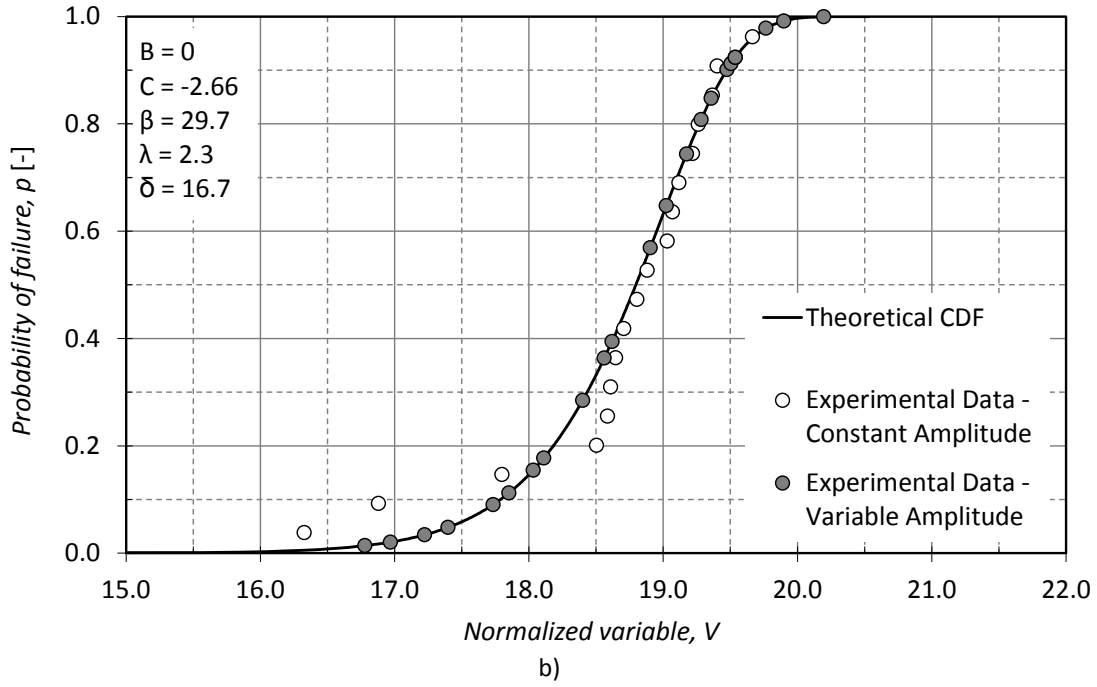

b)

Figure 7.8 – Cumulative distribution of the normalized variable *V* (smooth specimens made of P355NL1 steel) computed using: a) variable amplitude loading histories; b) constant amplitude versus variable amplitude data.

Miner numbers and LogMiner numbers are computed for the experimental data, using Equations (7.4) and (7.5). In order to apply these equations, the computation of the number of cycles to failure for given specific constant amplitude loading conditions is required. To this end, the *ε-N* field was used taking into account a failure probability of

50% (50% percentile). The experimental cumulative distributions of the resulting Miner and LogMiner numbers are plotted in Figure 7.9. These experimental distributions are obtained using the data ranking by Hazen (p=(i+0.5)/n)) [17,18]. We realize that the Miner numbers range between 0.8 and 1.8, with a non-symmetric distribution about the unity (p=0.5 $\rightarrow M$=1.25). Concerning the LogMiner numbers, they ranged between 0.90 and 1.07. In this case an almost symmetrical distribution is obtained (p=0.5 $\rightarrow LM$~1.0) with less scatter.

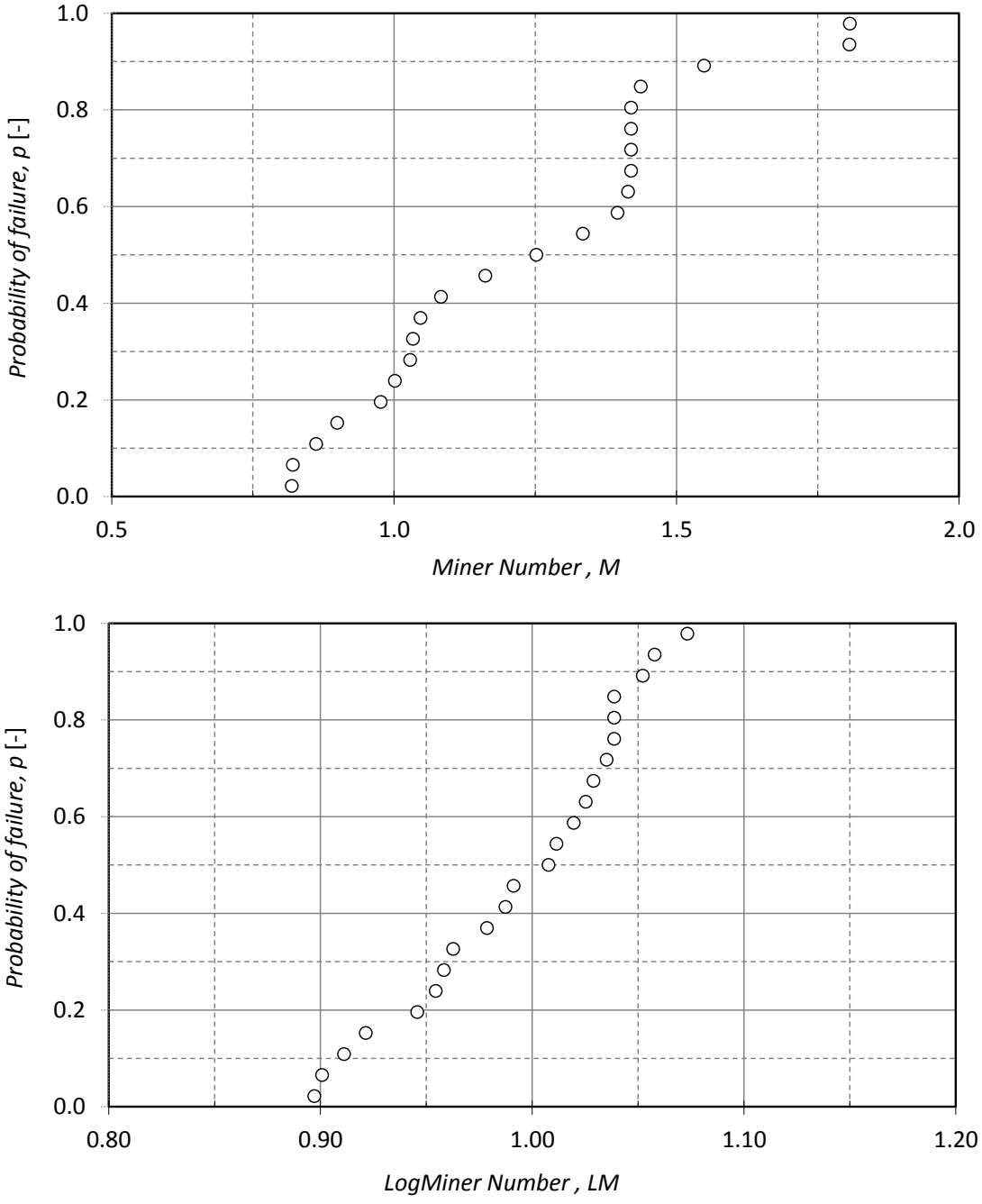

Figure 7.9 – Experimental distributions of Miner and LogMiner numbers obtained using data ranking according to Hazen (smooth specimens made of P355NL1 steel).

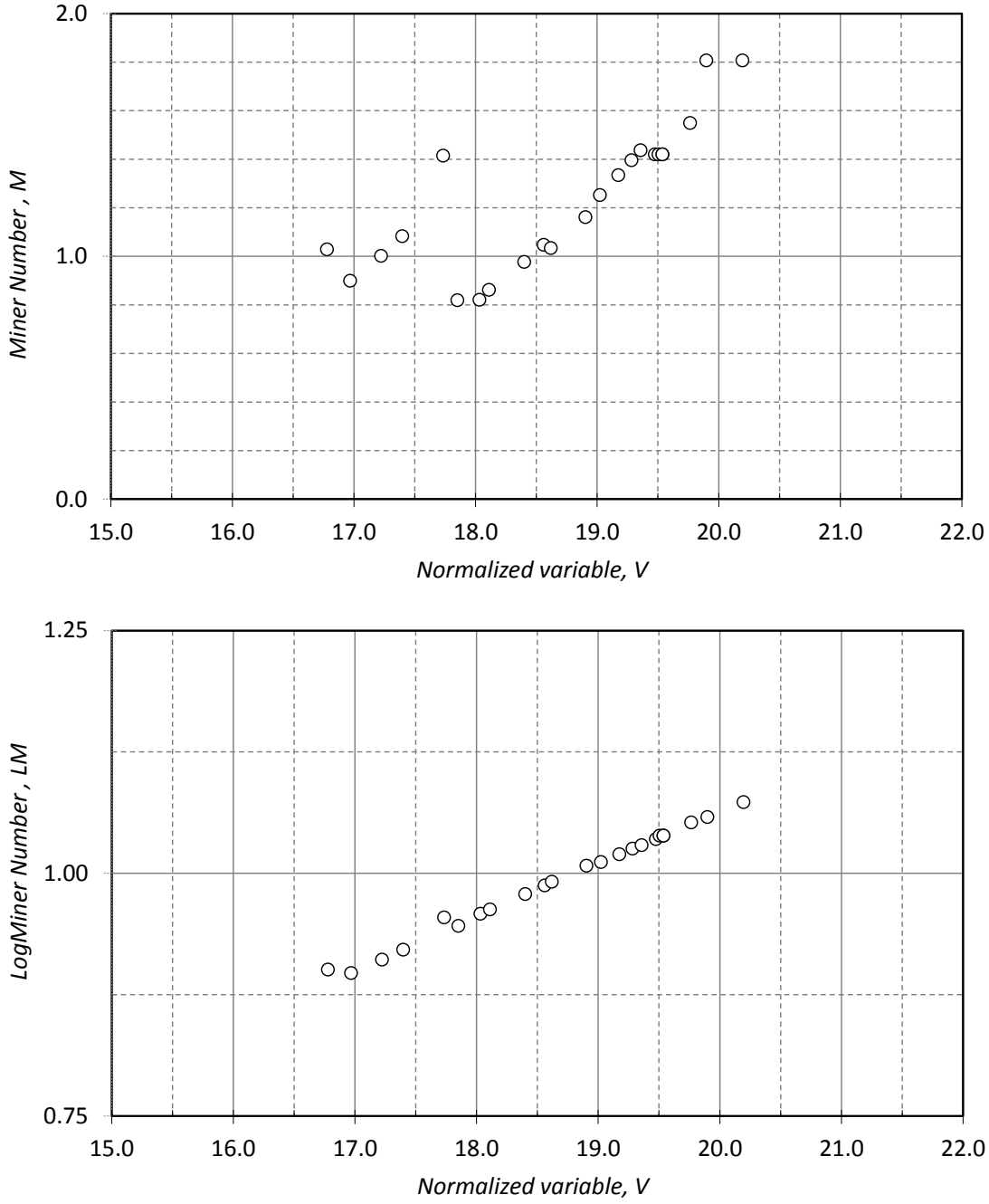

Figure 7.10 – Miner and LogMiner numbers versus normalized variable *V* (smooth specimens made of P355NL1 steel).

In Figure 7.10, the Miner and LogMiner numbers are plotted against the normalized variable *V*, in order to assess the respective relation between these variables. In the case of the Miner number, a non-monotonic relation is verified between the variables while an almost monotonic relation is observed between the LogMiner numbers and the normalized variable *V*. Using these relations between the Miner and LogMiner numbers and the normalized variable *V*, and taking into account the distribution of the normalized variable of Figure 7.8 the resulting distribution for the Miner and LogMiner numbers are

found as represented in Figures 7.11 and 7.12, respectively for the Miner and LogMiner numbers. The resulting distribution or the Miner number does not increase monotonically pointing out some inconsistencies in the computation of M and V for low failure probability data. On the contrary, the LogMiner distribution shows no contradictory trends resulting in a very reliable with a monotonic increasing “s shape”.

Figure 7.12 compares the computed cumulative distribution for the LogMiner number with the one resulting from ranking experimental data according to the plotting point position rule of Hazen. Both distributions approximately give the same LogMiner number for the 50% failure probability. However, assuming that both distributions could be fitted by a Weibull distribution, the experimentally-based distribution would exhibit a lower shape parameter, β.

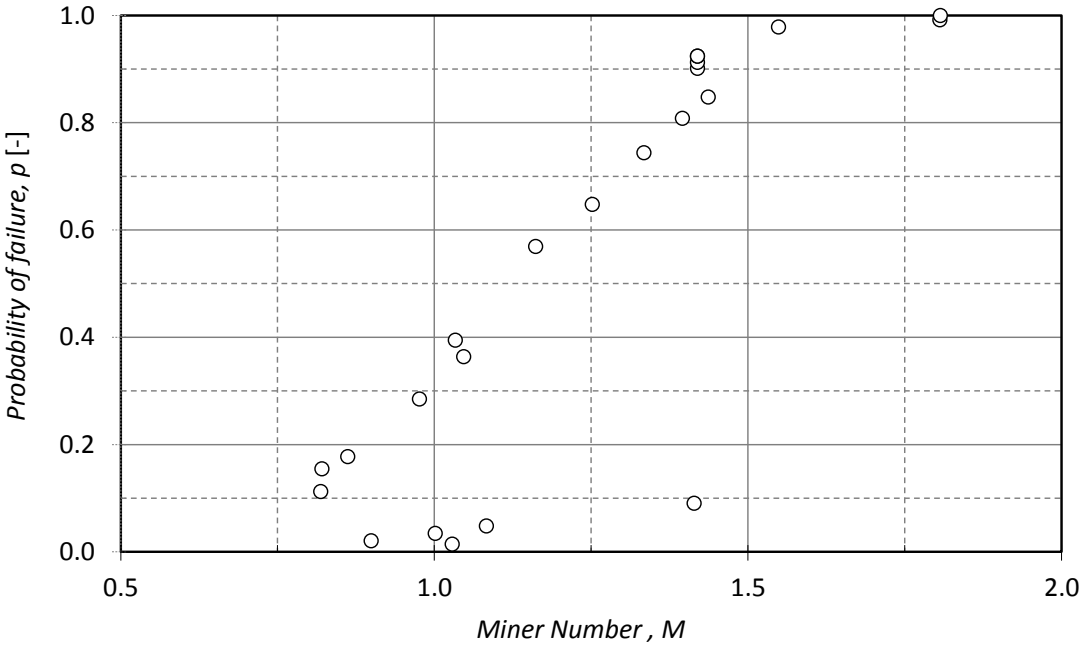

Figure 7.11 – Failure probability computed for the Miner number (smooth specimens made of P355NL1 steel).

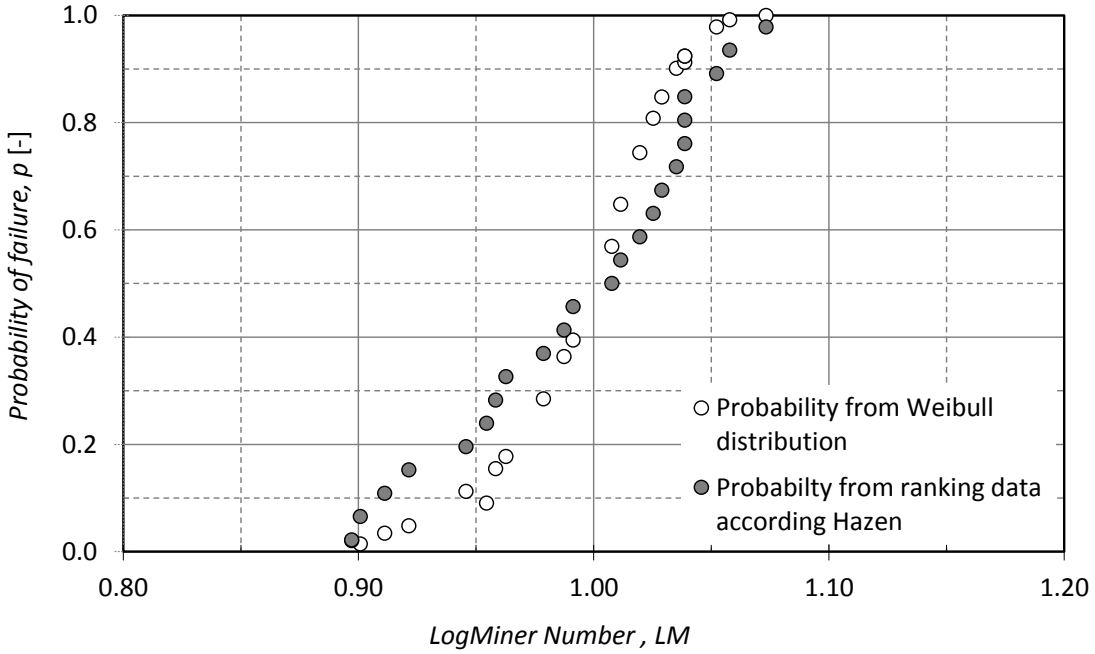

Figure 7.12 – Failure probability computed for the LogMiner number (smooth specimens made of P355NL1 steel).

7.3.2 Stress controlled test data for structural component

In this section, the experimental results of the fatigue tests performed under constant and variable amplitude stresses on riveted joints, available in the literature [15, 16] will be used to illustrate the proposed methodology to attribute a probability of failure to the Miner or LogMiner numbers. These experimental results were obtained for a simple riveted joint made of puddle iron extracted from the centenary Fão riveted bridge (refer to Figure 7.13 for geometry details). Fatigue tests were performed under stress control and null stress ratio (R_σ=0). Using constant amplitude data, the *P-S-N* field for the riveted joint was generated. This probabilistic fatigue field is illustrated in Figure 7.14. A significant 1%-99% failure probability band is observed which may be justified by the inclusion of experimental fatigue in the plastic regime (two data points). Censoring these two data points would result in a narrowed probabilistic field. Figure 7.15 compares the experimental and theoretical distributions for the normalized variable, V. A very satisfactory agreement mostly for higher failure probabilities is observed.

Figure 7.16 illustrates the variable amplitude stress applied to the riveted joints. Three distinct stress spectra were applied corresponding to a repetition of the blocks illustrated in Figure 7.16. The first block is composed of individual stress cycles with stress ranges in

the interval of 170 and 360 MPa. The second block is composed of individual stress cycles with stress ranges in the interval of 45 and 360MPa. The last block shows a central region with higher stresses. In this latter block, the stress ranges also vary between 170 and 360 MPa. Each block is formed by 100 cycles with null stress ratio. A total of 8 specimens were tested: 2 specimens under spectrum 1; 3 specimens under spectrum 2 and 3 specimens under spectrum 3. Table 7.2 summarizes the experimental results for the tested riveted joints, in terms of both blocks to failure and cycles to failure.

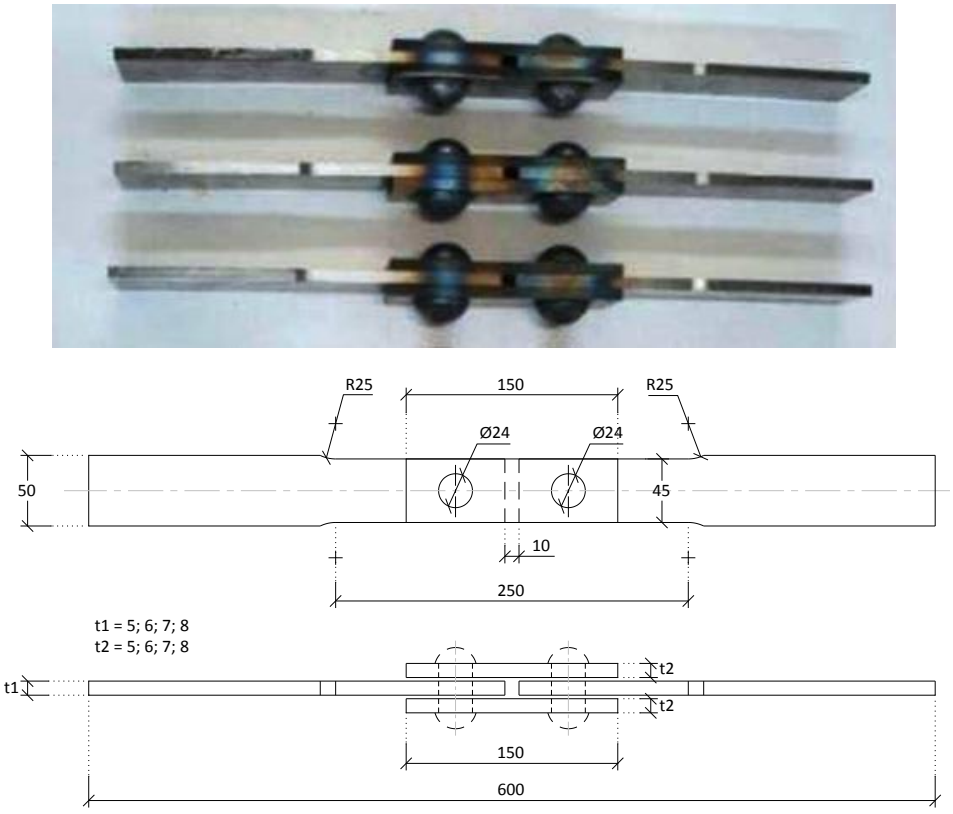

Figure 7.13 – Riveted joints made of Puddle iron, tested under constant and variable amplitude fatigue loading (dimensions in mm) [15,16].

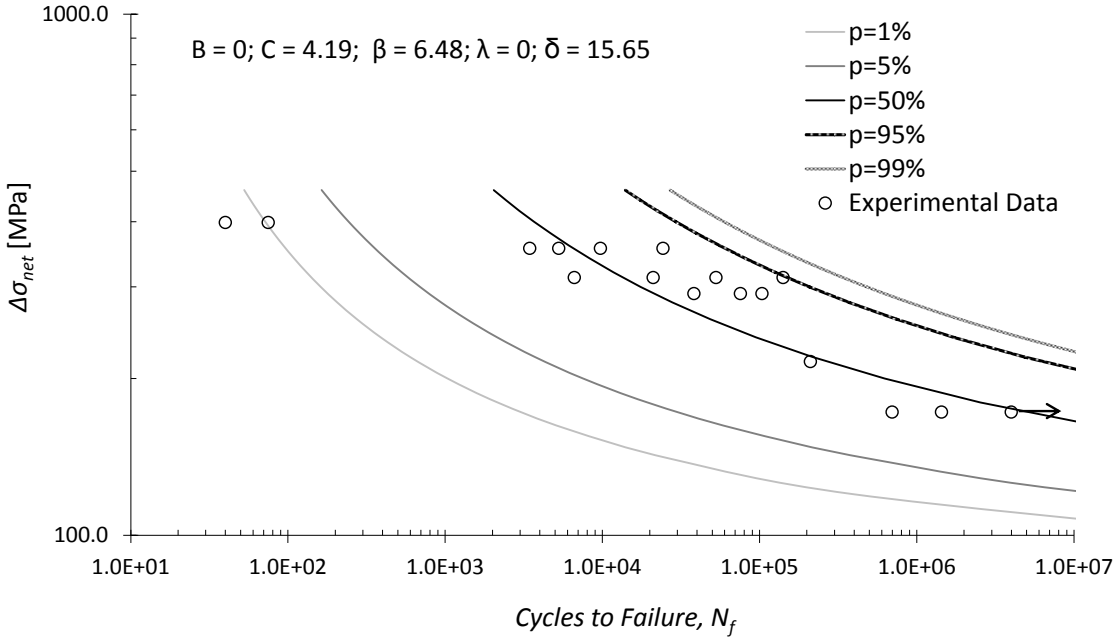

Figure 7.14 – Probabilistic *S-N* field obtained for the riveted joints using the Weibull probabilistic model proposed by Castillo and Fernández-Canteli.

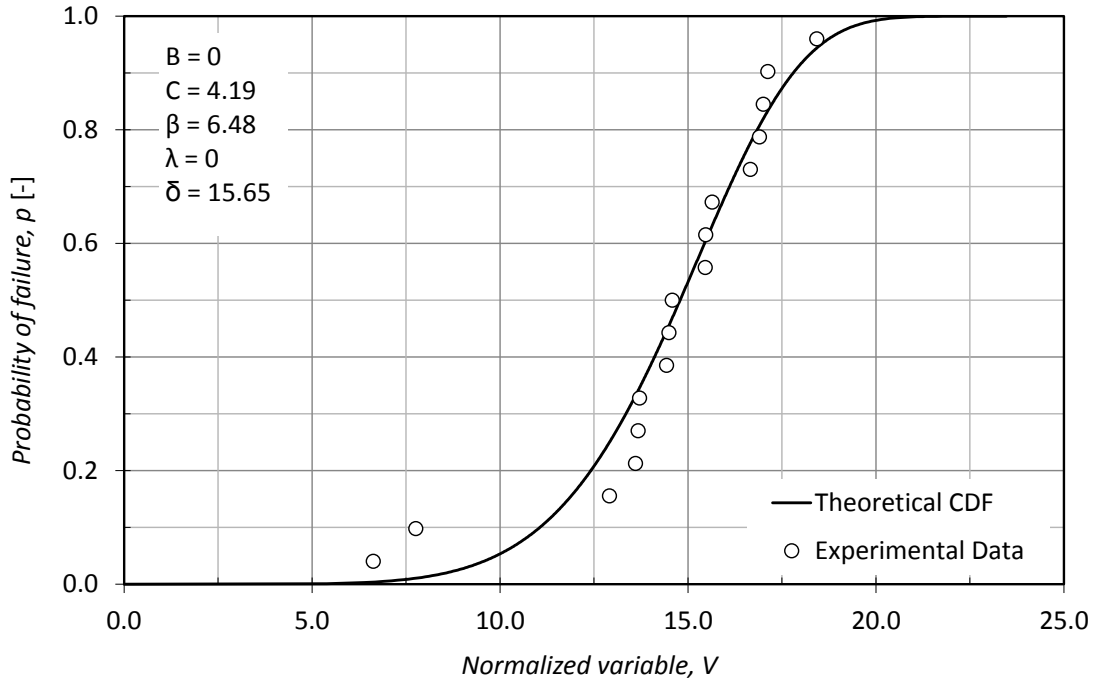

Figure 7.15 – Comparison of experimental and theoretical cumulative distribution function obtained for normalized variable V associated to the S-N data of the riveted joints.

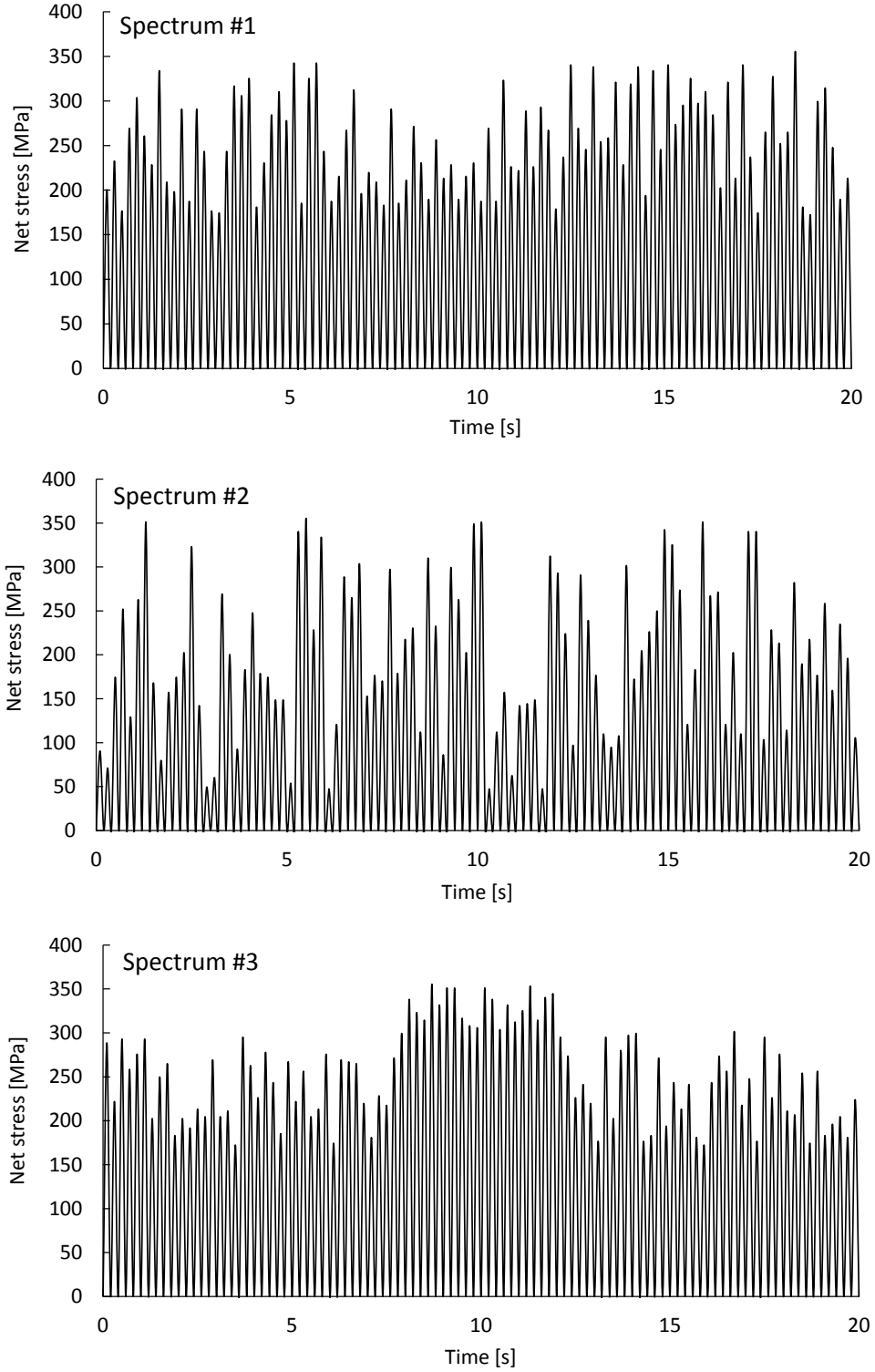

Figure 7.16 – Variable amplitude blocks applied to the riveted joints made of puddle iron from the Fão bridge [15,16].

Table 7.2 – Experimental programme of variable amplitude tests performed on riveted joints [15,16].

Specimens	Block Type	Interval of stress ranges (MPa)	No. of Blocks to Failure	Cycles to Failure
57	Spectrum #1	170 - 360	601	60100
58	Spectrum #1	170 - 360	701	70100
59	Spectrum #2	45 - 360	1309	130900
60	Spectrum #2	45 - 360	574	57400
61	Spectrum #2	45 - 360	1301	130100
62	Spectrum #3	170 - 360	282	28200
63	Spectrum #3	170 - 360	894	89400
64	Spectrum #3	170 - 360	660	66000

Figure 7.17 illustrates the cumulative distribution function of the normalized variable *V*, computed for each variable amplitude fatigue test. Only a total of eight data points were available from specimens 57 to 64 given in Table 7.2. The probabilities of failure were computed using the Weibull field obtained for the riveted joints, represented in Figure 7.14, using the procedure depicted in the workflow of Figure 7.3. The points of Figure 7.17 fall within the failure probabilities of 30-65%, the cumulative distribution function being almost linear in this region. This linear trend of the cumulative distribution function was also observed for the smooth fatigue data of the P355NL1 steel, presented in the previous section (Figure 7.8) for the same range of failure probabilities. Extreme failure probabilities were not calculated which may be justified by the fact that only a very low number of experimental observations were available.

Miner and LogMiner numbers were computed using, respectively, Equations (7.4) and (7.5). For this purpose the denominator of these equations were computed using the 50% percentile (median S-N curve) of the P-S-N field of the riveted joint. The results were plotted in Figures 7.18 and 7.19, respectively for Miner and LogMiner numbers, against the normalized variable, V. Both representations are approximately linear, but the linearity is higher in the case of the LogMiner number versus *V* relation. It is also worth mentioning that Miner numbers range from 0.97 to 3.11 with 6 points above 2; concerning the LogMiner numbers, they range between 0.93 and 1.05. The LogMiner number produces results that are much more close to the unity as suggested by the empirical failure condition. Replacing the normalized variable V in Figures 7.18 and 7.19

by the cumulative distribution function of Figure 7.17, results the representations of Figures 7.20 and 7.21. These figures also include an experimental cumulative distribution for the Miner and LogMiner numbers that were computed using the data ranking according to Hazen. The two distributions (theoretical and experimental) produced approximately the same Miner and LogMiner numbers for the 50% probability of failure. For other failure probabilities, distinct but consistent Miner and LogMiner numbers are predicted using distributions.

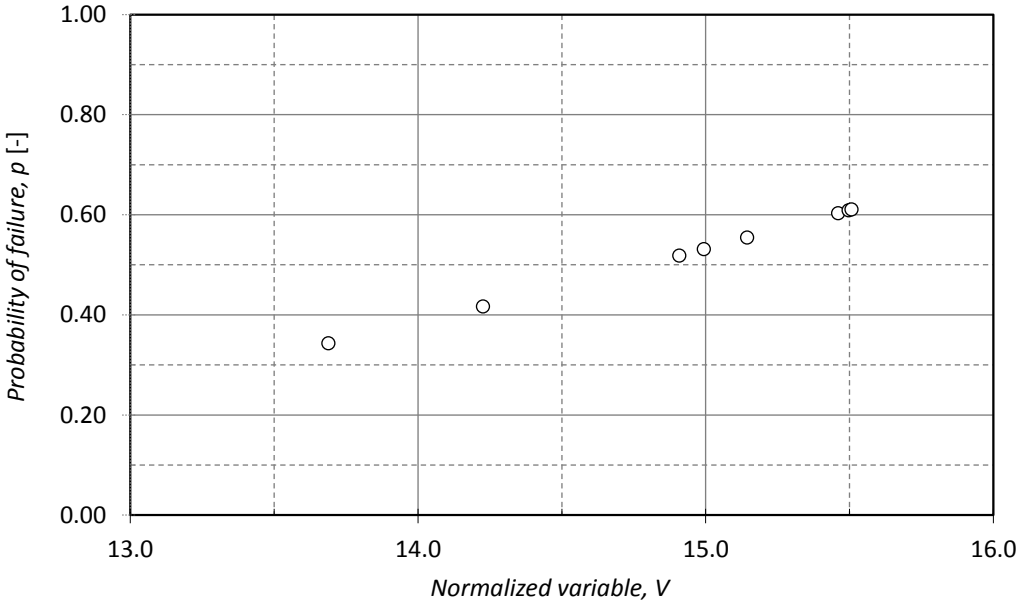

Figure 7.17 – Normalized variable *V* computed for the each loading history and corresponding failure probability computed using the Weibull distribution (riveted joints).

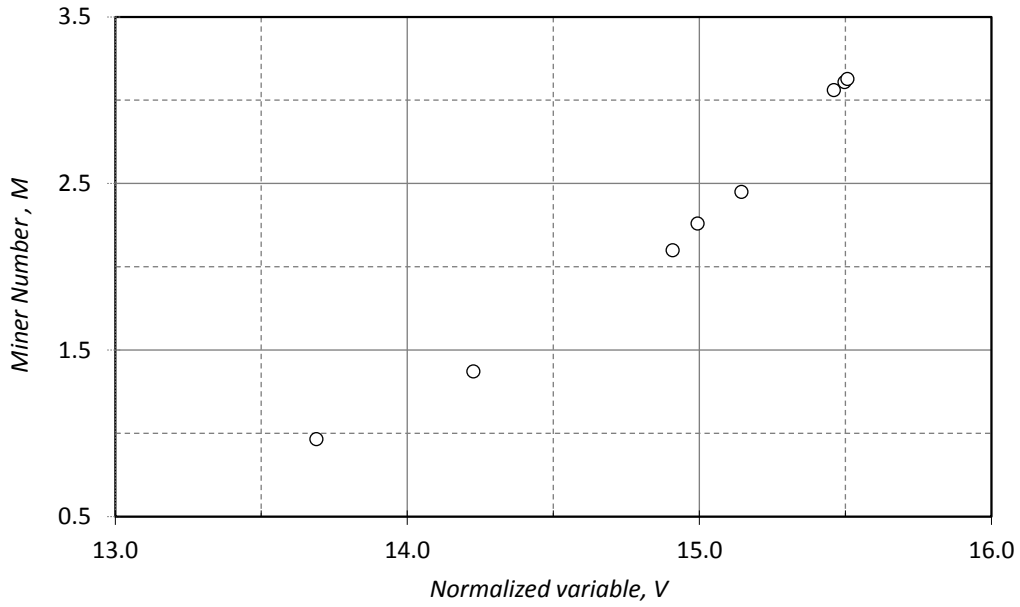

Figure 7.18 – Normalized variable *V* versus Miner number (riveted joints).

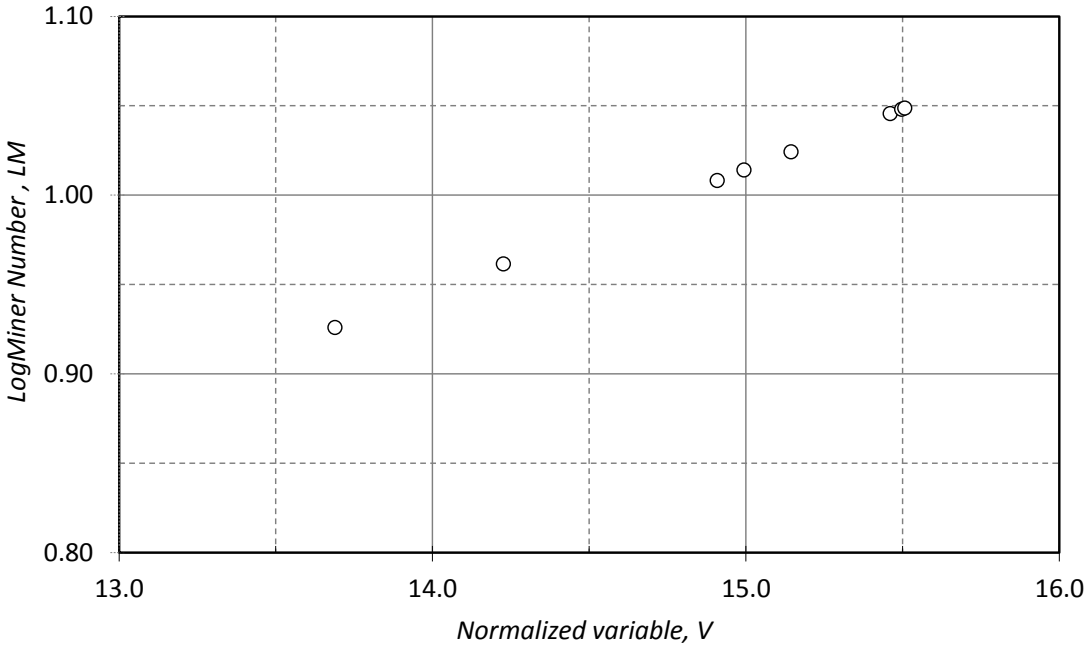

Figure 7.19 – Normalized variable *V* versus Logarithmic Miner number (riveted joints).

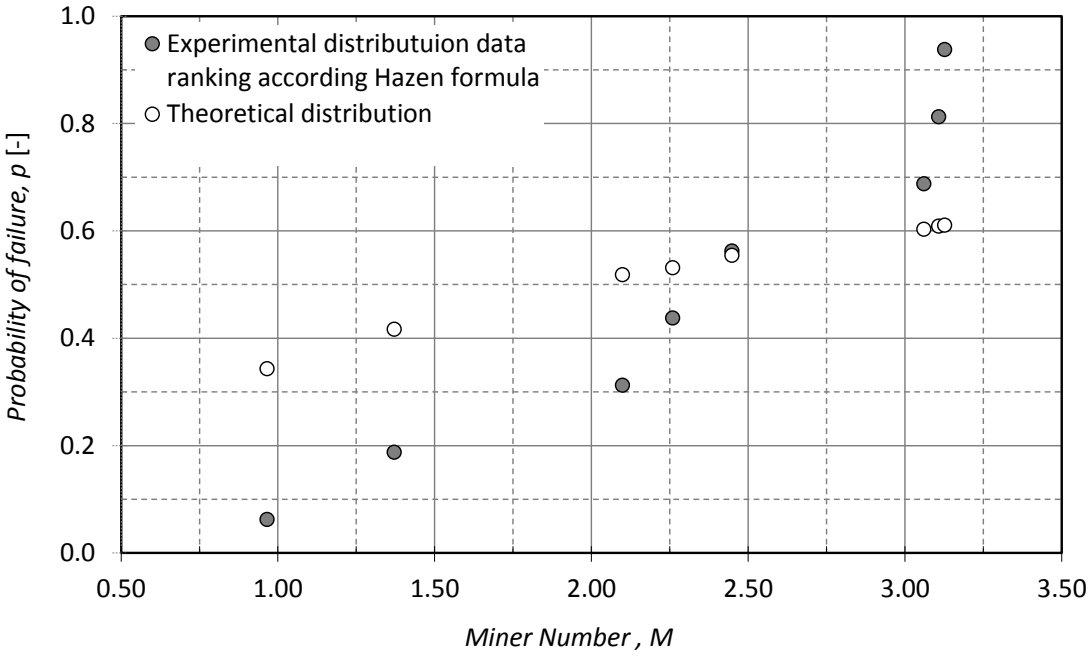

Figure 7.20 – Failure probability computed for the Miner number (riveted joints).

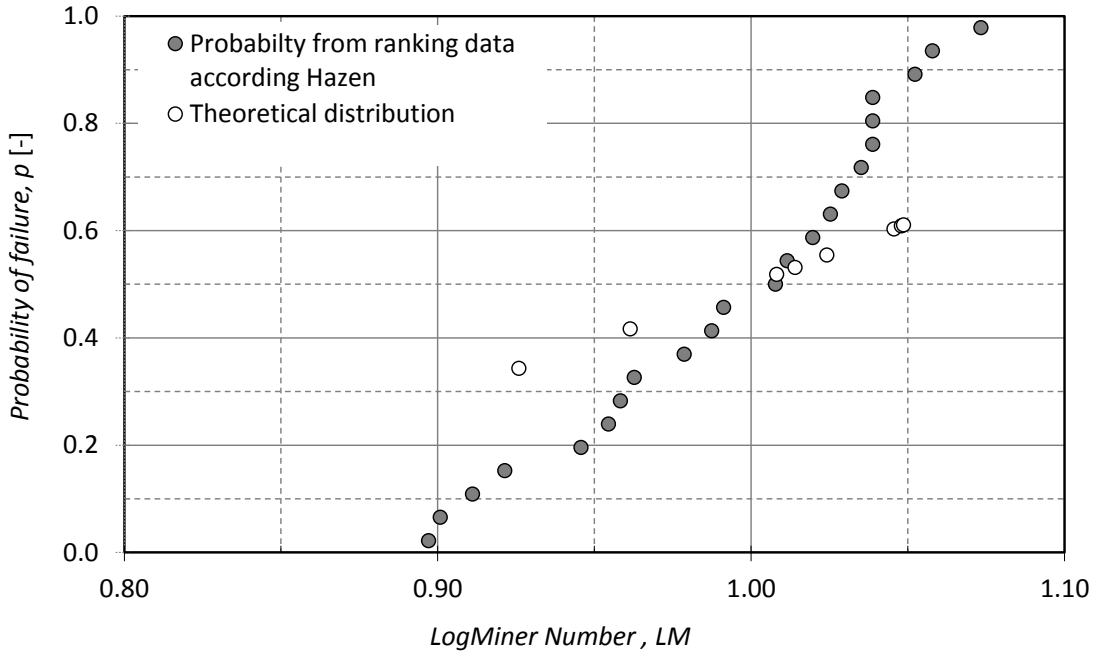

Figure 7.21 – Failure probability computed for the LogMiner number (riveted joints).

7.3.3 Results discussion

The probabilistic model, as proposed by Castillo and Fernández-Canteli [13] allows a probabilistic interpretation for the fatigue damage even under variable amplitude loading histories to be made, taking the normalized variable, *V*, as a damage indicator. Using this normalized variable, both constant and variable amplitude data can be correlated with the same theoretical distribution, as illustrated for the P355NL1 steel (see Figure 7.8).

The distribution of the normalized variable, *V*, obtained from the constant amplitude Weibull field, provides a failure probability that can be associated to classical damage parameters such as the Miner number or the Logarithmic Miner number, allowing the probability distributions for these parameters to be derived. This requires a monotonic relation between the normalized variable *V* and the damage parameter, which was observed for both Miner and LogMiner numbers computed for the riveted joints (see Figures 7.18 and 7.19) but only for the LogMiner number in the case of smooth specimens made of P355NL1 steel (see Figure 7.10)). Considering the LogMiner distribution for the smooth specimens (see Figure 7.12), some degree of agreement was verified between the experimental based and the computed distribution, both distributions crossing each other at approximately 50% failure probability. For the riveted joints this level of agreement was not verified (see Figures 7.20 and 7.21), but distributions still cross each other at

approximately 50% failure probabilities. The major deviation in the case of the riveted joints may be attributed to the low number of experimental data points which results in lower confidence for the experimentally-based cumulative distribution.

A detailed observation of the experimental data available for the smooth specimens, evidences that if the random block data is excluded from the analysis, a roughly linear relation between the Miner number and the normalized variable *V* results, as illustrated by Figure 7.22. Figure 7.23 compares the cumulative distributions of the Miner numbers for the smooth specimens, resulting from censoring experimental data from random blocks. In this case a better agreement was observed for the extreme failure probabilities. Several experimental tests yield the same fatigue lives, what provokes the sudden jump in the experimental based cumulative distribution.

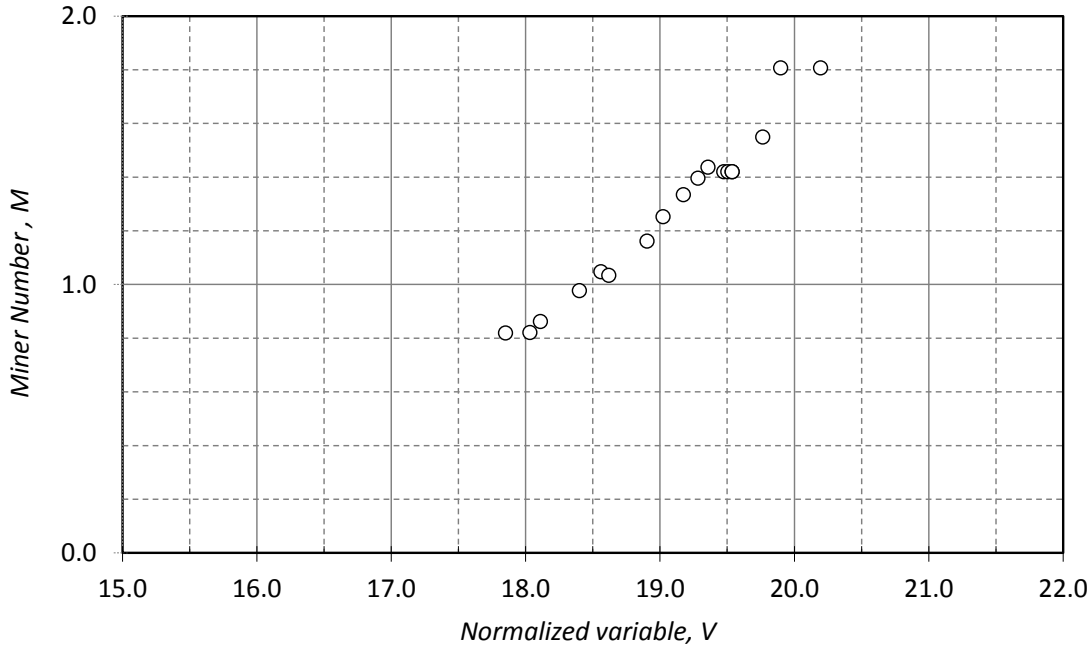

Figure 7.22 – Normalized variable *V* versus Miner number (smooth specimens).

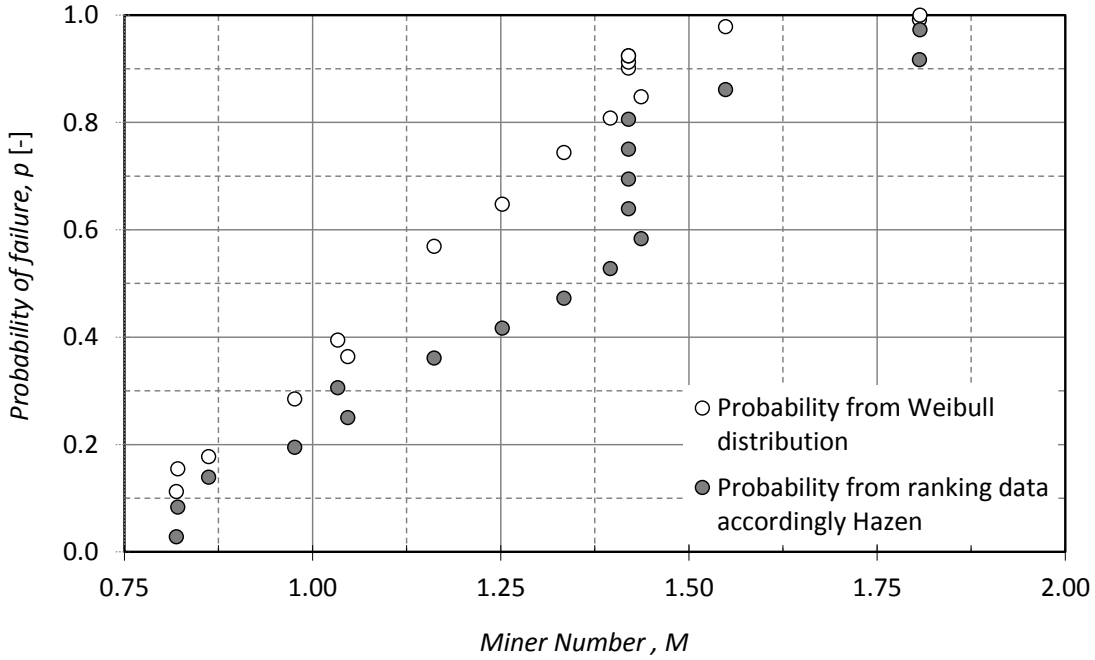

Figure 7.23 – Failure probability computed for the Miner number (smooth specimens).

It is interesting to note that the experimental LogMiner numbers are distributed symmetrically in a narrow band around the unity, making this damage indicator to more coherent with the classical assumption for the failure condition.

Taking advance of the use the probabilistic model proposed by Castillo and Fernández-Canteli [13] to assess distribution functions for the classical Miner and LogMiner numbers, the distribution of the normalized variable can be used to compute the fatigue damage for variable amplitude loading directly with evident advantages over the classical approaches based on Miner or LogMiner numbers. The application of Miner number or LogMiner number accounts for fatigue scatter into separate steps. Firstly one need to compute the Miner or LogMiner numbers using available constant amplitude fatigue data. In this case, a failure probability needs to be specified to allow the definition of the appropriate constant amplitude S-N curve. Usually the 50% percentile curve is adopted, but other failure probabilities can also be specified. In a second step the computed Miner numbers of LogMiner numbers need to be correlated with an appropriate statistical distribution in order their scatter to be appropriately accounted for. Using the normalized variable, a unified approach is used to determine the scatter. It is assumed that variable amplitude and constant amplitude data are correlated by the same probabilistic field or by the same cumulative distribution for the normalized variable. The constant amplitude

probabilistic field can be used to compute failure probabilities for given variable amplitude data (extrapolation). Alternatively, constant and variable amplitude experimental fatigue data can be combined together in the identification of the probabilistic field, scatter from both sources being accounted in this process.

In a recent paper [19], co-authored by the author of this thesis, a study similar to the one presented in this chapter was performed for concrete specimens. In this study a very significant number of tested specimens were considered. In this case the theoretical cumulative distributions for the Miner number and the experimental one from data ranking agreed satisfactorily if a scale effect type correction is applied to the theoretical distribution to compensate the non-conservative trend of the predicted results.

7.4. CONCLUSIONS

A statistical interpretation of the Miner is possible, without practically maintaining the simplicity of its calculation in the conventional approach allowing an increase of reliability in the lifetime prediction of structural and mechanical components.

In order to proceed to an adequate probabilistic evaluation of the Miner number, a probabilistic definition of the *S*-*N* field is required.

For the smooth specimens, some degree of agreement was achieved between the experimental based and the computed distribution. On the contrary, the low number of experimental data points in the case of riveted joints does not guarantee high confidence for the experimentally-based cumulative distribution.

Higher scatter is found by the distribution obtained from the experimental data compared to that predicted from the theoretical model.

Since the Miner rule is not able to reproduce interaction loading effects or shifting downwards of the fatigue limit, the latter being caused by crack growth due to loads overpassing the fatigue limit, inherent to any variable loading process, some non-conservative result should be expected in the probabilistic prediction. Nevertheless, this is not the case in the present study, at least for 50% probability of failure, which can be

attributed to retardation effects due to overloads compensating the above mentioned limitation of the Miner rule.

The probabilistic results are comparable when a LogMiner model is used. This proves that that the Miner rule does not respond to a “linear cumulative damage hypothesis” as general believed.

Other fatigue programs under variable loading with other materials should be considered in order to confirm the properties of the Miner distribution as exposed here.

7.5. REFERENCES

[1] Miner MA. Cumulative damage in fatigue. Transactions of The ASME. Series E. J. Appl. Mech., Vol. 12, pp. 159–164, 1945.

[2] Pereira HFSG. Comportamento à Fadiga de Componentes Estruturais Sob a Acção de Solicitações de Amplitude Variável. Mestrado em Engenharia Mecânica – Ramo de Construções Mecânicas, FEUP, 2006.

[3] Pereira HFSG, De Jesus AMP, Fernandes AA, Ribeiro AS. Analysis of Fatigue Damage under Block Loading in a Low Carbon Steel. Strain, Vol. 44, pgs. 429-439; 2008.

[4] Pereira HFSG, De Jesus AMP, Ribeiro AS, Fernandes AA. Cyclic and Fatigue Behavior of the P355NL1 Steel under Block Loading. Journal of Pressure Vessel Technology, Vol. 131, No. 2, Paper No. 021210 (9 pages); 2009.

[5] CEN-TC 250. EN 1993-1-9: Eurocode 3, Design of steel structures – Part 1-9: Fatigue. European Committee for Standardization, Brussels; 2003.

[6] EN13445. Unfired Pressure Vessel Code, European Standard; 2009.

[7] ASME – ASME Boiler and Pressure Vessel Code, NY,USA; 2010.

[8] Birnbaum ZW, Saunders SC. A probabilistic interpretation of Miner’s rule. SIAM J. of Applied Mathematics, Vol.16, No. 3 (1968), 637-652.

[9] Van Leeuwen J, Siemes AJM. Miner’s rule with respect to plain concrete. Heron, Vol. 24, Nr. 1, Delft, (1979).

[10] Van Leeuwen J, Siemes AJM. Fatigue of concrete. Report No B 76-443/04.2.6013, Tables, TNO-IBBC, Delft (1977).

[11] Holmen JO. Fatigue of concrete by constant and variable amplitude loading. Institutt for Betongkonstruksjoner, Norges Tekniske Høgskole, Universitet i Trondheim (1979).

[12] Fernández-Canteli A. Statistical interpretation of the Miner-number using an index of probability of total damage. Fatigue of Steel and Concrete Structures, IABSE, Zürich, (1982).

[13] Castillo E, Fernández-Canteli A. A Unified Statistical Methodology for Modeling Fatigue Damage.

Springer, 2009.

[14] Castillo E, Fernández-Canteli A. Statistical models for damage accumulation. Encyclopedia of Statistical Sciences, John Wiley & Sons, Balakrishnan (Editor), Chapter 5, (2011) 1-30. N.

[15] Silva JFN. Comparação entre o comportamento à fadiga de ligações rebitadas e aparafusadas. Universidade de Trás-os-Montes e Alto Douro, Vila Real; 2009.

[16] De Jesus AMP, Silva ALL, Correia JAFO. Fatigue of riveted and bolted joints made of puddle iron-an experimental approach. Journal of Constructional Steel Research, 2014, under review.

[17] Schijve J. Statistical distribution functions and fatigue of structures. International Journal of Fatigue, 2005; 27, 1031–1039.

[18] Castillo E. Extreme value theory in Engineering. Academic Press, San Diego Ca, 1988.

[19] Fernández-Canteli A., Blasón, S, Correia JAFO, De Jesus AMP. A probabilistic interpretation of the Miner number for fatigue life prediction. The First Multi-Lateral Workshop on "Fracture and Structural Integrity related Issues" Catania (Italy), September 15-17, 2014.

CHAPTER VIII

CONCLUSIONS

This chapter concludes the study carried in this thesis about the topic "an integral probabilistic approach for fatigue lifetime prediction of mechanical and structural components". It summarizes the main results of the conducted study. The contributions of this thesis and new lines for future research work are also presented.

8.1. OVERVIEW OF MAIN RESULTS

The main results of this study are presented in the following points:

1. Fatigue behaviour of materials and connections from ancient Portuguese riveted steel bridges

In general, materials from Portuguese riveted steel bridges tested or compiled in this study showed a significant correlation between their mechanical performance, including the fatigue properties, and the age of the materials. The materials from the Eiffel, Luiz I, Fão and Pinhão bridges are very likely puddle irons due to their age, the high microstructural heterogeneities and the low ductility properties. The material from the Trezói bridge is a low carbon structural steel.

Regarding the cyclic elastoplastic behaviour, the materials from Eiffel and Luiz I bridge may be satisfactorily described by the Masing model, since some apparent deviation from the Masing behaviour may be justified by scatter in material properties rather than by phenomenological reasons. The material from Trezói

bridge does not follow the Masing behaviour. The material from Fão bridge shows a cyclic elastoplastic behaviour dependent on strain ratio.

The fatigue crack propagation tests showed that the Paris law gives a good description of the fatigue crack growth data, for each stress ratio. The exponent of the Paris law resulted always greater than the value suggested by codes of practice (m=3). The C coefficient was in a range lower than recommended in literature for modern construction steels.

S-N fatigue data from original riveted joints was compared with existing design curves. The comparison performed with literature *S-N* data suggests the need for a riveted joint categorization, in particular the consideration of single and symmetric double shear splices. Also, a slope, m=5 seems to be more appropriate for the riveted joints, rather than m=3, as suggested by the code design curves.

2. A proposal for generalization of existing probabilistic fatigue damage models

A generalization of the probabilistic model originally proposed by Castillo and Fernández-Canteli [1,2] is proposed, which opens new perspectives for the application of the probabilistic model to a number of very general problems of lifetime involving fatigue modelling, instead of use deterministic approaches. Energetic parameters as reference for fatigue damage for both uniaxial and multiaxial fatigue are considered and adequately estimated using the probabilistic model.

3. Procedure to derive probabilistic fatigue crack propagation fields

Based on probabilistic local approaches to fatigue, *p-da/dN-ΔK-R* fields were derived allowing the description of stress *R*-ratio effects on fatigue crack propagation rates as well as the scatter on these fatigue crack propagation rates, which are significant for materials from old bridges. Predictions taking into account the p-ε_a-N material field produced satisfactory crack propagation fields for the materials from the Fão bridge and for the P355NL1 steel, since these materials showed crack propagation rates with relative small stress *R*-ratio sensitivity. For the material from the Eiffel bridge and the S355 structural steel, the *p-da/dN-ΔK-R* fields were obtained using the *p-SWT-N* material fields since these materials showed fatigue crack propagation rates that are more sensitive to stress ratio.

4. Procedure to derive probabilistic S-N fields for structural details

A unified approach for global *p-S-N* field prediction for structural/mechanical details was proposed. Both crack initiation and crack propagation were accounted in the approach using a similar methodology based on the failure of successive material elementary blocks. This was applied to the P355NL1 steel and to the puddle iron from the Eiffel bridge resulting satisfactory correlation of the experimental *S-N* data. The crack initiation was the dominant damaging process; the fatigue crack propagation only exerted a small influence on global *p-S-N* field, mainly in the high-cycle fatigue regime. The procedure proposed to derive the probabilistic *S-N* curves for structural details proved to be quite efficient, since it can be used to reduce the need for extensive testing.

5. A probabilistic interpretation of fatigue damage under variable amplitude loading

An approach for a probabilistic interpretation of fatigue damage under variable amplitude data, based on the probabilistic model by Castillo and Fernández-Canteli [2] was discussed. The possibility to associate a failure probability to the classical Miner number reduces the need of to perform extensive variable amplitude testing to identify the wanted cumulative distributions by direct ranking of data.

8.2. SUMMARY OF CONTRIBUTIONS

The original contributions of this thesis are summarized as follows:

- The generalization of existing original probabilistic fatigue damage model proposed by Castillo and Fernández-Canteli [1,2], proposing several fatigue damage parameters [3,4] for both uniaxial and multiaxial fatigue, opened new perspectives for the application of the probabilistic model to a number of very general problems of fatigue lifetime modeling instead of using classical deterministic approaches;

- A procedure to derive probabilistic fatigue crack propagation fields using local approaches to fatigue, based on probabilistic material (smooth) fatigue data was

proposed. To demonstrate this procedure, local approach to fatigue crack propagation as proposed by Noroozi et al. [5,6,7] was used with some modifications;

- The procedure to derive probabilistic *S-N* fields for structural details, including crack initiation and crack propagation, is presented as a unified approach. The probabilistic fatigue crack initiation fields is determined using a local elastoplastic approach together with a material probabilistic *S-N* fatigue (smooth) representation (e.g. $p–\varepsilon_a–N$ or *p–SWT–N* fields) to calculate the fatigue damage of the first elementary material block, ahead of the notch root. The crack propagation is modelled using the same local approaches to fatigue assuming that fatigue crack propagation is a process of continuous re-initializations, as argued in the UniGrow model proposed by Noroozi et al. [5,6,7]. The proposal was demonstrated to be satisfactory for structural/mechanical details.

-Finally some research was performed about fatigue damage assessment under variable amplitude fatigue loading and the potentialities of using the probabilistic *S-N* fields as proposed by Castillo and Fernández-Canteli were illustrated to serve as an alternative to the classical Miner analysis.

8.3. FUTURE WORKS

The future work after this thesis will consist in the following:

- To perform fatigue tests of materials from other ancient Portuguese riveted steel bridges with the purpose of extending the existing fatigue properties database;

- To search for more fatigue damage parameters candidates that could be used together with the base probabilistic model as proposed by Castillo and Fernández-Canteli [2]. A damage parameter that could transform the current hyperbolic *S-N* field into a sigmoidal one would be a very significant contribution;

- Development and validation of probabilistic fatigue life models using an equivalent initial flaw size distribution, and fatigue crack propagations estimated according to probabilistic fatigue models proposed in this thesis. This concept of

equivalent initial flaw size may be considered physically justified for the old materials from bridges (puddle irons) that show a significant number of intrinsic heterogeneities working as defects;

- Apply the proposed procedures in this thesis to the prediction of *p-S-N* fields to complex structural/mechanical details more representative of the real structures such as riveted or bolted connections;

- More studies in the field of fatigue damage accumulation under variable amplitude loading, using a probabilistic emphasis would be required. For example, more experimental validation is required to demonstrate the goodness of the normalized *V* parameter as a damage measure indicator. Also, the possibility of including loading sequential effects in damage computation using the normalized *V* parameter has to be investigated due to its relevance for some loading histories.

8.4. REFERENCES

[1] Fernández-Canteli A, Castillo E, Correia JAFO, De Jesus AMP, Przybilla C. Extending the applicability of probabilistic S-N models to the LCF region using energetic damage parameters. XVI International Colloquium Mechanical Fatigue of Metals. Brno – Czech Republic, 2012.

[2] Castillo E, Fernández-Canteli A. A Unified Statistical Methodology for Modeling Fatigue Damage. Springer, 2009.

[3] Ellyin F. Fatigue damage, crack growth and life prediction. Chapman & Hall, 1997.

[4] Smith KN, Watson P, Topper TH. A Stress-Strain Function for the Fatigue of Metals. Journal of Materials 1970; 5(4): 767-78.

[5] Noroozi AH, Glinka G, Lambert S. A two parameter driving force for fatigue crack growth analysis. International Journal of Fatigue 2005; 27: 1277-1296.

[6] Noroozi AH, Glinka G, Lambert S. A study of the stress ratio effects on fatigue crack growth using the unified two-parameter fatigue crack growth driving force. International Journal of Fatigue 2007; 29:1616-1633.

[7] Noroozi AH, Glinka G, Lambert S. Prediction of fatigue crack growth under constant amplitude loading and a single overload based on elasto-plastic crack tip stresses and strains. Engineering Fracture Mechanics 2008; 75: 188-206.

ANNEX

LIST OF PAPERS

This annex contains papers published by author in scientific journals and conferences:

- Scientific Journals

1. J.A.F.O. Correia, A.M.P. Jesus, M.A.V. Figueiredo, A.S. Ribeiro, A.A. Fernandes – "*Overview of Recent Portuguese Research on Fatigue Behaviour of Ancient Portuguese Riveted Steel Bridges*". *Revista de Mecânica Experimental*, ISSN 1646-7078, Vol. 16, pgs.73-79, 2009.

2. A.M.P. de Jesus, Hernán Pinto, Fernández-Canteli, Enrique Castillo, J.A.F.O. Correia, "*Fatigue Assessment of a Riveted Shear Splice Based on a Steel Probabilistic Model*". *International Journal of Fatigue*, ISSN 0142-1123, Issue 2, Vol. 32, 2010, 453-462. {http://dx.doi.org/10.1016/j.ijfatigue.2009.09.004}

3. B. Silva, J.A.F.O. Correia, F. Nunes, P. Tavares, H. Varum, J. Pinto, "*Bird Nest Construction – Lessons for Building with Earth*". *Journal WSEAS Transactions on Environment and Development*, ISSN 1790-5079, Issue 2, Vol. 6, February 2010, 95-104. {http://hdl.handle.net/10773/5785}

4. A.M.P. de Jesus, A.L.L. da Silva, M.V. Figueiredo, J.A.F.O. Correia, A.S. Ribeiro, A.A. Fernandes, *"Strain-Life and Crack Propagation Fatigue Data From Several Portuguese Old Metallic Riveted Bridges"*. *Engineering*

Failure Analysis, ISSN 1350-6307, Issue I, Vol. 18, Janeiro 2011, 148-163. {http://dx.doi.org/10.1016/j.engfailanal.2010.08.016}

5. J.A.F.O. Correia, A.M.P. Jesus, A.L.L. Silva – *"Simulação por Elementos Finitos de Curvas S-N de Ligações Rebitadas"*. *Revista de Mecânica Experimental*, ISSN 1646-7078, Vol. 19, pgs.9-18, 2011.

6. J.A.F.O Correia, A.M.P. de Jesus, A. Fernández-Canteli, "*A procedure to derive probabilistic fatigue crack propagation data*". *International Journal Structural Integrity*, ISSN 1757-9864, Issue 2, Vol. 3, 2012, 158-183. {http://dx.doi.org/10.1108/17579861211235183}

7. M. H. Hafezi, N. Nik Abdullah, J.A.F.O. Correia, A.M.P. de Jesus, "An *assessment of a strain-life approach for fatigue crack growth*". *International Journal Structural Integrity*, ISSN 1757-9864, Issue 4, Vol. 3, 2012, 344-376. {http://dx.doi.org/10.1108/17579861211281173}

8. B.Silva, F. Nunes, J.A.F.O. Correia, P. Tavares, H. Varum, J. Pinto, *"Aprender a construir com terra através da andorinha-dos-beirais". DigitAR, Revista Digital de Arqueologia,* ISSN 2182-844X, N. 1, 2013, pp. 95-101. {http://hdl.handle.net/10316.2/9136}

9. A.M.P. De Jesus, J.A.F.O. Correia – "*Critical assessment of a local strain-based fatigue crack growth model using experimental data available for the P355NL1 steel". Journal of Pressure Vessel Technology*, ISSN 0094-9930, Vol. 135, N.º 1, 2013, 011404:1-9. {http://dx.doi.org/10.1115/1.4006905}

10. J.A.F.O. Correia, A.M.P. de Jesus, A. Fernández-Canteli, "*Local unified model for fatigue crack initiation and propagation: application to a notched geometry*". *Engineering Structures*, ISSN 0141-0296, Vol. 52, 2013, 394-407. {http://dx.doi.org/10.1016/j.engstruct.2013.03.009}

11. A.M.P. de Jesus, A.L.L. Silva, J.A.F.O. Correia "*Fatigue of riveted and bolted joints made of puddle iron - A numerical approach*". *Journal of*

Constructional Steel Research, ISSN 0143-974X, Vol. 102, 2014, 164-177. {http://dx.doi.org/10.1016/j.jcsr.2014.06.012}

12. A.M.P. de Jesus, A.L.L. Silva, J.A.F.O. Correia "*A Probabilistic Fatigue Approach for Riveted Joints Using Monte Carlo Simulation*". *Journal of Constructional Steel Research*, ISSN 0143-974X (minor revision).

- Scientific Conferences

1. J.A.F.O. Correia, A.M.P. Jesus, M.A.V. Figueiredo, A.S. Ribeiro, A.A. Fernandes – "*Overview of Recent Portuguese Research on Fatigue Behaviour of Ancient Portuguese Riveted Steel Bridges*". *7.º Congresso Internacional de Mecânica Experimental (APAET)*; 3 pgs., Vila Real, 23-25 de Janeiro de 2008.

2. A.M.P. Jesus, J.A.F.O. Correia, M.A.V. Figueiredo, A.S. Ribeiro, A.A. Fernandes – "*Low-Cycle and Crack Growth Fatigue Data of a Steel from the Trezói Railway Riveted Bridge*".*11th Portuguese Conference on Fracture (PCF 2008)*, SPM; Lisboa, 13-15 de Fevereiro de 2008.

3. J.A.F.O. Correia, A.M.P. Jesus, M.A.V. Figueiredo, A.S. Ribeiro, A.A. Fernandes – *"Fatigue Assessment of Riveted Railway Bridge Connections. Part I: Experimental Investigations". 7th International Conference on Steel Bridges (ICSB'08)*; 9 pgs., Guimarães, Portugal, 4-6 June 2008.

4. A.M.P. Jesus, J.A.F.O. Correia – "*Fatigue Assessment of Riveted Railway Bridge Connections. Part II: Numerical Investigations". 7th International Conference on Steel Bridges (ICSB'08)*; 9 pgs., Guimarães, Portugal, 4-6 June 2008.

5. J.A.F.O. Correia, A.M.P. Jesus, M.A.V. Figueiredo, A.S. Ribeiro, A.A. Fernandes – "*Variability Analysis of Fatigue Crack Growth Rates of Materials from Ancient Portuguese Steel Bridges". Bridge Maintenance,*

Safety and Management (IABMAS'08); Proc. intern. conf., Korea, 16-19 July 2008. {http://dx.doi.org/10.1201/9781439828434.ch155}

6. J.A.F.O. Correia, A.M.P. Jesus, J.T.Q.S. Pinto – "*Simulação da Resistência à Fadiga de Ligações Rebitadas*". *1.º Congresso de Segurança e Conservação de Pontes (ASCP'09)*; 13 pgs., Lisboa, Portugal, 1-3 Julho 2009.

7. B. Silva, J.A.F.O. Correia, F. Nunes, P. Tavares, H. Varum, J. Pinto – *"Earth Construction: Bird Teaching". 2nd WSEAS International Conference on Urban Rehabilitation and Sustainability (URES'09), Environmental Science and Sustainability - Proceedings published by WSEAS Press (printed and in CD*), pp. 72-78 - Baltimore, USA, 7 a 9 de Novembro de 2009. {http://hdl.handle.net/10773/8000}

8. J.A.F.O. Correia, A.M.P. Jesus – "*Estimativa do campo de tensão-vida probabilístico para uma ligação rebitada com corte simples com base em análises elasto-plásticas por elementos finitos*". *VII Congresso de Construção Metálica e Mista (CMM)*; Centro de Congressos do LNEC, Lisboa, Portugal, 19-20 Novembro 2009.

9. J.A.F.O. Correia, A.M.P. Jesus, L. Silva – *"Simulação por Elementos Finitos de Curvas S-N de Ligações Rebitadas"*. *Congresso Nacional de Mecânica Experimental (CNME2010)*; Guimarães, Portugal, 21-23 Abril 2010.

10. A.M.P. Jesus, J. Silva, M.A.V. Figueiredo, A.S. Ribeiro, A.A. Fernandes, J.A.F.O. Correia, A.L.L. Silva, J. Maeiro – "Fatigue Behaviour of Resine-Injected Bolts: Na Experimental Approach".*Iberian Conference on Fracture and Structural Integrity 2010*, Porto, 17-19 de Março de 2010.

11. A.M.P. Jesus, A.L.L. Silva, J.A.F.O. Correia, M.A.V. Figueiredo, J.M.C. Maeiro, A.S. Ribeiro, A.A. Fernandes – "Analysis of *Low-Cycle Fatigue Data of Materials from several distinct Portuguese Riveted Steel*

Bridges".*Iberian Conference on Fracture and Structural Integrity 2010*, Porto, 17-19 de Março de 2010.

12. B. Silva, F. Nunes, P. Tavares, J.A.F.O. Correia, H. Varum, J. Pinto – "Aprender a construir com terra através das andorinhas-dos-beirais". *Seminário Ibero-Americano de Construção e de Arquitectura em Terra (6.º ATP / 9.º SIACOT)*; Coimbra, Portugal, 20-23 Abril 2010. {http://hdl.handle.net/10773/7046}

13. A.M.P. Jesus, J.A.F.O. Correia – "*Stress intensity factors evaluation for riveted beams applying FEA with VCCT*". *Bridge Maintenance, Safety and Management (IABMAS'10)*, Pennsylvania, USA, 11-15 July 2010. {http://dx.doi.org/10.1201/b10430-480}

14. J.A.F.O. Correia, A.M.P. Jesus – "*A procedure to derive probabilistic fatigue strength data for riveted joints*". *Bridge Maintenance, Safety and Management (IABMAS'10)*, Pennsylvania, USA, 11-15 July 2010. {http://dx.doi.org/10.1201/b10430-475}

15. N. Nik Abdullah, J.A.F.O. Correia, A.M.P. de Jesus, M. H. Hafezi, S. Abdullah – "*Assessment of fatigue crack growth data available for materials from Portuguese bridges based on UniGrow model*". *International Conference on Mechanical behaviour of materials, Lake Como, Italy, 5-9 Junho 2011*.
{http://dx.doi.org/10.1016/j.proeng.2011.04.160}

16. B.F.C. Fontoura, J.A.F.O. Correia, A.L.L. da Silva, A.M.P. de Jesus, Rui Matos, Carlos Rebelo, Luís Simões da Silva – "*Comparação da resistência à fadiga entre o aço S355 e o aço de alta resistência Domex 600*". *ASCP'2011 – 2º Congresso sobre Segurança e Conservação de Pontes , Univ. Coimbra, 29 Junho – 1 Julho 2011*.

17. J.A.F.O. Correia, A.M.P. de Jesus, A.L.L. da Silva, A. Fernández-Canteli – "*Comportamento à Fadiga do Material da Ponte Eiffel de Viana do*

Castelo". *ASCP'2011 – 2º Congresso sobre Segurança e Conservação de Pontes, Univ. Coimbra, 29 Junho – 1 Julho 2011*.

18. J.A.F.O Correia, A.M.P. de Jesus, A. Fernández-Canteli – "*A procedure to derive probabilistic fatigue crack propagation data*". *ACE-X 2011 - 5th International Conference on Advanced Computational Engineering and Experimenting, 3-6 Julho 2011*, Algarve – Portugal.

19. A.M.P. De Jesus, J.A.F.O. Correia – "*Assessment of fatigue crack growth data available for the P355NL1 steel using a local strain-based approach*". *PVP2011 – ASME 2011 Pressure Vessels and Piping Conference, 17-21/07/2011, Baltimore, USA*. {http://dx.doi.org/10.1115/PVP2011-57980}

20. A.M.P. de Jesus, J.F. da Silva, A.L.L. da Silva, J.A.F.O. Correia, A.S. Ribeiro, A.A. Fernandes – "*Fatigue Behaviour of Riveted and Bolted Connections Made of Puddle Iron - Part I: Experimental Investigation*". *COBEM 2011 - Congresso Brasileiro de Engenharia Mecânica, 24-28 de Outubro de 2011, Natal, Brasil*.

21. A.M.P. de Jesus, J.F. da Silva, A.L.L. da Silva, J.A.F.O. Correia, A.S. Ribeiro, A.A. Fernandes – "*Fatigue Behaviour of Riveted and Bolted Connections Made of Puddle Iron - Part II: Numerical Investigation*". *COBEM 2011 - Congresso Brasileiro de Engenharia Mecânica, 24-28 de Outubro de 2011, Natal, Brasil*.

22. A. Silva Ribeiro, J.A.F.O. Correia, A.M.P. de Jesus – "*Assessment of fatigue crack growth data available for the AA6061-T651 using a local strain-based approach*". *COBEM 2011 - Congresso Brasileiro de Engenharia Mecânica, 24-28 de Outubro de 2011, Natal, Brasil*.

23. A. Silva Ribeiro, J.A.F.O. Correia, A.L.L. da Silva, A.M.P. de Jesus – "*Evolution of fatigue history*". *COBEM 2011 - Congresso Brasileiro de Engenharia Mecânica, 24-28 de Outubro de 2011, Natal, Brasil*.

24. J.A.F.O. Correia, A.M.P. Jesus, A. Fernández-Canteli – "*Local Unified model for fatigue crack initiation and propagation: application to a notched geometry*". *13th Portuguese Conference on Fracture (PCF 2012)*, SPM; Coimbra, 2-3 de Fevereiro de 2012.

25. J.A.F.O Correia, A.M.P. de Jesus, A. Fernández-Canteli – *"Fatigue Probabilistic Behaviour of a Structural Detail of Puddle Iron from de Viana Bridge"*; *International Conference Durable Structures – ICDS12, 31/05-01/06 de 2012,* Lisboa – Portugal.

26. A.A. Fernandes, A.M.P. de Jesus, A.L.L. da Silva, J.A.F.O Correia – "*Retrofitting of old riveted Portuguese bridges. Past and current remnant life assessment research*"; *ICEM15 – 15th International Conference on Experimental Mechanics, 22-27 Julho 2012,* Porto – Portugal.

27. H.F.S.G. Pereira, J.A.F.O Correia, A.M.P. de Jesus – "*A discussion on fracture mechanics crack growth-based life prediction applied to a notched detail*"; *1st International Conference of the International Journal of Structural Integrity, 25-28 Julho 2012,* Porto – Portugal.

28. A. Fernández-Canteli, E. Castillo, J.A.F.O Correia, A.M.P. de Jesus, C. Przybilla – *"Extending the applicability of probabilistic S-N models to the LCF region using energetic damage parameters"*; *XVI International Colloquium Mechanical Fatigue of Metals, 24-26 Setembro 2012,* Brno – Republica Checa.

29. J.A.F.O. Correia, A.M.P. Jesus, Alfonso Fernández-Canteli, Rui A.B. Calçada – "*Modelling probabilistic fatigue crack propagation rates of mild strength steels*". *ASCP'2013 – 3º Congresso sobre Segurança e Conservação de Pontes, Faculdade de Engenharia da Universidade do Porto, de 26 a 28 de Junho de 2013.*

30. J.A.F.O. Correia, A.M.P. Jesus, A. Fernández-Canteli, Rui A.B. Calçada – "*Probabilistic fatigue behaviour of structural details of puddle iron from the Eiffel bridge*". *ASCP'2013 – 3º Congresso sobre Segurança e Conservação de Pontes, Faculdade de Engenharia da Universidade do Porto, de 26 a 28 de Junho de 2013.*

31. J.A.F.O. Correia, A.M.P. Jesus, A. Fernández-Canteli, R.A.B. Calçada – "*Modelling probabilistic fatigue crack propagation rates of mild and high strength steels*". *14th Portuguese Conference on Fracture (PCF 2014)*, SPM; Peso da Régua, 6-7 de Fevereiro de 2014.

32. A. Fernández-Canteli, S. Blasón, J.A.F.O Correia, A.M.P. de Jesus – *"A probabilistic interpretation of the Miner number for fatigue life prediction"*; *The First Multi-Lateral Workshop on "Fracture and Structural Integrity related Issues", 15-17 Setembro 2014,* Catania – Italy. {http://dx.doi.org/10.3221/IGF-ESIS.30.40}

33. J.A.F.O. Correia, A.M.P. Jesus, A. Fernández-Canteli, R.A.B. Calçada – "*A proposal for generalization of existing probabilistic fatigue damage models*". *ASCP'2015 – 4º Congresso sobre Segurança e Conservação de Pontes, Laboratório Nacional de Engenharia Civil (LNEC), Lisboa, de 25 e 26 de Junho de 2015. (Submitted).*